An experimental investigation of flow processes in dual-intake valve engines.

Mahmood, Zulshan

AN EXPERIMENTAL INVESTIGATION OF FLOW PROCESSES IN DUAL-INTAKE VALVE ENGINES

by

Zulshan MAHMOOD

A Thesis Submitted for the Degree of
Doctor of Philosophy
in the Faculty of Engineering
of the
University of London

Department of Mechanical Engineering
King's College London

January 1998

To My Parents

Abstract

This thesis describes an experimental investigation into the flow structures produced in the ports and cylinders of internal combustion engines by dual-intake valve cylinder head designs. The velocity characteristics of a production engine were studied using four different experimental techniques.

The effects of inlet valve lift on the flow structures were examined under steady flow conditions using an acrylic engine replica and a liquid mixture as the working fluid. Flow visualisation and laser-Doppler anemometry (L.D.A.) were employed to obtain mean velocity and turbulence data at both equal and asymmetric valve lifts. The influence of valve de-activation was examined, in addition to the effects of the combination of different inlet port designs.

Unsteady in-cylinder flow processes during the induction stroke were investigated using a dynamic water-analog rig. Flow visualisation was employed to study tumble and swirl development and particle image velocimetry (P.I.V.) was applied to measure velocity characteristics at B.D.C. of induction.

A stereoscopic flow visualisation method was used to investigate gas motion during the induction and compression strokes of a low-speed motored optical engine. High speed flows were simulated by using a high-density gas at various inlet pressure conditions and by operating the engine at several speeds. Image processing methods were used to extract velocity information from the gas flow images.

The steady flow experiments indicated the presence of tumble-like motions inside the cylinder with equal valve lifts. With one inlet port closed, a strongly swirling flow is generated in the cylinder. Flow visualisation and P.I.V. data from the dynamic water-analog rig showed organised tumble motion at B.D.C. and tumble ratio values calculated were found to be comparable to those previously reported for high-tumble engine designs. Results from the motored engine study verified

this and showed that the tumble motion is maintained during compression.

The results acquired using the different techniques are compared and their implications for engine design and operation are discussed. The ramifications of the results for numerical predictions of the flows are also discussed.

Acknowledgements

I would like to acknowledge the assistance of a number of people who were instrumental during the course of the research. It gives me great pleasure to acknowledge with gratitude, the constant supervision, valuable advice, encouragement and guidance generously provided by Professor Michael Yianneskis. I am obliged to Dr. Kalok C. Lee and Dr. Stavroula Balabani for offering their time and knowledge in acquiring and processing flow visualisation and L.D.A. data.

My thanks go to Dr. Gopal Ganti of Ford Motor Company Limited, Advanced Vehicle Technology, for providing technical advice and suggestions for research, as well as for arranging the provision of some of the experimental apparatus used in the study.

I am grateful to Professor Morgan Heikal and Messrs. Marc Fauré and Laurent Pommier of the University of Brighton for allowing use of their dynamic water-analog rig and assisting with the acquisition and processing of the P.I.V. data presented in Chapter 5. I am also obliged to Mr. Bob Marshall of Ford Motor Company Limited, for guidance in the operation of the optical engine discussed in Chapters 2 and 6.

I would like to thank Messrs. David Elgar, Ray Moslin, Paul Leforte and Alex Heaney for their help in the construction of the experimental facilities employed at King's College London.

I am indebted to the Engineering and Physical Sciences Research Council and the directors and management of Ford Motor Company Limited for providing financial support for the work.

Above all, I would like to thank my parents for encouraging me to pursue higher education and supporting me throughout the research programme.

Contents

List of Figures

List of Tables

Nomenclature

ROMAN CHARACTERS

Symbols		Units
b_0	Diameter of the beam leaving a laser at $1/e^2$ intensity	m
b_x	Diameter of measurement volume	m
b_y	Length of measurement volume	m
B, D	Dimension of engine cylinder bore	m
C_d	Coefficient of discharge of an inlet port	-
C_f	Flow coefficient	-
d	Characteristic dimension used in Reynolds number calculations	m
D_v	Inlet valve head diameter	m
f	Frequency	Hz
$f_{1,2,3}$	Focal lengths of lenses $L_{1,2,3}$ of the L.D.A. system	m
f_c	Crystal oscillation frequency of L.D.A. frequency counter	Hz
$f_{D,m}$	Doppler frequency	Hz
f_s	Frequency shift	Hz
i	Angle of incidence of a light beam to a surface	°
i_c	Critical angle of an incident light beam	°
k	Kinetic energy of turbulence	m^2/s^2
L	Inlet valve lift	m
$L_{1,2,3}$	Lenses 1,2,3 of the L.D.A. system	-
m	Order of the diffracted laser beams	-
n	Number of lines on the diffraction grating	-
$n_{1,2}$	Refractive indices of media 1 and 2	-
N_D	Number of Doppler cycles timed over counting period	-
N_g	Rotational speed of the diffraction grating	r.p.m.
r	Angle created by a light beam after refraction from a surface	°
Re	Reynolds number	-

St	Strouhal number	-
t	A timescale	s
T_r	Tumble ratio	-
u'	R.m.s. velocity in the x-direction	m/s
U	Mean velocity in the x-direction	m/s
V	Mean velocity in the y-direction	m/s
V_b	Bulk flow velocity	m/s
V_p	Piston velocity	m/s
w'	R.m.s. velocity in the z-direction	m/s
W	Mean velocity in the z-direction	m/s
x, y, z	Co-ordinates in the three orthogonal directions	m

GREEK CHARACTERS

Symbols		Units
γ	Isentropic exponent of a gas	-
ε	Dissipation rate of kinetic energy of turbulence	m^2/s^3
ζ	Vorticity	1/s
θ	Intersection angle of laser beams in L.D.A.	°
λ	Wavelength	m
μ	Dynamic viscosity of a fluid	Pa.s
ν	Kinematic viscosity of a fluid	m^2/s
ρ	Density of a fluid	kg/m^3
σ_3	Scattering volume dimension near the Kolmogorov timescale	m
$\sigma_{b,f,g,i,t}$	R.m.s. broadening contributions due to brownian motion, small scalle fluctuations within the measurement volume, velocity gradient, finite instrument bandwidth and finite transit time respectively	m/s
ω	Engine crank speed	rad/s

ABBREVIATIONS

A.F.R.	Air-fuel ratio

A.T.D.C.	After top-dead-centre
B.D.C.	Bottom-dead-centre
B.T.D.C.	Before top-dead-centre
C.A.	Crankangle
C.F.D.	Computational fluid dynamics
CO	Carbon monoxide
CO_2	Carbon dioxide
E.G.R.	Exhaust gas recirculation
F.F.T.	Fast Fourier transform
HC	Hydrocarbons
H.W.A.	Hot wire anemometry
I.C.	Internal combustion (engine)
L.D.A.	Laser-Doppler anemometry
L.S.P.	Laser speckle photography
L.S.V.	Laser speckle velocimetry
NO_x	Oxides of nitrogen
p.d.f.	Probability density function
P.I.V.	Particle image velocimetry
P.L.I.F.	Planar laser induced fluorescence
P.T.V.	Particle tracking velocimetry
r.m.s.	root mean square
SF_6	Sulphur hexafluoride
S.I.	Spark-ignition
T.D.C.	Top-dead-centre

Chapter 1

INTRODUCTION

1.1 PREAMBLE

The study of charge motion within internal combustion engines has become a topic of very active interest in the last two decades. A combination of international concern regarding the cost and availability of petroleum crude and environmental legislations calling for a reduction in pollutant exhaust emissions, has served to maintain an enthusiastic interest in I.C. engine flows. The influences of in-cylinder air motion on the performance of an engine are well established; it controls the combustion process in spark-ignition (petrol) engines and the fuel-air mixing and combustion processes in compression-ignition (diesel) engines.

Future advances in engine technology will essentially be defined by new emissions regulations, in addition to a desirable progress in vehicle fuel economy. Current international standards have specifically called for reductions in carbon dioxide (CO_2) gas - the major contributor to global warming - carbon monoxide (CO), hydrocarbon (HC) and oxides of nitrogen (NOx) emissions. For instance, Germany has specified that CO_2 emissions from all on-road vehicles must be reduced by 25% by the year 2005 [Endres et al 1992]. In Europe, the current E.C. Stage 2 emissions limits for light duty vehicles with spark-ignition engines - CO: 2.2 g/km and HC+NOx: 0.5 g/km - will be reduced further by the E.C. Stage 3 Proposal Standards to CO: 1.5 g/km and HC+NOx: 0.2 g/km for the 1999/2000 model year [Hadded et al 1995]. Legislations in the United States are stricter due to greater volumes of traffic. In California, concern over pollution hazards is so great that by the 2001 model year, over 5% of all new vehicles will have to conform to zero emissions standards.

Hence, in order for vehicles to meet increasingly stringent regulations, the combustion and pollutant formation processes within the engine must

be controlled to ensure efficient fuel consumption. One of the most effective methods for achieving these objectives is the creation of a well-defined in-cylinder flow pattern prior to combustion, and through this the generation of an optimised level of turbulence and/or charge distribution at the end of the compression stroke.

This chapter provides an introduction to the flow processes in the inlet ports and cylinders of modern I.C. engines. In section 1.2 the progress of engine flow research from early studies to the present is briefly described, while section 1.3 outlines the most commonly used experimental methods for flow visualisation and measurement. In section 1.4, a summary of the advances made in engine flow research up to the present date is provided, especially in four-valve per cylinder designs, based on a survey of the published literature. A summary of the important findings from the literature review relating to engine design is given in section 1.5, and areas requiring further research are identified. The objectives of the current research are given in section 1.6 and the chapter is concluded with an outline of the thesis in section 1.7.

1.2 THE DEVELOPMENT OF ENGINE FLOW RESEARCH

1.2.1 Early Work

Research into in-cylinder flows has been has been considered as an important subject since the development of internal combustion engines. Indeed, the earliest investigation into air motion in engines was undertaken by Otto, the inventor of the four-stroke cycle, to study combustion in his engine design. Preliminary studies were also performed by Sir Harry Ricardo, who developed a "turbulent chamber" engine comprising a combustion chamber design to provide ideal combustion through control of flow in the cylinder. Clerk (1912) identified that combustion rate was directly proportional to the turbulence generated during pre-ignition, and Alcock (1934) demonstrated that by introducing swirl to the in-cylinder motion, the efficiency of the diesel engine could be enhanced.

These early studies, among others, established the necessity for controlled engine flow and thereby set the scene for the start of ardent investigations into the nature of engine flows and the manners in which they may be manipulated. Initial attempts at flow visualisation are

illustrated by the research of Lee (1939) who devised a motored engine consisting of a transparent cylinder and observed intake flow circulation and swirl configurations with the aid of feathers introduced into the cylinder.

Even with this seemingly simplistic technique, Lee was able to make important observations on the circulatory flow patterns produced during the intake stroke, in addition to the swirl produced by a shrouded valve. Moreover, his results clearly identified the relationship between the intensity of vortex motions and engine speed, inlet swirl and inlet velocity. These observations, when considered with contemporary studies relating flow with combustion and flame speed, demonstrated that the relation between flame speed and engine speed is dependent on the fluid dynamic behaviour.

Subsequent research showed that the in-cylinder motion during the induction and compression strokes is largely influenced by the manner in which the flow is introduced into the cylinder; highlighting the requirement for appropriate intake port/valve configurations. This latter observation has stimulated great attention into the design of intake ports and valves which are advantageous for the creation of flows appropriate for efficient combustion.

Much of the early research, and that carried out up to the last ten years or so, has focused on the generation of swirl during the intake stroke, with a view to optimising the fuel combustion via a thorough and controlled mixing of the fuel and air. Extensive investigations have been performed on axisymmetric and off-axis inlet valve configurations for both S.I. and diesel engines, resulting in many new improvements in the design of inlet ports and valves.

1.2 .2 Recent Developments

Many studies have been conducted in conventional two-valve engines on the effects of in-cylinder motions such as swirl and squish on turbulence generation, air-fuel mixing and combustion, some of which will be mentioned later. Within the last decade though, an increasing number of motor vehicle manufacturers have moved away from traditional two-valve cylinder heads, to the employment of multi-valve (more specifically, dual-intake valve) engines. This trend has been stimulated by a desire for increased engine power and higher fuel efficiency. In spark-ignition

engines, use of a greater number of valves raises the engine torque and allowable engine speed, and this is an efficient method for achieving higher specific power output from the engine.

In dual-intake valve S.I. engines,*tumble* motion has been noted to offer good possibilities for the enhancement of turbulence and combustion. This type of flow is created during the induction stroke and comprises a large-scale in-cylinder vortex with its axis perpendicular to the cylinder axis. Engines with cylinder head configurations which encourage tumble flows during intake have improved combustion and emissions characteristics [e.g. Kent et al 1989, Hu et al 1992]. This is discussed in detail in section 1.4. The different techniques used to study engine flows in recent years are outlined in the following section.

1.3 EXPERIMENTAL TECHNIQUES FOR ENGINE FLOW INVESTIGATIONS

A variety of techniques has been employed for the purposes of in-cylinder flow visualisation, measurement and simulation. Flow visualisation methods are essentially concerned with observation of the qualitative flow characteristics and the regions of interest are primarily jet flows, recirculation regions and areas of high or low turbulence. Experimental methods for the measurement of velocity and turbulence characteristics have largely utilised two techniques - *hot-wire anemometry (H.W.A.)* and *laser-Doppler anemometry (L.D.A.)*. As most of the current knowledge has been acquired through the use of these two techniques, they will be described in greater detail.

Both H.W.A. and L.D.A. measure flow parameters at a single point at a given time. In recent years multi-point measurement methods, including *particle tracking velocimetry (P.T.V.)* and *particle image velocimetry (P.I.V.)*, have also been developed to evaluate velocities at many locations at the same instant in time. Since these techniques are becoming increasingly valuable and have been applied to many studies of engine flows, they are also reviewed in this section.

The computational techniques used most frequently involve mathematical modelling of the flow using a finite volume approach and an appropriate turbulence model. Results are often highly dependent on the turbulence model used, and much effort is currently being invested into the

development of improved prediction methods. This thesis is concerned with experimental investigations of engine flows and only brief references to computational methods are made where relevant to the following text.

1.3.1 Flow Visualisation

The flow patterns produced from different intake configurations may be viewed directly with flow visualisation methods. Most methods involve the introduction of particles into the flow, and the illumination of the flow-field with a light source allows the progression of the particles to be monitored. Records of flow development are obtained via still or high-speed photography or by video recording for real-time observation.

For internal combustion engines, optical access is obviously required, and is usually achieved by utilising transparent cylinders produced from Perspex in motored engines and by incorporating quartz or sapphire windows into the cylinders of firing engines. The quality of the flow visualisation, and subsequently, the results and conclusions derived from a study are dependent on the tracer particles inserted into the flow. Particles must follow the path of the flow faithfully, and for firing engines, offer the additional constraint of durability against combustion whilst retaining light scattering efficiency. The variety of different tracer particles employed for in-cylinder flow visualisation are described by Arcoumanis et al (1990 a).

For firing engines, techniques such as *shadowgraphy, Schlieren photography,* and *interferometry* have also been used to visualise spray development and flow propagation during combustion. The variations in engine phenomena from one cycle to the next are best observed by shadowgraphy and high-speed photography methods. The Schlieren method involves the use of a knife-edge or aperture to partially block the light, and takes advantage of the fact that density variations in the fluid give rise to variations in the refractive index. A summary of studies on combustion using these techniques is provided by Arcoumanis et al (1990 a).

1.3.2 Hot-Wire Anemometry

Hot-wire anemometry is a technique for measuring velocities at a single point. The method operates on the principle that the resistance of a piece of fine metal filament is dependent upon its temperature. As electrical

resistance is related directly to temperature, if this filament is placed in a cross-flow, its temperature, and hence its resistance, changes. The voltage variation resulting from this is monitored by electronic instrumentation, which gives an output related to the variations in the flow velocity.

Witze (1980) has assessed hot-wire anemometry as an engine flow measurement technique and notes that its advantages include the fact that it provides a continuous analogue output signal and has a good frequency response. Furthermore, it provides a high signal-to-noise ratio, essential for correct interpretation of the results. From economic and complexity viewpoints, the electronic circuitry involved in the technique is simple and fairly inexpensive.

On the negative side, however, a major disadvantage of H.W.A. is that the probe intrudes into the flow in the swept and clearance volume and may also impinge onto the moving piston. Whilst probe intrusion cannot be avoided, its effect can be minimised by careful designing and positioning into the flow. At any one time, the probe responds to both velocity components in a plane perpendicular to the wire and the direction of the flow cannot be distinguished. Another serious disadvantage is that calibration of each individual probe is required, and if this is not performed over the full range of temperatures and pressures encountered in the engine, then major errors may occur. Other disadvantages of H.W.A. include the facts that: output is dependent on gas temperature and pressure, as well as air velocity; there is an upper limit to the intensity of turbulence that may be measured; the method cannot be readily applied to firing engines, and as the wire is very delicate, it is prone to frequent breakage.

In spite of the above disadvantages, significant research has been performed with hot-wire anemometry into in-cylinder flow motions, much of which has resulted in improved designs for intake ports and valves.

1.3.3 Laser-Doppler Anemometry

L.D.A. has lately become the most widely implemented single-point velocity measurement technique. This may be accounted to one of its most attractive features - it is unobtrusive, causing no disturbance to the flow field and does not require calibration. A typical laser-Doppler anemometer, presented on Figure 1.1, comprises an optical system and a signal processing system.

As indicated by the figure, the beam from the laser is split into two beams having equal intensity. The beams are then collimated and focused to cross at a location within the flow, producing a *control volume* containing interference fringes. Micron-sized particles introduced into the flow scatter light as they cross the fringe pattern, and this is collected by a photomultiplier. The frequency of the scattered light is proportional to the component of the particle velocity perpendicular to the fringes. The direction of the velocity is determined by introducing a frequency shift between the two intersecting laser beams; the value of this shift is then either added or subtracted from the measured frequency to give the Doppler frequency.

The signal processing system consists of a bandpass filter which removes low frequency pedestal and high frequency noise from the signal from the photomultiplier tube. The signal is then amplified and may be viewed on an oscilloscope. An optical shaft encoder attached to the engine provides a gating circuit with information about the range of crankangle over which measurements are to be taken, and used for evaluation of ensemble-averaged velocities over many engine cycles.

The L.D.A. method for I.C. engine flows has also been assessed by Witze (1980). The advantages of the technique include that it is suitable for all applications, including those involving high temperatures and pressures - for example combustion. It is also an absolute technique as the measured frequency varies linearly with the flow velocity and is independent of the flow conditions. The ability to resolve the flow direction is also an advantage, as this implies that the local velocity vector can be completely resolved without any prior knowledge. Moreover, it has no restrictions on the measurement of turbulence intensity and, indeed, high levels of turbulence may be recorded.

From the perspective of information that may be acquired with regard to in-cylinder flows, L.D.A. presents a number of principal disadvantages. One of these is the requirement for optical access. If it is desired to measure three components of the velocity vector, then at least two mutually perpendicular windows must be built into the combustion chamber. The necessity for addition of particles into the flow results in the nature of the signal being intermittent, as it is produced by individual realisations from each particle. In terms of cost, L.D.A. equipment is expensive compared with H.W.A. A detailed discussion of the theory relevant to L.D.A. is provided in Chapter 2.

1.3.4 Multi-Point Fluid Measurement Techniques

The techniques of particle image velocimetry (P.I.V.) and particle tracking velocimetry (P.T.V.) have been employed by many researchers within the last decade to study the development of flow in reciprocating I.C. engines. In two-dimensional P.I.V., a pulsed laser sheet is passed through the cylinder of an optical engine and the calculated displacement of seeding particles in the flow between two successive pulses is used to determine flow velocities within a plane. Typical time intervals between pulses range from several nano- or micro-seconds for very high speed gas flows, to several milli-seconds for low-speed or water analog simulations. A laser sheet is also employed in P.T.V. to illuminate particles in the flow. Fluid velocities are calculated by measuring the length of particle streaks produced over a given exposure time, and dividing the displacement by the time interval. P.T.V. is generally applied to low-speed flows.

P.T.V. has been used to study in-cylinder flow patterns during induction in water models. By achieving conditions of dynamic similarity between the water rig and a motored engine, useful results can be acquired. A transient water analog was employed by Khalighi and Huebler (1988) to visualise intake flows. Through the use of an automated image processing system, the streaks produced by the particle motions in the flow were monitored, and flow-field velocities were evaluated. P.T.V. was used again later by Khalighi (1990) to investigate intake swirl and tumble motions; by Rönnbäck et al (1991) to study induction tumble, and by Kent et al (1989) to study large-scale flow structures produced by changes in intake port design. Examples of studies utilising P.I.V. include those by Reuss et al (1989) and Reeves et al (1996). The advantages and shortcomings of both P.I.V. and P.T.V. are outlined in Chapter 2, where the principles of the techniques are described in detail.

Each of the methods mentioned in this section plays an important and distinctive role in the study of flow motion in internal combustion engines. Flow visualisation techniques are useful to gain a general understanding of the qualitative nature of a flow process and are easiest to apply, as they tend not to require specialist research equipment or expertise. Hot-wire anemometry is an inexpensive method for measuring flow velocities, though it has now been superseded by laser techniques. L.D.A. is most

useful when detailed measurements of mean and cycle-averaged flow characteristics are necessary, and is also valuable to accurately calculate turbulence parameters, for instance turbulence kinetic energy, Reynolds stresses and energy dissipation. With multi-point techniques such as P.I.V., flow velocities over entire planes or volumes can be measured at the same instant in time, which is not possible with laser anemometry. Therefore, by combining the use of these methods, a far better insight into engine flows can be acquired than would be available through the use of one method alone.

1.4 LITERATURE SURVEY

A review of previous experimental investigations of in-cylinder flows is presented in this section. In the first instance, a brief summary of research performed on traditional two-valve (one inlet valve and one exhaust valve) cylinder head configurations will be provided, with emphasis on induction stroke air motions. Following this, an in-depth review of the current state of research on multi-valve engines is provided, based on a survey of published literature and dealing with aspects of particular importance to current engine design. The conclusions from this survey will be utilised to identify areas of research into multi-valve engines which call for further investigation.

1.4.1 Flow Through 2-Valve Engines

A large number of studies of flow in single intake valve engines has been performed. In an effort to understand the characteristics of in-cylinder flows and thereby manipulate their motions to the designer's advantage, extensive research has been undertaken into the vortices and turbulence generated during the induction and compression strokes.

Axisymmetric inlet ports, though not representative of practical cylinder heads, have been employed in research since the flow in this type of port is easier to understand than flows produced by helical or directed ports. Moreover, as the resultant flow is normally symmetric, fewer measurements have to be made in order to understand the flow processes inside the inlet port and the cylinder.

With regard to induction flows in axisymmetric designs, Tindal et al (1988) have indicated that steady flow in the port could be likened to a pipe flow if swirl was absent. The study revealed that the flow at the valve gap emerges as an annular jet to produce a ring vortex below the cylinder head and a larger ring vortex directly underneath the valve. In addition, the inlet port flows and the vortices have low levels of turbulence, whilst high turbulence is detected in the jet as a result of turbulence generation in the shear layers.

In motored engines, variation in valve lift produces no significant change in the location of the main vortex in the cylinder [Ekchian and Hoult 1979]. Both the size and location of this vortex do vary, however, with different crankangles [Ekchian and Hoult 1979, Vafidis and Whitelaw 1986] until mid-induction, after which vortex size and location remain approximately constant.

When swirl is introduced into the cylinder using swirl vanes in the inlet port, the jet flow from the inlet valve moves closer to the cylinder head, increasing the size of the main vortex, and making the upper vortex smaller. At high levels of swirl, a third vortex is produced below the valve due to a swirl-induced radial pressure gradient [Morse et al 1980]. Swirl velocities after mid-induction in the radial plane are larger nearer the surface of the piston than close to the cylinder head as swirl develops during the intake stroke. Turbulence levels within the flow tend to increase with the intensity of the swirl, possibly due to greater shear forces in the flow.

The flow emanating from directed ports enters the cylinder as two main jets [Tindal et al 1982] to produce two counter-rotating vortices near the cylinder head in the radial plane and a single vortex further downstream [Tindal and Williams 1977]. A ring vortex is also produced below the valve in the diametral plane. The intake jet leaves the directed port with high velocity, particularly at low valve lifts, and bypasses the upper portion of the cylinder; at B.D.C. the flow structure near the cylinder head is more complex than near the piston, where an organised swirling motion is formed.

Swirling motion in engines with helical ports is produced upstream of the port exit about the valve axis, and spirals towards the exit as observed by Tindal et al (1988). The flow, upon entering the cylinder, comprises two counter-rotating vortices near the cylinder head in the radial plane in addition to a single swirling vortex further downstream [Tindal and

Williams 1977]. This single swirling vortex forms closer to the cylinder head at high valve lifts than at low valve lifts and "solid-body" swirling rotation of the flow is reached sooner for a port producing high swirl than one producing low swirl.

Fluid motions in the cylinders of both single and two-valve engines are discussed in considerable detail in review articles by Gosman (1986), Arcoumanis and Whitelaw (1987) and Heywood (1987).

1.4.2 Investigations in Multi-Valve Engines

It was indicated earlier that the present trends towards the use of multi-valve cylinder head configurations for medium-size spark-ignition engines have been initiated by a desire for lower fuel consumption, lower exhaust emissions and higher engine power. Multi-valve induction and exhaust systems increase the volumetric efficiency of the engine and give the designer greater control over the development of the flow. Four valves per cylinder head has been the standard on virtually all aircraft engines of the reciprocating piston type since the First World War and are common in racing cars. However, it was not until the start of the 1980s that this configuration became popular for passenger cars. The main reason for this delay in implementation was the additional complexity and cost involved in manufacture, which could not be justified at a time when low-rated engines were sufficient for family car and urban driving applications.

Newton et al (1989) have provided a summary of the major advantages of four valve engines over their two valve counterparts. When four valves are employed, a greater proportion of the head area can be used for porting. Furthermore, as the spark plug can be positioned as close to the centre of the combustion chamber as desired, the flame path is short, leading to improved combustion. With only two valves used on the cylinder head, the valve diameter is large in relation to the cylinder bore, so that gas flow past valve edges adjacent to the cylinder wall tends to be masked by it. There is hardly any masking with four valves, however, and the interaction of the two intake flows further improves mixing and subsequently combustion characteristics. Moreover, when two exhaust valves are used instead of one, the ratio of seat length to area exposed to hot gases is higher, as is therefore the rate of cooling by conduction through the seats.

The employment of *lean-burn engines* has helped to solve some of the demands that the modern engine designer is faced with. Lean fuel mixtures

utilising air-fuel ratios of up to 20:1 or greater allow good fuel economy and reduced NOx and CO emissions. These advantages, however, are offset by observations that the resultant burn rates are slower, leading to greater cyclic combustion variability [Matekunas 1983]. This factor can be alleviated by generation of an optimum level of turbulence prior to ignition, hence the great interest devoted to the study of induction and compression flows.

(a) Intake Swirl and Tumble Flow Development

The pentroof combustion chamber has become the standard design for multi-valve engines, as the pentroof shape is close to the ideal spherical shape for a combustion chamber [Gruden et al 1984]. For these types of engines, an alternative flow movement to conventional swirl has been devised. *Tumble*, which may be described as a large rotational motion about an axis perpendicular to the cylinder axis, has been found to be advantageous, as it may be created using a straight dual-intake port configuration and hence without any loss in flow coefficient. Tumble motion is sometimes referred to as *"Barrel Swirl"*.

A study on tumble in a four-valve engine was carried out by Benjamin (1988) on a lean-burn engine and provides a summary on tumble flow development from intake to its dissipation during compression. Essentially, the tumble vortex is generated during the induction stroke and its intensity is determined by the design of the intake ports and combustion chamber. The vortex is created by the incoming airflow detaching from the port and thereby flowing over the top of the valve head. With progression of the induction stroke, the vortex can be made to increase in rotational speed and size, such that by the time the piston reaches B.D.C., a single tumbling air motion covers the entire cylinder.

During the compression stroke the tumble vortex is enhanced, i.e. it undergoes "spin-up", where its rotational velocity increases due to conservation of angular momentum. At the same time, the vortex experiences some degradation due to shearing effects. As the piston progresses upwards, the tumble motion begins to break down just after mid-compression due to distortion and very high shear, resulting in high levels of turbulence. The spin-up phenomenon was observed by Gosman et al (1985) in a combined computational and experimental investigation performed on an engine with a single shrouded inlet valve placed in an axisymmetric location in the cylinder head.

Khalighi (1990) studied the development of swirl and tumble in five different intake port configurations using a transient water-analog engine and flow measurement by particle tracking velocimetry. The configurations differed only in the number of inlet valves open and shrouds employed to direct the flow. It was found that when both inlet valves were open, no well-defined tumble flow structure is created and vortices dissipate quickly, before the piston reaches B.D.C. of the induction stroke. However, the strongest tumble flow at B.D.C. induction was generated when one inlet valve was kept closed and a 180° shroud was added to the open valve, and Khalighi observed the tumble flow to be highly repeatable from cycle to cycle.

The effects of the intensity of tumble motion during the induction stroke on the precombustion turbulence in a four-valve motored optical engine were investigated by Rönnbäck et al (1991) using P.T.V. Three cylinder head configurations were tested, viz. 'low tumble', 'medium tumble' and 'high tumble' designs. The study reports that at low valve lifts, no major tumble motion develops for all three designs due to the predominantly downward direction of the flow entering the cylinder. The medium and high tumble cylinder heads produced greater values of tumble ratio, as the intake flow had larger horizontal velocity components. It is also indicated in this study that the kinetic energy imparted to the tumble vortex during the induction is partly maintained during compression. Furthermore, a high intensity tumble vortex will produce large turbulent length scales and high turbulence intensities in the flow field prior to combustion.

Omori et al (1991) applied laser-Doppler anemometry to a motored optical engine operating at wide-open-throttle to investigate the influence of different intake ports on the in-cylinder flow structure. Three types of inlet port were tested: a conventional smoothly curved port, a tumble port which directed the flow tangentially, and the same tumble port with a shroud added to intensify tumble motion. It was noted that if, early in the intake stroke, the intake valve flow is projected towards the exhaust valves, strong vortical flow is produced in the cylinder, which is identifiable as tumble by the end of the induction stroke. The tumble, if intense enough, may be retained until after mid-compression.

It was observed that the conventional port also produced tumble flows; however, the effects of the upward flow under the exhaust valves is weakened by the downward flow under the intake valves, resulting in a

vortex with low tumble intensity. At the same time, steady flow tests performed by Omori et al revealed that port designs which increase tumble intensity also tend to decrease the flow discharge coefficient. This calls for the designer to make a compromise between flow discharge coefficient and tumble ratio.

Arcoumanis et al (1993) performed tests on two cylinder heads, of 'low tumble' and 'high tumble' types, to assess the suitability of four-valve cylinder heads to produce tumble under steady flow conditions. Flow velocities were measured using laser-Doppler anemometry. The tumbling air motion was converted to swirl using a 'tumble adaptor' device, to allow conventional swirl measurement methods to be employed to characterise the tumble. The study showed that when air mass flowrate is kept constant, the inlet port discharge coefficient (C_d) decreases with increasing valve lift, and that the high-tumble design gave lower C_d values than the low-tumble system. The tumble intensity on the steady flow rig was noted to become higher as the inlet valve lifts were increased above 3 mm. Measurements taken by Arcoumanis et al in a motored optical engine indicated that the tumble vortex ratio reaches a maximum between 280° CA and 320° CA, corresponding to the 'spin-up' and decay processes described earlier.

The development of tumble and swirl was studied by Kent et al (1989) on two Ford 1.6 litre I4 4-valve engines, which differed in bore/stroke ratios. A total number of six cylinder head configurations were employed, some with valve masking and each engine was tested with both one and two intake valves open. Swirl was seen to be the dominant motion when only one inlet valve was operated and tumble was created when both valves were opening. However, valve masking produced 'tipped swirl' - a combination of both swirl and tumble - when only one valve was opened, and the axis of the vortical motion was inclined to the cylinder axis by 30°. At the same time, the strongest tumble at B.D.C. induction was also observed in this configuration.

Cylinder heads with intake port configurations which produce 'inclined tumble' and 'inclined swirl' flows - consisting of a combination of tumble and swirl components - have been noted to give good mean flow and turbulence characteristics which are useful for the efficient burning of lean air-fuel mixtures at low engine speeds and at part load operating conditions. The swirling component is introduced to the tumble by either de-activating one inlet valve, or by restricting the flow through one of the intake ports with a valve mechanism fitted at the port entrance [Henriot et

al 1989, Furuno et al 1990, Nakanishi et al 1992, Stone et al 1993]. Both numerical and experimental studies have shown that an intense tumble component develops inside the cylinder during the induction stroke, which breaks down soon after mid-compression. However, the swirl component produced during induction is largely maintained up to T.D.C. compression [Henriot et al 1989, Arcoumanis et al 1990 b]. It has been observed that the distortion of the swirl component could be employed to generate additional turbulence during combustion, by which time the turbulence produced through the decay of the tumble may have reduced to a level too insignificant to influence combustion characteristics [Arcoumanis et al 1990 b, Le Coz et al 1990, Neusser and Geiger 1996].

(b) Influence of Swirl and Tumble on Turbulence Generation

The production of an optimum level of turbulence at pre-ignition being the primary objective of both swirl and tumble creation in the engine cylinder, a number of investigations have been performed to determine the levels of turbulence that can be generated at the end of the compression stroke.

A combined computational/experimental investigation employing C.F.D. and forward-scatter L.D.A. to study flow in a four-valve engine was undertaken by Fujii et al (1989). Velocity measurements made during the early compression stroke showed that swirl flow at this stage is far weaker in comparison to the overall flow. Axial velocities were much larger due to strong tumble vortices generated by the intake valves. As the compression stroke continued with time, the tumble vortices moved and reduced in size. Changes in axial velocity revealed that the influences of the downward flow during induction are present at the start of compression and the tumble vortex centres move upwards as the piston rises. At around 60° B.T.D.C., the swirl, already small in comparison to tumble, ceases to exist as tumble takes over the flow. Hence, experimental results revealed that for the four-valve engine in the study swirl motion is small and tumble motion is dominant during both the induction and compression strokes. Different pentroof combustion chamber geometries were also modelled with C.F.D. by varying the apex angle of the pentroof. The results suggested that the strength and location of the tumble vortices vary with combustion chamber configuration.

Hadded and Denbratt (1991) used L.D.A. to test four different engine types, ranging from low tumble to high tumble systems. The results indicated that although high tumble ports generate the strongest tumble at the start of induction, the flow starts to decay early, reducing the kinetic energy stored in the mean flow during compression. Levels of ensemble-averaged turbulence were found to increase near to T.D.C. with increasing tumble ratio, and peak r.m.s. turbulence with tumbling flow was noted to occur closer to T.D.C. in an engine with a pentroof combustion chamber than with a disc chamber.

An investigation by Furuno et al (1990) was concerned with how the inclination of swirling flows affects turbulence characteristics. Two configurations were tested, one having a straight intake port with a swirl control valve (SCV) and a helical port, while the other had one straight port with a SCV and one straight port with a shroud whose angle could be altered. It was shown that the swirl inclination angle produced by the configuration with the shrouded port varied from 90° when the shroud angle was 0°, to 31° when the shroud angle was set to 90°. A 19° swirl inclination angle was reported for the design with the helical port. More significantly, Furuno et al observed that the intensity of the pre-ignition turbulence, between 30° B.T.D.C. and T.D.C. of the compression stroke, varied greatly with the inclination angle of the swirling flow in the cylinder. The results suggested that the highest turbulence intensity near T.D.C. compression occurs when the swirl is inclined between 30° and 45°. Subsequent improvements to this design are reported by Nakanishi et al (1992).

Le Coz et al (1990) performed a combined experimental and computational analysis of the turbulence generated in a four-valve engine. L.D.A. was employed as the measurement technique. Three cylinder heads were tested - each of these varied in the number of inlet ports open and types of shrouds employed to direct flow into the cylinder.

The results for both systems utilising only one open inlet valve indicated that inclined tumble was produced in the cylinder, with the flow in the shroud configuration being more intense. As the piston approached T.D.C. of compression, the greatest levels of turbulence were measured in the configuration with a shroud fitted on the open valve. This higher turbulence corresponded to a stronger tumble vortex. The tumble motions broke down during compression to produce turbulence, whilst the swirl component of inclined tumble suffered lesser decay, suggesting that tumble

motion makes a greater contribution to turbulence generation just before ignition than swirl. However, the swirl component can make a contribution to flame front propagation during early combustion. Investigations into cycle-resolved turbulence indicated that the turbulence created by the intake configurations consists of low frequency and high frequency components, the ratios of which are independent of intake configuration.

The above comments on the influence of swirl and tumble on the generation of in-cylinder turbulence at ignition were also verified in a combined experimental and computational study carried out by Trigui et al (1994). A water-analog rig was employed to simulate intake flow motion through a four-valve engine cylinder head with both ports open and with port de-activation. Velocity measurements made using three-dimensional particle tracking velocimetry showed that tumble was the dominant motion with both ports open, while a strong swirling component was present in the flow at B.D.C. induction as a result of port de-activation. Gas flow during the compression stroke was modelled with C.F.D. and the initial conditions for compression were based on the P.T.V. results. The computations indicated that for both configurations the tumble vortex intensified during compression up to 280° A.T.D.C. The swirl component with port de-activation did not decay rapidly and was still strong at the time of ignition. Volume-averaged turbulence intensity values increased during compression in both cases, as the energy of the mean flow converted to turbulence.

(c) Correlations Between In-Cylinder Flow, Combustion and Emissions

Lean-burn engines, it was mentioned earlier, whilst offering the highly desirable characteristics of low fuel consumption and reduced NOx and CO emissions, do suffer from one inherent disadvantage, in that highly diluted mixtures result in slow burning rates, which in turn can lead to partial burn events and misfires. To this end, some studies of in-cylinder flow and turbulence have been complemented by investigations of the effects of velocity characteristics on combustion.

Hadded and Denbratt (1991) indicated that an increase in tumble intensity during induction and compression is reflected directly in a reduction in the delay angle of the combustion, i.e. the time required from ignition to burn 10% mass fraction. This rapid initial burn assists the combustion system to burn leaner mixtures without compromising on combustion cyclic variability. An increase in strength of tumble also results

in higher tolerance of exhaust gas recirculation (EGR), the use of which further reduces the delay angle, when combined with tumbling flows.

The results of the study by Kent et al (1989), based on data for a 0-90% mass fraction burn duration, also confirmed the relation between increased swirl and tumble strength at B.D.C. induction, and faster combustion rates. Moreover, it was revealed that of the six configurations tested, those employing one open intake valve to create the flow field had lower burn durations than those in which both valves were open during induction - although these too exhibited a decrease in combustion rates with more intense tumble motions. In addition, steady flow tests performed on the configuration with valve masking revealed that an increased burn rate acquired through stronger tumble was also accompanied by a reduction in the effective flow area of the port and valve.

Four-valve engines employing high tumble induction systems have been noted to give lower combustion times in addition to reductions in harmful exhaust emissions. De Boer et al (1990) assessed the combustion characteristics of three engines fitted with low to high tumble generating cylinder heads. High tumble systems gave rise to the shortest values for ignition delay and combustion duration in comparison to the others throughout the AFR range tested. Cyclic variability was also observed to be lower at high air-fuel ratios. Moreover, de Boer et al note that the higher EGR tolerance of a tumble build resulted in reductions in pumping loss, leading directly to 6.3% gain in urban fuel economy and 3% in motorway cycles. HC and CO emissions from the engine were reduced by 18% and 25% respectively.

Similar trends were also observed by Endres et al (1992), who compared engines offering different levels of tumble intensity and swirl with a four-valve engine having conventional ports. Engine performance tests showed that at part load, tumble systems have a lower brake specific fuel consumption, and can operate at higher values of air-fuel ratio. In addition, the high tumble system had the lowest value of ignition delay, taking almost half the time required by the conventional port design to burn 5% mass fraction from ignition. The same trend was observed for the combustion duration. Endres et al also found that the greater tolerance to exhaust gas recirculation allowed by swirl and tumble systems resulted in a reduction of approximately 4% in the specific fuel consumption compared to the conventional system. Emissions tests indicated that by combining swirl

and/or tumble with use of exhaust gas circulation, an up to 80% reduction in NOx emissions may be achieved.

The flow and combustion characteristics of engines fitted with low and high tumble generating cylinder heads were compared by Hu et al (1992); the low tumble system had a tumble ratio of 0.4, while the high tumble engine gave a tumble ratio of 1.74. It was shown that the high tumble engine had a lower ignition delay (0-5% mass fraction burned) by 20-30°CA than the low tumble system. Similarly, the burn duration (5-95% mass fraction burned) was lower by 25-30% for the high tumble configuration, implying that the higher turbulence produced by this engine enhanced the flame propagation rate. Moreover, this engine also gave rise to a 5% reduction in specific fuel consumption over the air-fuel ratio examined, and low levels of NOx emissions are also reported at an air-fuel ratio of 21, in addition to good EGR tolerance.

The disablement of one of the two inlet valves in a 4-valve S.I. engine has been found to be an effective technique for increasing the strength of swirl, which is necessary for effective combustion of lean mixtures at part load conditions and at low engine speeds. At higher load and wide open throttle conditions both inlet ports have to be operated in order to achieve an appropriate amount of charge for combustion and high engine power. Stone et al (1993) assessed the influence of inlet valve disablement on swirl, and subsequently, combustion and emissions on a 4-valve four cylinder engine with a pentroof combustion chamber. It was noted that disabling one inlet valve completely would result in a 43% increase in the axial swirl ratio and a 46% increase in the tumble ratio. Tumble ratio was almost doubled when an inlet valve was disabled, compared to when the valve was open by 1 mm instead of being completely closed.

This increase in vortex strength was due to the doubling of velocities through the open port as a result of valve disablement, since the mass flowrate was fixed. Consequently, valve disablement is reported to lead to more rapid combustion and the MBT ignition timing becomes less advanced. This in turn leads to higher in-cylinder temperatures and a faster laminar flame speed, reducing the duration of the early flame period. Tests performed by Stone et al indicate that an approximately 23% reduction in both 0-10% and 0-90% burn duration is achieved in comparison to the case where both valves are operated. Combustion tests performed in the study also suggest that large reductions in cycle-by-cycle variations result from inlet valve disablement. The reasons given for this feature are that faster

early burn duration means that there is less time for development of any random displacement of the flame kernel away from the spark plug. Moreover, the increase of the axial swirl component also leads to lower cyclic variations [Liou et al 1984] as all cycles burn closer to the mean, for which ignition timing is set. This leads to a reduction in fuel consumption, and indeed an average 5.6% reduction is reported as a direct consequence of inlet valve disablement. A possibility for a significant cut in NOx emissions is also mentioned in the study. Improvements in engine performance due to additional swirl resulting from port de-activation in modern lean burn S.I. engines are also reported by Neusser et al (1995) and Neusser and Geiger (1996).

The effects of tumble intensity on flow and combustion in an optical engine were examined by Arcoumanis et al (1994 a). The tumble ratio of a four-valve engine cylinder head was determined under both steady flow and motored engine conditions, and results indicated that both were of similar magnitude. L.D.A. measurements in a motored engine revealed that organised tumble motion was produced in the cylinder during induction. During compression, as the tumble velocity component deteriorated due to shear, the turbulence energy resulting from this was redirected to the other two velocity components. Volume averaged turbulence levels in compression were found to be 60% higher than those achieved for conventional single intake valve cylinder heads. By fitting sleeves into the inlet ports of the same four-valve cylinder head, a stronger tumble flow was generated in the engine, which resulted in 100% higher mean velocities and 30% larger r.m.s. velocities at the time of spark. Combustion tests performed in the study showed that the extra turbulence levels near the spark plug due to the intake port sleeves produced 6% faster combustion compared to the standard tumble head.

For lean-burn spark-ignition engines, the inclination angle of the inlet ports also plays an important role in defining the strength of tumble motion, and thereby the combustion efficiency of lean air-fuel mixtures. This was verified in an investigation by Kang et al (1996), who examined three cylinder head configurations with the same pentroof combustion chamber and directed siamesed inlet ports at different inclination angles to the horizontal; (i) 15°, (ii) 20° and (iii) 25°. Tumble ratios at various valve lifts were measured on a steady flow test rig. The results showed that the configuration with 25° inlet ports produced the weakest tumble. At small valve lifts the 15° ports produced the strongest tumble, while the 20° port

configuration gave the highest tumble ratios at larger valve lifts. L.D.A. measurements in a motored engine confirmed that with 25° ports, the tumble started to break down towards the end of the induction stroke, and no organised flow motion was noted at ignition. Both the 15° and 20° intake systems displayed strong tumble characteristics towards the end of compression, but the 20° system gave the highest volume averaged turbulence intensities at spark. This resulted in lower combustion times at all lean air-fuel ratios tested and reduced cyclic variations compared to the other two designs. The study suggests a 20° inclination angle as appropriate for siamesed intake configurations with directed ports.

Other recent studies which correlate in-cylinder tumble and swirl in four-valve engines with improved engine combustion and emissions characteristics include those by Saito et al (1994), Ohsuga et al (1995), Urushihara et al (1995), Kühn et al (1996) and Neusser and Geiger (1996).

(d) Concepts for Charge Stratification in Multi-Valve S.I. Engines

The advantages of lean burn strategies in four-valve engines have already been outlined. In order to further improve the combustion and emissions characteristics of engines running with overall lean air-fuel mixtures, a variety of concepts have been devised which make use of swirl and tumble motion to transport the greatest quantity of injected fuel as close as possible to the vicinity of the spark plug at the time of ignition. Most of the charge stratification concepts for multi-valve engines described here have been developed within the 1990s, and charge stratification is a topic of intensive research at the present moment.

In single-intake valve engines, *axial stratification*, whereby the richest air-fuel mixture in an engine cylinder is created near the top of the combustion chamber and the leanest mixture near the piston top, was found to be a useful method for reducing vehicle fuel consumption, cyclic variation in combustion and pollutant exhaust emissions [Quader 1982]. Charge is axially stratified by imparting swirl to the intake air and by injecting fuel into the inlet port shortly before the end of the induction stroke. As the vertical velocity component in the flow field is small due to swirling motion, vertically stratified charge layers are maintained until T.D.C. compression.

Researchers at Mitsubishi Motors Corporation developed a three-valve engine, named the 'Mitsubishi Vertical Vortex (MVV) Engine, which

makes use of intense tumble motion to stratify fuel and air/EGR in the cylinder. Referred to as 'Barrel Stratification' [Iwamoto et al 1992, Kiyota et al 1992], the concept makes use of two separated intake ports designed to generate very strong tumble motion during induction while the production of swirling flow is minimised. Fuel is introduced via only one of the intake ports such that a rich mixture is created downstream of this port and a lean mixture downstream of the other, through which only air is brought in. The tumble intensity ensures that the separation between rich and lean mixture is maintained up to ignition, when the rich mixture layer is ignited by a spark plug positioned directly opposite the port through which fuel was introduced.

Kiyota et al (1992) have shown via combustion tests that tumble greatly increases flame propagation in the engine cylinder. At an early stage of combustion, large-scale eddies enhance flame propagation, while at a later stage of combustion the eddy burning rate is enhanced by small-scale turbulence. It was noted that compared to homogeneous charge engines fitted with standard or tumble-generating ports, the MVV engine gives a 15% improvement in indicated thermal efficiency and thereby in engine fuel economy, due to reductions in pumping loss, heat loss and thermal dissociation. The MVV engine has a significantly higher lean air-fuel limit and combustion stability can be maintained at high air-fuel ratios, whilst achieving significant reductions in NOx emissions.

A further engine design employing the Barrel-Stratification concept is reported by Kuwahara et al (1994) of Mitsubishi Motors. A four-valve per cylinder, centre-spark plug engine was developed, with partitions fitted in the intake ports. Fuel is injected in the inside of both port partitions and lean mixture is introduced on the outside. The strong tumble motion produced during induction creates a three-layer stratification regime inside the cylinder, with a rich mixture layer in the centre and lean mixture layers on either side of this. Mixing of charge between the rich and lean fuel layers by swirling vortices is prevented by a 'tumble-control piston', which has a curved top profile designed to accentuate the tumble and inhibit swirl formation. At the end of compression, the rich mixture is concentrated in the centre of the cylinder around the spark plug. Kuwahara et al report that the advantages of the inlet port partitions include the improvement of port flow coefficient and stronger tumble. The tumble control piston also contributes to the destruction of tumble to turbulence with small eddies. The low bulk flow velocities close to the spark plug at the time of ignition

reduce the risk of misfire and lead to the enhancement of eddy burning and extension of the lean limit of the engine.

Stratified charge combustion systems incorporating swirl and tumble on a four-valve engine have also been developed by researchers at Ricardo Consulting Engineers - refer to e.g. de Boer et al (1993), Stokes et al (1994) and Lake et al (1994). The CCVS (Combustion Control by Vortex Stratification) system utilises well-defined air motion to stratify air-fuel mixture and EGR. The CCVS system can operate in four distinct modes to create either a homogeneous or stratified mixture inside the engine, depending on engine load. The inlet ports are separate from each other and the spark plug is located in an offset position in the cylinder head.

At idle speed conditions, one inlet port is deactivated and 100% air is introduced through the open port. A strong swirling motion is therefore produced in the engine. Both inlet ports are employed at part load conditions and 100% EGR enters through one port at variable rates. At EGR rates lower than the air flowrates, swirl is still the dominant in-cylinder motion and provides a homogeneous mixture for combustion. As EGR rates increase due to higher engine load and speed, strong tumble motion develops and two separate regions of EGR and stoichiometric mixture are created downstream of the corresponding ports, and these are maintained until combustion. When the engine runs at wide open throttle, the requirement for a greater quantity of air for efficient combustion means that air is introduced through both ports at the same rate. A CCVS concept employing strong swirl motion to create a layer of EGR adjacent to the cylinder wall and stoichiometric mixture within this was proposed by de Boer et al (1993). This concept was noted to be less promising than the system using tumble [Stokes et al 1994].

In order to verify the applicability of the CCVS system, de Boer et al performed combustion tests on a Ricardo Hydra single-cylinder engine employing lateral stratification, i.e. using tumble flow motion. When compared against a similar baseline engine operating with homogeneous EGR and under part load conditions, the CCVS system maintains good combustion stability. Engine fuel economy is also increased by up to 8.2% (2400 rpm, 2.5 bar BMEP), an amount greater than the 5% achieved by the baseline configuration through the introduction of EGR under similar operating conditions. The system also gives much lower increases in HC emissions and an up to 92% reduction in NOx emissions (1500 rpm, 1.5 bar BMEP) when compared against a similar engine with zero EGR.

Furthermore, it is believed by the authors that the CCVS system may offer EGR rates approaching 50% under certain situations, greatly beyond the tolerance levels of any homogeneous EGR systems devised to date. A *Variable Tumble Inlet System (VTIS)* addition to the CCVS system is also suggested by Stokes et al (1994). This allows the maximum valve lift of the engine to be varied using a variable valve timing mechanism and further improvements to engine performance and emissions are reported as a result of this.

Ohm et al (1993) report the development of an axially stratified dual-intake valve engine by Hyundai Motor Company. Strong intake swirling flow motion is generated in the cylinder by the combination of one swirl port and one straight port. In addition to the requirement for a high swirling ratio, Ohm et al indicate that for axial stratification injection timing for fuel is also a major factor which influences the location of fuel vapour at the end of compression. A swirl ratio of 3.7 was selected for the Hyundai engine from a number of inlet port configurations, and the favourable fuel injection timing was noted to be 110° - 130° A.T.D.C. crankangle during the induction stroke. Swirl ratio and injection timing as well as injection flowrate were also noted to affect the engine lean misfire limit. Fuel economy tests compared the axial stratification engine running in a vehicle against a conventional engine with two straight intake ports, and showed that up to 23% improvement in fuel economy was achieved when driving the vehicle at a constant speed of 60 kilometres per hour. By combining lean combustion and EGR, an 80% reduction in NOx emissions was also reported.

The influence of the stratification of fuel and air on combustion was also tested by Deschamps et al (1994) using a number of different intake configurations employing shrouds fitted onto the inlet valves at various angles. Tumble was produced by opening both inlet ports, while swirl was created through port de-activation. L.D.A. measurements of the flow and turbulence in each tumble configuration showed that with both inlet valves opening, much stronger tumble motion at the end of compression was produced by the shrouded valve configuration than when no shrouds were fitted, resulting in significantly higher mean and fluctuation velocities at the time of ignition. A planar laser-induced fluorescence (P.L.I.F.) study with the tumble heads on the influence of fuel injection revealed that with enhanced tumble stratified flow was created by injecting fuel through only one port and introducing pure air through the other. Injecting fuel through

both ports resulted in a homogeneous mixture at spark. Deschamps et al speculate that a successful engine design would include both strategies, i.e. fuel injection through one port at part load and through both ports at full load to improve the combustion of lean mixtures.

A number of other researchers have confirmed the above points regarding the advantages of charge stratification in four-valve S.I. engines and suggest various concepts of achieving this, e.g. studies in a constant volume combustion chamber by Arcoumanis et al (1994 b), the development of an engine by Mazda Motor Corporation capable of running at air-fuel ratios of over 40 through stratified charge [Tabata et al 1995] in addition to strategies investigated by Arcoumanis et al (1996) and Queenan et al (1996).

(e) Direct-Injection Multi-Valve S.I. Engines

The most recent state-of-the-art technologies in multi-valve engines employ fuel injection systems to introduce petrol directly into specific regions of the in-cylinder flow to create charge stratification or homogeneous mixture, as opposed to conventional port injection systems. The potential advantages of gasoline direct injection (G.D.I.) engines have been known for many decades and include fuel economy equivalent to diesel engines and major reductions in engine emissions. However, the main reason for the delay in their development was the problem of ignition fouling due to liquid fuel impinging onto the spark plug. A successful G.D.I. engine design would require very strong in-cylinder motion to transport liquid fuel droplets away from the spark plug at the time of injection.

A four-valve G.D.I. concept has been developed by researchers at Mitsubishi Motors [Kume et al 1996]. The cylinder head incorporates upright straight intake ports to create an intense 'reverse tumble' flow during the induction stroke, as shown on Figure 1.2, compared to the tumble motion generated by standard four-valve cylinder heads. Swirl formation is prevented by a 'tumble-control piston' with a specially designed spherical cavity to intensify the reverse tumble. The Mitsubishi engine operates on two different injection strategies, depending on engine load. At part load conditions fuel is injected at a late stage during the compression stroke to create stratified charge in the cylinder. Homogeneous charge is produced at high engine load by injecting petrol early in the induction stroke. The reported advantages of late injection at part load include improved combustion, since a compact spray with well-atomised

droplets is produced by impingement of fuel into the piston cavity and directed towards the spark plug by the flow. A widely dispersed fuel spray is necessary at high load and the injection timing should be arranged to avoid the fuel impinging onto the piston or the cylinder wall, since this could lead to soot formation.

Engine performance tests indicated that the Mitsubishi G.D.I. engine has significantly better combustion characteristics at all load conditions compared to standard engine configurations. As a consequence of the reverse tumble and optimum injection timing, the engine is able to operate at air-fuel ratios of over 40, leading to stable combustion at even high EGR rates. Fuel economy is reported to be at a similar level to diesel engines and emissions are also significantly lower. The engine has recently been put into production in a passenger car.

Further information on the benefits of G.D.I. four-valve engines are provided by Ando (1996) of Mitsubishi Motors, Jackson et al (1996) of Ricardo Consulting Engineers who have a similar engine design to the Mitsubishi concept and by Wirth et al (1996) of AVL-List.

(f) Other Methods for Improving Engine Efficiencies

The achievement of an increase in the performance characteristics of an engine, for instance volumetric efficiency, break mean effective pressure (BMEP) and mechanical efficiency, can greatly improve the overall running of the engine, and this, subsequently, can lead to lower fuel consumption. A number of recent developments in engine design have succeeded in obtaining better performance via a slight change in the mechanical operation of the engine.

The technique of *VARIABLE VALVE TIMING (VVT)* for example, has been identified as a means of achieving significant reductions in fuel consumption. The employment of *Variable Intake Valve Closing (VIVC)* methods can improve the mechanical efficiency of an engine through manipulation of the volumetric efficiency to control the power output. For example, Fujimoto et al (1995) observe that late intake valve closure prevents the early decay of intense tumbling vortices and can result in greatly increased levels of turbulence kinetic energy at the end of the compression stroke.

Ziegler and Köningstein (1993) provide a summary of the benefits and disadvantages of VVT through early intake valve closing and late intake

opening. In both instances, the advantages of lower gas exchange work, lower fuel consumption and improved mixture preparation can be gained. Furthermore, early intake closing offers the additional advantage of lower NOx emissions and late intake closing allows less residual gas formation and improves idling. Both systems, however, suffer from the disadvantages in that higher HC emissions result and combustion efficiency deteriorates. The study also suggests that improvements in emissions reduction and engine performance may also be derived from *variable (asymmetric) valve lift* - where one valve may have a greater lift than the other - and through *valve deactivation*, the benefits of which have already been mentioned.

The effects of asymmetric inlet valve lift strategies on engine combustion and emissions were assessed in a study by Wilson et al (1993). Seven valve lift concepts based on a four-valve S.I. engine were tested; in each case one inlet valve opened to its designed maximum value, while the maximum lift of the second valve was different for each concept. Combustion tests revealed that all the configurations showed reductions in ignition delay and combustion duration with increasing steady flow swirl and tumble ratios compared to the baseline case which had equal valve lifts. The lower ignition delay values led to reduced total hydrocarbon emissions, while smaller amounts of NOx emissions were noted as a result of the shorter combustion duration times. A 75% improvement in NOx emissions occurred for all concepts through the introduction of an 18% EGR rate relative to the baseline configuration with a 15% EGR rate. Promising improvements in engine fuel economy and emissions were reported with all the strategies, while the best idle stability was obtained with valve deactivation.

Increasing the number of valves in the engine from four to five has also been found to be a successful method for improving engine performance. Aoi et al (1986) report the development of a five-valve engine (three-intake, two exhaust) at Yamaha Motor Company Ltd., which is able to produce higher torque than an equivalent four-valve engine. Some advantages of five-valve cylinder heads are that the intake valve opening area is increased by 20 - 25% based on the same cylinder bore as the four-valve engine. The design also leaves greater room in the centre of the cylinder for spark-plug location, as the valves are located closer to the outer edge of the engine cylinder, so spark plug sizes can be easily varied. In addition, if four-valve and five-valve engines are designed based on equal

intake valve open area, the five-valve engine would have a 10% smaller bore, resulting in a more compact combustion chamber.

Accordingly, tests were performed on firing four- and five-valve 125 cc engines, each having equal bore/stroke ratios and compression ratios. The results showed that over a range of low to high speeds, the five-valve engine displayed a better volumetric efficiency, particularly at high speeds, where volumetric efficiency increased by around 10%. Combustion tests indicated that, again, that if a four and a five valve engine design is based on equal valve opening area, then the five-valve system gives a higher thermal efficiency and, therefore, has a wider power curve. Similar trends have been reported for production five-valve S.I. engines developed for passenger cars by Tickford Limited [Downing and Bale 1990, Sykes 1995] and by Audi A.G. [Ohrnberger and Mann 1994].

1.5 CONCLUSIONS OF LITERATURE SURVEY

Sections 1.2 to 1.4 have outlined primarily recent work that has been performed on in-cylinder flows and the manner in which the flow can be manipulated in order to acquire the desirable characteristics of improved fuel economy and lower pollutant emissions from a four-valve engine. The principal observations derived from the literature review are as follows:

1. The creation of a tumble flow in the engine cylinder is an effective method for the development of an organised flow pattern during induction, since a strong tumble vortex covers the entire cylinder volume at the beginning of compression, and minimises any random flow motions [Khalighi 1990].

2. The destruction of the tumble vortex during compression can lead to the generation of high levels of turbulence, an essential requirement for rapid burning of fuel during combustion.

3. Modern designs for four-valve engines, employing a pentroof combustion chamber, are well suited to the initial development of tumble flows.

4. The production of well-defined tumble during the induction stroke is dependent on how early the vortex develops. If the air motion during early

induction is random or poorly directed, a regular flow pattern will not develop until later on into the stroke, and any large vortices that result, quickly decay by the start of compression [Henriot et al 1989, Khalighi 1990, Kang et al 1996].

5. The parameters relating to the intake port and valve geometry which have a direct effect on tumble generation are:

A - The geometry of the port
B - The inclination angle of the valve
C - Valve lift

6. By varying the intensity of the tumble vortex via the appropriate type of inlet port, the turbulence intensity and length scale can be altered to influence the rate of combustion [Hadded and Denbratt 1991, Arcoumanis et al 1994 a].

7. The combination of swirl and tumble vortices to produce a complex 3D inclined flow (inclined tumble) can produce high levels of turbulence immediately before ignition, which are higher than turbulence levels produced by either swirl or tumble alone [Furuno et al 1990, Arcoumanis et al 1990, Neusser et al 1995]. The influences of such flows on combustion have not been investigated fully, although short burn durations and cyclic variations of lean mixtures at part load and the ability to vary combustion characteristics have been reported [Le Coz et al 1990, Nakanishi et al 1992]. Methods via which inclined tumble can be quickly created and its subsequent effects on turbulence, combustion parameters and emissions is an area that warrants further investigation.

8. As the intensity of the intake flow is increased during induction, the ignition delay and combustion duration both decrease greatly [e.g. Kent et al 1989, De Boer et al 1990, Hadded and Denbratt 1991, Endres et al 1992].

9. Engines fitted with high tumble generation systems exhibit improvements in specific fuel consumption in the region of 5%, in comparison with conventional 4-valve engines. In addition these engines increase the lean air-fuel limit and show a greater tolerance to exhaust gas recirculation [De Boer et al 1990, Hadded et al 1991, Endres et al 1992, Hu et al 1992, Kang et al 1996].

10. A substantial reduction in NOx emissions (up to 80%) may be achieved through the employment of both swirl and tumble in an engine, when combined with exhaust gas recirculation [Endres et al 1992, Hu et al 1992]. However, no reduction in HC emissions has yet been achieved, and methods by which HC emissions too may be cut down demand further research.

11. By keeping one of the two intake valves in a four-valve engine closed for part load operation with lean mixtures, it is possible to generate swirl and tumble flow structures which are stronger than those produced with both valves open, leading to higher turbulence intensities near the combustion chamber approaching T.D.C. compression [Henriot et al 1989, Kent et al 1989, Khalighi 1990, Stone et al 1993]. This, subsequently, leads to more rapid combustion and an average 5.6% reduction in engine fuel consumption is reported when compared against a similar engine with both intake valves in operation [Stone et al 1993]. Investigations into reasons for this result are urgently needed in addition to how this technique may be further utilised to enhance engine operation of lean mixtures.

12. Stratification of charge in a multi-valve engine leads directly to improved combustion and emissions characteristics, as typified by Mitsubishi's Barrel Stratification systems [Kiyota et al 1992, Kuwahara et al 1994], and the Ricardo CCVS combustion system [Stokes et al 1994]. By making use of a strong tumble motion to laterally stratify stoichiometric fuel mixture and EGR, substantial reductions in engine fuel consumption, cyclic combustion variation and NOx emissions can be achieved when compared against similar homogeneous-charge engines. Greater improvements can be achieved by direct-injection gasoline engines. However, this technology is still in its early stages and more research is required in order to develop methods whereby stratified charge can be quickly created within an engine cylinder, without greatly compromising on the design of the combustion chamber.

13. Variable valve timing and variable valve lift have been successfully used to improve engine performance and reduce fuel consumption [Wilson et al 1993, Ziegler et al 1993]. However, few studies relating to flow patterns produced and measurements relating to flow and turbulence characteristics

have been performed as yet. Methods by which the flow generated by VVT/variable valve lift systems may be manipulated to further to improve engine performance and to minimise emission characteristics need to be determined.

14. Comparisons of a five-valve 125 cc engine with a similar four-valve engine having equal intake valve open area have indicated that the five-valve engine has a higher volumetric efficiency and offers potential for a more compact engine [Aoi et al 1986]. Passenger car engines developed by Audi A.G. and Tickford Limited also report these benefits [e.g. Sykes 1995].

1.6 OBJECTIVES OF THE PRESENT INVESTIGATION

The literature review has been used to highlight the main findings relating to fluid motion in dual-intake valve engine designs and aspects which require further investigation. It is evident that more fundamental research is necessary into how in-cylinder flow motion may be manipulated by modification of the inlet port design. Very few published studies up to now have described detailed measurements of ensemble-averaged mean and r.m.s. velocities in the inlet ports and the cylinder of a four-valve engine. In addition to this data being useful for cylinder head and combustion chamber design, it would also be very valuable to compare the experimental data with numerical results obtained through C.F.D. engine models. C.F.D. is becoming an increasingly important tool for engine research and development, since it allows an engine design to be quickly evaluated before the more expensive and time consuming tasks of prototype building and testing are carried out. However, the results are highly dependent on the numerical scheme and the turbulence model employed, so that accurate and detailed experimental data is necessary for validation purposes.

Previous investigations into engine flows have confirmed the similarity of steady and unsteady intake flow through an engine cylinder head. Bicen et al (1985) among others showed that fluid motion in the early part of the induction stroke may be treated as quasi-steady. Traditionally, tumble and swirl ratios as well as port discharge and flow coefficients are measured under steady flow conditions for inlet port optimisation. It would therefore be very useful to perform detailed L.D.A. measurements inside the

engine cylinder - and in the inlet ports too if possible - with steady flow, as measurement time and effort would be considerably reduced. This would allow the affects of inlet port shape and inlet valve lift on the intake fluid motion, and especially on tumble creation, to be examined without interference from transient effects caused by valve and piston motion.

The literature review showed the direct relationship between the inclination of tumble axis and high turbulence levels at the point of ignition. Two methods for achieving this are reported; by valve de-activation and through combinations of directed and swirl ports and both strategies should be investigated with steady flow. This would also help to identify flow features which are not inducive to strong tumble creation. The flows at the exit of the inlet valves should be looked at and the effects of port direction, valve direction and inlet port type should be investigated separately to isolate effects of individual parameters.

The development of swirl and tumble motion during the induction and compression strokes of reciprocating four-valve engines also require further research. Dynamic water analog rigs and model engines have been used effectively to simulate transient flow inside the engine cylinder. Through the use of flow visualisation and multi-point fluid measurement techniques such as particle image velocimetry, intake tumble and swirl processes should be studied in detail. More importantly, the progression of tumble during the compression stroke should be examined in detail and the effects of engine load and speed could be determined.

Therefore, the above review indicates that new and/or more detailed knowledge and clarification is required in the following areas:

1. Quantification of the influence of inlet port design and inlet valve lift on steady flow processes in the engine cylinder, through a combination of flow visualisation and laser-Doppler anemometry.

2. Determination of the effects of valve disablement, asymmetric valve lift strategies and combinations of different inlet port designs on in-cylinder flow.

3. Visualisation and measurement of unsteady intake swirl and tumble motions and their effects during compression.

4. Comparison of steady and transient flow measurement data with C.F.D. results where possible in order to assess the suitability of numerical schemes and turbulence models to calculate velocity and turbulence characteristics.

1.7 OUTLINE OF THE THESIS

The remainder of this thesis consists of six chapters. Chapter 2 describes the experimental techniques employed in the present investigation and the arrngement of the experimental apparatus. In Chapter 3, results of steady flow investigations in a model of a dual-intake valve engine with equal inlet valve lifts are discussed. Chapter 4 presents flow visualisation and L.D.A. results of asymmetric valve lift and inlet port configurations. Flow visualisation and P.I.V. measurements of unsteady intake motion in a four-valve engine using a dynamic water-analog rig are reported in Chapter 5. Gas motion during the induction and compression strokes in a low-speed motored engine is described in Chapter 6, and the effects of engine load and engine speed on the tumble flow are reported. Finally, Chapter 7 provides a summary of the main findings of the investigation, as well as recommendations for future work.

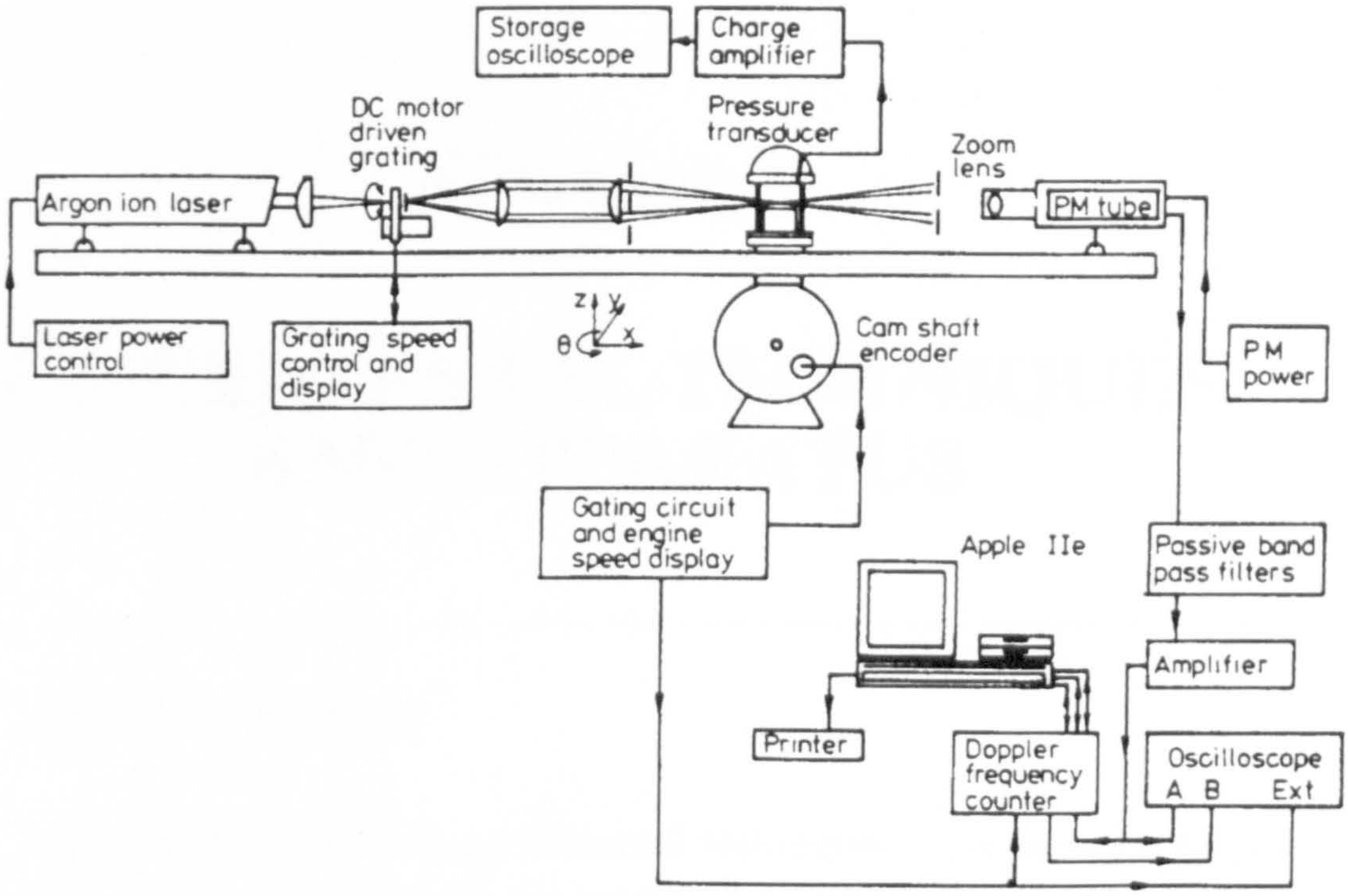

Figure 1.1 A typical laser-Doppler anemometry system arrangement for engine flow investigations
(From Suen and Yianneskis, 1988)

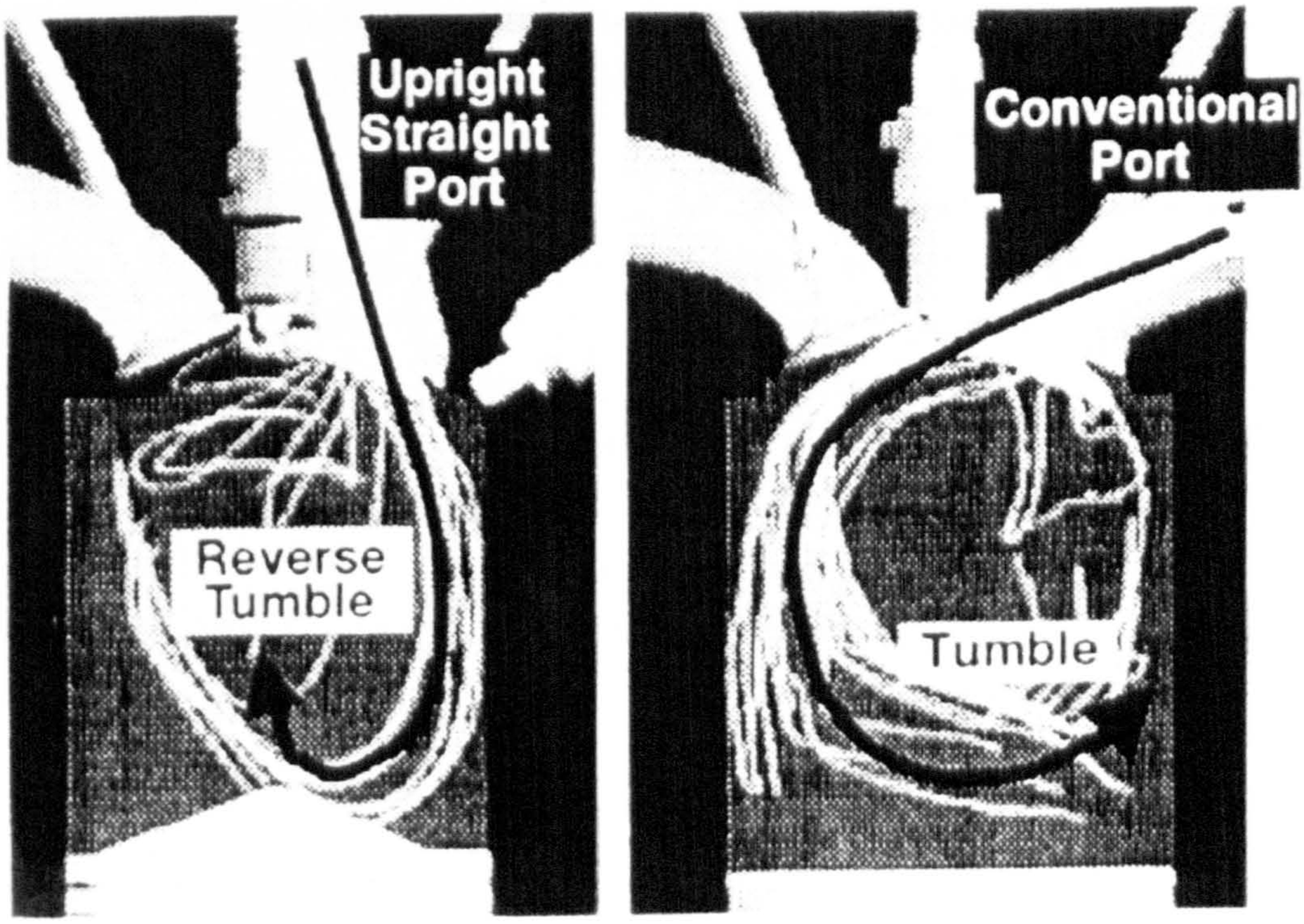

(a) Direct-injection engine (b) Conventional 4-valve engine

Figure 1.2 Illustration of the 'Reverse Tumble' concept produced by the Mitsubishi G.D.I. engine, compared to conventional tumble motion
(From Kume et al, 1996)

Chapter 2

EXPERIMENTAL TECHNIQUES AND APPARATUS

2.1 INTRODUCTION

A number of different experimental techniques have been employed during the present investigation, in order to determine a broad range of both qualitative and quantitative information relating to the intake flow characteristics of multi-valve spark ignition engines. These are described in this chapter. A refractive index matching technique was used to study liquid flow motion through a model of the intake ports and cylinder of a four-valve per cylinder engine under steady flow conditions. Details of the laser-sheet flow visualisation and laser-Doppler anemometry systems chosen are provided.

The development of in-cylinder flow during the induction stroke of a four-valve-per cylinder engine was investigated using flow visualisation and particle image velocimetry applied to a dynamic water-analog rig. A brief introduction of the P.I.V. method is given in this chapter, in addition to a description of the system used in the present study. A stereoscopic flow visualisation and three-dimensional velocity measurement technique was also employed to examine gas motion in a motored optical research engine. The experimental rig and the flow measurement technique are discussed here.

2.2 THE REFRACTIVE INDEX MATCHING TECHNIQUE

Flow visualisation in internal combustion engine ports and cylinders, and velocity measurements by L.D.A. are dependent upon optical access into

the region of interest. The complex shape of engine ports does not easily permit the inclusion of windows for optical access. This problem can be resolved by creating a replica of the desired test section from a transparent material, thus allowing extensive optical access.

With air as the working fluid, it is still difficult to visualise the flow due to refraction of the laser light at the interfaces between air and port material. Moreover, engine ports and cylinder heads are most often produced by a casting process so their internal surfaces are usually rough. These internal surface effects should be reproduced in a port model in order to ensure that the flow being studied is as close as possible to that in a real engine. Laser light, however, would be diffused from the surface, as well as refracted, so flow visualisation and measurement difficulties would still exist. If, on the other hand, a working fluid with the same refractive index as that of the engine model is employed, then the aforementioned problems can be resolved.

2.2.1 The Refraction of Light Rays

As a ray of light travels from one medium to another with a different refractive index, its behaviour corresponds to *Snell's law:*

$$n_1 \sin i = n_2 \sin r \tag{2.1}$$

where n_1 and n_2 are the refractive indices of the two media; i and r are the angles created by the ray of light to the normal of the surface at the point of incidence before and after refraction, respectively. If $n_2 < n_1$, then the light beam is refracted away from the normal to the interface, and towards the normal if $n_1 < n_2$, as depicted on Figure 2.1(a). When the angle of incidence is too large, then the ray may not cross the surface, but rather may reflect off it. The *critical angle* of the incident beam, i_C, is determined by:

$$i_c = \sin^{-1}\left\{\frac{n_2}{n_1}\right\} \tag{2.2}$$

Thus, rays with an incident angle greater than the critical angle undergo *total internal reflection*, as indicated on Figure 2.1(b).

For the case of light passing through a curved surface from one medium to another, Snell's law still applies. Figure 2.2 shows a beam of light incident

upon a curved interface. With $n_2 < n_1$ the light rays are unable to penetrate through the interface in regions where the dimension 'h' is large as the critical angle is exceeded. In this instance, light approaching this region is totally reflected. This may occur when laser light reaches the internal surface of a transparent engine cylinder. Again, employing a working fluid with a refractive index matching that of the material used for the cylinder will remedy this difficulty, so that light can penetrate through all parts of the transparent wall.

When L.D.A. is used, the location of the actual measurement volume will be different to the desired location due to refraction effects, if refractive index matching is not employed. The relationship between the real depth (BR) and the apparent depth (AB) of the measuring location at small angles of incidence is given by:

$$\frac{BR}{AB} \approx \frac{BR\cos(i)}{AB\cos(r)} = \frac{n_2}{n_1} \qquad (2.3)$$

Therefore, this effect must be accounted for when locating the measuring volume in cases where the laser beam passes through two mediums with differing refractive indices.

2.2.2 Application of Refractive Index Matching in Complex Geometries

In order to allow laser access for flow visualisation and laser-Doppler anemometry, windows have to be fitted into an engine test section, as was indicated earlier. However, the complex shape of engine inlet ports does not easily allow the addition of windows without introducing changes to the geometry and internal roughness of a port which could lead to a modification of the flow structure. Moreover, the size of the window would also limit the extent of optical access. By producing an exact replica of the inlet ports from a transparent material, the above difficulties can be minimised or eliminated.

The position of the crossing point of two laser beams passing through a simple curved surface, such as a cylinder, can be determined as shown by Bicen (1981). For the case of more complicated geometries with randomly varying boundaries, e.g. inlet ports, the laser beams may be forced to undergo a number of deviations before they intersect. Therefore a more complex procedure is required in order to evaluate the required correction

factor [Taylor et al 1982] and protracted three-dimensional calculations may be necessary. When the refractive indices of the test section and the working fluid are different, the continuous change in the contour of a port wall may result in that beam characteristics cannot be determined exactly. For flow visualisation this could cause diffusion of the laser light sheet to an increased thickness, thereby reducing the resolution of images, while for L.D.A., the half angle of the two intersecting beams and the location of the measurement volume could be affected. All of the above difficulties can be resolved by employing a working fluid whose refractive index is equal to that of the material used for the test section.

2.2.3 Refractive Index Matching Fluids

For internal combustion engine flow visualisation and measurement purposes, the cylinder is most often made out of either Perspex plastic, quartz or Pyrex glass. Cheung (1989) and Budwig (1994) have provided information on liquids that have been used to refractive index match these materials in previous studies. For this investigation, a mixture of *tetrahydronaphthalene* (tetraline) and rectified *oil of turpentine* was employed as the working fluid within a Perspex engine model. The properties of these two liquids are provided on Table 2.1.

	Oil of Turpentine	**Tetraline**
Density (kg/m³)	855 - 868	967 - 970
Dynamic viscosity (cP)	1.6	2.2
Refractive index (n_{20}^{D})	1.467 - 1.470	1.546

Table 2.1 Properties of oil of turpentine and tetraline liquids

Table 2.2 presents data relating to the properties of tetraline/turpentine mixtures by volume at temperatures at which they are refractive index matched with Perspex, where $n_{Perspex}$ = 1.4894 at 21.7°C and 1.4892 at 23°C for the laser wavelength used (632.8 nm). The refractive indices of both Perspex and the liquid mixture are temperature dependent, so both should be maintained at the correct temperature to achieve proper matching.

By allowing a beam of laser light to pass through normal to the test section, the effectiveness of the matching can be assessed. To this end, the

beam from a laser mounted on a compound traversing table is firstly shone onto a point - on a wall, say - 3 metres to one side of the test section, whilst ensuring that the beam is normal to the test section. This point is classified as the datum and marked as such.

	30.8% / 69.2%	*31.3% / 68.7%*
Refractive Index	1.4894	1.4892
Temperature (°C)	21.7	23
Density (kg/m^3)	894	899
Kinematic Viscosity (m^2/s)	1.71×10^{-6}	1.67×10^{-6}

Table 2.2 Properties of tetraline/turpentine mixtures used for the refractive index matching of Perspex

The compound table is then traversed to a location such that the laser beam passes through the region of maximum cylinder curvature, where the greatest amount of beam deviation is likely to take place. The distance between the datum and the new position on the wall is compared to the distance traversed by the laser. For exact refractive index matching, these two distances should be equal. The composition and/or temperature of the mixture can be varied in order to achieve perfect matching of the refractive indices of fluid and test section material.

2.2.4 The Ford Zetec Port Model

The test section configuration was produced to actual scale according to the 1.8 litre medium-output Ford Zetec engine, with two intake valves per cylinder. Exhaust ports were not created within the model, as it was desired only to study inlet flows. The intake ports were of fixed geometry, high velocity, siamesed type, known as *High Velocity Tumble (H.V.T.)* ports - designed, as the name suggests, to generate a strong tumble motion into the engine cylinder, although the velocity characteristics of flow through the cylinder head had not been determined in any detail.

The ports and cylinder head profiles were produced into the Perspex block at King's College London in a number of stages. Initially, molten rubber was poured into an actual aluminium cylinder head provided by Ford Motor Company, to create a male mould, shown on Figure 2.3(a), which was

extracted in two parts. A female mould was then made out of plaster of Paris from this rubber mould. A fusible alloy mould (Figure 2.3(b)) produced using the plaster mould, was sent to a company manufacturing acrylics (Stanley Plastics Ltd., U.K.), who made a casting of a rectangular shape Perspex block with a flat surface using the fusible alloy. Finally, the cylinder of the test section was machined to appropriate dimensions at King's College London, and the outer surfaces polished. The valves and valve guides did not require any special manufacturing techniques, but were machined from Perspex according to the Ford Zetec specifications. Figure 2.4 shows two photographs of the Perspex port model, and Figure 2.5 presents diagrams of the engine cylinder head, outlining its main characteristics and dimensions.

Studies were also performed in two variants of the standard Zetec cylinder head design, and in this case the aluminium cylinder head from an actual engine was mounted onto a Perspex block which included the appropriate cylinder bore. A photograph of one of the engine models is given on Figure 2.6, while Figures 2.7(a) and (b) show the inlet port configuration of each cylinder head. L.D.A. measurements were taken within the cylinder region of each engine model.

2.2.5 Annealing of the Perspex Test Section and Valves

Both tetraline and oil of turpentine are organic fluids which cause deterioration of Perspex due to chemical attack. Annealing relieves stress within the test section and thereby minimises chemical reaction. In the annealing procedure, the port, inlet valves and inlet valve guides were placed in a bath of water. The temperature of the water was initially raised from room temperature to 70°C (the softening temperature of Perspex) at a rate of 0.3°C/minute via a constant temperature bath. The test section was then held at this temperature for a period of 32 hours, the time period being evaluated from the relation prescribed by ICI's Perspex Technical Service Note PX128:

$$T_{Holding} = 0.32\,Y \quad \text{(hours)}$$

where Y, in mm, is the greatest dimension within the largest single piece of Perspex within the port - in this case, 100 mm for the standard Zetec test section. The port and valves were finally cooled very slowly from 70°C to room temperature over a period of 26 hours, the cooling time being given by:

$$T_{Cooling} = 0.26\,Y \quad \text{(hours)}$$

After annealing, each of the individual components were checked for changes in dimension, and were found to be satisfactory. The cylinder block for the other test sections was also annealed in the same way.

2.2.6 The Steady Flow System

Flow visualisation in the Ford Zetec ports was carried out under steady flow conditions, and a schematic diagram of the rig is provided on Figure 2.8. Essentially, the liquid mixture was pumped up from the lower tank to the upper tank using two pumps, each having a maximum pumping capacity of 54.5 litres per minute. The upper tank was employed to provide a constant head, and an overflow pipe led back from this to the lower tank. Liquid from the upper tank flowed into the test section through the inlet manifold of an actual Zetec engine, to ensure that the flow entering the inlet ports was as close to flow into a real engine as possible.

The flowrate within the system was controlled via a valve connected to a rotameter located downstream of the test section. This rotameter had a maximum measuring capacity of 216 litres per minute. The liquid temperature was maintained constant by means of a temperature control unit which allowed the temperature to be specified to within 0.02°C. Two temperature sensors, one located in each tank, provided input to the control unit. A heating coil and a cooling coil were fitted into the lower tank, the cooling coil being able to be provided with either mains water or refrigerant. Each coil, therefore, came into operation as and when required to maintain the liquid temperature at the desired level.

Detailed descriptions of the development of this steady flow rig and research previously performed on it are provided by Yianneskis et al (1988), Cheung (1989), Cheung et al (1990) and Nadarajah (1992).

2.3 FLOW VISUALISATION

Once exact refractive index matching had been achieved, flow visualisation was performed and recordings of the flow at various valve lifts were made using a C.C.D. video camera. Air bubbles were used as flow

tracers: they were created in the lower tank of the steady-flow rig and carried up to the upper tank and through the test section by the pumps. These bubbles were of minute size - on average between 50 to 60 μm in diameter, and followed the flow faithfully. When a plane of laser light was passed throughout the test section, the bubble paths indicated the flow motion by appearing as streaks. Due to the small bubble size, the bubble rise velocity as a result of buoyancy forces was negligible - it can be shown that the bubble rise velocity is less than 2 mm/s [Nadarajah 1992].

A 2W Argon-Ion laser (model: Coherent Radiation Innova 90) operating at a wavelength of 514 nm was used as the light source. The laser beam was passed through a cylindrical lens to produce a sheet of light, and mirrors were used to direct it to the required location in the test section, as indicated on Figure 2.9. For flow visualisation, the laser was mounted on its own bench and not on the compound traversing table on which the optics were installed. Through a combination of adjusting the mirrors, the cylindrical lens and traversing the compound table, the light plane could be positioned at different locations so as to provide flow field information wherever desired.

2.4 LASER-DOPPLER ANEMOMETRY

2.4.1 Background

Laser-Doppler anemometry (L.D.A.) is used extensively for the investigation of the flow structure of both liquids and gases. The technique offers a number of advantages compared to other methods for flow measurement, as was described in Chapter 1, including (i) it is non-intrusive, (ii) it provides high spatial and temporal resolution, and (iii) it has a well-defined directional response. The laser anemometer measures the frequency of light scattered from seeding particles travelling with the fluid, and the time-dependent velocity of the particles is calculated from this.

In a 'fringe mode' L.D.A. system, two incoming laser beams are made to intersect, and a fringe pattern is created at the crossing point, as illustrated on Figure 2.10. As small particles moving with the flow pass through the light and dark fringes of the intersection volume, the intensity modulation of the scattered light is collected by a photodetector and the resulting signal is known as a "Doppler burst". Figure 2.11 shows a typical Doppler signal. The

two Doppler-shifted scattered beams are combined by the fringe mode L.D.A. system and a light-sensitive detector measures the difference between the two beams. By employing signal processing methods, the flow velocity can be calculated from the signal produced by the detector. The velocity component U in a direction perpendicular to the fringes of a particle crossing the intersection volume is related to the Doppler frequency f_D by the following expression (Drain 1980):

$$f_D = \frac{2\,U \sin\left(\frac{\theta}{2}\right)}{\lambda} \tag{2.4}$$

where λ is the wavelength of the laser light, and θ is the intersection angle of the two laser beams.

The above expression allows evaluation of only the magnitude of the particle velocity. In order to obtain information with regard to flow direction, 'frequency shifting' of the laser beams is normally employed. This is achieved by causing the two incident laser beams to have slightly different optical frequencies and results in the movement of the interference fringes within the control volume. Therefore any particles travelling in the opposite direction to the movement of the fringes will seem to be moving faster, and the light detector will sense a higher modulating frequency. By taking the frequency increase caused by the fringe movement into account, the actual frequency of the scattered light can be determined, and thereby the particle velocities.

A number of different apparatus can be used for beam splitting and to introduce the frequency shift, including Bragg cells, diffraction gratings and rotating prisms. If, as in the present investigation, a rotating diffraction grating is chosen, then the following expression is used to calculate the shift frequency f_s from the rotational speed of the grating:

$$f_s = \frac{2\,m\,n\,N_g}{60} \tag{2.5}$$

where m is the order of the pair of diffracted beams employed, n is the number of lines on the grating, and N_g is the rotational speed of the grating in rpm.

Hence, velocity measurements are obtained from the expression below:

$$U = (f_D \pm f_s)\frac{\lambda}{2 \sin(\theta/2)} \qquad (2.6)$$

The optical arrangement and signal processing system employed in the present work will be described in the following sections.

2.4.2 Optical Arrangement of L.D.A. System

The laser-Doppler anemometer was operated in dual beam forward-scatter fringe mode. The anemometer comprised of a Spectra-Physics 106-2 10 mW helium-neon laser, a rotating diffraction grating (produced by Optical Manufacturing Tools) and a photomultiplier (model EMI 9817B) fitted with a zoom lens. Figure 2.12 presents a schematic diagram of the optical arrangement.

Laser:	Wavelength: 632.8 nm (red) Power: 10 mW Beam diameter: 0.83 mm
Lenses:	L_1: f = 200 mm L_2: f = 500 mm L_3: f = 200 mm
Diffraction Grating:	No. of lines: 21600 Rotational speed: 4700 rpm Frequency shift: 3.384 MHz Half-angle between incident beams: 1.79° (measured)
Measurement Volume Dimensions: (at $1/e^2$ intensity)	Diameter (b_x): 77.91 μm Length (b_y): 1.005 mm No. of fringes: 19 Frequency / velocity conversion factor: 4.096 (m/s/MHz)

Table 2.3 L.D.A. system characteristics

The diffraction grating had 21600 lines etched at mean track diameter of 133.2 mm and was rotated at speeds of up to 4700 rpm by means of a bi-directional electric motor. Using the first-order beams, a frequency shift of 3.384 MHz was achieved. The grating and motor assembly was fitted on a 45°

table, so that by moving the complete assembly up or down the table, different velocity components could easily be measured. Table 2.3 provides the L.D.A. system characteristics.

The measurement volume dimensions and the number of fringes were evaluated from the optical characteristics of the L.D.A. system. The measurement volume diameter, b_x, is given by:

$$b_x = \frac{b}{\cos\left(\frac{\theta}{2}\right)} \tag{2.7}$$

and its length, b_y, is calculated from:

$$b_y = \frac{b}{\sin\left(\frac{\theta}{2}\right)} \tag{2.8}$$

where θ is the intersection angle of the beams. The parameter b is calculated from the following expression:

$$b = \frac{4 \lambda f_1 f_3}{\pi b_0 f_2} \tag{2.9}$$

where b_0 is the diameter of the beam leaving the laser. The number of fringes inside the control volume, N_{fr}, is given by:

$$N_{fr} = \left(\frac{2 b}{\lambda}\right) \tan\left(\frac{\theta}{2}\right) \tag{2.10}$$

As seen on Figure 2.12, light from the laser was focused onto the diffraction grating by a bi-convex lens of 200 mm focal length. The pair of first order beams from the diffraction grating were selected using an optical mask and collimated by a plano-convex lens of focal length 500 mm. The collimated beams were then focused by another plano-convex lens of focal length 200 mm to create the control volume. The entire optical system was mounted on a compound table which could be traversed along two horizontal directions and in the vertical direction to give three degrees of freedom. Artificial seeding of the flow was not required as the liquid mixture contained a sufficient amount of micron-sized contaminant particles. The scattered light from particles crossing the control volume was focused onto a

pinhole of 0.5 mm diameter at the front housing of the photo multiplier tube by a zoom lens of 80 - 200 mm focal length. The photomultiplier was powered by a Brandenburg 10-2000 Volts DC power supply.

The experimental test section had mutually perpendicular and completely flat outer surfaces, and before aligning the optics on the bench it was ensured that the beam from the laser was positioned normal to the side from which measurements were to be taken. Therefore there was no requirement for correction factors to account for the change in refractive indices as the beams passed through the outer surfaces of the test section, from air to Perspex and vice versa, other than those related to apparent depth.

2.4.3 Signal Processing System

A schematic representation of the signal processing system employed is shown on Figure 2.12. The output from the photomultiplier was firstly amplified by a pre-amplifier and bandpass filtered in order to remove low frequency pedestal and high frequency noise. Hence, the amplified signal was passed through a low pass filter (produced by TTE Inc., USA) of 20 MHz cut-off frequency and then a high pass filter of 1.5 MHz cut-off frequency fitted in the input module of the frequency counter. The quality of the filtered signal was monitored continuously with an oscilloscope (Telequipment model DM63).

The frequency counter used for signal processing (Thermofluids Section 'Model 3' Phase Doppler Counter) was designed and constructed at the Mechanical Engineering Department at Imperial College, London, [Hardalupas and Laker 1993] for performing phase-Doppler anemometry measurements. In the present study, however, it was employed as an L.D.A. counter, so that only one of the three channels available for the input of Doppler signals was selected for use.

The counter required a minimum signal amplitude of approximately 30 mV in order to activate the amplitude validation logic. The beginning of a Doppler burst was detected by the first correctly sequenced crossing of the threshold level, and the end of the burst was assumed when its amplitude became lower than the threshold setting. Once initiated, the counter made one measurement for every Doppler burst detected and the elapsed time of eight Doppler cycles was measured in addition to the time of the first five of those eight cycles, for estimating the Doppler frequency and for signal

validation in the time domain. Detailed diagrams of the counter modules and counter control logic have been provided by Hardalupas and Laker (1993).

The frequency counter was linked to a commercial interface card (National Instruments AT-DIO-32F) installed in an IBM PC-compatible computer for the transfer of data. Two computer programs responsible for the remote programming of the counter were installed onto the microcomputer. In addition to allowing the initiation and ending of a particular measurement cycle, these programs enabled specification of the operating parameters of the L.D.A. system used as well as the display and plotting of results. The software displayed and updated results for mean and r.m.s. velocity after every 512 data samples. In the present study a length of 2048 data samples was chosen for each measurement at every control volume location. The measurements were repeated, on average, three times in each location.

2.4.4 Sources of Error in the L.D.A. System

This section examines some of the factors which may have led to errors and uncertainty in the L.D.A. measurements. The major causes of error may stem from the seeding, frequency shifting, count ambiguity, broadening, positioning, statistical uncertainty and bias effects. The influence of each of these will be discussed individually.

Seeding

No seeding particles were added to the flow for L.D.A. measurements in the liquid system used, as a sufficient amount of micron-sized particles were taken to be present within the system. The actual size of the particles and their velocity fidelity could not be determined. The liquid mixture was regularly filtered by passing it through a 10 micron sieve and layers of filter paper, cotton wool and de-colorizing charcoal. Hence, particles within the filtered liquid were micron sized and their velocity fidelity at large turbulence frequencies was suitably high. For example, the sink velocities for a 1 μm and a 5 μm diameter particles in the liquid mixture are 7.5×10^{-4} mm/s and 0.02 mm/s respectively.

Frequency Shifting

The diffraction grating used to produce the frequency shift was rotated by a bi-directional variable speed motor with feedback control. It has already

been shown that the maximum fluctuation of the motor was 0.3% in the long term and 0.8% in the short term [Cheung 1989]. Melling (1977) has shown that such a variation would have a very small influence on the measured r.m.s. values. During the measurement procedure, the rotational speed of the grating was regularly checked with an optical tachometer and appropriate adjustments were made to the frequency shift value specified within the L.D.A. software.

Count Ambiguity

Counting systems inherently have an error of ±1 clock count, as it is possible for the gate to miss one pulse generated by the crystal oscillator as it opens or closes. Therefore, the maximum timing error is $\pm\frac{1}{f_c}$, and the corresponding fractional error is $\frac{f_m}{N_D f_c}$, where f_c is the oscillation frequency of the crystal, f_m is the measured frequency of the signal, and N_D is the number of Doppler cycles to be timed. The frequency counter had a 500 MHz oscillator (i.e. a time resolution of 2 ns). For measured frequencies of 4 MHz over 8 Doppler cycles, the error is, therefore, 0.1%.

Broadening Errors

A variety of different factors can produce broadening of the measured velocity probability distribution function (p.d.f.). Some causes which can induce broadening are [Durst et al, 1981]: small scale velocity fluctuations within the measurement volume (σ_f), gradients in mean velocity (σ_g), the finite time taken by scattering particles to cross the measurement volume (σ_t), instrument broadening (σ_i), brownian motion and laser linewidth. Durst et al (1981) showed that the effect of the last two contributions is negligible, so that the total mean square contribution of broadening errors, σ_b^2, is given by:

$$\sigma_b^2 = \sigma_t^2 + \sigma_g^2 + \sigma_f^2 + \sigma_i^2 \qquad (2.11)$$

Finite transit time and instrument broadening are negligible and do not affect measurements taken with a frequency counter such as the present one.

George and Lumley (1973) expressed broadening from small scale velocity fluctuations within the measurement volume as:

$$\sigma_t^2 \approx \frac{2}{15}\,\sigma_3^2\left\{\frac{4\pi\sin\theta}{\lambda}\right\}^2\frac{\varepsilon}{\nu} \qquad (2.12)$$

where σ_3 is the scattering volume dimension near the Kolmogorov microscale, ε is the dissipation of turbulence energy and ν is the kinematic viscosity of the fluid. In order to evaluate this error, the Kolmogorov microscale and turbulent energy dissipation must be known, and a more complex calculation is required for larger scattering volume dimensions. This error was estimated by Melling (1975) to be of the same order as the velocity gradient broadening.

For measurements made across a velocity gradient, particles passing through different sections of the control volume will have different velocities, irrespective of any turbulent velocity fluctuations which may exist in the flow. This can cause the p.d.f. of a velocity component to be skewed and broadened compared to that for a point measurement [Durst et al, 1981]. If the velocity gradient is almost linear along the longer axis of the measurement volume, the broadening of the mean velocity would be small. Large errors can occur, however, if the mean velocity gradient is steep and linear.

Positioning Errors

If perfect refractive index matching between the working fluid and the test section is achieved, then accurate location of the measurement volume is only dependent on the accuracy of defining the datum point within the test section and measuring the table movement. Nadarajah (1992) determined the accuracy of positioning the compound traversing table as 0.1 mm and the random error in locating the measurement volume to be ±0.25 mm.

Cheung (1989) examined the errors which could arise in measured velocity values if perfect refractive index matching was not achieved, and therefore the measurement volume was not located accurately. He found that for a variation of 0.25°C in the liquid temperature from the ideal refractive index matching temperature, the positional error was negligible as the displacement of the measurement volume was very small. It was also shown that a 1°C change in liquid temperature from that of the test section produced only a small difference in the measured velocity (0.027 m/s) in a region of steep velocity gradient. In the present rig, it has been previously established

(Cheung 1989) that the liquid temperature could be accurately controlled to within ±0.02°C.

Statistical Errors

Errors in ensemble-averaged results can occur if too few velocity measurements are taken, leading to statistical inaccuracies. In the present study, a sample size of at least 2048 measurements by the counter was chosen at each control volume location. The errors for velocity measurements were calculated as suggested by Yanta (1973), and were 2% for mean velocity, with a confidence level of 95% and assuming a turbulence intensity of 0.5, and 3% for r.m.s. velocity. In order to check for accuracy and repeatability of the results, measurements were repeated at least twice at every location.

Velocity Bias Effects

Bias in velocity measurements can occur when ensemble-averaged measurements are taken with a constant seeding density in the flow. A greater number of particles with large velocities will be recorded over a given measuring period than slow moving particles, causing skewness of the measured p.d.f. towards the higher velocities region [McLaughlin and Tiederman, 1973]. A number of correction methods have been suggested to minimise this error - e.g. randomising time intervals between measurements [Drain, 1980], weighting of the velocity data from individual particles with their residence time [Hoesel and Rodi, 1977] and random sampling of the measured velocities recorded by individual particles after sorting the data obtained by all particles [Durao and Whitelaw, 1975]. An appropriate correction method for highly three-dimensional flows is not available, especially when the measurements of the three velocity components are not made simultaneously. The liquid flows in the present study had high turbulence intensities, and therefore bias effects are expected to be minimal.

The principal causes of uncertainty in the L.D.A. measurements have been described above. The errors will vary with measurement location, so that it is difficult to identify individual error types and compensate for them. Cheung (1989) and Suen (1992) checked the accuracy of similar L.D.A. systems to the one employed in the current investigation. The known velocity of a pin rotated by a d.c. motor was measured with each of their systems. In both instances, it was found that the mean and r.m.s. velocities were calculated within 1% and 2% respectively of the known value.

Although no corrections could be made for some of the error types described earlier, the overall errors in the mean and r.m.s. values have been assessed by Cheung (1989) and Suen (1992) to be around 5% and 10% respectively, and therefore are not expected to have any significant influence on the results.

2.5 PARTICLE IMAGE VELOCIMETRY

2.5.1 Introduction

The technique of Particle Image Velocimetry (P.I.V.) has now successfully been employed for over twelve years for the experimental study of fluid motion. The method has essentially developed from laser-sheet flow visualisation methods, where flows are seeded with particles which follow fluid behaviour to the smallest temporal and spatial scales of motion, and laser light scattered by the particles provides a qualitative view of the flow.

P.I.V. extends this to give quantitative results of velocity magnitude and direction, at many points in a given plane at one instant in time. Hence, it differs from single-point velocity measurement techniques, such as hot-wire anemometry and laser-Doppler anemometry, in that whereas these methods can only measure a velocity component at usually one location in the flow field at a time, P.I.V. can potentially be used to measure the velocity of all particles in a light plane at the same time.

Particle image velocimetry has developed from the techniques of laser speckle photography (L.S.P.) and laser speckle velocimetry (L.S.V.). L.S.P. has been used in the field of solid mechanics for measuring displacement fields. A solid surface is illuminated with laser light and two speckle image exposures, taken before and after a given displacement are superimposed onto a single photographic frame. In any given local area, the two individual speckle patterns will be separated by a constant displacement. When a low power laser beam is shone through this area, Young's fringes are created by the interference of diffracted light waves from each exposure. The separation and orientation of the fringes are used to arrive at the magnitude of displacement.

Laser speckle velocimetry operates on the same principle, and was first applied by Barker and Fourney (1977) to the study of a low Reynolds number fluid flow. Dudderar and Simpkins (1977), Grousson and Mallick (1977) and Meynart (1983 a, b) also performed early investigations using L.S.V.

methods. In particle image velocimetry, the particle concentrations in the fluid medium are considerably lower than for L.S.V., so that individual particles can be identified on each exposure, as opposed to merely a speckle pattern. The P.I.V. images may be acquired either by photography or from video recordings of the flow. A pulsed laser light sheet is used to illuminate particles in the fluid, and a photographic lens positioned perpendicular to the light sheet collects scattered light from the particles. The recorded images, photographic or video, are then transferred to a computer for analysis and data processing. The analysis procedure is known as 'interrogation' and is usually the most time-consuming part of the P.I.V. technique. Interrogation methods are discussed in section 2.5.2.

Adrian (1992) has identified three categories of P.I.V. systems. The first type, 'high resolution P.I.V.', is the conventional system and uses photography to capture images. The substantial information capacity of photographic film means that large arrays of velocity vectors can be measured with good spatial resolution and a high degree of accuracy. For instance, a film of 125 mm by 100 mm would normally be divided into a grid of 125 by 100 interrogation regions. If each interrogation spot, of 1 mm by 1 mm size, is digitised into a 256 by 256 pixel grid, then a total number of 8.192 x 10^9 pixels will be present in each P.I.V. image. Photographic recording media are employed for high resolution and wide dynamic velocity range measurements.

The second and third P.I.V. systems employ video techniques to record images of the flow. When the entire flow field is recorded with a video camera, the technique is referred to as 'low resolution P.I.V.' or sometimes 'Digital P.I.V.'. This is because most video cameras have resolutions far lower than photographic film, typically containing from 512 x 512 pixels up to 2000 x 2000 pixels per video array. This disadvantage can be overcome by dividing the total flow regime into small regions, and recording each region with a video camera. By combining together all the arrays from each interrogation region, the total flow regime can be reconstructed at high resolution. Adrian (1992) refers to this method as 'video-probe P.I.V.'.

Although two-dimensional P.I.V. is the most extensively used method, three-dimensional velocity measurement techniques have also been developed, and these make use of multiple light sheets, stereoscopic imaging or holography to acquire 3D data in either a single plane or in a particular volume. With the development of high-performance computer systems to analyse images and process data, three-dimensional techniques are becoming

increasingly important tools for the visualisation and quantitative analysis of complex 3D flows. Coupland and Halliwell (1992) have discussed 3D P.I.V. techniques in some detail. In-depth discussions of the P.I.V. technique have been provided by Adrian (1991), Gray (1992), Buchhave (1992) and Adrian (1996).

2.5.2 P.I.V. Interrogation Techniques

The interrogation of P.I.V. images involves the use of electronic hardware and computer software to implement a processing algorithm on images, in order to compute a grid of displacement or velocity values. A number of different factors characterise the performance of an interrogation system. These include accuracy, reliability and speed of processing. Ideally, the interrogation system should be able to measure particle displacements from images with even low information content, without being greatly influenced by the systematic and random uncertainties corresponding to individual measurements (Gray (1992)).

In the same way, the choice of technique will also be influenced by the amount of time taken and the effort required to process images. Hence, although photographic methods in P.I.V. do give better resolution in the recorded images, the procedure of developing film to produce images is nowadays often seen as an unwelcome interruption to the measurement process. This has led to the increasing use of digital techniques to record images, which can then be directly transferred to computer for analysis, in spite of the lower resolution of current C.C.D. cameras.

At the present moment, the two mathematical methods most commonly used to compute velocity magnitudes and directions from particle images are 'auto-correlation' and 'cross-correlation'. If the two successively recorded particle fields are developed onto one image for analysis, then the auto-correlation method is used to evaluate the velocity magnitude from each particle pair in the image. The cross-correlation technique is employed when the two successive particle fields are stored as separate images. The theory and application of these techniques will now be outlined.

The Auto-Correlation Method for P.I.V. Processing

The auto-correlation method for interrogation of P.I.V. images is most commonly implemented on double-exposure images of particle fields, and

can be performed on a computer. During interrogation, small areas of the P.I.V. image are successively illuminated by a light source, such as a laser and recorded by an image-resolving electronic detector (e.g. a C.C.D. camera) onto the computer. The aim of the analysis is to evaluate a vector displacement that will translate particles from the first image field onto the second image field.

Figure 2.13(a) illustrates the auto-correlation algorithm. A two-dimensional fast Fourier transform routine (F.F.T.) is applied to the double-exposure image, as it is digitised, followed by a squaring of the image data to obtain the power spectrum. This results in a pattern of bright and dark Young's fringes. These fringes are positioned perpendicular to the mean vector displacement, and their spacing is inversely proportional to the displacement magnitude. The displacement, and thereby the velocity, of the particles can therefore be calculated from the wavelength of the fringes and their orientation. An inverse F.F.T. is then carried out on the power spectrum to obtain the auto-correlation function.

Since digital F.F.T. operations require high performance computer systems in order to process data rapidly, when such computer resources are not available, the auto-correlation procedure can be speeded up by incorporating optical analysis methods. In this instance, the P.I.V. image is interrogated by a laser beam and the scattered light is passed through a converging lens with Fourier transforming properties. The image is digitised and transferred to a computer by an image-resolving camera placed in the Fourier transform plane.

Due to the detection process being sensitive to light intensity, a squaring process is inherently constituted on the image, so that the digitised image on the computer is a power spectrum of the object image. Hence the computer is required to perform only one Fourier transform operation in order to compute the auto-correlation function, thereby significantly reducing the processing time. This method has been referred to as the 'Young's fringes' interrogation technique (Adrian 1991, 1996, Buchhave 1992).

One disadvantage in the use of double-exposure images is that there is a 180° directional ambiguity in the velocity data calculated from the auto-correlation function. In order to resolve this ambiguity, Adrian (1986) developed an 'Image Shifting' technique, where the image field is shifted between exposures, such that the displacement always has one positive component. The negative velocities in the processed data are determined

after interrogation, by subtracting the additional shift. Other methods of resolving directional ambiguity are described in Gray (1992), Adrian (1991) and Adrian (1996).

The Cross-Correlation Method for P.I.V. Processing

With the increasing implementation of digital techniques for the capture of P.I.V. images, the cross-correlation method has been developed to compute the velocity data. The cross-correlation algorithm is used for evaluation of data from two successive video images. It was not commonly used until recently, as the fixed time interval between video frames restricts the velocity magnitudes which can be measured. The method is computationally intensive and requires the use of high speed computers for data processing.

However, technical improvements in digital cameras and the fact that all analysis can be performed computationally, means that the technique has attracted great interest. The most significant advantage of the method is that direction of the velocity data is resolved without ambiguity, since separate single-exposure images are used in the analysis procedure.

The cross-correlation algorithm has been illustrated on Figure 2.13(b). In the P.I.V. systems used by Willert and Gharib (1991) and Heckmann et al (1992) both of the particle images are scanned by a 32 x 32 pixel moving window. The pattern produced by the window in the first frame is then cross-correlated with the pattern of the corresponding window in the second particle image frame. A fast Fourier transform is then applied to the patterns from both images, and then the complex conjugate product of the two F.F.T.'s is calculated. The cross-correlation function is obtained by implementing an inverse F.F.T. on the complex conjugate product. The maximum peak of the cross-correlation is employed to calculate the particle displacement between the two images in consideration.

Detailed descriptions of the cross-correlation algorithm, including mathematical analyses, are provided in articles by Willert and Gharib (1991) and Keane and Adrian (1993). Some developments in the method are also discussed in Rouland et al (1994).

2.5.3 The Experimental System - Hardware and Software

The experiments were carried out on a low-speed dynamic water-analog rig located in the Department of Mechanical Engineering, University of Brighton. A schematic diagram of the rig is presented on Figure 2.14(a). The engine cylinder head was positioned horizontally onto the rig, and a glass cylinder was pressed against it. An actuator system which was connected to a personal computer through an electronic interface, was used to drive a transparent Perspex piston within the cylinder, to simulate piston motion during the induction stroke. Water was employed as the working fluid. A glass box with straight glass panels was fitted around the cylinder, and the space between the outer surface of the cylinder and the inner surfaces of the glass panels was filled with water. This was required in order to minimise optical distortion caused by differences in refractive indices between glass, water and air, and to reduce refraction of laser light from the curved surface of the cylinder.

The inlet valves on the cylinder head were driven by stepper motors linked to an electronic interface, as shown in Figure 2.14(a). The inlet valve lift profile during the induction stroke was specified using a personal computer. During the induction stroke, the inlet valves and the piston actuator were operated to allow water from a tank to flow through the cylinder head and cylinder. At the end of the induction stroke, the water was returned to the tank through the exhaust ports on the cylinder head by the piston, as it returned to the top-dead-centre position. A detailed description of the dynamic flow visualisation rig is given in Jackson et al (1995).

The illumination system consisted of a continuous 10 W Argon-ion laser (Lexel Laser Inc.) and a multi mode fibre-optic link with a built-in lens system to produce a sheet of laser light. The laser sheet could be positioned at any desired position and orientation through the test section by repositioning the fibre-optic probe. Neutrally-buoyant particles of approximately 80 μm diameter were added to the water tank to trace the flow inside the glass cylinder.

For flow visualisation studies, the flow in various planes inside the cylinder at different crankangles was recorded using a video camera connected to a super-VHS video recorder. The Genloc system was used to combine together video and computer images, in order to obtain a high quality video of the flow visualisation.

For the P.I.V. experiments, the laser sheet was double-pulsed using a P.I.V. timer (Dantec 'Flow Grabber' DPIV Timer 100). The separation and the duration of the pulses could be adjusted through the timer to suit the flow under consideration. Two successive particle images of the flow were grabbed with a high-speed cross-correlation camera (Dantec 'Flow Grabber' Double Image 700 Camera) connected to a frame grabber card installed inside a personal computer. In order to compute an ensemble-average of the flow, to determine the mean flow characteristics, the process was repeated ten times for each plane inside the cylinder. The images were grabbed at the point when the piston reached 180° crankangle position of the induction stroke.

The captured images were interrogated using a commercial P.I.V. processing package - VISIFLOW™ produced by A.E.A. Technology Limited. The software applied a cross-correlation algorithm to the two images to evaluate the particle velocities and directions. A map of around 900 raw instantaneous vectors was produced in approximately twenty seconds. Vectors which appeared to be incorrect, with unrealistic magnitudes and directions, were selected and deleted using the software. A number of different interpolation algorithms were available within the VISIFLOW™ package to create vectors locally in those areas. The boundary of the vector field was then adjusted to correspond with the plane under consideration. In addition to particle velocity, vorticity was also calculated at each vector location. The data was then saved in a file for postprocessing.

The commercial software MATLAB™ was employed for postprocessing and plotting the P.I.V. results. The programs used had been developed at the University of Brighton, and calculated flow parameters including tumble ratio, swirl ratio, minimum velocity and maximum velocity. Averaged velocity maps were also produced from the ten instantaneous plots processed for each plane. Further details of the postprocessing procedure are provided in articles by Faure et al (1996 a and b).

2.5.4 Errors in P.I.V. Results

Errors and uncertainties may be introduced into velocity and vorticity measurements made by P.I.V. through a number of factors relating to image recording, interrogation and data processing. The experience of the user in the measurement technique also plays an important role in the definition of measurement errors. During image capture and double-exposure recording,

distortion of the scene being viewed by the camera lens, three-dimensional effects and limitations in film and lens resolution can contribute to inaccuracies. Large velocity gradients in the flow can lead to bias effects and uncertainties also result from errors due to signal processing and image analysis algorithms.

During the interrogation of double-exposed P.I.V. images, velocity magnitudes are determined from the location of the peak in the auto-correlation function. If the peak of the auto-correlation function is not properly identified, then velocity magnitudes evaluated may not be accurate. Lourenco and Krothpalli (1995) have assessed errors in velocity and vorticity resulting from this and offer a number of different numerical schemes to improve the identification of the peak location, though no explicit values are provided.

Adrian (1996) reports that with images recorded on high resolution film using optimum lighting conditions, an accuracy of 0.1% to 1% may be achieved in velocity results, which is comparable to the accuracies offered by advanced laser-Doppler anemometer systems. Buchhave (1992) reports that errors of between 1 and 10% of the maximum flow velocity may be present in P.I.V. results obtained with all-numerical processing, akin to the one used in this work. Systems with hybrid optical/numerical processing methods or all optical processing methods offer similar or slightly better accuracies in the measured particle image displacement.

2.6 PARTICLE TRACKING VELOCIMETRY

2.6.1 Introduction

Many of the considerations involved in the measurement of fluid flow processes using particle image velocimetry are also pertinent for particle tracking velocimetry (P.T.V.). Adrian (1991) describes P.T.V. as a type of 'low-image-density P.I.V.' technique, since the number of particles per interrogation region in a image is far fewer than in P.I.V. images. However, the essential difference between the two methods is that a P.T.V. image contains streak lines which represent the trajectory of particles over a typical time interval. The velocity magnitude is evaluated by measuring the length of the streak and dividing this by the time interval.

In order for P.T.V. to be successful, the particle images must not contain overlapping streaks, which could cause ambiguity in the measurement process. At the same time, the particle streak should not be truncated, and this is ensured by employing a sheet of laser light with a thickness which takes the out-of-plane velocity of the flow into account. Therefore, the technique is very practical for the quantitative visualisation of two-dimensional flows, but difficulties can arise when the method is applied to complex three-dimensional fluid flows with large out-of-plane velocity components, due to shortened streak lines in the captured images. Ideally, the laser light sheet should be as thin as possible.

P.T.V. images are captured either by photography or by using video techniques. As with P.I.V. images, the use of video recordings can restrict the application of the method to the study of low-speed flows due to fixed video frame rates, but the convenience of digital recordings means that this is the most popular way of capturing images. At the same time, the resolution of the video camera used is also an important factor, since low resolution images will contain poorly-defined particle streaks.

From a given particle streak in a two-dimensional P.T.V. image the magnitude of two velocity components can be evaluated without difficulty, but a 180° ambiguity is present in the results if the streaks are continuous. For very low speed flows, it is possible to determine the direction of the streaks by comparing two or more successive images, but this can be impractical or inaccurate for flows with higher velocities, where large changes in the flow are present between successive frames. In such cases, the streaks can be encoded in way that defines the starting point and the end point of the line, for example a dot-dash arrangement, and the direction can be deduced from this. This can be achieved either by pulsing the laser or by employing a rotating chopper-wheel to chop the laser beam. During postprocessing the encoded line is replaced by an arrow representing velocity magnitude and direction.

Two-dimensional particle tracking velocimetry techniques have been used in many studies to investigate flows in I.C. engines. Khalighi and Huebler (1988) and Khalighi (1989) report an automatic analysis technique for processing P.T.V. images to determine velocity information. The particle streaks were encoded in a 'dot-dot-dash-dot' pattern using an acousto-optic modulator, with 'dot-dot' representing the source of the processed vector. An image processing system was developed to identify the coded pattern and calculate velocity. Similar methods have been applied by Marko and Rimai

(1985) and Adamczyk and Rimai (1988) among others to study flows in I.C. engines.

Three-dimensional P.T.V. systems have also been developed and applied to investigate engine flows. These systems offer the advantage of being able to measure all three velocity components of a particle simultaneously, and therefore allow the instantaneous three-dimensional flow structure to be determined. Ensemble-averaged results can be obtained by interpolating instantaneous results from many cycles onto a regular grid, and then calculating the average of these.

Adamczyk and Rimai (1988) recorded the three-dimensional flow field inside the cylinder of a model engine using two video cameras positioned orthogonally to each other. The entire cylinder volume was illuminated with light from an argon-ion laser, and the laser light was intensity-modulated by a Bragg cell and an aperture to generate encoded tracks of the seeding particles in the flow. The output from each video camera was combined onto a single video frame using a video mixer.

During the reconstruction procedure, particle tracks in each image on a frame were matched and a mathematical transformation was applied to reconstruct the flow and to calculate all three velocity components of the particle track. A detailed mathematical analysis of the reconstruction procedure is provided in Adamczyk and Rimai (1988). A similar method was applied in the present study, and the system used will be described in greater detail in the following sections. Further details of stereoscopic methods are provided in articles by Adrian (1991), Saneyoshi et al (1991) and Prasad and Adrian (1993).

2.6.2 The Motored Optical Research Engine

The in-cylinder flow inside a low-speed motored optical research engine was investigated using stereoscopic particle tracking methods. The engine rig was a model of a motored internal combustion engine, with working inlet and exhaust valves, and a moving piston. The arrangement of the engine was designed for maximum flexibility, and allowed different cylinder head designs to be quickly fitted onto the rig. Figure 2.15 shows two different views of the rig. In order to allow maximum optical access into the engine, a transparent glass tube was used as the engine cylinder and the piston crown was produced from transparent Perspex, permitting laser access into the cylinder through the piston. Cylinder bore sizes, piston sizes and engine

stroke could all be changed quickly and without difficulty, to simulate any desired engine configuration.

The optical engine consisted of a motor-driven variable stroke crankshaft mechanism which was used to operate the extended piston. The camshafts on the engine cylinder head were driven by a stepper motor connected to an electronic control unit. When operational, the valve train was synchronised with the crankshaft by an electronic link established between the two. There was no mechanical connection between the cam and the crank, so that the valve timings could be adjusted without affecting the crank timings, before the electronic link was switched on. The engine speed was varied using a speed control panel.

The engine was operated at speeds up to 100 r.p.m. during the current investigation. Instead of air, a high density gas - sulphur hexafluoride (SF_6) - was used under pressurised inlet conditions as the working fluid. By applying dynamic similarity, high speed engine flows were modelled at greatly reduced engine speeds, since SF_6 has a high density and low kinematic viscosity compared to air. Some properties of SF_6 gas are provided in Table 2.4.

Density (20°C, 1 bar):	6.07 kg/m^3
Specific gravity, gas (air = 1):	5.04
Dynamic viscosity (0°C, 1.01 bar):	1·4 x 10^{-5} Pa.s
Kinematic viscosity (0°C, 1.01 bar):	2·3 x 10^{-6} m^2/s
Isentropic exponent: (specific heat ratio)	1.08 (30°C, 1 bar)

Table 2.4 Some physical properties of sulphur hexafluoride (SF_6) gas

The main advantages of implementing low speed dynamic similarity modelling for I.C. engine flows have been mentioned by Ma et al (1986 a). Gas flow in high speed engines during the induction and compression strokes is highly complex and the measurement of velocity and turbulence characteristics requires very expensive equipment, and can be labour-intensive. Steady flow models and dynamic water analog rigs may provide useful information about flow in the induction stroke, but the influence of intake flow on turbulence at the end of compression is difficult to determine from these techniques. Modelling high speed gas motion at considerably lower

speeds allows standard video apparatus to be used to record the flow processes from T.D.C. induction to T.D.C compression, and this information is very valuable in assessing the design features of cylinder heads.

Ma et al (1986 a) have discussed the main criteria for producing a dynamically similar flow inside a low speed motored engine. Three non-dimensional groups are important: Reynolds number, Mach number and the specific heat ratio (γ). The role of each group is briefly described below.

Reynolds Number - The definition of Reynolds number is:

$$Re = \frac{\rho V d}{\mu} \qquad (2.13)$$

where for flow in an I.C. engine, ρ is the fluid density, V is the engine speed in m/s or a characteristic fluid velocity, d is a characteristic dimension, and μ is the dynamic viscosity of the fluid.

Hence, if a similar Reynolds number is to be achieved at a low engine speed, then the working fluid should have a low kinematic viscosity. Ma et al specify that fluorocarbons satisfy these criteria and have been successfully used to obtain velocity reductions of between 6 and 7, and greater reductions by pressurising the gas at inlet. Investigations into in-cylinder motion using Freon-12 gas are reported in the same article and in Ma et al (1986 b). The reduction factors for the present study are given in Appendix 3.

Mach Number - Since maximum velocities inside an engine cylinder occur within the intake jet and would rarely exceed Mach 0.5 at high engine speeds and wide-open-throttle operating conditions, then Mach number equality is not important when modelling engine flows at low speeds and part load conditions (Ma et al (1986 a)). Even at conditions of choked flow in the engine due to flow reversal into the inlet ports caused by the cylinder pressure being higher than inlet pressure, Mach number similarity is not necessary, as the turbulence generated by such a flow will decay due to the following inlet flow. Ma et al estimate only a 6% error in the dynamic head by assuming incompressible flow, even at gas velocities as high as Mach 0.5.

Specific Heat Capacity Ratio (γ) - The specific heat ratio of a gas does not greatly affect the properties during induction, since there is little temperature change throughout the stroke. It does, however, play an important role in influencing the properties of the gas during the compression stroke,

particularly pressure and temperature. If the gas chosen to model air flow does not have a similar value of γ, then pressure and temperature will rise differently from air as the flow is compressed. The dynamic viscosity, μ, is strongly dependent on temperature and critical temperature, so that viscosity variation during compression may not be modelled correctly.

It is possible to adjust the value of γ by altering the mixture proportions of two or more modelling gases, though this can be costly as mixtures which give γ values similar to air require expensive gases. Ma et al (1986 a) employed Freon-12 as the working fluid - $\gamma = 1.14$ compared to 1.4 for air - and accept that variations up to 23% in Reynolds number will occur towards the end of compression, which will affect modelling of the smallest scales of turbulence. However, they point out that the process of generation of large scale eddies is unaffected, if the Reynolds number is matched at inlet conditions.

2.6.3 Flow Visualisation - Image Capture and Recording

The in-cylinder gas flow was seeded with hollow silicate glass spheres of around 100 μm diameter. Since each particle had the equivalent mass of a solid 1 micron diameter glass particle, the spheres would follow the flow motion faithfully. Figure 2.16 illustrates the system setup for image recording. A 5 Watt argon-ion laser (model: Coherent Innova 90) was used as the light source. The laser beam was converted to a laser sheet of 3 mm thickness using a system of lenses. A 45° mirror positioned directly underneath the piston reflected the laser sheet through the Perspex piston crown, to illuminate the required plane inside the engine cylinder. Figure 2.17(a) shows the geometry of the cylinder head combustion chamber, and the actual optical setup is pictured on Figure 2.17(b).

The flow recording system depicted on Figure 2.16 consisted of two C.C.D. video cameras (Siemens K230), a half-frame format video multiplexer (A.E.A. Technology Ltd. Model 7830), a timecode generator (Imp Electronics Model V9000A), a Super V.H.S. video recorder (Panasonic Model AG-7330-B) and a stereoscopic television system (A.E.A. Technology Limited). The C.C.D. video cameras were positioned to record the flow stereoscopically.

The output from the left and right cameras was connected to the corresponding video multiplexer inputs. The video multiplexer placed the images from each camera next to each other to show both cameras views together, and the multiplexer output was sent to a timecode generator, which

stamped a timecode onto each frame of the S.V.H.S. video recordings. A three-dimensional view of the in-cylinder flow could be observed on the stereoscopic T.V. monitor by viewing through polarizing glasses.

2.6.4 Image Grabbing and Flow Velocity Evaluation

Capture of Images from Video

The apparatus used to grab images from the flow visualisation video recordings was developed by A.E.A. Technology Limited, Harwell, U.K. The system comprised a S.V.H.S. video recorder, a timecode reader, a digital framestore (C.E.L. Electronics, Model P147-20), a video de-multiplexer, and a stereoscopic television system. An Apple Macintosh IICX personal computer was fitted with a video input card to capture video images of the flow. Figure 2.18 presents the arrangement of the image grabbing system.

During replay, the signal from the video recorder was connected to the time code reader, which recognised the timecode on each video frame. The output from the timecode reader was entered into the digital framestore. This was used to automatically grab desired frames from the video, and also contained controls to introduce enhancement effects into the video images. A framestore control switch was connected between the timecode reader and the framestore, and was used to observe the odd and even fields of an image either separately or together. The de-multiplexer unit separated the left camera and the right camera views on the video images, so that each camera view could be seen separately on the left and right screens of the stereoscopic T.V. system. The output from the framestore was connected to the video input card in the Apple Macintosh computer. The required images from the flow visualisation video were grabbed and saved in TIFF format using the QuickCapture™ software for further image processing and velocity evaluation.

Image Analysis and Velocity Evaluation

The captured images were processed using software packages installed on the Apple Macintosh computer. Figure 2.19 describes the image analysis and data processing methods employed to determine three-dimensional velocity results from the captured images. A transparent layer was applied over the image containing particle streaks, using the UltraPaint™ software package. This allowed any lines drawn over the image to be saved

independently, and was similar to the method of using tracing paper to copy drawings.

Matching particle tracks were identified manually on each pair of camera images. The tracking procedure involved drawing a line over the length of a chosen streak in the image, as shown on Figure 2.19. Careful attention was required at this stage, as mistakes in the track position and length could lead to errors in the velocity magnitudes and directions calculated in subsequent stages. During the tracking process, a particle streak was selected from the left hand camera image, and a line drawn over its length. The same particle streak on the right hand camera image was then identified and tracked. The direction of the streak in a particular frame was determined by comparing the flow in preceding and successive frames. Direction information was recorded by drawing the tracks such that the starting point of the line represented the source of the vector, and the end point of the line therefore determined the magnitude and direction of the flow. This process was repeated until all well-defined streak pairs in the image were tracked. The picture was then saved in PICT format.

The particle track images of the two camera views were then examined using the Super 3D™ software, as seen on Figure 2.19. In order for a three-dimensional image of the flow to be constructed from the two 2D images, it was necessary to translate both images along the horizontal axis so that they would be superimposed. The co-ordinates of lines in the images were determined with Super 3D™, and this information was utilised to calculate the number of pixels each camera view would be translated by. The image data was then saved in text format so that the translation could be applied using the Microsoft Excel™ spreadsheet package.

The three dimensional particle position and velocity data was calculated by a spreadsheet containing the required data and formulas. The spreadsheet required the input of data relating to the camera characteristics and system setup. Some of the characteristics have been listed in Table 2.5.

The formulae used to calculate the 3D particle track co-ordinates and velocities are provided in Appendix 1. Essentially, the modified x- and y- co-ordinates of each pair of left hand and right hand particle tracks were firstly divided by the scaling ratio. These values together with the system parameters given in Table 2.5 were then employed to calculate the co-ordinates of the head and tails of the three-dimensional particle tracks. Velocity magnitudes along the x-, y- and z-directions were calculated by

dividing the length of the 3D particle streak with the time interval for each image, which was fixed at 20.0 ms.

Focal length of cameras (f):	16.0 mm
Measured camera separation (t + 2h):	92.0 mm
Camera convergence distance (u):	450.0 mm
Calculated lens offset (h):	1.64 mm
Calculated lens separation (t):	88.73 mm
Calculated lens back focal distance (v):	16.59 mm
Scaling ratio (pixel no./target mm):	92.05
Time integration interval (T):	20.0 ms
Camera constant (vt):	1472.0

Table 2.5 Some measured and calculated system parameters used to evaluate 3D particle positions and velocities

Using the calculated co-ordinates, a three-dimensional representation of the particle tracks was constructed with the aid of Super 3D™ software. The resulting image could be rotated about different axes, to allow the tracks to be viewed from any chosen perspective and in 3D space. The velocity magnitude results could also be replotted as vectors with appropriate plotting software, such as UNIRAS™ or Mathematica™.

2.7 SUMMARY

Four fluid measurement techniques have been used in the present study to examine engine in-cylinder flow motion: laser-sheet flow visualisation, laser-Doppler anemometry, particle image velocimetry and stereoscopic flow visualisation. At the same time, these techniques were applied to the study of three distinctive types of flow motion, viz. (i) steady liquid flow through an engine model, (ii) a dynamic water-analog rig to simulate transient flow during the induction stroke of a four-stroke engine, and (iii) unsteady gas motion inside a motored optical research engine during the induction and compression strokes.

Each of these methods provide an individual insight into the nature of flow in an internal combustion engine, and are therefore equally valuable as

design tools for engine development. When used together, they are able to give the designer a more thorough understanding of the nature of engine flows, than may be obtained through the use of only one particular method. The results acquired through the application of the above techniques are described in the following chapters.

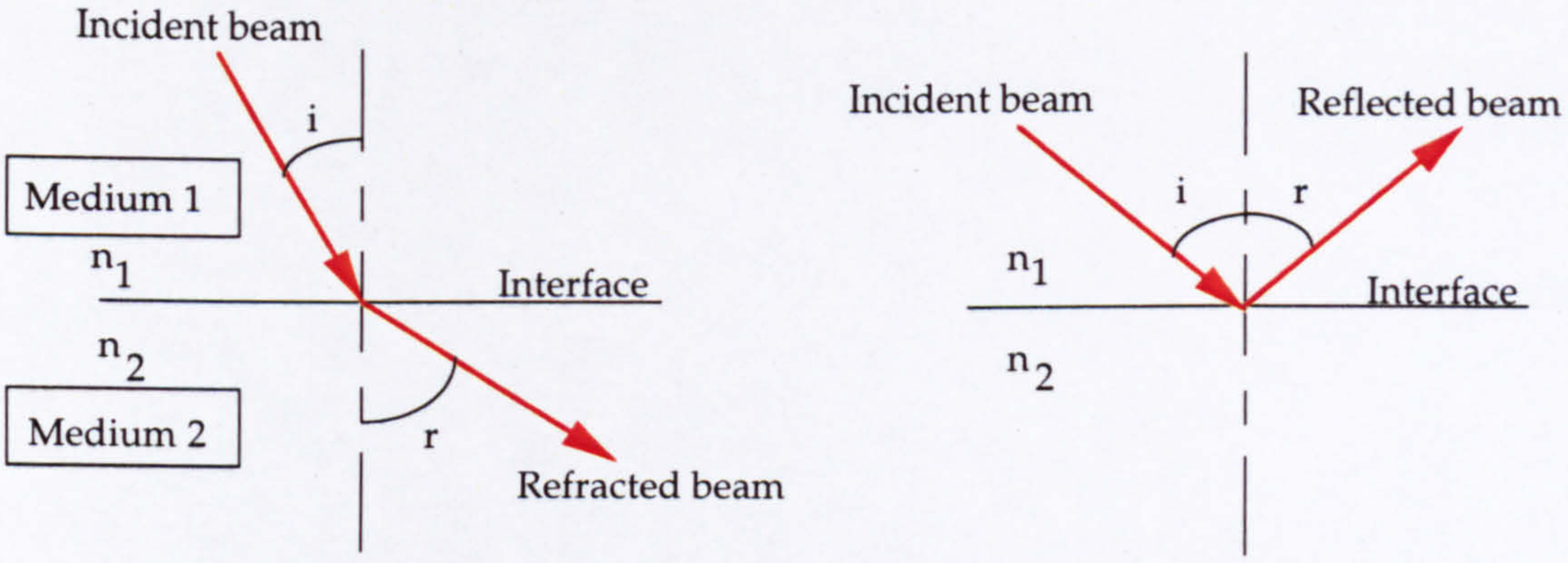

(a) (b)

Figure 2.1 Refraction and reflection of light rays

(a) light is refracted when incidence angle is less than the critical angle

(b) reflection of the beam occurs when incidence angle is greater than the critical angle

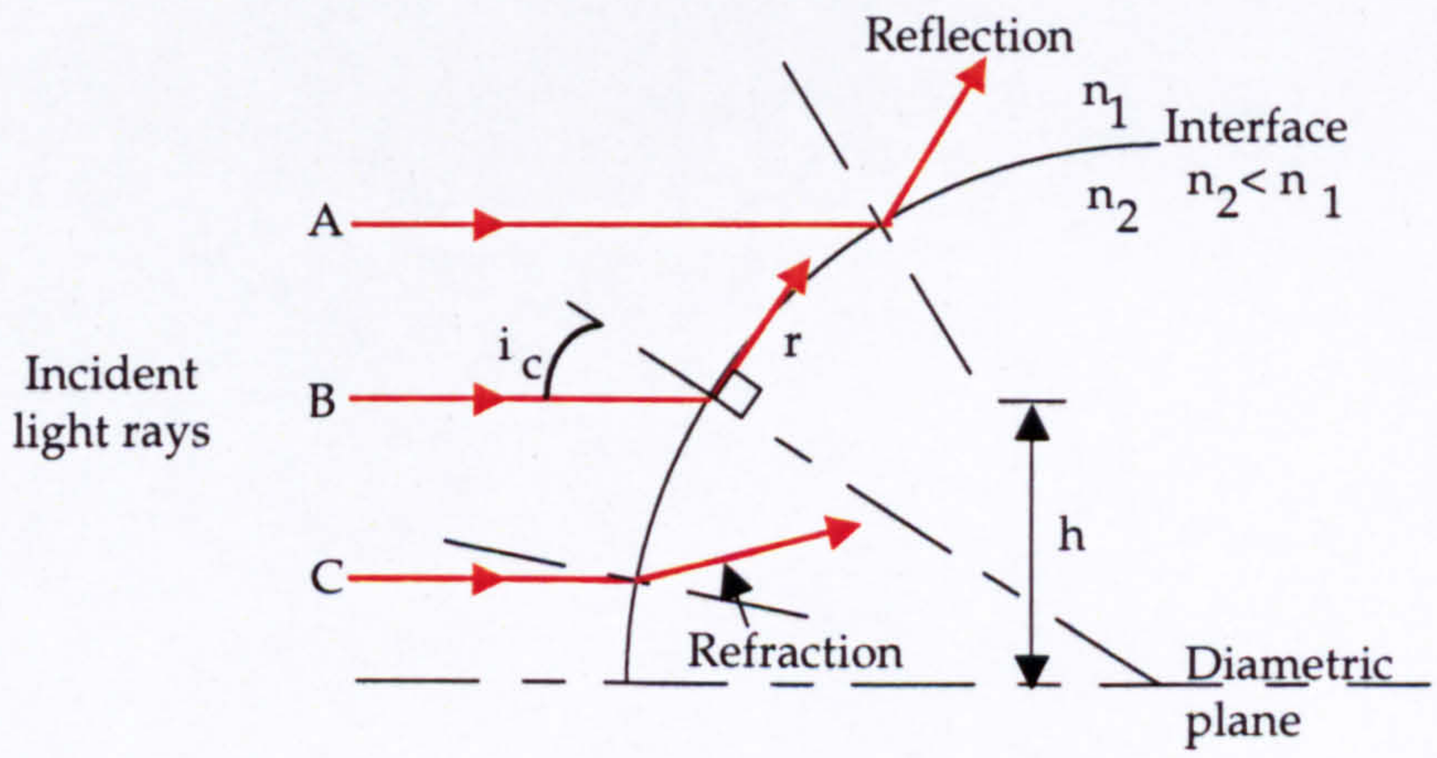

Figure 2.2 Refraction of light rays on a curved surface

Figure 2.3(a) Mould of engine inlet ports, combustion chamber and cylinder produced from rubber Vynamold material

Figure 2.3(b) Fusible alloy mould used to cast Perspex engine model

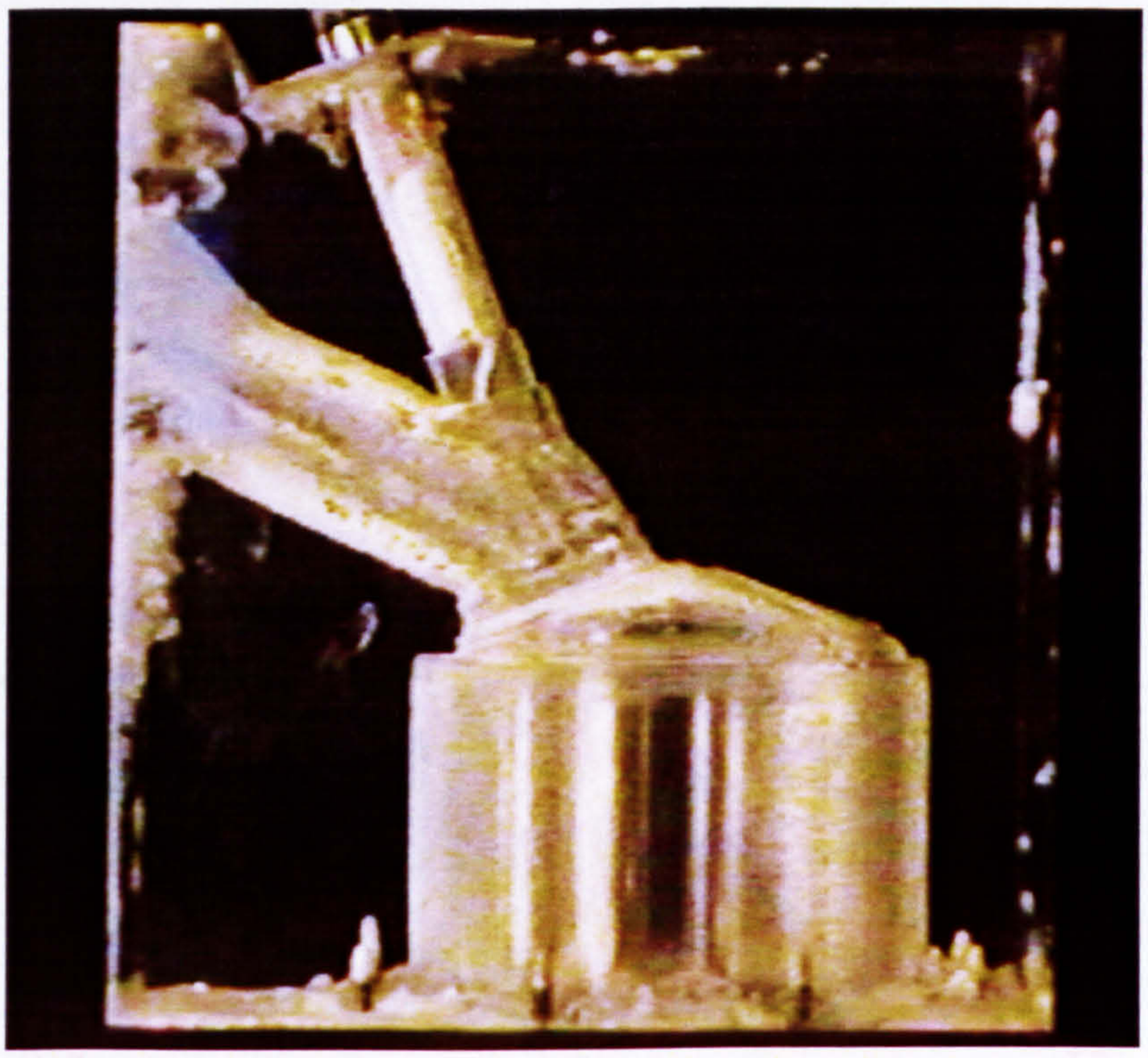

(a) Side View

(b) Front View

Figure 2.4 Perspex replica of the Ford Zetec medium output engine inlet ports and cylinder

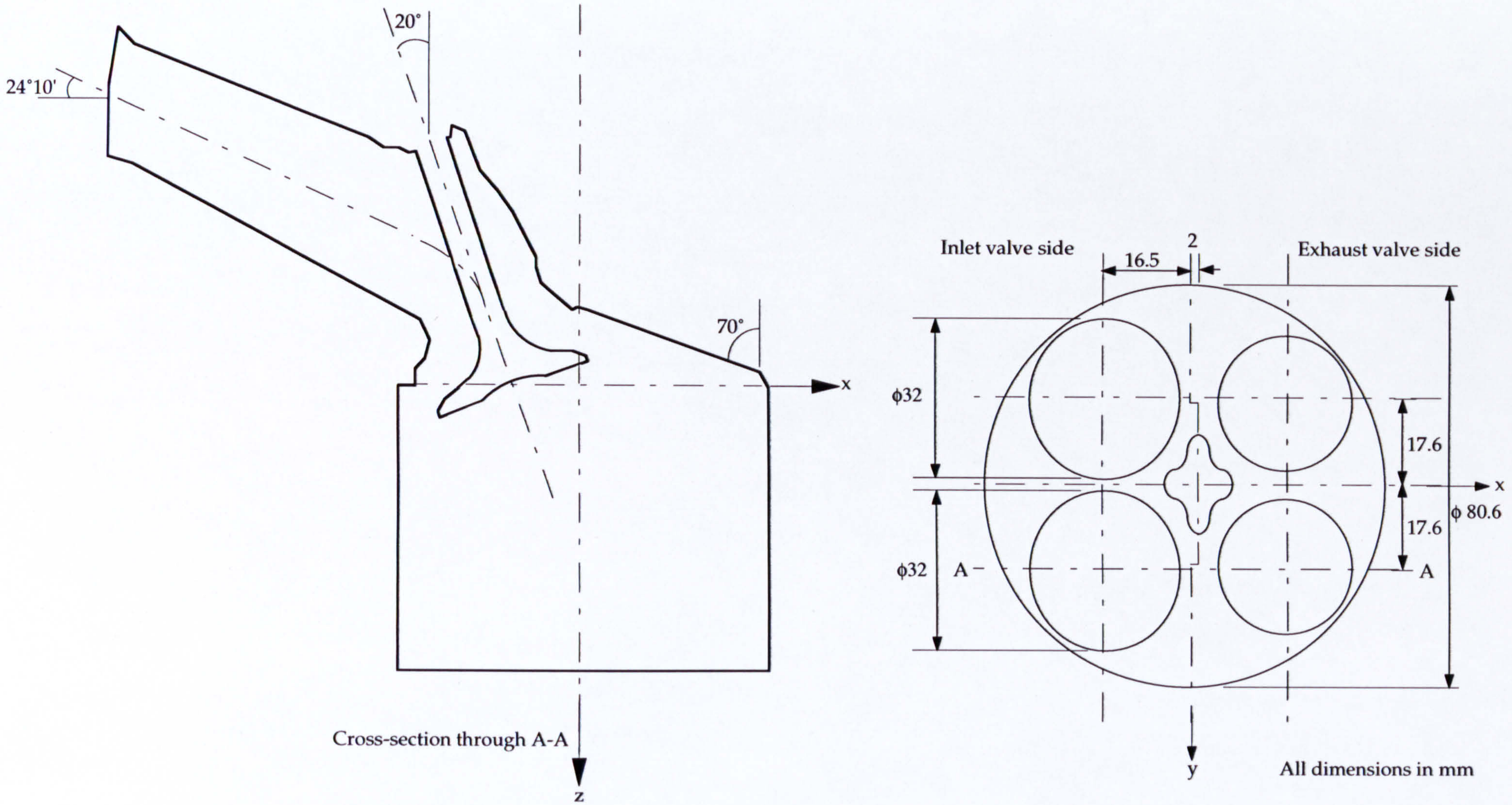

Figure 2.5 Outline of the Ford Zetec engine intake port in a vertical plane through the centre of one inlet valve and major cylinder head dimensions

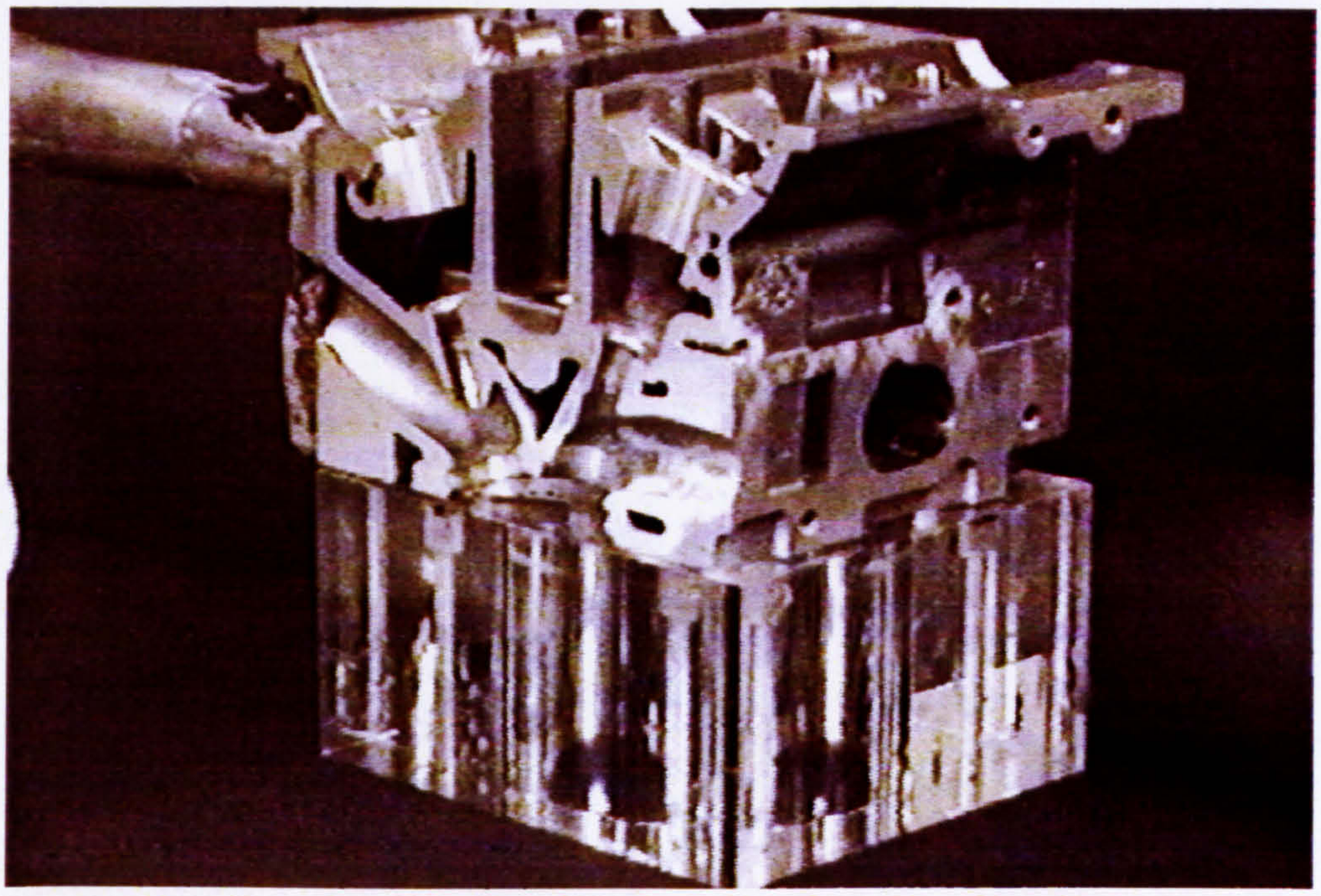

Figure 2.6 Engine model produced by mounting an aluminium cylinder head onto a Perspex cylinder block

Figure 2.7(a) Ford Zetec inlet port configuration with one straight port and one swirl port

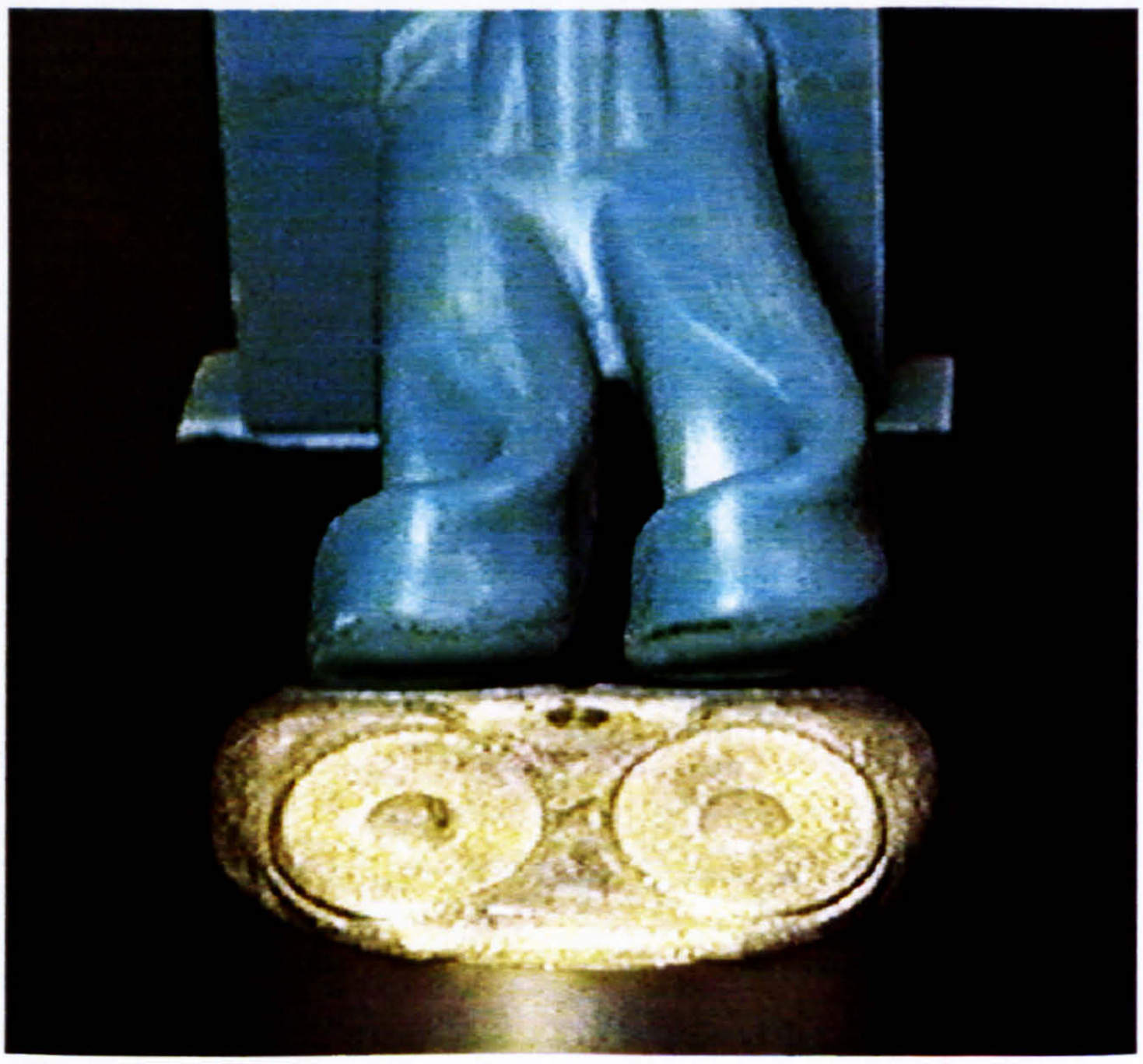

Figure 2.7(b) Ford Zetec inlet port configuration with twin swirl ports

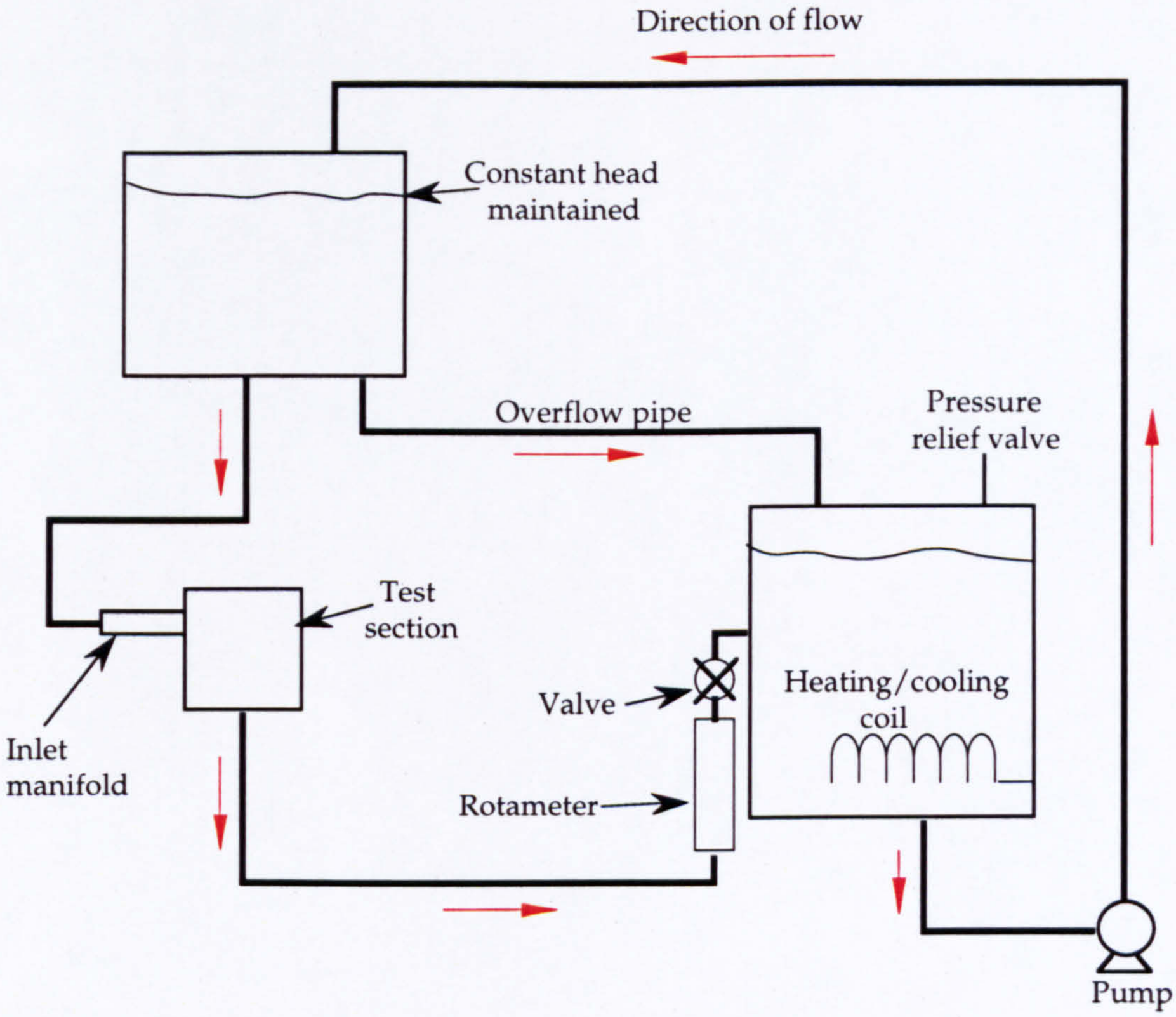

Figure 2.8 Schematic diagram of steady flow rig

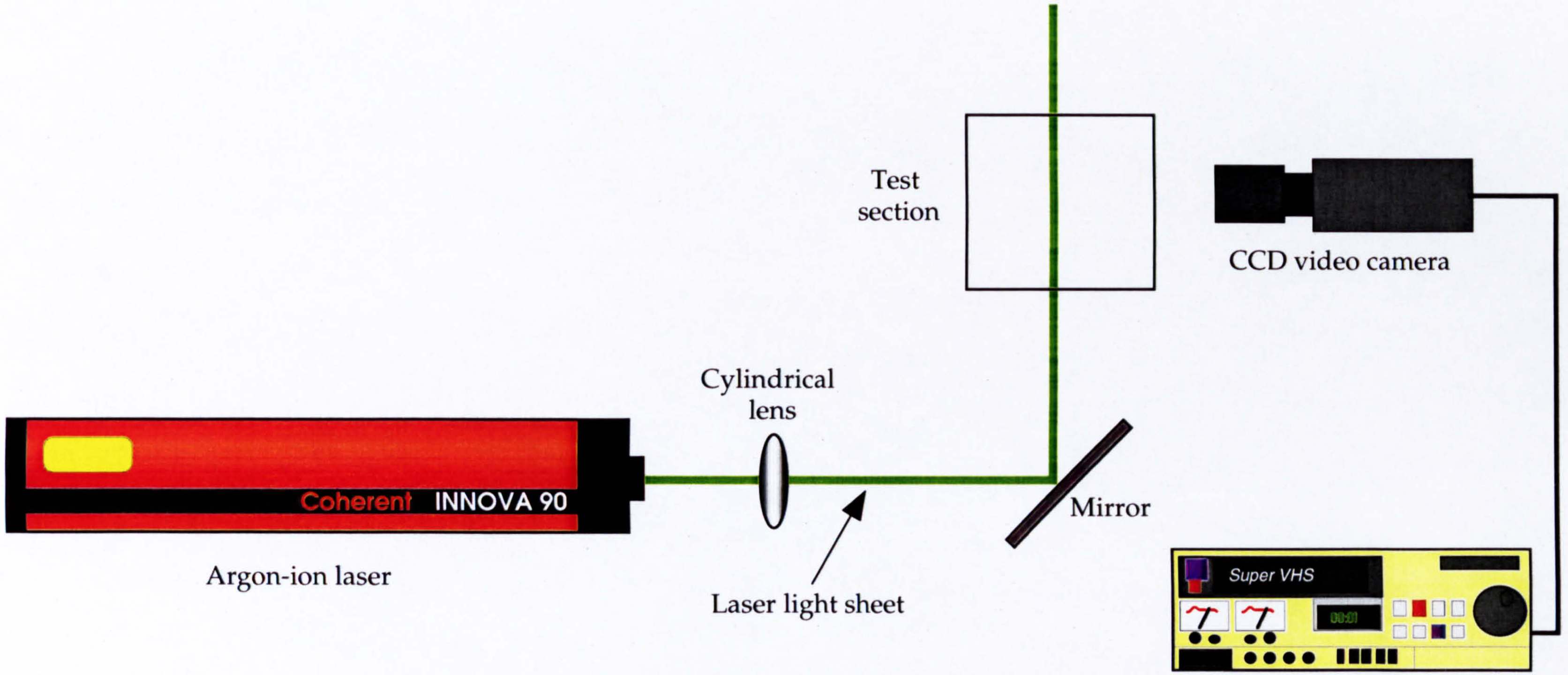

Figure 2.9 A typical experimental arrangement for laser-sheet flow visualisation

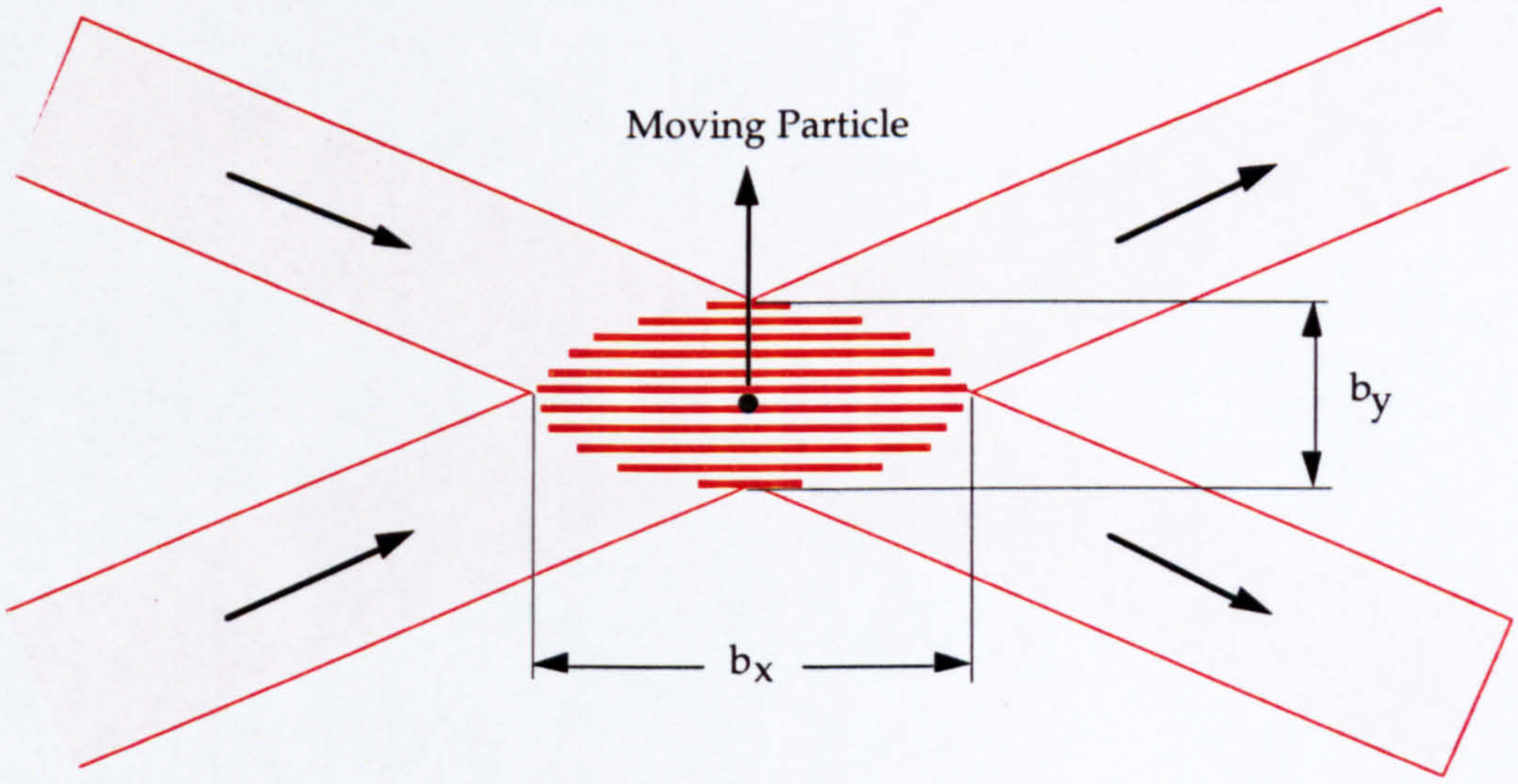

Figure 2.10 Interference fringe pattern produced at the intersection point of two laser beams

Figure 2.11 A typical Doppler Burst signal produced by a particle crossing the control volume

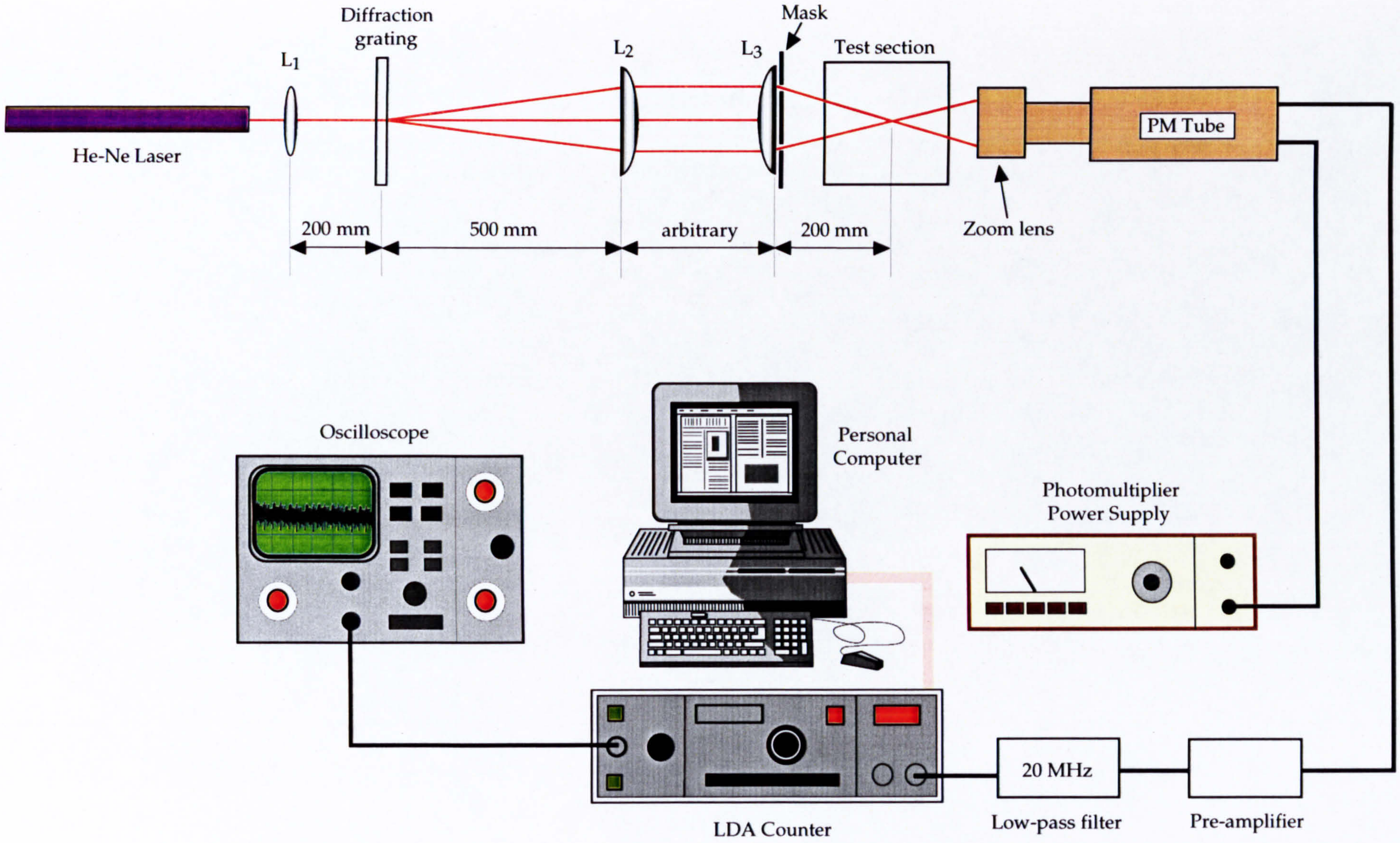

Figure 2.12 LDA optical and signal processing systems

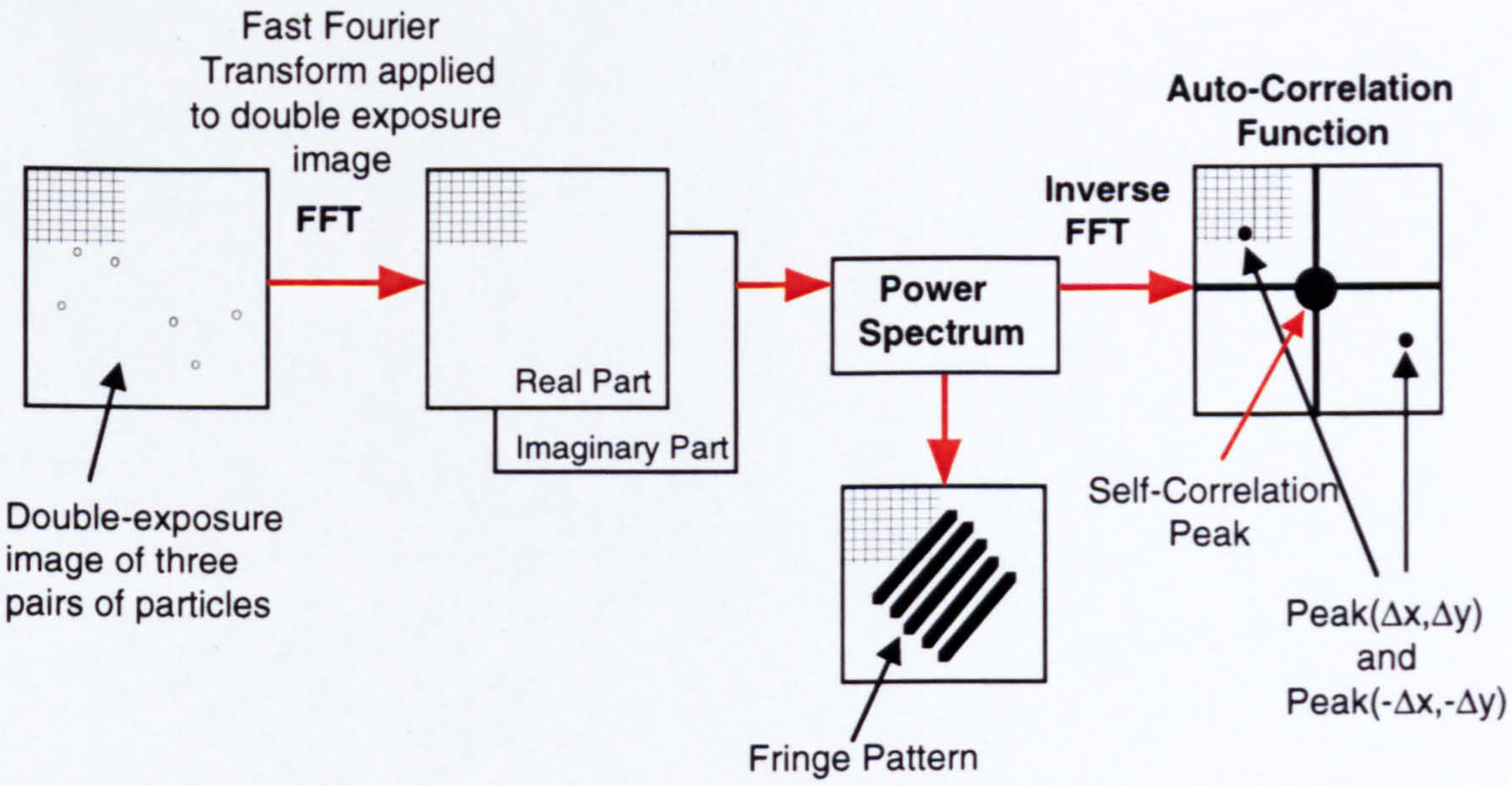

(a) The Auto-Correlation algorithm

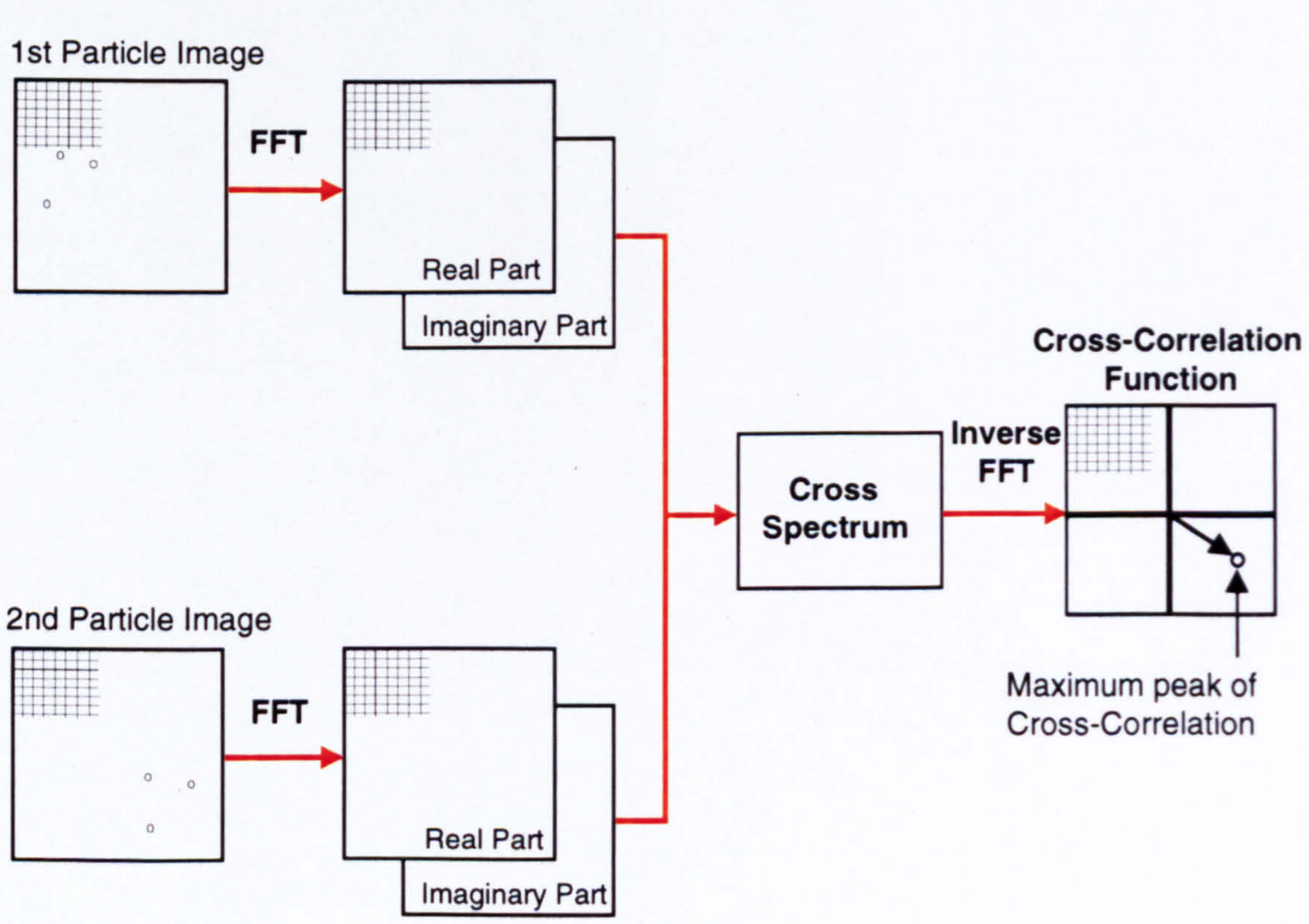

(b) The Cross-Correlation algorithm

Figure 2.13 Commonly used interrogation algorithms for P.I.V. processing
(Adapted from Rouland et al (1994))

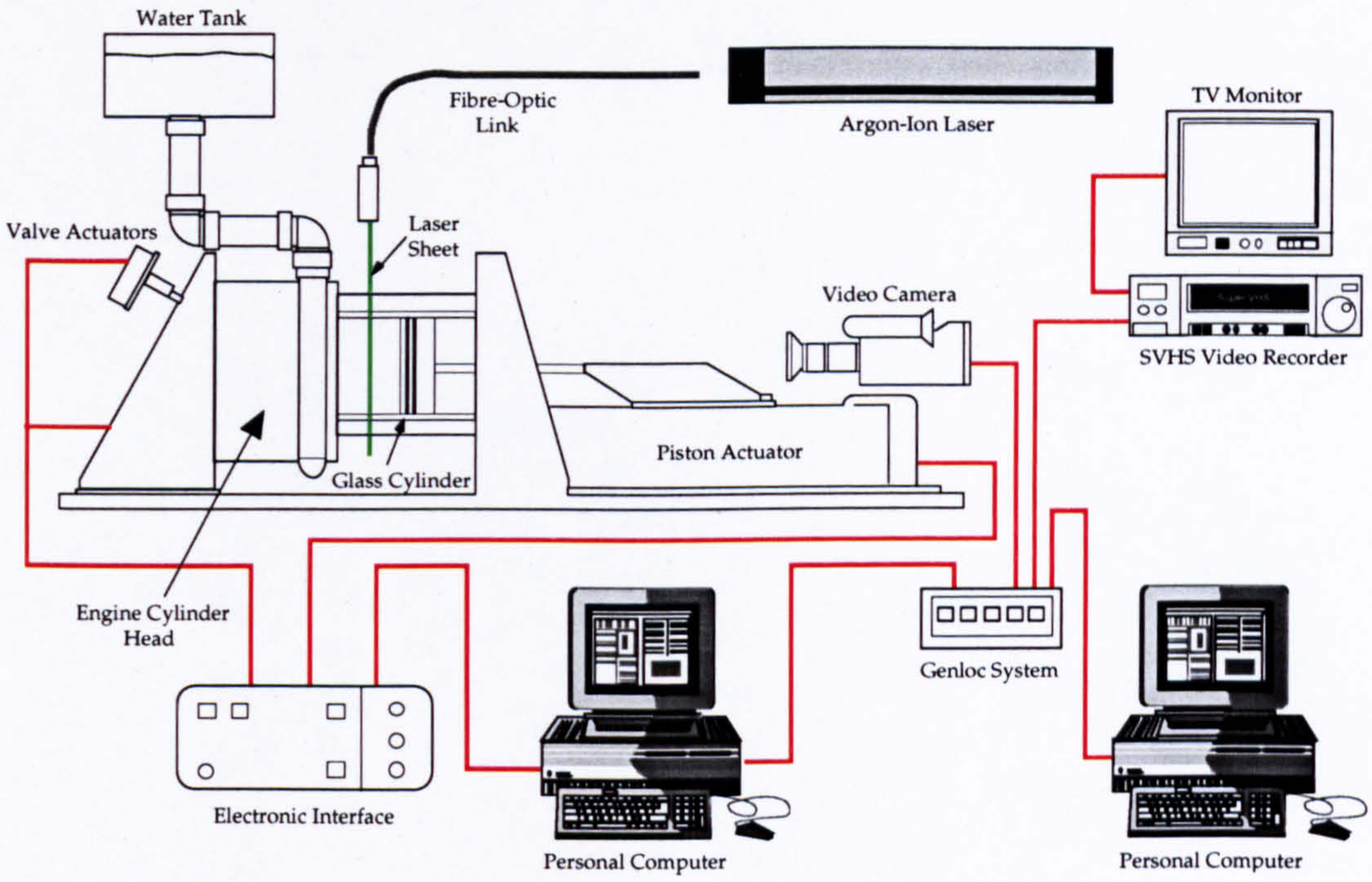

(a) Schematic diagram of the dynamic flow visualisation rig at the Department of Mechanical Engineering, University of Brighton

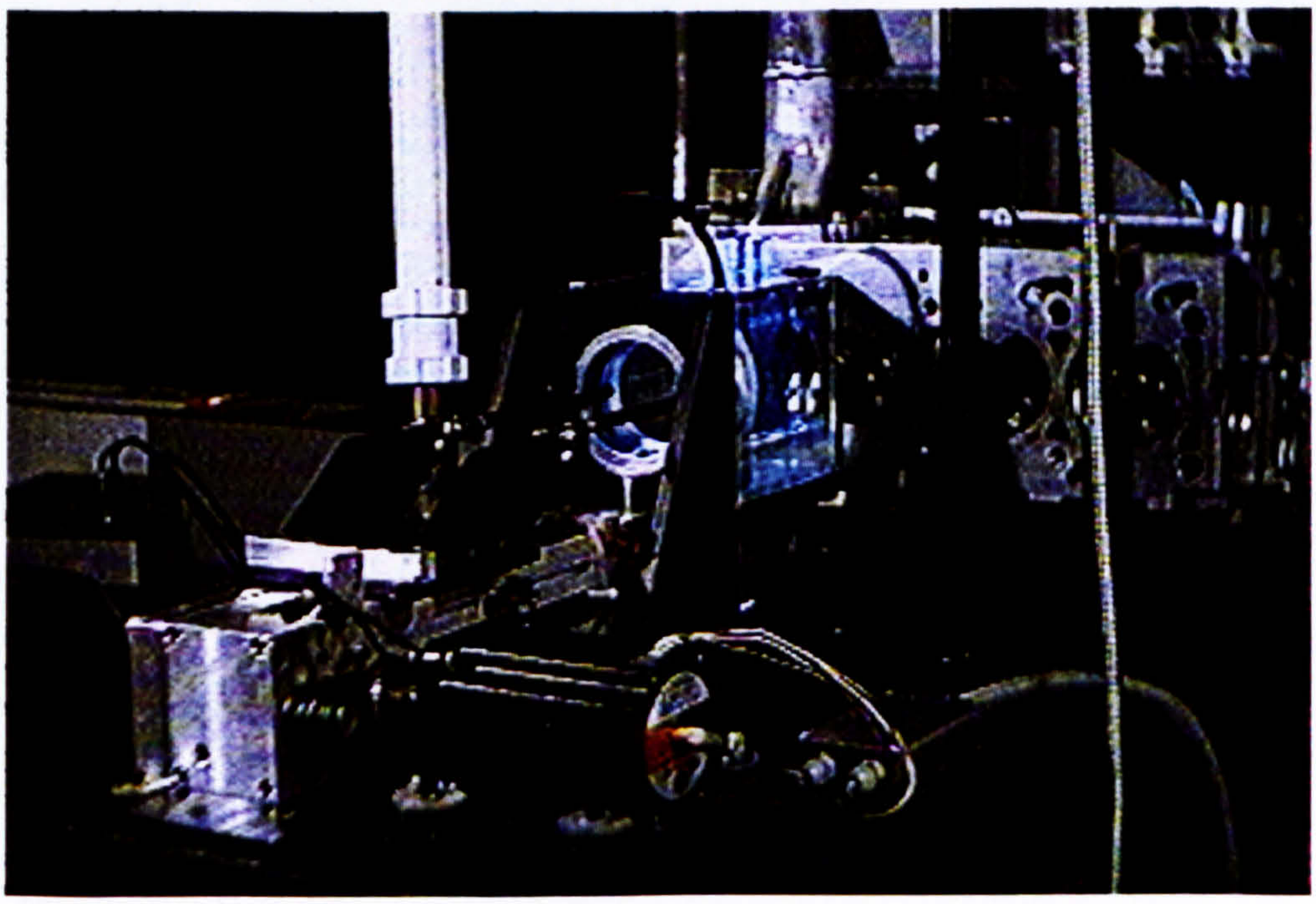

(b) Flow visualization rig with Ford Zetec engine cylinder head fitted

Figure 2.14 Experimental setup of the water analog rig used in the study

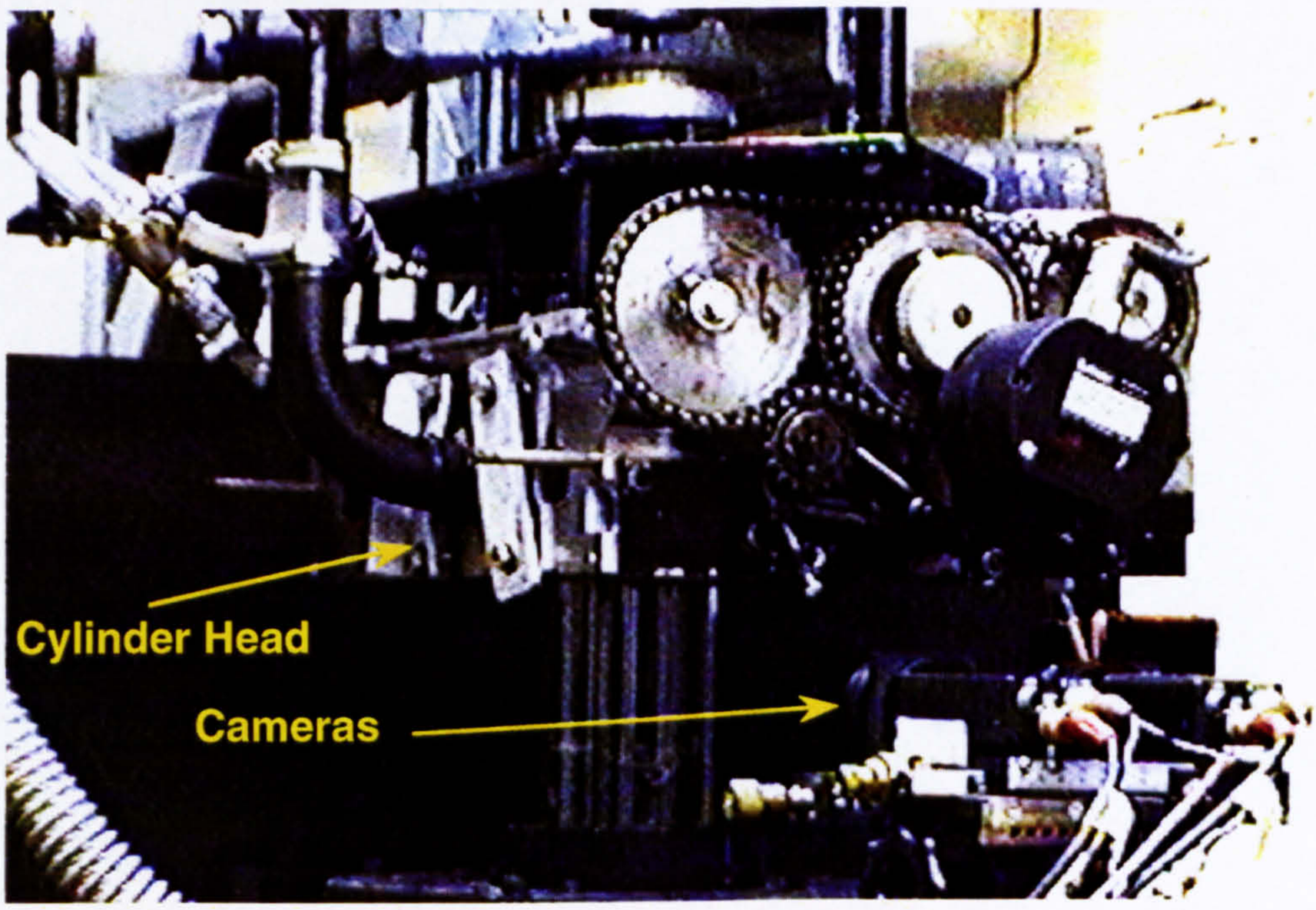

(a) View of optical engine showing cylinder head and stereoscopic camera position

(b) View showing glass cylinder and piston

Figure 2.15 The optical research engine fitted with a Ford Zetec engine cylinder head

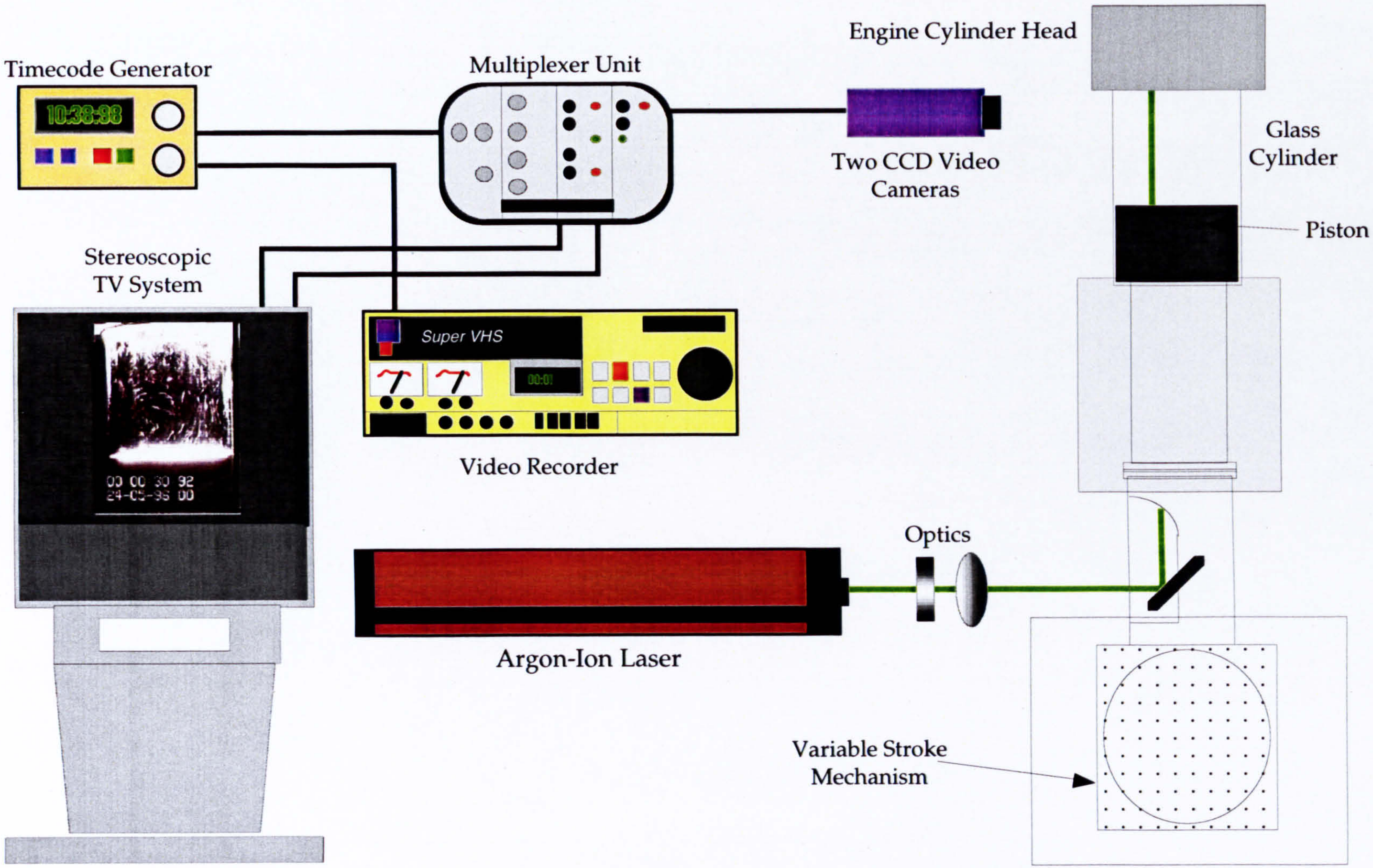

Figure 2.16 Arrangement of experimental equipment for stereoscopic image recording

Figure 2.17(a) Combustion chamber design of the Ford Zetec engine cylinder head used in the study

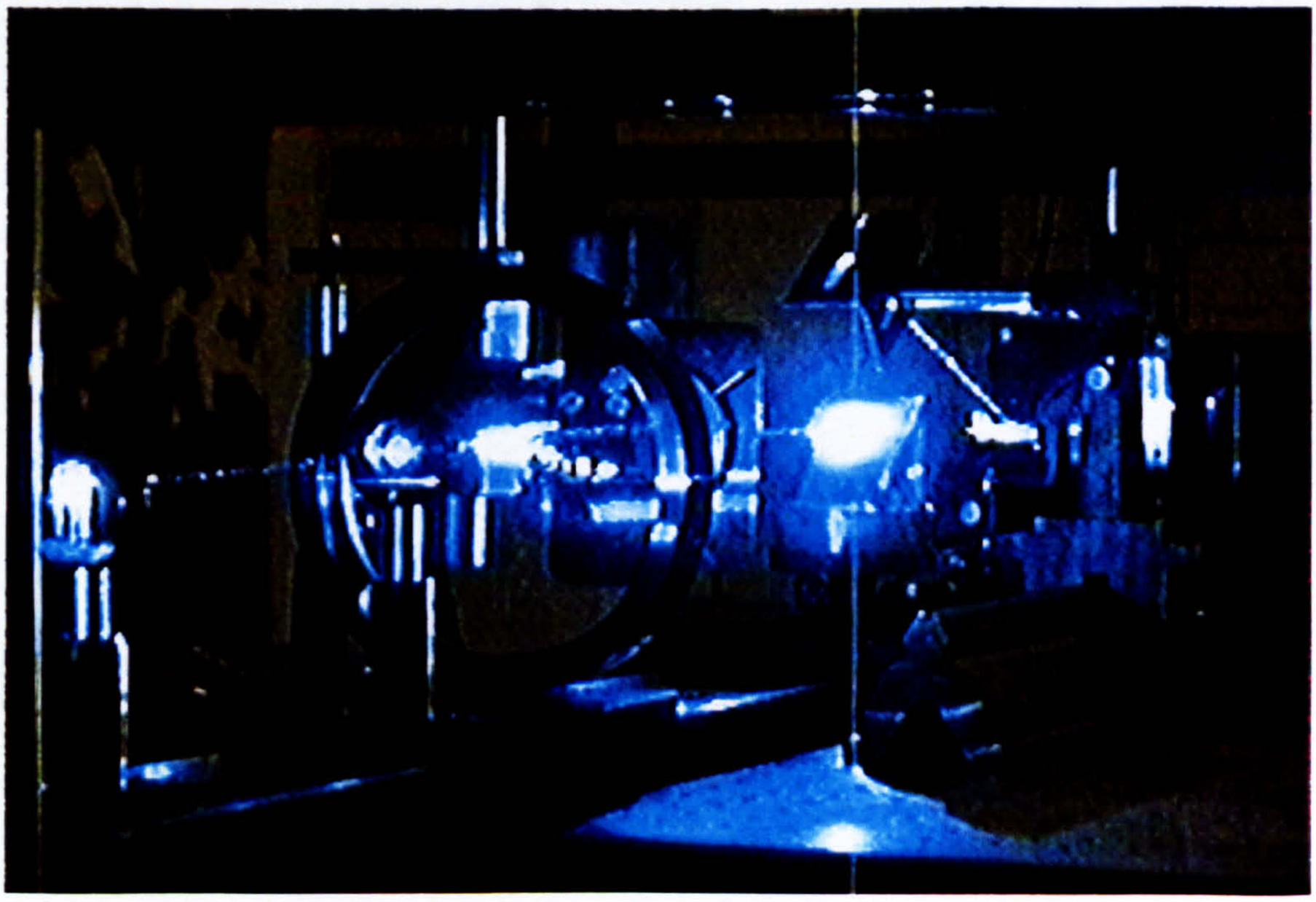

Figure 2.17(b) Photograph of the optical system setup

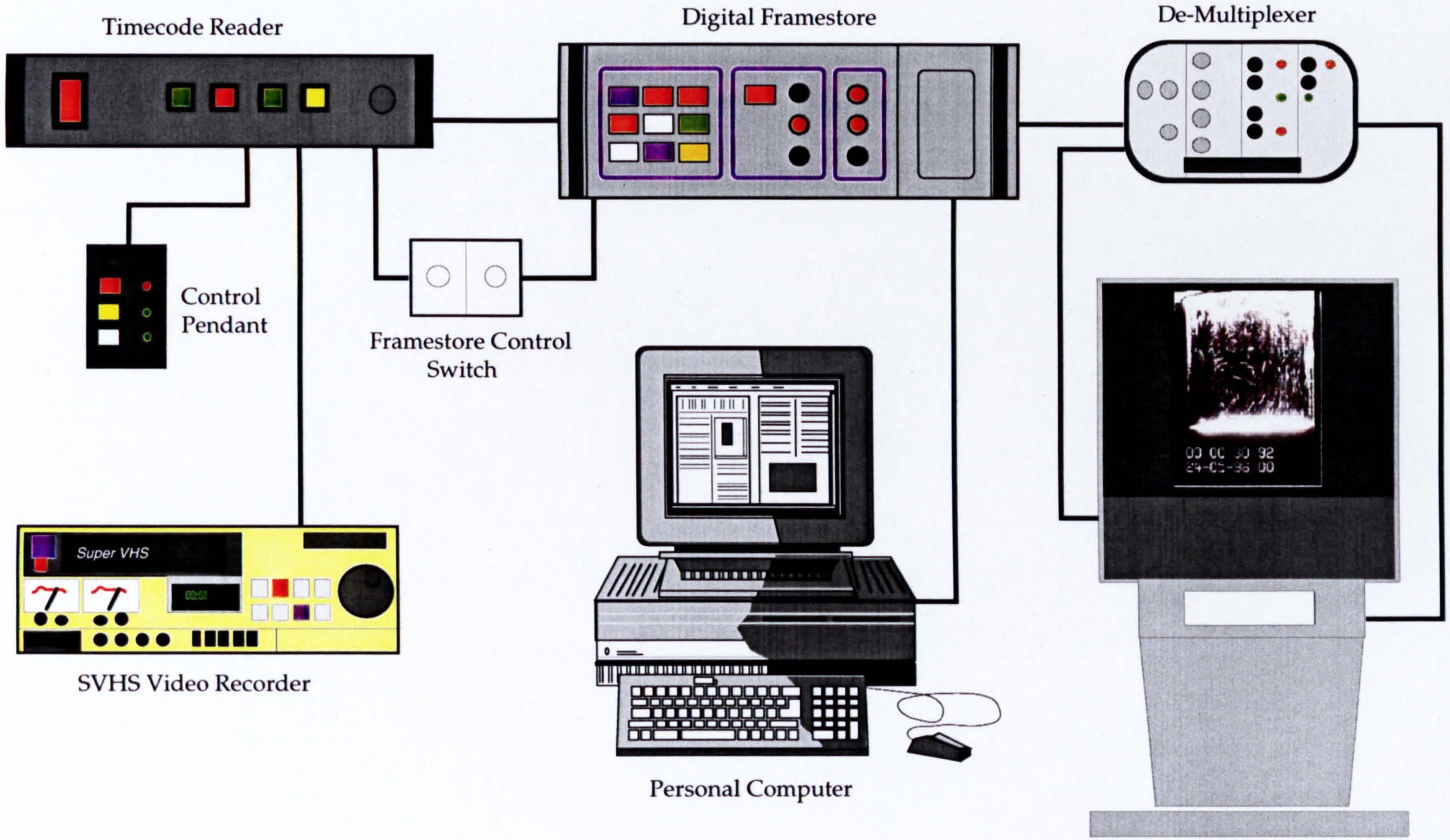

Figure 2.18 Experimental system for grabbing stereoscopic flow visualisation images from video

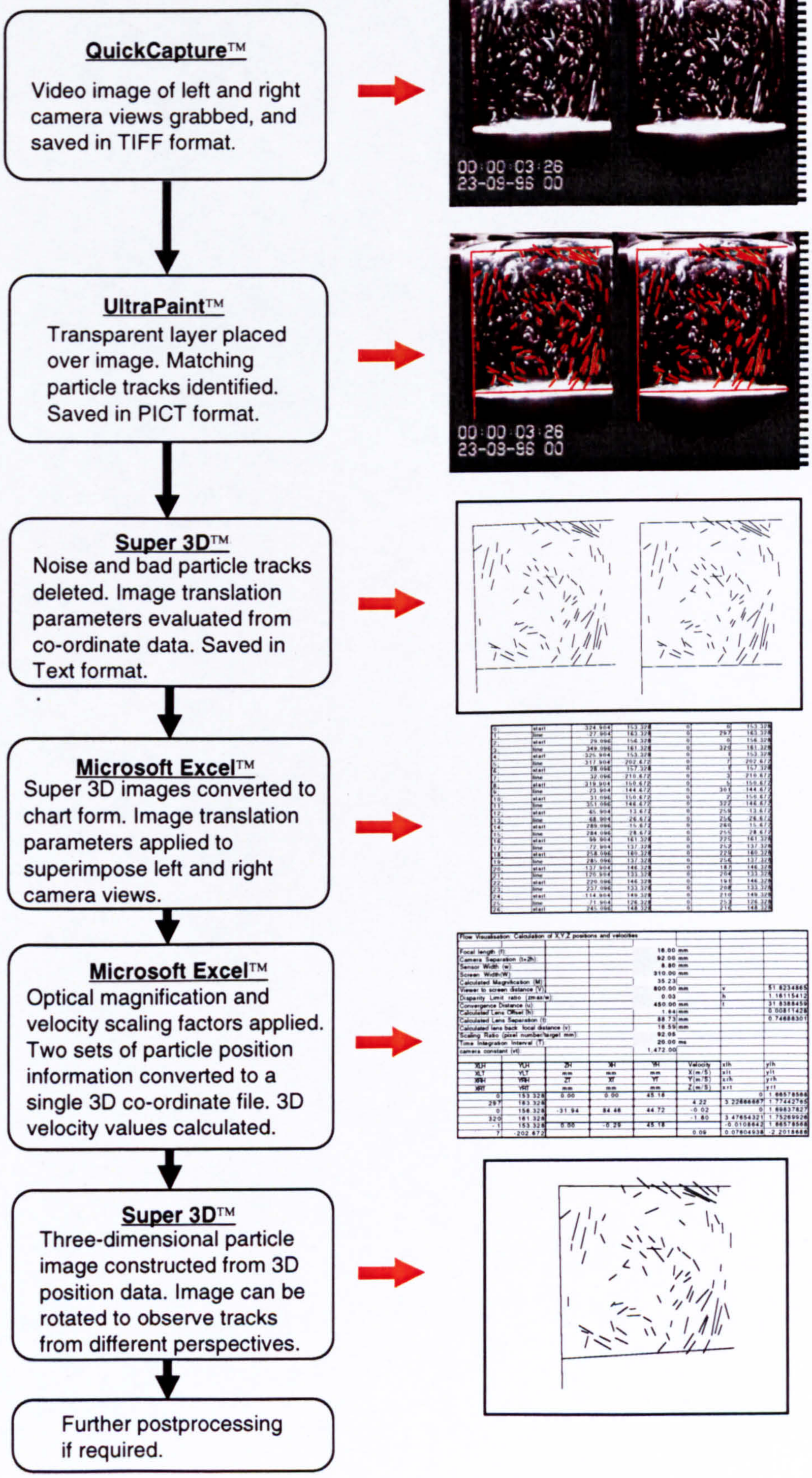

Figure 2.19 Image analysis and data processing procedure for stereoscopic flow visualisation

Chapter 3

STEADY FLOW STRUCTURE THROUGH DUAL-INTAKE PORTS WITH EQUAL VALVE LIFTS

3.1 INTRODUCTION

The behaviour of flow motion through the inlets ports of the 1.8 litre 'medium-output' Ford Zetec engine was examined experimentally under conditions of both equal and asymmetric fixed valve lifts. This chapter describes investigations performed under steady flow conditions with both inlet valves having identical lifts. Engine in-cylinder flows are highly three-dimensional and therefore flow visualisation and L.D.A. was applied in many different vertical and horizontal planes in order to acquire as full an understanding as possible of the effects of inlet port shape and inlet valve lift. It is anticipated that the results will be useful for the assessment of future engine designs and cylinder head concepts.

It should be noted that for the steady flow work in this and the following chapter, relatively few, if any, comparisons can be made with previously published work: the reasons for this are the relative lack of dual-intake port steady flow studies of of a similar detail to the present one. Steady flow investigations have been traditionally used in engine development to examine the breathing characteristics of cylinder heads, since results can be obtained quickly without complex and expensive equipment. Intake port designs are most commonly assessed using steady flow rigs to optimise pressure drop, discharge coefficients and flow coefficients as well as swirl and tumble ratios. These parameters in themselves provide a good indication of the likely combustion behaviour of an engine, when compared

to combustion data acquired from an engine dynamometer. However, current legislations calling for engines with advanced fuel economy and low emissions systems also require an understanding of the pre-combustion gas flow and turbulence behaviour in addition to the aforementioned parameters.

Previous steady flow studies have shown the similarities between steady and unsteady intake flow motion, particularly through the intake ports [Bicen et al 1985] and during the early portion of the induction stroke. Due to the lack of published experimental data for dual-intake port configurations it was decided to perform extensive investigations into the flow structure under steady flow conditions. The three-dimensional flow field inside the test section was analysed firstly by laser sheet flow visualisation in order to determine detailed qualitative information with regard to the influence of intake port design and inlet valve lift on in-cylinder flow structure. Measurements of ensemble-averaged mean and r.m.s. velocity were then performed by L.D.A., and the measurement planes, locations and flow velocity components were selected on the basis of results from the flow visualisation study. The main features of the flow processes observed through the use of both flow visualisation and L.D.A. techniques are discussed and the main conclusions are outlined at the end of the chapter.

3.2 FLOW VISUALISATION STUDY

The experimental procedure for the flow visualisation study has already been reported in the previous chapter and in Mahmood and Yianneskis (1994). Four fixed inlet valve lift settings were chosen to determine the effect of valve lift on flow structure; these were: (i) 2.5 mm, (ii) 5.0 mm, (iii) 7.5 mm and (iv) 10.0 mm. Although the maximum inlet valve lift of the 1.8 litre Zetec engine is 9.3 mm [Hirsch 1991], the 10.0 mm setting was selected on the basis that this investigation was of a generic nature.

The planes inside the test section in which visualisation was carried out and the Cartesian co-ordinate system employed are each given on Figure 3.1. The inlet valves have also been labelled as 'Valve 1' and 'Valve 2' as indicated on the figure, in order to assist with the description of the flow. In the x-z direction, the vertical planes y = -17.6 mm and y = 0 mm were chosen to study the motion of the liquid mixture as it passed through the ports and entered the cylinder. The y = -17.6 mm plane passed vertically through the axis of Valve 2 and presented the flow field over the valve head, while the y =

0 mm plane passed vertically through the plane of symmetry of the cylinder head. It was established that fluid motion through the test section was essentially symmetric about the y = 0 mm plane and hence flow through the centre of Valve 1 was not visualised.

The development of swirl inside the section at each valve lift was studied by passing laser light sheets horizontally through the cylinder at locations below the cylinder head. The z = 10 mm plane (10 mm below the cylinder head) showed flow motion in the upper portion of the cylinder, while the z = 30 mm and z = 40 mm planes presented swirling flow further downstream of the valves. In the y-z direction, plane x = -16.5 mm passed vertically through the centre of the inlet valve heads to show the impingement of jets from the ports, and plane x = 0 mm visualised flow through the cylinder axis.

3.2.1 Effect of Liquid Mass Flowrate on Flow Structure

In order to ascertain that variation of liquid mass flowrate through the test section had a minimal effect on the qualitative flow field under steady flow conditions, flowrate tests were carried out. Flow visualisation was performed at three different mass flowrate settings:

(i) 0.41 kg/s (Re = 7930),
(ii) 0.98 kg/s (Re = 18940), and
(iii) 1.54 kg/s (Re = 29800)

The value of the Reynolds number corresponding to the liquid mass flowrate was based on the dimensions and area of the flow passage at entry into the cylinder head, upstream of the inlet ports (see Appendix 2 for Reynolds number calculations). The low value of Re with the 0.41 kg/s flowrate suggests that the flow may possibly not have been fully turbulent at this setting.

At the lowest flowrate setting, 0.41 kg/s, the in-cylinder velocities appear to be very low. Vortices created inside the cylinder are not well-defined and display oscillations about their centres. Figure 3.2(a) is a schematic drawing of the flow field visualised in the plane y = -17.6 mm with 5 mm lifts for both inlet valves. The dominant flow features in this plane at the lowest flowrate are the tumble-type vortex created by the intake motion over the valves and along the combustion chamber roof, as well as the elliptic

vortex produced by flow to the left of the valves. Both of these vortices appeared to oscillate in vertical and horizontal directions, indicating flow instability. A small recirculation region is noted to the left of the inlet valve, close to the port exit, and this is due to flow separation from the sharp edge at the back of the port. In the central region of this plane, as Figure 3.2(a) shows, flow velocities are so low that no organised motion can be observed, and this has been specified as 'random flow motion' on the figure. Figure 3.2(b) is a schematic diagram of the flow field in the y = 0 mm vertical plane, at the 0.41 kg/s flowrate setting. In this plane, flow motion is observed down the cylinder walls, but in the central region of the cylinder no structured vortices are noted.

At the higher mass flowrate settings of 0.98 kg/s and 1.54 kg/s, a more intense fluid motion is achieved. Flow in the y = -17.6 mm plane for the m = 0.98 kg/s and the m = 1.54 kg/s flowrate cases are shown on Figures 3.2(c) and 3.2(e) respectively. Both the tumbling vortex on the right of the inlet valve and the elliptic vortex underneath the valve are better defined as a result of the larger in-cylinder velocities, and no oscillations were observed in the flow. The most structured flow field is observed at the 1.54 kg/s flowrate setting, as Figure 3.2(e) shows. In the central plane y = 0 mm, tumbling of the fluid is seen in both Figures 3.2(d) and 3.2(f), and again this motion is better-defined at the higher flowrate.

When the valve lifts are set at 10 mm, the flow structure obtained with each of the flowrates is qualitatively very similar in each plane, as Figures 3.3(a) - (f) indicate. In the y = -17.6 mm plane, Figure 3.3(a) illustrates that the tumble-like vortex on the right of the figure has become considerably more larger and rounder, and the elliptic vortex adjacent to it is also bigger. However, fluctuation of the intake jets and oscillation of the vortices are apparent at the 0.41 kg/s setting.

Hence, under steady flow conditions, very little qualitative change was observed in the flow field. At low flowrates, the flow structure displays instabilities which can be attributed to the very low velocities of the working fluid. At larger values of liquid mass flowrate flow patterns are well-defined, with fewer regions where random motion is noted. Hence, the rest of the flow visualisation study was performed with the maximum liquid mass flowrate of 1.54 kg/s.

3.2.2 Flow Structure with 2.5 mm Valve Lifts

In order to determine the effect of increasing valve lift on the in-cylinder flow field, the visualisation study was initiated with the first case of 2.5 mm valve lift setting for both inlet valves. Figure 3.4(a) illustrates the flow pattern observed in the plane y = -17.6 mm. The flow through the upper portion of the inlet port, upstream of the inlet valves, is uniform and appears to travel in a direction parallel to the walls. Closer to the cylinder, a strong jet is directed by the intake valve to follow the profile of the combustion chamber and move downwards along the cylinder wall. A small elliptical vortex corresponding to the early formation of tumble in a reciprocating engine is created by the intake flow, with its centre of rotation very close to the combustion chamber roof. Similar vortices will be termed 'tumble-like' hereafter for brevity.

To the left of the inlet valve, a very small recirculation region is formed adjacent to the rear wall of the port. An elliptical vortex is also seen underneath the inlet valve, to the left of the figure, the centre of which tends to oscillate in the horizontal direction. This oscillation may be partly attributed to the fact that some flapping of the rear wall jet is also observed.

In the central plane, y = 0 mm, the intake flow is again complex, as shown on Figure 3.4(b). The prominent feature is the large tumble-like vortex of approximately half the cylinder diameter that is produced by the intake jet. At the top left hand corner of the cylinder, the flow behind the intake valves creates a recirculation region of approximately 15 mm in height. A turning motion of the flow is observed further down Figure 3.4(b), which may be due to a weak vortex.

The horizontal visualisation planes z = 10 mm, z = 30 mm and z = 40 mm were chosen to study the development of swirl inside the engine cylinder under steady flow conditions. Contrary to expectations, the flow configuration was not symmetrical in the swirl planes when both inlet valve lifts were set at 2.5 mm. Figure 3.4(c) presents the flow structure in the z = 10 mm plane for this case. Here it can be seen that the flow comprises of a large swirling vortex on the right hand side of the plane, whilst smaller vortices are present on the left side. This flow asymmetry was not believed to be due to geometrical irregularities in the test section. Moreover, the flow pattern in this plane was seen to change instantaneously on some occasions to the structure indicated on Figure 3.4(d), where the large swirling vortex is

located on the left of the figure. On closer inspection, it may be noted that the flow pattern in Figure 3.4(d) is akin to a mirror image of Figure 3.4(c). On the whole, though, the structure of Figure 3.4(c) was noted to occur more frequently than the other. The asymmetric nature of the flow was seen to persist in planes further down the cylinder.

The flow asymmetries seen at the 2.5 mm valve lift setting may be due to instabilities in the flow, which are accentuated at lower values of valve lift. Moreover, at valve lifts of between 2 and 3 mm, the flow discharge coefficient for dual-intake port cylinder heads is often maximum [Arcoumanis et al 1993], and the highest velocities in the cylinder may occur for these lifts. Factors such as internal roughness of ports and slight irregularities in cylinder head design can lead the flow to be prone to asymmetry and/or oscillation. In the present instance, if geometrical irregularities such as sharp edges were the cause of the asymmetry, then they were more likely to be located upstream of the intake ports, within the pipe connected to the inlet manifold, or within the inlet manifold itself. Nevertheless, flow asymmetries and oscillations in geometrically symmetric cylinder head configurations are not uncommon, owing to the highly three-dimensional and turbulent nature of in-cylinder flows.

3.2.3 Flow Structure with 5.0 mm Valve Lifts

When the lift of the inlet valves is set at 5.0 mm, the tumble-like vortex seen in the y = -17.6 mm vertical plane becomes larger, as shown in Figure 3.5(a), and its centre of rotation also moves further down from the roof of the combustion chamber than with the 2.5 mm valve lift. This is partly due to the intake jet having a greater spread as a result of the higher valve lift. The width of the recirculation region on the left of the valve, on the rear wall port, is also seen to increase to approximately 2 mm in width. The elliptical vortex to the left of the figure is of similar dimensions to that seen in Figure 3.4(a).

In the vertical plane y = 0 mm, only a slight change is noted in the flow pattern from that seen with the 2.5 mm valve lift setting and the flow diagram is not shown for economy of presentation. Firstly, the recirculation region seen at the top left of Figure 3.4(b) reduces from 15 mm to approximately 10 mm in height. This is because the amount of valve lift has a large influence on the angle at which the flow to the left of the inlet valve enters the cylinder. At low valve lifts, such as 2.5 mm, the jet has a greater inclination to the combustion chamber roof, so that it strikes the cylinder wall

further down than at instances where the valve lift is higher. The second difference noted is that the tumbling vortical motion seen to the right of Figure 3.4(b) is located further down the plane when the valve lift increased to 5 mm.

Figure 3.5(b) presents the flow configuration visualised in the horizontal z = 10 mm plane. The flow is symmetrical about the y = 0 mm plane and consists of two large counter-rotating elliptical vortices on both sides of the cylinder centre. The vortices near the cylinder wall are larger and stronger, being greatly influenced by strong flow against the cylinder wall. Small vortices are observed at the bottom of Figure 3.5(b), at the exhaust valve side of the test section.

At 30 mm below the cylinder head, the flow is different. Figure 3.5(c) shows that in the centre of the plane random flow regions are present, whereas two counter-rotating vortices were present in the z = 10 mm plane. Strong swirling vortices are still noted on the left and right sides of the figure, which are accompanied by smaller and weaker vortices seen towards the top of the figure, in the region underneath the inlet valves. In the z = 40 mm plane, not shown for brevity, some break-up of the flow was noted, but two large vortices of similar dimensions to those of Figure 3.5(c) could still be distinguished to the left and right of the plane, the vortex on the left side appearing to be weaker than its companion.

The flow patterns in a vertical plane through the centre of both inlet valves (plane x = -16.5 mm) are drawn on Figure 3.5(d). In this case, the strongest flow is between the valves and consists of two jets from the valves merging in the centre of the plane, and travelling downwards. Two vortices are produced underneath the inlet valves by the jet flow. At the outer edges of the vortices, the liquid is moved upwards and then travels downwards after joining the high velocity fluid along the cylinder wall.

3.2.4 Flow Structure with 7.5 mm Valve Lifts

Figure 3.6(a) illustrates the flow pattern seen in the y = -17.6 mm plane when the valve lifts are set at 7.5 mm. The intake flow produces a vortex to the right of the inlet valve which has increased in size compared to the 5 mm lift case, now being around 27 mm in height. Its centre of rotation has also moved further down. Moreover, the intake jet leaves the valve with a higher inclination angle to the horizontal and does not follow the combustion chamber roof as closely as was the case with lower valve lifts. This is likely to

be a consequence of the smaller in-cylinder velocities at higher valve lifts. The width of the recirculation on the rear wall of the port has now increased to 3 mm. Swirling flow can be detected about the sides of the cylinder wall to the right of Figure 3.6(a) and the elliptic vortex at the left of the figure shows little change in its dimensions from the lower valve lift flows, still being approximately 40 mm in height.

Two pairs of counter-rotating vortices are again noted for flow in the horizontal z = 10 mm plane, as shown on Figure 3.6(b). The flow pattern in this plane is symmetric and very similar to that described already for the 5 mm valve lift case (Figure 3.5(b)). Groups of small vortices are also apparent at the bottom of the figure. In the z = 30 mm plane, Figure 3.6(c) shows that strong swirling vortices are present at the left and right hand side, with no structured flow visible in the central region of the plane. For flow in the vertical plane x = -16.5 mm (Figure 3.6(d)) the main features are once again the two counter-rotating vortices underneath the valves, as well as flow down the cylinder walls, which returns back up to create a rotating motion, as described earlier.

3.2.5 Flow Structure with 10 mm Valve Lifts

With the 10 mm valve lift case, the in-cylinder flow structure is better defined in vertical planes than in horizontal planes. In Figure 3.7(a) a still frame from the video flow visualisation study is presented, showing the flow field observed in the y = -17.6 mm plane. The image shows that the large tumble-like vortex occupies over half the plane, and the elliptical vortex at the left hand side can also be seen. It should be noted that these vortices are part of the same three-dimensional toroidal vortex which is formed in the cylinder by liquid flow over the valve head. A three-dimensional diagram of the flow with 10 mm valve lifts is presented on Figure 3.7(e). A large recirculation region of approximately 5 mm thickness can be seen to the left of the valve head at the port exit. Strong motion is noted close to the cylinder wall at the right of the figure, while no organised fluid motion is apparent next to the combustion chamber roof.

The swirling vortices produced in the horizontal planes with the 10 mm valve lift are much smaller than those seen for the lower lifts. On Figure 3.7(b), showing the z = 10 mm plane, strong flow motion is evident along the cylinder wall and as a jet in the centre of the plane, which travels across the plane from the inlet valve side to the exhaust valve side. Small groups of

vortices are present at the sides of the figure and towards the bottom, but on the whole, velocities appear to be very low in this plane and no structured flow is apparent in most of the central region. The same is true for flow in the z = 30 mm plane, which is displayed on Figure 3.7(c). Higher velocity flow is again noted along the cylinder walls, in addition to groups of small vortices, but in general no organised flow motion is observed over most of the plane. In the z = 40 mm plane, no vortices or jets were apparent in the flow structure.

Figure 3.7(d) illustrates the flow structure in the vertical x = -16.5 mm plane. The two counter-rotating vortices underneath the inlet valves are much more rounder and smaller than those seen with 5 mm and 7.5 mm valve lifts, and no structured motion is noted towards the bottom of the figure. The 3-D flow structure inside the cylinder comprises of two toroidal vortices placed about the plane of symmetry, one of which is illustrated on Figure 3.7(e) to assist with the explanation. In general, tumble is the dominant flow type at this valve lift and swirl-like vortices are small.

3.3 LASER-DOPPLER ANEMOMETRY STUDY

3.3.1 Introduction

L.D.A. measurements were performed in the test section at three different intake valve lift settings; these were: (i) both valves having 5 mm lift ($L/D_V = 0.15625$) , (ii) both valves having 10 mm lift ($L/D_V = 0.3125$) and (iii) one valve closed and one having 10 mm lift. The results for the last lift combination are presented in the following chapter and also described in Mahmood and Yianneskis (1995). Initially, in order to ascertain that for the steady flow within the experimental rig, the in-cylinder flow velocities scaled with mass flowrate, flowrate tests were carried out. Three mass flowrate settings were selected for each of the above valve lift cases: 0.98 kg/s (Re = 18940), 1.26 kg/s (Re = 24380) and 1.54 kg/s (Re = 29800). In the L.D.A. study the 0.41 kg/s flowrate setting was not chosen for this test since the flow visualisation study suggested that the flow may not have been fully turbulent in this case. The Reynolds number for each of the flow configurations was based on the dimensions of the flow passage at entry into the cylinder head (see Appendix 2).

Figures 3.8(a) and (b) show the variation of the U and u' velocities along the x = 0 mm profile in the plane z = 30 mm for the case of 5 mm lifts for both inlet valves. The mean velocity profiles show that at the highest flowrate setting of 1.54 kg/s, the flow within the cylinder is symmetric. Velocity profiles at the lower settings of 0.98 kg/s and 1.26 kg/s are similar in shape, but indicate a more asymmetric in-cylinder flow structure, where mean U velocities are higher in the right hand portion of Figure 3.8(a) than on the left hand side and therefore velocity magnitudes do not scale with mass flowrate at every measurement location. This would imply that at lower values of Reynolds number, the in-cylinder flow structure can be more asymmetric even when the valve lifts are the same for both cases. This flow asymmetry appears to be a feature of the flows through twin-intake ports and will be discussed further below. Similar trends are shown on Figure 3.8(b) for the r.m.s. velocities, and on Figure 3.9, for the 10 mm valve lift case. However, the asymmetry in the r.m.s. profiles and with the high valve lifts is considerably smaller.

A possible explanation for this could be that even though both inlet ports and valve lifts are identical, the flow entering the ports at the lower flowrates may not be splitting equally in that more liquid may be flowing through one port than the other. This would give rise to the asymmetric flow features noted in both Figures 3.8 and 3.9. When one inlet valve on the test section was completely closed, both mean and r.m.s. velocities scaled perfectly with mass flowrate, as discussed in Chapter 4.

Having established that flow velocities did in fact satisfactorily scale with change in mass flowrate, the remaining L.D.A. measurements were carried out at the maximum flowrate of 1.54 kg/s. Figure 3.10 indicates the planes within the test section in which measurements were taken, in addition to the measurement locations. These planes were selected on the basis of previous flow visualisation work done on the same test section, which had revealed flow features within the inlet ports and cylinder that merited further investigation.

For each valve lift case, the U, u', W and w' mean and r.m.s. velocity components were measured along the z = 10 mm, z = 20 mm, z = 30 mm and z = 40 mm horizontal planes, with a view to assessing the swirl characteristics of the engine model. Optical restrictions (such as the inlet manifold) prohibited the orientation of the anemometer in the y-coordinate direction, so that the V and v' velocity components could not be measured. The velocity data presented in this chapter has not been normalised against the bulk flow

velocity for the purposes of presentation. This is because features such as flow asymmetries could not be easily distinguished with normalised results.

3.3.2 Flow with 5 mm Valve Lifts

a) Vertical Plane Flows

The velocity vectors obtained from measurements in the vertical plane y = -17.6 mm with both valve lifts set at 5 mm are shown on Figure 3.11. The flow within the ports follows the port inclination angle and the velocity vectors indicate that the port flow is relatively uniform. Two-dimensional flow velocities within the port are typically around 1.8 m/s. In-cylinder flow velocities are highest near the cylinder head, where the fluid exits the port and enters the combustion chamber. The jet issuing from the inlet valve generates a strong motion into the engine cylinder, causing fluid to travel downwards as it strikes the cylinder wall. A small vortex with its centre at approximately x = 12 mm and z = -2 mm is created. Flow velocities decrease as the liquid travels back upwards towards the inlet valve, being around 1 m/s in the cylinder centre and 0.5 m/s close to the inlet valve. A jet is also generated on the left of the inlet valve, with velocities of approximately 2.2 m/s being reached at 2 mm away from the l.h.s. cylinder wall. A small, narrow vortex is also produced by this jet to the left of the main vertical vortex.

Profiles of the mean velocity components U (radial) and W (axial) for the 5 mm valve lift case in the plane y = -17.6 mm are shown on Figures 3.12(a) and 3.12(c) respectively, while the corresponding fluctuation velocities u' and w' are displayed on Figures 3.12(b) and 3.12(d) respectively. Figure 3.12(a) indicates that the U mean velocity component has the largest values within the intake port. The flow entering the engine cylinder also has large U velocity magnitudes, as a result of the strong intake jet from the valve, and velocities of up to 1.4 m/s were measured in the profile z = -5 mm. Within the engine cylinder, however, the U velocities are negative almost everywhere, which is a result of the vortical motion of the flow. The highest in-cylinder U velocities, up to 0.8 m/s, occur within the central region of the plane, and low values are achieved towards the cylinder walls, where the W velocity component is of high magnitude.

R.m.s. u' velocities corresponding to Figure 3.12(a) are presented on Figure 3.12(b). The levels of r.m.s. velocities are lowest within the port region,

between 0.1 and 0.2 m/s, and are almost constant along each profile, due to the uniform flow in the ports. Higher levels of u' velocities occur within the cylinder near the l.h.s. wall, whereas in the centre of the test section, the profiles indicate that u' levels are fairly constant at approximately 0.38 m/s, and similar for each profile.

The W component of the mean flow in the test section is lower inside the intake port than the corresponding U component, as Figure 3.12(c) shows. W-velocity magnitudes are almost constant along the z = -35 mm and z = -45 mm profiles, at around 0.73 m/s. The profile at z = -25 mm is nearly linear, with velocities varying from 0.72 m/s to 1.03 m/s. The intake jets caused by flow over the valve give rise to W-velocities close to both the right and left edges of the cylinder wall and velocity magnitudes of up to 1.9 m/s near the right and left wall respectively. On the right side of the cylinder, the vortical motion results in a fairly steep velocity gradient, in which the W-velocity direction changes from positive to negative. Velocity magnitudes in the central region of the cylinder are again relatively constant.

Figure 3.12(d) shows that the shape of the w' r.m.s. velocity profiles within the test section is similar to those for the u' profiles already discussed. Within the port, w' levels are low, and almost constant along each profile. The highest in-cylinder w' velocity in this plane, 0.56 m/s, occurs in the z = -5 mm profile within the intake flow, and levels of around 0.5 m/s are also noted adjacent to the rear wall. Levels in the central region of the test section are constant at around 0.27 m/s.

Contours of local turbulence intensity magnitude in the vertical plane y = -17.6 mm plane are plotted on Figure 3.13. It should be noted that as a result of the lower resolution of the measurement grid in the z-direction compared to the x-direction the contours levels appear to be elongated along the z-axis, so the results should be interpreted with care. The turbulence intensity was calculated by dividing the r.m.s. velocity measured at each location with the corresponding mean velocity and have been expressed as a percentage. Figure 3.13(a) shows contours of u'/U and indicates that u'/U levels are below 75% in the central region of this plane, where the U-velocity component is greater than the value of the r.m.s. velocity. As noted in the vector plot of Figure 3.11, the flow in this section is uniformly moving up towards the inlet valves. Larger magnitudes, from between 200% to around 800% are found in regions close to the cylinder wall, where the flow is changing direction, so that magnitudes of mean radial velocities are close to zero.

Contours of the w'/W turbulence intensity are shown in Figure 3.13(b). On the right of the figure it is noted that magnitudes of w'/W are the smallest, at below 75%, due to strong flow motion in the downwards direction, as mentioned earlier and noted on Figure 3.12(c). A vertical strip of high w'/W values is also present in the right hand side of this plane, and corresponds to measurement points where the mean W velocity component is very small, i.e. where the flow changes direction. In the majority of Figure 3.13(b), however, w' values are comparable to the W magnitudes, at between 75% and 150% of the mean velocity.

The difference between the magnitudes of the fluctuation velocity components u' and w' measured at each location was calculated and normalised with the bulk flow velocity V_b - giving $|(u'-w')/V_b|$ - in order to obtain an indication of the degree of anisotropy present within the flow. In any turbulent fluid flow which is not strongly influenced by shear at a solid wall, such as atmospheric flows well away from the ground and many other types of free flows, the magnitudes of the r.m.s. velocity components along the principal co-ordinate directions will inherently tend to be equal to each other [Davies 1972]. In internal flows directed by solid boundaries, energy transfer within the fluid may be directed towards a particular orientation especially if vortices are present, leading to r.m.s. components which differ from each other and thereby to anisotropy within the measured turbulence.

However, in computations of internal flows made with C.F.D. techniques, the most commonly used turbulence model, the k-ε model, is based on an implicit assumption that turbulence within the flow is isotropic, i.e. that at any location in the flow, the magnitudes of the fluctuation velocities along the three Cartesian co-ordinate directions are the same. This assumption can lead to C.F.D. methods inaccurately calculating turbulence levels present within a particular flow configuration and thereby the velocity magnitudes and amount of mass transfer taking place. Therefore, it is useful to ascertain the level of anisotropy present in a flow.

Figure 3.14 shows the difference between u' and w' measured at locations within the y = -17.6 mm plane expressed as contour levels. In the main, the differences in u' and w' are very small within the majority of the plane, at below 5% of the bulk flow velocity (V_b = 1.38 m/s, as given in Appendix 2). Higher values of up to 12% of V_b, are noted in areas where vortices are present. It has been shown by Bradshaw (1971) and Tennekes and Lumley (1972) that anisotropy within vortical flows is related to the

concept of 'vortex stretching' due to the rate strain applied to a vortex along a particular direction.

In order to accurately determine the degree of anisotropy present within flow inside the engine model, it would have been necessary to measure all three velocity components at each location, and to calculate vorticity and rate of strain. Since this has not been possible in the present investigation, it is sufficient to note that Figure 3.14 shows that turbulence within this flow appears to be anisotropic along the x-coordinate direction, as on the whole u' velocities measured in this plane were higher than w' velocities at the same location.

b) Swirl Plane Flows

Figure 3.15(a) presents the mean flow structure within the cylinder in the horizontal plane z = 10 mm. The U velocity profiles indicate the presence of two large vortices at the left and right hand sides of the cylinder, which are of approximately equal strength. These are accompanied by two counter-rotating vortices in the cylinder centre of smaller dimensions. The highest velocities are achieved at locations close to the cylinder wall, and are around 1.5 m/s for the profile at x = 12 mm. The velocity in the centre of the cylinder increases as the flow travels in the positive x-direction, up to the profile x = 36 mm, where the U velocity component reduces in magnitude as a result of downward motion of the fluid. High values of the in-cylinder velocity are also found in the negative x-direction, being around 0.7 m/s within the profile at x = 12 mm. On the whole, the mean velocity profiles for the plane z = 10 mm indicate that the flow structure for this valve lift configuration is symmetric, as was noted from the flow visualisation study. The assymetry in the x = -36 mm profile has been referred to earlier and will be discussed further below.

The r.m.s. results corresponding to the profiles presented on Figure 3.15(a) are shown on Figure 3.15(b). The profiles indicate that r.m.s. velocities within this plane are higher at locations where high mean velocity gradients are present, viz. at the sides and in the middle of the cylinder. The maximum r.m.s. velocity is similar for each profile in this plane, and is around 0.5 m/s.

The mean flow field in the plane z = 20 mm for the 5 mm valve lift case is displayed on Figure 3.16(a). At first glance, there appears to be little change in the flow from that of z = 10 mm. The fluid velocities at the extreme left and extreme right locations on each profile are similar and reach magnitudes of

around 1.3 m/s in the profile at x = 12 mm. In the centre of the cylinder, U velocities in the positive x-direction are lower. This would imply that either the two counter-rotating vortices in the cylinder centre have reduced in strength and size, or that the flow is turning back from the front of the cylinder wall (bottom of the figure) as a result of tumbling motion. At the back of the cylinder, in the x = -36 mm profile for this figure, negative flow velocities are achieved, which are a result of fluid flow behind the inlet valves.

The r.m.s. velocity profiles for the plane z = 20 mm, given on Figure 3.16(b), show that turbulence levels at the front end of the engine cylinder (bottom of the figure) are evenly distributed and are almost the same, on average around 0.3 m/s, at each measurement location. Larger r.m.s. velocity values, on average 0.48 m/s, are achieved at the back of the cylinder (top of the figure). The bigger values for turbulence in this case could be due to interaction of the jet flows from the two ports in the central region. Moreover, Figure 3.11 shows that the downward W velocity component and associated gradients large within this region, due to the high velocity jet flow from behind the inlet valve and due to this jet striking the cylinder wall.

By the plane z = 30 mm for this configuration, mean velocities in the positive direction are considerably lower than in the planes previously described, as Figure 3.17(a) illustrates. Profiles are still symmetric with less steep gradients, implying that the flow begins to settle at the lower regions of the test section. In the main, the velocity profiles show that the vortices at the sides of the cylinder have grown in size, while the two centrally located vortices seen in planes closer to the cylinder head are not as well defined as before. This was also seen in the flow visualisation results, as shown in Figure 3.5(c). High values of negative U velocities occur, towards the top of the figure, which correspond to fluid travelling due to tumble motion. U-component velocities are very low along the profiles x = -36 mm and x = 36 mm because the flow is travelling straight downwards at these locations where the W-velocity component is comparatively large. The r.m.s. velocity profiles for this plane (Figure 3.17(b)) display similar characteristics to those described for Figure 3.16(b).

By the z = 40 mm plane the flow velocities have become significantly lower, as Figure 3.18(a) illustrates. For example, in the profile x = 0 mm, velocity magnitudes at the outer edges of the profile have reduced from 1.56 m/s and 1.1 m/s in the z = 10 mm plane, to 0.35 m/s and 0.26 m/s in the z = 40 mm plane. Velocities in the negative x-direction reach 0.7 m/s in the

central region of the cylinder. The structure of the velocity profiles would indicate that the flow field in this plane still comprises two counter-rotating swirling vortices each of which are approximately half the cylinder diameter in width. The profiles are, in the main, symmetric about the cylinder centre indicating that the two vortices are of similar intensities. Levels of r.m.s. u' velocities in the z = 40 mm plane - presented on Figure 3.18(b) - are uniform and very similar to those of Figure 3.16(b), in the z = 20 mm plane.

Contours of turbulence intensity u'/U for flow in the horizontal planes have been plotted on Figures 3.19(a) to 3.19(d). The contour plot for the z = 10 mm plane, Figure 3.19(a), consists of alternate vertical bands of low and high levels of u'/U, which can be used to identify the vortices in the plane; though it is appreciated that the appearance of the bands may be an artefact of the lower grid resolution along the x-axis. When this figure is examined in conjunction with the mean velocity profile plot shown on Figure 3.15(a), it is seen that the low levels, below 75%, correspond with the high velocity jet flows present in the figure. Turbulence intensities over 900% are present at locations where U velocity magnitudes are very small.

Figure 3.19(b) shows levels of u'/U in the z = 20 mm plane. Again, levels below 75% are present at the left and right edges of the plot where mean velocity magnitudes are the highest. In the centre of the figure, the turbulence intensity magnitudes along the y = 0 mm direction have increased from 0 - 75% in Figure 3.19(a), to 75 - 150% as a result of the lower mean velocities in the central jet of fluid. R.m.s. levels for flow in the z = 30 mm and z = 40 mm planes are very similar, so that the main differences between the two contour plots of Figures 3.19(c) and (d) are due to variations in the mean velocity profiles. In general, it is seen that the higher levels of turbulence intensity are found towards the top of the contour plots, indicating that the flow is more turbulent in the region directly below the inlet valves. Moreover, comparison of the four contour plots reveals that in horizontal planes close to the cylinder head, as shown in Figures 3.19 (a) and (b), distinct bands of high and low u'/U exist, whereas further down the cylinder the turbulence appears to spreading within the plane.

A further estimation of the levels of turbulence present in the flow with 5 mm valve lifts has been obtained by computing a single average r.m.s. value for each plane from all the measurement locations. Thus, for flow in the y = -17.6 mm plane the average of the u' r.m.s. velocities is: u'_{ave} = 0.30 m/s, while the average of the w' fluctuation component is: w'_{ave} = 0.27 m/s. Although accurate conclusions can only be drawn with data obtained from a

very large number of measurement locations, the approximately 10% difference in these two values may indicate that the flow is anisotropic along the tangential velocity direction. In the horizontal planes, the average values of the u' velocity component are as follows: (i) z = 10 mm: u'_{ave} = 0.36 m/s; (ii) z = 20 mm: u'_{ave} = 0.35 m/s; (iii) z = 30 mm: u'_{ave} = 0.33 m/s and (iv) z = 40 mm: u'_{ave} = 0.29 m/s. These values would suggest that for this particular flow configuration, turbulence levels are the highest at positions close to the cylinder head and that they tend to reduce at locations further downstream.

3.3.3 Flows with 10 mm Valve Lifts

a) Vertical Plane Flows

When both intake valve lifts are increased to 10 mm, major changes are noted in the flow structure. Figure 3.20 shows the mean velocity vectors in the vertical plane y = -17.6 mm for this configuration. The flow within the intake ports is uniform, with velocities of approximately 1.75 m/s. These port velocities are very similar to those achieved with the 5 mm valve lift case, which were typically around 1.8 m/s. The flow within the cylinder in this plane is dominated by a large vortex of size approximately half the cylinder diameter, as observed in the flow visualisation. The highest in-cylinder velocity for this valve lift case, 1.9 m/s, was measured at the x = 4 mm location in the z = -5 mm plane, which is about 3 mm away from the valve tip. Further away from the valve, the intake jet has lower velocities. The jet does not follow the combustion chamber roof shape as for the 5 mm valve lift case.

Flow velocities reduce as the liquid turns back upwards towards the inlet valve. A strong intake jet is also created by the flow behind (left side of) the inlet valve, where mean velocities are approximately 0.7 m/s at locations closest to the cylinder wall. An elliptically shaped vortex is also created by this flow.

Mean U velocity profiles in the axial plane y = -17.6 mm for this valve lift configuration are presented on Figure 3.21(a). The average U velocity component within the port is approximately 1.6 m/s. Mean U velocities reach 1.67 m/s within the intake jet close to the inlet valve. Lower velocities are noted at points close to the front cylinder wall, due to the primarily downward motion of the liquid. Negative U velocities occur in the central area of the test section.

Figure 3.21(b) shows the corresponding r.m.s. u' velocity profiles. R.m.s. levels within the inlet ports appear to be constant along each profile at approximately 0.1 m/s. In the z = -5 mm profile, within the intake jet, u' peaks to 0.57 m/s. Turbulence levels are higher in the regions occupied by the intake jet within this plane, especially along the z = -5 mm, z = 2 mm and z = 10 mm profiles, due to the shearing effects of the intake jet on the flow. Low values, around 0.16 m/s, are noted in regions underneath the inlet valves within these profiles. Further down the cylinder, the energy of the intake jets appears to have diffused; u' levels in the z = 20 mm, z= 30 mm and z = 40 mm profiles are almost constant at an average value of 0.25 m/s.

The W velocity component for the 10 mm valve lift case has been plotted on Figure 3.21(c). Within the intake ports, velocity magnitudes are generally constant, at around 0.7 m/s. In the z = -25 mm profile, velocities vary linearly from 0.63 m/s close to the port wall to 0.95 m/s near to the valve stem. W velocities in the downward direction are predominant in the lower portion of the cylinder, especially at locations close to the cylinder wall at the right of the figure, where velocities as high as 1.1 m/s were measured. This is because the fluid is moving primarily in the downward direction in these regions, so that the W component is larger than the U velocity component.

Figure 3.21(d) presents the r.m.s. w' velocity profiles within the test section. Inside the ports, w' is slightly lower than u' at the same locations, being on average between approximately 0.075 m/s and 0.1 m/s. R.m.s. velocities are in the upper portion of the cylinder do not vary along each profile as much as the u' values at the same locations. R.m.s. levels in the z = -5 mm profile are similar at each measurement location, with an average value of 0.28 m/s. Within the z = 2 mm, z = 10 mm and z = 20 mm profiles, higher w' levels are noted amidst the area occupied by the high velocity intake jets; w' varies from 0.174 m/s in the low velocity region to around 0.4 m/s in the intake jets within the z = 10 mm velocity profile. Further downstream, r.m.s. w' velocities are similar in the z = 30 mm and z = 40 mm profiles, and are on average approximately 0.25 m/s, which is equivalent to the u' velocities shown on Figure 3.21(b) at the same measurement locations.

Figure 3.22 displays contours of both u'/U and w'/W turbulence intensities for flow in the y = -17.6 mm plane. On Figure 3.22(a) the magnitudes of u' range from below 75% of the corresponding U-velocity to over 200 % in the majority of the plane. As with the contours for the 5 mm valve lift case, shown on Figure 3.13(a), u'/U magnitudes are highest at

locations close to the cylinder wall, where the radial mean velocities are small. The highest values of u'/U, at over 900%, are indeed present at locations to the left and right sides of the figure. A contour plot of w'/W turbulence intensities is displayed on Figure 3.22(b). At the right of this figure w'/W levels are low at 0-75% due to a strong jet of fluid travelling downwards. In the central region of the plane contour levels vary from 75% up to 600% at locations where the velocity gradients are large. A small area at the bottom left of Figure 3.22(b) has values over 900%, where very low values of mean velocity were measured.

An indication of the anisotropy of flow in the y = -17.6 mm plane is given by Figure 3.23, which displays contours of the difference between the u' and w' r.m.s. velocity magnitudes normalised against the bulk fluid velocity, V_b. The plot illustrates that in the majority of the plane the differences amidst the two r.m.s. components are very small, at less than 2.5% of V_b, and this is verified by Figures 3.21(b) and 3.21(d), which are very similar in appearance at almost locations. The greatest difference is noted towards the upper portion of the plane, to the right of the inlet valve. In this area $|(u'-w')/V_b|$ values of between 0.15 and 0.18 have been computed; this is due to the fact that larger u' r.m.s. velocities were measured within the intake jet, in the z = -5 mm, z = -2 mm and z = 10 mm profiles.

b) Swirl Plane Flows

Flow characteristics within horizontal planes through the engine cylinder with a 10 mm valve lift setting are presented on Figures 3.24, 3.25 and 3.26. Figure 3.24(a) shows mean U velocity profiles in the z = 10 mm plane. Mean velocities are low at almost all locations except in the centre of the plane and close to the cylinder wall. These low velocities are due to the predominantly upward (or downward) motion of the flow at these locations, as the velocity vectors on Figure 3.20 show, so that the W mean velocity component is much larger than the U component. The profiles indicate the presence of two small vortices adjacent to the left hand and right hand cylinder walls. In the x = 0 mm profile, velocities vary from around 1.3 m/s at the location closest to the l.h.s. cylinder wall, to a minimum of 0.02 m/s.

A flow motion can be identified on Figure 3.24(a) in the cylinder centre along the x-direction. When travelling in the positive direction, velocities in this flow vary from 0.47 m/s in the x = -12 mm profile to 1.02 m/s in the x = 12 mm profile. A similar flow is also produced in the negative direction, and

U velocities peak at 0.77 m/s in the x = -36 mm profile within this particular jet. The velocity profiles are by and large symmetrical about the y = 0 plane. However a small asymmetry in the flow can be seen to develop in the x = 24 mm and x = 36 mm profiles. A possible reason for this could be the fact that the mass flowrate of liquid entering each intake port is not identical despite the fact that the valve lifts are equal. As the central flow appears to be drifting towards the bottom right hand side of Figure 3.24(a), more fluid is likely to be entering the test section through the port with Valve 1, as specified in Figure 3.1. This was verified by a C.F.D. study reported in Mahmood et al (1996), where the total mass flowrate through the engine model was split 45%/55% through the inlet ports and an asymmetry similar to that noted here was observed in the in-cylinder flow.

R.m.s. u' levels within the z = 10 mm plane are shown on Figure 3.24(b). In general, u' levels in this plane with 10 mm valve lifts are slightly lower than those measured at the 5 mm valve lift settings - shown on Figure 3.15(b) - although similar trends can be observed within the profiles. In the top part of the plot, u' velocities of between 0.3 m/s and 0.43 m/s are noted in the x = -36 mm profile. Higher values are seen in the centres of each profile and at the sides of the cylinder walls, where the higher velocity gradients are located. For instance, in the x = -24 mm profile velocities in the three central points are around 0.4 m/s, and approximately 0.16 m/s to the left and right of these locations.

In Figure 3.24(b), the x = -24 mm and x = -12 mm profiles - and to some extent the x = 0 mm profile too exhibit locally small peaks due to the various velocity gradients and corresponding higher r.m.s. values. Further along the plane the x = 12 mm and x = 24 mm profiles are more uniform. R.m.s. velocities are high in the x = 24 mm profile, varying gradually between adjacent points from 0.28 m/s at the cylinder walls to 0.48 m/s in the centre of the profile. The higher r.m.s. levels in this particular profile may be accounted for by the fact that the flow velocities off the inlet valve are amongst the highest in this region.

Mean velocity profiles in the plane z = 20 mm are presented on Figure 3.25(a). U velocities are still in the main low within all regions of the plane. The major difference in the flow structure to that of the z = 10 mm plane is that the flow velocities near the cylinder walls and in the centre have lower magnitudes. In the x = 0 mm profile, the maximum velocity is 0.87 m/s compared to 1.3 m/s at the same location in the z = 10 mm plane. At the same time, whereas velocities in the central flow in the positive x direction reached

a maximum value of 1.02 m/s in the z = 10 mm plane, the maximum velocity has now been reduced to 0.48 m/s. The shape of the profiles still indicates the presence of two vortices against the cylinder walls, and flow asymmetry can again be noted in the x = 24 mm and x = 36 mm profiles.

In Figure 3.25(b), r.m.s. velocities profiles in the z = 20 mm plane show similar trends to those presented on Figure 3.24(b). One immediately visible difference in the structure of the profiles is that those on Figure 3.25(b) are more uniform, so that there is less of a change in r.m.s. velocity magnitude between successive measurement locations than in the z = 10 mm plane. In the x = -36 mm profile, u' is almost constant at around 0.37 m/s at all points, and r.m.s. levels in the x = 0 mm and x = 12 mm profiles are very similar, with an average of around 0.28 m/s for each of these profiles.

Mean U velocities in the z = 30 mm plane - shown on Figure 3.26(a) - are lower still than the in the two planes already described. Maximum velocities in both the x = -24 mm and x = -36 mm profiles are only 0.17 m/s and 0.12 m/s respectively and very near to zero at most other points. Flow velocities along the cylinder wall increase from 0.25 m/s in the x = -12 mm profile to approximately 0.5 m/s in the x = 12 mm profile. In the centre of the cylinder, velocities are very low so that the flow noted in Figures 3.24(a) and 3.25(a) is not as pronounced. Peaks in the x = 0 mm and x = 12 mm profiles corresponding to mean velocities of around 0.45 m/s imply that strong backward flow is occurring in these regions. This flow occurs at points where fluid in the main vertical vortex shown on Figure 3.20 is turning to travel from a downward to an upward direction. R.m.s. velocity profiles for the z = 30 mm plane are shown on Figure 3.26(b). The turbulence seems evenly spread across the plane; u' is almost constant along each profile, and has an average value of approximately 0.25 m/s.

Figure 3.27 shows contour plots of u'/U turbulence intensity magnitude for flow in the horizontal planes. In Figure 3.27(a), the lowest values of u'/U in the z = 10 mm plane are obtained in regions with high velocity jets, i.e. at the left and right sides of the plot and within the jet in the centre. As mean U velocities are close to zero at many points, the turbulence intensity is high within these regions, varying from 300% to over 900%. This is also observed in Figures 3.27(b) and (c), the contour plots for the z = 20 mm and z = 30 mm planes respectively. Here, two bands of high u'/U magnitude are noted, which follow the low velocity measurement locations in the plane. In each of the horizontal planes, u'/U varies from 0 to 225% in the majority of the flow regions.

Average values of the r.m.s. have been computed for flow in each of the measurement planes. For the y = -17.6 mm plane, u'_{ave} = 0.23 m/s, while w'_{ave} = 0.21 m/s. As reported earlier for the 5 mm valve lift case, the fact that u'_{ave} is greater than w'_{ave} suggests that the turbulence in the flow is anisotropic in the radial direction, but again the differences (9-11%) may result partly from the measurement grid employed and should be interpreted with care. For the horizontal planes, average values of u' are: (i) z=10 mm: 0.29 m/s; (ii) z = 20 mm: 0.29 m/s and (iii) z = 30 mm: 0.25 m/s. The turbulence is again higher in planes closer to the cylinder head, probably due to interactions between high velocity jets and between vortices. Further downstream, the lower average r.m.s. value indicates the flow settling down with less steep gradients and reduced turbulence levels.

3.3.4 Comparison of Experimental and Computational Results

In a parallel study to the experimental investigations described in this chapter, steady flow inside the Ford Zetec engine was evaluated at King's College London using computational fluid dynamics. A three-dimensional grid incorporating all the features of the engine inlet ports, valves, combustion chamber and cylinder was constructed using C.A.D. data provided by Ford Motor Company Limited. Some details of the computational techniques and the turbulence model employed to calculate the flow are provided in Chen et al (1996) and Mahmood et al (1996). The measurement data from the present investigation was used to validate the computational results.

Figures 3.28(a) to (f) present comparisons of the calculated and measured mean and r.m.s. velocities in selected vertical and horizontal planes for 5 mm and 10 mm valve lifts. Axial velocity component profiles for flow in the vertical plane y = -17.6 mm are given on Figures 3.28(a) and (b). These figures show good qualitative and quantitative agreement between both computational and experimental results at most locations, and particularly in the central region of the plane for both valve lift cases. The calculated velocity profiles show steeper velocity gradients in the inlet ports than the experimental results, which indicates that the C.F.D. model may not have accurately predicted the size of the small recirculation that exists at the port exit. This influences the computed intake flow behind the inlet valves, so that greater differences are noted at points close to the test section walls seen at the left of each plot, where the measured velocity values are higher.

Radial velocity profiles for flow in the horizontal plane z = 10 mm are shown on Figures 3.28(c) and (d). Again, both figures show that the C.F.D. model is able to evaluate all the main features of the flow at 5 mm at 10 mm valve lifts. However, the flow asymmetry seen at the bottom of Figure 3.28(d) is not shown by the computational results. Comparisons of the u' r.m.s. velocity, shown on Figures 3.28(e) and (f), indicate that experimental results have significantly greater magnitudes than the C.F.D. data. The fact that the flow model assumes isotropic turbulence is likely to be one major reason for the differences. The flow inside the ports is likely to be anisotropic since it is directed by the ports. Moreover, it is well known that experimental engine flows include non-random fluctuations within the measured r.m.s. values, which can give the impression that turbulence levels are higher than they may really be. These variations are not calculated by standard turbulence models, such as the k-ε turbulence model. By employing Large-Eddy Simulation models in C.F.D. studies, the variation of the mean velocity could be predicted.

The actual random velocity fluctuations can be determined by employing time-resolved L.D.A., followed by removal of the non-random variation component through the use of F.F.T. signal processing methods. The resulting r.m.s. magnitudes can be up to 50% lower in regions of intense vorticity than the initial measured values [Balabani 1996], and comparison of this data with that calculated using C.F.D. may show much closer agreement between experimental and computational results. Since time-resolved L.D.A. measurements were not performed in the present study, it is not possible to define the the contribution of non-random components to the r.m.s. velocity results presented in this chapter.

3.4 CONCLUSIONS

The aim of the research described in this chapter was to acquire an understanding of the flow characteristics present within an engine through detailed velocity measurements. On the whole, this study has revealed that the flow in an dual-intake port engine cylinder is highly three-dimensional and that large changes in flow structure can occur with slight alteration in geometric characteristics such as valve lift. The main findings with regard to the flow configurations investigated using both flow visualisation and L.D.A. are provided below:

1. The variation of mass flowrate of the working fluid through the test section, for a particular valve lift case, displayed very little effect on the in-cylinder flow structure, i.e. on vortex shapes and sizes. At low values of flowrate, however, instabilities in the flow such as jet flapping and oscillation of vortex centres were detected, particularly at small values of valve lift. L.D.A. measurements showed that velocity magnitude only approximately scale with variation of flowrate (see Figures 3.8 and 3.9). This could be accounted by uneven split between the two intake ports, as indicated by the C.F.D. study referred to above.

2. For equal valve lift configurations, tumble-like vortices produced in vertical planes became larger and stronger as valve lift was increased. At low values of lift, the intake jet closely followed the roof of the combustion chamber, while at larger lifts the flow entered the cylinder with a greater angle to the roof. At higher valve lifts, the angle of the intake flow increases relative to the cylinder head (Figure 3.20), so that mean velocity magnitudes near the cylinder wall are lower.

3. Flow motion behind the inlet valve created a recirculation region at the exit of the port, which became greater in size as valve lift was increased.

4. With equal valve lifts, the in-cylinder flow was generally symmetrical in all the examined planes, as both the flow visualisation and L.D.A. studies indicated. However, at very low valve lifts, instabilities were introduced into the flow, which resulted in asymmetries in the flow structure in spite of the geometric symmetry in the cylinder head. With valve lifts set at 2.5 mm, a bold asymmetry was seen in horizontal planes. The asymmetry was observed to suddenly transfer from one side of the cylinder to the other at random intervals.

5. Swirl vortices were larger and better-defined at lower valve lifts. At higher values, swirl motion rapidly diminished as the fluid travelled down the cylinder, whereas at lower valve lift settings, organised flow motion was retained in a larger volume of the cylinder. Overall swirl magnitudes were small in the configurations evaluated, as the counter-rotating swirl vortices observed in the horizontal planes appeared to cancel each other out. Hence, tumble-like motion was dominant inside the cylinder in this instance.

6. Mean velocities inside the ports at both 5 mm and 10 mm equal valve lifts were found to be very similar, with maxima of approximately 1.8 m/s. Flow inside the inlet ports was uniform with high mean radial and axial velocity components. R.m.s. velocity levels in the inlet ports were low and almost constant along each profile, due to flow uniformity.

7. R.m.s. velocities in vertical planes in the cylinder showed little change along profiles where velocity gradients are low. High values were noted within regions of strong flow, e.g. inside jets. R.m.s. levels were also generally lower in profiles lower down in the cylinder, with fewer variations in magnitude along the profile.

8. R.m.s. velocity profiles in horizontal planes indicated that flow was more turbulent in the upper portion of the cylinder than within lower planes. This was judged from the shape of the profiles, which have a more jagged appearance in the z = 10 mm and z = 20 mm planes, than in the z = 40 mm plane. This indicates that turbulence is localised into specific locations near the top of the cylinder, but spreads out more evenly with the flow further downstream.

9. Contour plots of local turbulence intensity u'/U and w'/W showed that turbulence intensities were lowest within regions which contained strong jet flows. High values of u'/U and w'/W were noted at locations with low mean velocities.

10. The anisotropy of the turbulence in vertical planes at both 5 mm and 10 mm valve lifts was estimated by calculating $|(u'-w')|/V_b$. The results showed little difference between u' and w' magnitudes, except at locations where vortices were present and within intake jets, where u' values were generally larger than w' values.

11. Comparison of the experimental results of mean and r.m.s. velocities presented in this chapter with previously reported C.F.D. simulations of the flow showed that the C.F.D. model was able to calculate all the main features of the flow at both 5 mm and 10 mm valve lifts. Good quantitative agreement for mean velocity results was obtained at most locations in vertical and horizontal planes. Comparisons of r.m.s. velocities indicated that computed r.m.s. levels were considerably lower than measured values. This was partly

due to the limitations of the turbulence model used in the flow calculations, as well as instabilities and fluctuations present in the actual flow which the C.F.D. model was unable to evaluate.

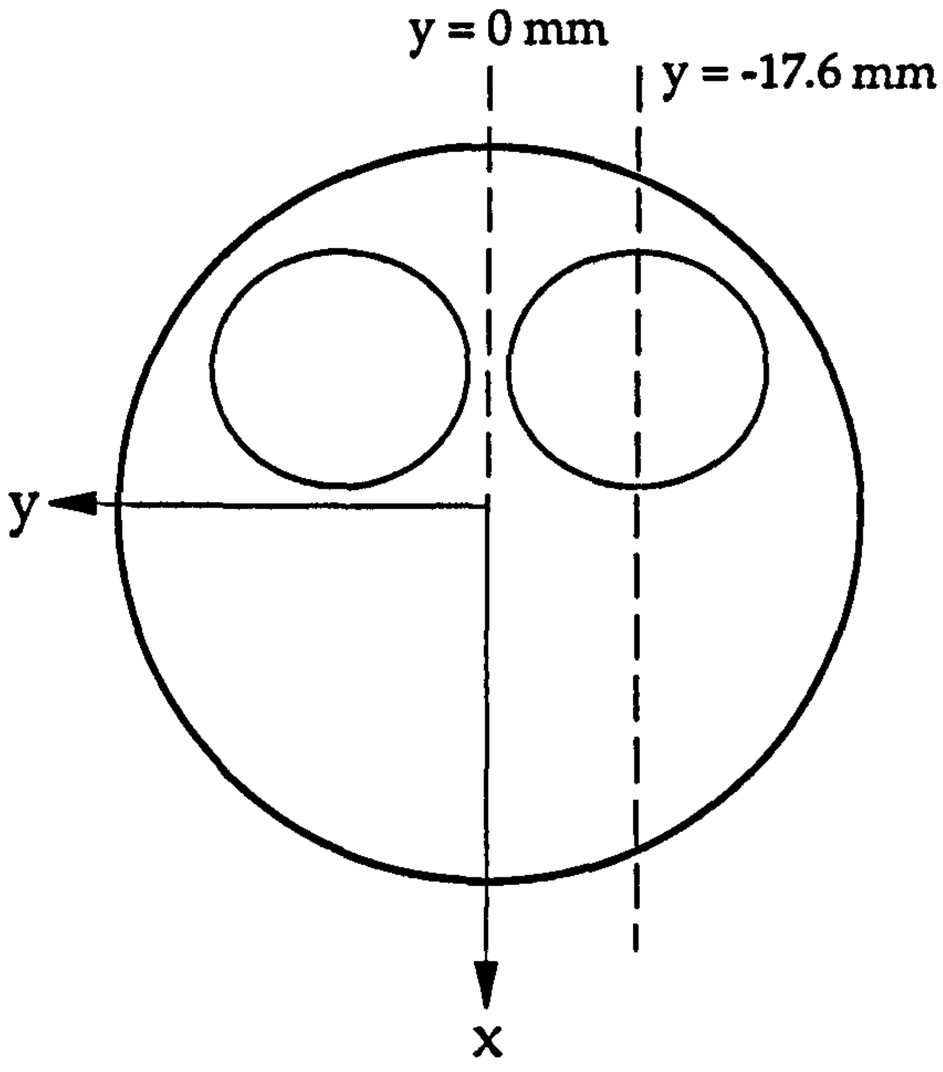

(a) Vertical x-z planes

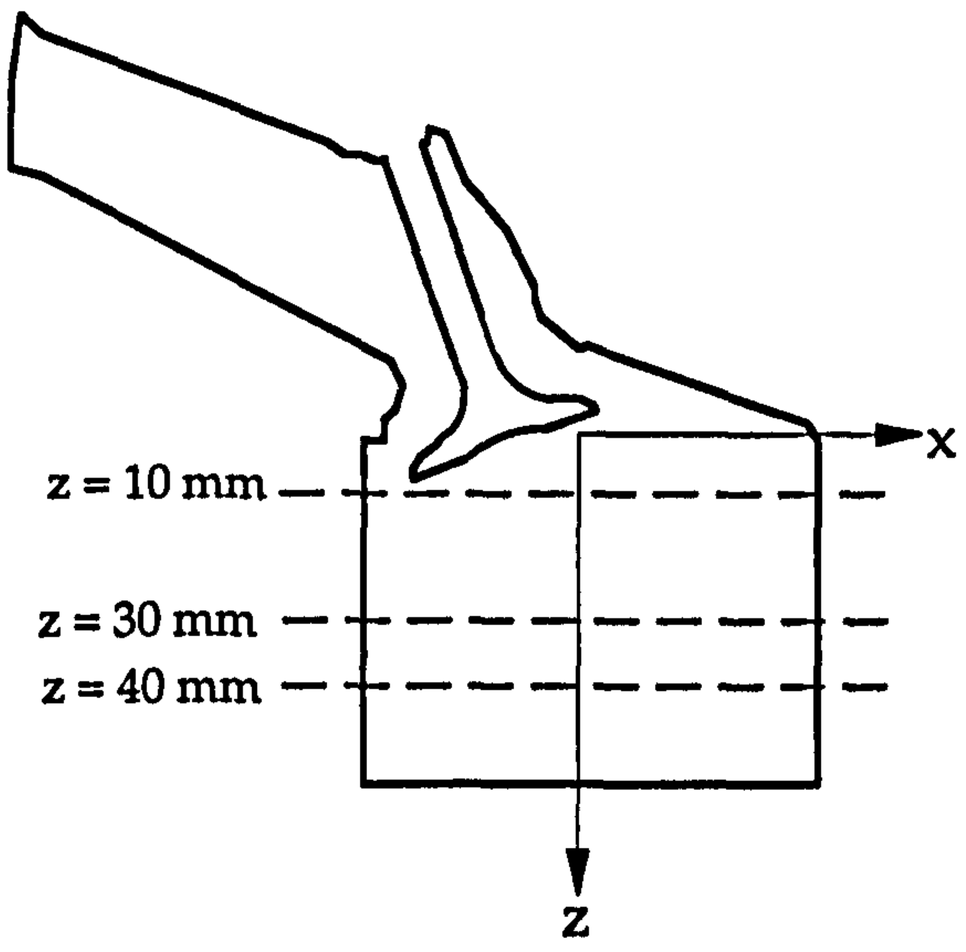

(b) Horizontal x-y planes

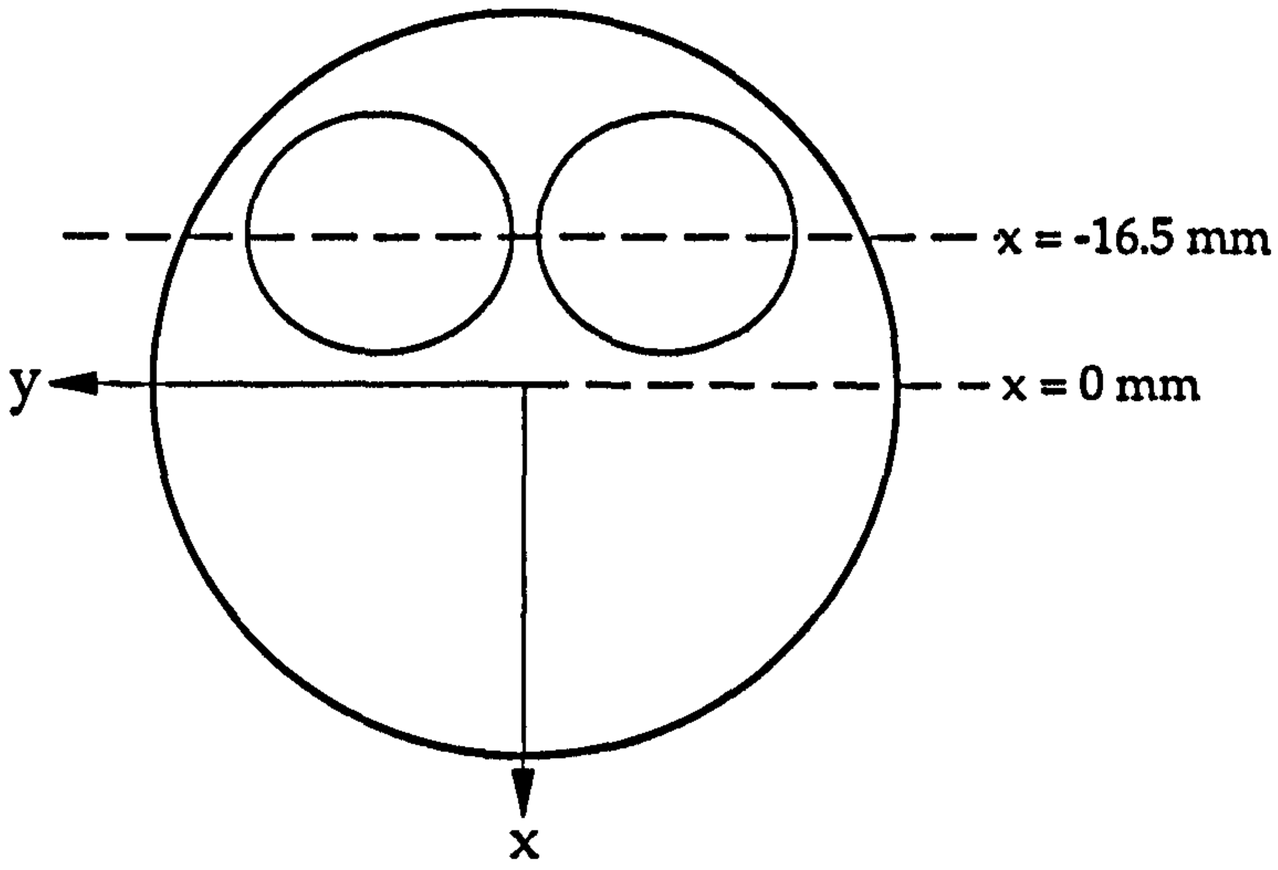

(c) Vertical y-z planes

Figure 3.1 Position of laser light sheet planes for flow visualisation study

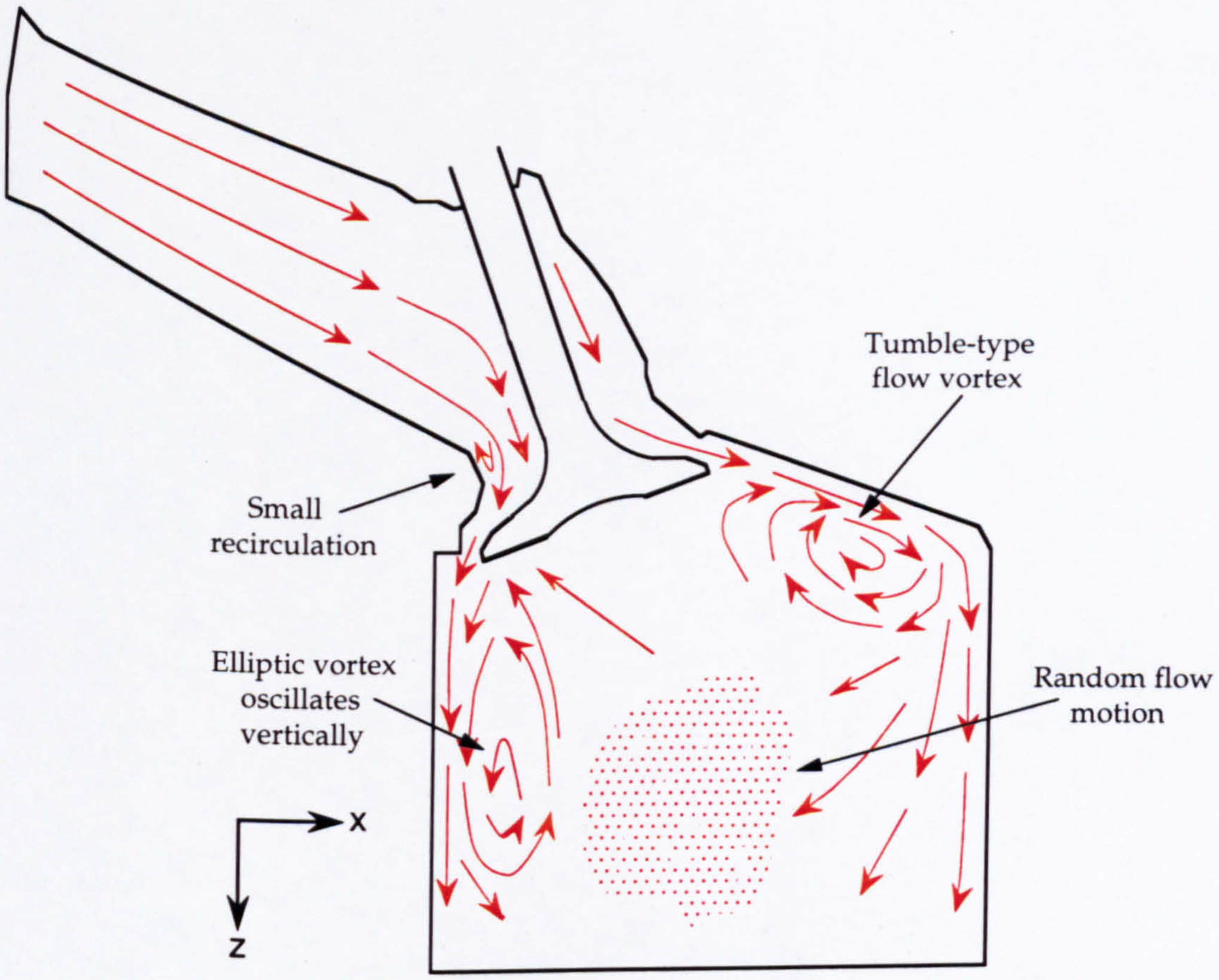

Figure 3.2(a) Flow structure in the y = -17.6 mm plane with mass flowrate m = 0.41 kg/s and 5 mm valve lifts

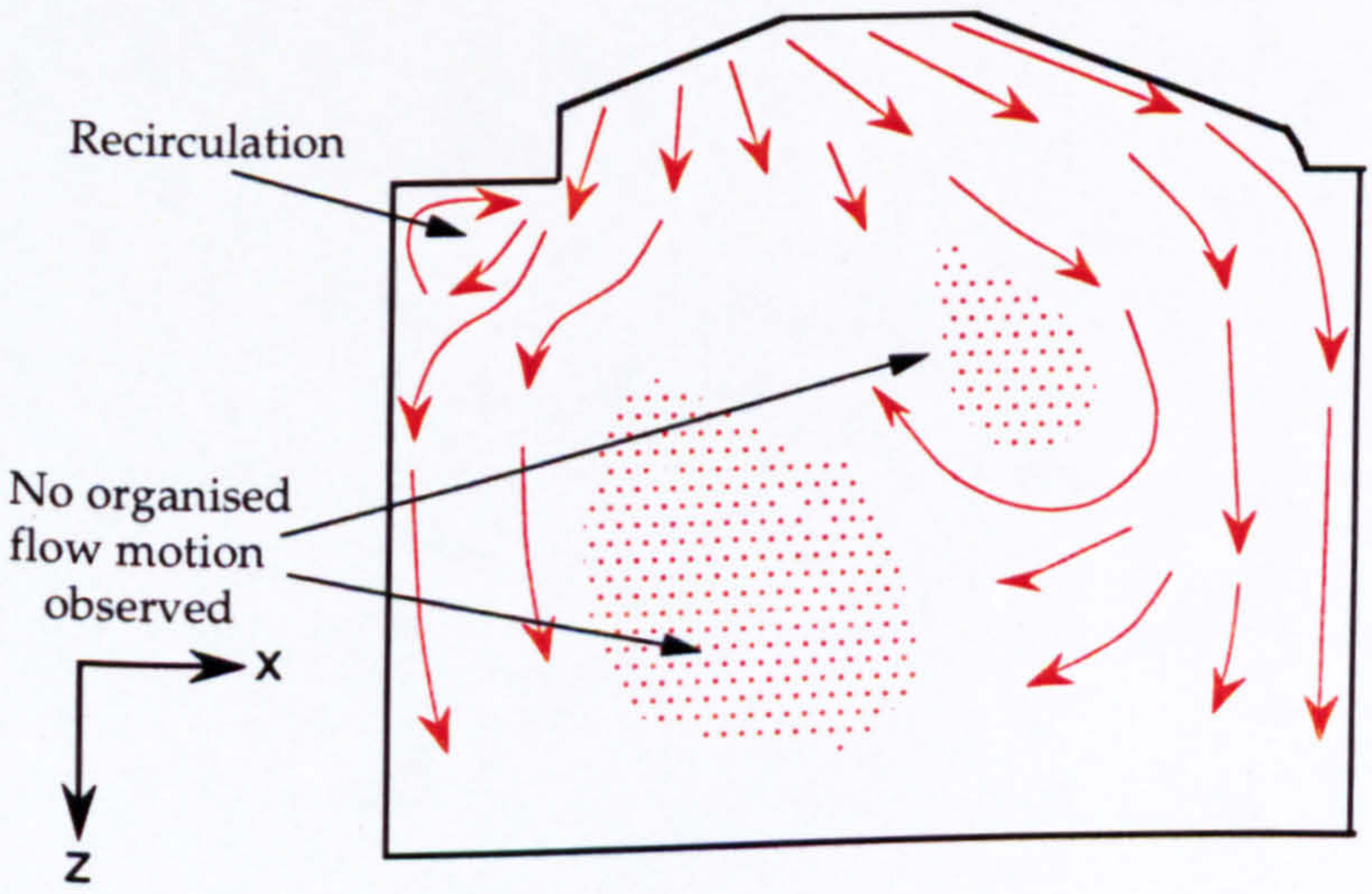

Figure 3.2(b) Flow structure in the y = 0 mm plane with mass flowrate m = 0.41 kg/s and 5 mm valve lifts

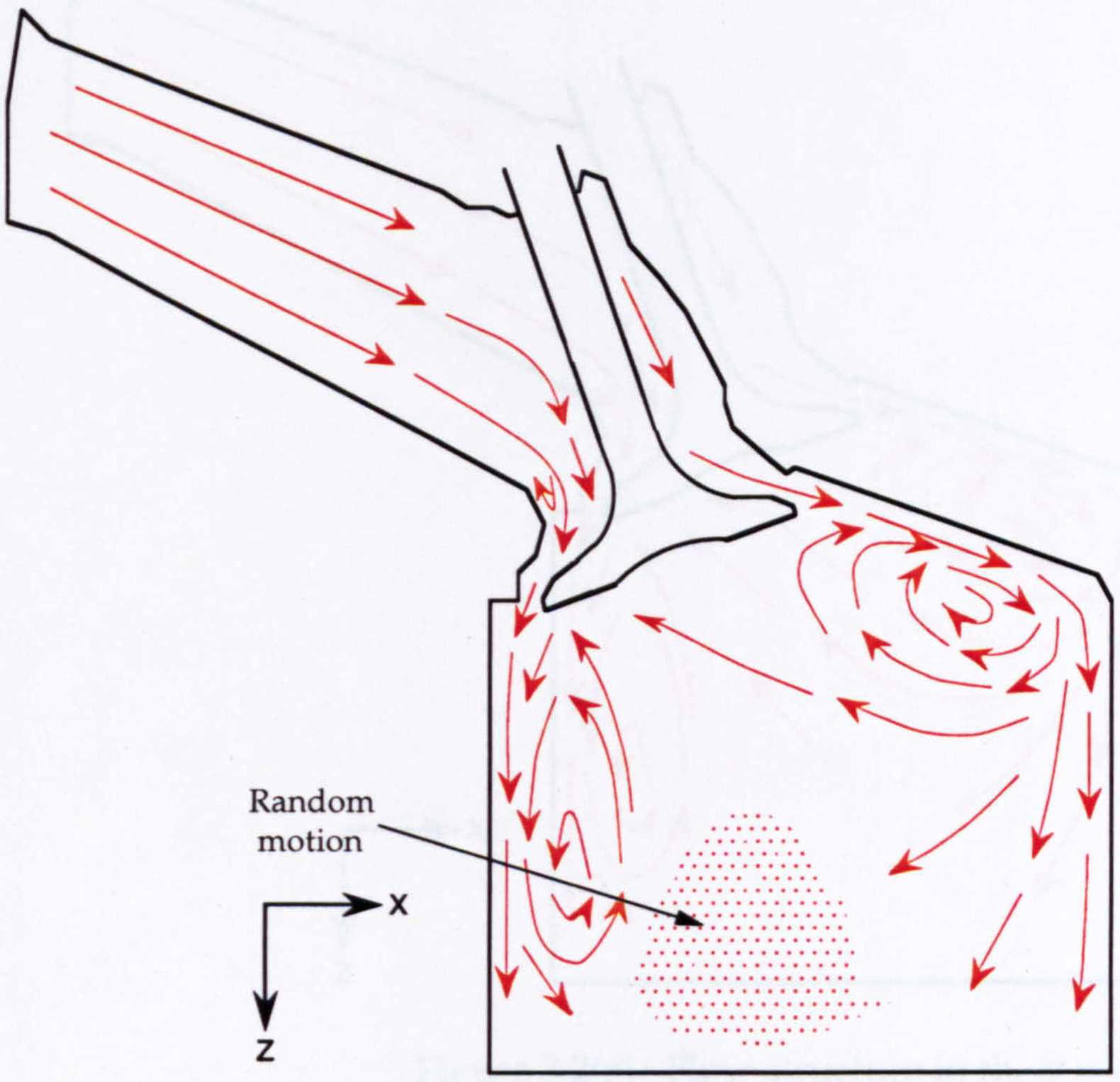

Figure 3.2(c) Flow structure in the y = -17.6 mm plane with mass flowrate m = 0.98 kg/s and 5 mm valve lifts

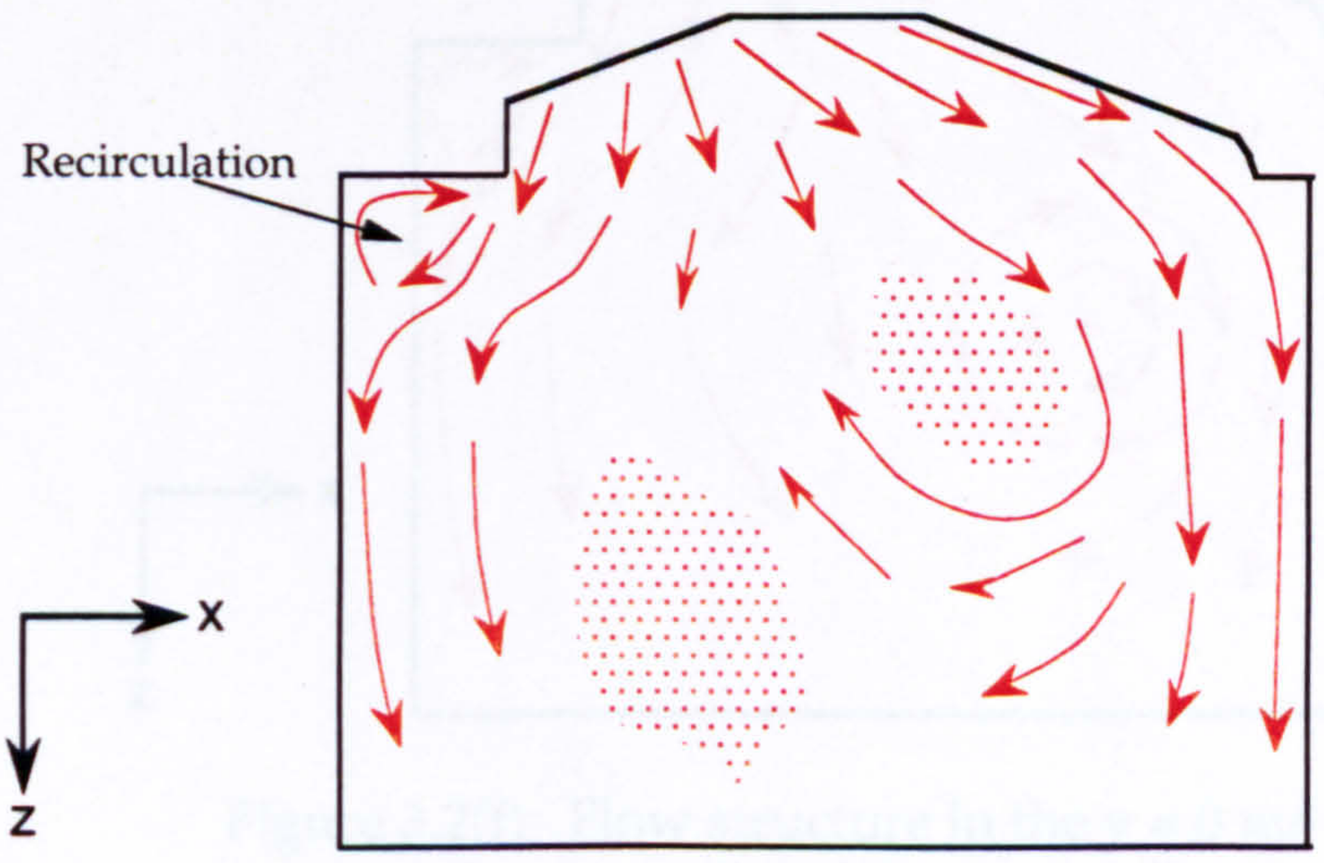

Figure 3.2(d) Flow structure in the y = 0 mm plane with mass flowrate m = 0.98 kg/s and 5 mm valve lifts

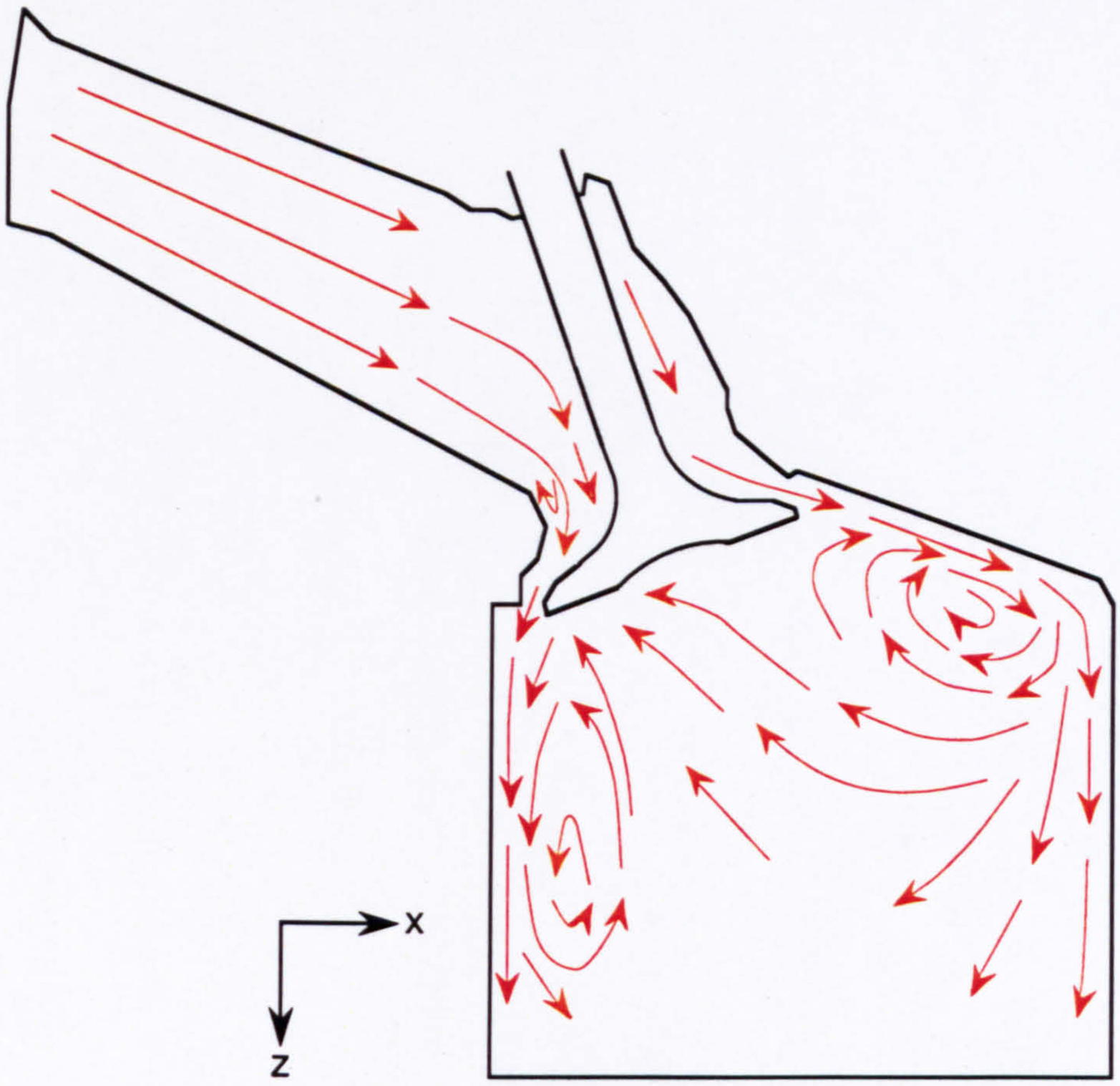

Figure 3.2(e) Flow structure in the y = -17.6 mm plane with mass flowrate m = 1.54 kg/s and 5 mm valve lifts

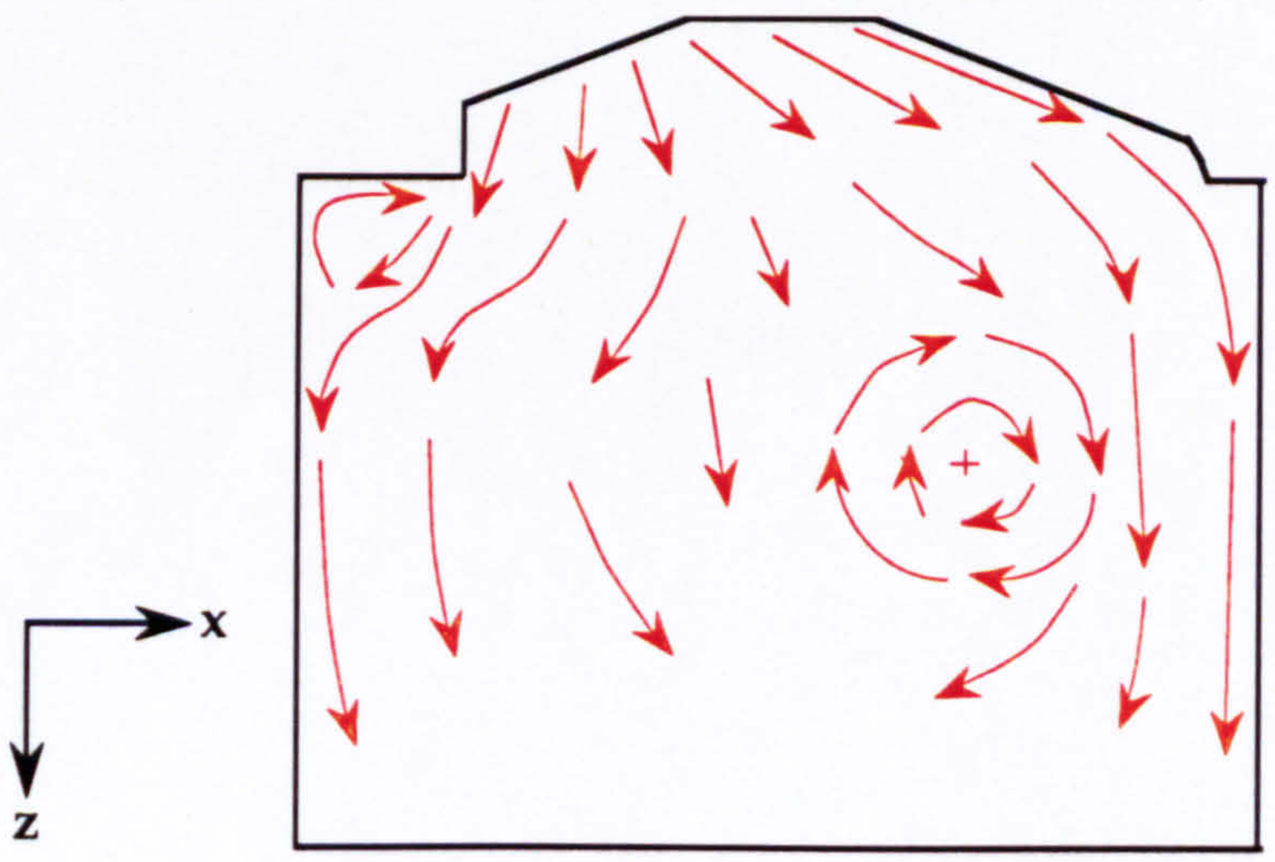

Figure 3.2(f) Flow structure in the y = 0 mm plane with mass flowrate m = 1.54 kg/s and 5 mm valve lifts

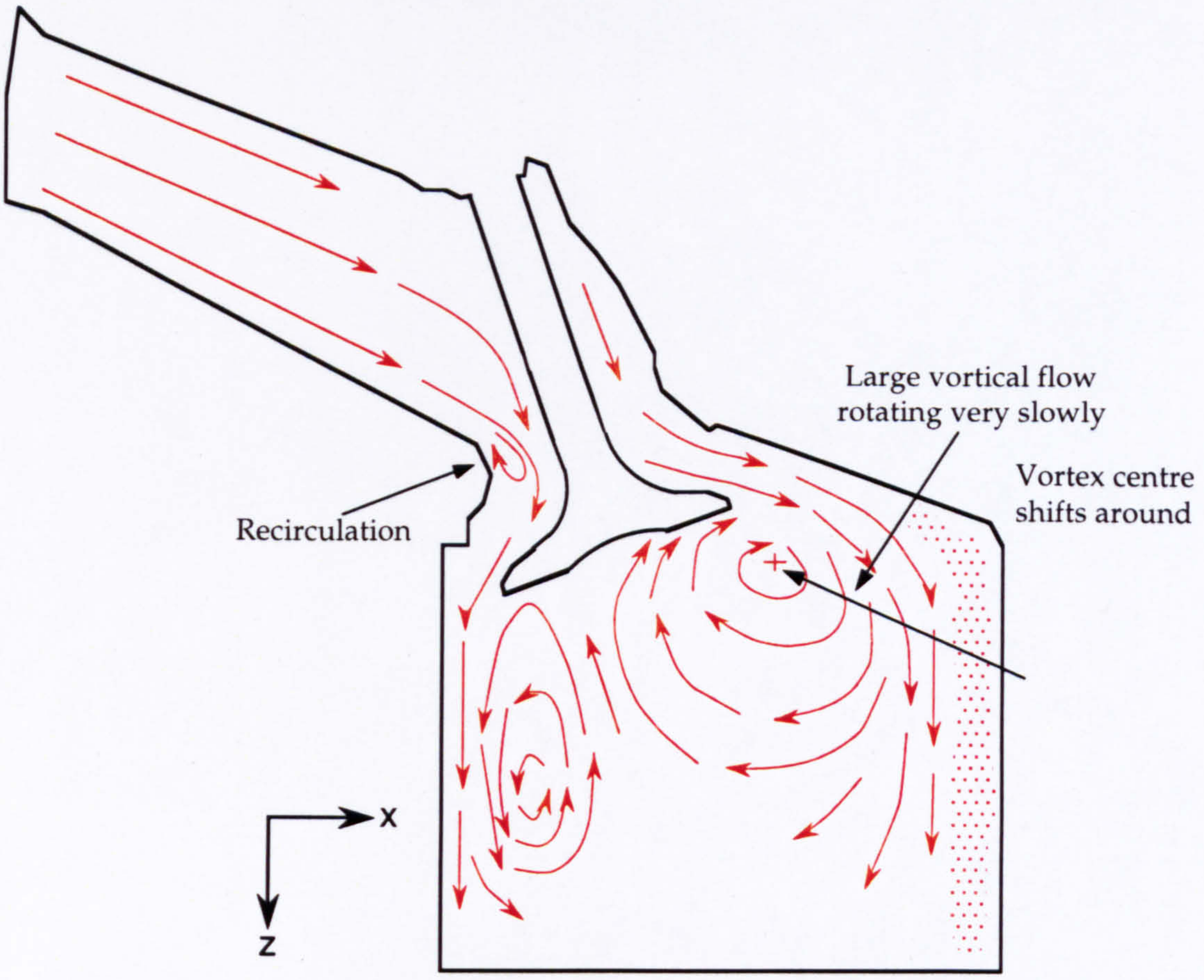

Figure 3.3(a) Flow structure in the y = -17.6 mm plane with mass flowrate m = 0.41 kg/s and 10 mm valve lifts

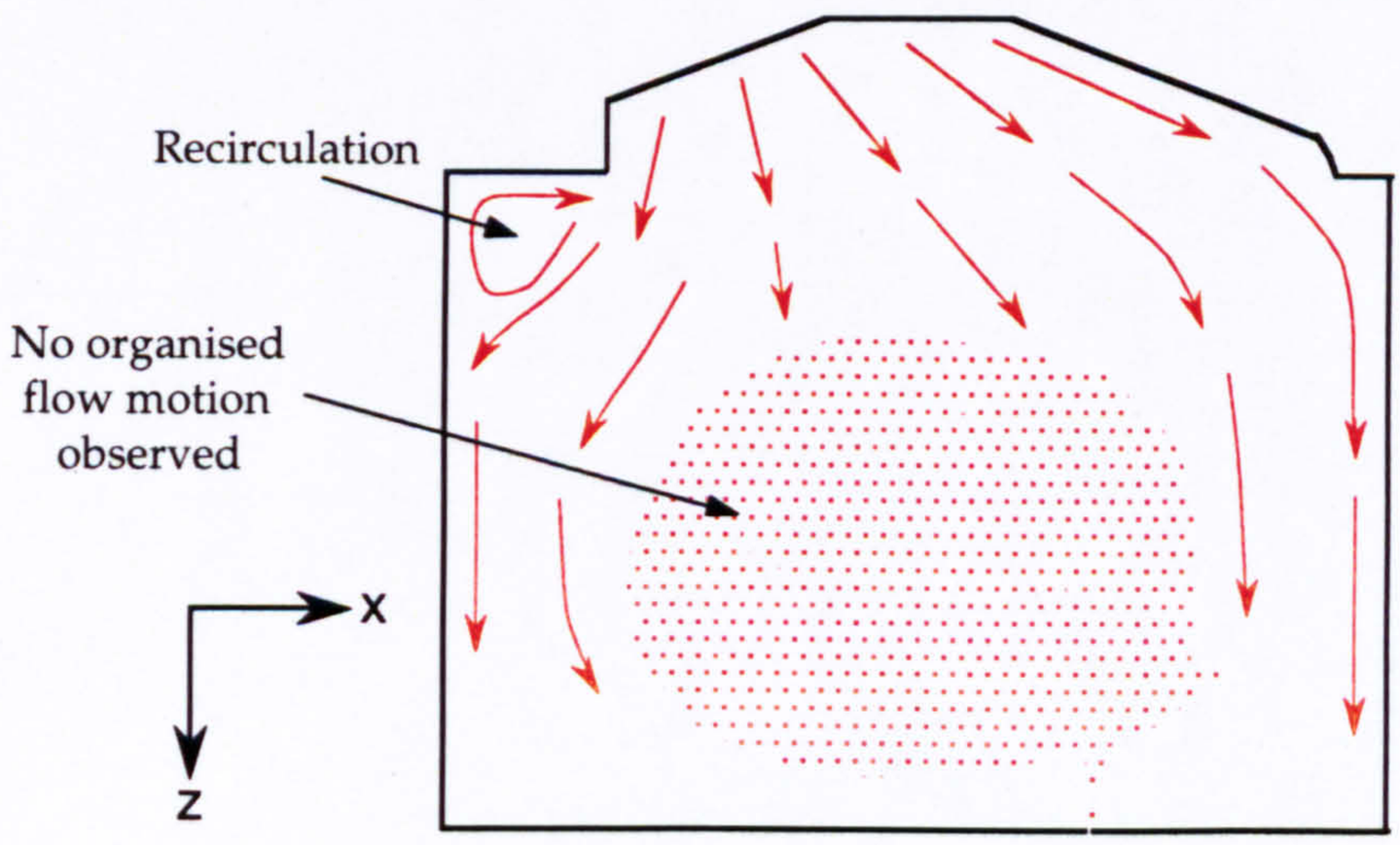

Figure 3.3(b) Flow structure in the y = 0 mm plane with mass flowrate m = 0.41 kg/s and 10 mm valve lifts

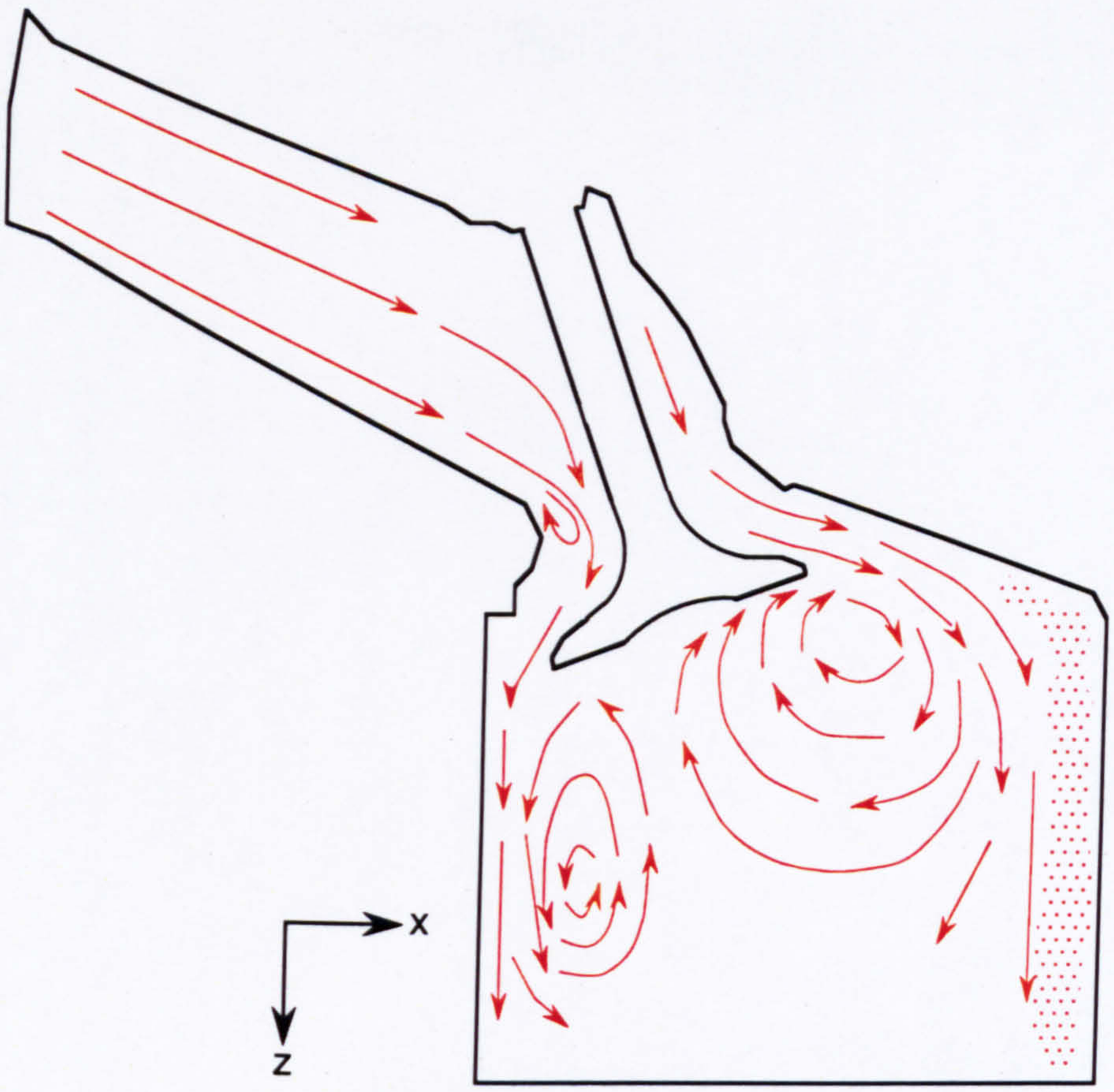

Figure 3.3(c) Flow structure in the y = -17.6 mm plane with mass flowrate m = 0.98 kg/s and 10 mm valve lifts

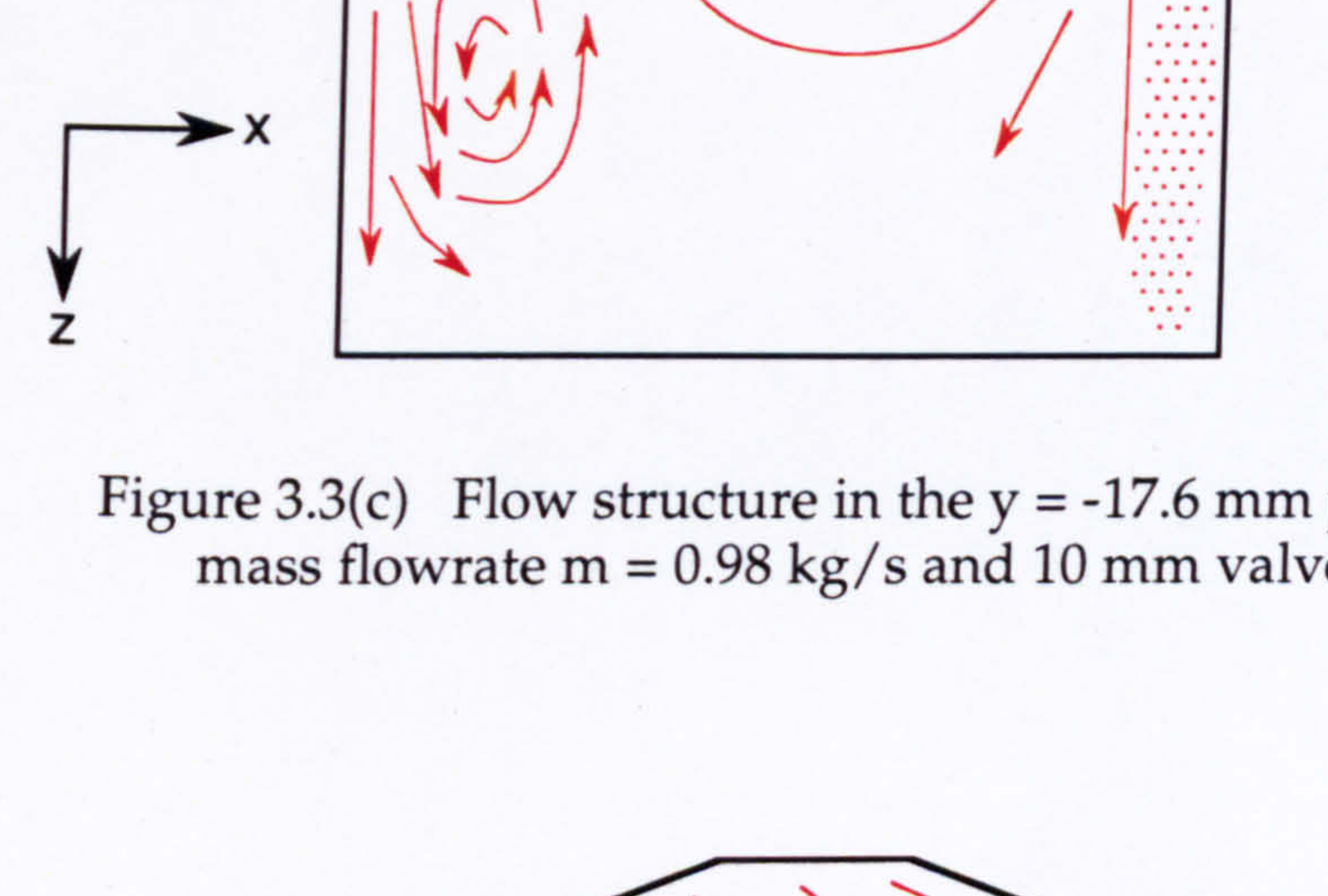

Figure 3.3(d) Flow structure in the y = 0 mm plane with mass flowrate m = 0.98 kg/s and 10 mm valve lifts

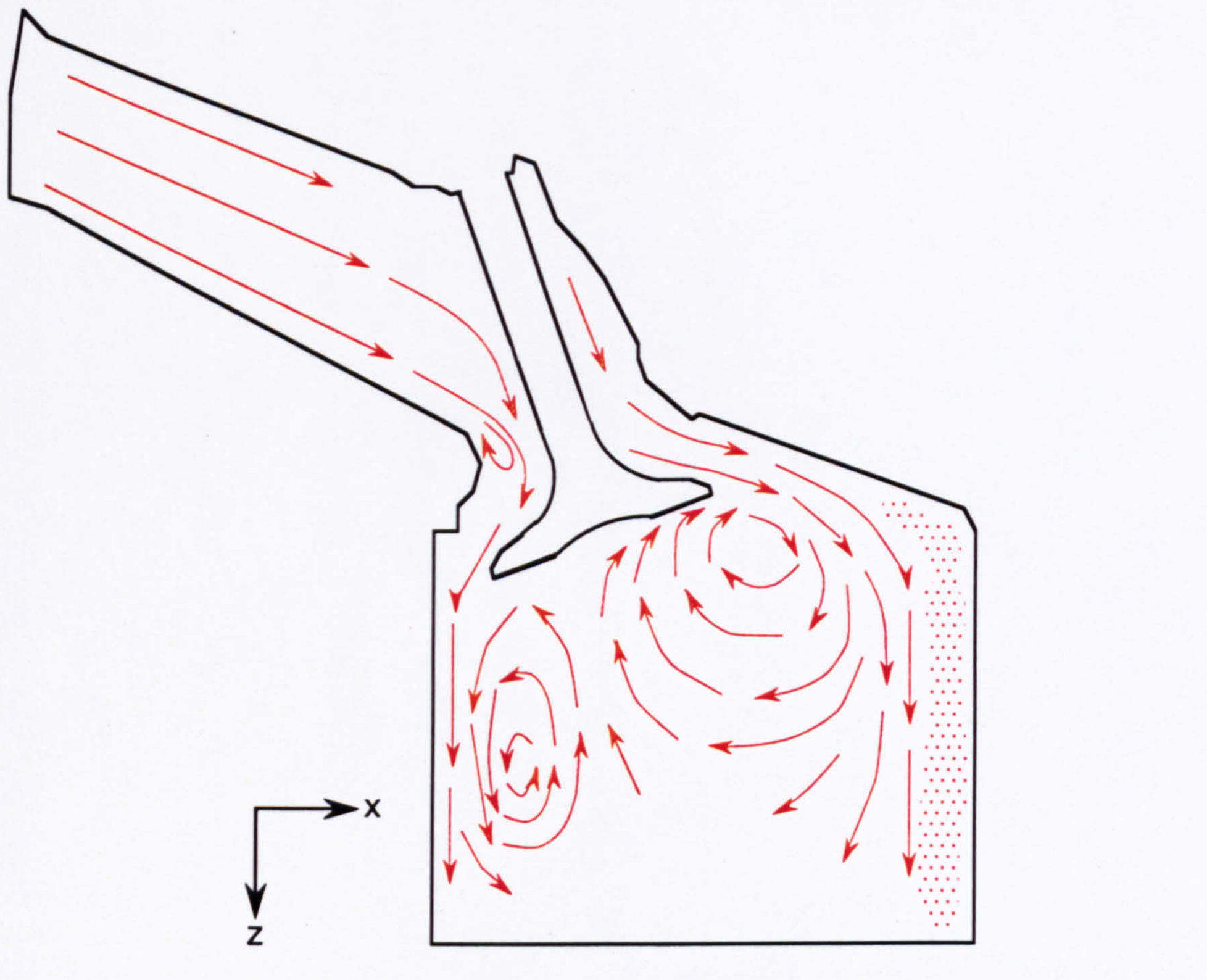

Figure 3.3(e) Flow structure in the y = -17.6 mm plane with mass flowrate m = 1.54 kg/s and 10 mm valve lifts

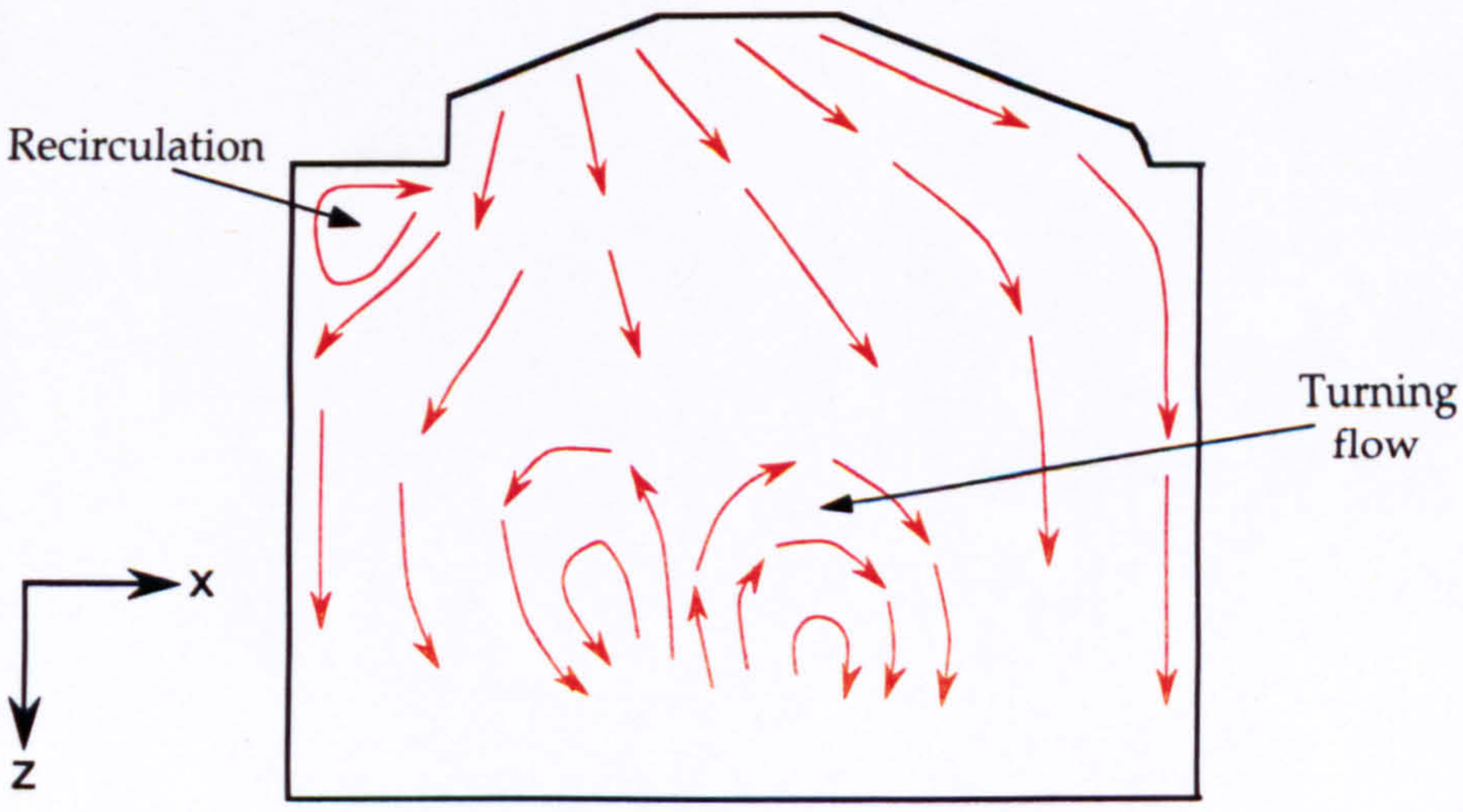

Figure 3.3(f) Flow structure in the y = -17.6 mm plane with mass flowrate m = 1.54 kg/s and 10 mm valve lifts

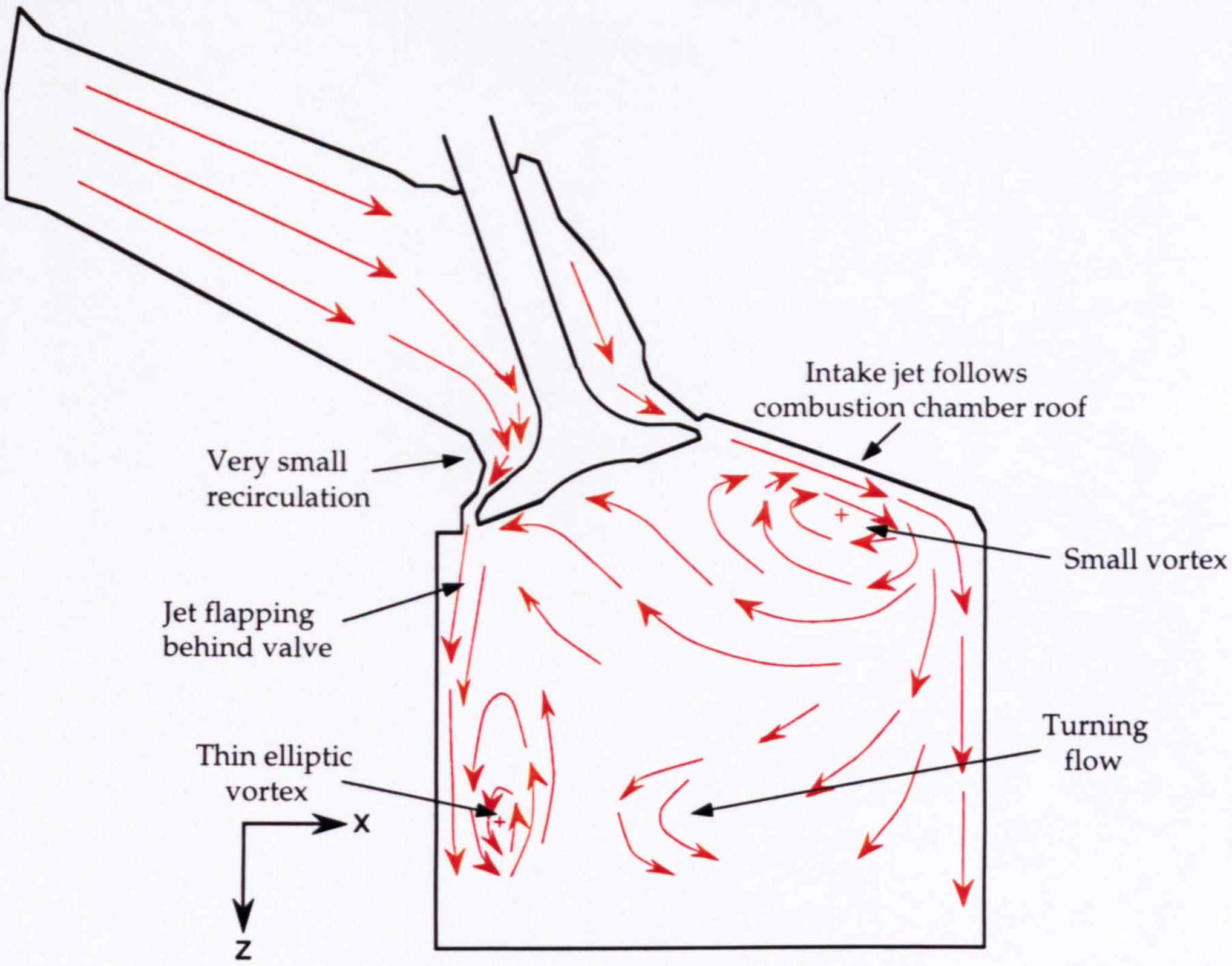

Figure 3.4(a) Flow structure in the y = -17.6 mm plane with both valve lifts set at 2.5 mm

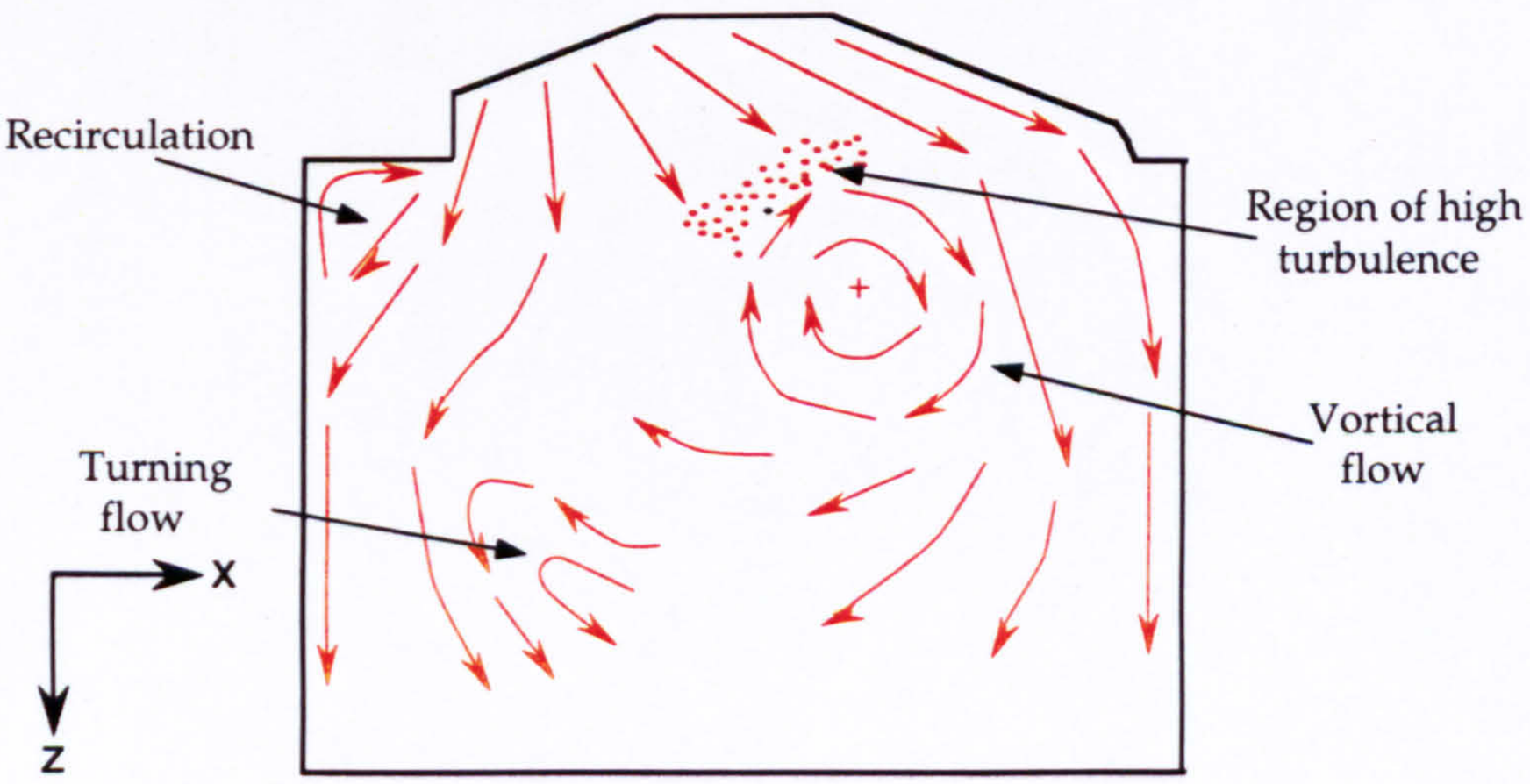

Figure 3.4(b) Flow structure in the y = 0 mm plane with both valve lifts set at 2.5 mm

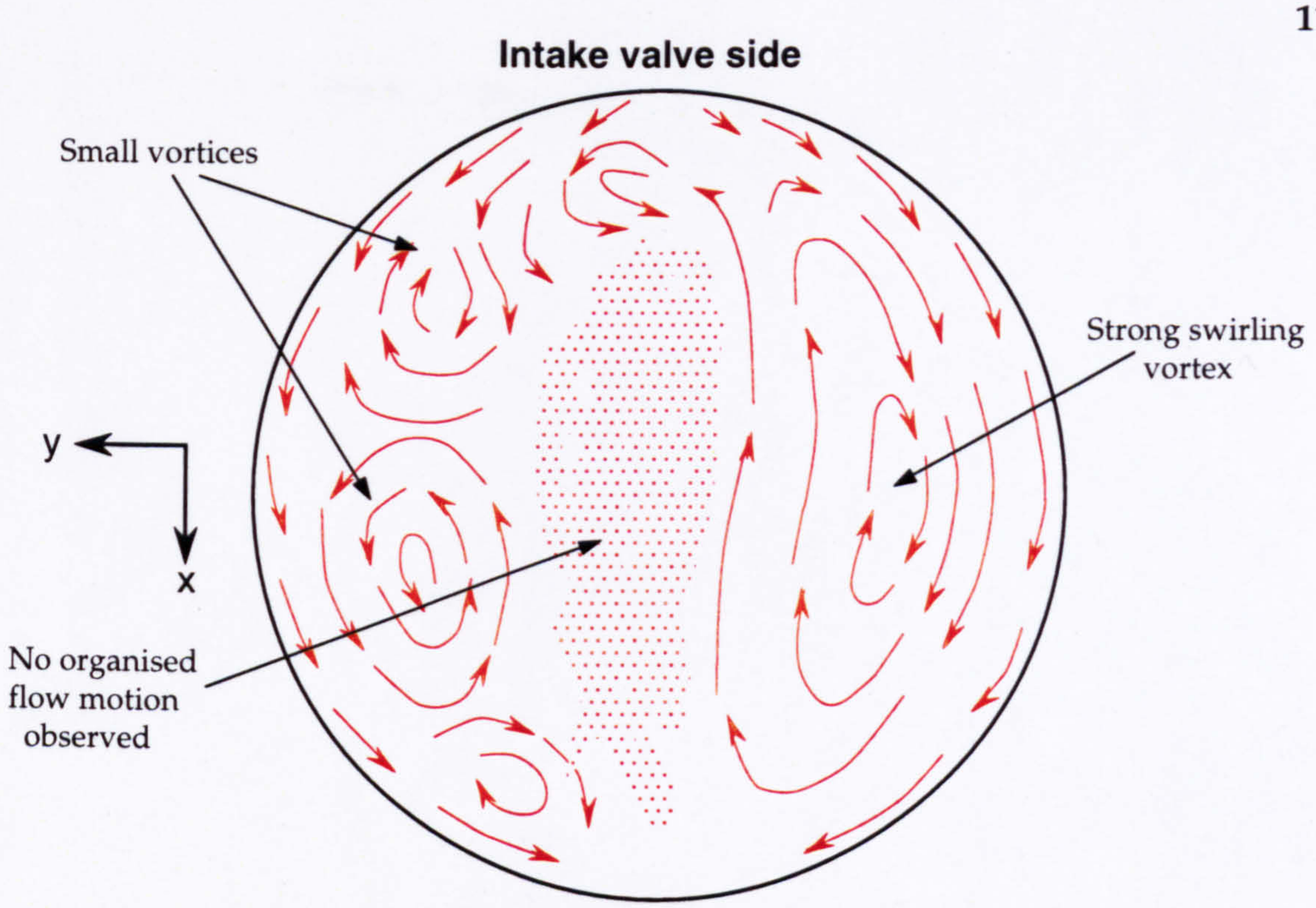

Figure 3.4(c) One of the two flow patterns observed in the z = 10 mm horizontal plane with both valve lifts set at 2.5 mm

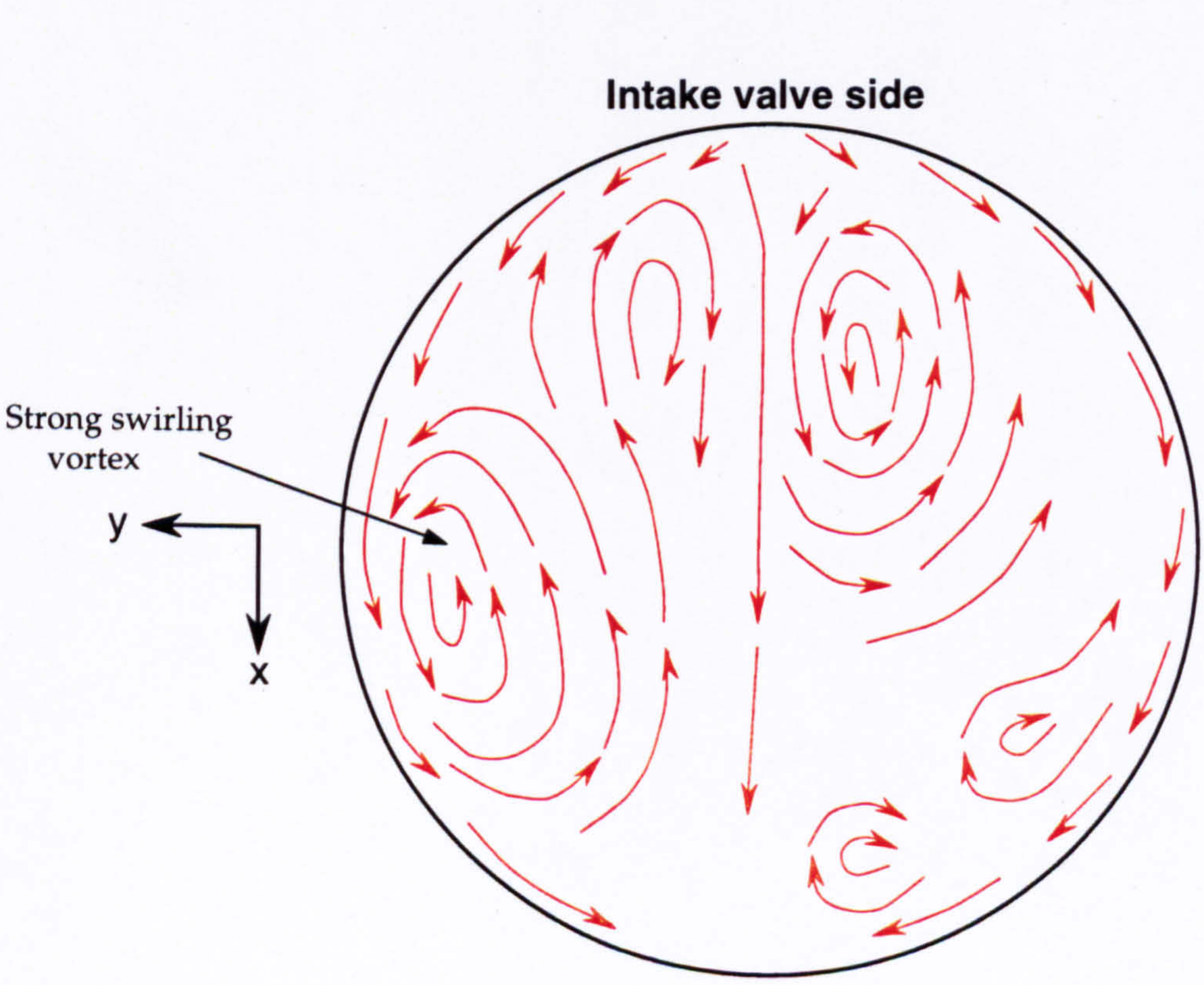

Figure 3.4(d) The other flow pattern observed in the z = 10 mm horizontal plane with both valve lifts set at 2.5 mm

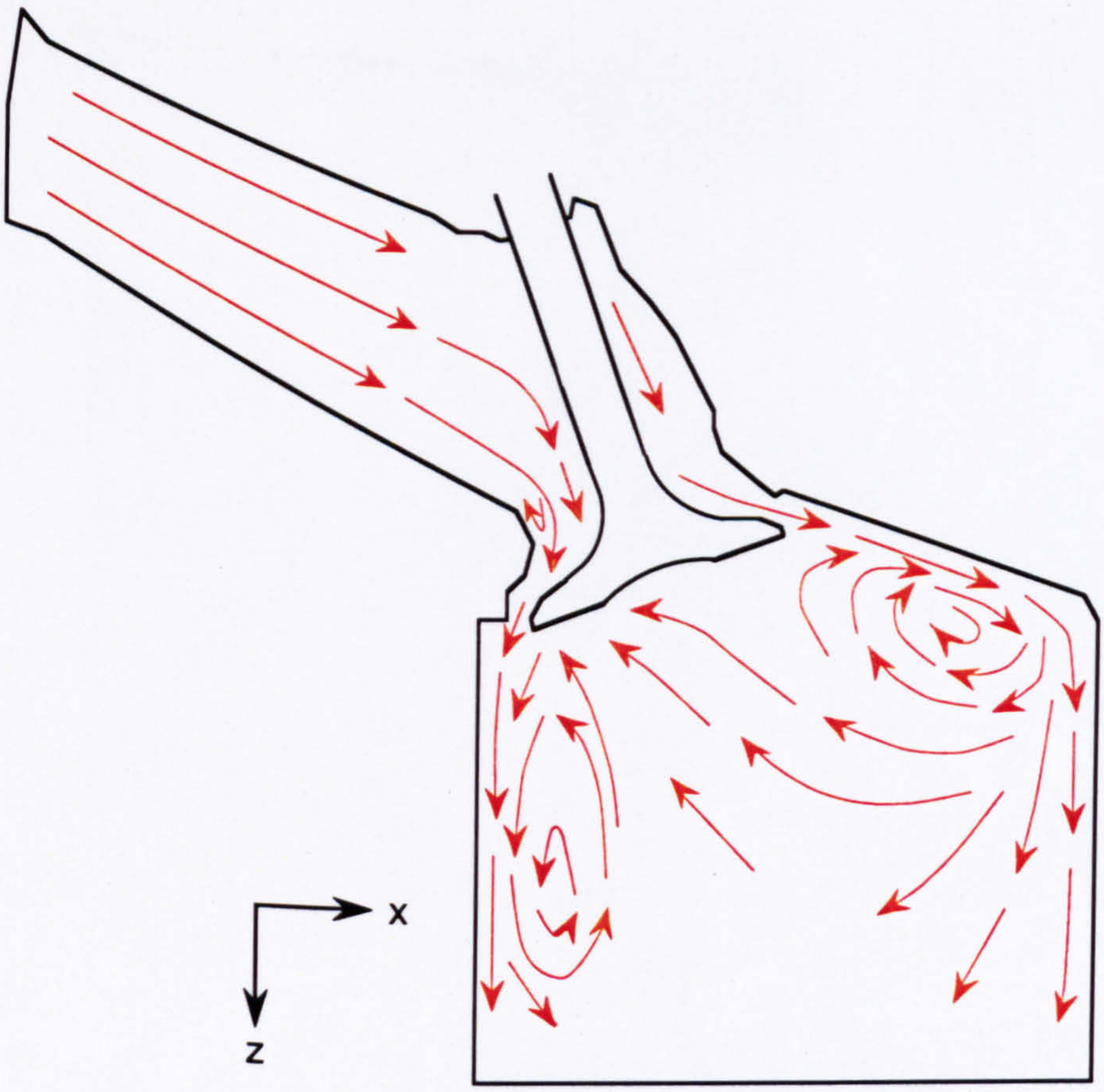

Figure 3.5(a) Flow structure in the y = -17.6 mm plane with both valve lifts set at 5 mm

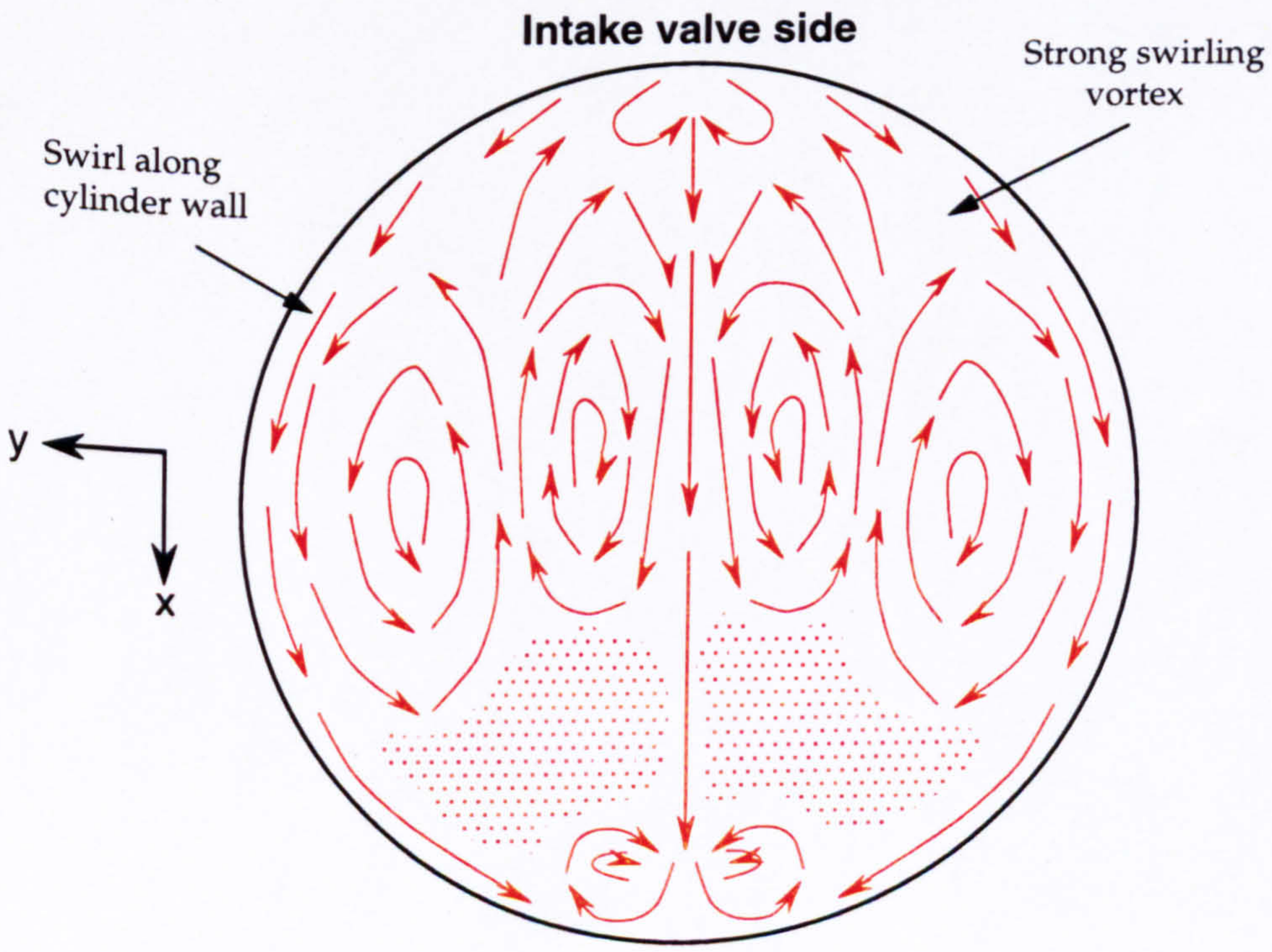

Figure 3.5(b) Flow structure in the z = 10 mm horizontal plane with both valve lifts set at 5 mm

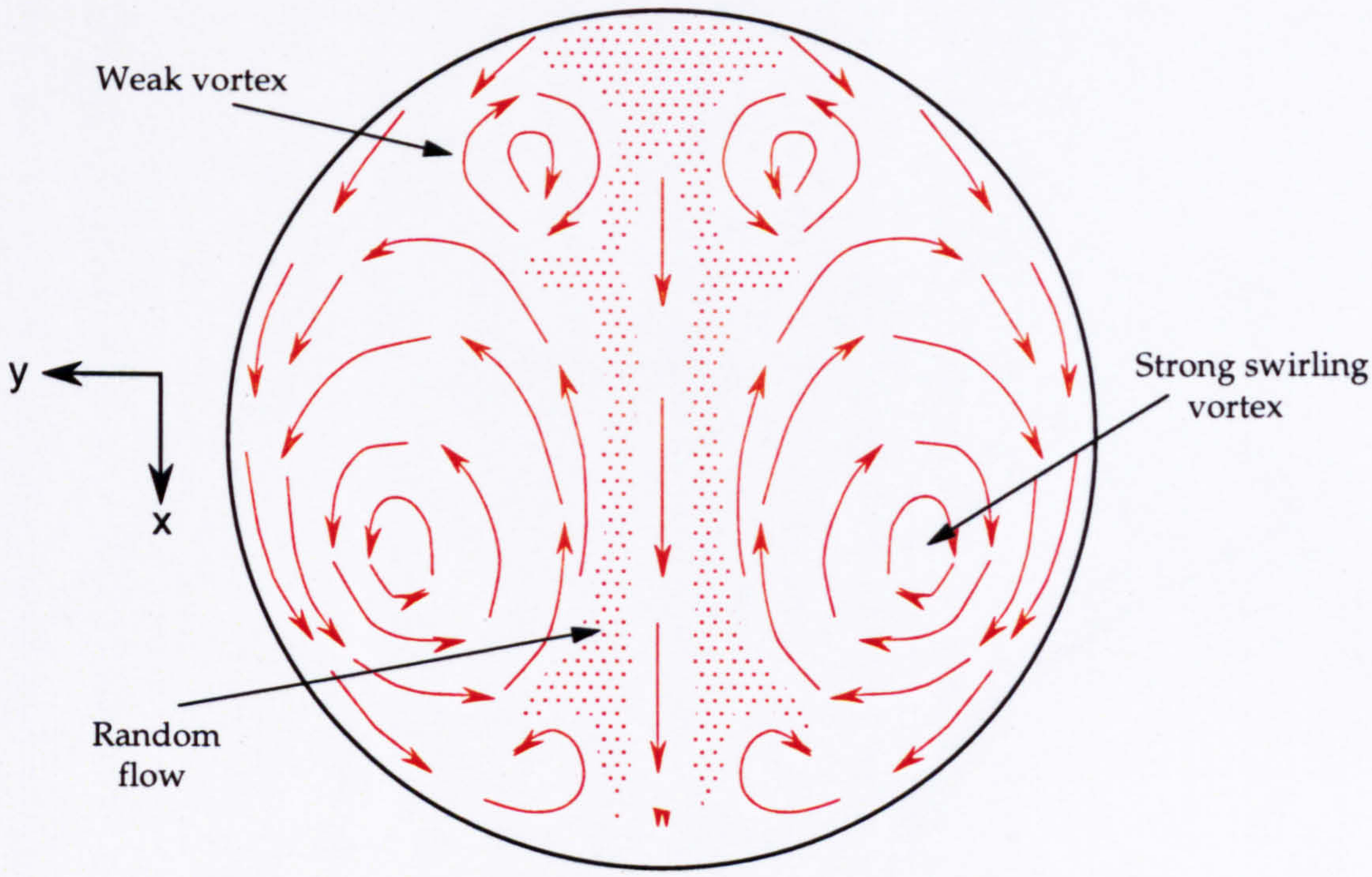

Figure 3.5(c) Flow structure in the z = 30 mm horizontal plane with both valve lifts set at 5 mm

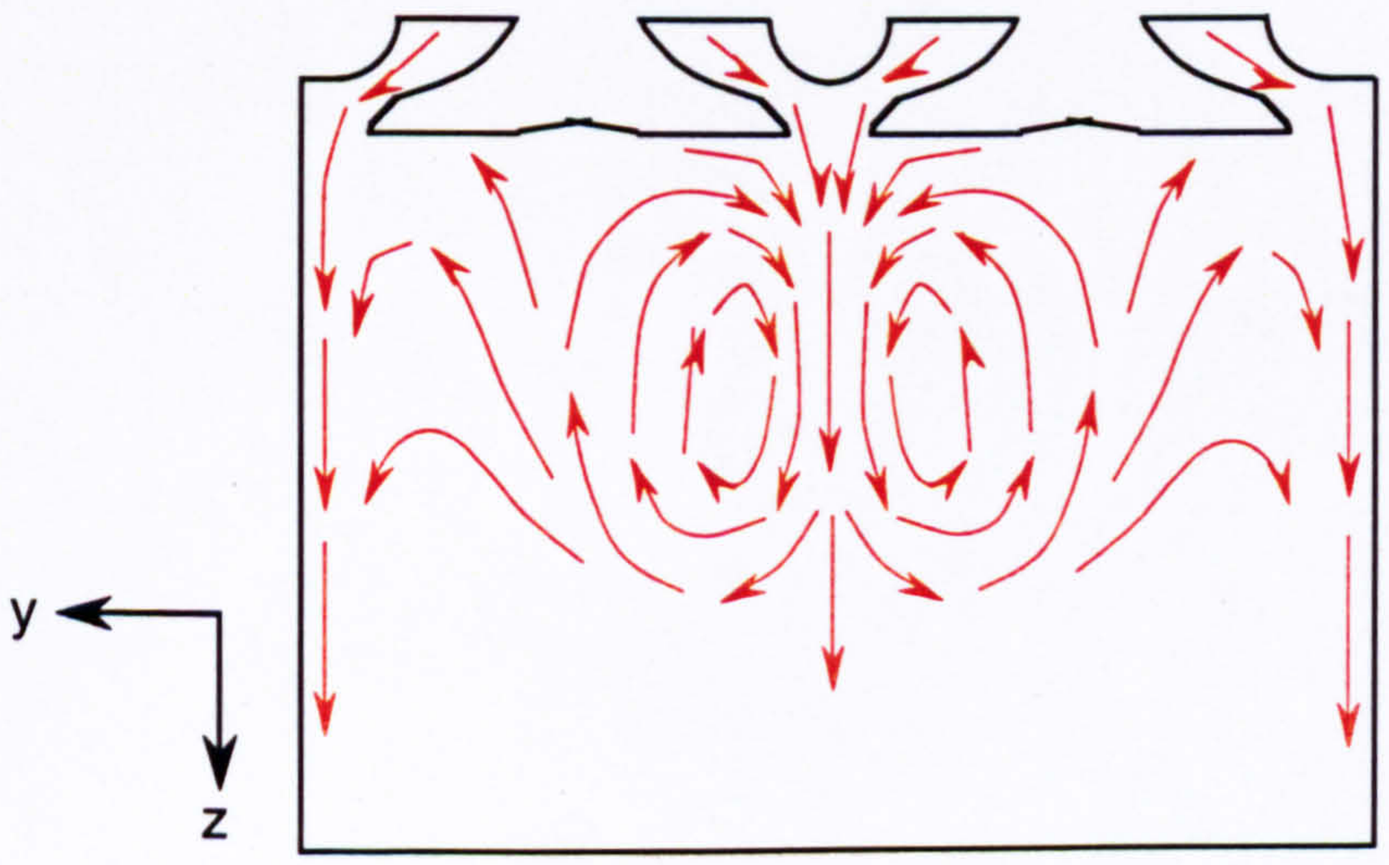

Figure 3.5(d) Flow structure in the x = -16.5 mm plane with both valve lifts set at 5 mm

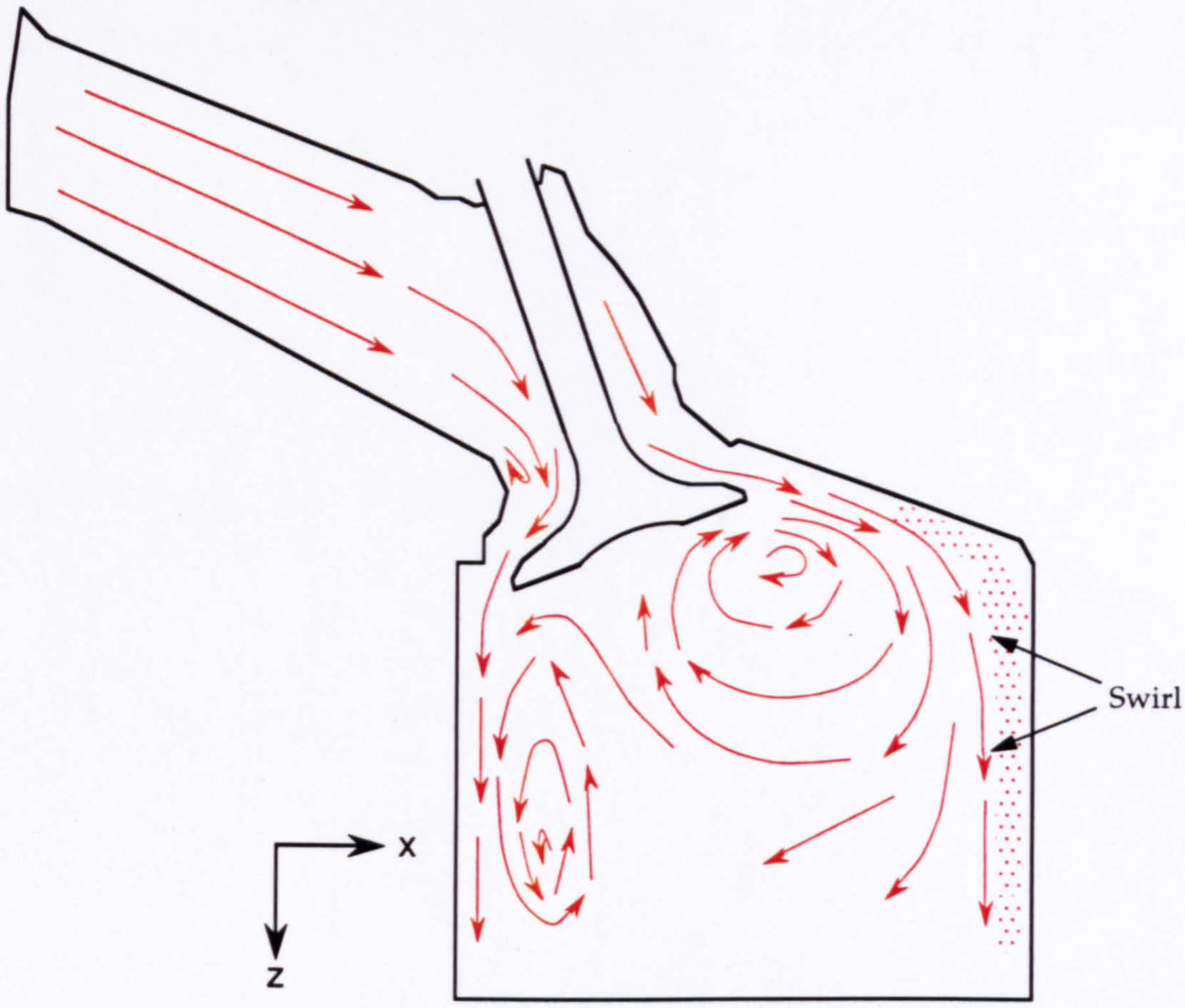

Figure 3.6(a) Flow structure in the plane y = -17.6 mm with both valve lifts set at 7.5 mm

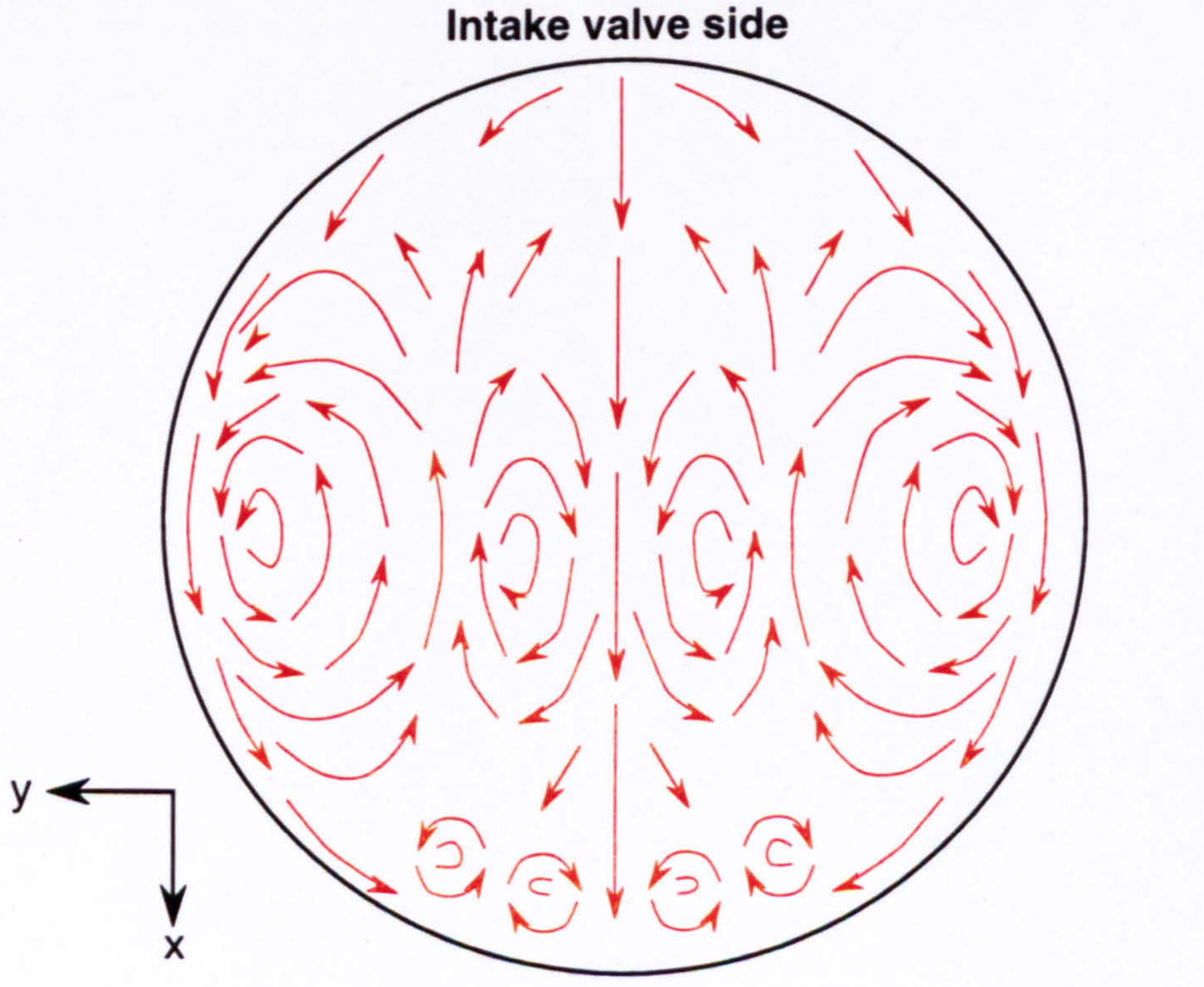

Figure 3.6(b) Flow structure in the z = 10 mm horizontal plane with both valve lifts set at 7.5 mm

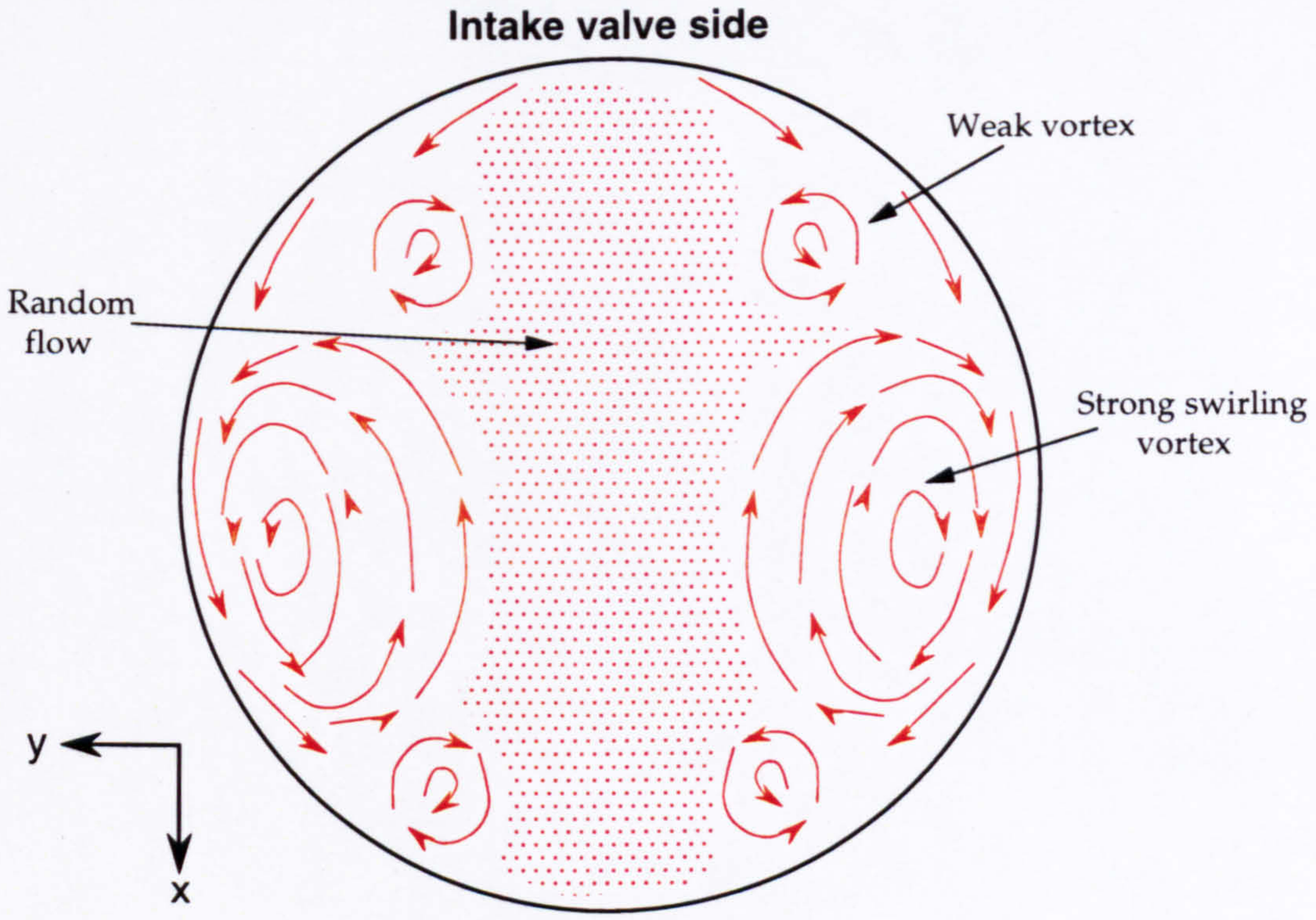

Figure 3.6(c) Flow structure in the z = 30 mm horizontal plane with both valve lifts set at 7.5 mm

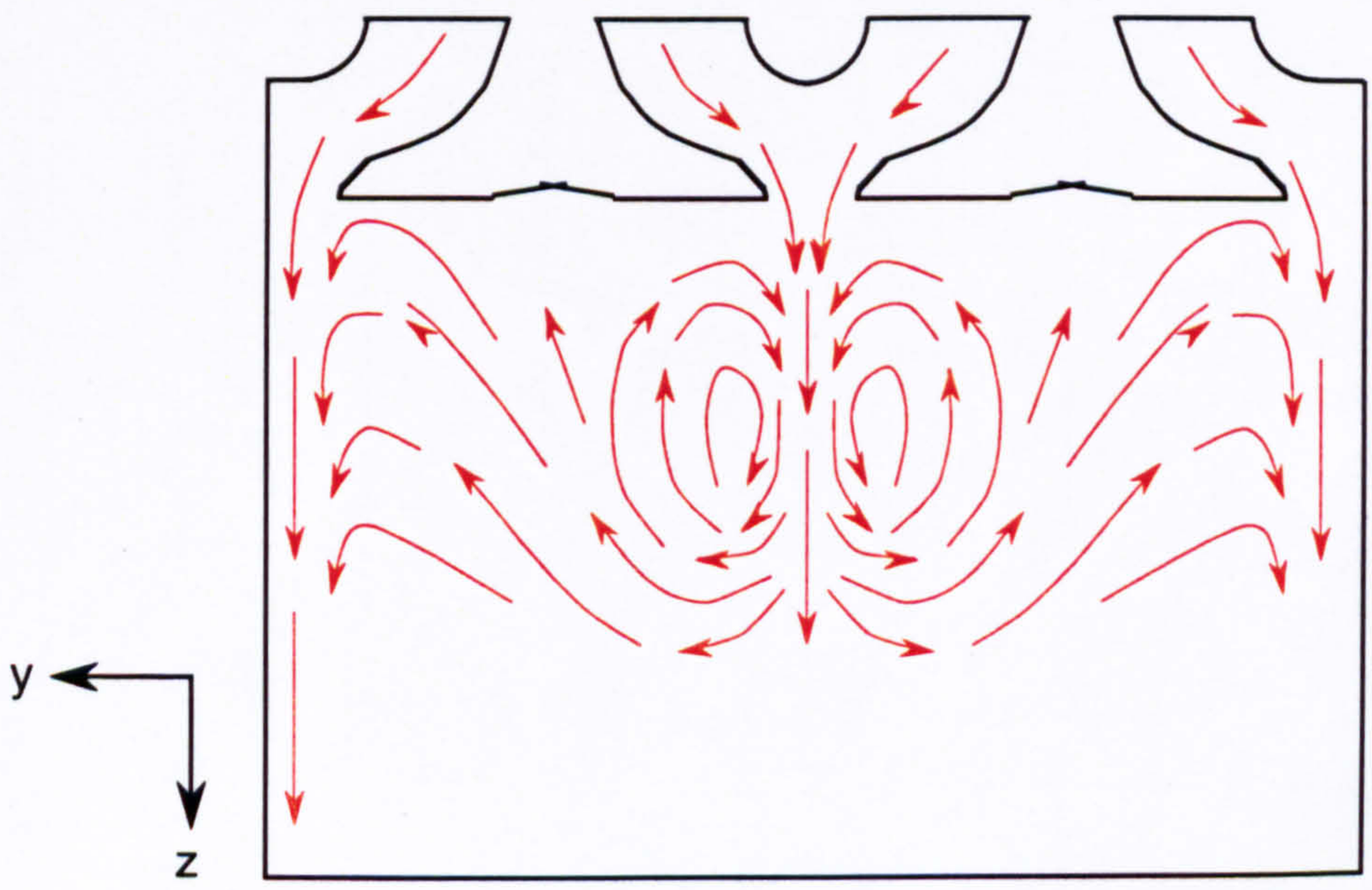

Figure 3.6(d) Flow structure in the plane x = -16.5 mm with both valve lifts set at 7.5 mm

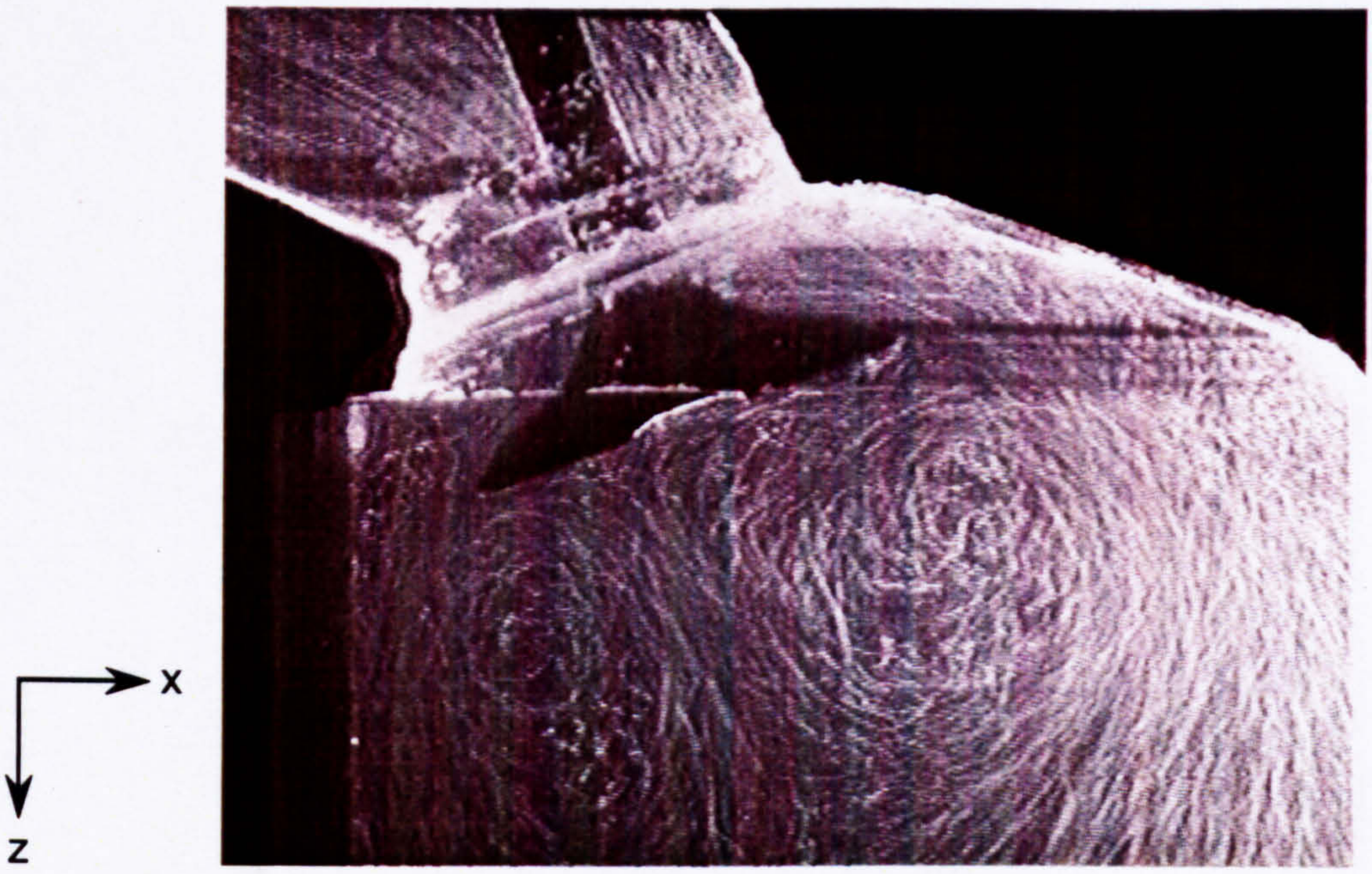

Figure 3.7(a) Flow structure in the vertical plane y = -17.6 mm with both valve lifts set at 10 mm

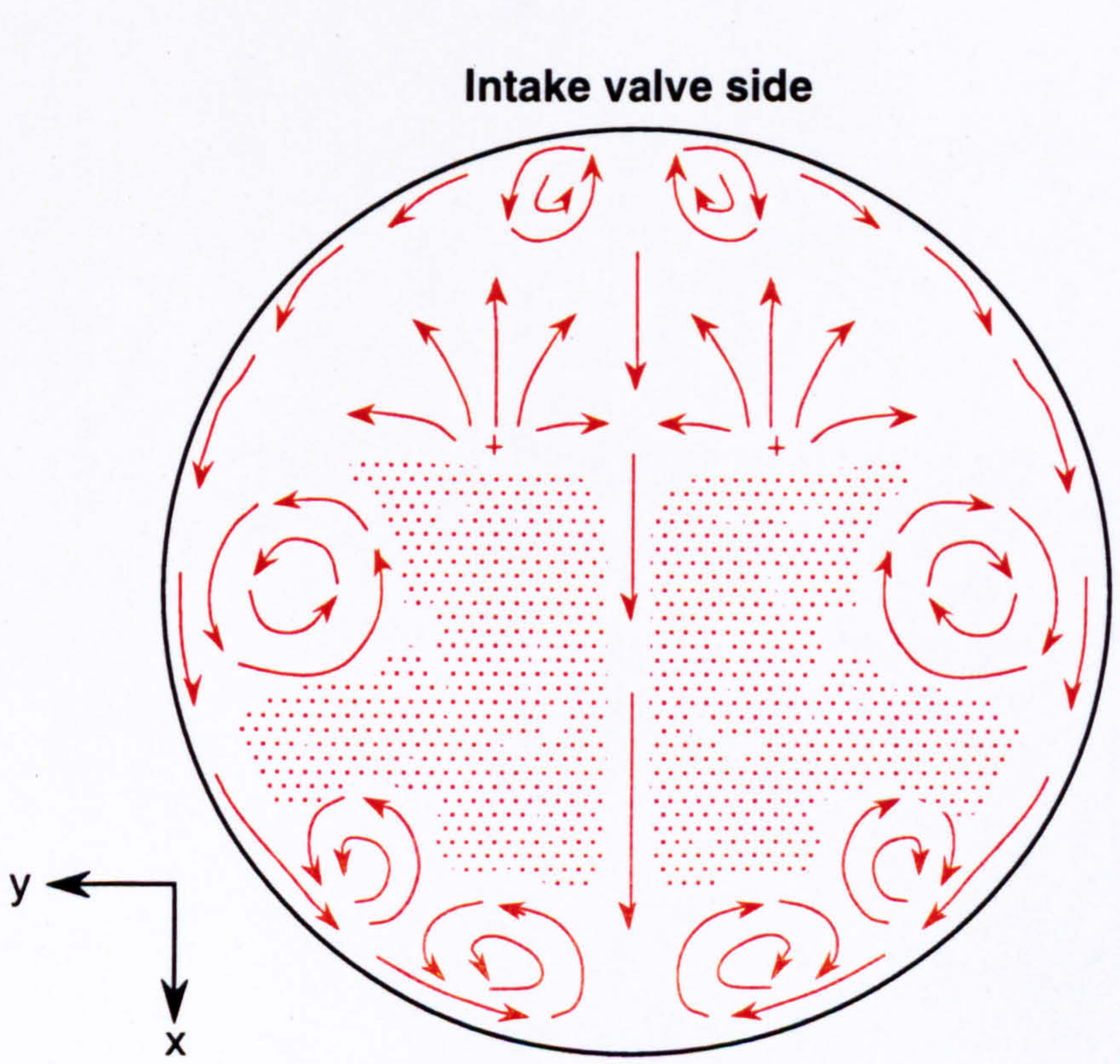

Figure 3.7(b) Flow structure in the z = 10 mm horizontal plane with both valve lifts set at 10 mm

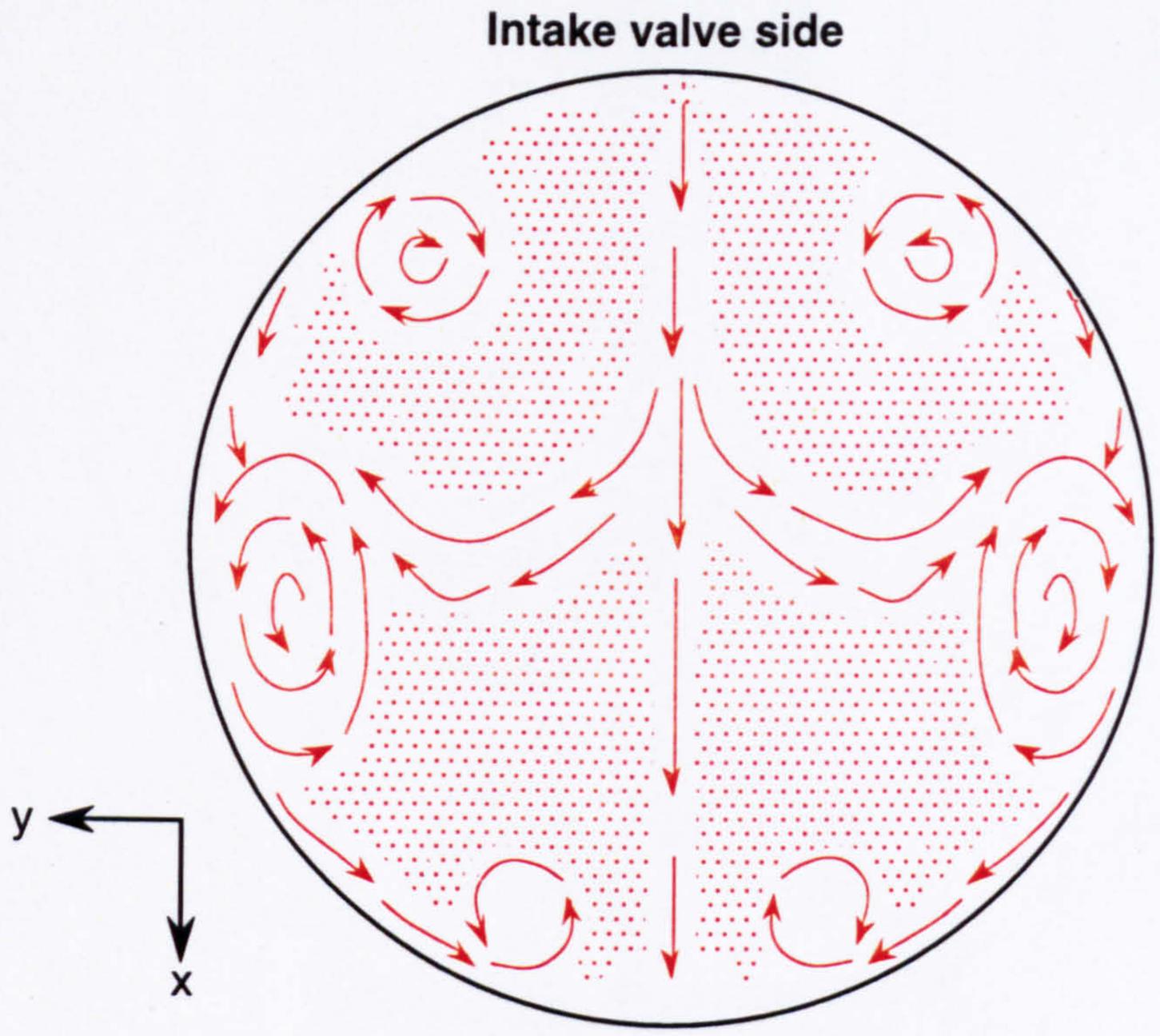

Figure 3.7(c) Flow structure in the z = 30 mm horizontal plane with both valve lifts set at 10 mm

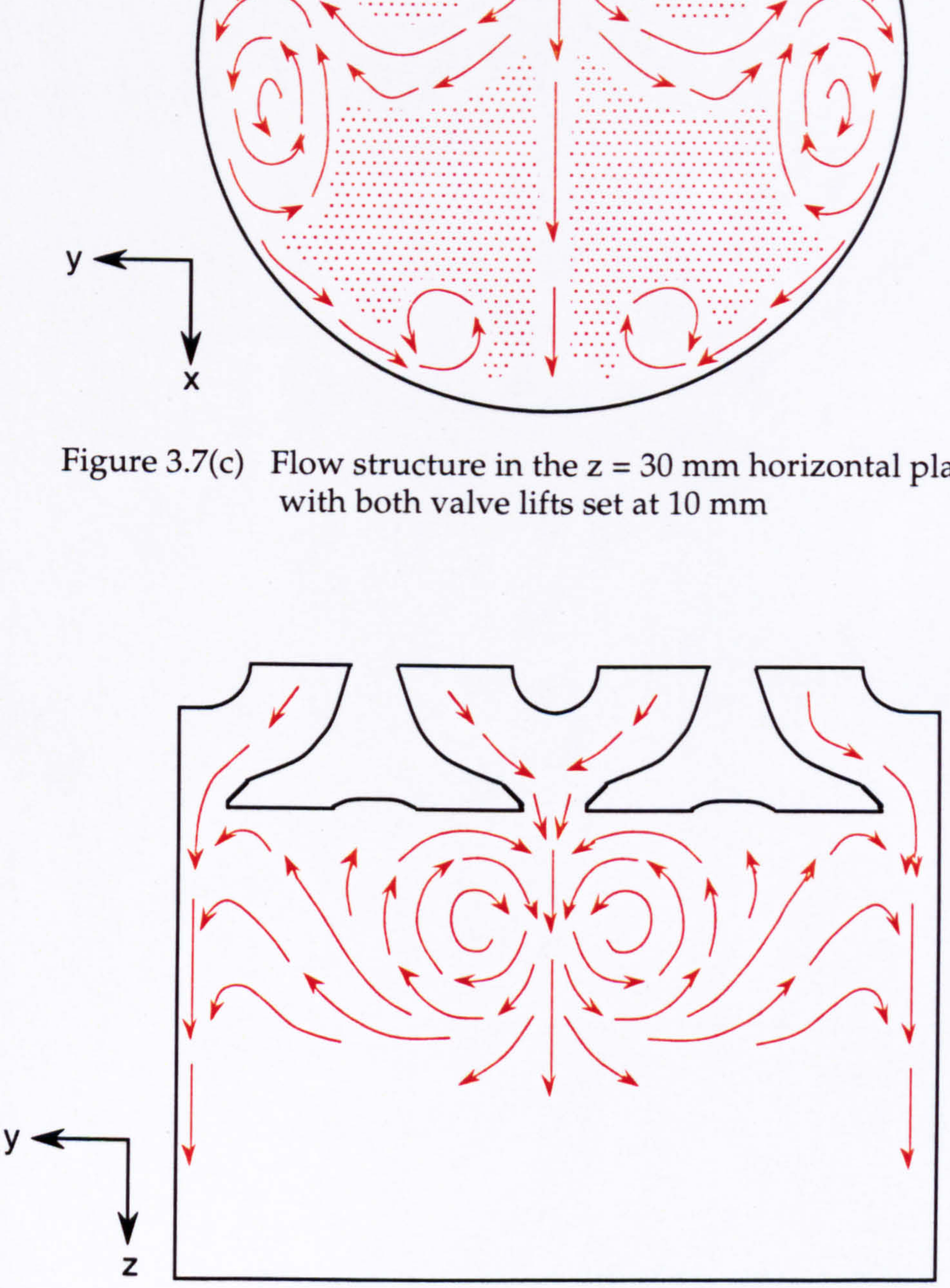

Figure 3.7(d) Flow structure in the x = -16.5 mm vertical plane with both valve lifts set at 10 mm

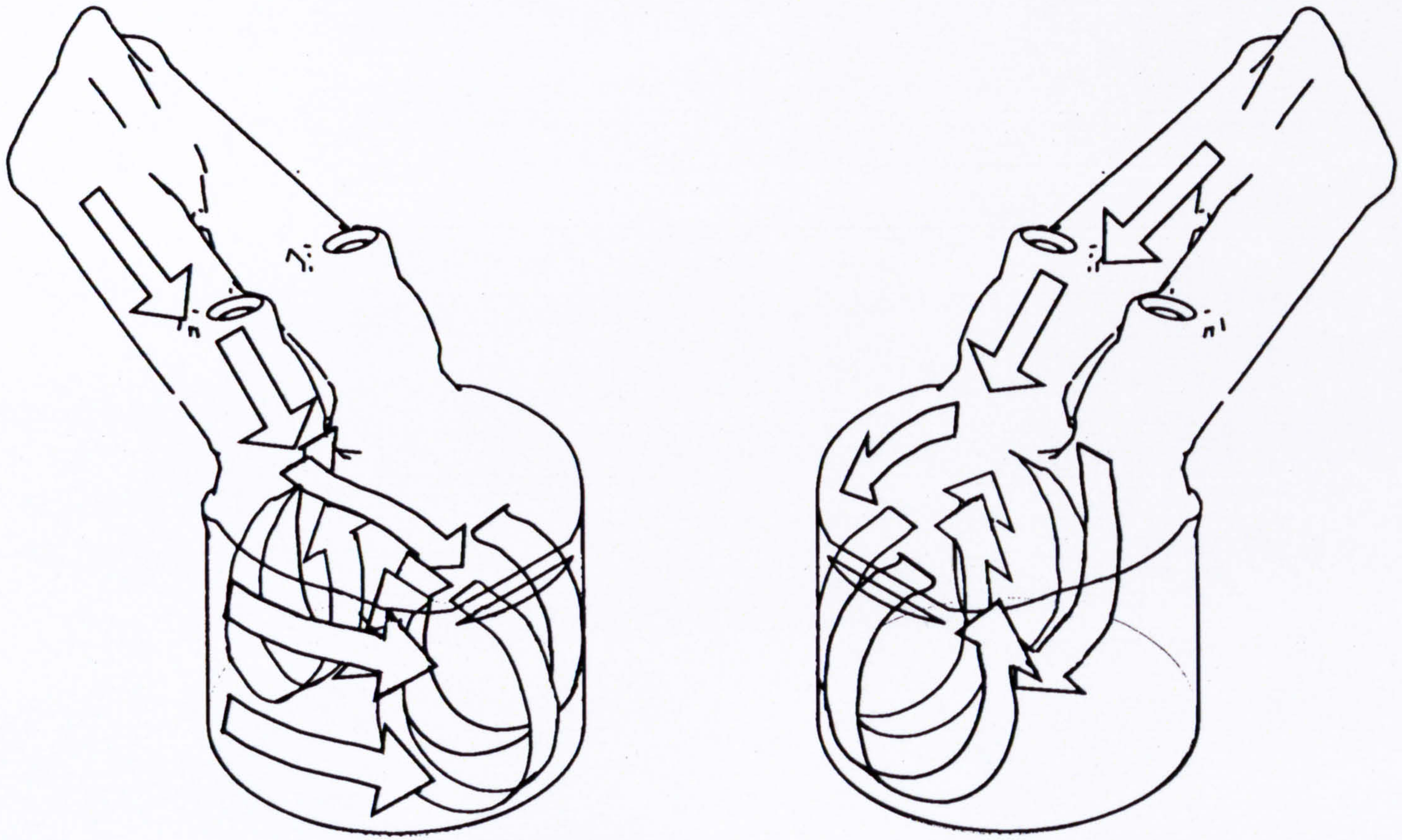

Figure 3.7(e) Three-dimensional flow pattern in the engine cylinder with 10 mm valve lifts
(one half of the flow structure shown)

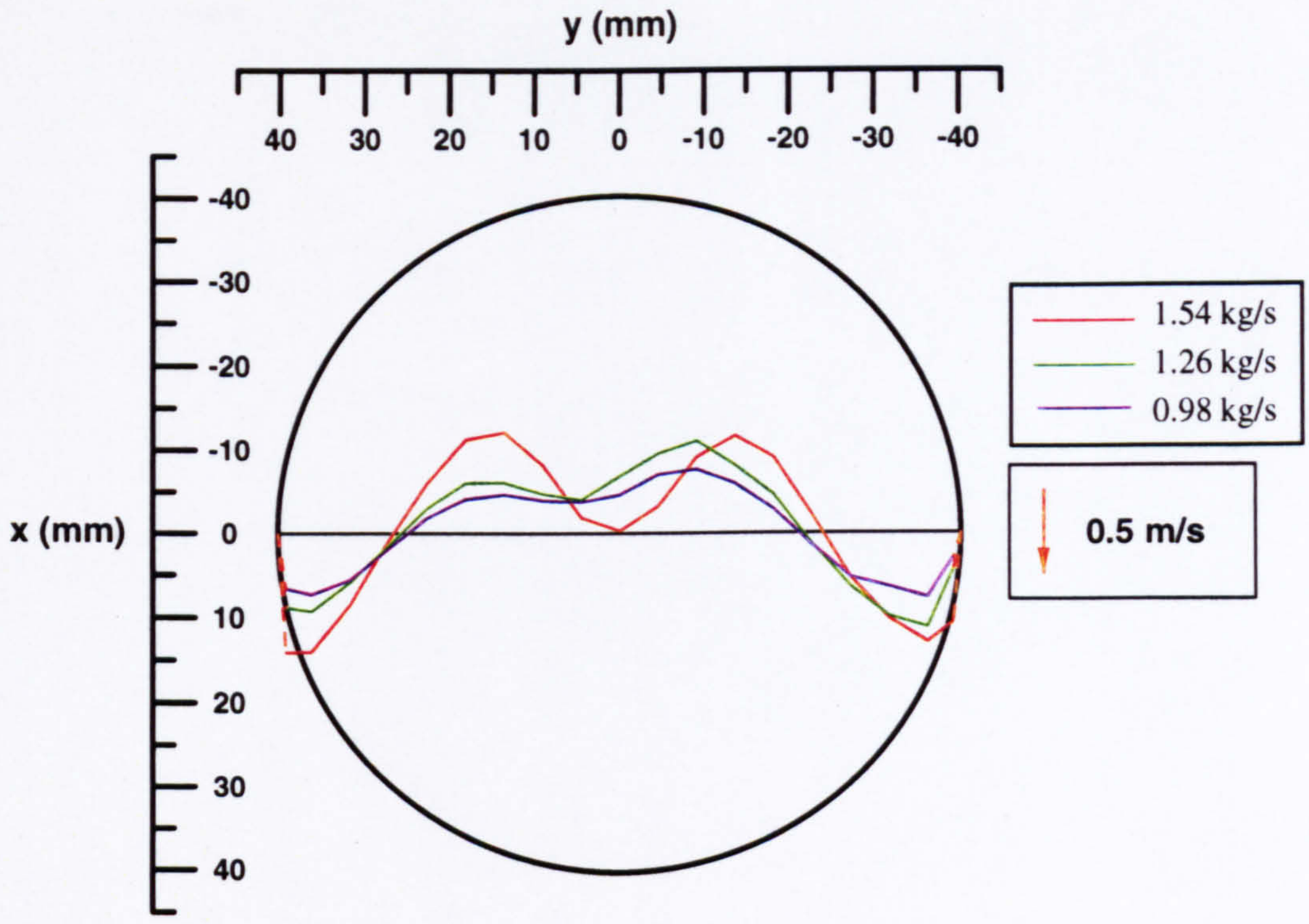

(a) Mean Velocities

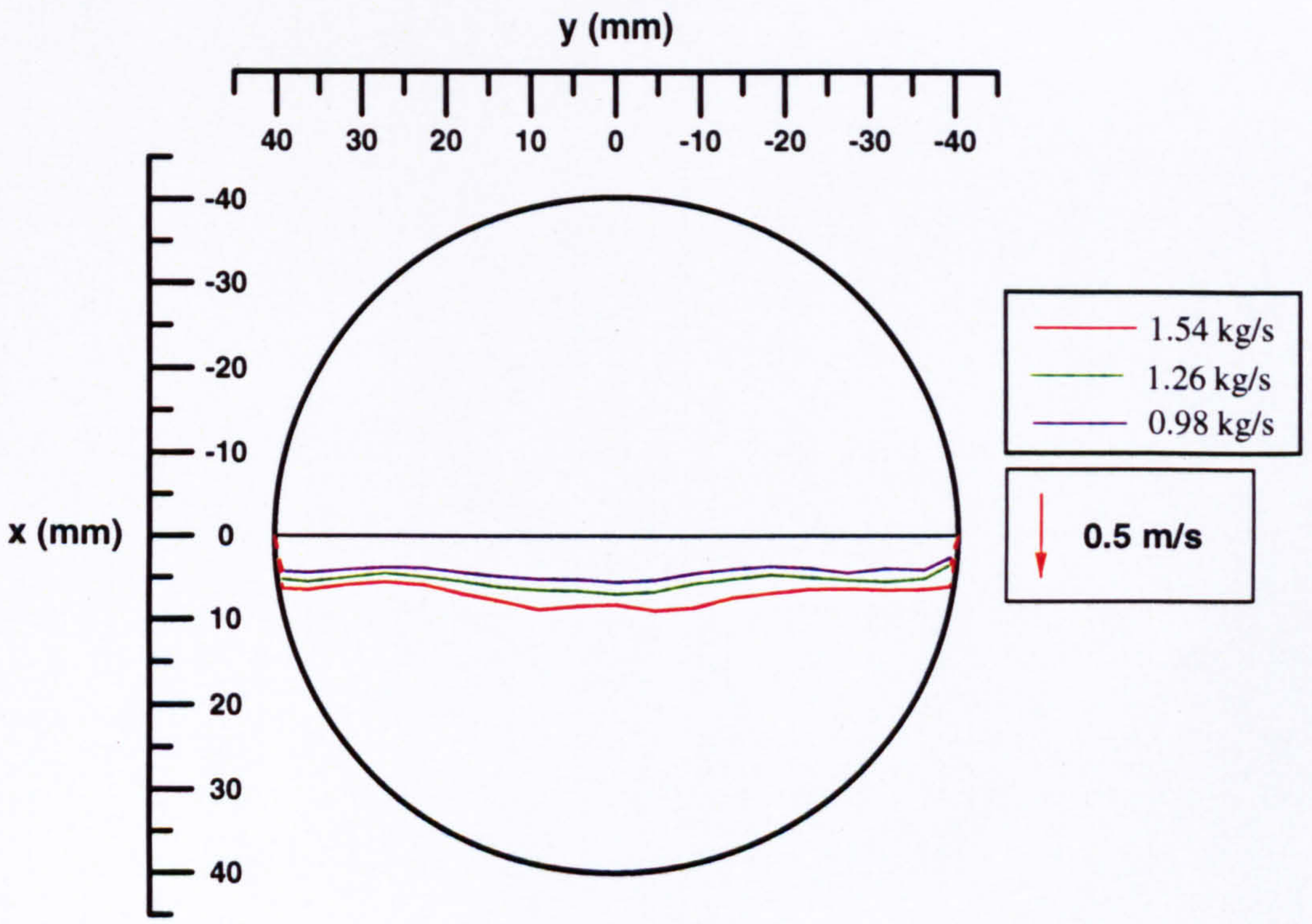

(b) R.m.s. Velocities

Figure 3.8 Variation of mean and r.m.s. in-cylinder velocities with liquid mass flowrate in the x = 0 mm profile and z = 30 mm plane (5 mm valve lifts)

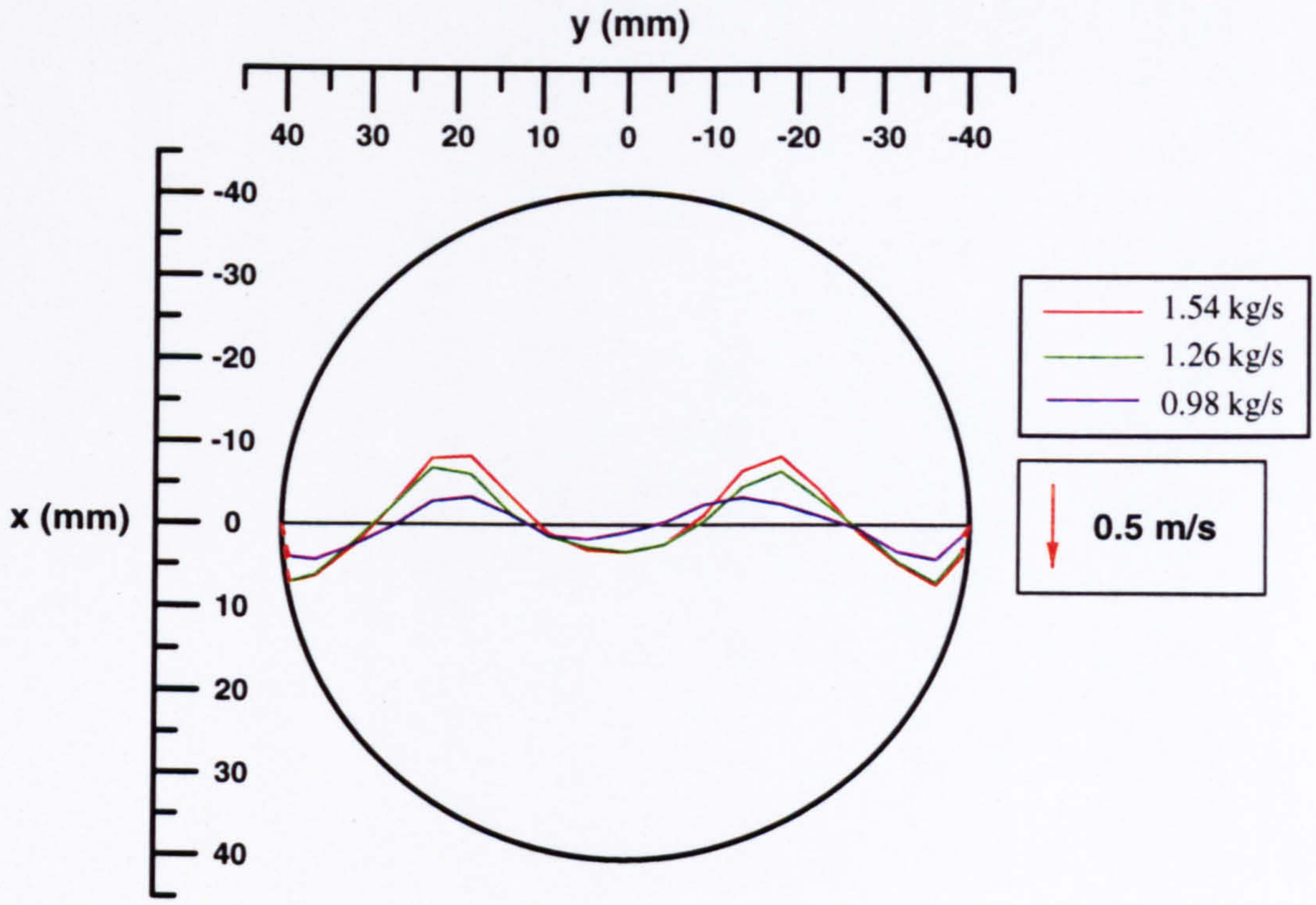

(a) Mean Velocities

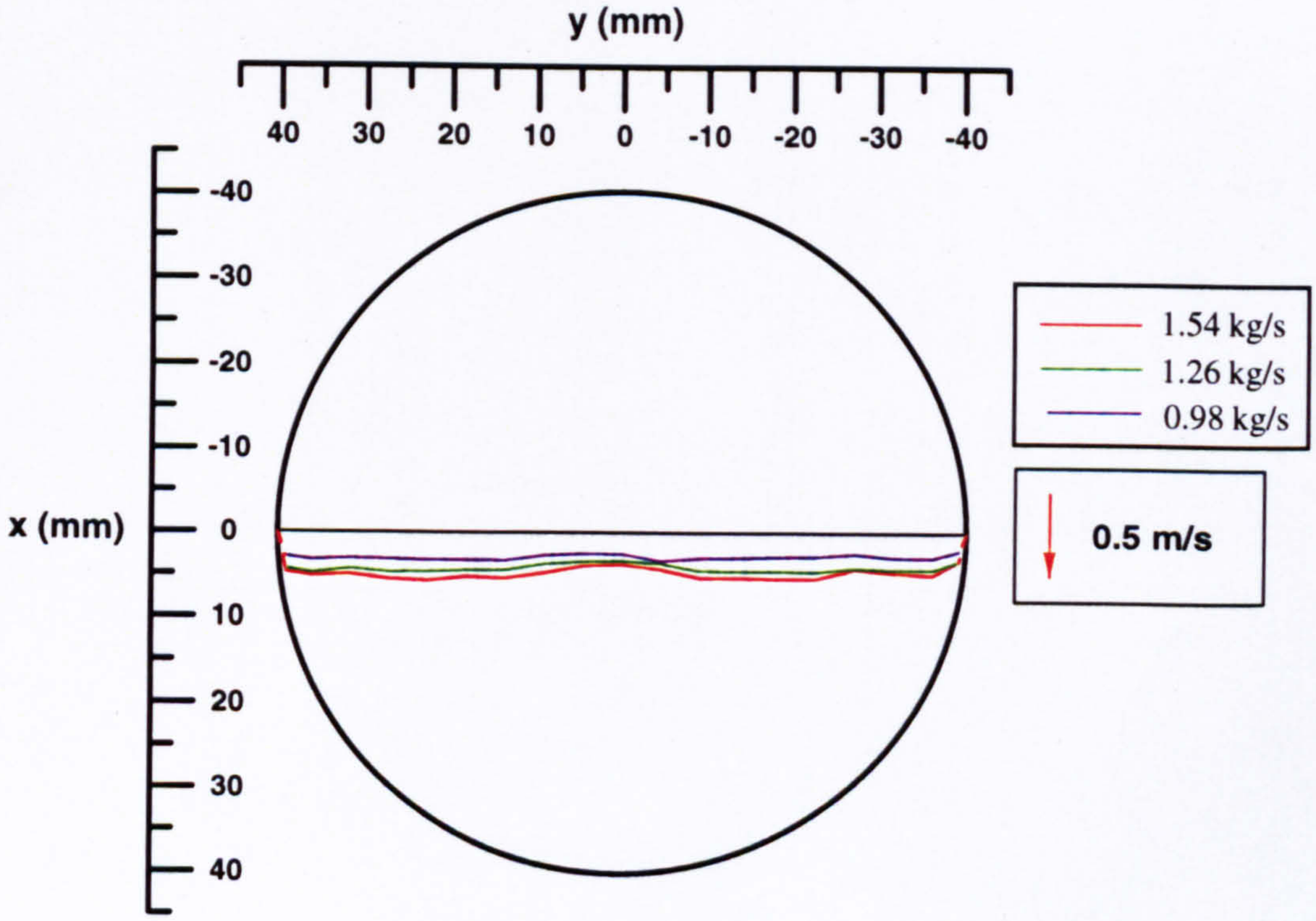

(b) R.m.s. Velocities

Figure 3.9 Variation of mean and r.m.s. in-cylinder velocities with liquid mass flowrate in the x = 0 mm profile and z = 30 mm plane (10 mm valve lifts)

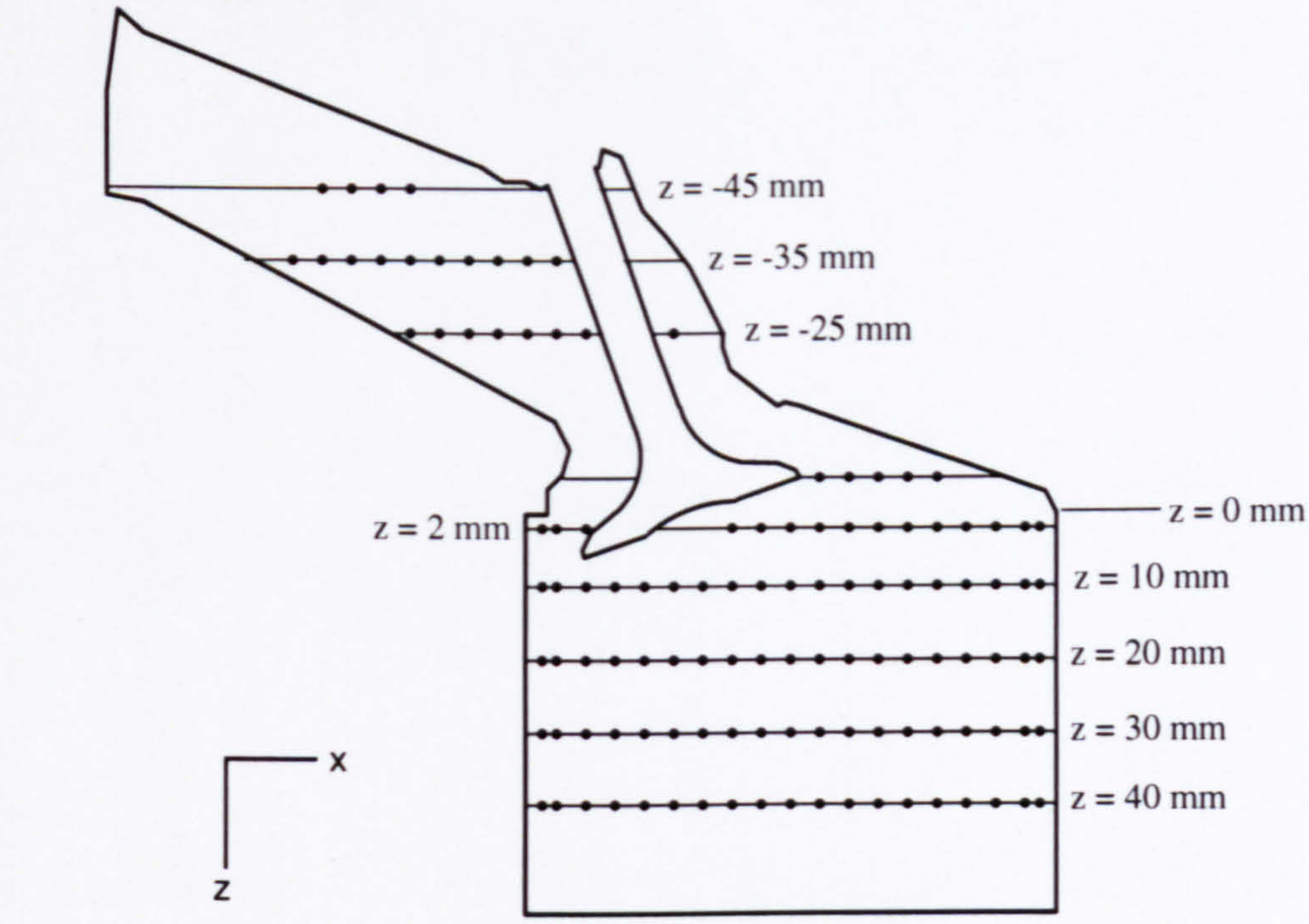

Figure 3.10(a) Measurement locations in axial planes y = -17.6 mm at valve lift setting of 10 mm

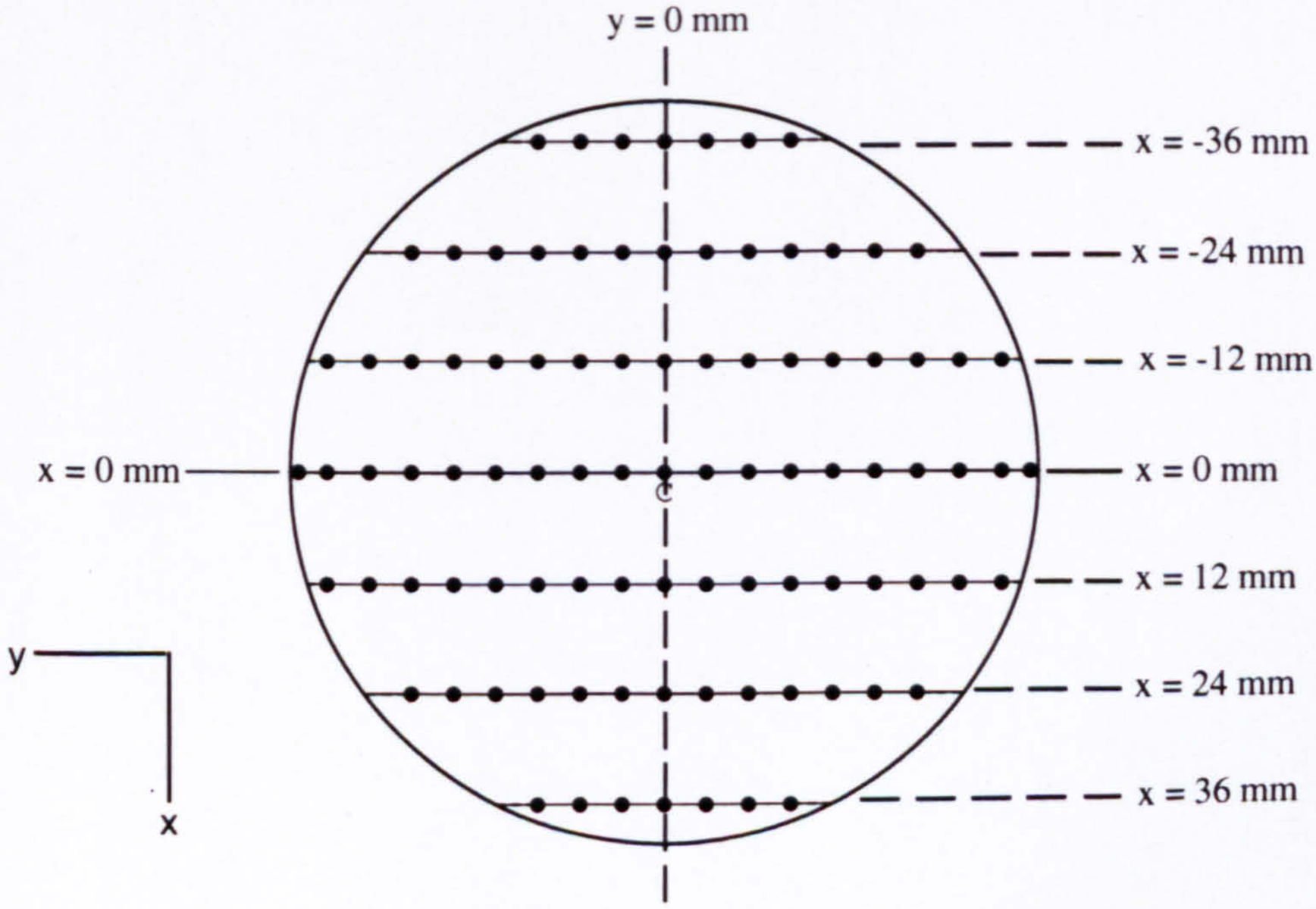

Figure 3.10(b) Measurement locations in horizontal planes

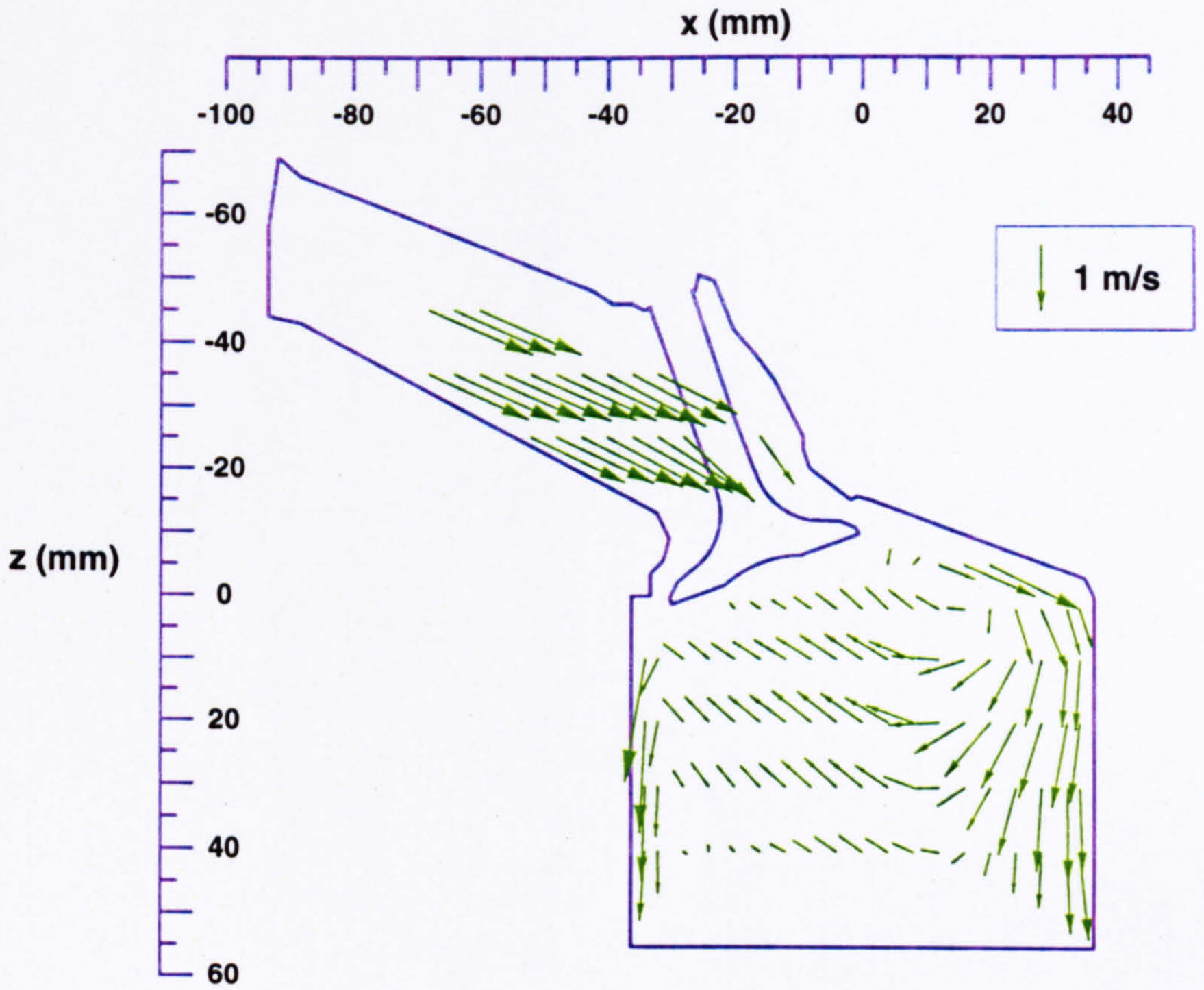

Figure 3.11 Vector plot of radial (U) and axial (W) mean velocities in the plane y = -17.6 mm with 5 mm valve lifts

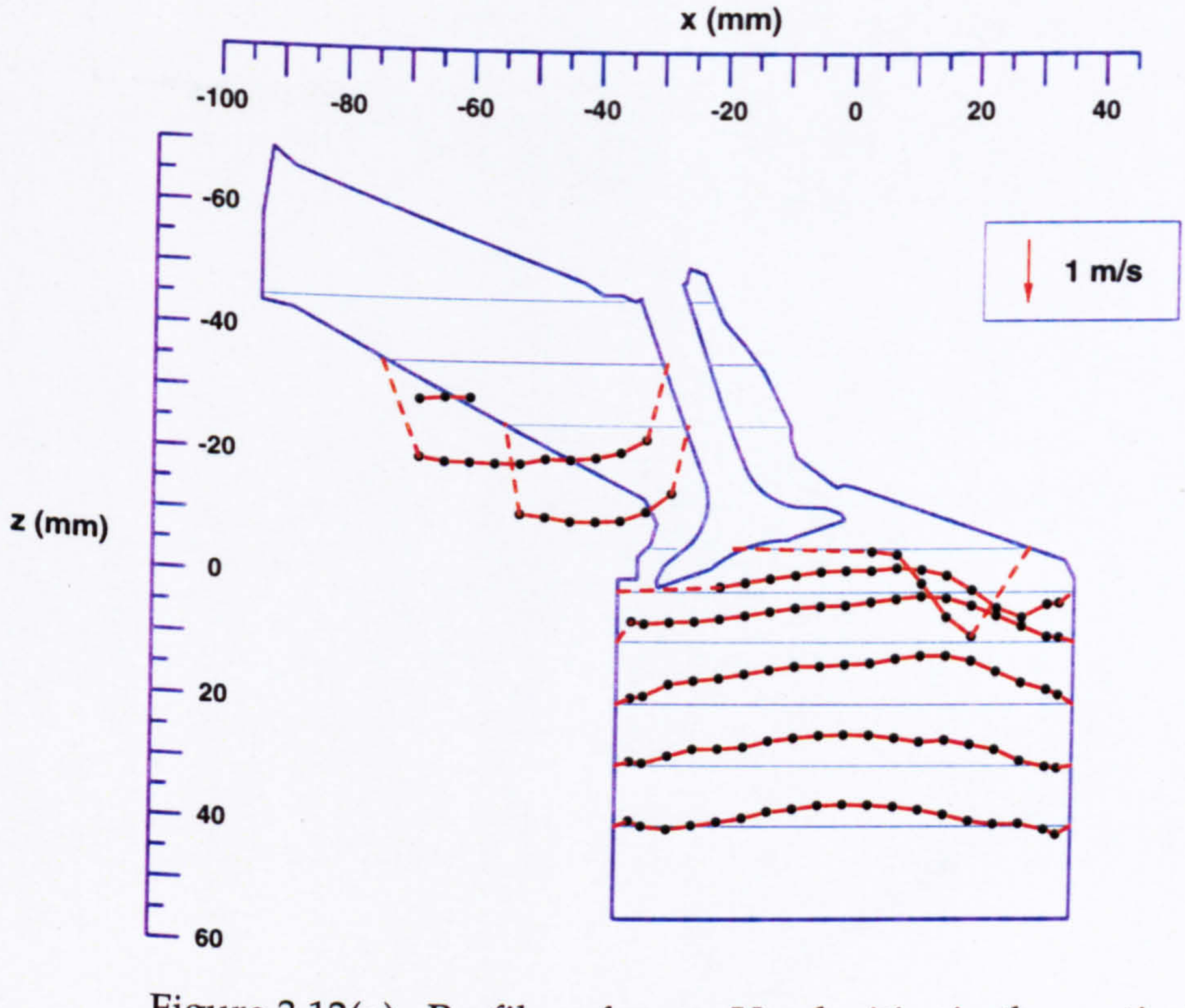

Figure 3.12(a) Profiles of mean U velocities in the vertical plane y = -17.6 mm with 5 mm valve lifts

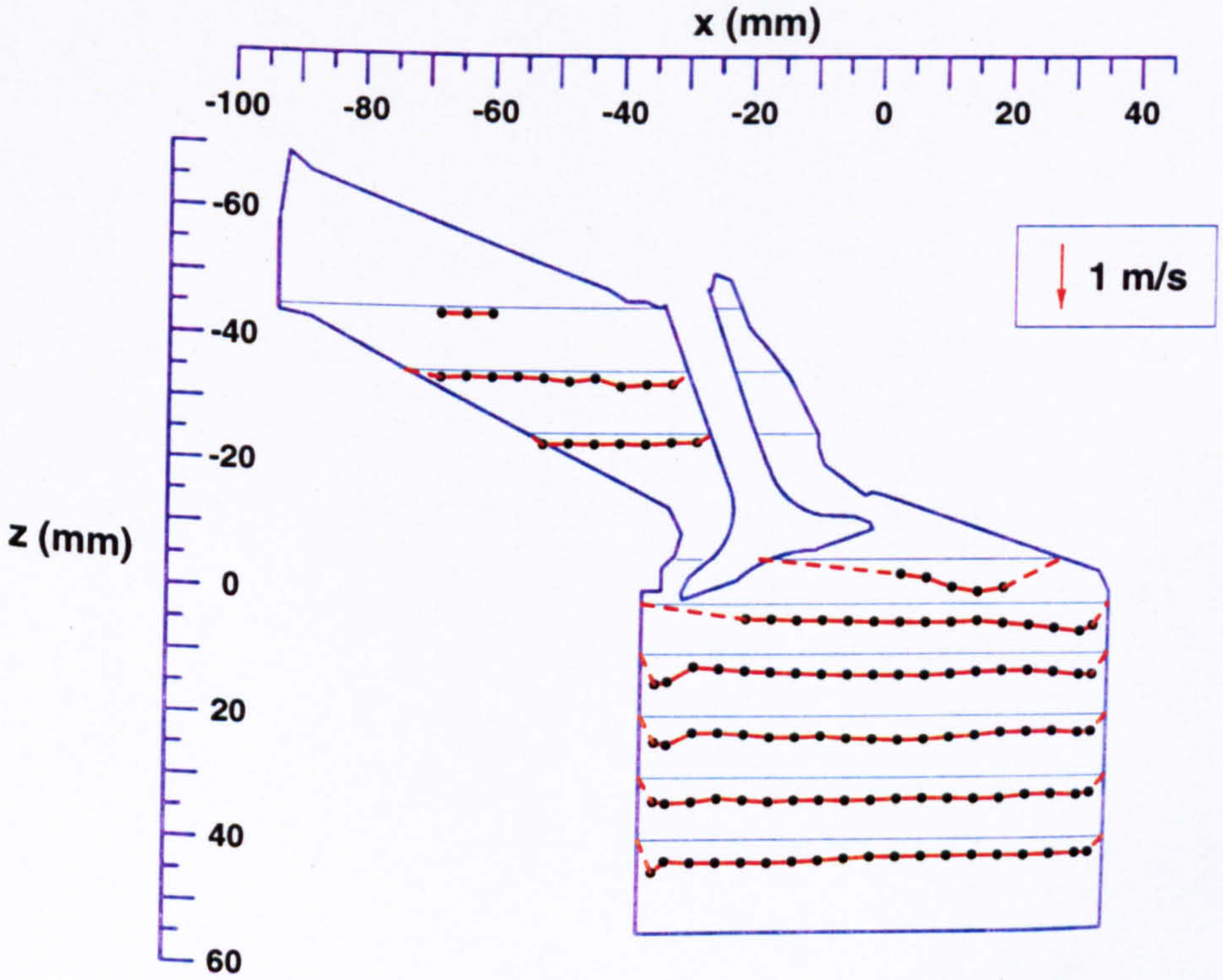

Figure 3.12(b) Profiles of r.m.s. u' velocities in the vertical plane y = -17.6 mm with 5 mm valve lifts

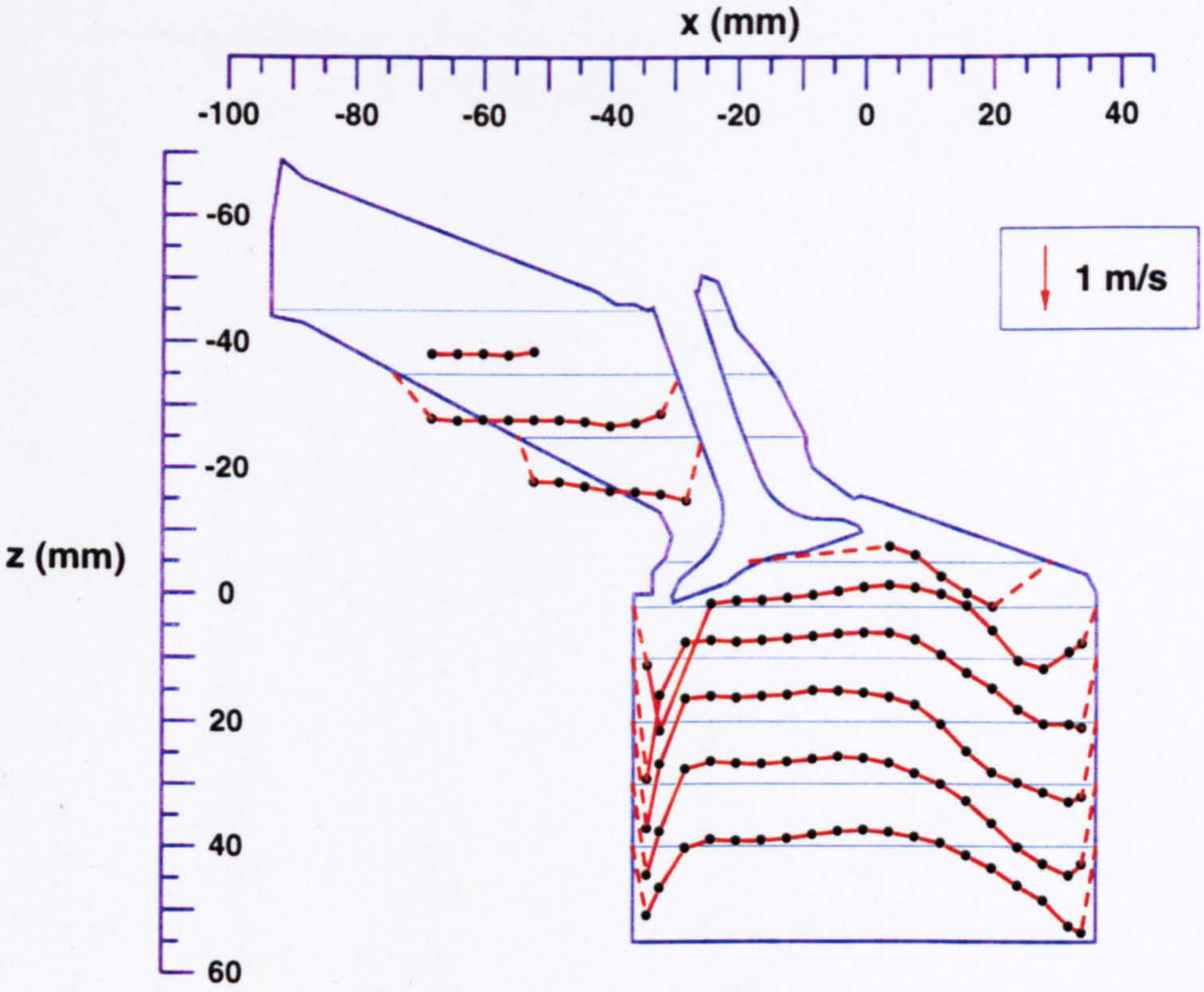

Figure 3.12(c) Profiles of mean W velocities in the vertical plane y = -17.6 mm with 5 mm valve lifts

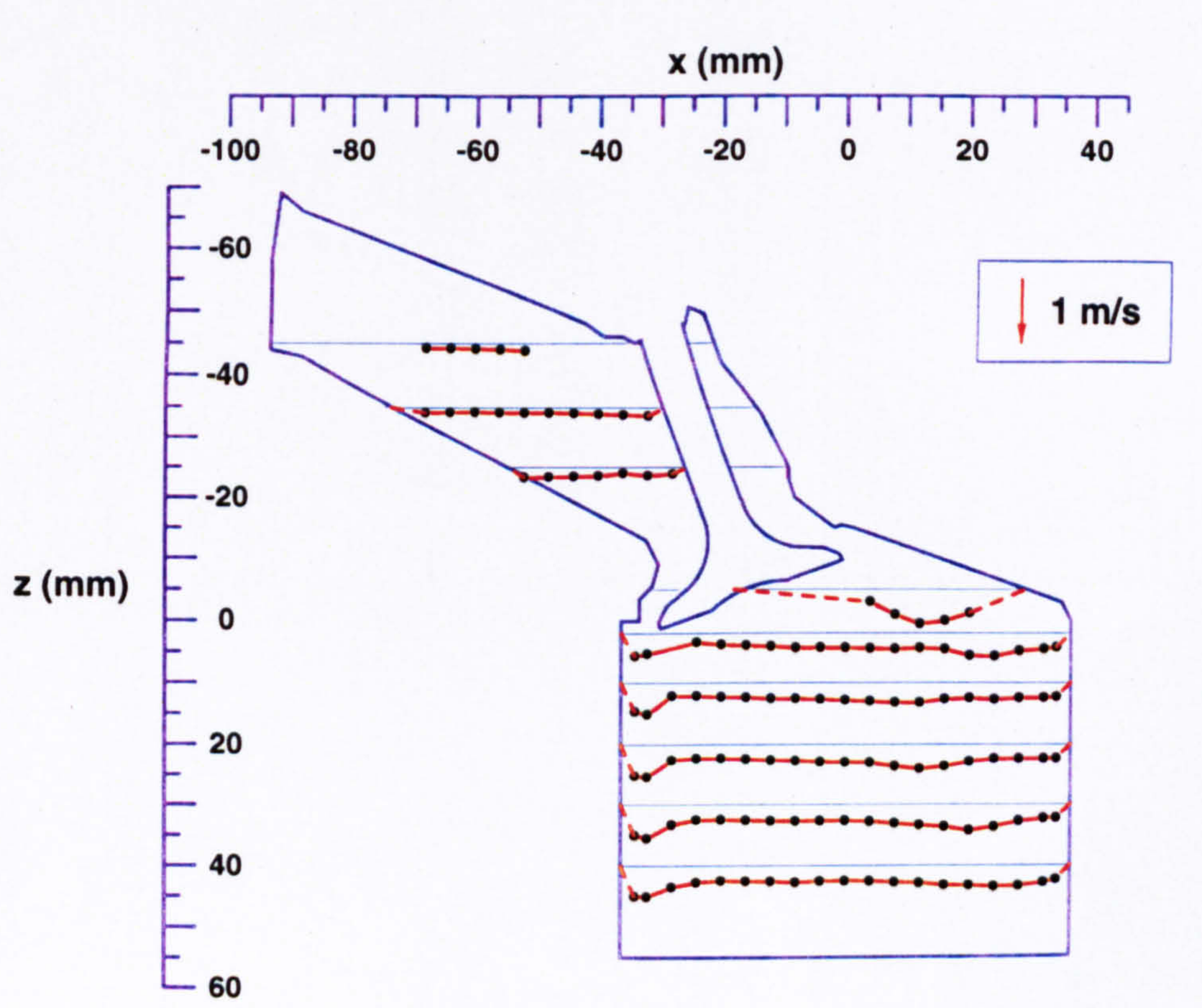

Figure 3.12(d) Profiles of r.m.s. w' velocities in the vertical plane y = -17.6 mm with 5 mm valve lifts

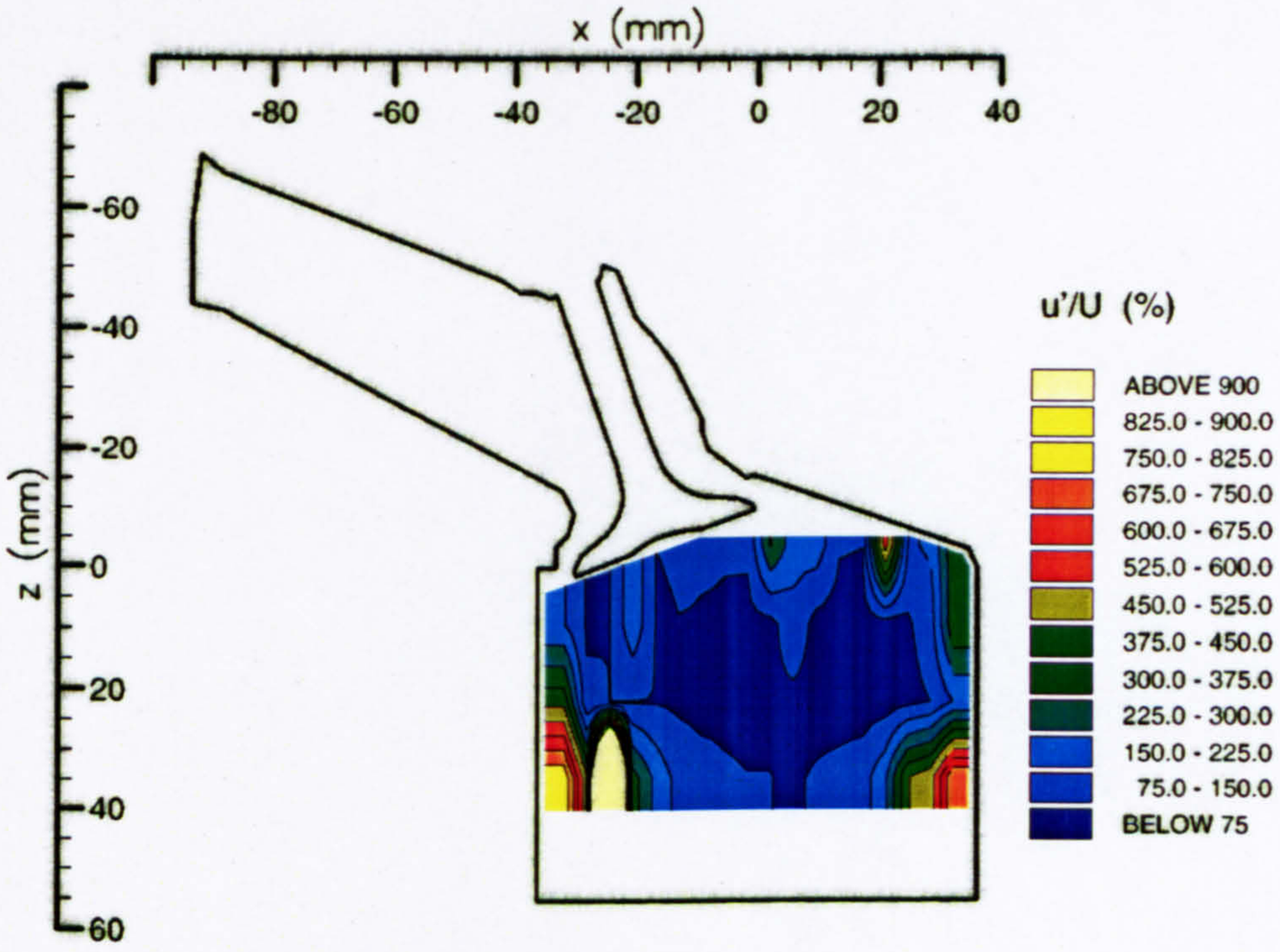

(a) Contours of u'/U

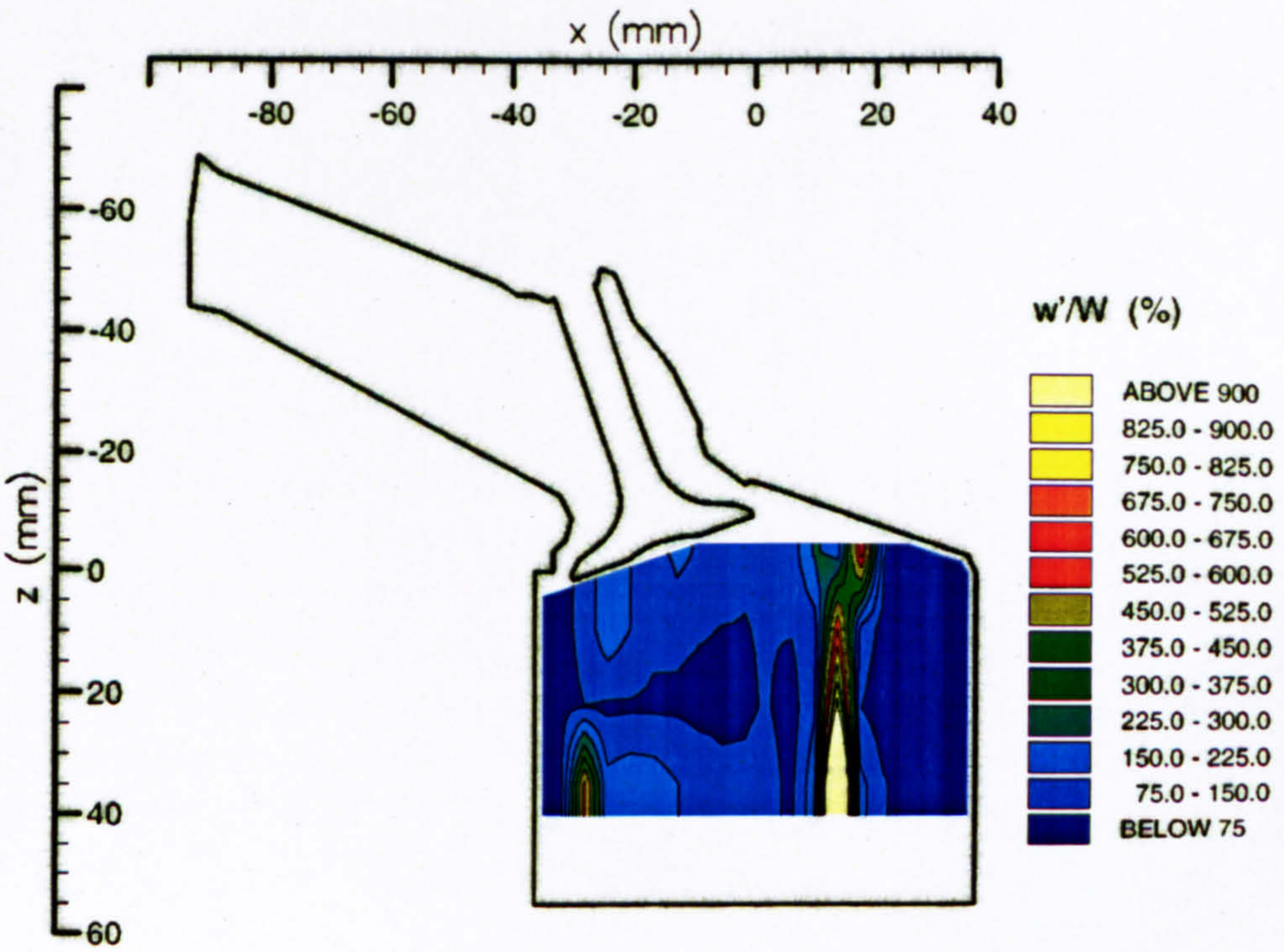

(b) Contours of w'/W

Figure 3.13 Contours of turbulence intensity for flow in the vertical plane y = -17.6 mm with 5 mm valve lifts

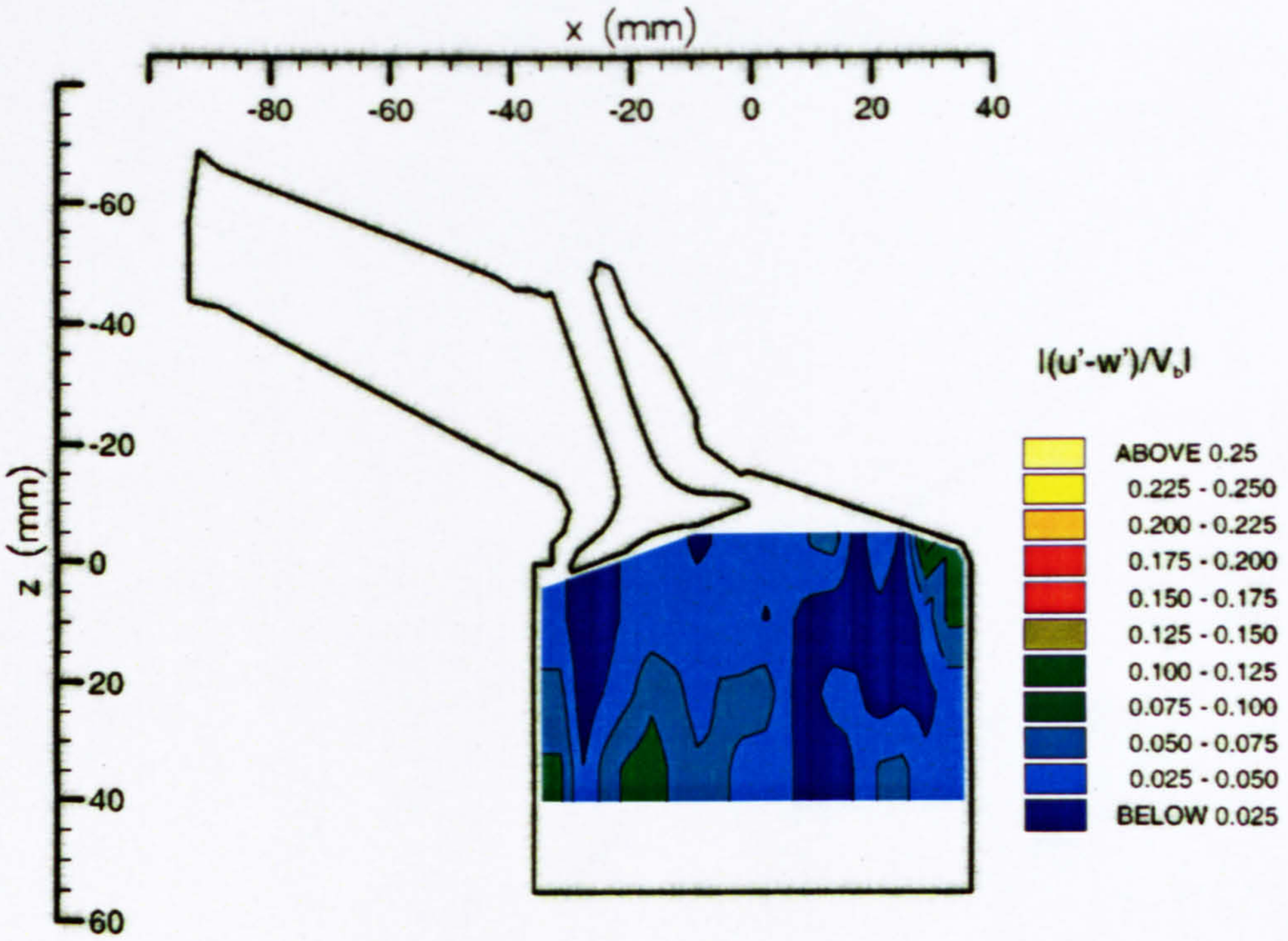

Figure 3.14 Contours of $|(u' - w')/V_b|$ for flow in the vertical plane y = -17.6 mm with 5 mm valve lifts

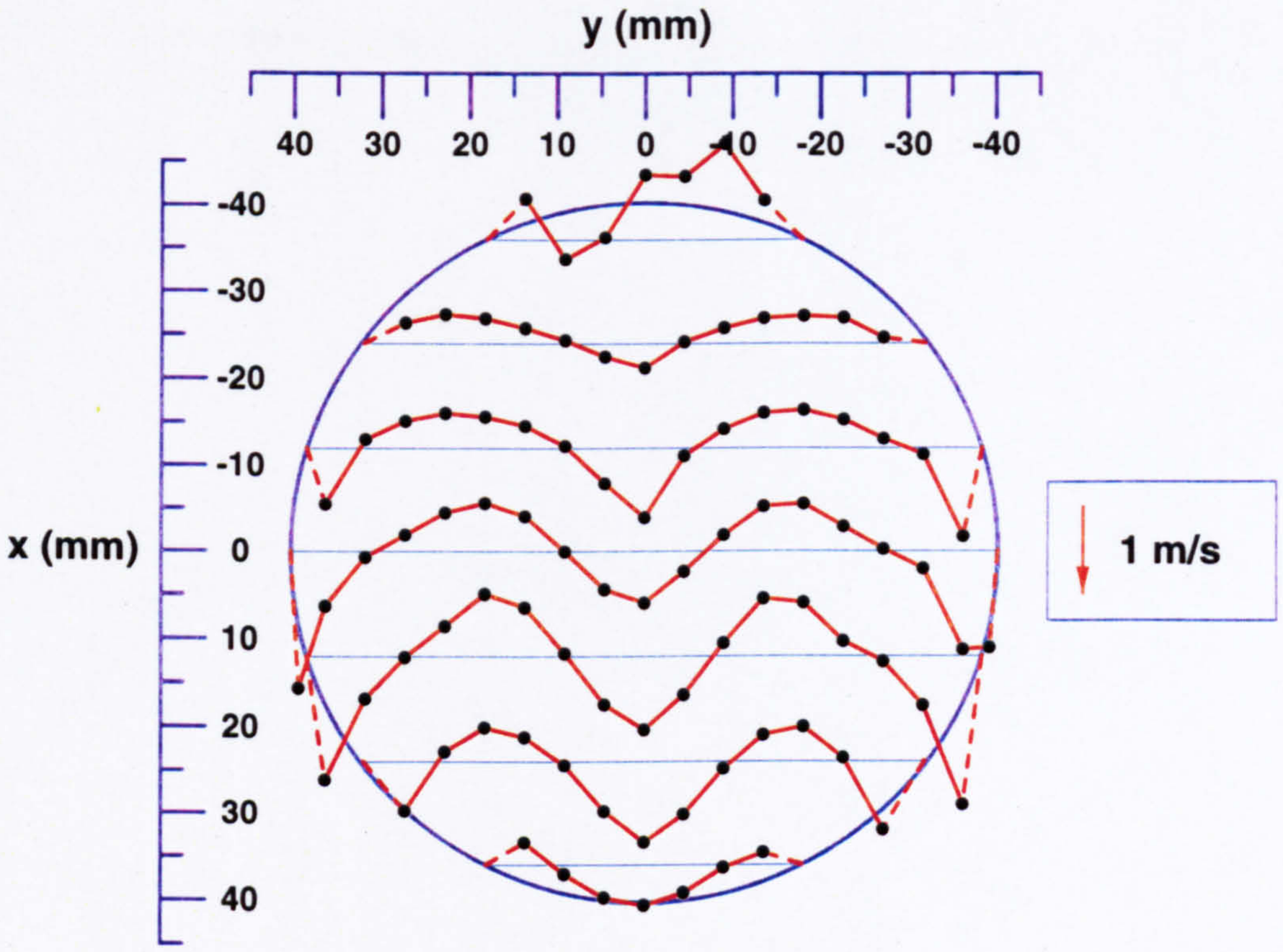

Figure 3.15(a) Profiles of mean U velocities in the horizontal plane z = 10 mm with 5 mm valve lifts

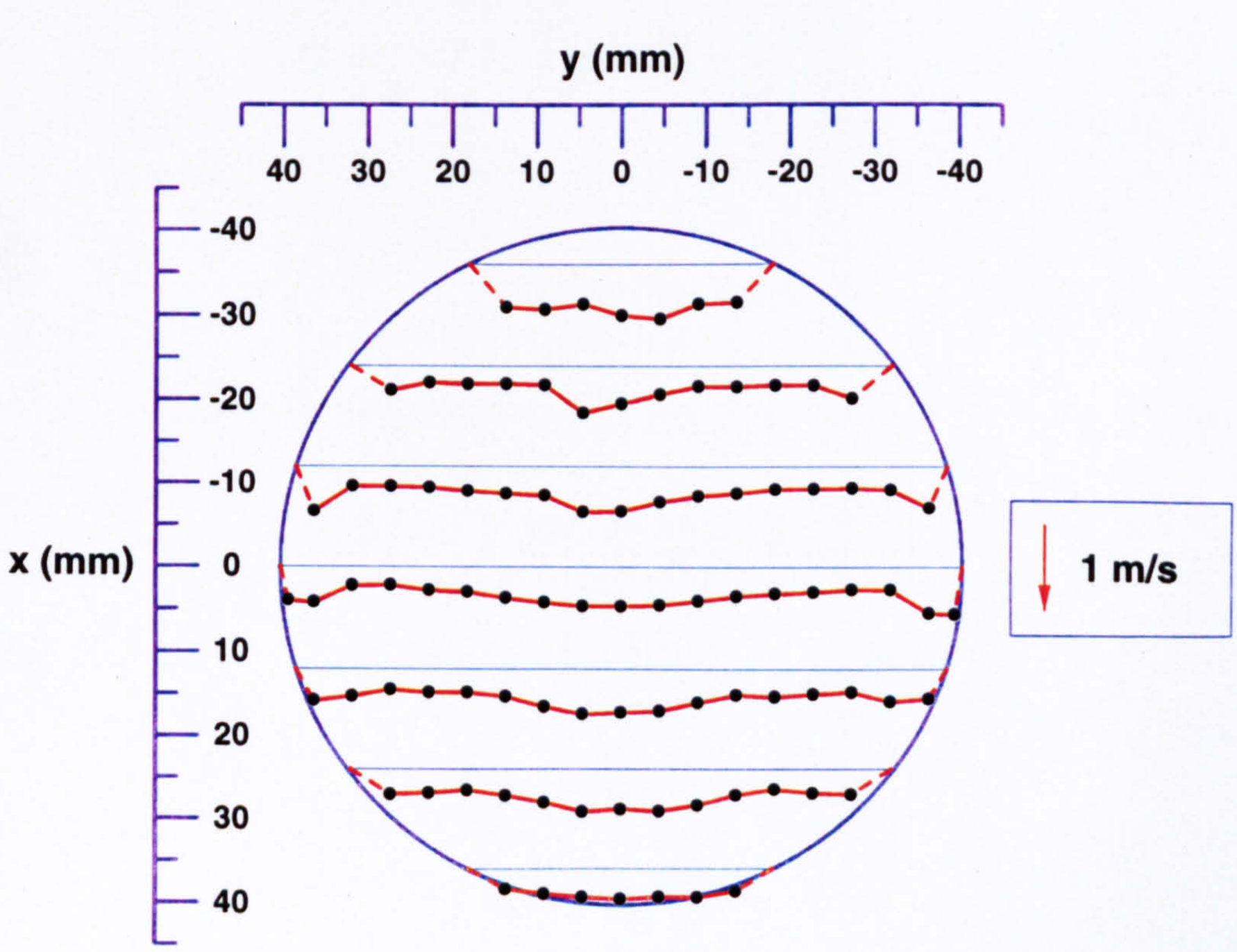

Figure 3.15(b) Profiles of r.m.s. u' velocities in the horizontal plane z = 10 mm with 5 mm valve lifts

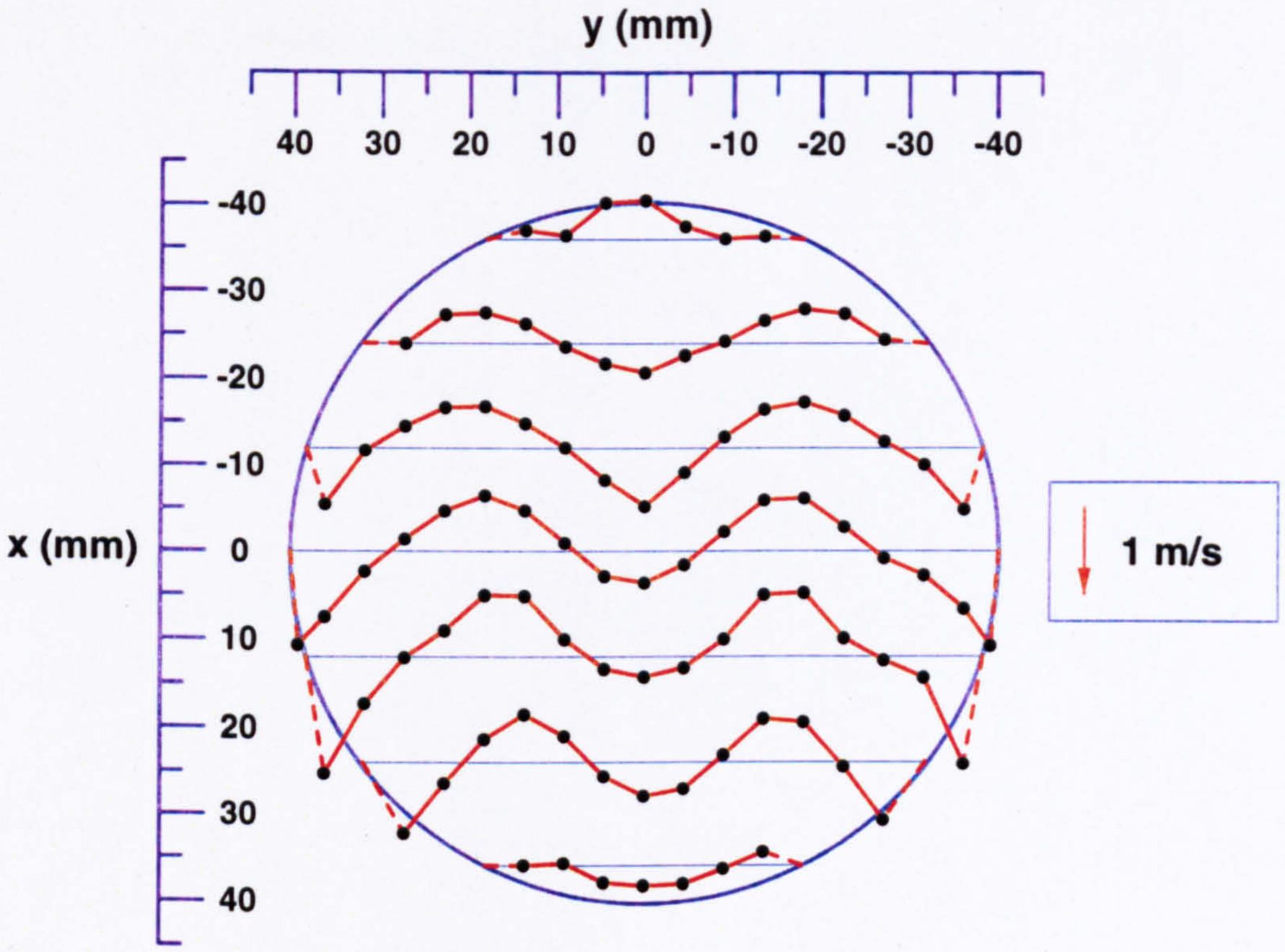

Figure 3.16(a) Profiles of mean U velocities in the horizontal plane z = 20 mm with 5 mm valve lifts

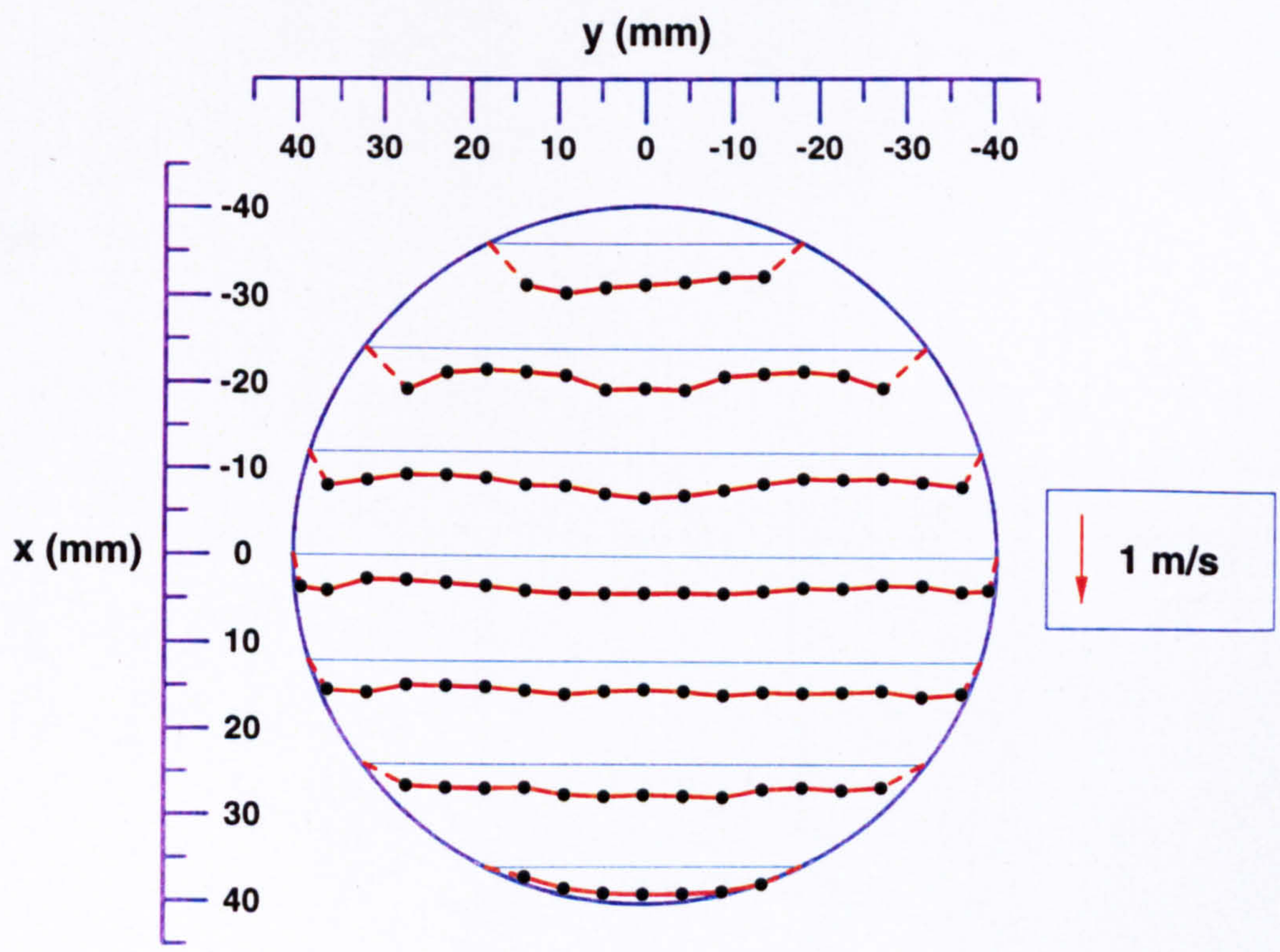

Figure 3.16(b) Profiles of r.m.s. u' velocities in the horizontal plane z = 20 mm with 5 mm valve lifts

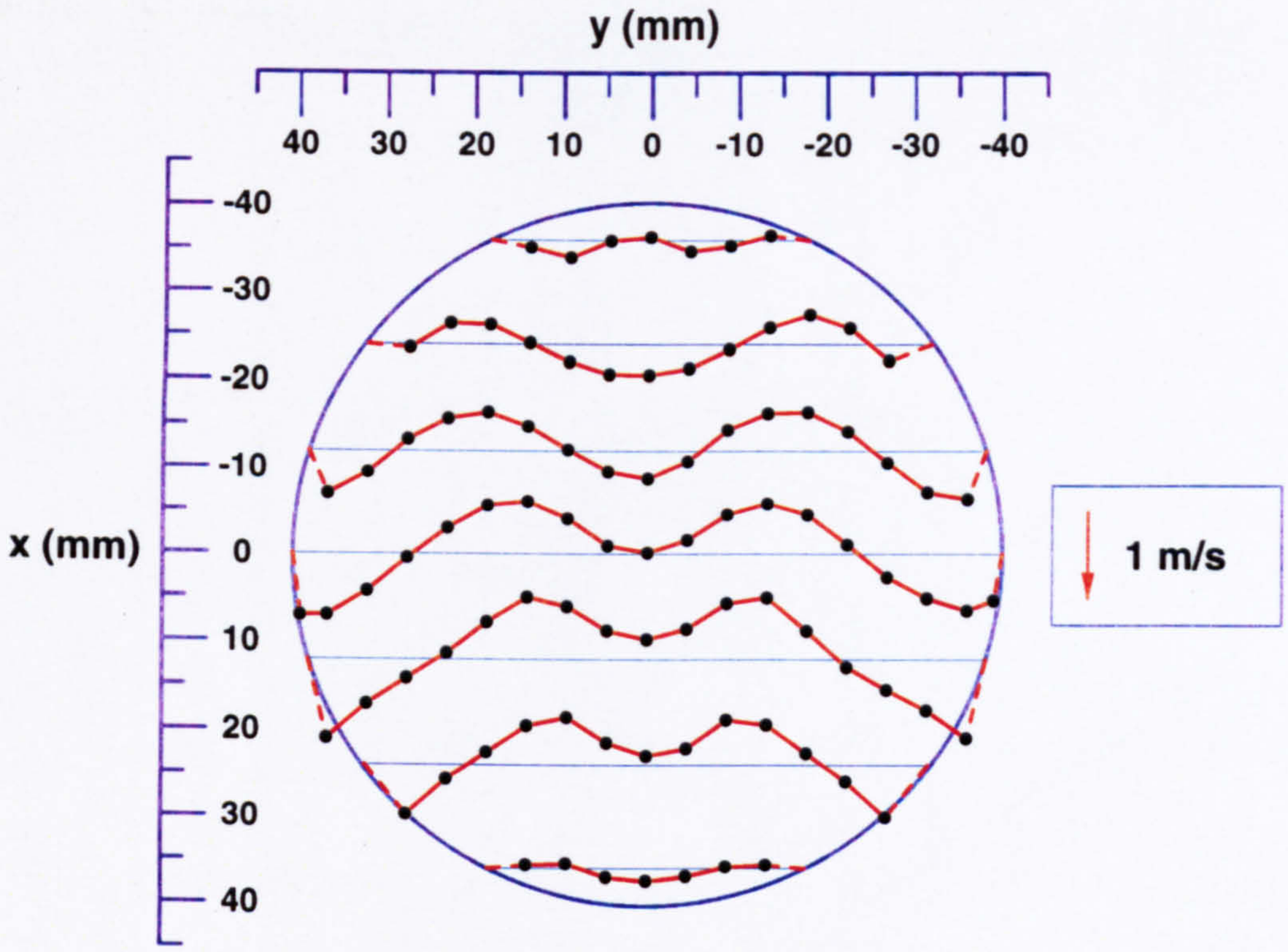

Figure 3.17(a) Profiles of mean U velocities in the horizontal plane z = 30 mm with 5 mm valve lifts

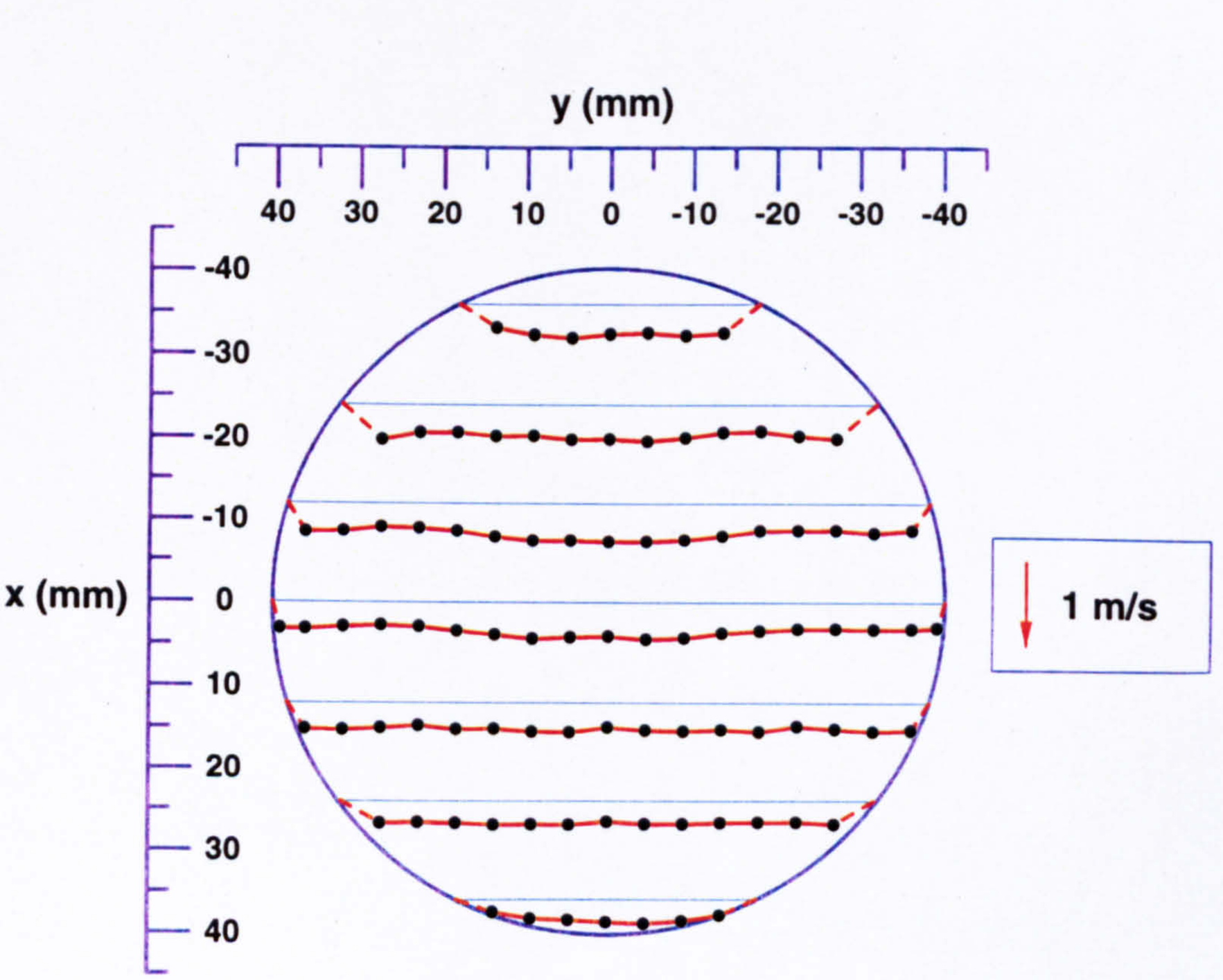

Figure 3.17(b) Profiles of r.m.s. u' velocities in the horizontal plane z = 30 mm with 5 mm valve lifts

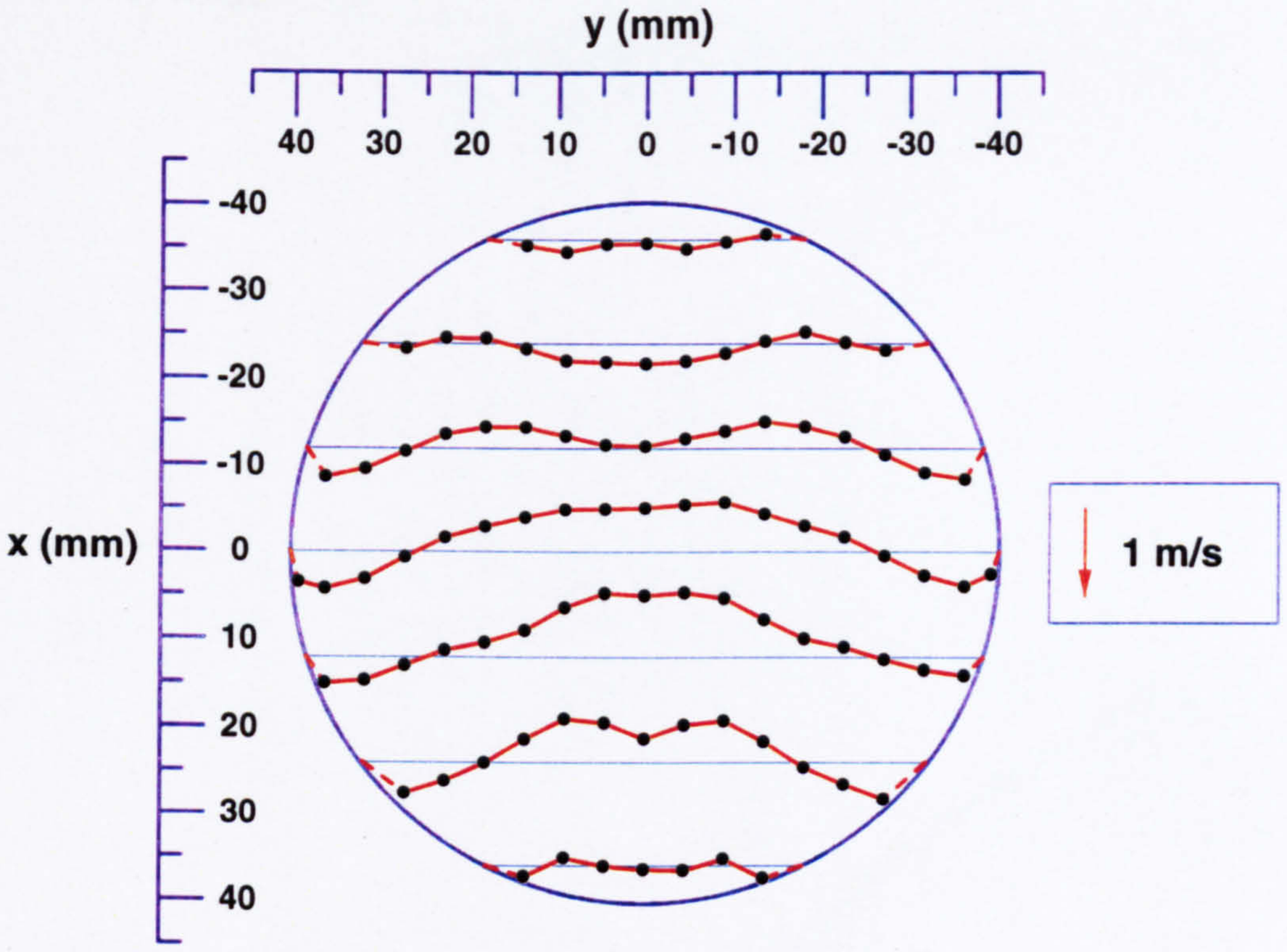

Figure 3.18(a) Profiles of mean U velocities in the horizontal plane z = 40 mm with 5 mm valve lifts

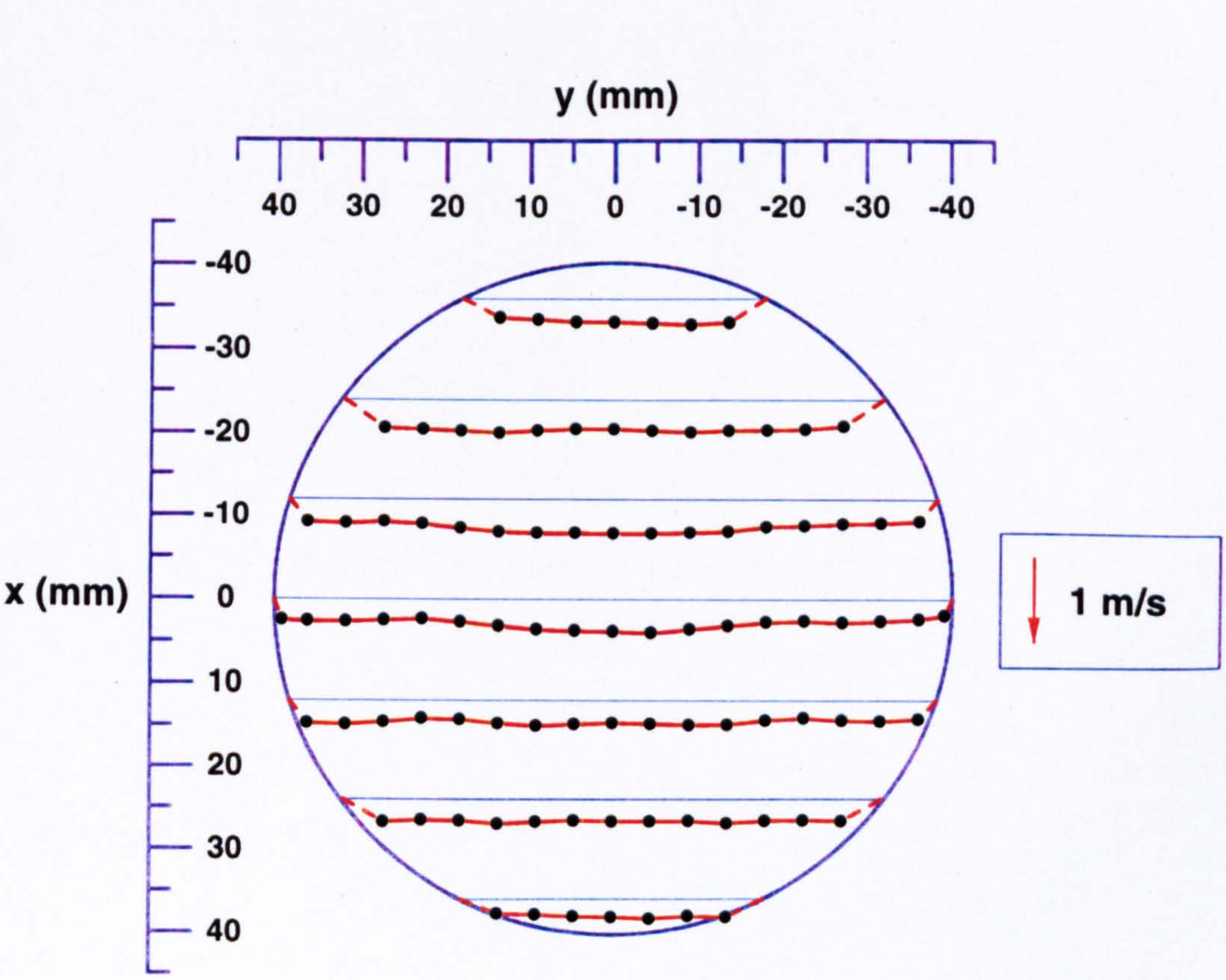

Figure 3.18(b) Profiles of r.m.s. u' velocities in the horizontal plane z = 40 mm with 5 mm valve lifts

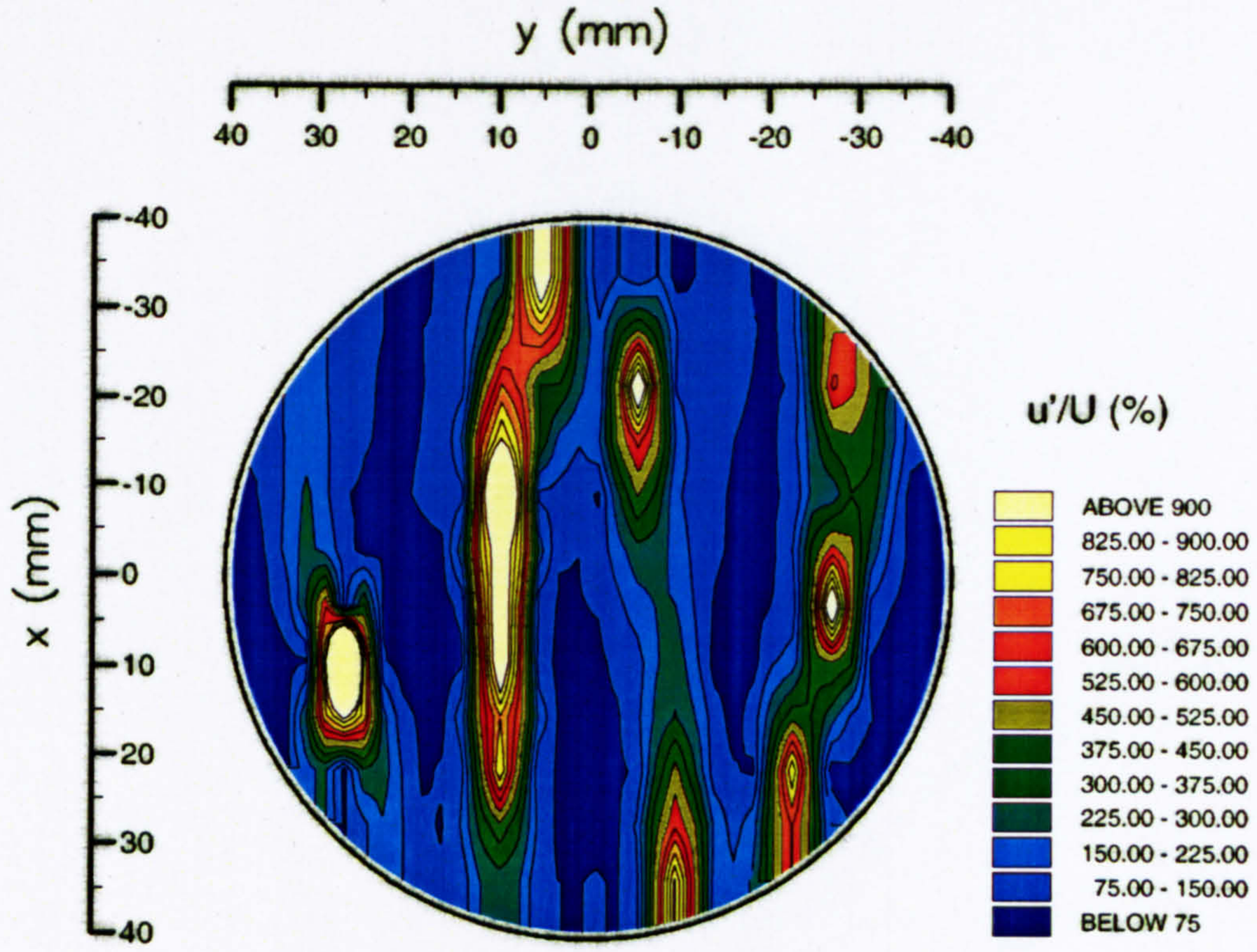

Figure 3.19(a) Contours of turbulence intensity u'/U for flow in the horizontal plane z = 10 mm with 5 mm valve lifts

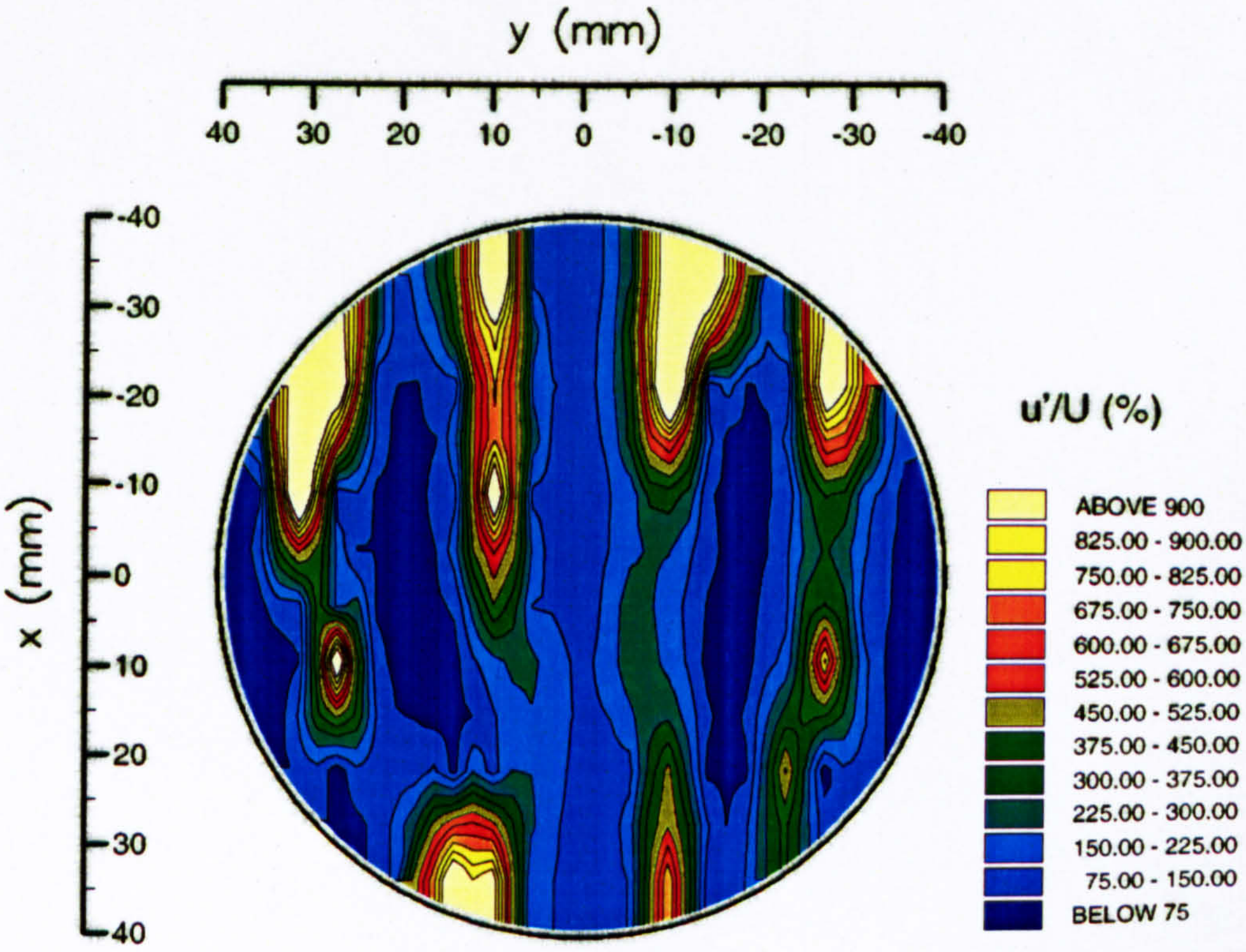

Figure 3.19(b) Contours of turbulence intensity u'/U for flow in the horizontal plane z = 20 mm with 5 mm valve lifts

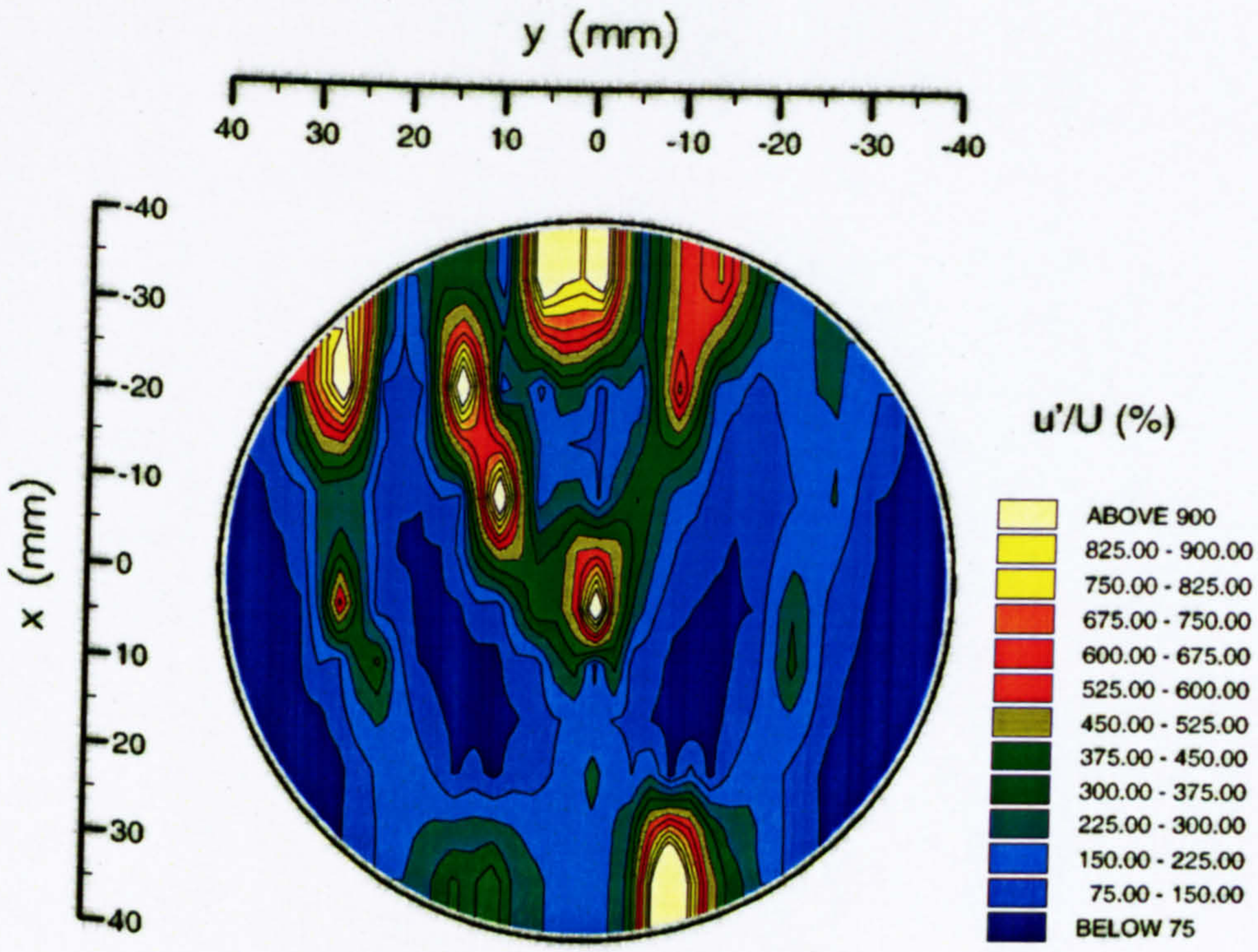

Figure 3.19(c) Contours of turbulence intensity u'/U for flow in the horizontal plane z = 30 mm with 5 mm valve lifts

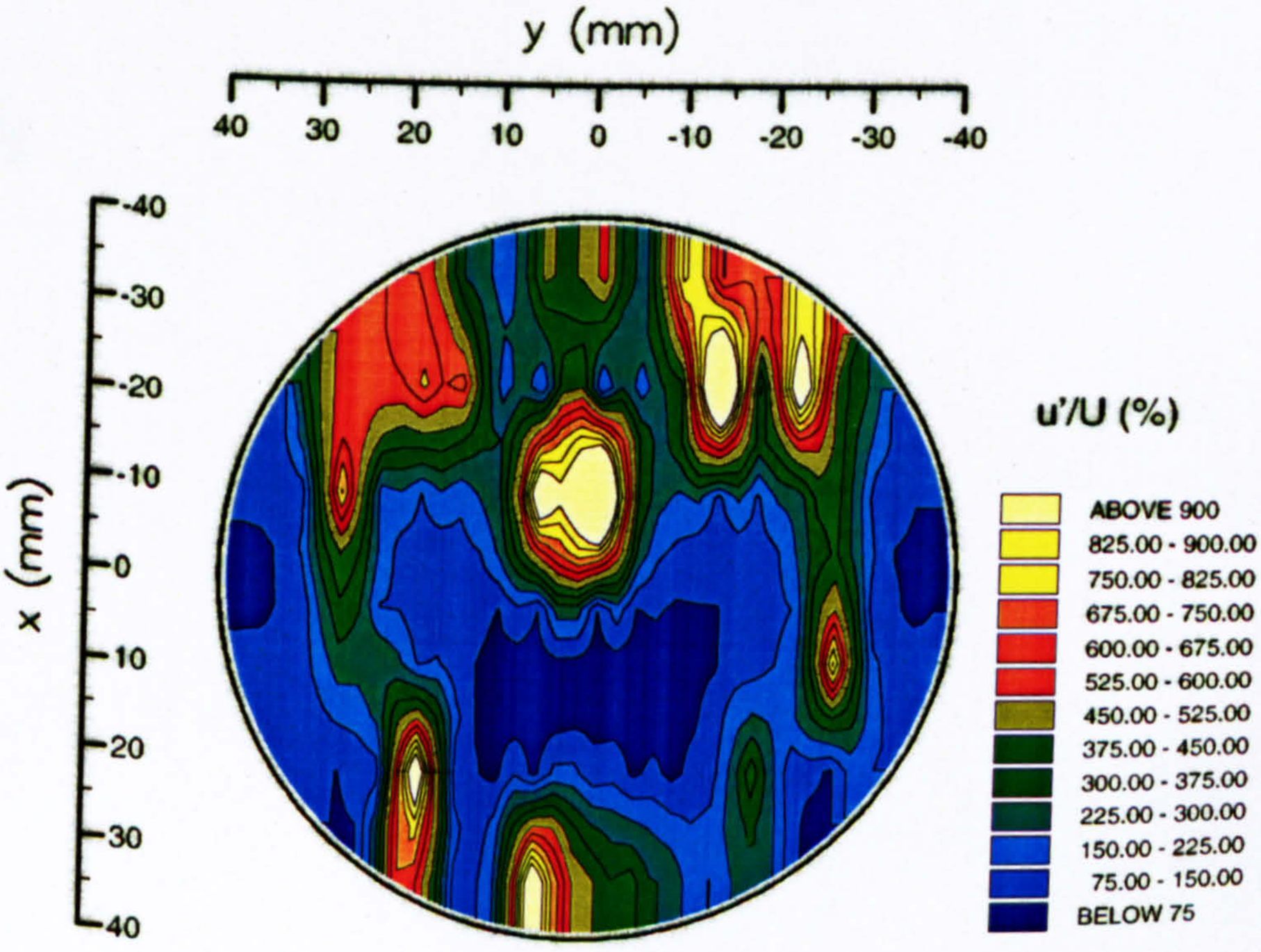

Figure 3.19(d) Contours of turbulence intensity u'/U for flow in the horizontal plane z = 40 mm with 5 mm valve lifts

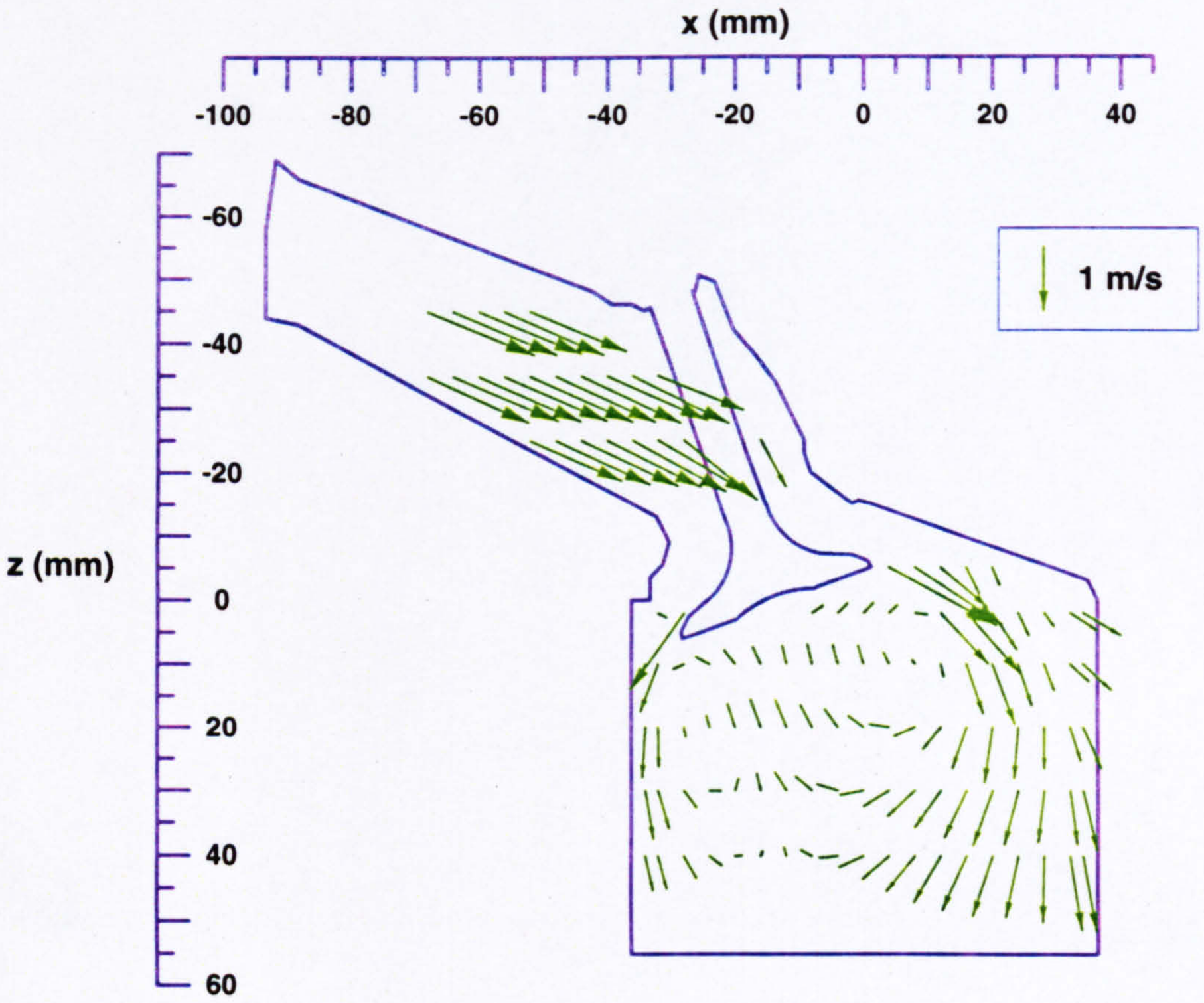

Figure 3.20 Vector plot of mean radial (U) and axial (W) velocities in the plane y = -17.6 mm with 10 mm valve lifts

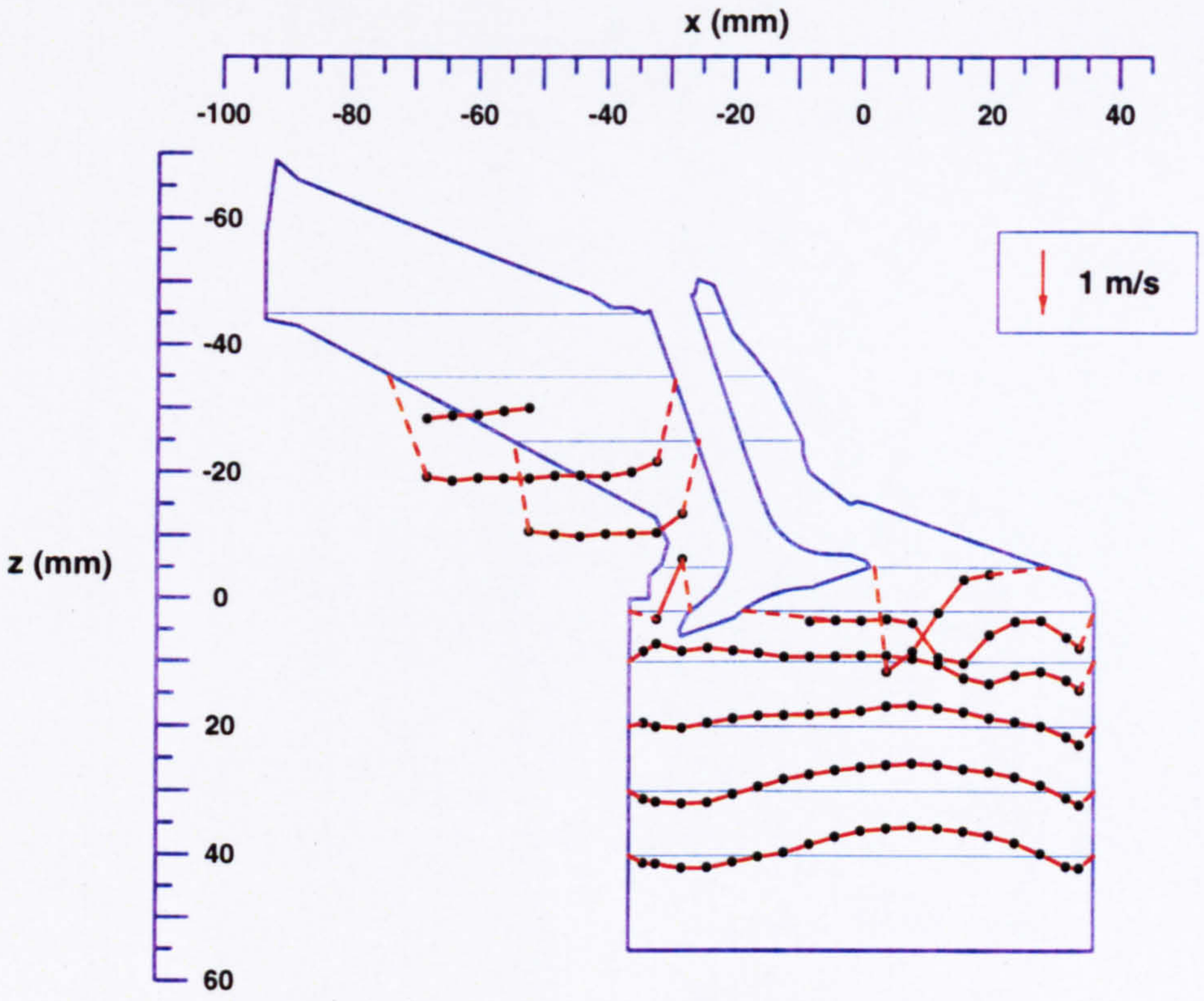

Figure 3.21(a) Profiles of mean U velocities in the vertical plane y = -17.6 mm with 10 mm valve lifts

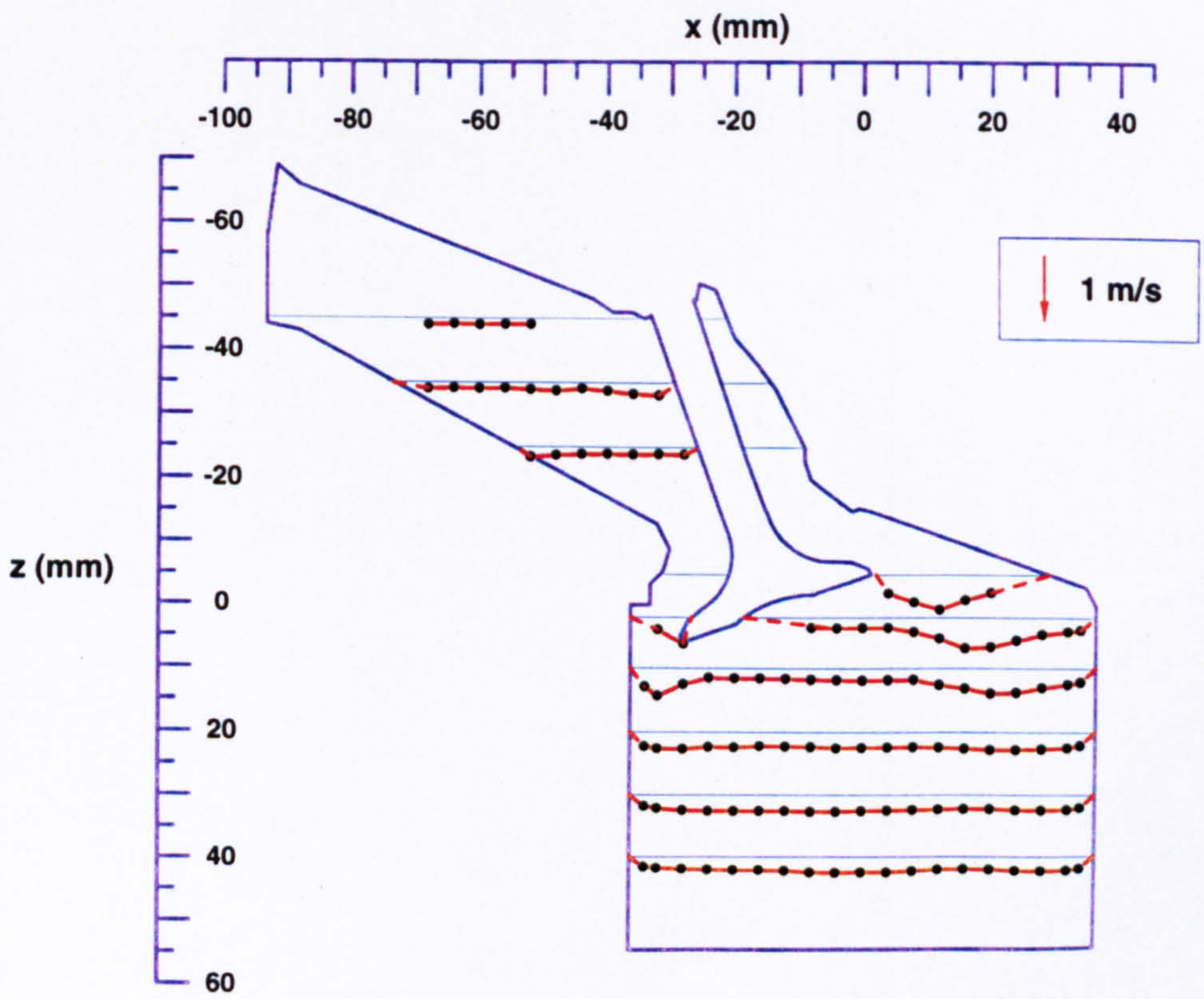

Figure 3.21(b) Profiles of r.m.s. u' velocities in the vertical plane y = -17.6 mm with 10 mm valve lifts

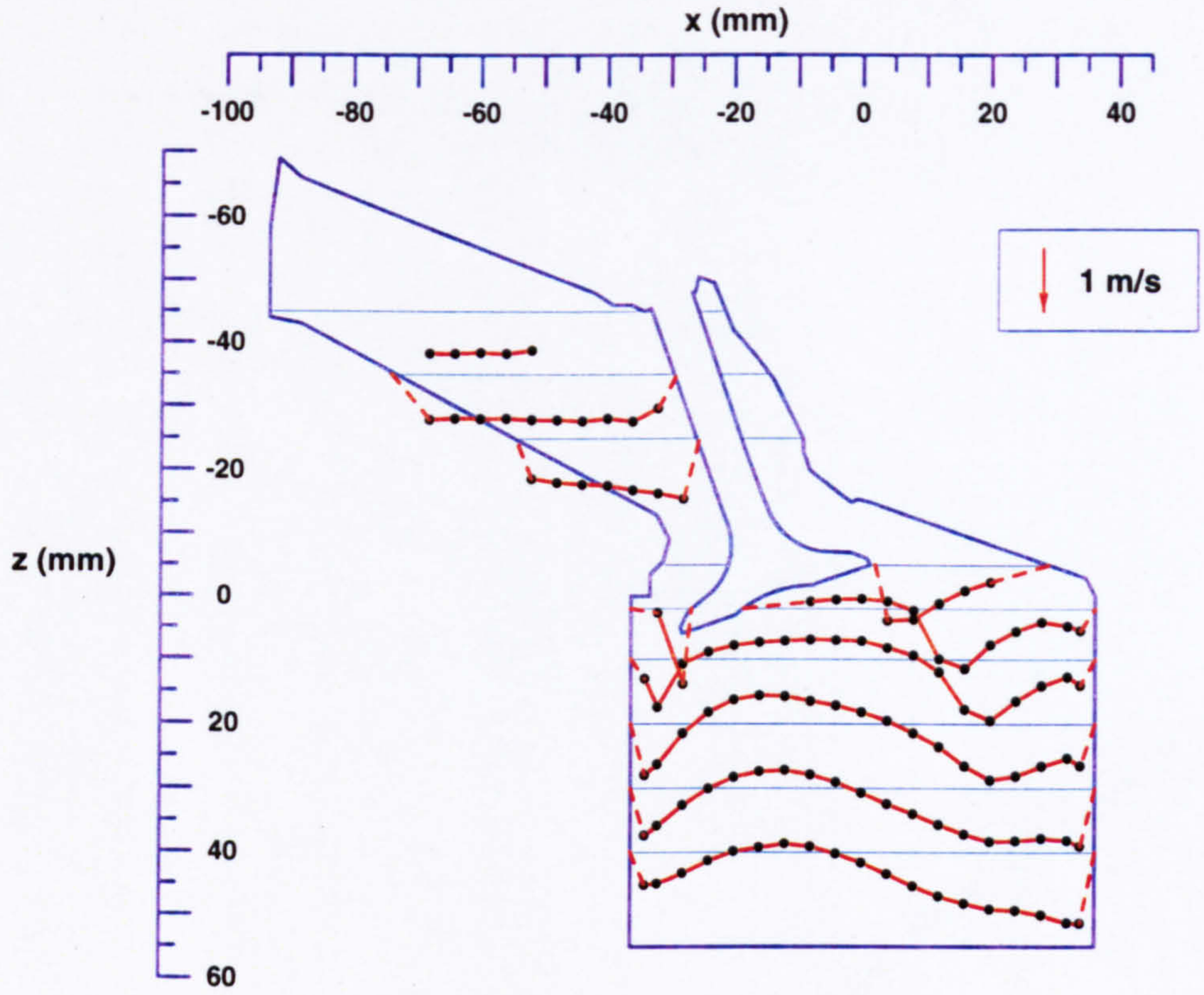

Figure 3.21(c) Profiles of mean W velocities in the vertical plane y = -17.6 mm with 10 mm valve lifts

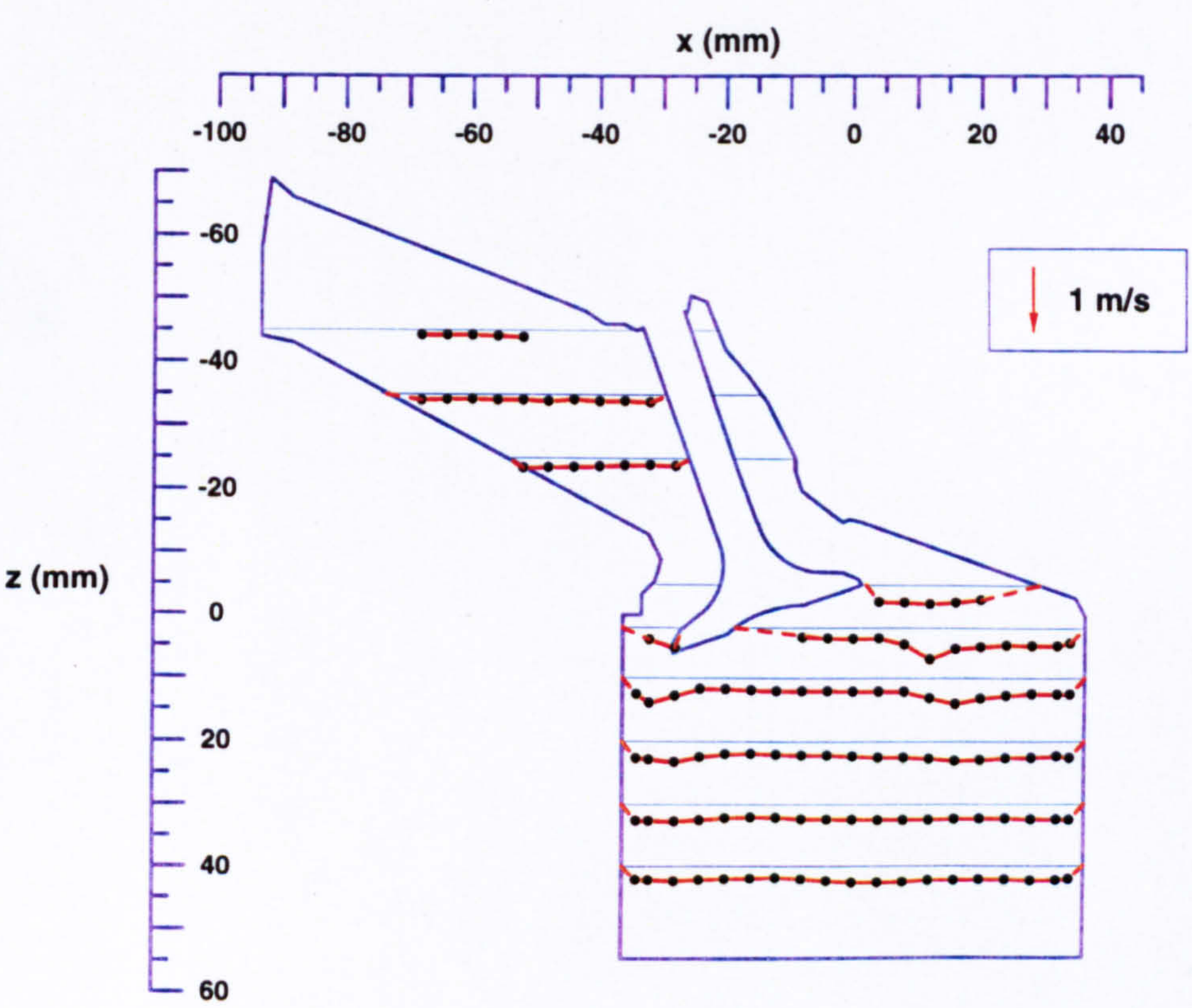

Figure 3.21(d) Profiles of r.m.s. w' velocities in the vertical plane y = -17.6 mm with 10 mm valve lifts

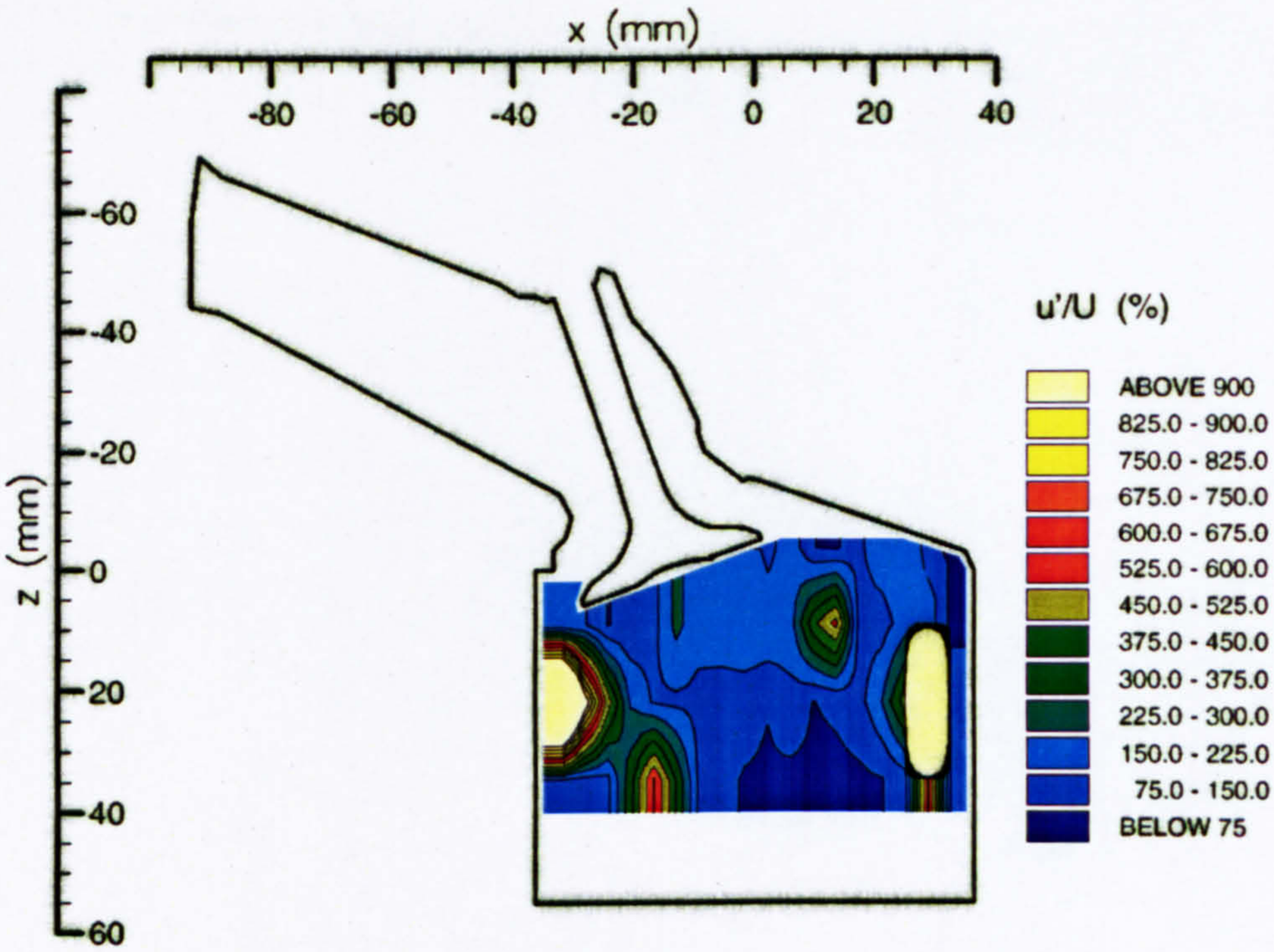

(a) Contours of u'/U

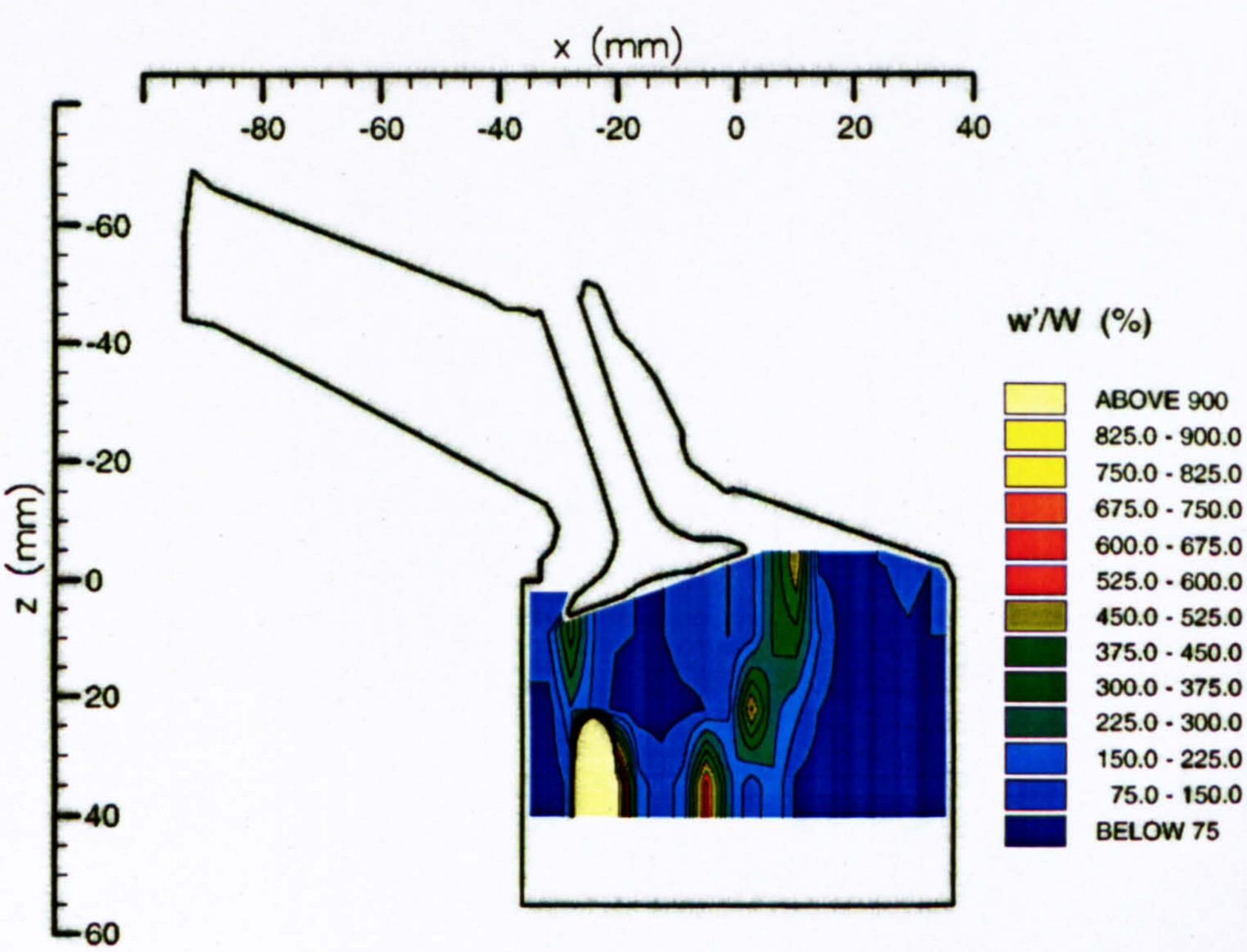

(b) Contours of w'/W

Figure 3.22 Contours of turbulence intensity for flow in the vertical plane y = -17.6 mm with 10 mm valve lifts

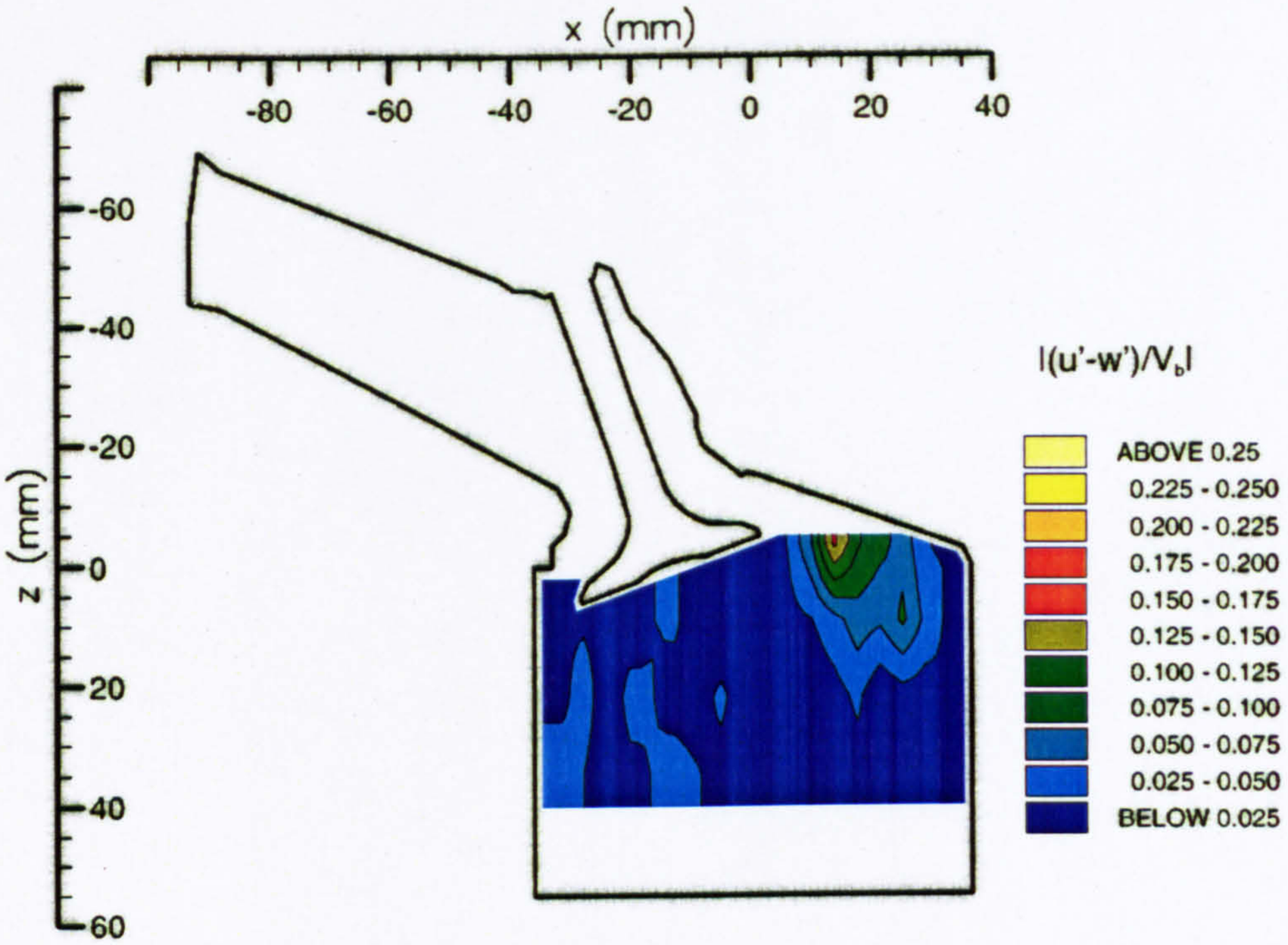

Figure 3.23 Contours of $|(u' - w')/V_b|$ for flow in the vertical plane y = -17.6 mm with 10 mm valve lifts

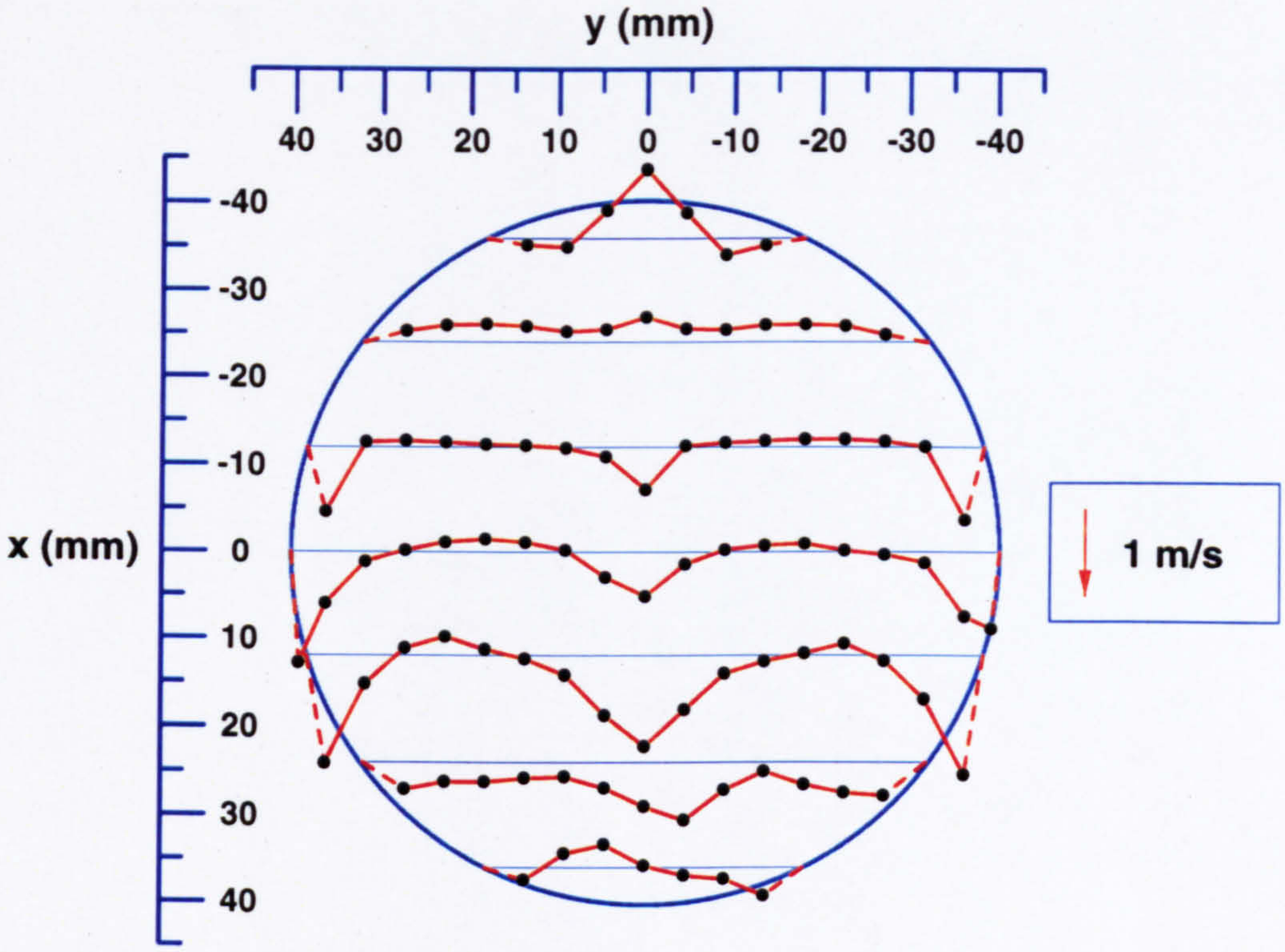

Figure 3.24(a) Profiles of mean U velocities in the horizontal plane z = 10 mm with 10 mm valve lifts

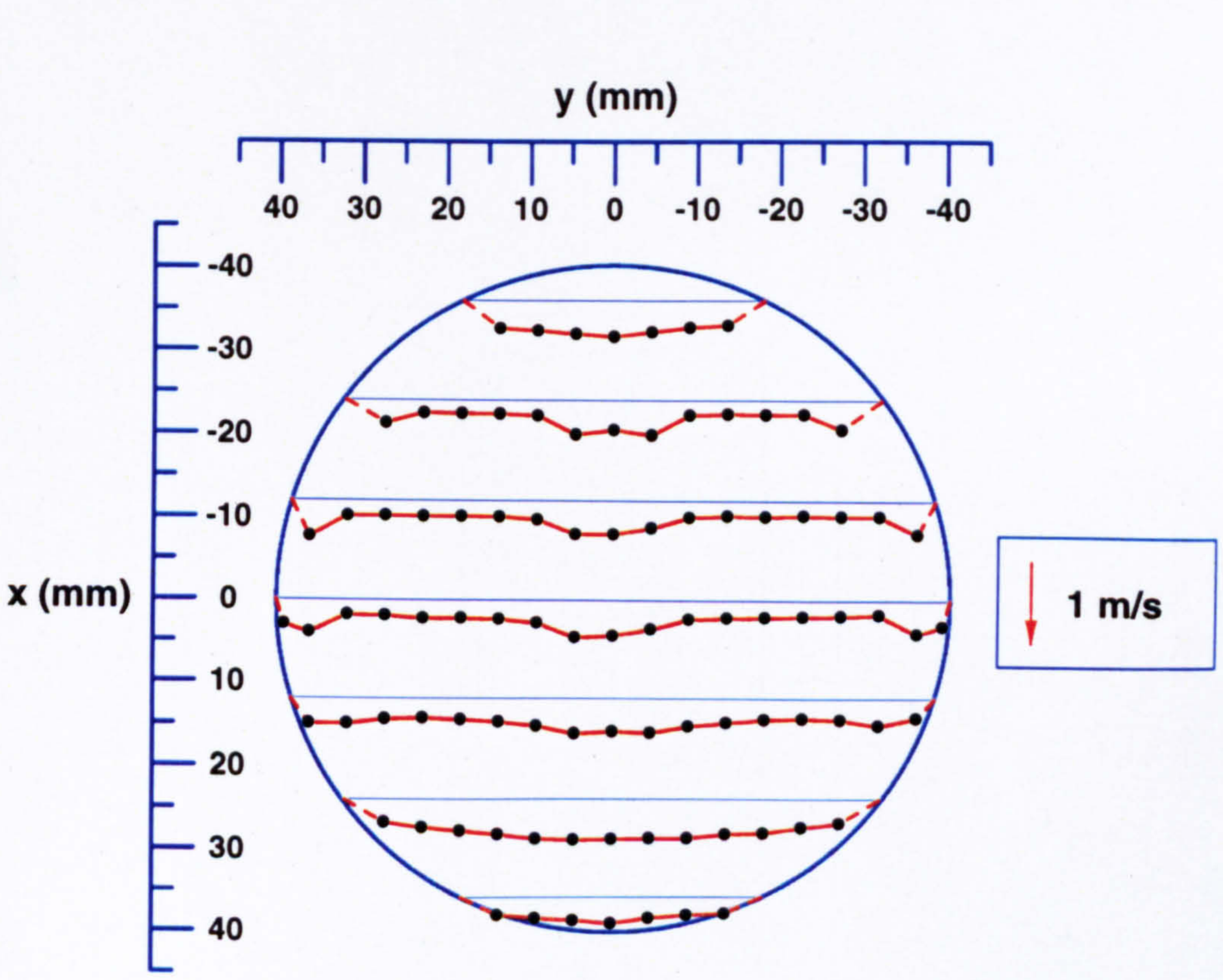

Figure 3.24(b) Profiles of r.m.s. u' velocities in the horizontal plane z = 10 mm with 10 mm valve lifts

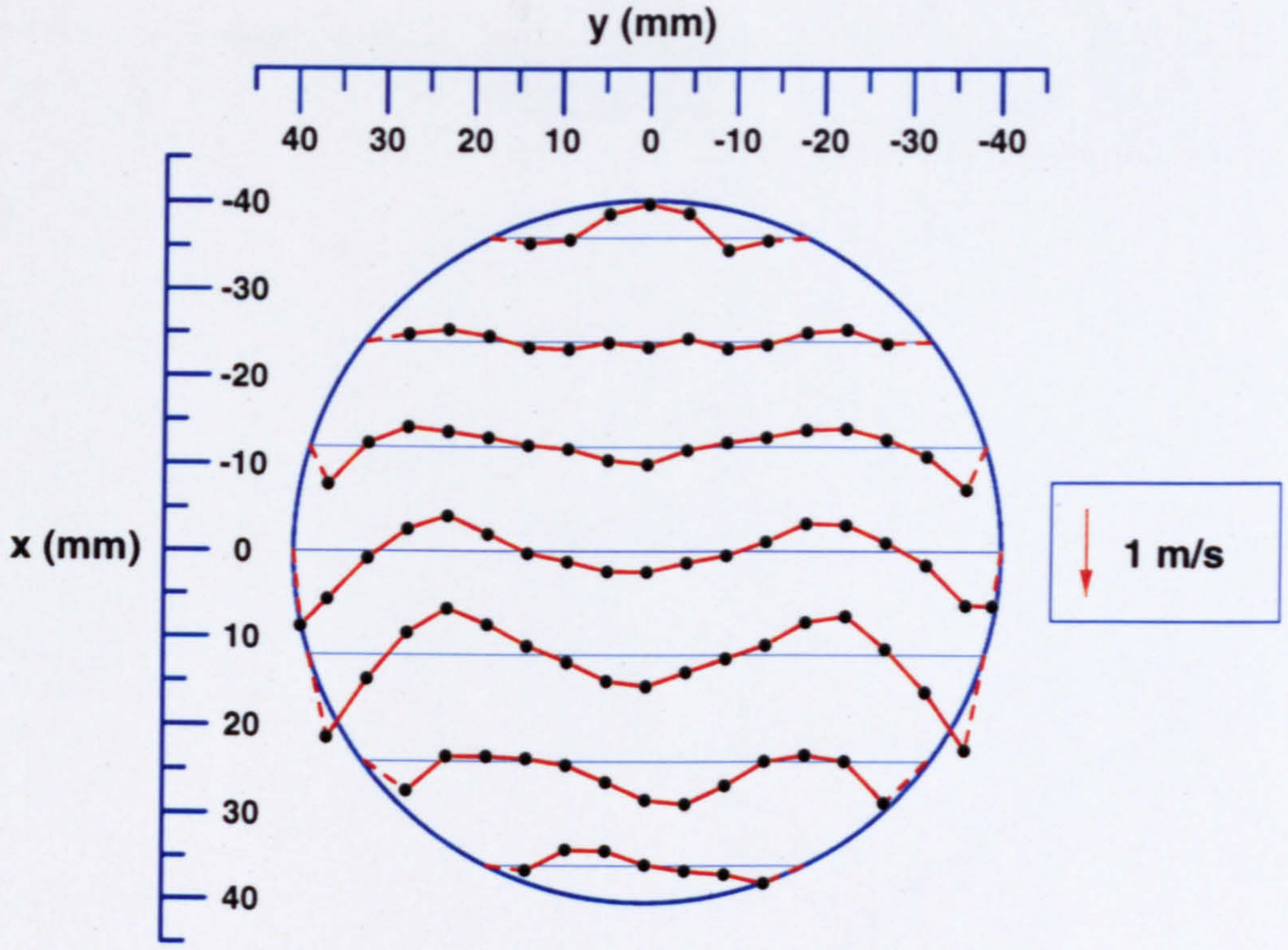

Figure 3.25(a) Profiles of mean U velocities in the horizontal plane z = 20 mm with 10 mm valve lifts

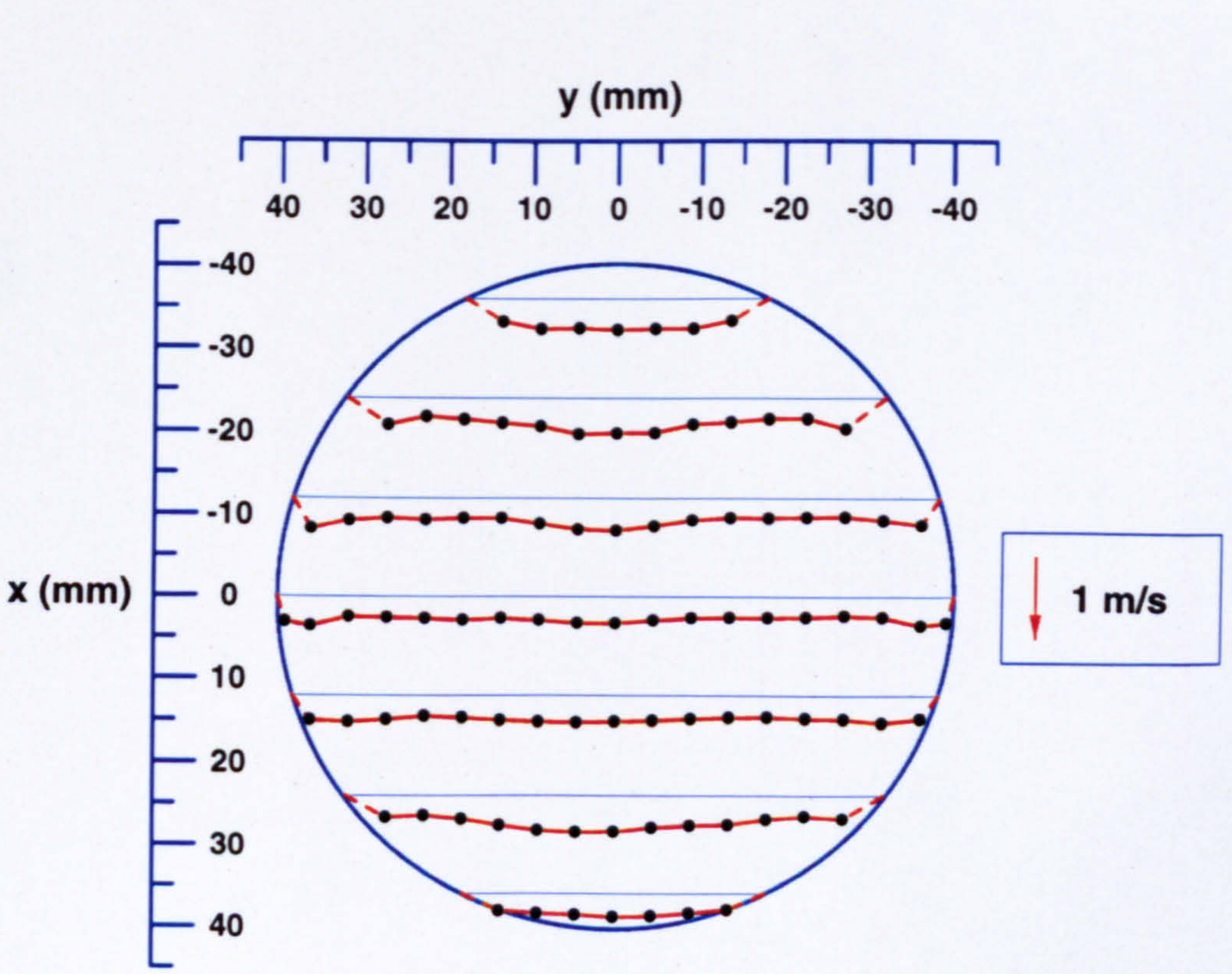

Figure 3.25(b) Profiles of r.m.s. u' velocities in the horizontal plane z = 20 mm with 10 mm valve lifts

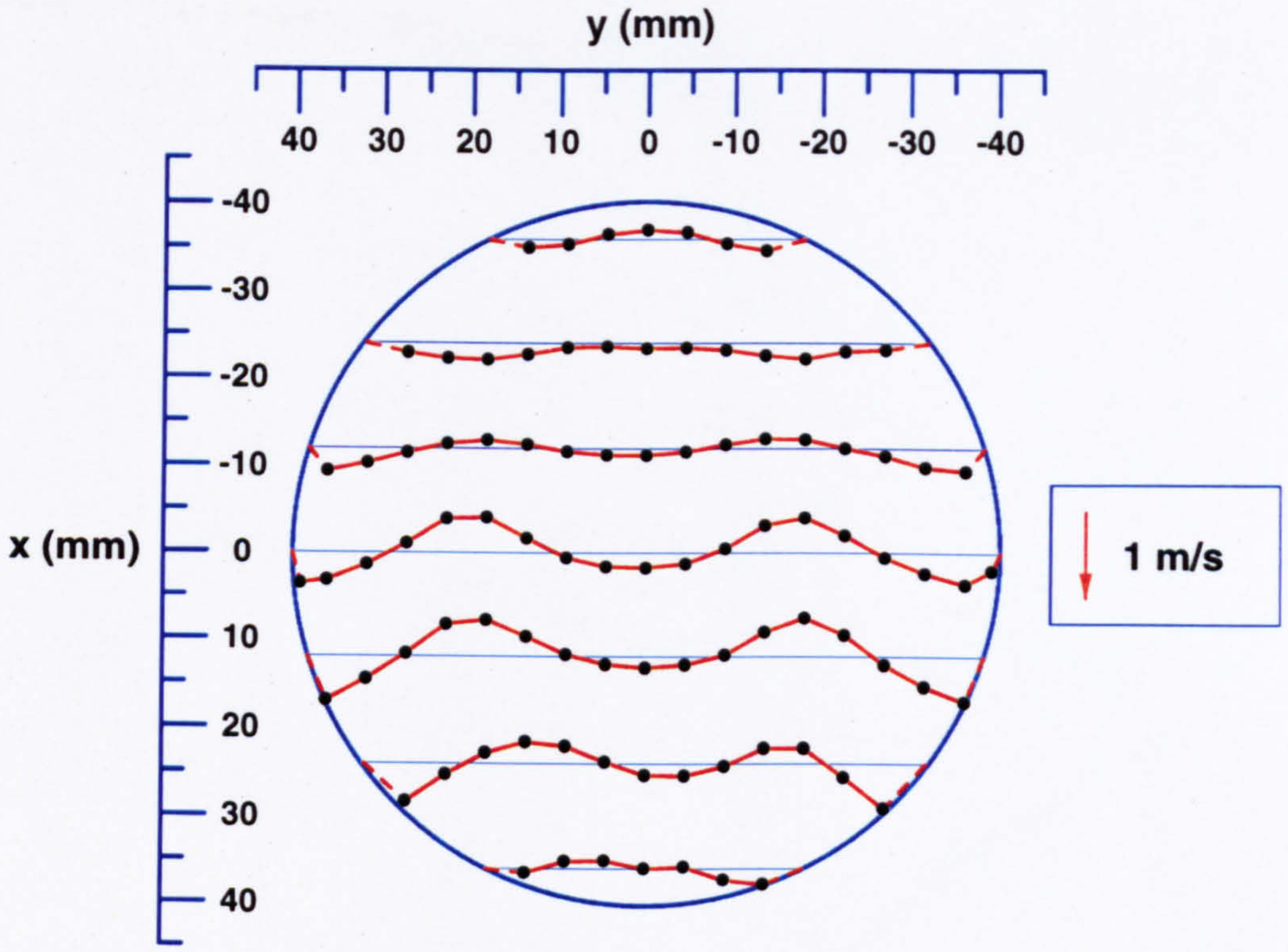

Figure 3.26(a) Profiles of mean U velocities in the horizontal plane z = 30 mm with 10 mm valve lifts

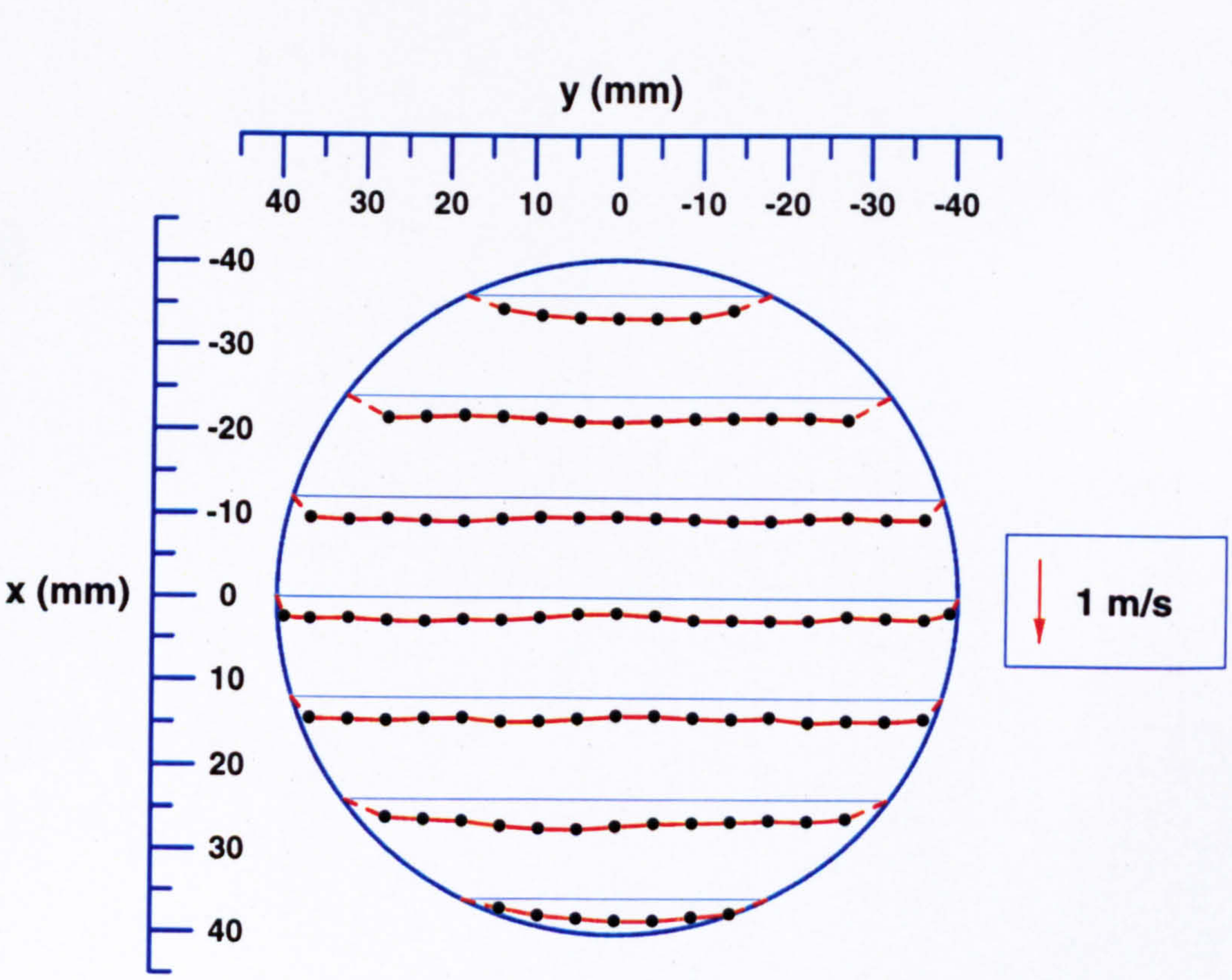

Figure 3.26(b) Profiles of r.m.s. u' velocities in the horizontal plane z = 30 mm with 10 mm valve lifts

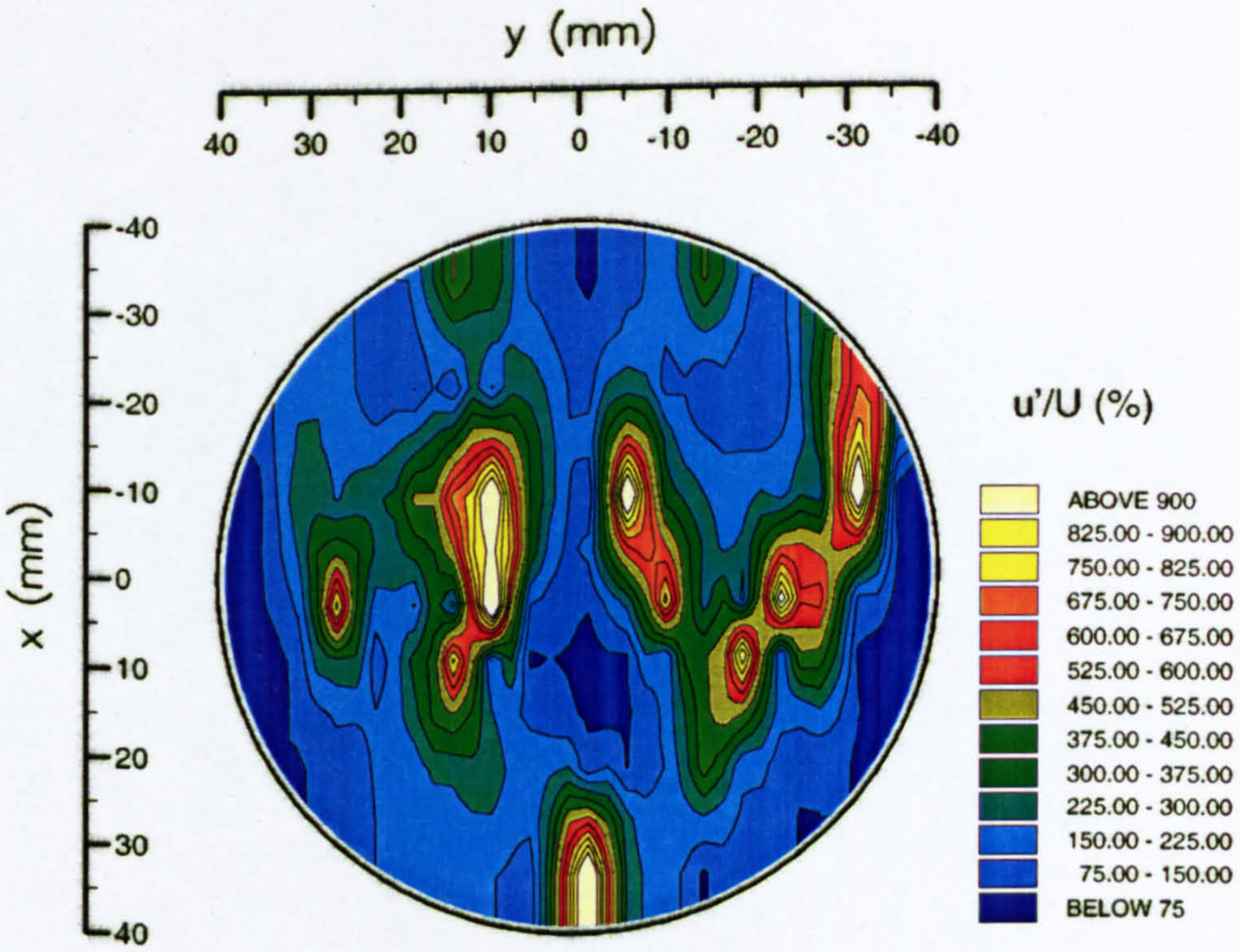

Figure 3.27(a) Contours of turbulence intensity u'/U for flow in the horizontal plane z = 10 mm with 10 mm valve lifts

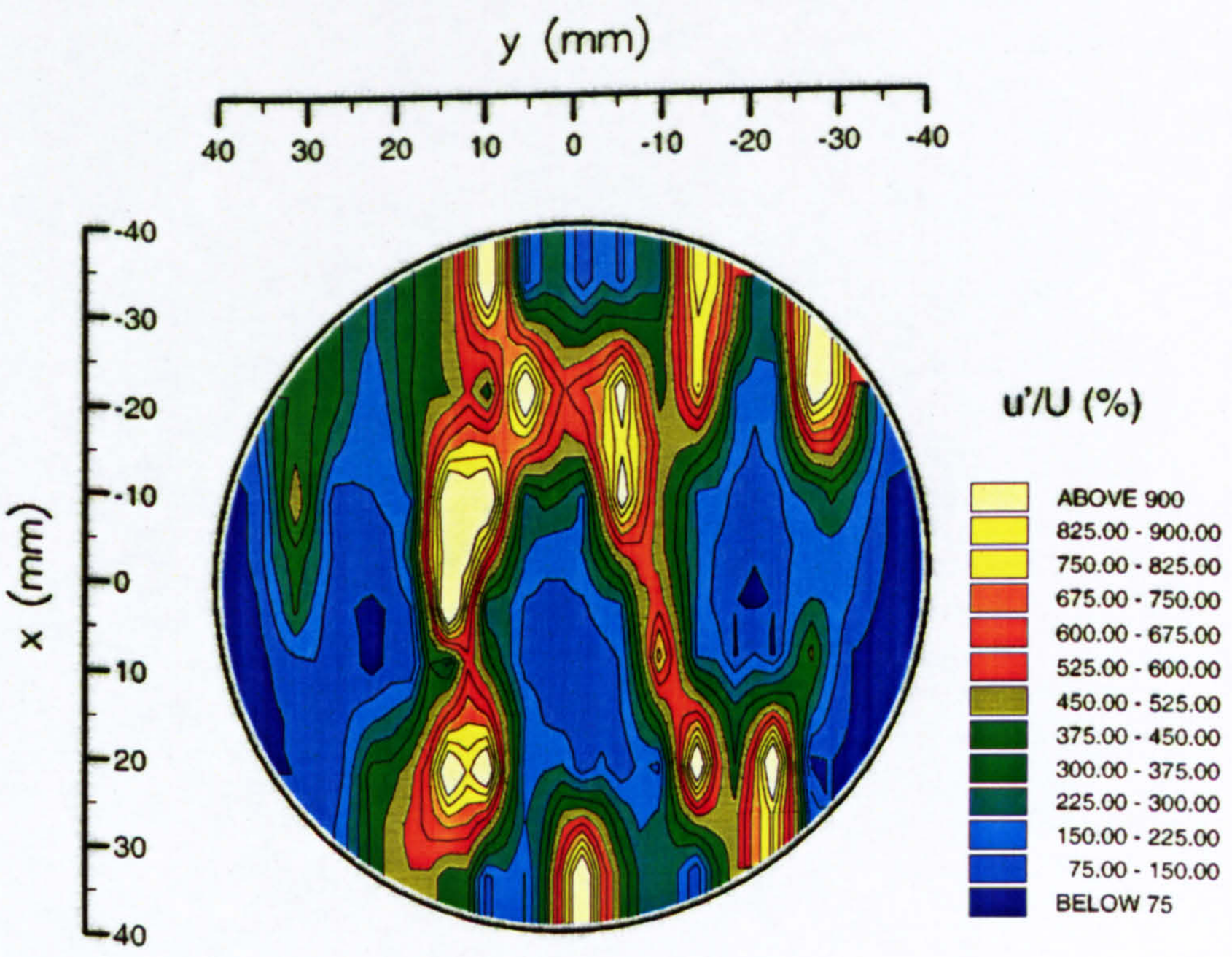

Figure 3.27(b) Contours of turbulence intensity u'/U for flow in the horizontal plane z = 10 mm with 20 mm valve lifts

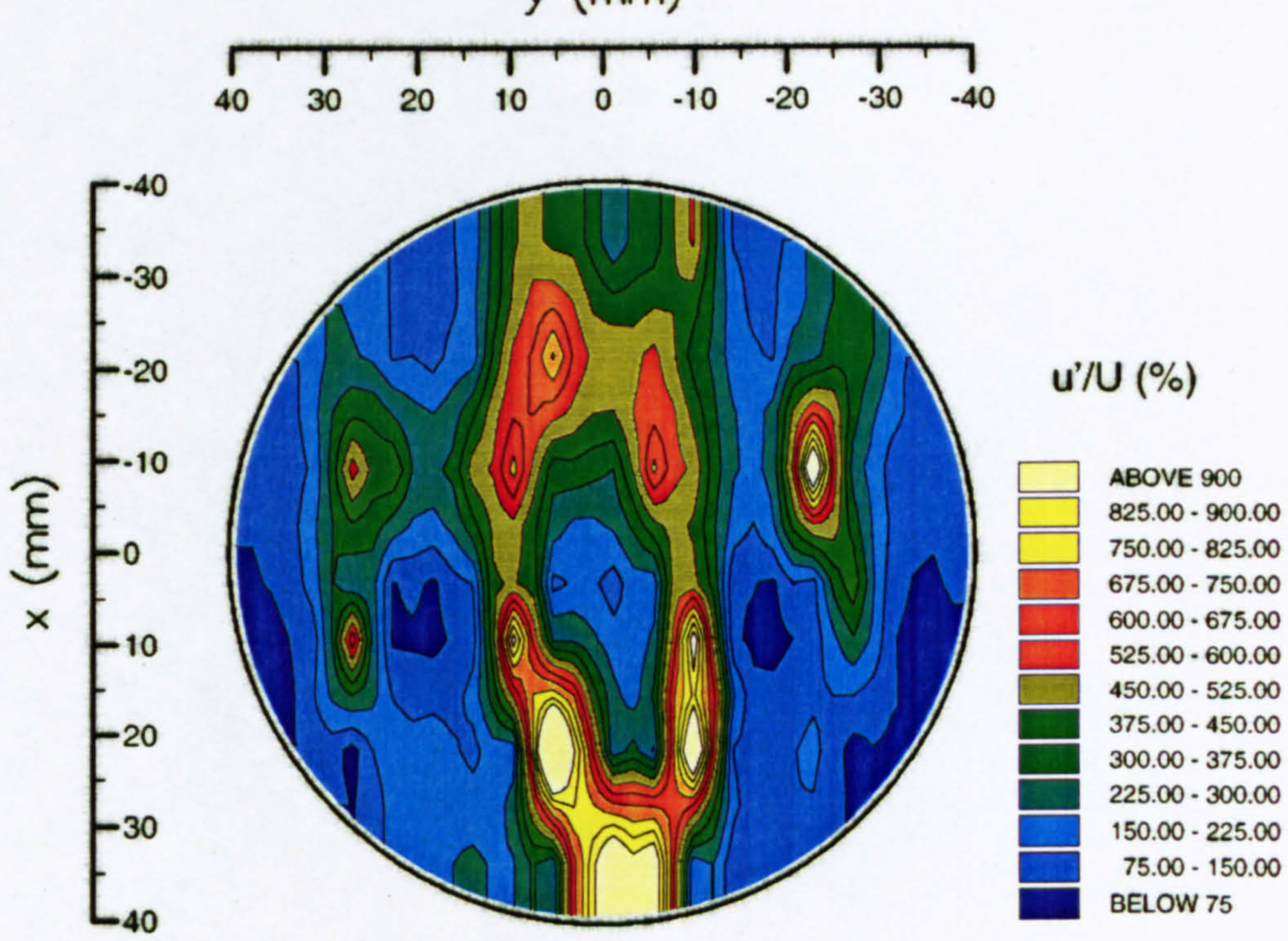

Figure 3.27(c) Contours of turbulence intensity u'/U for flow in the horizontal plane z = 30 mm with 10 mm valve lifts

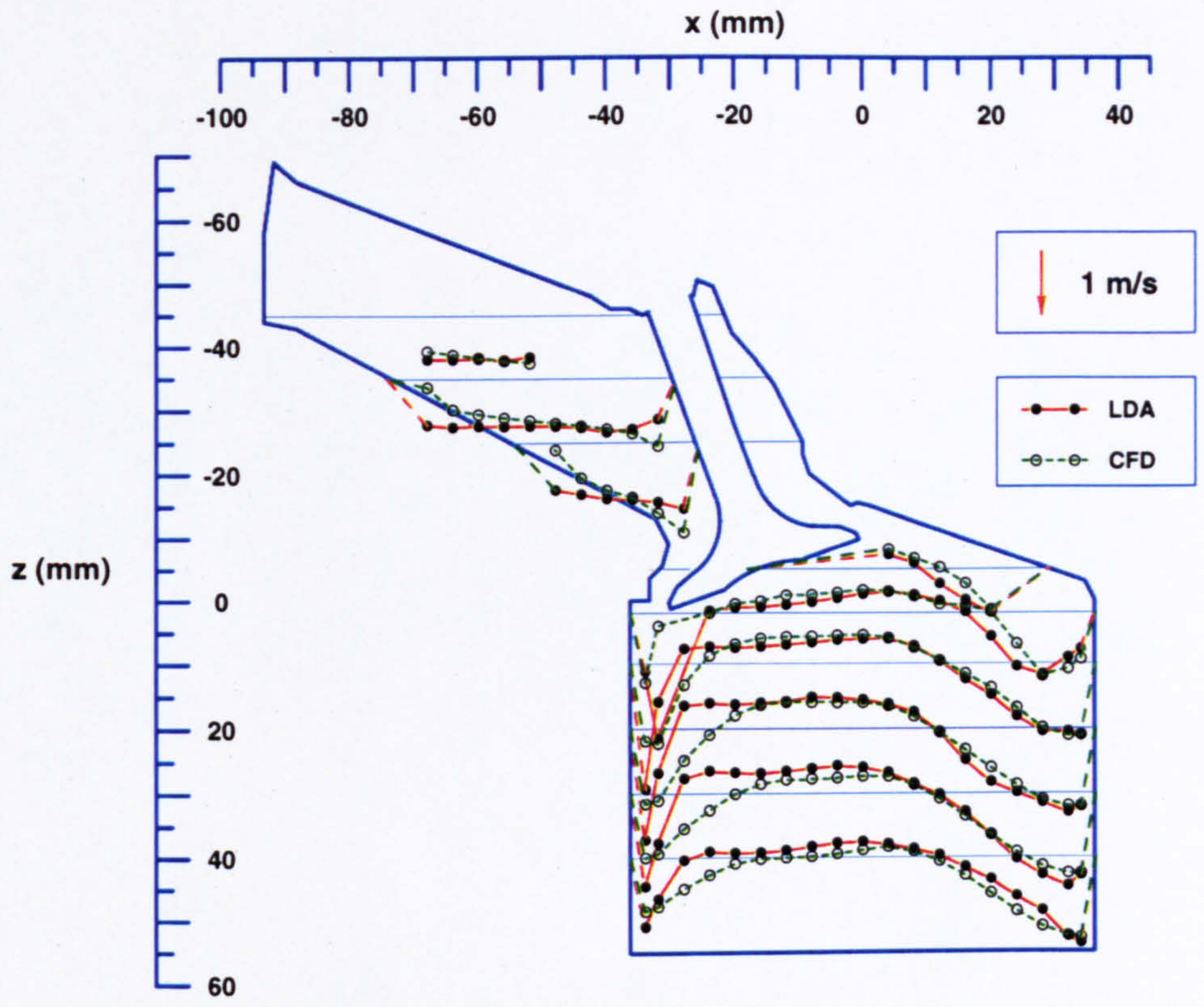

Figure 3.28(a) Comparison of the calculated and measured axial W-component velocities in the y = -17.6 mm plane, with 5 mm valve lifts

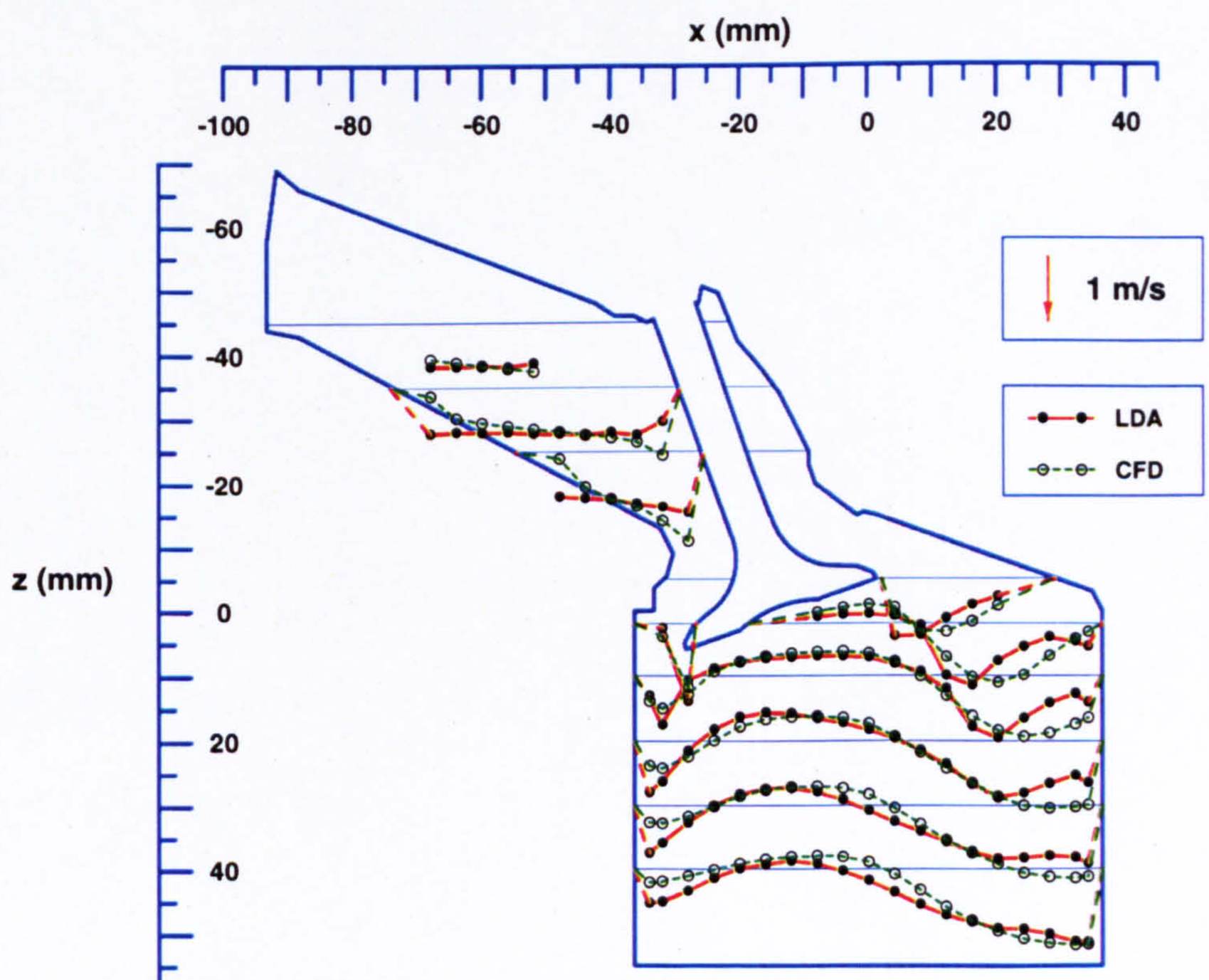

Figure 3.28(b) Comparison of the calculated and measured axial W-component velocities in the y = -17.6 mm plane, with 10 mm valve lifts

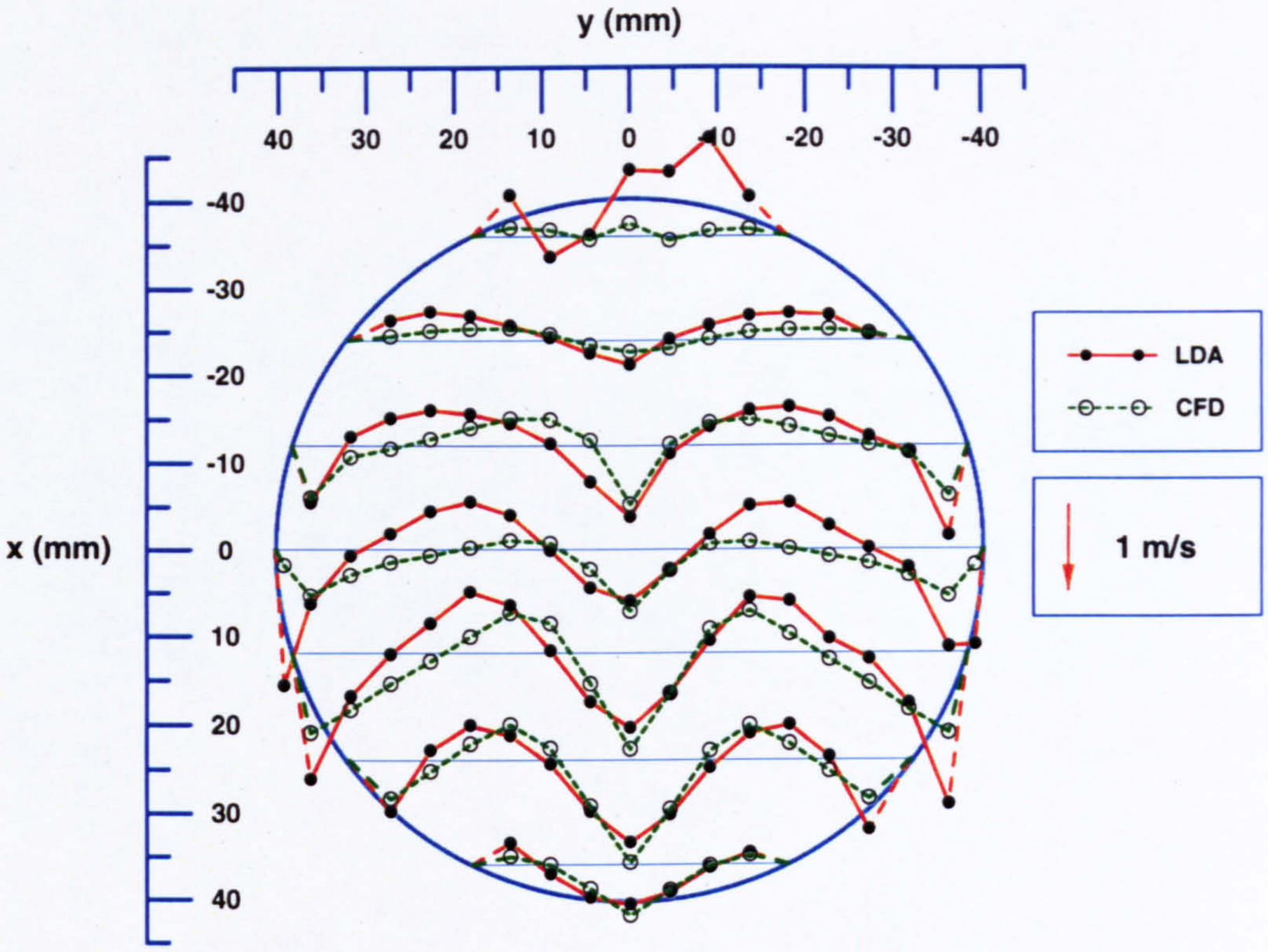

Figure 3.28(c) Comparison of the calculated and measured U-component velocities in the z = 10 mm plane, with 5 mm valve lifts

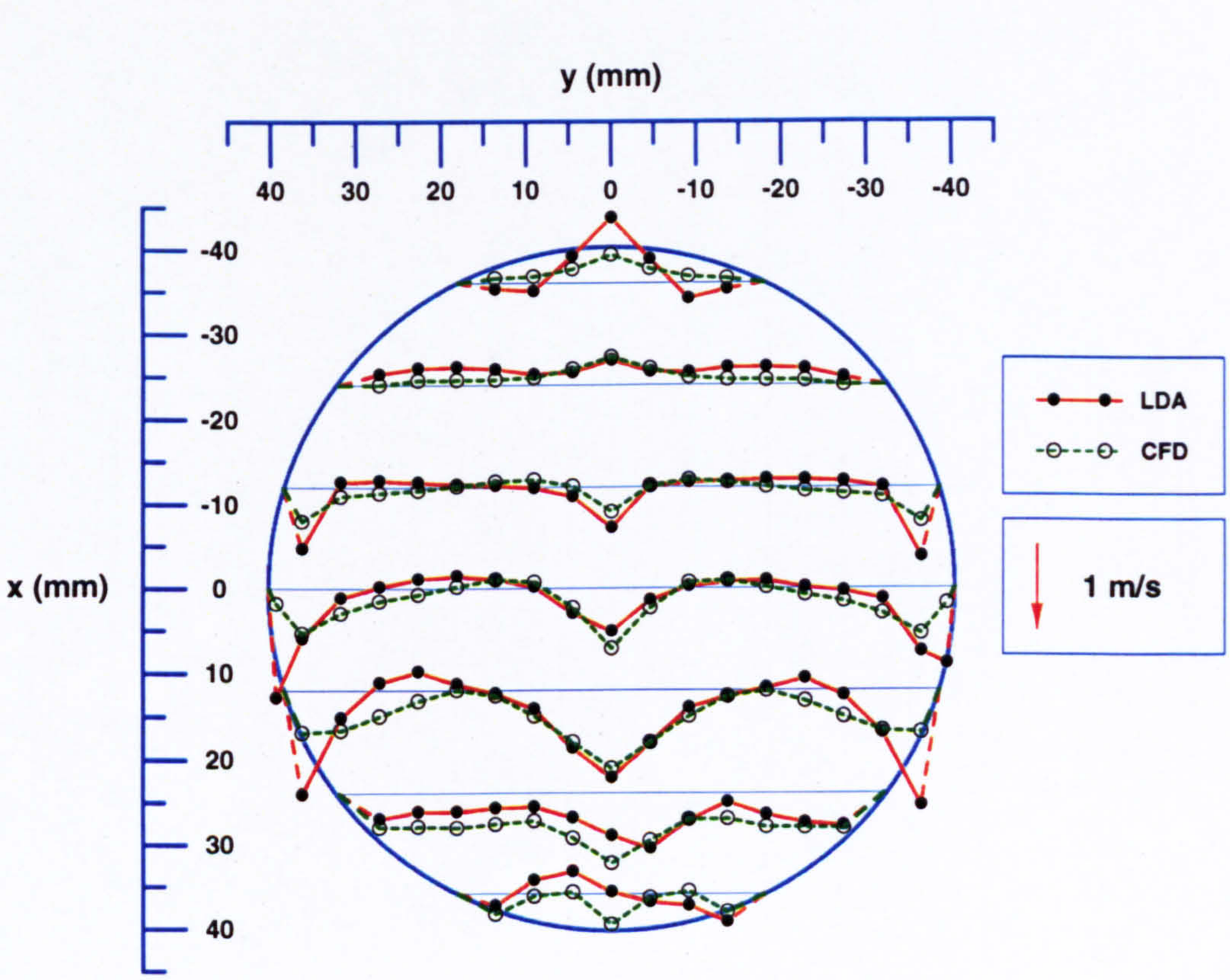

Figure 3.28(d) Comparison of the calculated and measured U-component velocities in the z = 10 mm plane, with 10 mm valve lifts

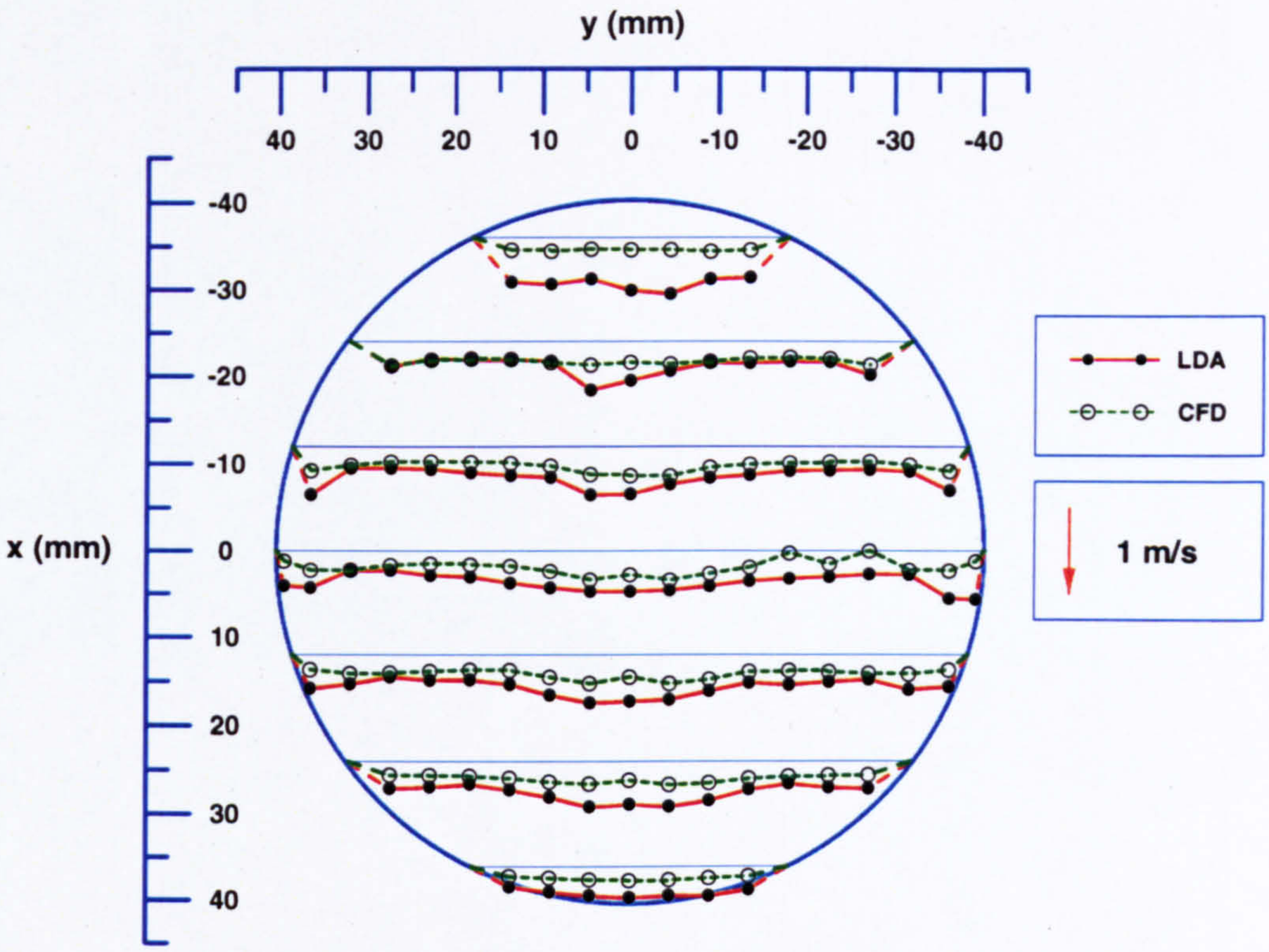

Figure 3.28(e) Comparison of the calculated and measured u'-component velocities in the z = 10 mm plane, with 5 mm valve lifts

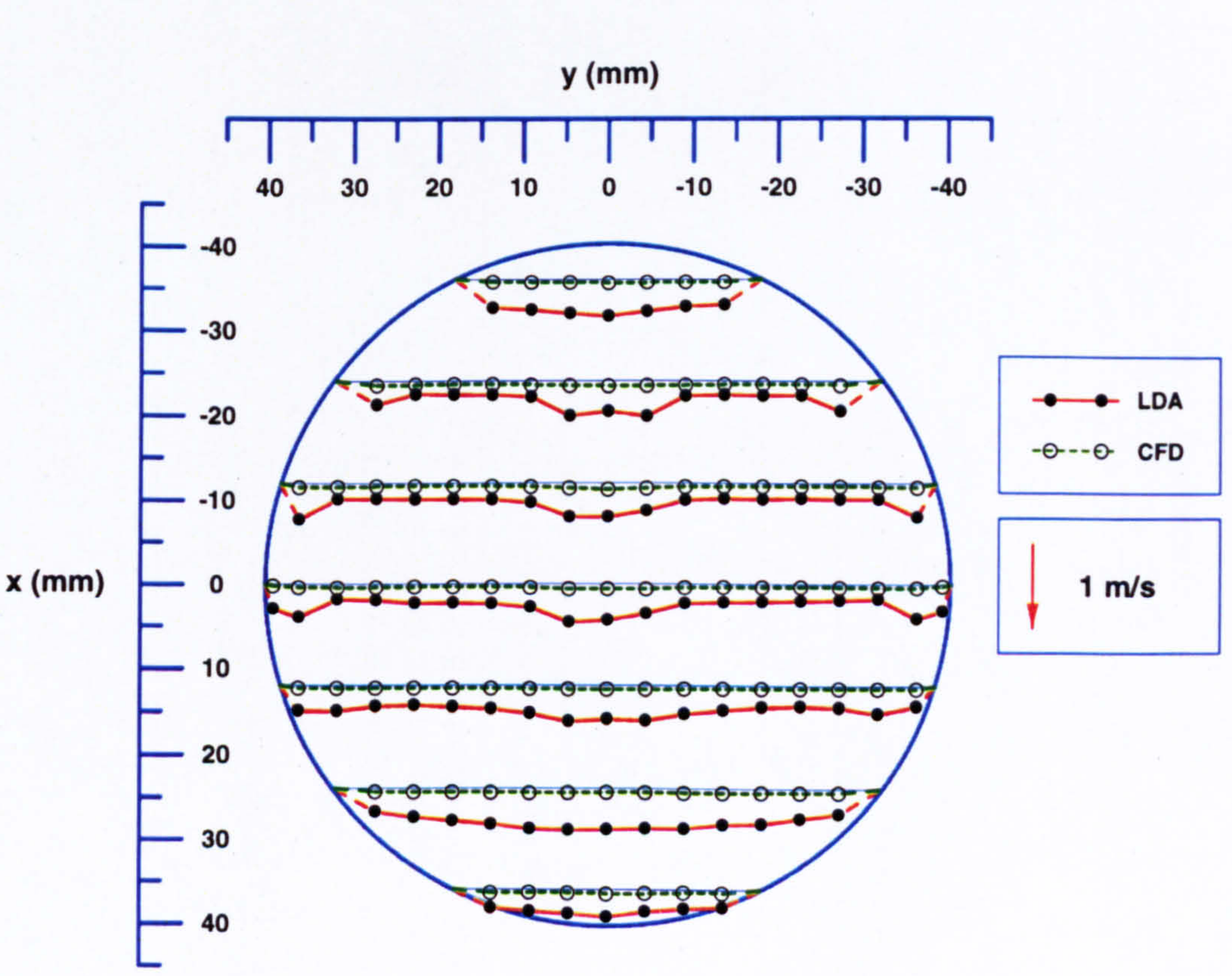

Figure 3.28(f) Comparison of the calculated and measured u'-component velocities in the z = 10 mm plane, with 10 mm valve lifts

Chapter 4

STEADY FLOW STRUCTURE WITH ASYMMETRIC VALVE LIFT AND INLET PORT CONFIGURATION STRATEGIES

4.1 INTRODUCTION

This chapter describes further investigations performed with Ford Zetec engine cylinder head designs to study the effects of asymmetric lift, valve de-activation and port shape combinations on the in-cylinder flow structure. In the first instance, laser-sheet flow visualisation was employed to study the different flow structures obtained with the 'medium output' cylinder head by varying the lift of one inlet valve relative to the other. Following this, detailed ensemble-averaged L.D.A. measurements of mean and r.m.s. velocity were performed with the medium output design for one case where one inlet valve was completely closed and the lift of the second valve was set at 10 mm. The steady in-cylinder flow field generated by two prototype Ford Zetec engine cylinder heads with combinations of straight and swirl inlet ports was also studied using laser-Doppler anemometry. Velocity measurements taken at selected locations in both vertical and horizontal planes are compared with earlier and more detailed investigations made for flow through the medium output cylinder head, with a view to identifying the influence of intake port design on flow characteristics.

4.2 FLOW VISUALISATION STUDY

The laser-sheet flow visualisation procedure has been previously described in Chapter 2. During the course of these tests the lift of one inlet

valve was varied with respect to the other, in order to determine whether any notable large-scale flow structures could be generated in the cylinder of the engine model. The benefits of asymmetric or variable valve lift and valve de-activation in a dual-intake valve engine have already been reviewed by Mahmood and Yianneskis (1994), and include improvements in engine performance and reduction of pollutant emissions.

For each test, the lift of Valve 2 - see Figure 3.1 in Chapter 3 - was set at a particular value, and the lift of Valve 1 was varied relative to this. Consequently, nine different valve lift configurations were examined, these being:

	Valve 1 Lift (mm)	Valve 2 Lift (mm)
(i)	0	10.0
(ii)	2.5	10.0
(iii)	5.0	10.0
(iv)	7.5	10.0
(v)	0	7.5
(vi)	2.5	7.5
(vii)	5.0	7.5
(viii)	0	5.0
(ix)	2.5	5.0

In all cases, the mass flowrate was 1.54 kg/s. Tests were not carried out with Valve 1 closed and Valve 2 set at 2.5 mm because it was not possible to achieve this flowrate in the rig with such a low lift.

4.2.1 Flow Structure with One Inlet Valve Closed

By far the strongest in-cylinder motion was achieved when one inlet valve of the test section was kept closed. Figure 4.1(a) presents the flow structure in the vertical plane y = -17.6 mm with Valve 1 closed and Valve 2 open by 10 mm. In this plane, a very strong vortex was observed which rotated in an anti-clockwise direction, generated by a powerful intake jet to the left of the inlet valve. This flow creates a large recirculation region at the exit of the port, shown to the left of the inlet valve on the figure. The intake flow passing over the right of Valve 2 is not as intense.

In the y = 0 mm plane the flow structure appears to be more complex, as shown on Figure 4.1(b), with the fluid seeming to travel in many different

directions. On closer inspection, however, it may be noted that the flow is actually spiralling in the clockwise direction down the cylinder. Thus, fluid on the right hand side of the figure is travelling in the opposite way in the y-direction to the flow on the left hand side.

Flow in the y = 17.6 mm is presented on Figure 4.1(c), and this is the vertical plane through the centre of the closed inlet valve. The strong tumble-type flow shown in this figure is actually part of the mainstream swirl, which is inclined to the side of Valve 1.

The fact that swirl is the predominant flow motion for the case of inlet valve closure is particularly noticeable in the horizontal planes z = 10 mm, z = 30 mm and z = 40 mm. Figure 4.1(d) shows the flow pattern in the z = 10 mm plane. The flow is rotating in a clockwise direction and is strongest close to the cylinder wall. The clockwise rotation can be attributed to the geometry of the intake ports, which are inclined in the horizontal as well as the vertical planes. When one inlet valve is kept shut, then the fluid is directed into the cylinder in the same manner as by a swirl port.

In Figure 4.1(d), two smaller swirling vortices are also apparent, both of which rotate in the clockwise direction in conjunction with the main flow. Planes z = 30 mm and z = 40 mm - shown on Figures 4.1(e) and 4.1(f) respectively - further describe the high level of swirl in the cylinder. In the z = 30 mm plane the flow has become more orderly and the two vortices have also become rounder in shape - and are of a similar size here. It is interesting that there is counter-rotation (with the likelihood of significant shear) in the boundary between the two vortices, Figure 4.1(e). This may be a reason for the reduction in size of the vortices, from around 25 mm diameter at z = 30 mm to approximately 15 mm diameter at z = 40 mm. The spiralling nature of the flow is indicated by the fact that these vortices have shifted to a different location and appear to be travelling in a clockwise direction with respect to the centre of the mainstream swirling flow in the cylinder. The actual strength of the swirl may be appreciated by noting that in z = 40 mm horizontal plane, the intensity of the overall flow is altered little from planes upstream. The flow in the vertical plane x = -16.5 mm is illustrated on Figure 4.1(g). Here it is seen that the intake flow from valve 2 is forced underneath this valve by swirl from the left hand side of the figure, which further enhances the clockwise motion of the working fluid. An illustration of the three-dimensional in-cylinder flow is shown on Figure 4.1(h). The diagram verifies that swirl is the dominant flow feature in this case.

Tests were also carried out with Valve 1 shut and Valve 2 opened first by 7.5 mm and then by 5.0 mm. The flow structure in both these cases was similar to that already described above.

4.2.2 Asymmetric Valve Lift Flows

Altering the lift between the two inlet valves produced very complex flow structures within the test section. Figure 4.2(a) shows the flow in plane y = -17.6 mm for the case when Valve 1 is opened by 2.5 mm and Valve 2 by 10 mm. Whereas inlet valve closure created a very strong and organised flow motion within the engine cylinder, opening Valve 1 greatly altered the characteristics of the flow. As Figure 4.2(a) indicates, a large proportion of the intake fluid still enters from left of the inlet valve to produce an elliptical vortex with rapid circulation. The flow from the right of the valve travels straight down the cylinder and no vortex is present in this region. This could be due to flow from the middle of the test section, which can be seen to travel upwards towards the right of the plane and back down and would thus prevent the formation of any tumble-type vortices.

A dominant tumbling flow motion can, however, be detected in the plane y = 0 mm for this configuration. Figure 4.2(b) shows a well-defined tumble-like flow of approximately half the cylinder diameter. Towards the left of the figure an elliptical vortex of approximately 25 mm height and 20 mm width is also noted, and is related to the vortex shown on Figure 4.2(a). The flow behind the valves also creates a recirculation region at the top left hand corner of the figure.

In the plane y = 17.6 mm, indicated on Figure 4.2(c), the flow is decidedly less well structured. Only two small vortices can be seen, a very small vortex close to the cylinder head and another located underneath the inlet valve. Flapping of the jet issuing to the left of Valve 1 was also observed, indicating flow instability within this region. The jet flapping may also partly be due to some flow from the rear of the cylinder which turns round and travels towards the exhaust valve side.

The flows in the swirl planes also portray the complexity of the in-cylinder motion. In plane z = 10 mm, shown on Figure 4.2(d), the fluid travels in a number of different directions. Near the centre of the cylinder, a region is seen where organised flow motion is indiscernible. Smaller vortices also exist close to the cylinder wall on the left hand side of the figure. The flow travelling towards the exhaust valve side from the cylinder centre can

be recognised as corresponding to fluid seen on Figure 4.2(a) flowing up from the middle of the test section and towards the exhaust valves. Similarly, flow motion towards the inlet valves in Figure 4.2(d) is likely to be the upper portion of the vortex underneath Valve 2, shown in plane y = -17.6 mm. Hence, the small region in z = 10 mm plane indicated as "random flow" is more possibly liquid that is moving upwards in the test section, which would appear as chaotic flow motion in a horizontal plane. Vortices depicted on Figure 4.2(e) are weak, and the flow structure is very complex, such that by plane z = 40 mm, no organised motion is observed.

Views from the exhaust valve side of the test section for this valve lift configuration confirm the above observations. The vertical plane x = -16.5 mm presented on Figure 4.2(f) shows the working fluid travelling down from between the inlet valves, and back up to create vortical motions. The in-cylinder velocities for this valve lift case appeared to be low.

Figure 4.2(f) also clearly indicates that flow from Valve 2 enters at an angle towards the region underneath Valve 1. This causes the intake flow from Valve 1 to turn round and curl underneath the valve head to produce a small vortex. Due to the liquid flowrate over Valve 2 being higher as a consequence of its greater lift, fluid to the right of the figure moves with a lower velocity.

When the lift of Valve 1 is increased to 5.0 mm, whilst maintaining that of Valve 2 at 10 mm, little change in the flow structure is observed. In Figure 4.3(a), a large elliptical vortex of around 40 mm height is again noted, the centre of which moves up and down, indicating flow instability. A small vortex is also created by the fluid motion towards the right of the figure. The flow in the vertical plane y = 0 mm at these valve lifts is indicated on Figure 4.3(b). Similar to the flow of Figure 4.2(b), a large tumble-type motion of approximately half cylinder diameter is apparent. At the same time, a vortex adjacent to the tumbling flow can also be seen, generated by intake flow at the left of the figure. These vortices appear to have a higher rotational velocity than was the case with valve 1 open by 2.5 mm. In the plane y = 17.6 mm, however, little change in the flow structure was distinguished from the previous valve lift configuration - the flow pattern being almost identical to that shown in Figure 4.2(c). The flow structure in the z = 10 mm plane was very similar to that already illustrated on Figure 4.2(d). At z = 30 mm, Figure 4.3(c), it can be observed that the overall flow structure shown on the left hand side of the figure is less well-organised as that seen on the right.

Increasing the lift of Valve 1 to 7.5 mm alters the flow to the effect that in plane y = -17.6 mm, presented on Figure 4.4(a), the tumbling flow vortex has achieved a size of approximately half the cylinder diameter. In the main, the flow in this plane is of a very similar nature to the case of 10 mm lift for both inlet valves, which was discussed in Chapter 3. A tumbling vortex motion is again apparent in the y = 0 mm plane - Figure 4.4(b) - whilst the vortex due to flow behind the inlet valves is noted to be weak in this plane. At y = 17.6 mm, shown on Figure 4.4(c), however, still largely has a low velocity and weak vortices, as observed in earlier cases. The observations suggested that in asymmetric valve lift cases, the flowrate through each valve is not proportional to the valve lift and that more fluid passes through the intake port with the higher valve lift than would be expected if proportionality between valve lift and flowrate was assumed.

Flows at the lower valve lift situations also follow the general trends outlined already. Notably, when the valve lifts are set at 2.5 mm for Valve 1 and 7.5 mm for Valve 2, a strong vertical tumble-like motion is present in plane y = 0 mm, as indicated on Figure 4.5(a). The patterns in swirl planes - Figures 4.5(b), 4.5(c) and 4.5(d) - show the presence of strong swirling flows in the cylinder for z ≥ 30 mm. When the lift of valve 2 is altered from 7.5 to 5.0 mm, a smaller vertical vortex is observed in plane B, shown on Figure 4.6(a). The flows in horizontal planes - presented on Figures 4.6(b), 4.6(c) and 4.6(d) - also identify flow characteristics similar to those observed with the 2.5/7.5 mm valve lifts.

4.3 LASER-DOPPLER ANEMOMETRY STUDY

4.3.1 Flow Structure with One Inlet Valve Closed

The flow visualisation study showed that when one inlet valve is shut, an intense and well-defined flow structure is created inside the cylinder of the engine replica under steady flow conditions. It was therefore decided to investigate this flow further by employing L.D.A. to determine mean velocity and turbulence characteristics with Valve 1 closed and the lift of Valve 2 set at 10 mm. The influence of the variation of liquid mass flowrate on in-cylinder velocities was firstly examined, and tests were performed with mass flowrate settings of: (i) 0.98 kg/s, (ii) 1.26 kg/s and (iii) 1.54 kg/s. The results are presented on Figure 4.7. In this instance, the profiles show that the in-

cylinder velocities are directly proportional to liquid mass flowrate. Very good scaling is achieved for both mean and r.m.s. velocities. This could be due to the fact that as all of the liquid is entering the test section via just one inlet port, then the possibility suggested in Chapter 3 of the uneven split of flow between the two inlet ports with identical valve lift settings will obviously not arise.

Subsequently, detailed measurements of the radial and axial velocity components were taken in the vertical planes y = -17.6 mm, y = 0 mm and y = 17.6 mm, similar to the flow visualisation study. The level of swirl inside the cylinder was determined through measurements of radial velocity in the horizontal planes z = 10 mm, z = 20 mm, z = 30 mm and z = 40 mm. The liquid mass flowrate was maintained at 1.54 kg/s during this study.

a) Vertical Plane Flows

The L.D.A. results confirmed the visualisation observations that closing one inlet valve gives rise to entirely different flow characteristics within the test section. Mean velocity vectors in the vertical plane y = -17.6 mm are presented on Figure 4.8. As one of the intake ports has been disabled while maintaining the mass flowrate entering the test section, twice as much liquid will pass through the one open port than with previous cases and high velocities are achieved inside the inlet port. Whereas with equal valve lift settings of 5 mm and 10 mm mean velocities of approximately 1.8 m/s were noted, velocities of up to 3.9 m/s were measured inside the open port in this case.

In the z = -5 mm profile the velocities are between 1.93 m/s and 3.4 m/s, the U velocity component being significantly larger than the corresponding W component. A high velocity jet is created by flow over the left side of the inlet valve. This produces a strong vortex underneath the inlet valve which rotates in the opposite direction to the tumbling flows referred to in Chapter 3. The fluid within this plane appears to be travelling primarily from the left to the right of the figure. However, it will be shown later (Figures 4.20 - 4.23) that the fluid is rotating in a clockwise direction. Hence, in the three-dimensional sense, liquid towards the right hand side of Figure 4.8 is expected to flow out of the plane of the figure, and that to the left of the figure into the plane, in the opposite direction.

The strength of the vortex underneath the inlet valve may be judged by the fact that a velocity vector of 2.1 m/s magnitude is noted at z = 10 mm,

which is one of the highest velocities measured below the inlet valve. High velocity magnitudes are present at locations closest to the right hand cylinder wall. The lowest velocities were measured in the z = 2 mm profile, where strong flow from the vortex underneath the valve collides with the strong intake flow shown on the z = -5 mm profile.

Figure 4.9(a) shows the mean U velocity profiles in the plane y = -17.6 mm. The U velocities are very high inside the port. In the x = -25 mm and x = -35 mm profiles, maximum velocities are about 3.5 m/s, whilst the highest magnitude of U measured in the x = -45 mm profile is 2.64 m/s. At the same time, whereas the profiles within the ports for the previous two valve lift cases showed that U remained relatively constant throughout the profile, in this instance variations in velocity magnitude are seen along each profile. For example, U varies from 2.45 m/s close to the port wall to approximately 3.5 m/s near the valve stem. Significant magnitude changes between successive measurement points can also be identified in the x = -45 mm profile. Mean U velocities within the intake jet reach 3.27 m/s (z = 5 mm) close to the inlet valve head, whilst further away from the valve velocities are smaller. The largest U velocity measured inside the cylinder is around 1.47 m/s, in the z = 20 mm profile.

R.m.s. u' velocities corresponding to the mean flow structure of Figure 4.9(a) are plotted on Figure 4.9(b). In the 5 mm and 10 mm equal valve lift cases, u' levels appeared to be largely constant along each profile at around 0.1 m/s, and little difference in velocity magnitude was noted between each of the three profiles taken inside the port. In this case, however, u' magnitudes of up to 0.38 m/s have been measured in the x = -45 mm profile. The z = -25 mm and z = -35 mm profiles also show higher u' values than with the equal valve lift flow.

The r.m.s. profiles taken within the combustion chamber and cylinder indicate an increase in the turbulence generated when one intake valve is closed. u' velocity levels at z = -5 mm profile have magnitudes between 0.7 m/s and 1.05 m/s. Levels of u' are high close to the cylinder wall, to the right of the figure. This could be due re-direction of high velocity liquid by the cylinder wall, as it is forced to follow the curvature of the cylinder. The levels in the upper portion of the cylinder are higher than those further below. For instance, in the z = 20 mm profile, u' values are between approximately 0.3 m/s and 0.58 m/s, while over most of the z = 30 mm profile they do not exceed 0.25 m/s..

Profiles of the axial (W) velocity component in the y = -17.6 mm plane are shown on Figure 4.9(c). Mean W velocities in the ports are expectedly lower than the corresponding U component due to the inclination of the port. Once again, whereas velocity magnitudes were almost constant along each profile inside the port with both inlet valves at 10 mm lift, in this case, large changes in velocity are seen in some parts of the profiles. Average velocities in the port are around twice those with equal 10 mm valve lifts. W varies from 0.92 m/s close to the port wall to 1.56 m/s near the valve stem in the x = -35 mm profile. Velocities are generally higher in the x = -25 mm profile.

Inside the cylinder, the profiles in Figure 4.9(c) indicate a rapidly changing flow structure. Jet flows from both the right and left of the inlet valve give rise to sharp peaks in the z = 10 mm profile. The rapid change in flow magnitude and direction shown on this figure is due to the vortex underneath the inlet valve shown on Figures 4.1 and 4.8. The z = 20 mm, z = 30 mm and z = 40 mm profiles all have a similar shape. A strong flow in the downward direction can be identified close to the right of the figure, and the W velocities associated with this vary from 1.96 m/s to 1.57 m/s.

The w' profiles shown on Figure 4.9(d) illustrate similar trends to those described already for u' velocities in this plane. R.m.s. values in the port are again the highest in the x = -45 mm profile, up to 0.4 m/s. Levels in the x = -25 mm and x = -35 mm profiles are relatively constant. Levels reduce in profiles further down the cylinder.

Figures 4.10(a) and (b) present contour plots of u'/U and w'/W turbulence intensity for flow in the plane y = -17.6 mm. The u'/U contours show low intensities at almost all locations within the plane, below 75%. This is a result of the high U velocity values in this plane, and as a result of the low mean velocity gradients present in the profiles in Figure 4.9(a). The contour plot of w'/W, Figure 4.10(b), illustrates greater variations, due to the steeper velocity gradients shown in the mean velocity profiles. Over most of the plane, w'/W levels vary from 0-75% up to 450%, and the highest values, over 900%, are found at locations which correspond to areas in the plane with low W magnitudes.

An estimation of the anisotropy of turbulence in the flow in the y = -17.6 mm plane was determined by evaluating the magnitude of the difference between the two r.m.s. velocity components measured. A contour plot of $|(u'-w')/V_b|$ is provided on Figure 4.11. The largest variations in u' and w' are between 0.2 and 0.3 m/s and are seen within the intense vortex underneath the inlet valve. The bulk flow velocity V_b is 1.38 m/s, so that the

maximum differences are over 20% of V_b, as the figure indicates. In most of the plane differences between u' and w' are considerably lower, up to 0.12 m/s, which is approximately 9% of V_b.

Flow in the axial plane y = 0 mm is very complex as velocity vectors on Figure 4.12 show. Strong flow to the right of the figure can be distinguished at z = -5 mm and z = 2 mm, where velocities of up to 2.92 m/s were measured. As was noted from the flow visualisation study, the overall flow configuration suggests that inclined swirl is the dominant motion in the test section when one inlet valve is closed. Strong downward motion can be observed close to the right hand side cylinder wall, while liquid is moving upwards at the left hand wall. In the centre of the plane a high velocity jet of fluid is produced. Mean U velocities in this plane (Figure 4.13(a)) are high close to the centre of the plane. At z = 2 mm, velocities vary from -0.04 m/s to 2.32 m/s within the jet flow.

u' velocities, profiles of which are shown on Figure 4.13(b), are generally higher in this plane than with equal valve lifts. Levels of u' are lower close to the left wall of the cylinder, approximately 0.2 m/s. Increases in u' magnitude up to 1.07 m/s can be noted at regions of mean velocity gradients, particularly in the z = 2 mm an z = 10 mm profiles. The profiles become more uniform and the turbulence decreases as the flow travels down the test section, as velocity gradients are smaller in the lower parts of the cylinder. The lowest (z = 40 mm) profile is almost uniform.

The W profiles in the y = 0 mm plane for this valve lift configuration are plotted on Figure 4.13(c). As was noted for the corresponding U profiles, W component also shows large variations along each profile. W magnitudes are higher in regions where downward flow motion of the liquid is dominant, such as close to the cylinder wall, at the right of the figure, where velocities of between 1.23 m/s and 1.71 m/s were measured.

On Figure 4.13(d), the w' profiles show similar trends to the u' profiles already discussed. Near the top of the figure, higher values of w' were again measured. The z = 30 mm and z = 40 mm profiles have similar levels of minimum and maximum r.m.s. velocities, around 0.23 m/s and 0.5 m/s respectively. w' levels in the z = 40 mm profile are not as uniform as the u' levels, due largely to the strong axial motion of the flow which is still present in this region.

Figure 4.14 shows contour plots of u'/U and w'/W turbulence intensity in the y = 0 mm plane. Both plots indicate that turbulence intensity levels are small at most locations within the plane. High levels are seen in some

locations where U magnitudes are lowest. On the whole, u'/U levels are greater throughout the plane than w'/W ones.

$|(u'-w')/V_b|$ in the y = 0 mm plane, shown on Figure 4.15, is generally smaller than that in Figure 4.11 for y = -17.6 mm. The maximum differences in the two r.m.s. components are found in the upper part of the plane, and range from 0.18 m/s to 0.24 m/s, which is 13 - 18% of the bulk flow velocity.

Mean flow in the vertical plane through the closed inlet valve (y = 17.6 mm) is shown by the velocity vectors on Figure 4.16. The vectors appear to be indicating the presence of one tumble vortex which covers almost the entire plane. Flow towards the top of the cylinder has a low angle of inclination, indicating that swirl is the dominant motion in this region, and it is anticipated that the third velocity component, V, not measured in this study, is also of large magnitude. Hence, axial mean velocities are low at most locations in the z = 2 mm and z = 10 mm vector profiles. The spiralling motion of the liquid as it moves down the cylinder results in axial velocities becoming larger further downstream.

Figure 4.17(a) shows the U velocity profiles for flow through the vertical plane y = 17.6 mm plane. As was seen on Figure 4.16, magnitudes of U are fairly low towards the upper part of the plane. U velocities in the z = 30 mm and z = 40 mm profiles are all in the negative x-direction and large throughout the profile.

u' velocity profiles in the y = 17.6 mm plane are shown on Figure 4.17(b). These profiles, when viewed alongside the flow vectors on Figure 4.16, show that r.m.s. velocities are the highest in regions where flows from different directions collide together, for instance towards the right hand side of Figure 4.10. In this region u' velocities reach 0.86 m/s. Low r.m.s. values are noted at locations where mean velocities are small, and/or the flow is moving in the same direction, e.g. in the left hand portion of the z = 10 mm profile. The U velocities in the z = 30 mm and z = 40 mm profiles are large, but as the flow at these locations is showing only a gradual change in direction, r.m.s. levels are relatively constant along both these profiles.

The W velocity component of the mean flow in this plane is plotted on Figure 4.17(c). The highest axial velocities are noted in the bottom half of the cylinder, at locations nearest to the right cylinder wall. Due to the primarily horizontal motion of the liquid in the central portions of the z = 30 mm and z = 40 mm profiles, magnitudes of W are low at these locations, while the axial component is also small at locations towards the left hand side of Figure 4.17(c), where the flow is moving upwards. The w' velocity profiles for flow

in the y = 17.6 mm plane are plotted on Figure 4.17(d). Increases in r.m.s. velocities are noted at locations where mean velocity profiles have a steep gradient.

Contours of u'/U and w'/W turbulence intensity, presented in Figure 4.18, exhibit higher values in the upper portion of the cylinder, close to the inlet valves. On Figure 4.19, contours of $|(u'-w')/V_b|$ illustrate the fact that over most of the plane u' and w' are similar. The largest differences are noted towards the right of the figure, between 0.12 and 0.3 m/s (9% to 22% of V_b).

b) Swirl Plane Flows

Figures 4.20, 4.21, 4.22 and 4.23 represent the mean and r.m.s. velocity profiles in horizontal planes within the cylinder. The swirling flow in the plane z = 10 mm is shown on Figure 4.20(a). The profiles verify the strong swirl in the clockwise direction along the cylinder wall observed in the flow visualisation study. Large variations in velocity can also be noted along each profile. The flow visualisation showed two swirl vortices in the centre of the plane, both rotating clockwise. This gives rise to the steep velocity gradients seen on Figure 4.20(a). In the x = 0 mm profile, five velocity peaks can be identified, in which velocities vary from 1.55 m/s at the extreme left, to 1.52 m/s at the right. In between these two points, velocity magnitude and direction changes rapidly, from 1.52 m/s to -0.65 m/s to 1.23 m/s amidst points only around 32 mm apart. Large velocity variations are also seen in the x = 12 mm profile.

Most of the velocity variations in the z = 10 mm plane occur in the right hand portion of the plane, where the open intake port is located. Velocity gradients on the closed valve side of the plane are almost linear. This results in higher u' levels on the right side of the figure, as shown by the u' profiles on Figure 4.20(b). At the left hand side of Figure 4.20(b), r.m.s. levels within the x = -12 mm profile are almost constant at approximately 0.33 m/s, after which there is a sudden increase in u' to 0.97 m/s at the centre of the profile. The highest r.m.s. velocity measured in the plane is 1.12 m/s at x = 0 mm. One reason for the increase in r.m.s. values is the higher shear forces generated between the two vortices rotating in the same direction, which were seen on Figure 4.1(d).

Mean velocity profiles in the z = 20 mm plane are plotted on Figure 4.21(a) and show a somewhat different flow structure to that seen in the z = 10 mm plane. The profiles in the upper portion of the plane, i.e. at x = -12

mm and x = -24 mm do not show sharp increases or reductions in U velocity, but rather indicate the development of a swirling flow. The intensity of the swirl may be judged by the x = -12 mm profile, in which velocities to the right of the profile centre are between 1.2 m/s and 1.5 m/s. The two vortices identified in the centre of Figure 4.21(a) appear now to have reduced in size and also to have shifted towards the front of the plane. The profiles in the z = 20 mm plane are also more uniform.

R.m.s. levels in the right hand portion of the x = -12 mm and x = -24 mm profiles in Figure 4.21(b) have reduced substantially, to become almost constant along each profile as a result of the more uniform mean flow. Although the x = 0 mm, x = 12 mm and x = 24 mm profiles each show similar trends to those seen at the same locations on Figure 4.20(b), with similar u' magnitudes, the profiles are also less jagged, principally due to the settling of the flow.

A single and almost solid-body-like rotation of the flow can be identified in the z = 30 mm plane, as Figure 4.22(a) shows. Maximum velocities in the region of 1.1 m/s were measured at the sides of the x = 0 mm profile and similar levels are also noted in the x = -12 mm and x = 12 mm profiles. The two vortices referred to in the discussion of the z = 10 mm and z = 20 mm planes cannot be identified in this plane, although flow visualisation work performed at this valve lift configuration showed that they persisted throughout this plane. Figure 4.22(b) shows that u' are more uniform than in the z = 20 mm plane.

U-component velocity profiles in the z = 40 mm plane are plotted on Figure 4.23(a). The profiles show that swirling flow has now developed fully. R.m.s. velocity profiles in Figure 4.23(b) indicate that turbulence in the cylinder is becoming uniform in the lower part of the cylinder. Levels are almost constant along all profiles with an average value of approximately 0.35 m/s for most profiles.

The contour plots of u'/U turbulence intensity are presented on Figures 4.24(a) to (d). Due to the presence of the flows in the upper region of the cylinder described above, the contour plots of Figures 4.24 (a) and (b) show more variations in u'/U. In the z = 30 and z = 40 mm planes, where swirling flow is better defined, u'/U magnitudes are below 75% at almost all locations, except at points within the centre of the figures, where mean velocity values are small.

The overall levels and development of turbulence with this particular configuration may be indicated by the average u' and w' r.m.s. values

calculated for each plane. These values were determined as averages of all the r.m.s. velocities measured in a plane. The u'_{ave} and w'_{ave} values for each plane are listed in Table 4.1.

Measurement Plane	Average R.m.s. Velocities (m/s)
y = -17.6 mm	$u'_{ave} = 0.41$; $w'_{ave} = 0.39$
y = 0 mm	$u'_{ave} = 0.51$; $w'_{ave} = 0.48$
y = 17.6 mm	$u'_{ave} = 0.44$; $w'_{ave} = 0.43$
z = 10 mm	$u'_{ave} = 0.54$
z = 20 mm	$u'_{ave} = 0.47$
z = 30 mm	$u'_{ave} = 0.39$
z = 40 mm	$u'_{ave} = 0.33$

Table 4.1 Average r.m.s. velocity values for each measurement plane

The table shows that in the vertical planes, u'_{ave} magnitudes are bigger than their corresponding w'_{ave} values, as was noted in Chapter 3 with the equal valve lift cases, which again suggests that the flow may be anisotropic in the radial velocity direction, as a result of the inclination angle of the directed port through which liquid enters the test section cylinder. However, the average values themselves are substantially larger than values obtained with both valves open. For instance, in the y = -17.6 mm vertical plane, the u'_{ave} and w'_{ave} of 0.49 m/s and 0.39 m/s respectively are almost twice as large as u'_{ave} = 0.23 m/s and w'_{ave} = 0.22 m/s which were calculated with both valves at a 10 mm valve lift. This is due to the higher in-cylinder velocities and shear flows present inside the test section, as has already been discussed.

Average values of u' for flow in the horizontal planes are also considerably larger than those obtained with both 5 mm and 10 mm equal valve lifts. Table 4.1 also indicates that the magnitude of u'_{ave} is decreasing from the z = 10 mm plane to the z = 40 mm plane. As mentioned earlier, this verifies that the turbulence is most intense at the top of the cylinder, while it decays further away from the cylinder head, as the swirling flow develops.

4.3.2 Flow Structure with Asymmetric Cylinder Head Configurations

The in-cylinder flow field generated by two prototype Ford Zetec engine cylinder heads under steady flow conditions was also studied using

L.D.A., in order to assess the influence of intake port design on the flow processes in the cylinder. The engine cylinder bore was machined into a transparent Perspex block and each aluminium cylinder head was mounted onto this in turn, to create a replica of the cylinder head and cylinder assembly, as has been described in Chapter 2. Velocity measurements taken at selected locations in both vertical and horizontal planes are compared with earlier and more detailed investigations made for flow with the standard medium output Zetec cylinder head.

One cylinder head had one straight intake port and one swirl intake port (Ford reference RE.99.XB.704.00.033 - henceforth referred to as 'No. 33' cylinder head) while the second cylinder head had twin swirl intake ports (Ford reference RE.99.XB.704.00.035 - henceforth referred to as 'No. 35' cylinder head). Both cylinder heads had the same flow area at entry as the standard medium output production 1.8 litre Zetec engine with straight High Velocity Tumble intake ports (henceforth referred to as 'H.V.T.' cylinder head), and identical pentroof combustion chambers.

The liquid mass flowrate through each of the No. 33 and No. 35 cylinder heads was maintained at 1.26 kg/s. The Reynolds number was calculated to be 24600, based on the cross section of the flow area at the inlet plane of each cylinder head at entry.

Velocity measurements were taken at 10 mm equal valve lifts for both the No. 33 and No. 35 heads and with Port 2 closed for the No. 33 head (Ports 1 and 2 are as identified on Figure 3.1 in Chapter 3). The previous L.D.A. investigations with the H.V.T. head were carried out at a higher liquid mass flowrate (1.54 kg/s), so that mean and r.m.s. velocity results were normalised for comparison purposes by dividing by the bulk flow velocity at entry into the cylinder head (V_b = 1.13 m/s when Q = 1.26 kg/s and V_b = 1.38 m/s when Q = 1.54 kg/s). It was also shown earlier in this chapter that no difference is observed in the flow structure when the mass flowrate of the working fluid is varied at a particular valve lift setting.

Flow with 10 mm Equal Valve Lifts

Mean and r.m.s. velocity results for the H.V.T. and No. 33 cylinder heads in the vertical y = -17.6 mm plane are compared on Figures 4.25(a) - (d), with both inlet valve lifts set at 10 mm. Profiles of the normalised U-velocity component are shown on Figure 4.25(a), and indicate some differences in the flow. The z = 20 mm profile for the H.V.T. head has

negative values in the central region, while with the No. 33 head at the same region velocity magnitudes are lower and/or positive. Levels of mean U velocity for the two cylinder heads are similar in the z = 40 mm profile, except at points close to the cylinder wall shown on the right of Figure 4.25(a), where flow is turning away from the cylinder wall with the No. 33 head, but towards the wall with the H.V.T. head. Magnitudes of normalised u' velocity are presented on Figure 4.25(b), and are very similar for both cylinder heads in the z = 20 mm and z = 40 mm profiles.

The corresponding results for the normalised axial W-velocity component are plotted on Figure 4.25(c). Both sets of profiles in this plane indicate that while the No. 33 cylinder head has higher velocity magnitudes for flow to the left of the Figure than those produced by the H.V.T. head, velocity magnitudes to the right of the figure are generally lower at z = 40 mm. This suggests that the combination of a swirl port and a straight port results in stronger motion of flow entering the cylinder from the left of the inlet valve, as seen in this plane, than is produced by two straight intake ports. Hence, a large vortex is produced underneath the inlet valve, which restricts the development of a tumble-like vortical flow to the right of the cylinder. Flow visualisation and L.D.A. studies on the H.V.T. Zetec engine revealed the presence of a large separation region against the valve seat of the open inlet port, which acted as a restriction to the flow entering the cylinder to the left of the inlet valve. A recirculation is less likely to be created at the same location at the valve seat with a swirl port, as the flow through this port is not uni-directional like through a straight port, but has a strong swirl velocity component. Hence, flow velocities at the rear of the cylinder are higher than those acquired with a H.V.T. port due to the possible absence of the recirculation, and the smaller angle of the intake flow relative to the inlet valve.

In Figure 4.25(d) the measured w' velocity components for the two cylinder heads are compared. The No. 33 head creates higher levels of turbulence in the flow than the H.V.T. head. This may be accounted by the interaction of the (asymmetric) flows from the two dissimilar port designs inside the cylinder as a result of fluid being introduced at different directions. In contrast, the H.V.T. head has two identical ports, so that interaction of the streams from each port is not as great. The No. 33 head shows greater mean velocity gradients on the left of this plane, which correspond to the higher levels of r.m.s. velocities in this region in Figure 4.25(d).

The flow characteristics produced by the No. 35 cylinder head (with twin swirl ports) in the y = -17.6 mm plane are presented on Figures 4.26(a) to (d). Comparisons of normalised U-component velocity with corresponding results for the H.V.T. head on Figure 4.26(a) show that in the z = 10 mm profile, flow velocity magnitudes and directions are similar except near the r.h.s. cylinder wall. The H.V.T. ports are designed to direct flow away from the inlet valve and along the combustion chamber roof in order to produce strong tumble motion. Measurements with the No. 35 head show that tumble-type motion in this plane is again not as prominent as with the H.V.T. cylinder head. As was noted with the No. 33 head, flow motion to the left of the plane is more intense due to the swirl ports than that resulting from the left of the H.V.T. port, leading to a large vortex underneath the inlet valve. Profiles of normalised r.m.s. u' velocity in this plane, displayed on Figure 4.26(b), indicate that turbulence levels created by both cylinder heads are comparable.

Figure 4.26(c) compares the normalised W-velocity component magnitudes for the H.V.T. and No. 35 cylinder heads in the plane y = -17.6 mm. These results again show that the jet of fluid travelling down the right cylinder wall has a smaller cross section with the No. 35 head than that created by the H.V.T. ports, leading to a smaller vortical flow at the right of the inlet valve. The stronger motion underneath the valve with the No. 35 is evident from the higher W-velocity magnitudes and gradients in this region. The normalised r.m.s. w' velocity results for these two cylinder heads are plotted on Figure 4.26(d). Turbulence levels produced by the two cylinder heads are similar at most locations along the z = 10 mm and z = 30 mm profiles. The No. 35 cylinder head gives slightly higher values of w'/V_b, which may be explained partly by greater interaction of the intake streams from the ports and by the larger mean velocity gradients noted in parts of this plane.

Flow characteristics within the z = 10 mm and z = 30 mm horizontal planes through the engine cylinder at a 10 mm valve lift setting are presented on Figures 4.27 and 4.28 respectively. Figure 4.27(a) shows that mean flow velocities in the z = 10 mm plane are small for all three cylinder heads, due to the predominantly downward motion of the flow, as already illustrated by the previous figures. The profiles produced by flow in the H.V.T. head are symmetric, which would be expected due to its identical intake ports and geometrically symmetric design. Results for flow in the other two cylinder heads indicate an asymmetric flow structure, with the No. 33 head

generating a greater degree of asymmetry in the x = 0 mm profile, and the No. 35 head showing the most asymmetry in the x = 24 mm profile. This can be accounted by the different directions at which liquid enters the cylinder. Maximum velocities obtained with each cylinder head are similar to each other. Measurements of normalised r.m.s. quantities are plotted on Figure 4.27(b). The profiles indicate that turbulence levels in the left portion of Figure 4.27(b) are alike for all three cylinder heads, while variations are noted on the right hand side of the plane. The No. 33 cylinder head in general gives the highest r.m.s. values due to, as explained earlier, the greater degree of interaction between the two intake jets from the ports.

In the z = 30 mm plane, Figure 4.28(a), the small counter-rotating swirling vortices on either side of the symmetry plane with the H.V.T. cylinder head are indicated (see Chapter 3). A swirling motion is also evident from the profile structure on the right of the plane with the No. 35 head, and smaller swirl vortices are apparent on the left of Figure 4.28(a). Results for the No. 33 head suggest that flow in this case is not as well organised compared to the other two heads, as velocities are lower at most measurement locations, and the velocity profiles have a more jagged appearance. Normalised r.m.s. u' results for the H.V.T. and No. 35 cylinder heads are very similar, while the No. 33 head again shows higher magnitudes, as is seen on Figure 4.28(b).

Flow With One Inlet Valve Closed

Investigations were performed with swirl port 1 of the No. 35 cylinder head closed in order to compare the in-cylinder flow characteristics generated by a swirl port and a H.V.T. port. The lift of the open valve was set as 10 mm. Figure 4.29(a) presents a comparison of the normalised U velocity profiles in the vertical y = -17.6 mm plane, i.e. through the centre of the open inlet valve. The profiles indicate that qualitatively the flow created by both cylinder heads is similar in this plane, though the H.V.T. port directs the fluid with greater intensity towards the right of the figure. The swirl port directs flow entering the cylinder to the left of the inlet valve, as is indicated by the negative U-velocity components underneath the valve in the z = 10 mm profile. The overall lower horizontal velocity magnitudes produced by the No. 35 cylinder head indicate that, surprisingly, the swirl generation capability of the swirl port design is not as great as that of the H.V.T. port. This is also shown by the W results presented below. Normalised r.m.s. u'

velocity results in the y = -17.6 mm plane are similar for both cylinder heads, as shown by Figure 4.29(b).

As mentioned above, the possible absence of a recirculation region against the valve seat allows flow to enter the cylinder with greater intensity from the left of the inlet valve, and this is indicated on Figure 4.29(c) by the measurements of the normalised mean W velocity component in the x = -17.6 mm plane. In the z = 10 mm profile, measurements taken at locations nearest to the left cylinder wall show significantly higher velocity magnitudes with the No. 35 cylinder head, than are achieved with the H.V.T. head. The flow structure in the central region of this plane is qualitatively similar for both cylinder head designs, and the H.V.T. port gives rise to higher velocities along the right hand cylinder wall. The z = 30 mm profile shows lower W-velocity magnitudes with the No. 35 head than with the H.V.T. head, suggesting that the swirling flow in this region has a smaller inclination angle to the horizontal. Profiles of w'/V_b in the y = -17.6 mm plane are presented on Figure 4.29(d) and, on the whole, show little difference in turbulence levels generated by each port design, except at measurement points close to the cylinder wall, where variations are due to differences in mean velocity gradients.

Figure 4.30(a) shows profiles of the normalised U velocity component in an axial plane through the centre of the cylinder, y = 0 mm. The structure of the profiles is indicative of intense inclined swirl motion. The results for both cylinder heads again show many similarities in the liquid motion in both qualitative and quantitative terms. The biggest differences in velocity magnitudes are noted in the z = 10 mm profile, close to the inlet valve and cylinder head, due to the different intake characteristics of the H.V.T. and swirl ports, whereas U/V_b magnitudes are closer further down the cylinder. This is also reflected by Figure 4.30(b), which shows the greatest differences in normalised r.m.s. values in the z = 10 mm profile.

The results for normalised W velocity in the y = 0 mm plane show steep velocity gradients are noted in the central region of this plane in both the z = 10 mm and z = 30 mm profiles and both types of cylinder head produce similar flow features. As was seen on Figure 4.29(c), the swirl port gives rise to higher W-component velocities at the left of the figure in the z = 10 mm profile than the H.V.T. port, though flow with the H.V.T. port generally shows the higher velocity gradients. The normalised r.m.s. results of Figure 4.30(d) show similar and high turbulence levels for both cylinder heads.

Figures 4.31 and 4.32 identify the swirl flow characteristics of the flow generated by the H.V.T. and No. 35 cylinder heads in horizontal planes. The flow field produced in the z = 10 mm plane is given on Figure 4.31(a) and it indicates that stronger swirl is produced by the H.V.T. port. The flow configuration comprises swirl vortices in the centre of the plane both rotating in the clockwise direction (see earlier discussion in this chapter), and this gives rise to the steep velocity gradients seen on Figure 4.31(a). Flow features are very similar, but the H.V.T. design generates higher velocities in the central region of the plane. The highest mean velocities in the centre of the z = 10 mm plane resulting from the H.V.T. port are close to those along the cylinder wall, whereas swirl velocities with the No. 35 head are much smaller relative to those at the cylinder wall. The steeper velocity gradients resulting from the H.V.T. port also produce large variations along the normalised u' profiles on Figure 4.31(b), whilst the profiles for flow with the swirl port are more uniform.

A well-defined flow structure is evident further down the cylinder in the z = 30 mm plane, as Figure 4.32 illustrates. Both cylinder heads display similar qualitative flow characteristics although the H.V.T. port again produces the higher mean velocities overall. This is also reflected by the normalised r.m.s. u' velocity values in the z = 30 mm plane which are, on the whole, slightly higher for the H.V.T. cylinder head.

4.4 CONCLUSIONS

This chapter has described flow behaviour within the cylinder of the Ford Zetec engine designs resulting from asymmetric inlet valve lift and inlet port configurations. The fluid motion produced inside the cylinder of a Ford Zetec 'medium-output' engine model as a result of asymmetric inlet valve lifts was initially examined by laser sheet flow visualisation, followed by detailed L.D.A. measurements for flow with one inlet valve closed.

The flow structure produced by two variations of the production 1.8 litre Ford Zetec engine was also investigated with L.D.A. One cylinder head had one swirl type intake port and one straight port of H.V.T. design. The other had twin swirl intake ports. Measurements taken inside the cylinder were compared with earlier measurements obtained in the standard Zetec engine cylinder under steady flow conditions.

The principal observations of these investigations are summarised below:

Standard Zetec Engine

1. Flow visualisation revealed that inlet valve disablement (keeping one inlet valve of a dual-intake valve cylinder head closed) generates a high level of swirl in the cylinder, in addition to intense vortices in vertical planes. This strong swirl is maintained over a large proportion of cylinder volume.

2. Varying the lift between the two inlet valves in the standard Zetec engine cylinder head produced stronger flow motion on the side of the cylinder with the higher valve lift. In-cylinder motion was always weaker on the lower valve lift side. Even when the comparable level of difference in the valve lifts was small, the flow on the lower valve lift side was weaker than would be expected if the flowrate through each intake port was assumed to be proportional to the corresponding valve lift. It is therefore concluded, that the large majority of the fluid passed through the port with the higher valve lift, and the flow through each port is not in proportion to the corresponding valve lift.

3. Variable valve lift configurations generated strong levels of inclined tumble. This was due to the fact that fluid from the port with the higher flowrate was directed towards the low valve lift side, as flow structures in this region were not large intense to prevent this.

4. Flow velocities inside the open valve port are doubled compared to when both ports are open, when one intake valve is closed and mass flowrate is kept constant. High velocities are achieved by flows both forward of and behind the inlet valve and a strong vortex is created underneath the inlet valve and to the rear of the cylinder. An inclined motion is created inside the cylinder as the flow moves down the test section, of which swirl is the larger component.

5. Two adjacent vortices which both rotate in the same direction are produced by flow into the cylinder for the configuration with one port disabled. R.m.s. velocity magnitudes at locations close to the cylinder head were high, due to the shear forces in the fluid resulting from these vortices.

Mean velocity measurements in horizontal planes at lower positions in the cylinder show that swirl levels increase as the fluid travels downwards. Average r.m.s. velocity values decrease with increasing distance from the cylinder head.

6. The u'/U and w'/W turbulence intensities were low partly due to the large radial and axial mean velocities in both vertical and horizontal planes.

7. Contour plots of $|(u'-w')/V_b|$ indicated anisotropic turbulence in regions where strong jet flows and vortices are present. Values of $|(u'-w')/V_b|$ were considerably greater than those noted when both inlet valve lifts were equal.

Prototype Zetec Engine Cylinder Heads

1. Measurements taken in both cylinder head designs with a 10 mm lift for both valves showed that the tumble-like motion seen in this plane is more pronounced with the H.V.T. design. The swirl ports direct flow into the cylinder at a lower angle relative to the inlet valve axis, so that higher velocity flow is introduced from behind the inlet valve. This creates an elliptical vortex underneath the inlet valve which is larger than the one observed with flow in the H.V.T. head, and inhibits the development of a large tumbling flow motion.

2. While the No. 35 and the H.V.T. cylinder heads generally produced similar r.m.s. velocity levels, the No. 33 head produced the highest levels of turbulence inside the cylinder.

3. With one port of the No. 35 head closed, strong inclined swirling motion was noted inside the cylinder and the flow structure was qualitatively similar to that noted with the H.V.T. port.

This work described in this chapter has shown that of the three cylinder head designs evaluated, the standard medium output Zetec engine design with High Velocity Tumble intake ports produced the optimum mean and r.m.s. velocity characteristics under steady flow conditions. The role of the intake ports during the induction stroke is to direct flow such that vortices are produced which will be maintained into the compression stroke, and the largest and most useful vortical structures were produced by the H.V.T.

ports. Although the highest comparable steady flow turbulence levels were generated by the No. 33 cylinder head design, this fact alone does not place it at any advantage over the other designs, since it should be remembered that high turbulence levels are required near the end of the compression stroke, immediately prior to combustion and not necessarily during the induction stroke.

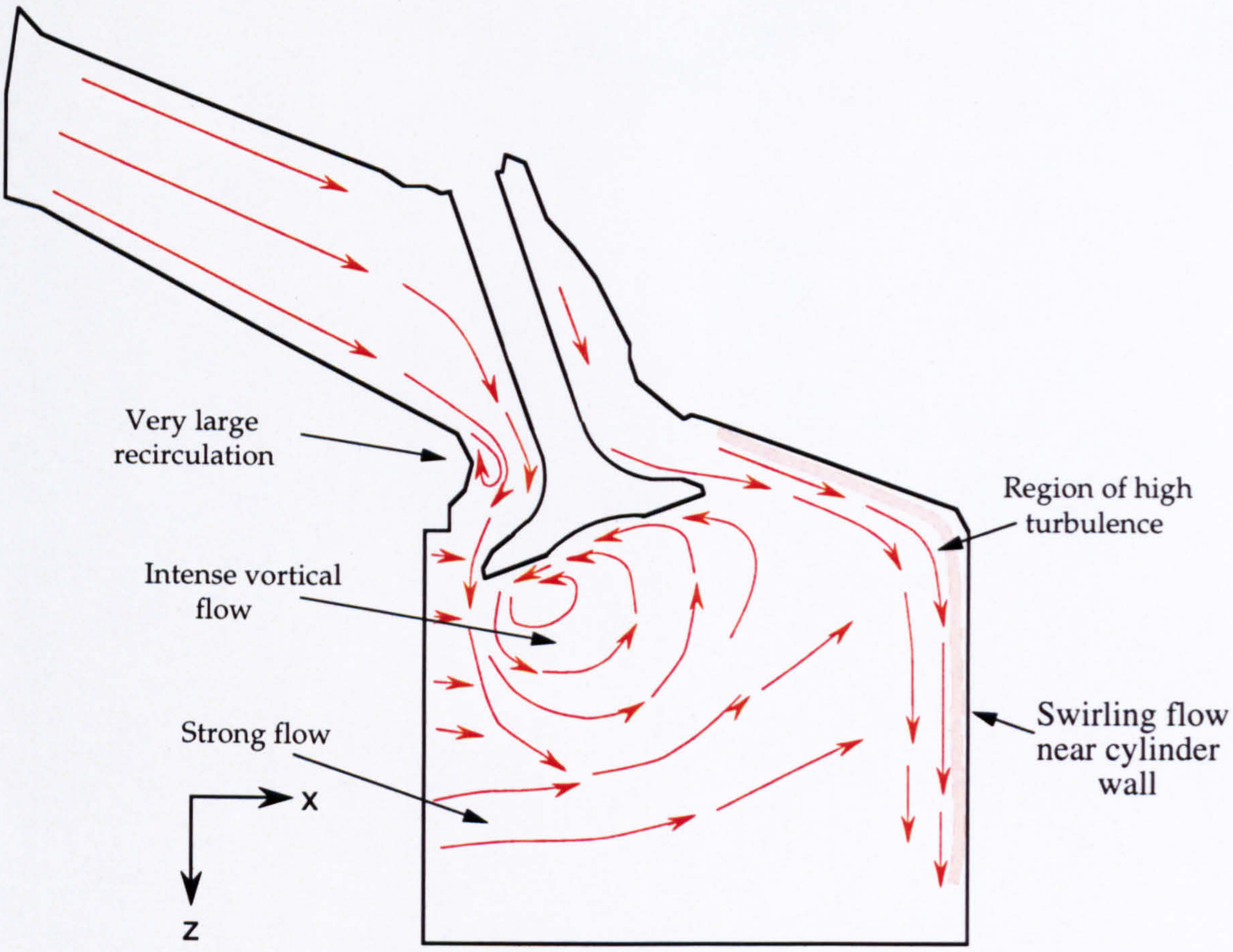

Figure 4.1(a) Flow structure in the y = -17.6 mm vertical plane with 0 mm / 10 mm valve lifts

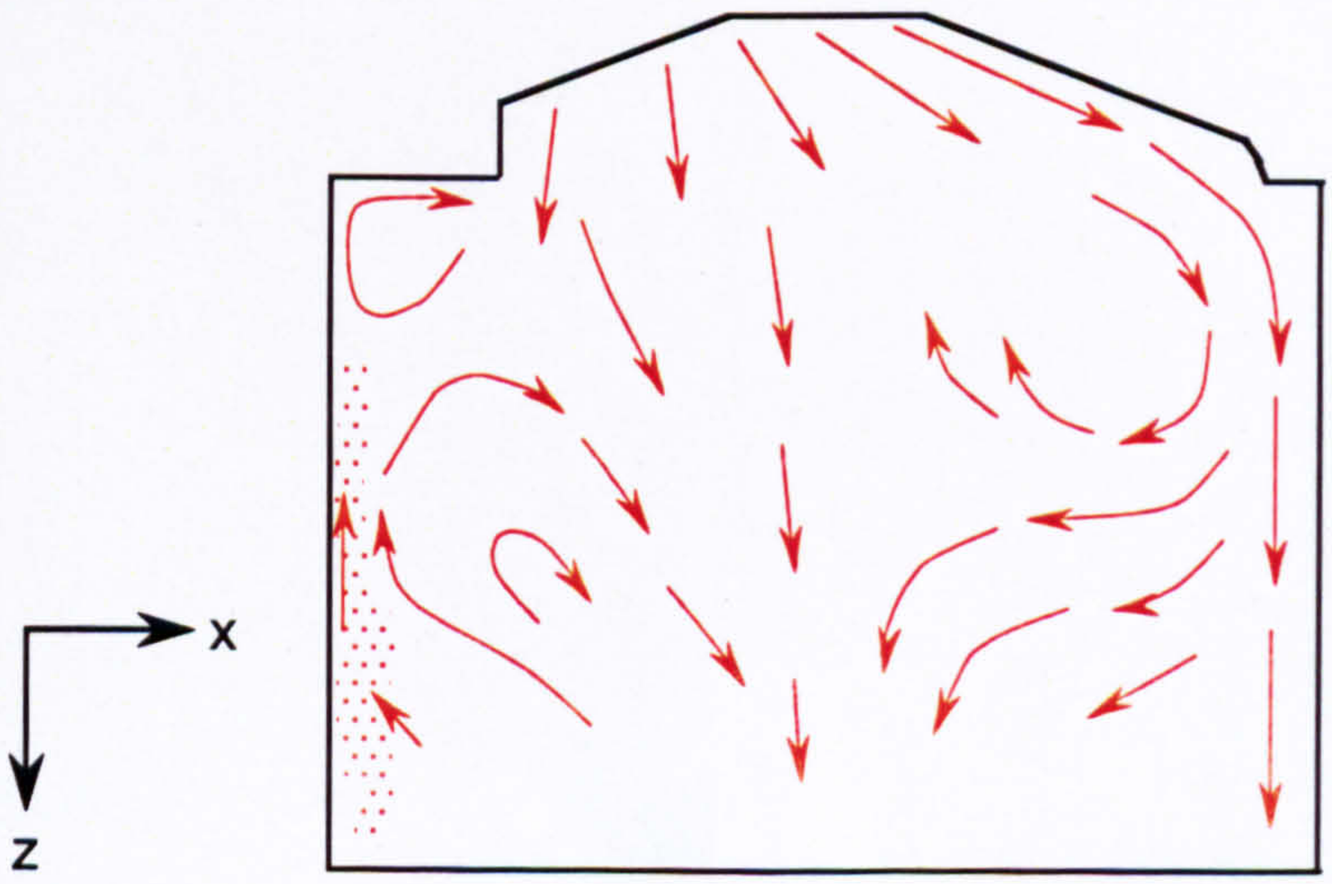

Figure 4.1(b) Flow structure in the y = 0 mm vertical plane with 0 mm / 10 mm valve lifts

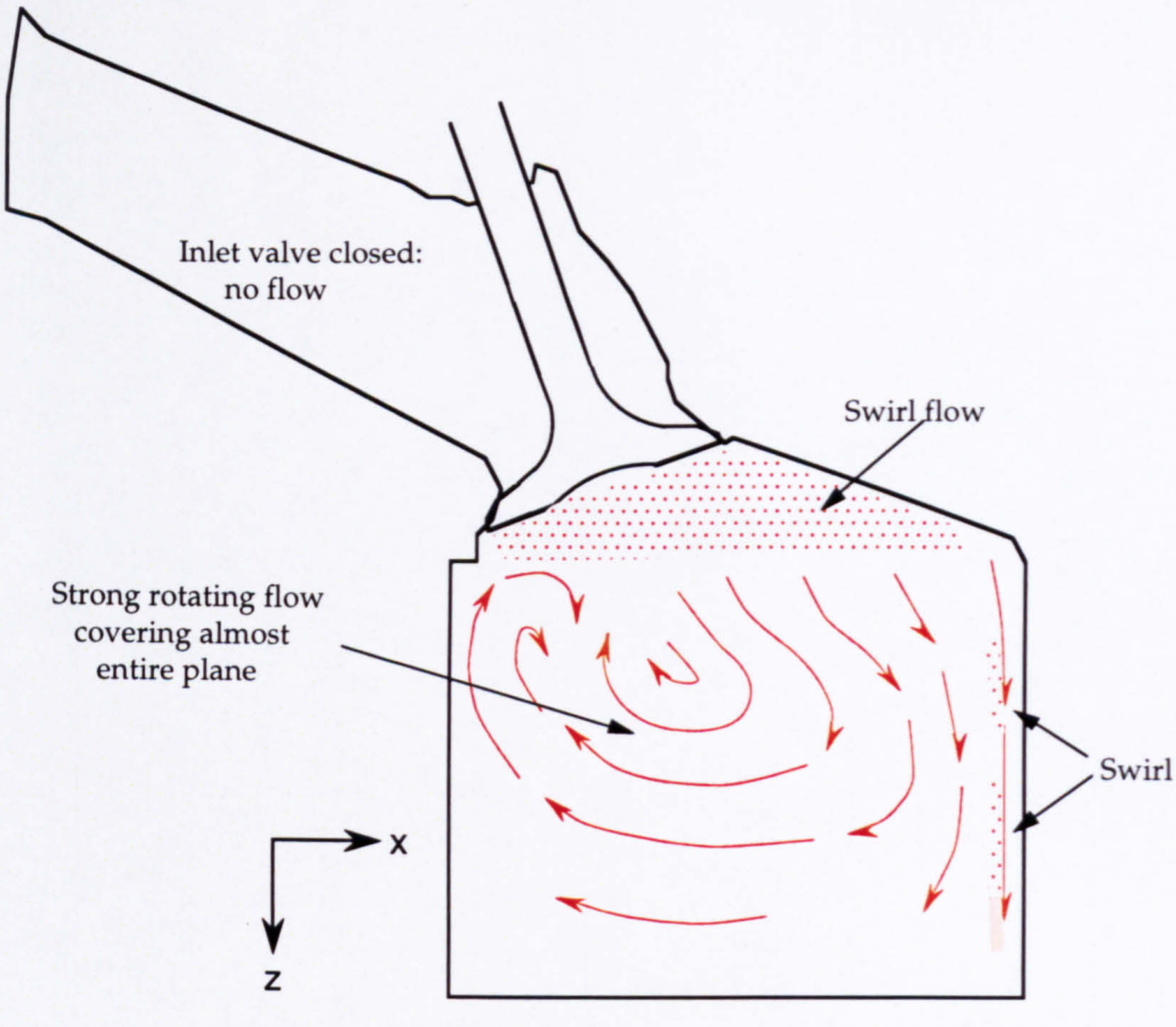

Figure 4.1(c) Flow structure in the y = 17.6 mm vertical plane with 0 mm / 10 mm valve lifts

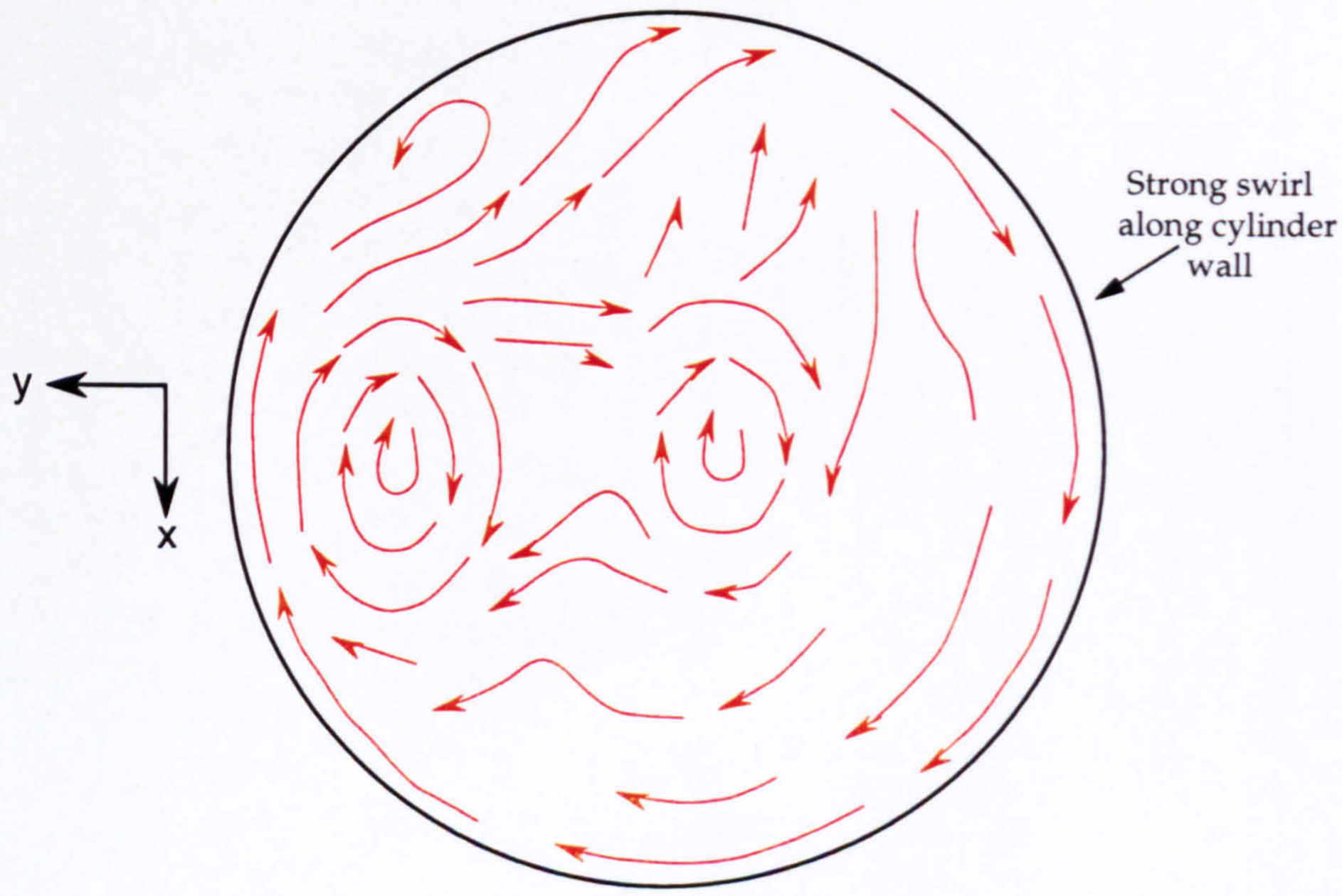

Figure 4.1(d) Flow structure in the z = 10 mm vertical plane with 0 mm / 10 mm valve lifts

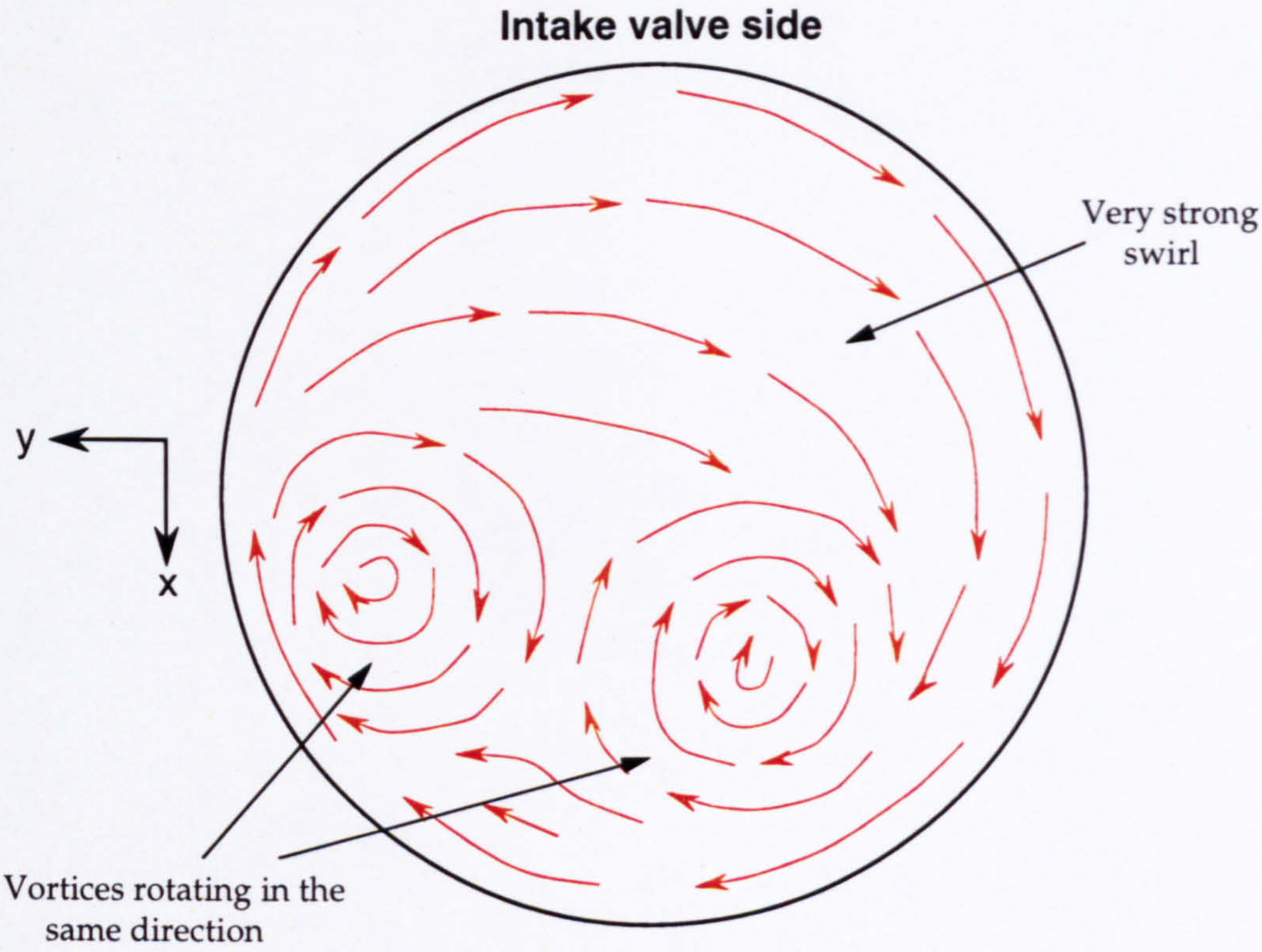

Figure 4.1(e) Flow structure in the horizontal plane
z = 30 mm with 0 mm / 10 mm valve lifts

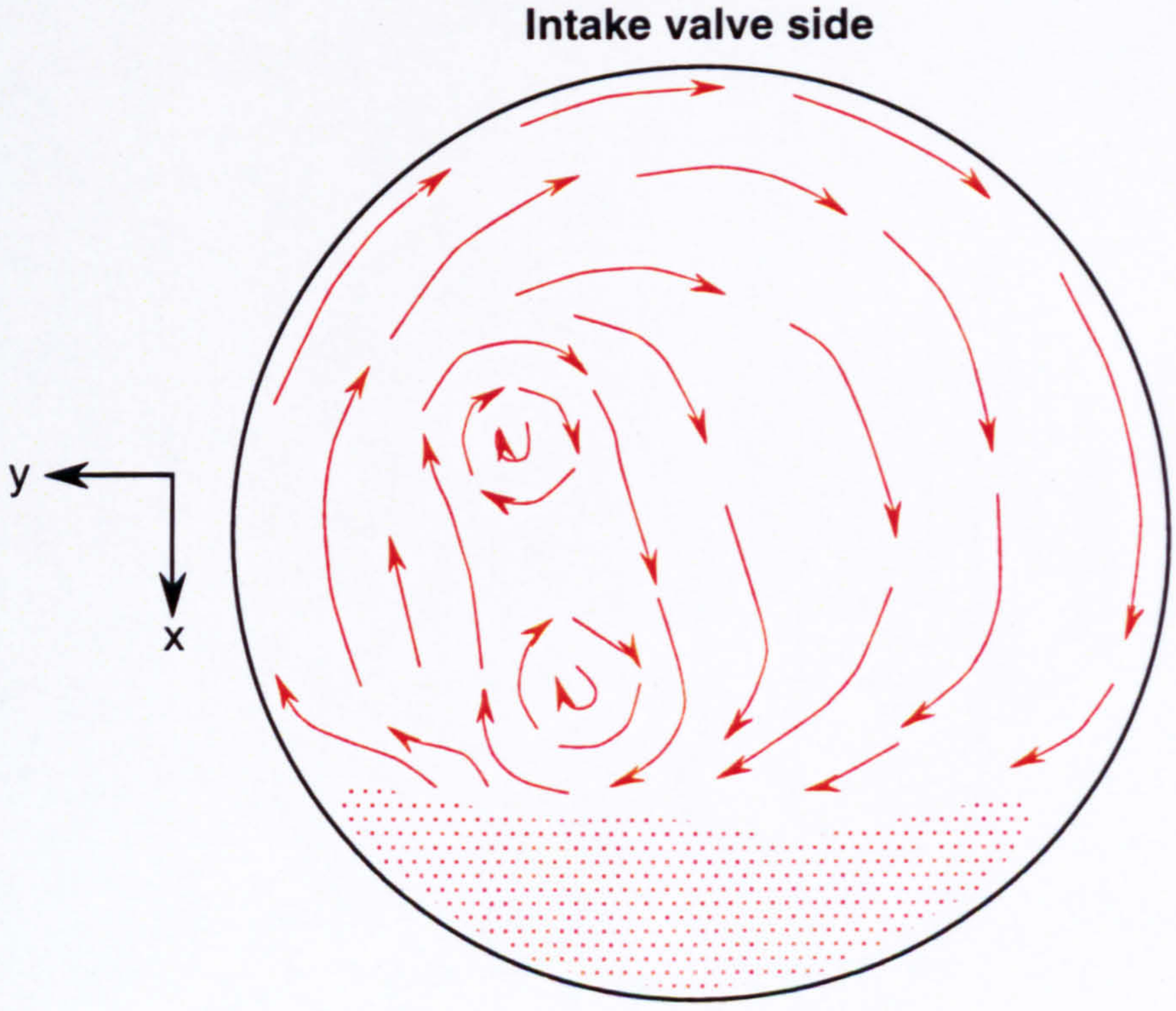

Figure 4.1(f) Flow structure in the horizontal plane
z = 40 mm with 0 mm / 10 mm valve lifts

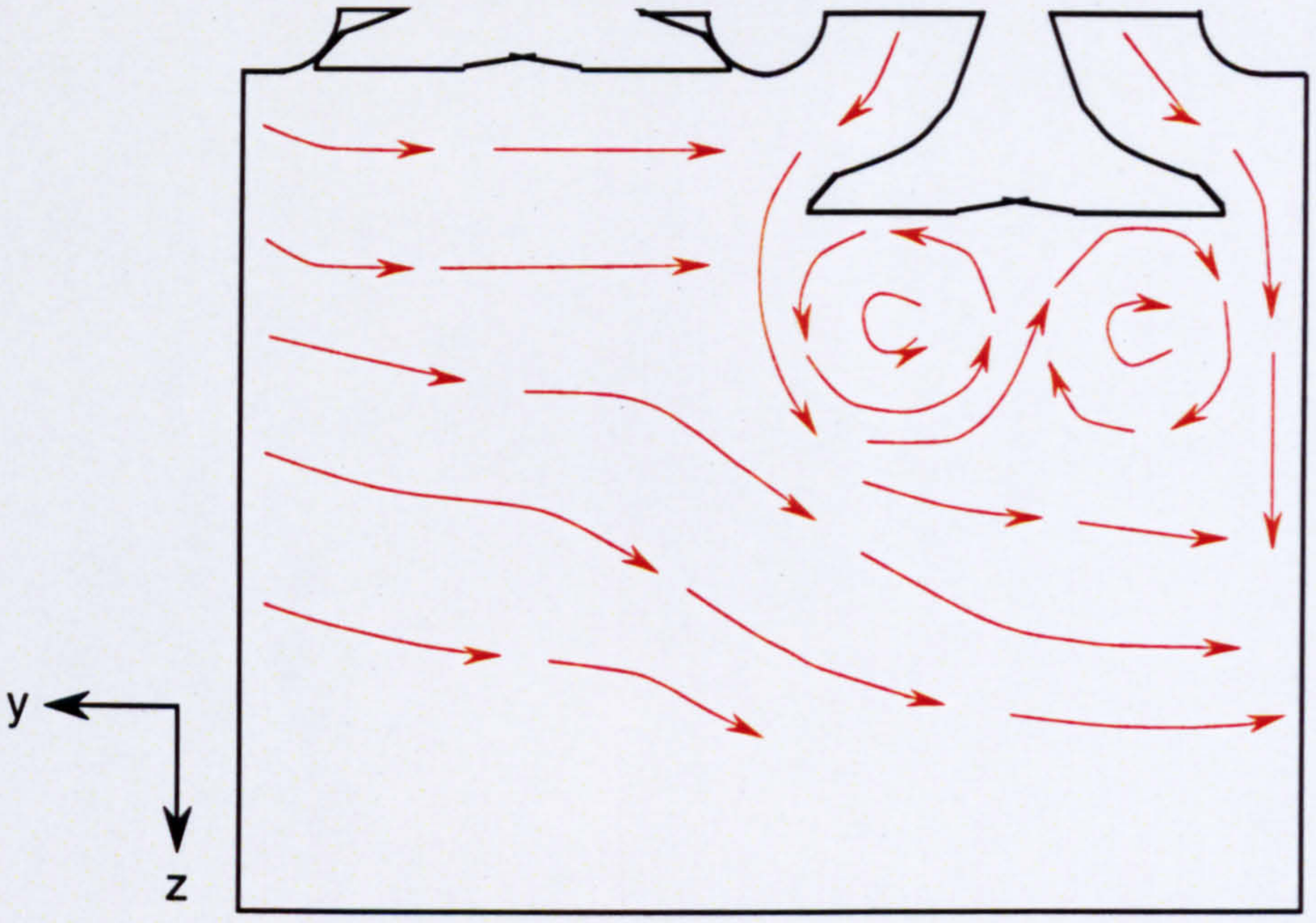

Fig 4.1(g) Flow structure in the x = -16.5 mm vertical plane with 0 mm / 10 mm valve lifts

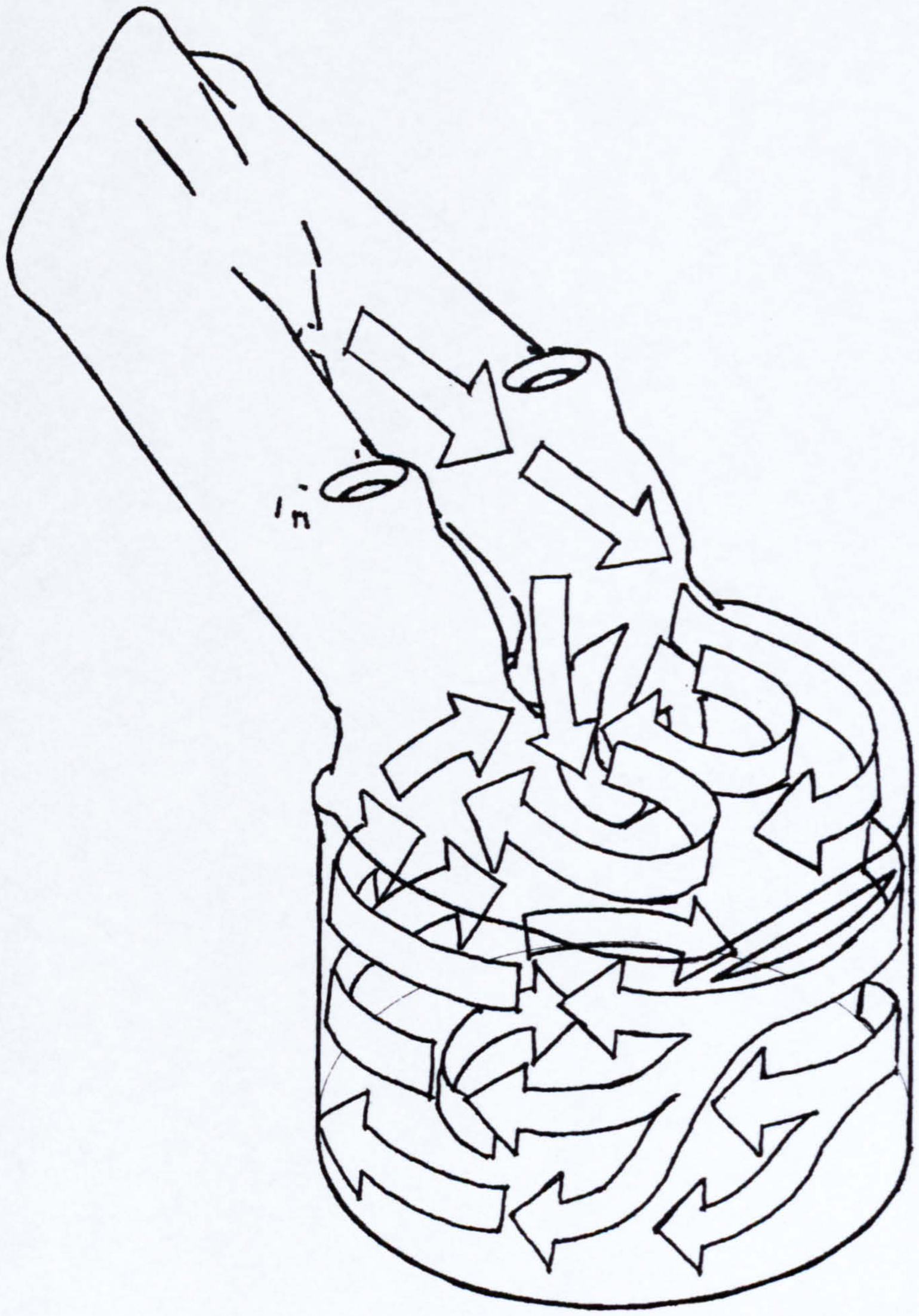

Figure 4.1(h) Three-dimensional in-cylinder flow pattern with 0 mm / 10 mm valve lifts

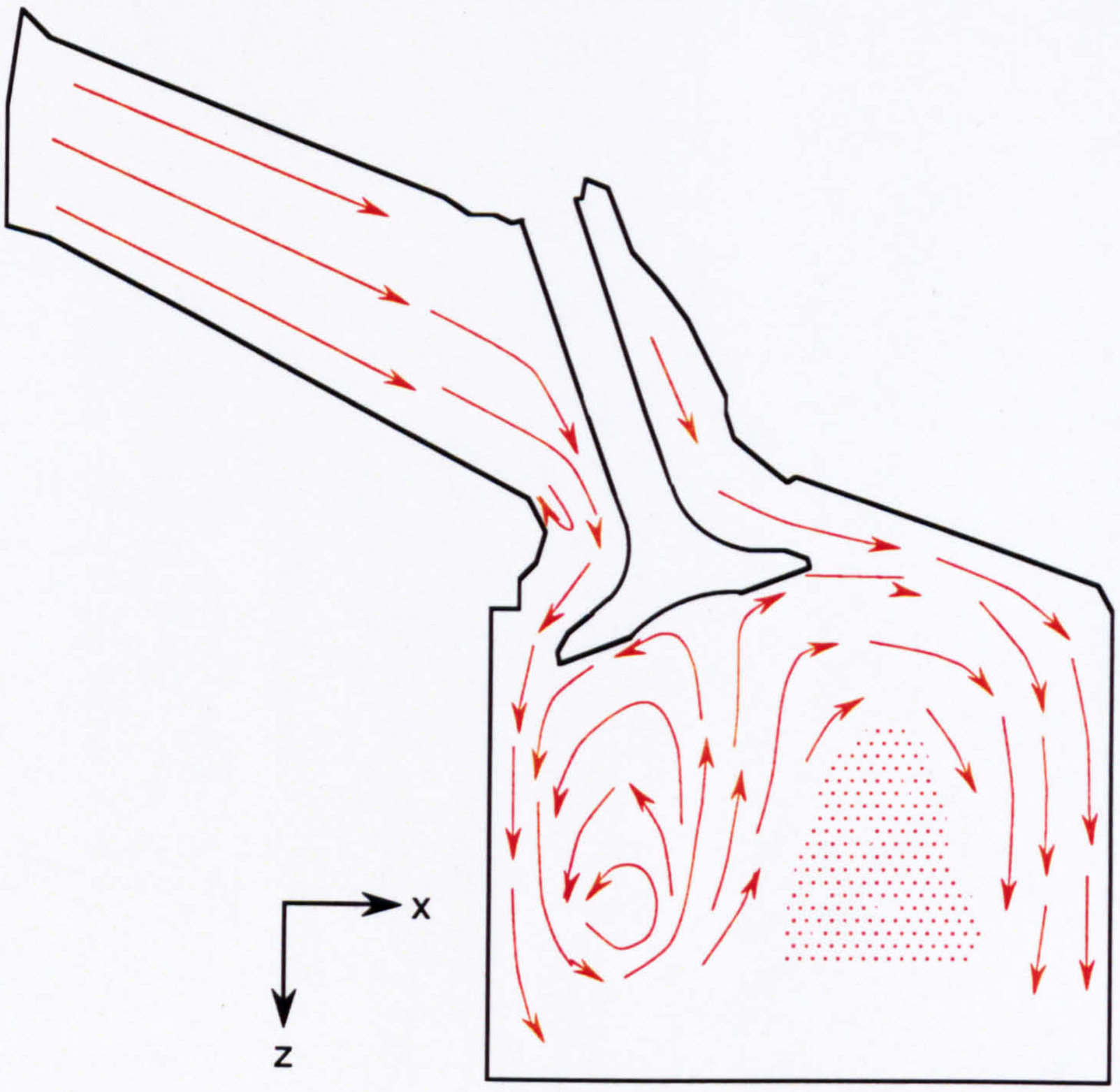

Figure 4.2(a) Flow structure in the y = -17.6 mm vertical plane with 2.5 mm/10 mm valve lifts

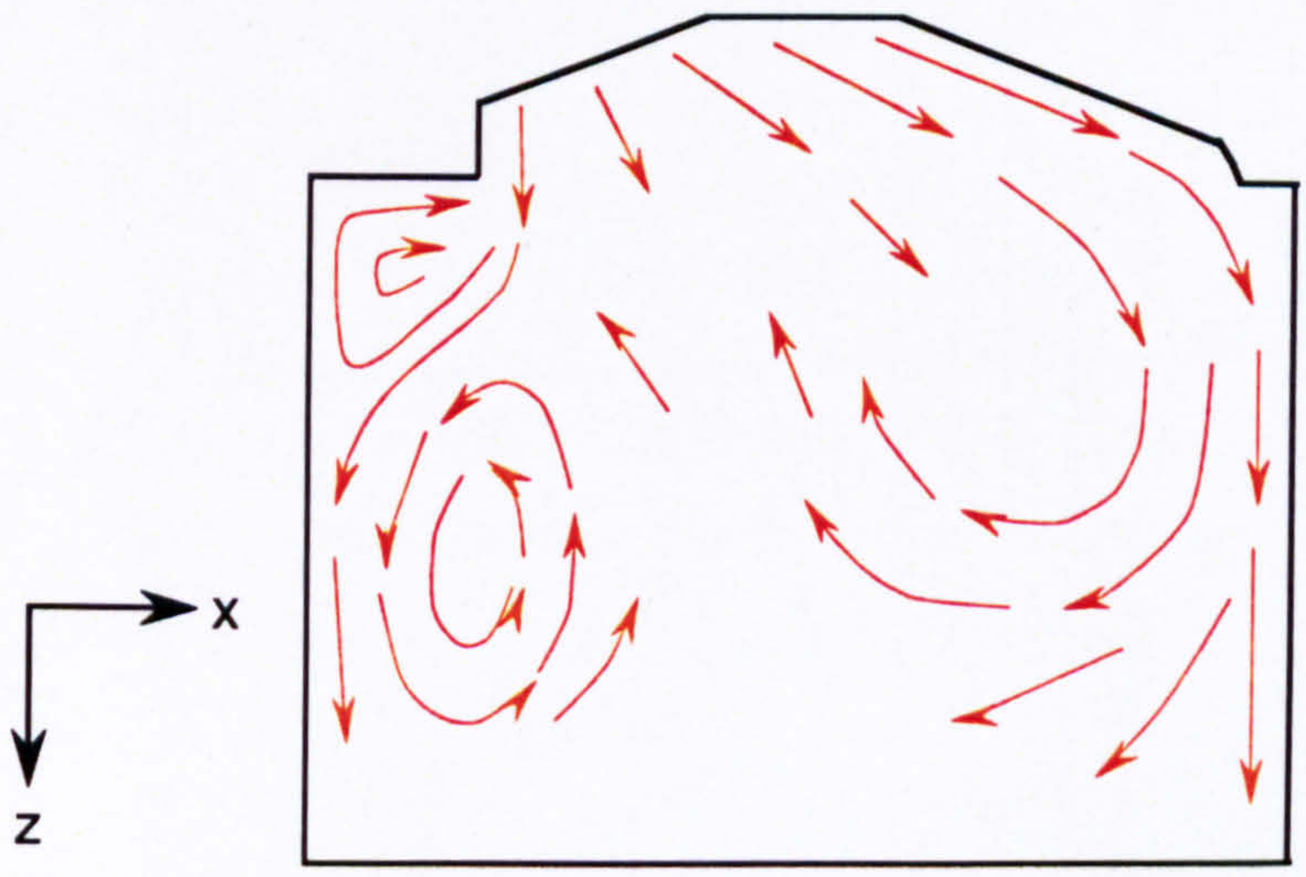

Figure 4.2(b) Flow structure in the y = 0 mm vertical plane with 2.5 mm/10 mm valve lifts

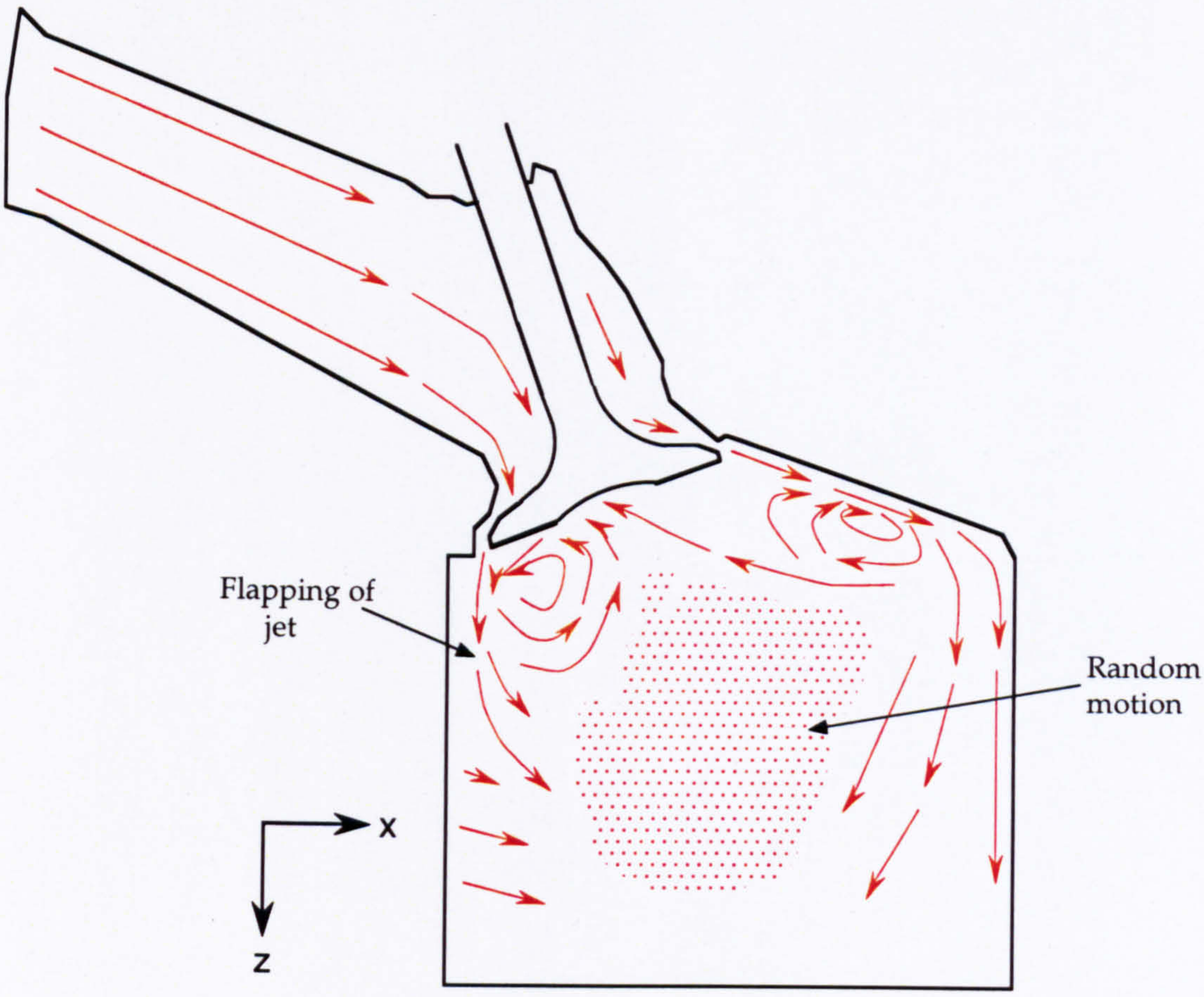

Figure 4.2(c) Flow structure in the y = -17.6 mm vertical plane with 2.5 mm/10 mm valve lifts

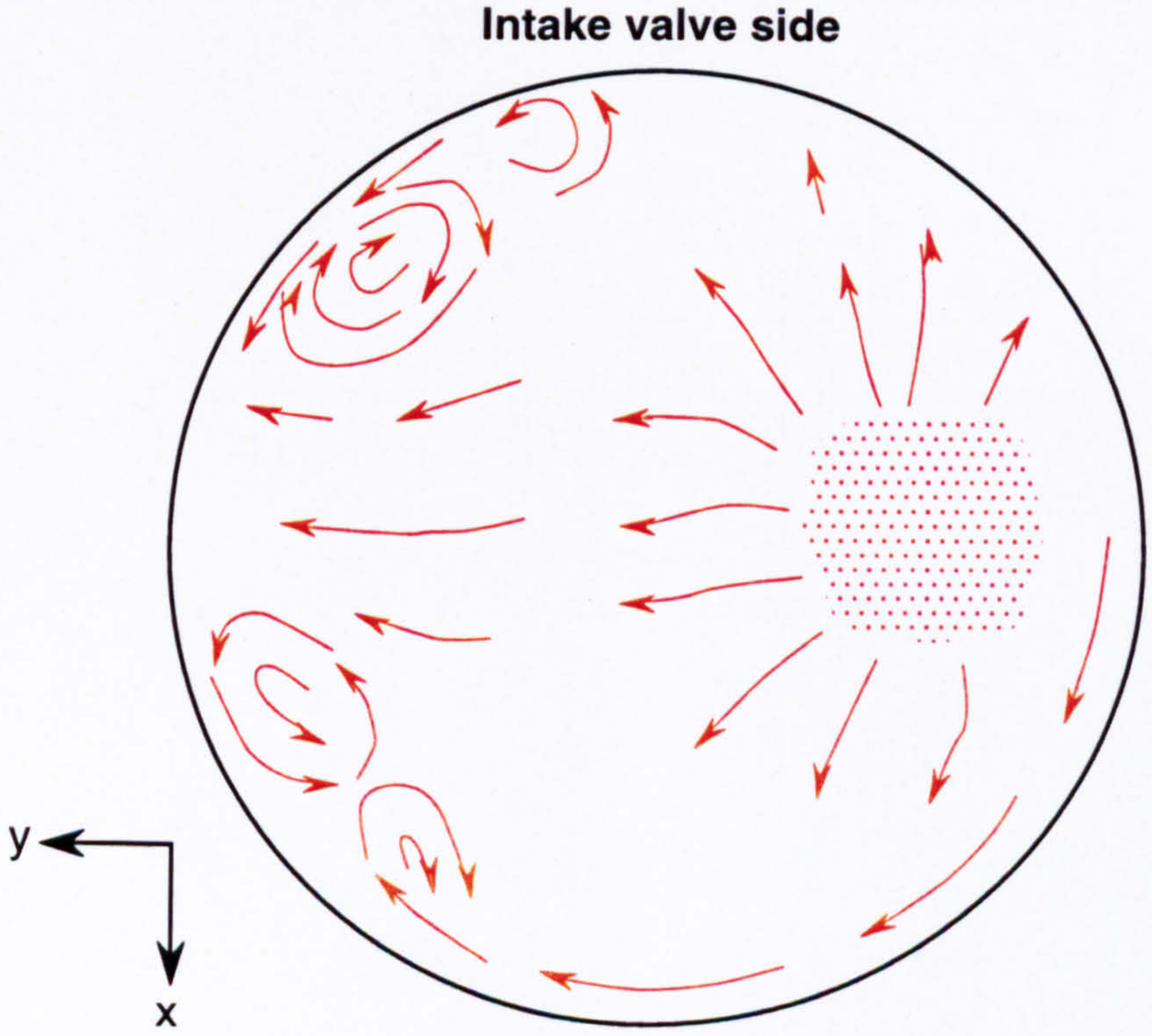

Figure 4.2(d) Flow structure in the horizontal z = 10 mm plane with 2.5 mm/10 mm valve lifts

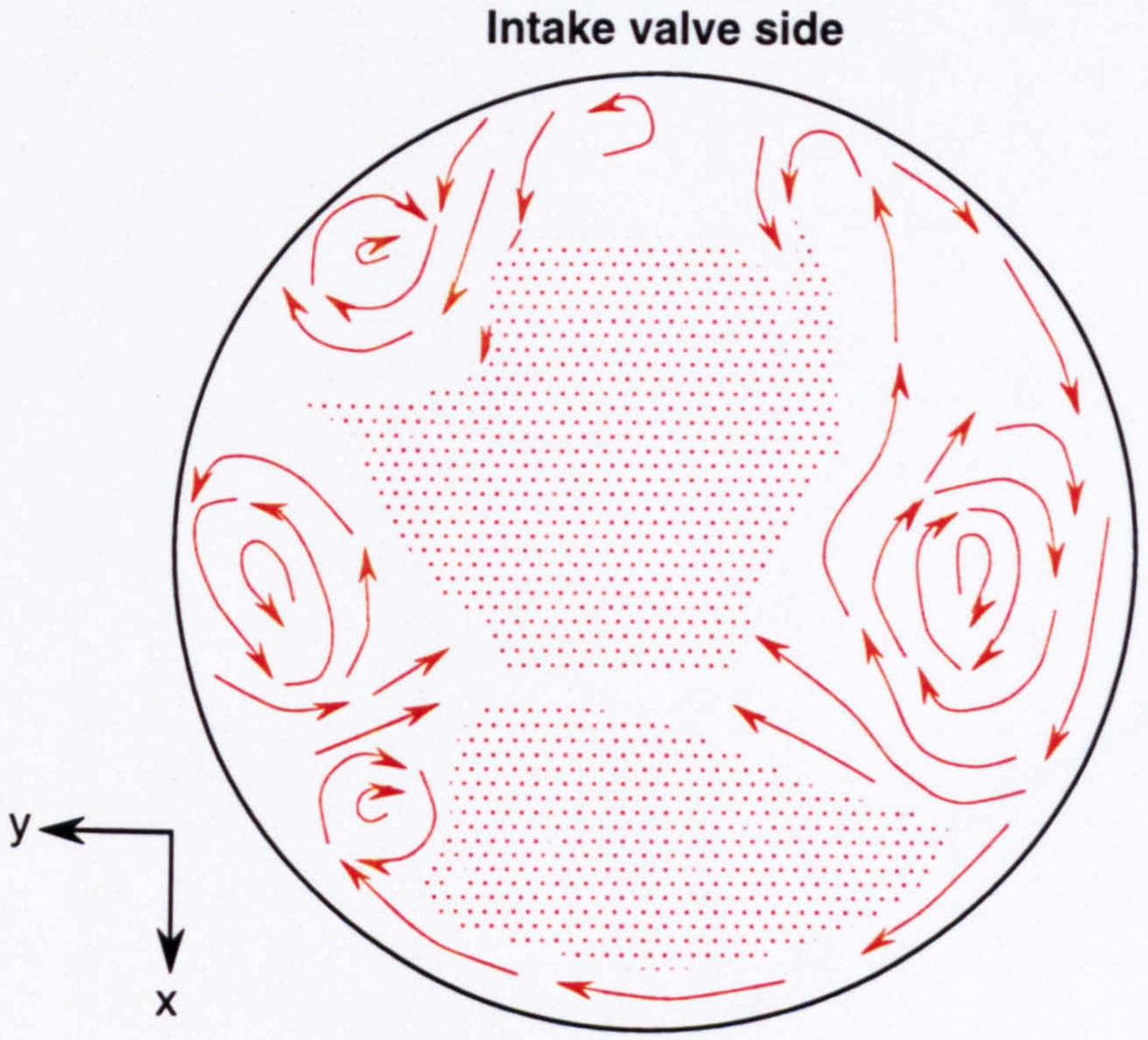

Figure 4.2(e) Flow structure in the horizontal z = 30 mm plane with 2.5 mm/10 mm valve lifts

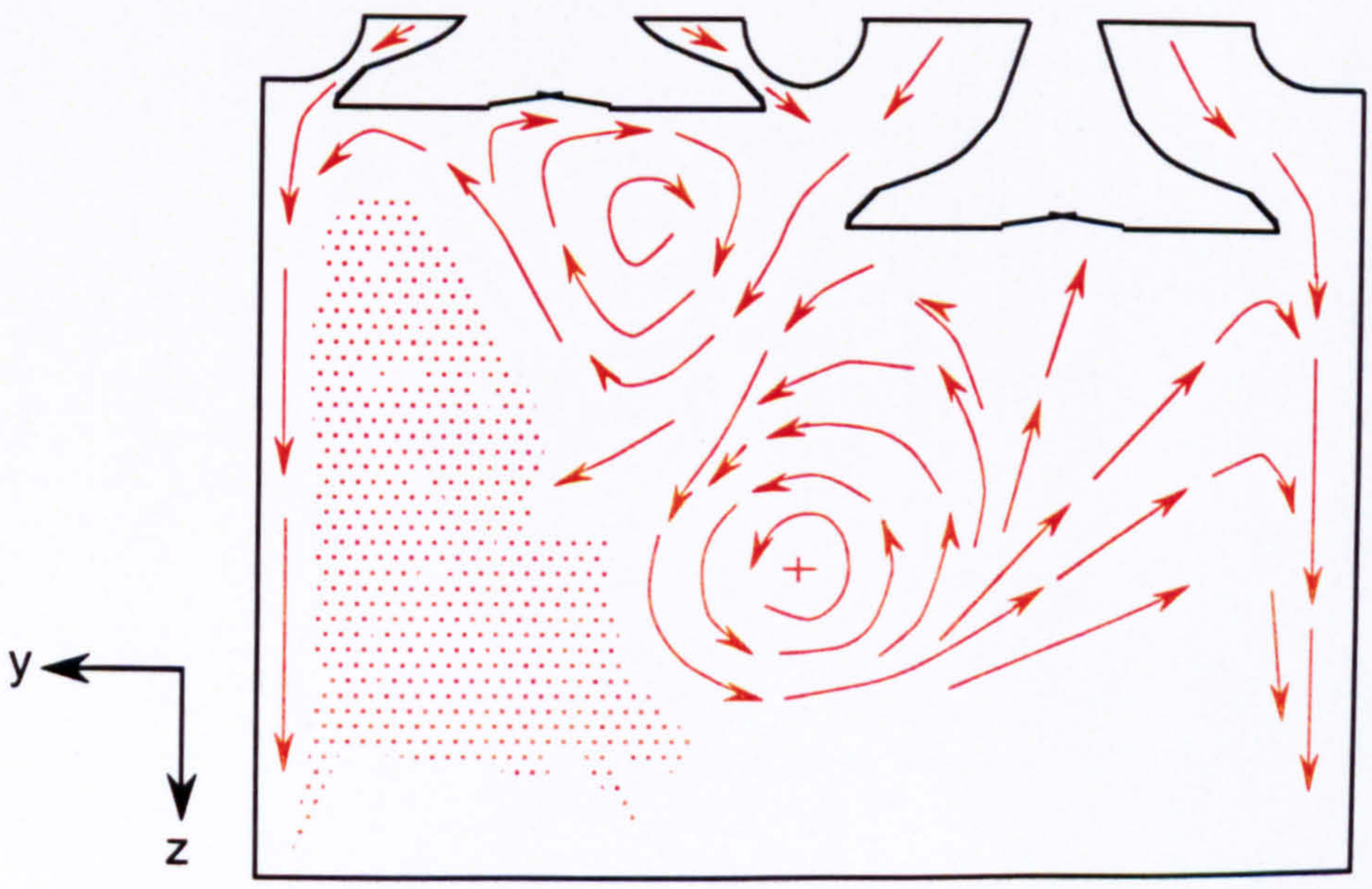

Figure 4.2(f) Flow structure in the vertical plane x = -16.5 mm with 2.5 mm/10 mm valve lifts

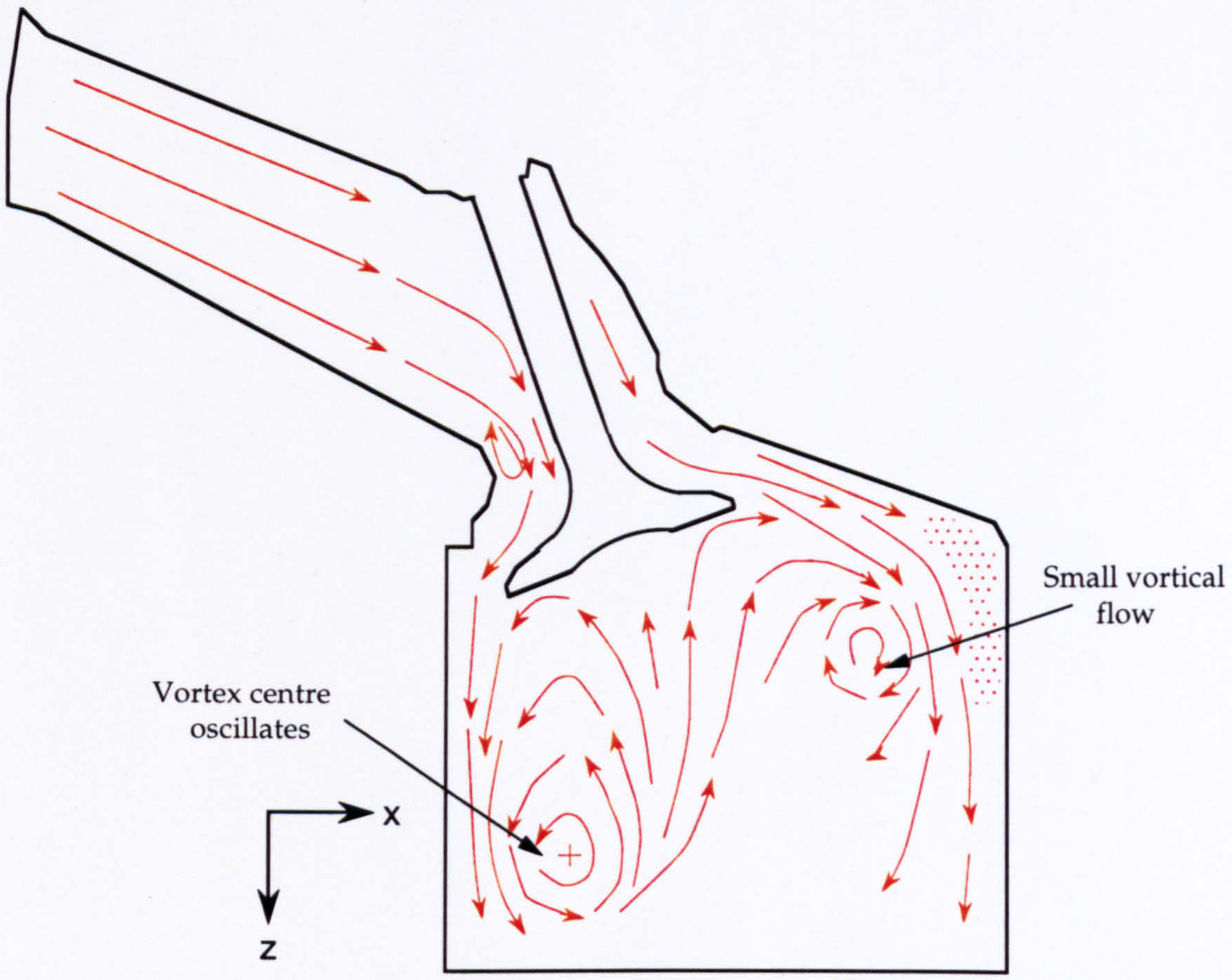

Figure 4.3(a) Flow structure in the vertical plane y = -17.6 mm with 5 mm/10 mm valve lifts

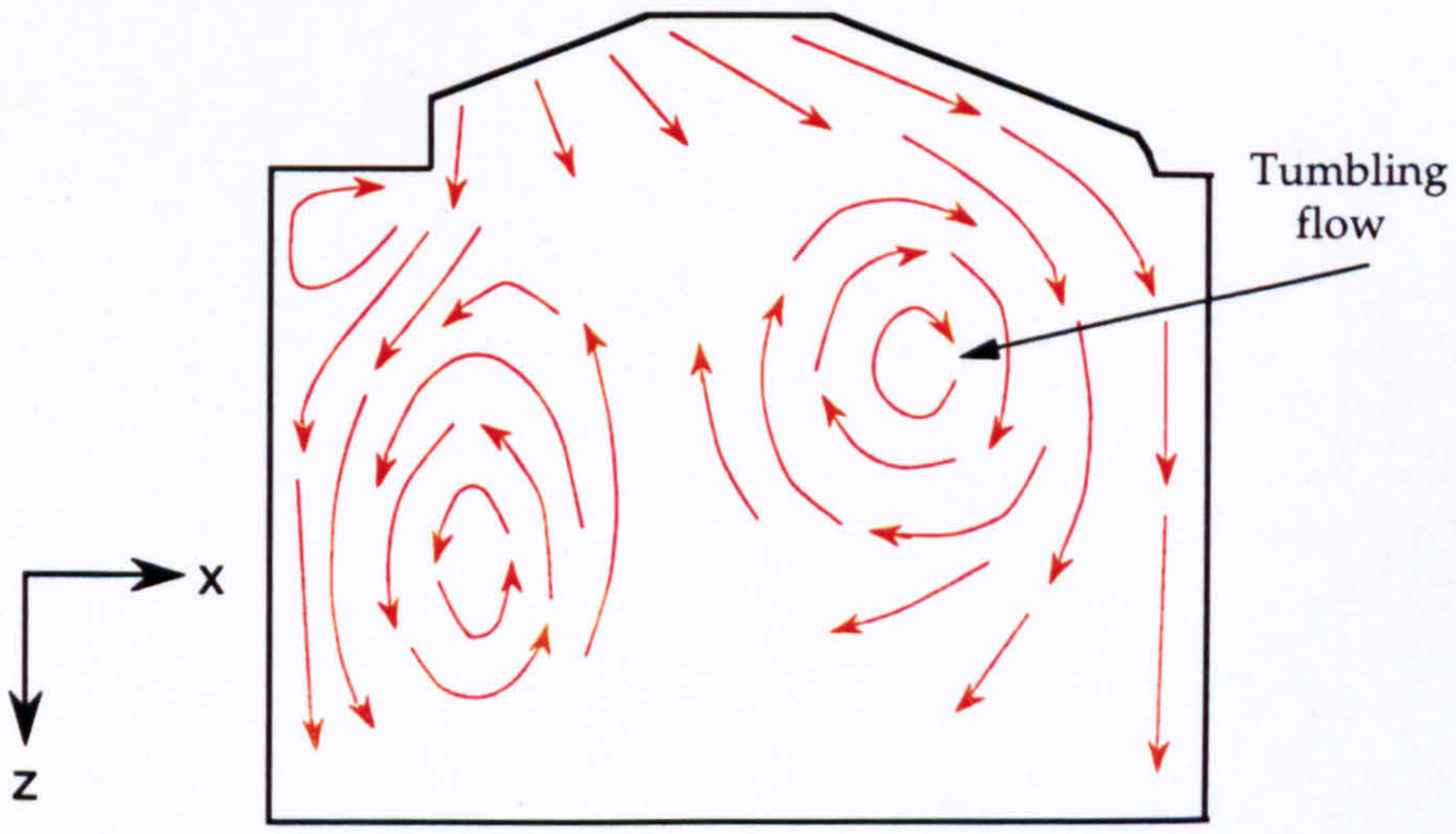

Figure 4.3(b) Flow structure in the vertical plane y = 0 mm with 5 mm/10 mm valve lifts

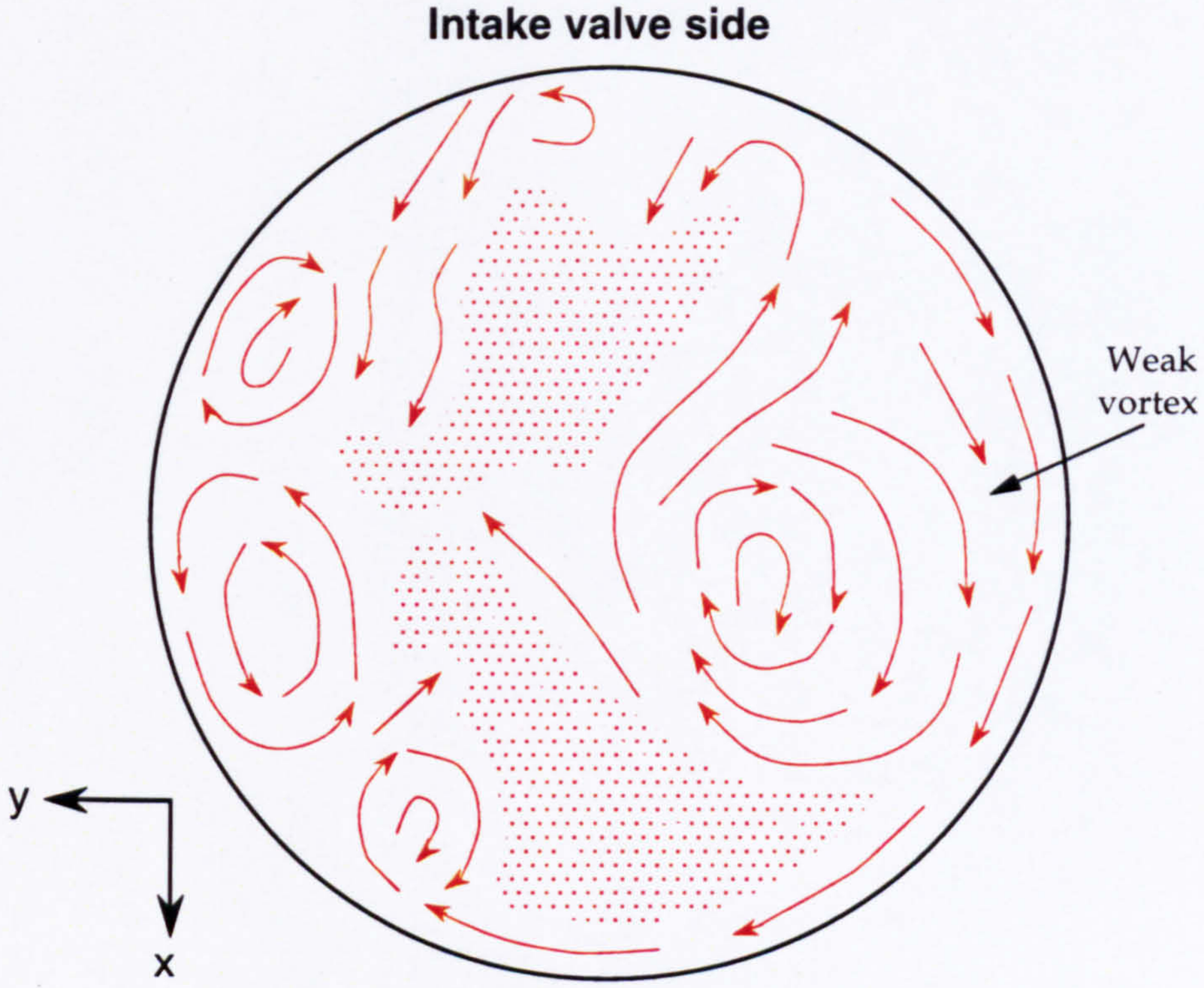

Figure 4.3(c) Flow structure in the horizontal plane z = 30 mm with 5 mm/10 mm valve lifts

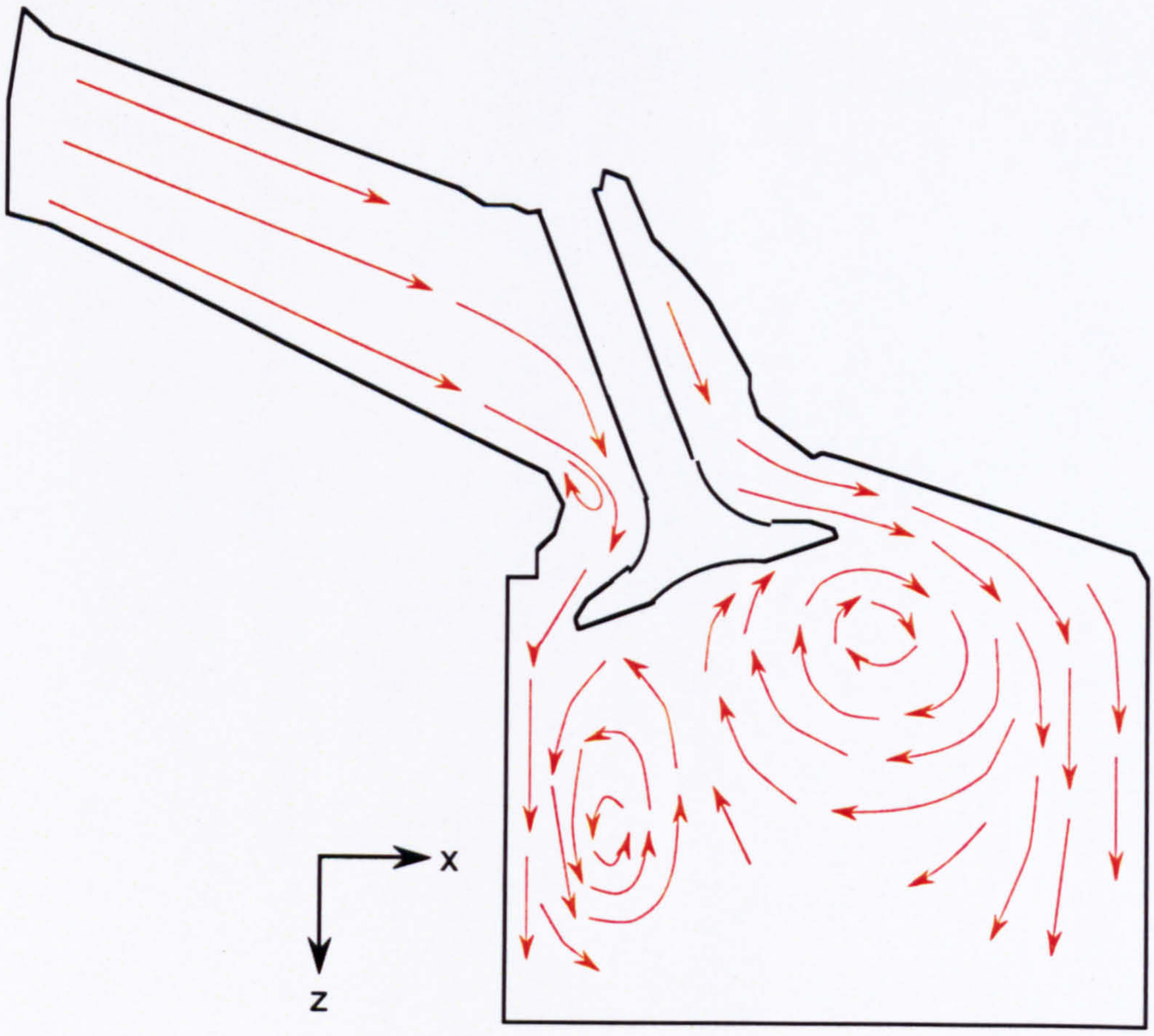

Figure 4.4(a) Flow structure in the vertical plane y = -17.6 mm with 7.5 mm/10 mm valve lifts

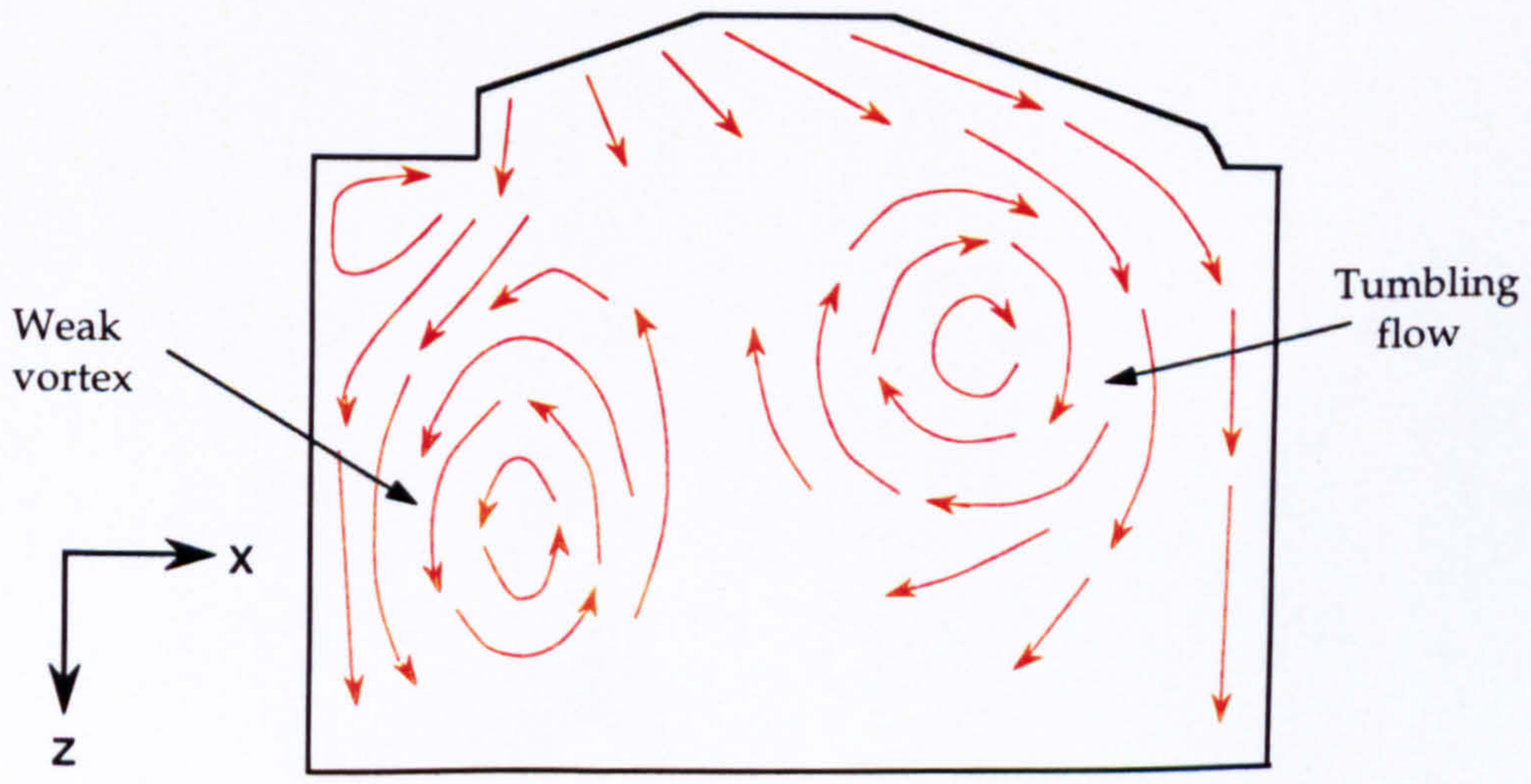

Figure 4.4(b) Flow structure in the vertical plane y = 0 mm with 7.5 mm/10 mm valve lifts

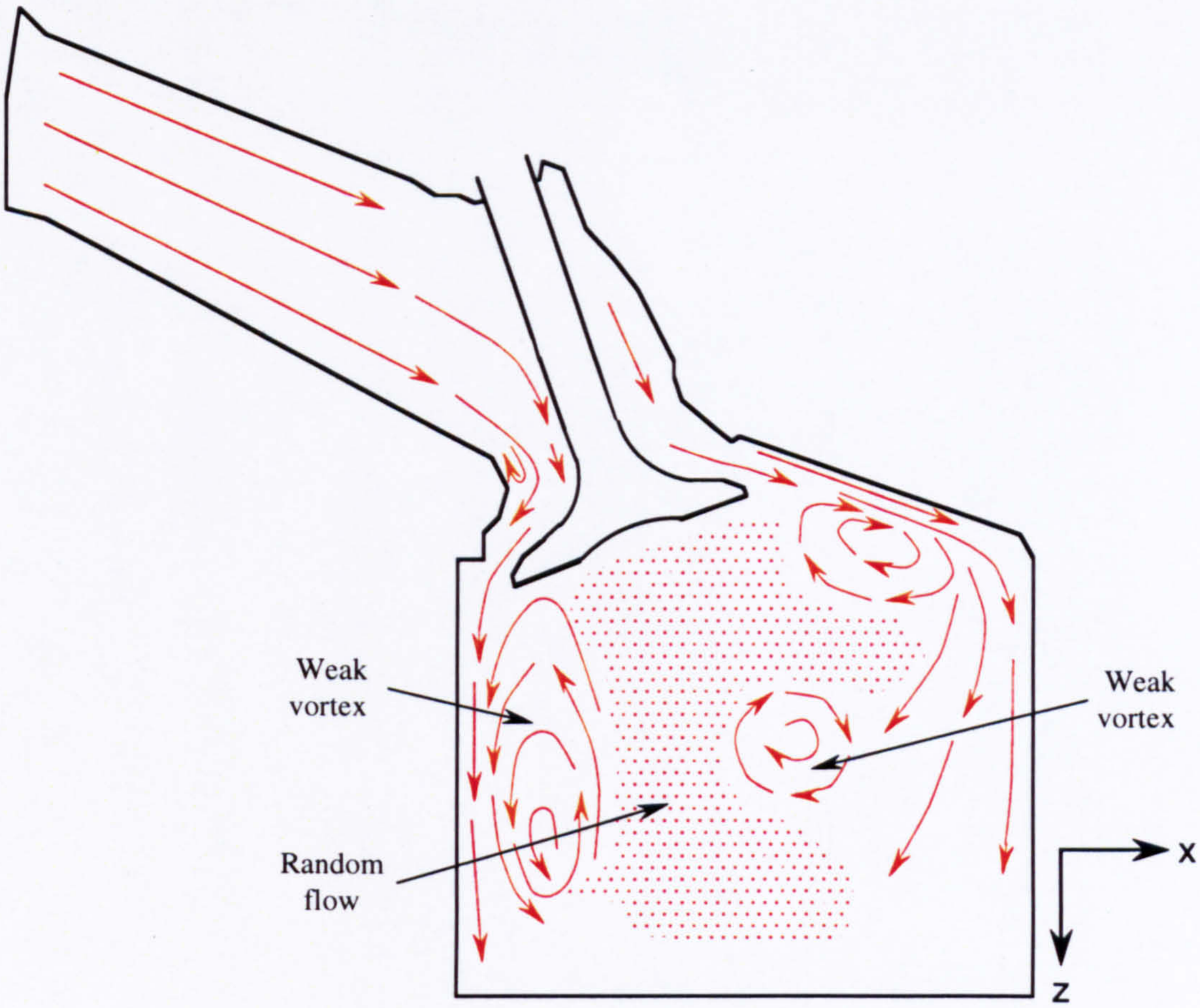

Figure 4.4(c) Flow structure in the vertical plane y = 17.6 mm with 7.5 mm/10 mm valve lifts

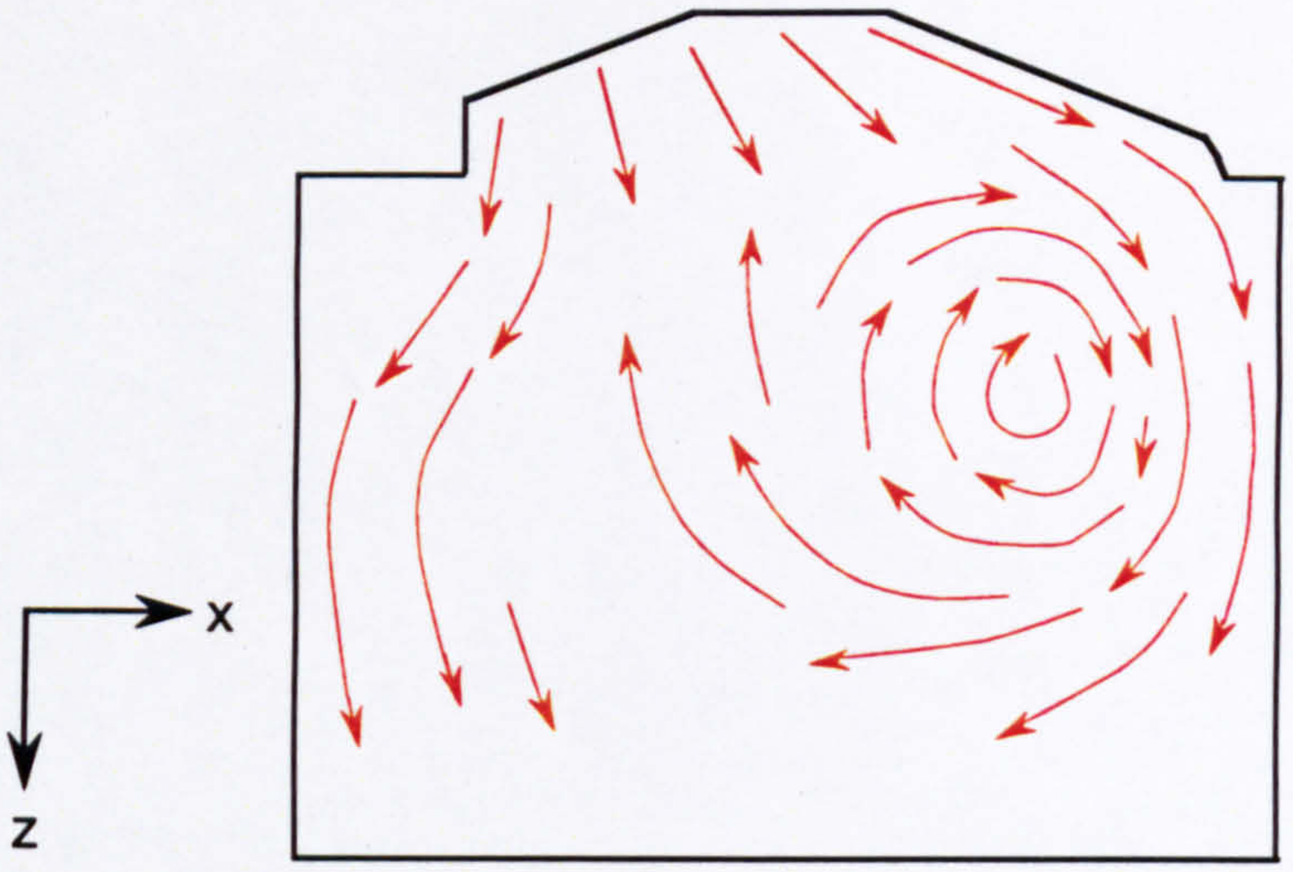

Figure 4.5(a) Flow structure in the vertical plane y = 0 mm with 2.5 mm/7.5 mm valve lifts

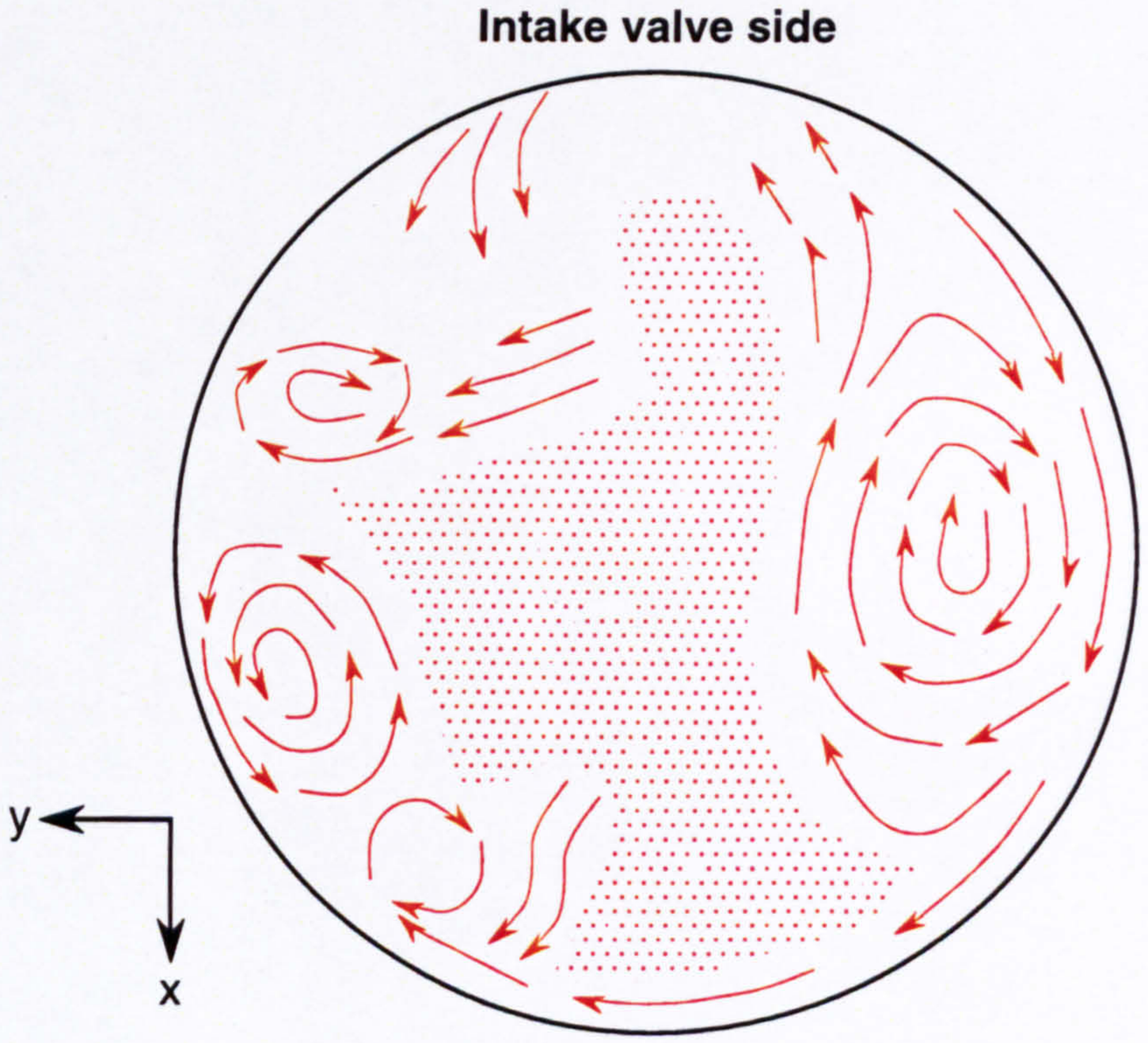

Figure 4.5(b) Flow structure in the horizontal plane z = 10 mm with 2.5 mm/7.5 mm valve lifts

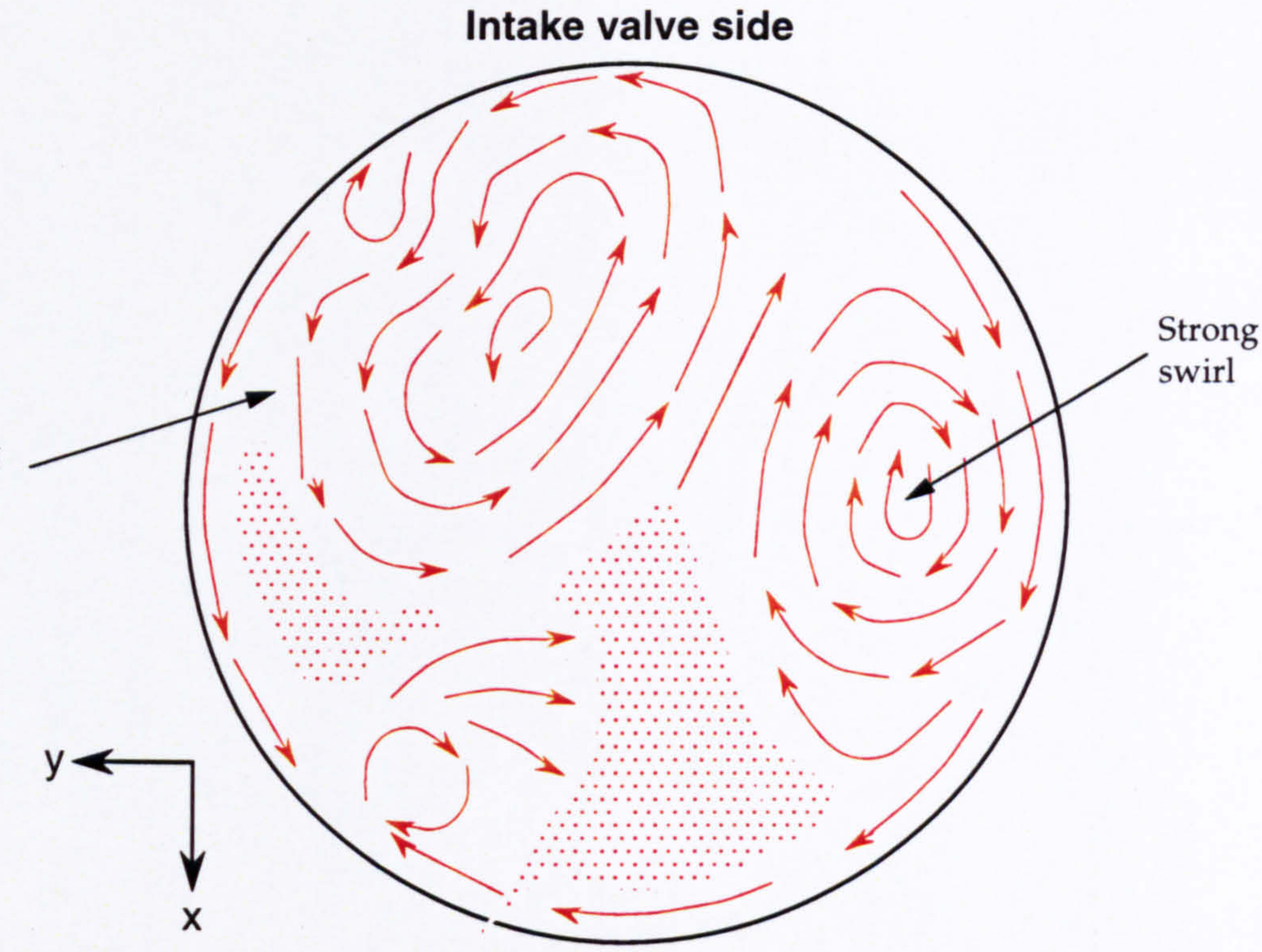

Figure 4.5(c) Flow structure in the horizontal plane z = 30 mm with 2.5 mm/7.5 mm valve lifts

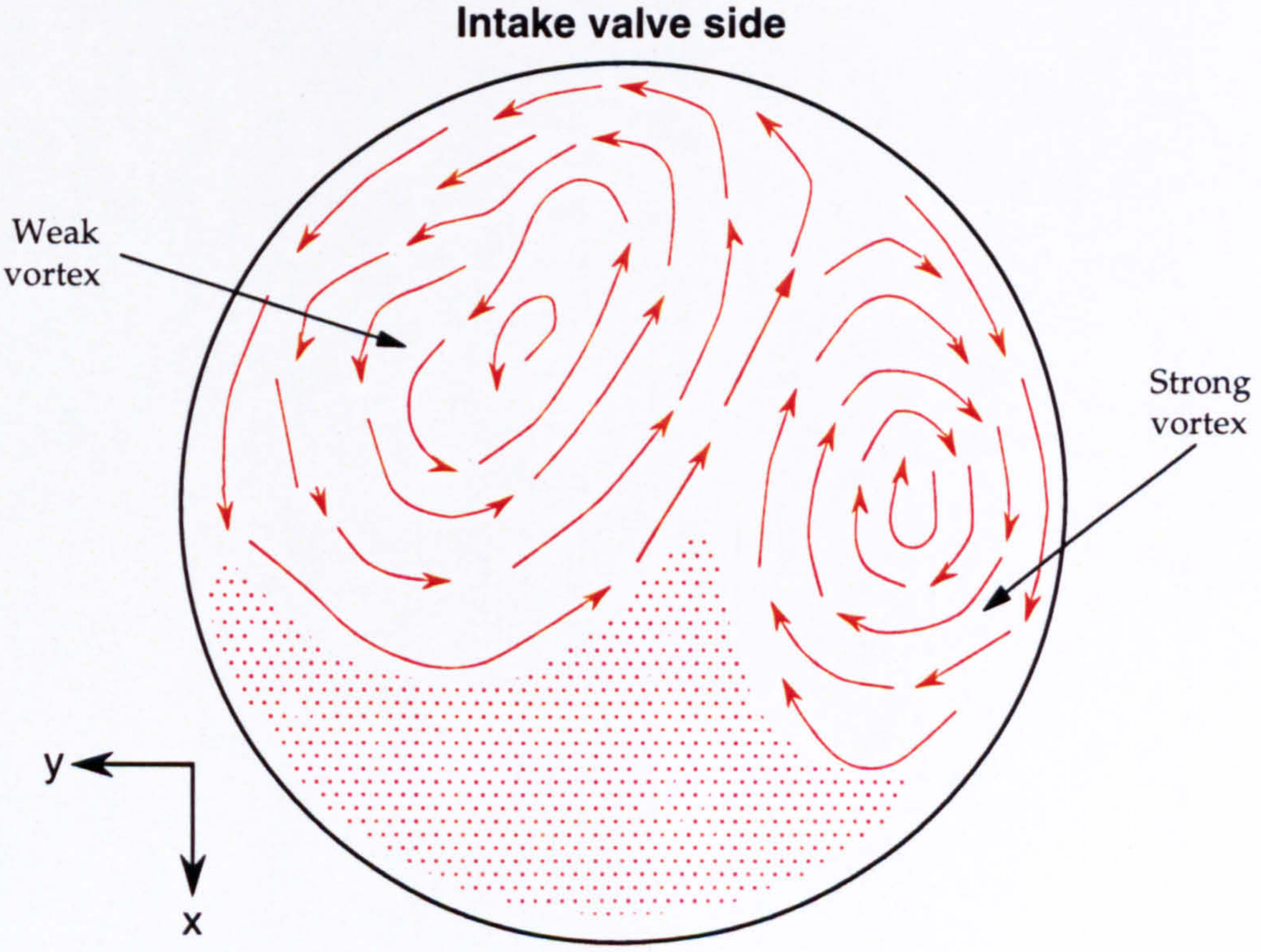

Figure 4.5(d) Flow structure in the horizontal plane z = 40 mm with 2.5 mm/7.5 mm valve lifts

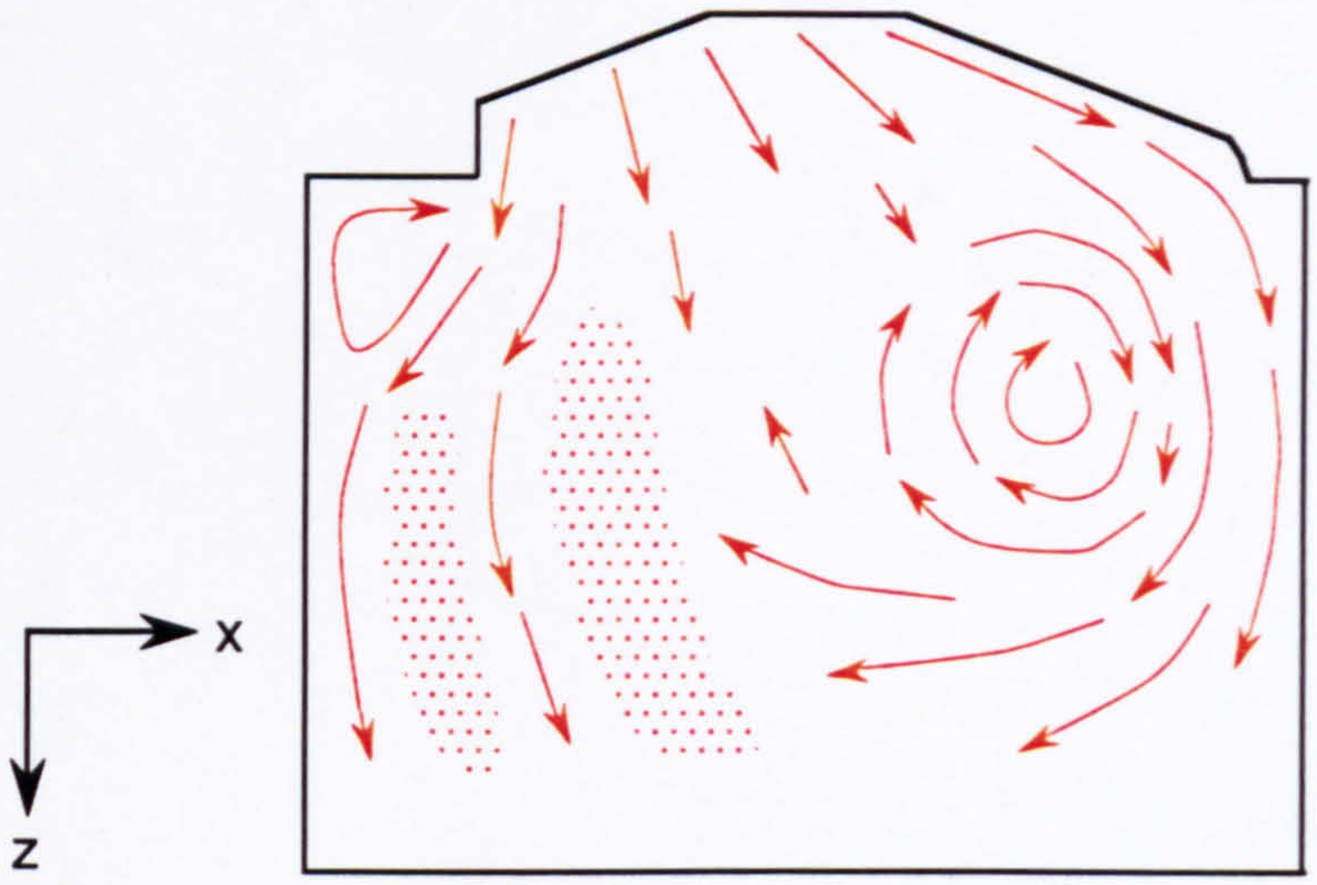

Figure 4.6(a) Flow structure in the vertical plane y = 0 mm with 2.5 mm/5 mm valve lifts

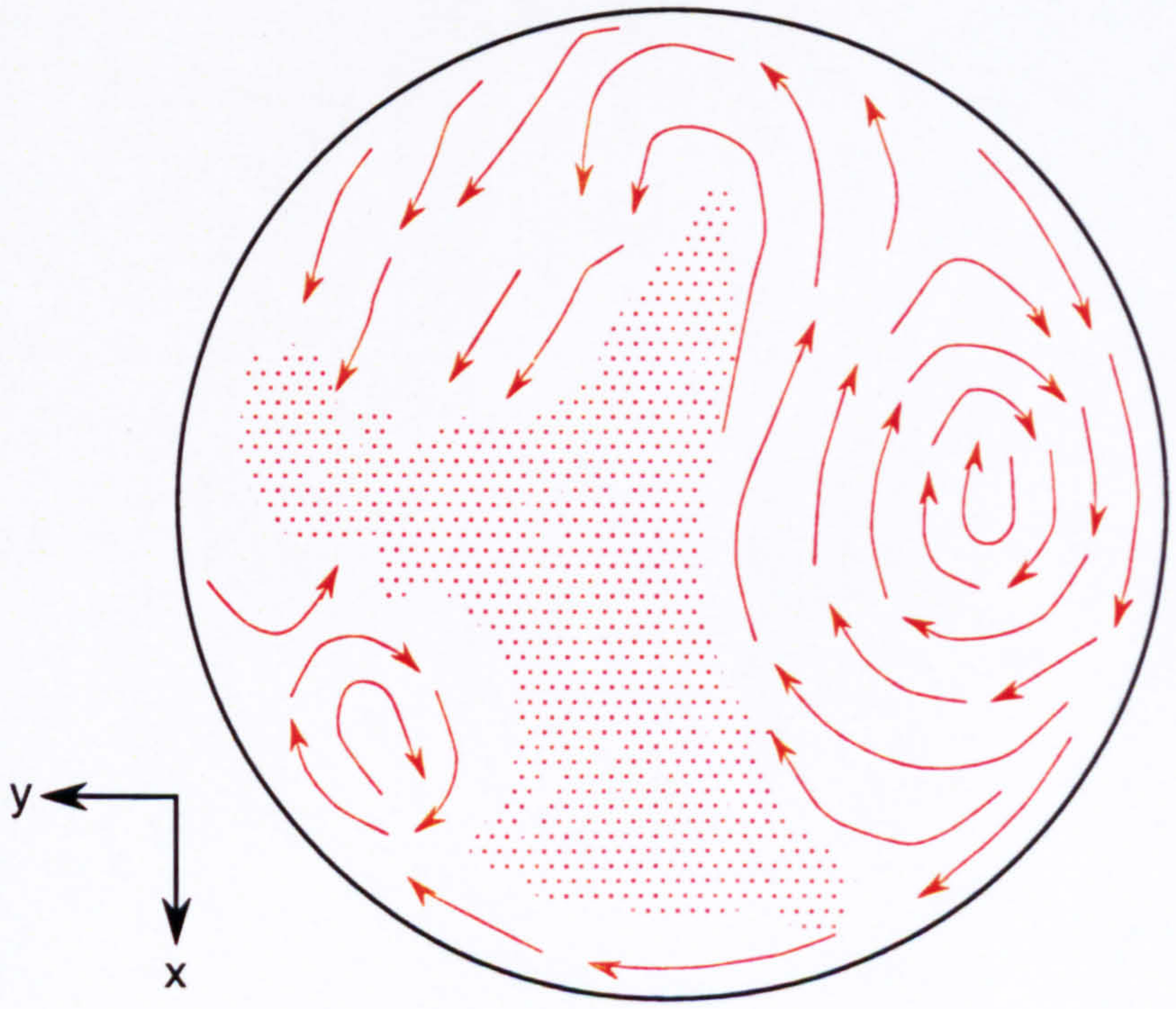

Figure 4.6(b) Flow structure in the horizontal plane z = 10 mm with 2.5 mm/5 mm valve lifts

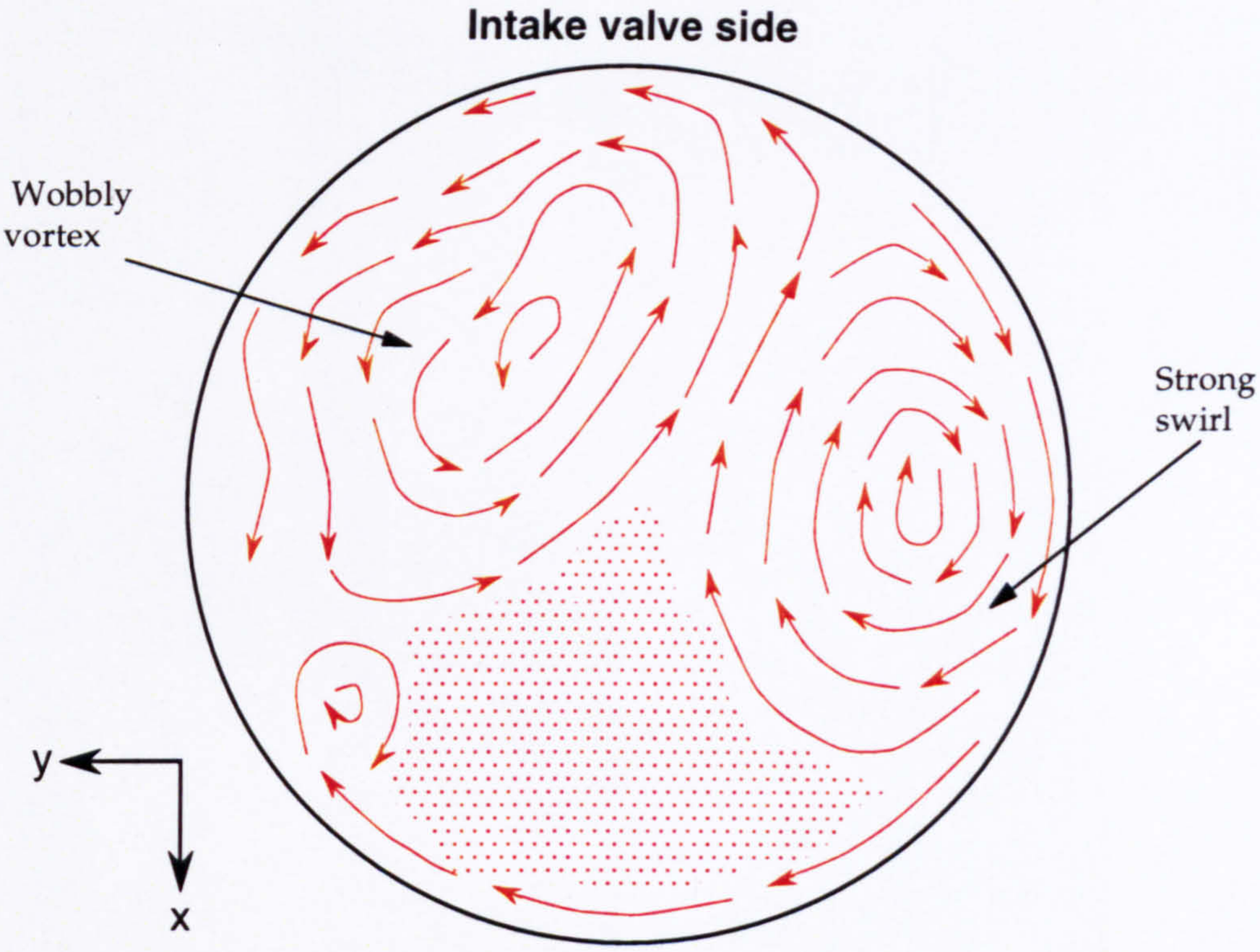

Figure 4.6(c) Flow structure in the horizontal plane z = 30 mm with 2.5 mm/5 mm valve lifts

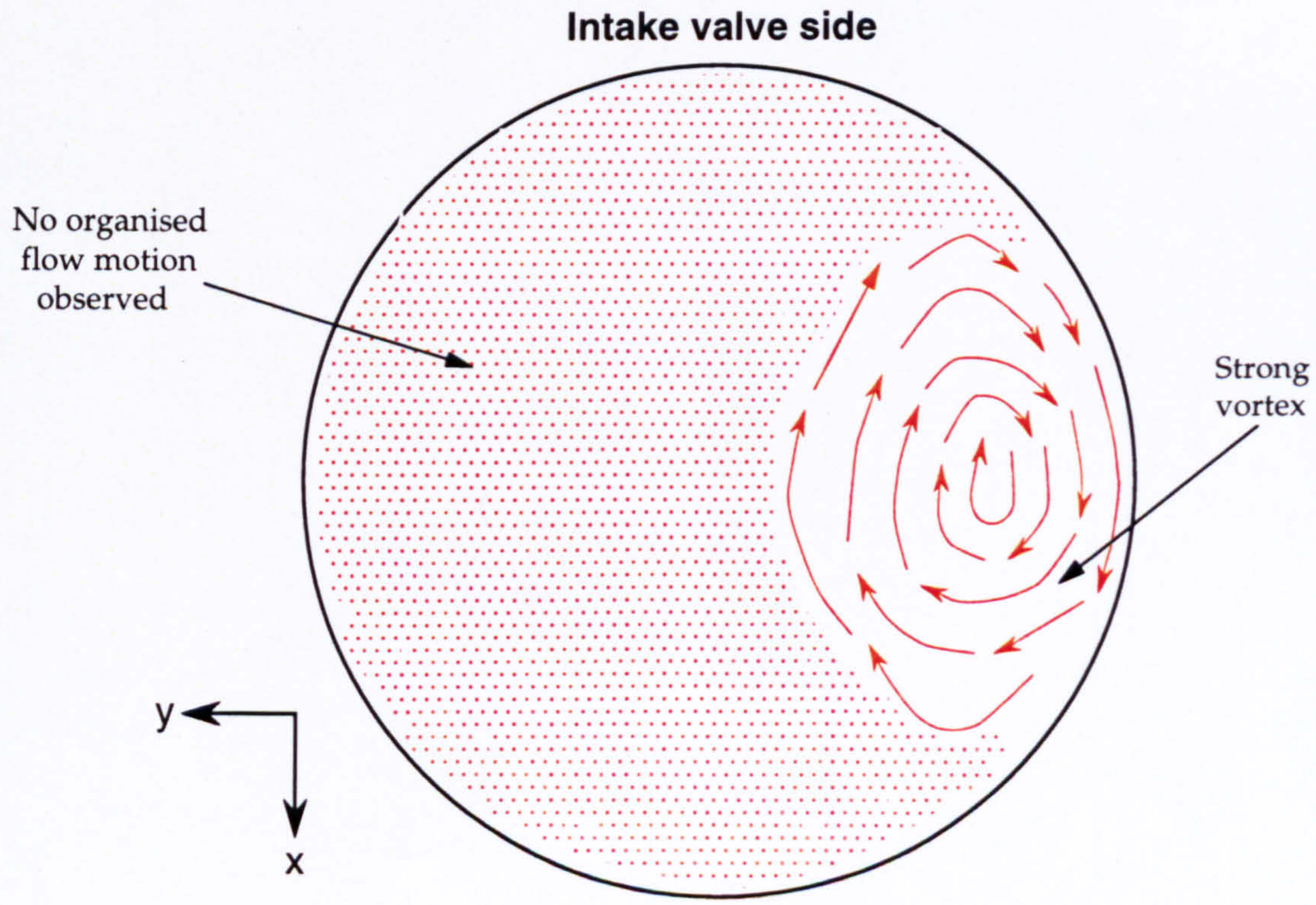

Figure 4.6(d) Flow structure in the horizontal plane z = 40 mm with 2.5 mm/5 mm valve lifts

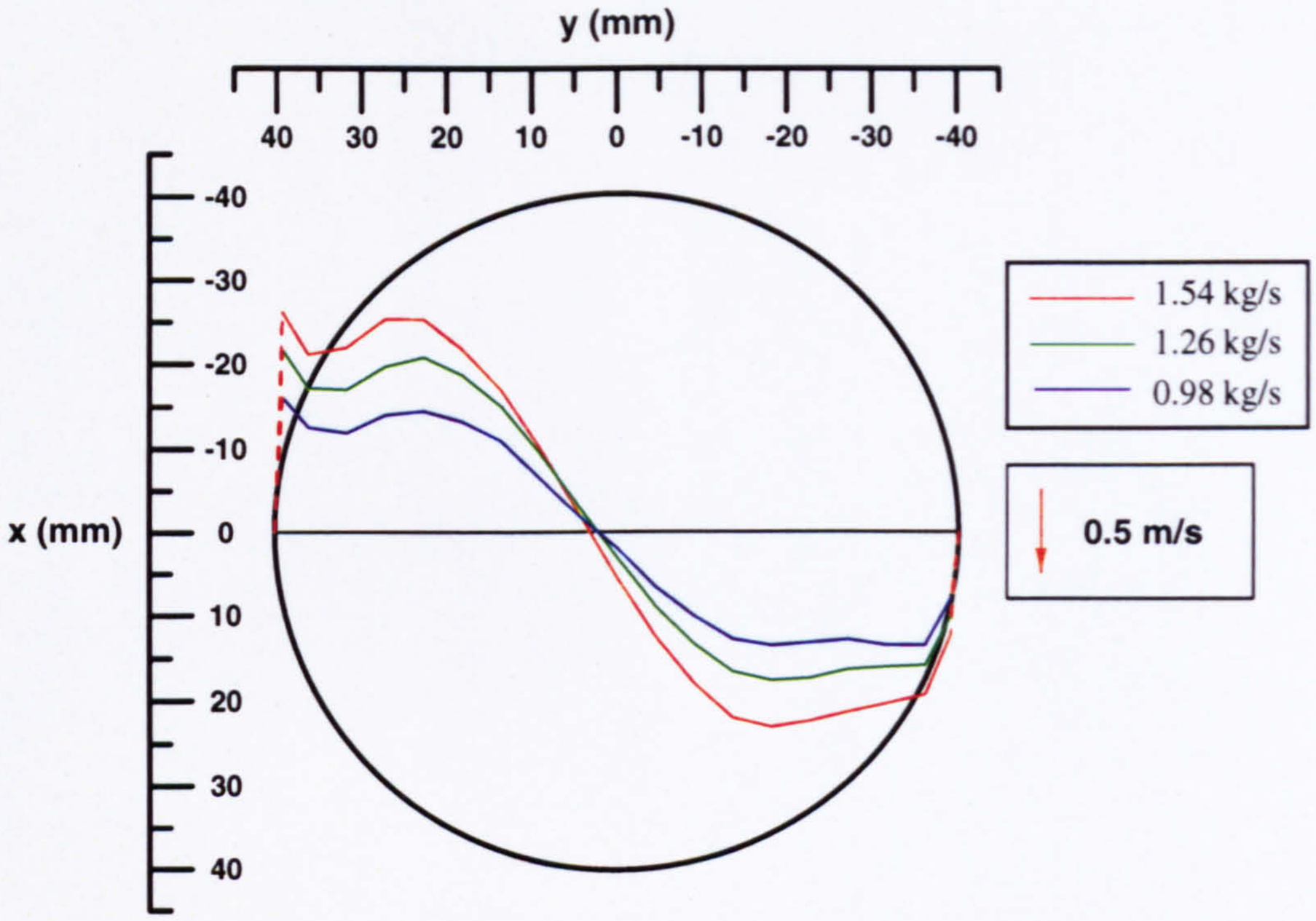

(a) Mean Velocities

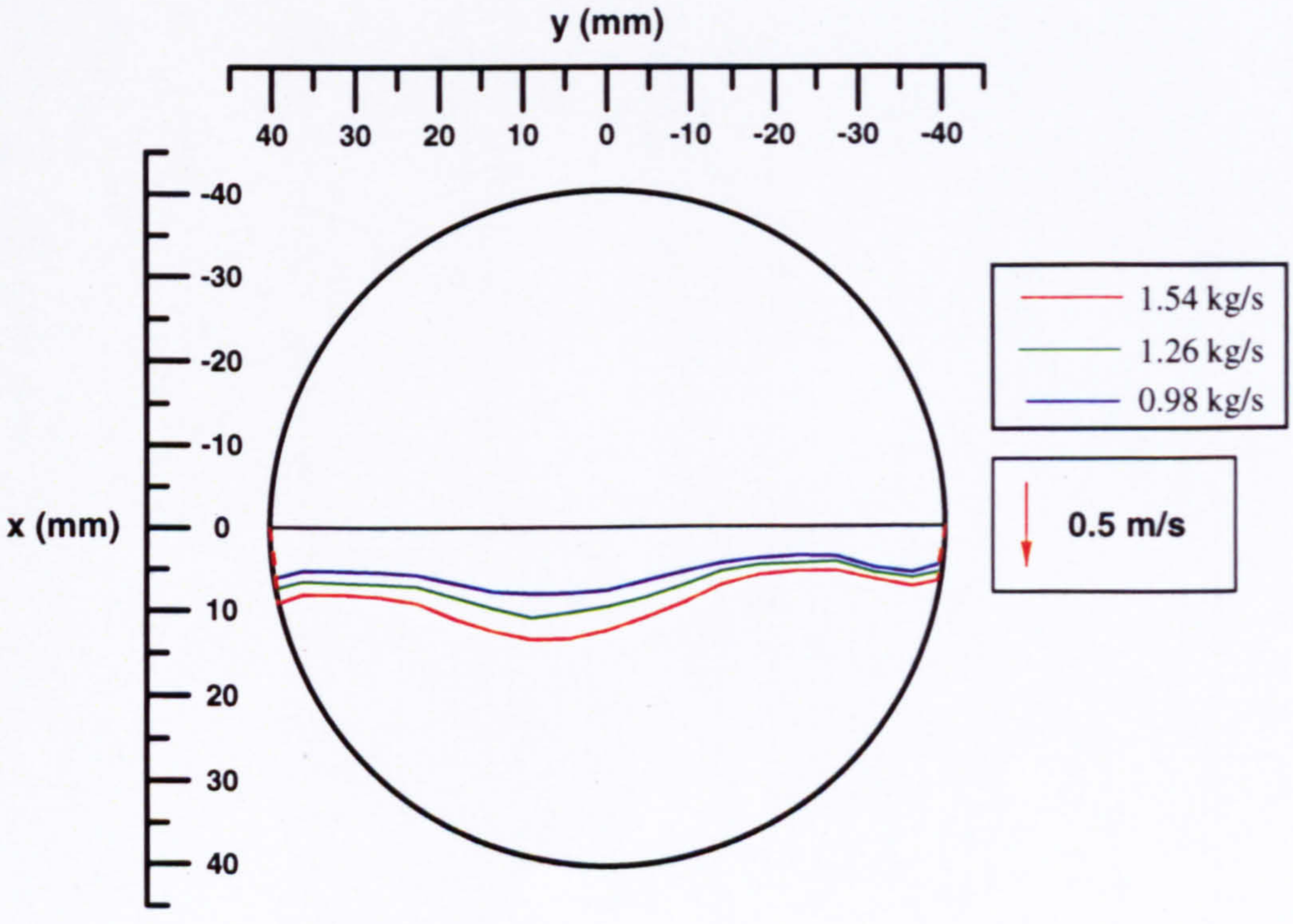

(b) R.m.s. Velocities

Figure 4.7 Variation of mean and r.m.s. in-cylinder velocities with liquid mass flowrate in the x = 0 mm profile and z = 30 mm plane (0/10 mm valve lifts)

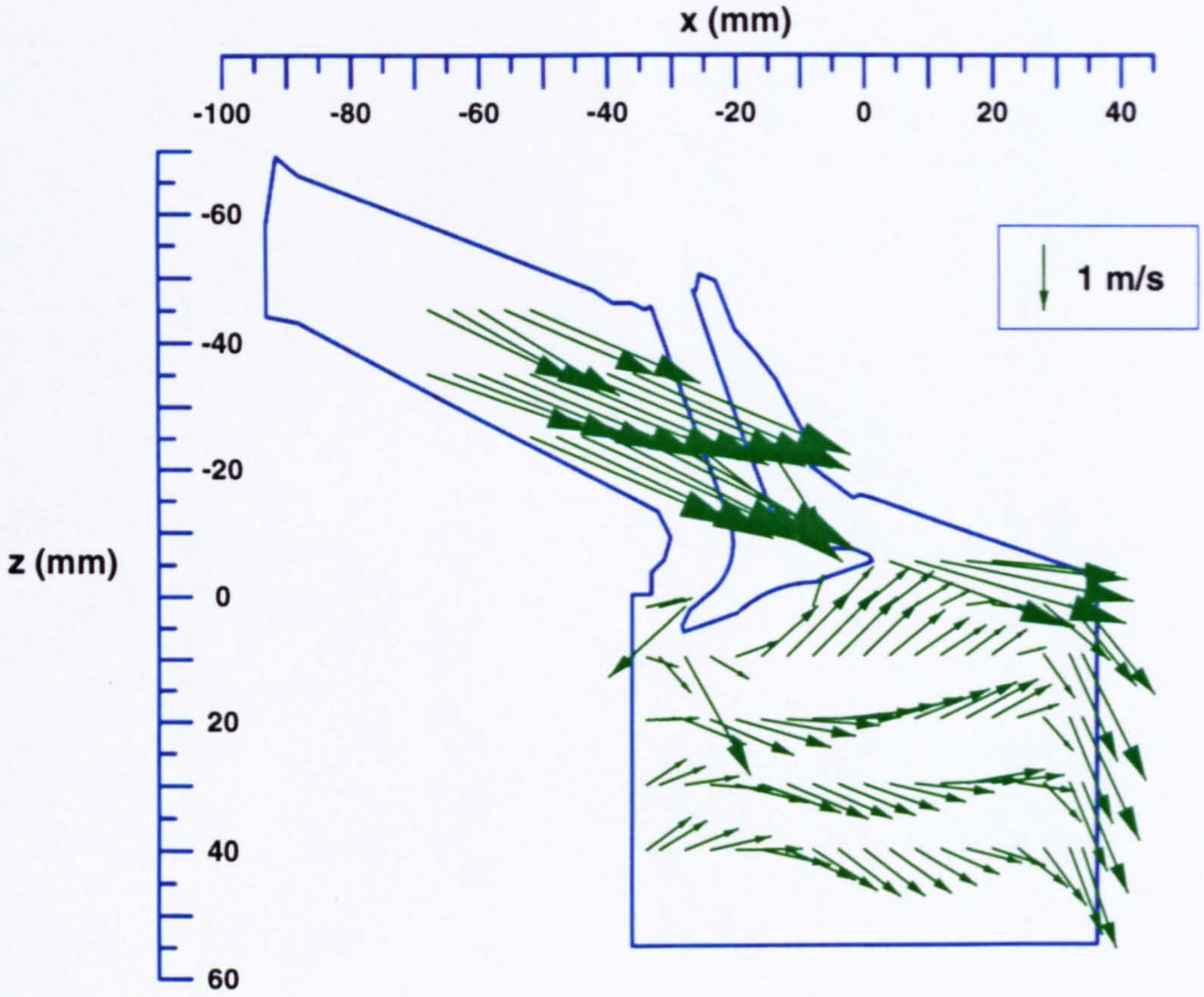

Figure 4.8 Vector plot of radial (U) and axial (W) mean velocities in the plane y = -17.6 mm with Valve 1 closed

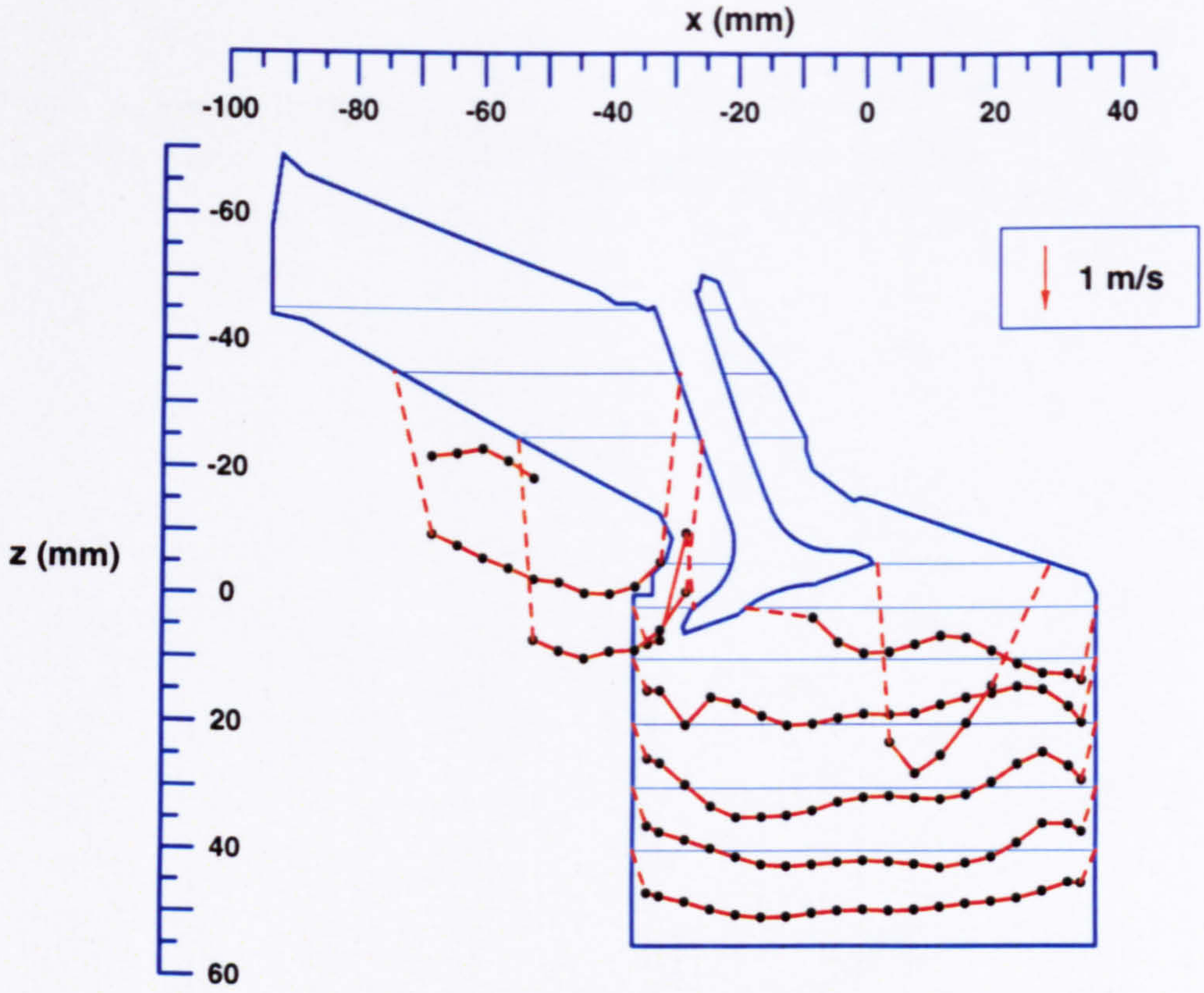

Figure 4.9(a) Profiles of mean U velocities in the vertical plane y = -17.6 mm with Valve 1 closed

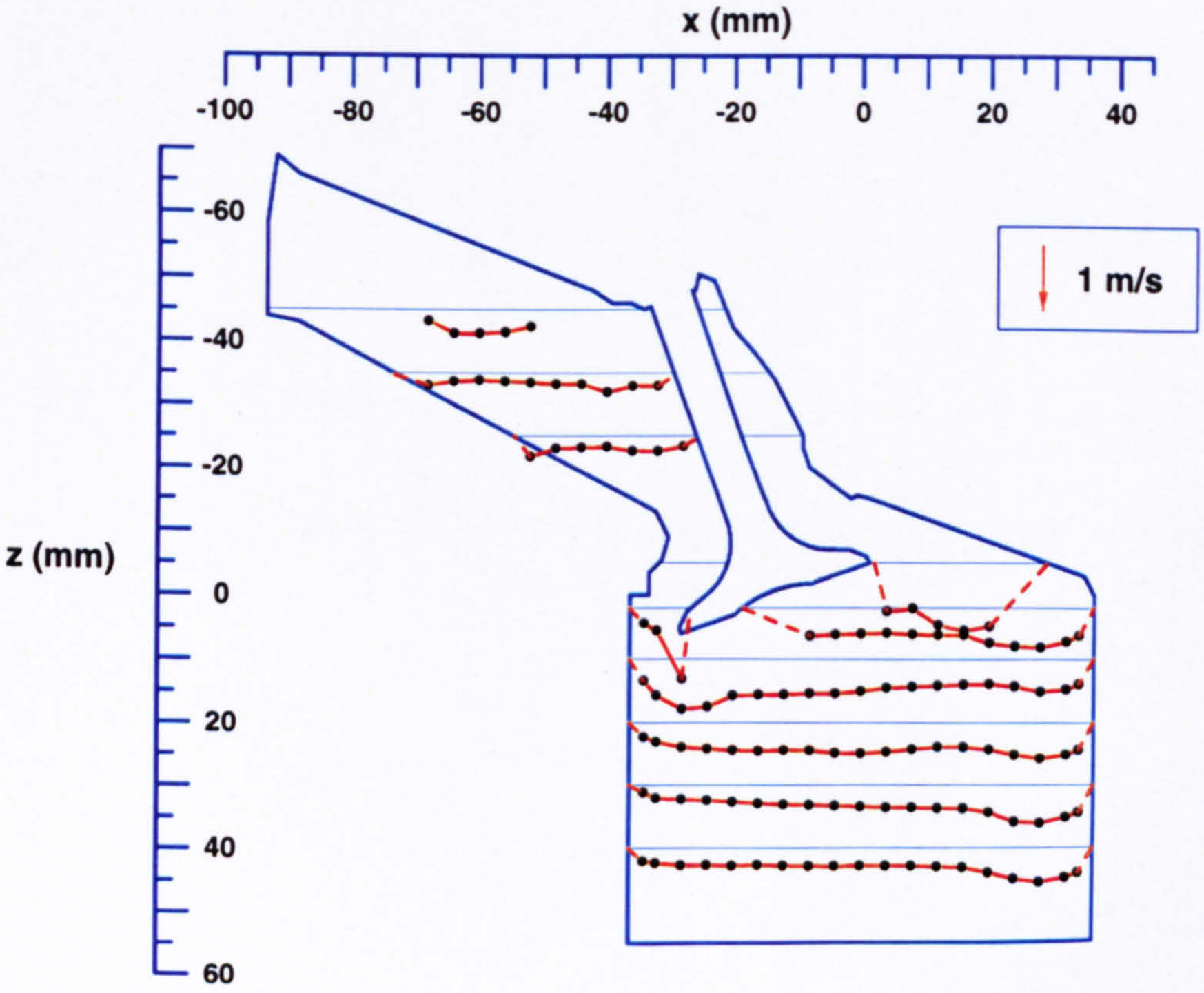

Figure 4.9(b) Profiles of r.m.s. u' velocities in the vertical plane y = -17.6 mm with Valve 1 closed

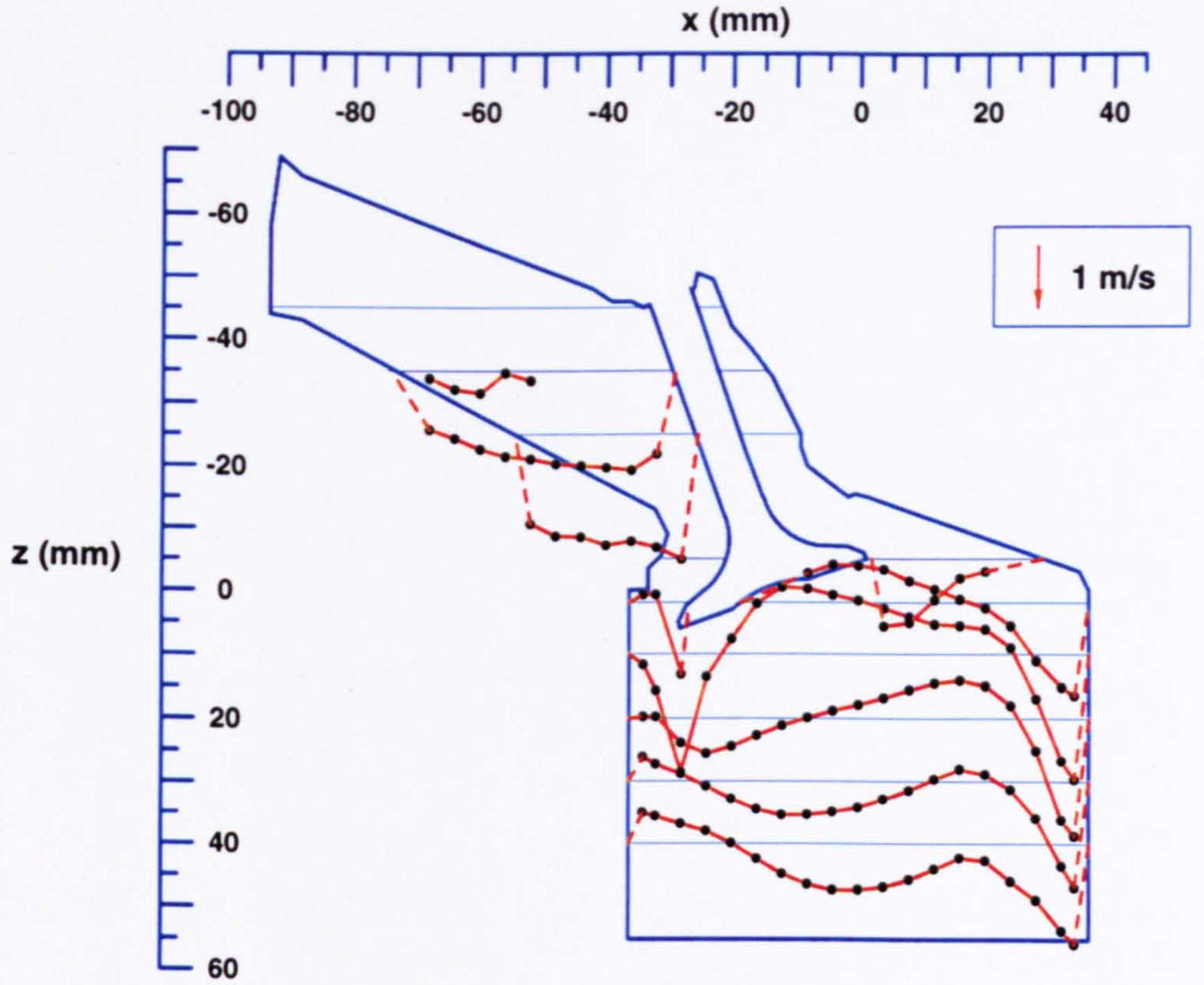

Figure 4.9(c) Profiles of mean W velocities in the vertical plane y = -17.6 mm with Valve 1 closed

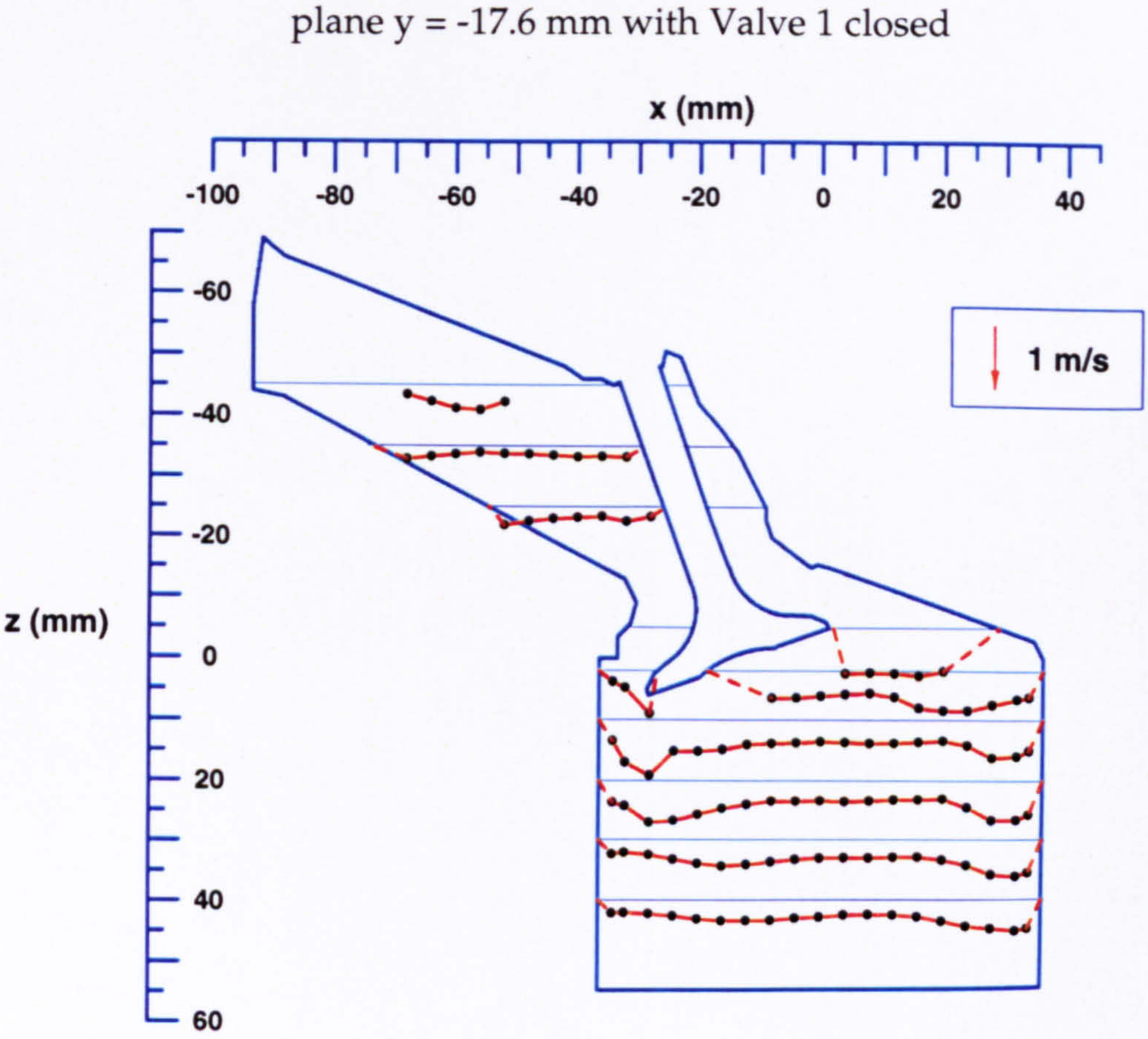

Figure 4.9(d) Profiles of r.m.s. w' velocities in the vertical plane y = -17.6 mm with Valve 1 closed

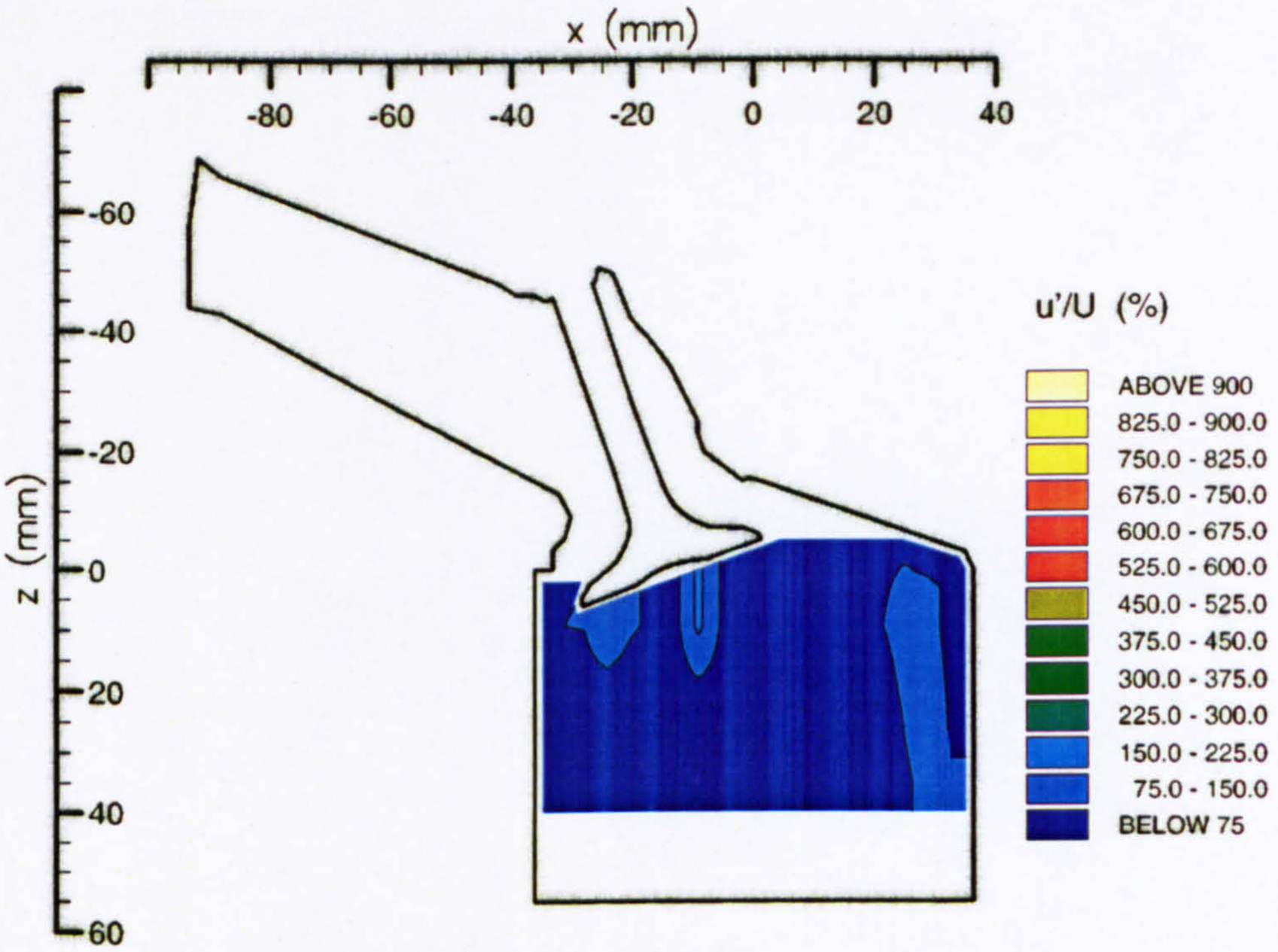

(a) Contours of u'/U

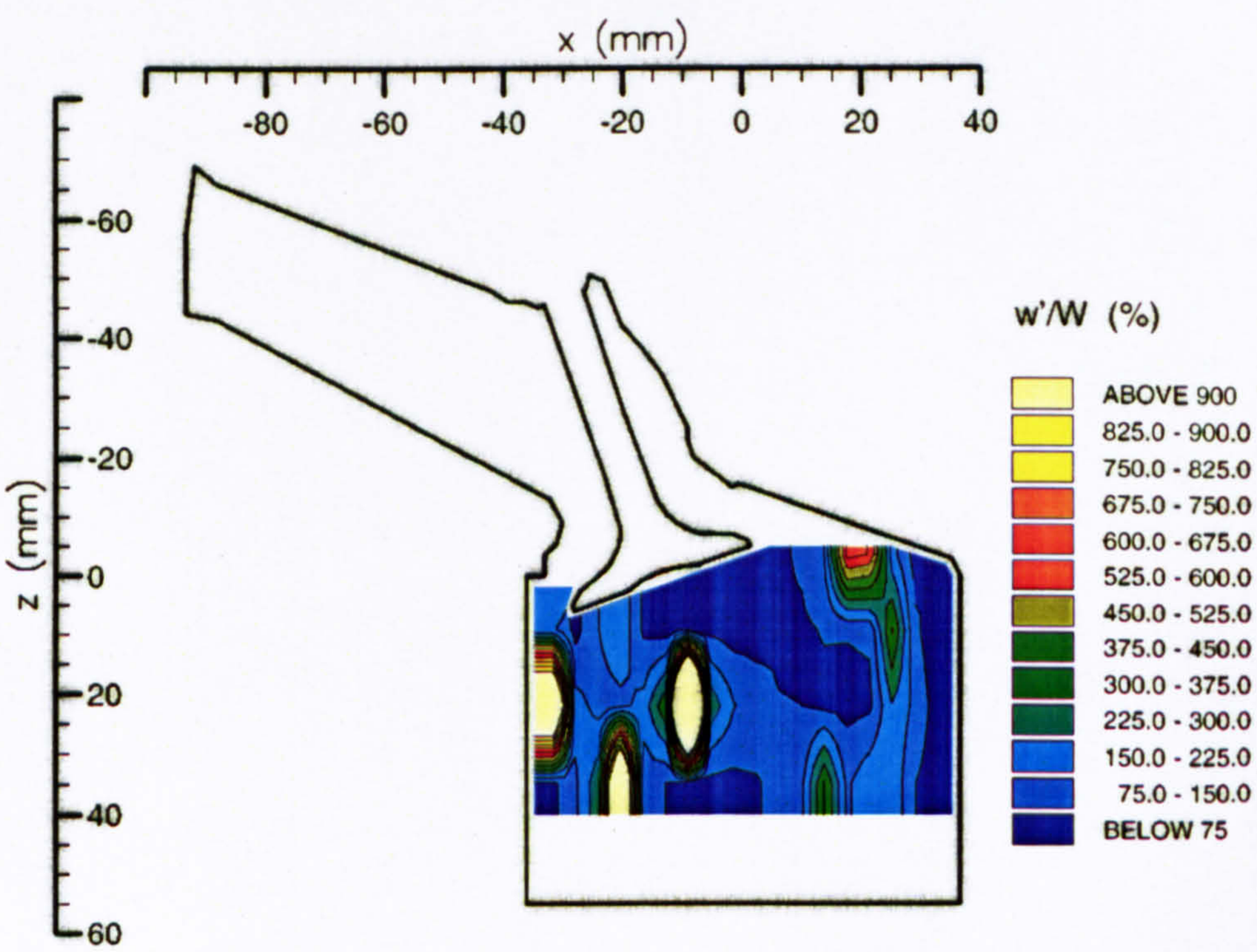

(b) Contours of w'/W

Figure 4.10 Contours of turbulence intensity for flow in the vertical plane y = -17.6 mm with Valve 1 closed

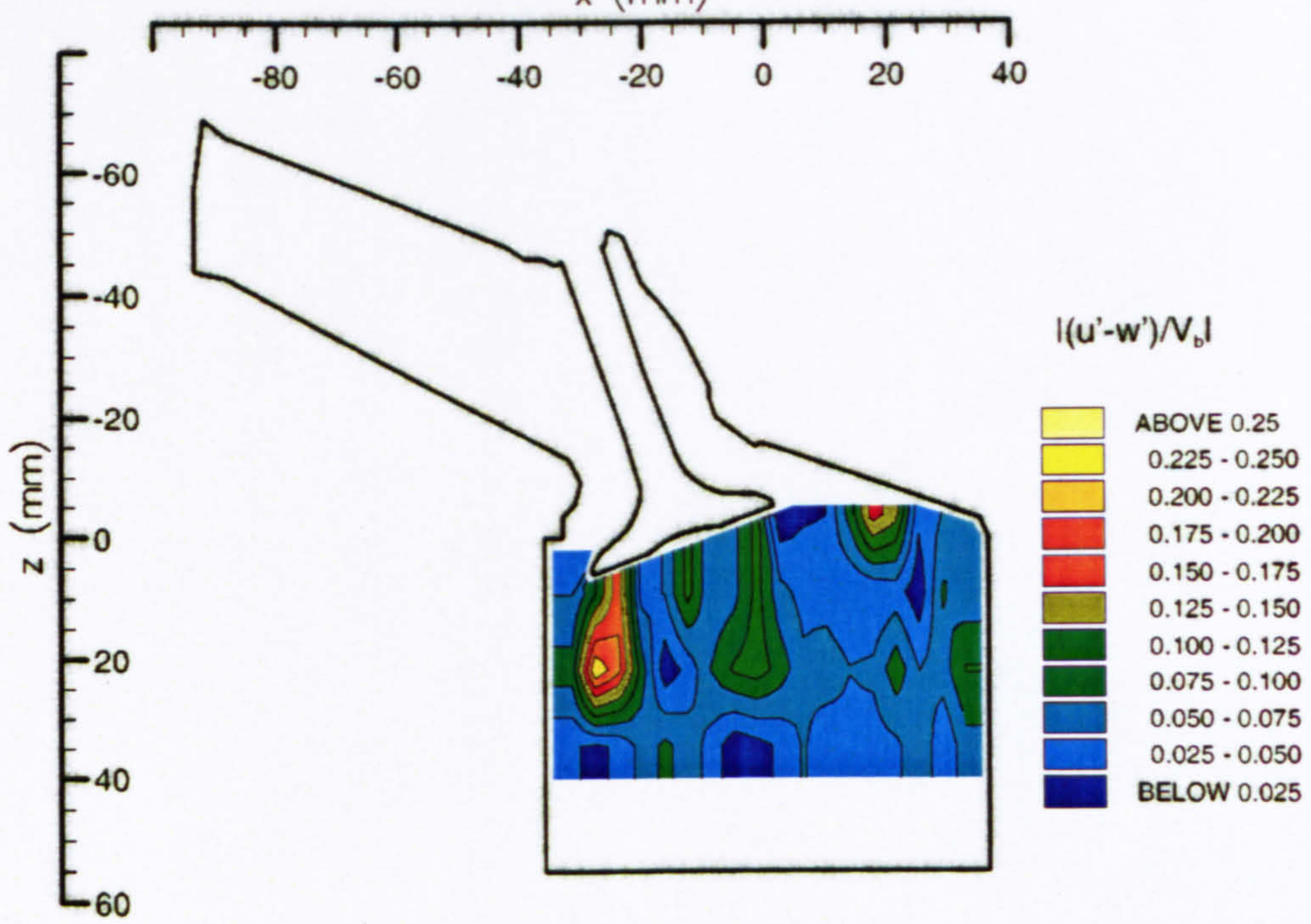

Figure 4.11 Contours of $|(u' - w')/V_b|$ for flow in the vertical plane y = -17.6 mm with Valve 1 closed

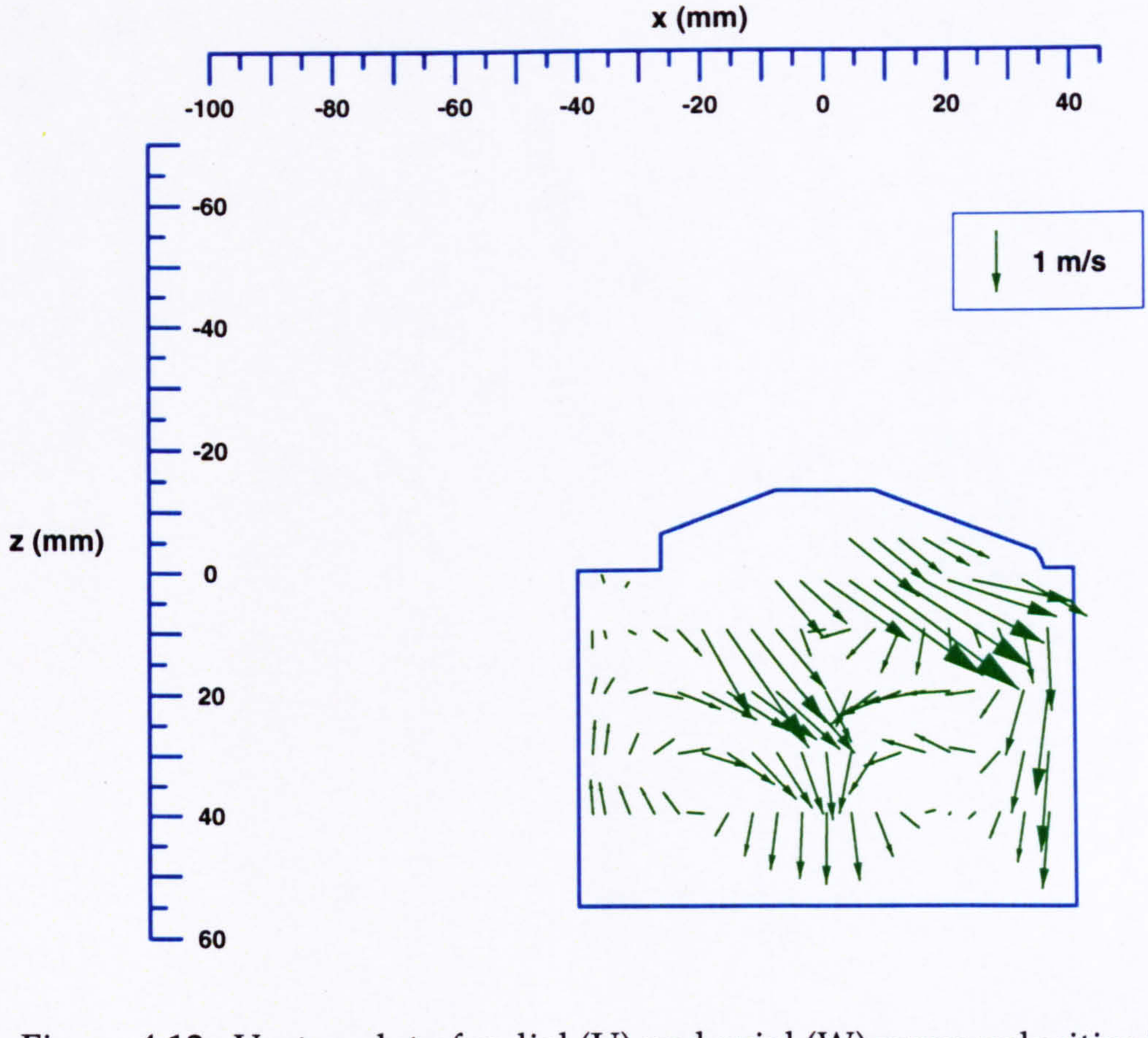

Figure 4.12 Vector plot of radial (U) and axial (W) mean velocities in the plane y = 0 mm with Valve 1 closed

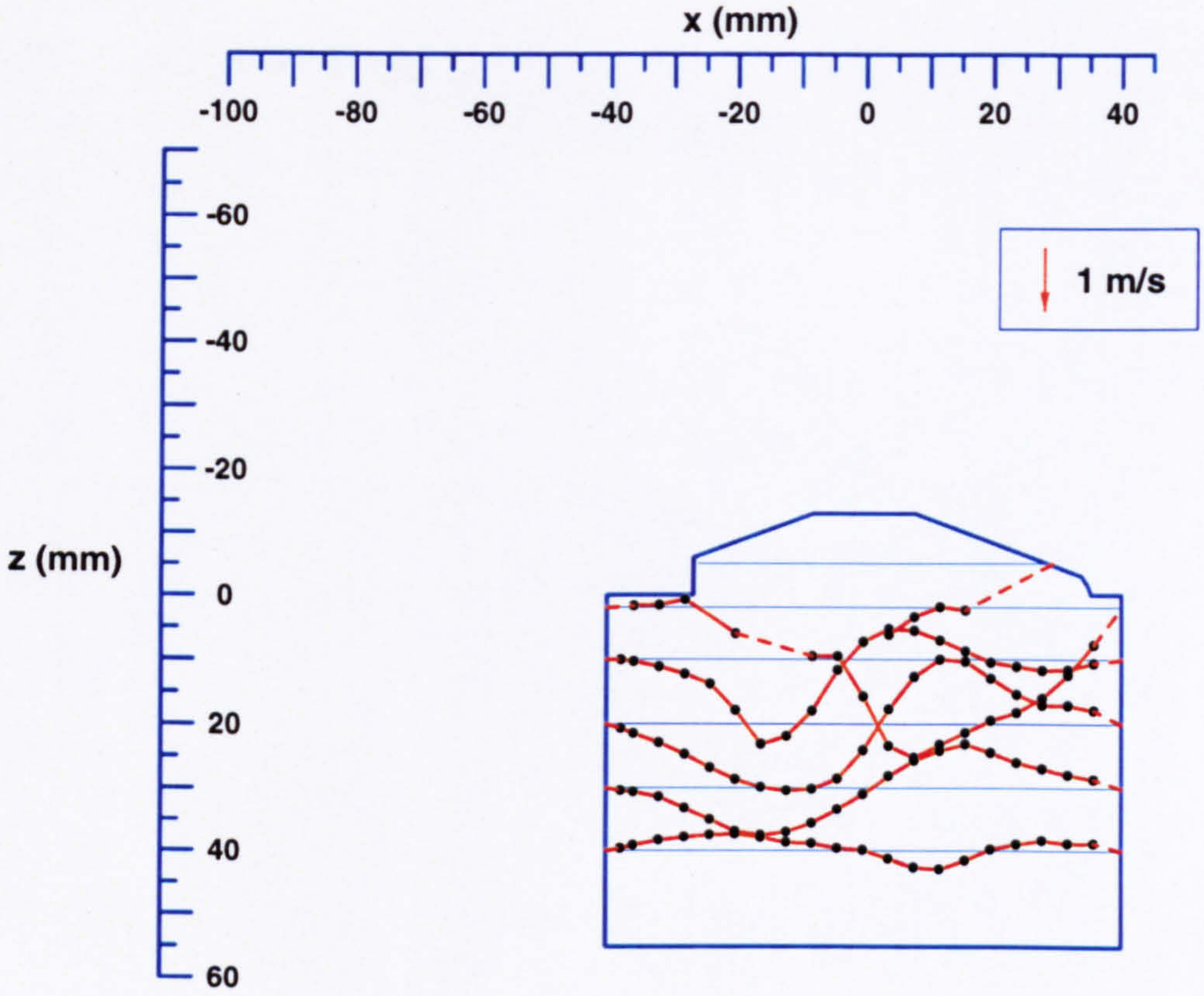

Figure 4.13(a) Profiles of mean U velocities in the vertical plane y = 0 mm with Valve 1 closed

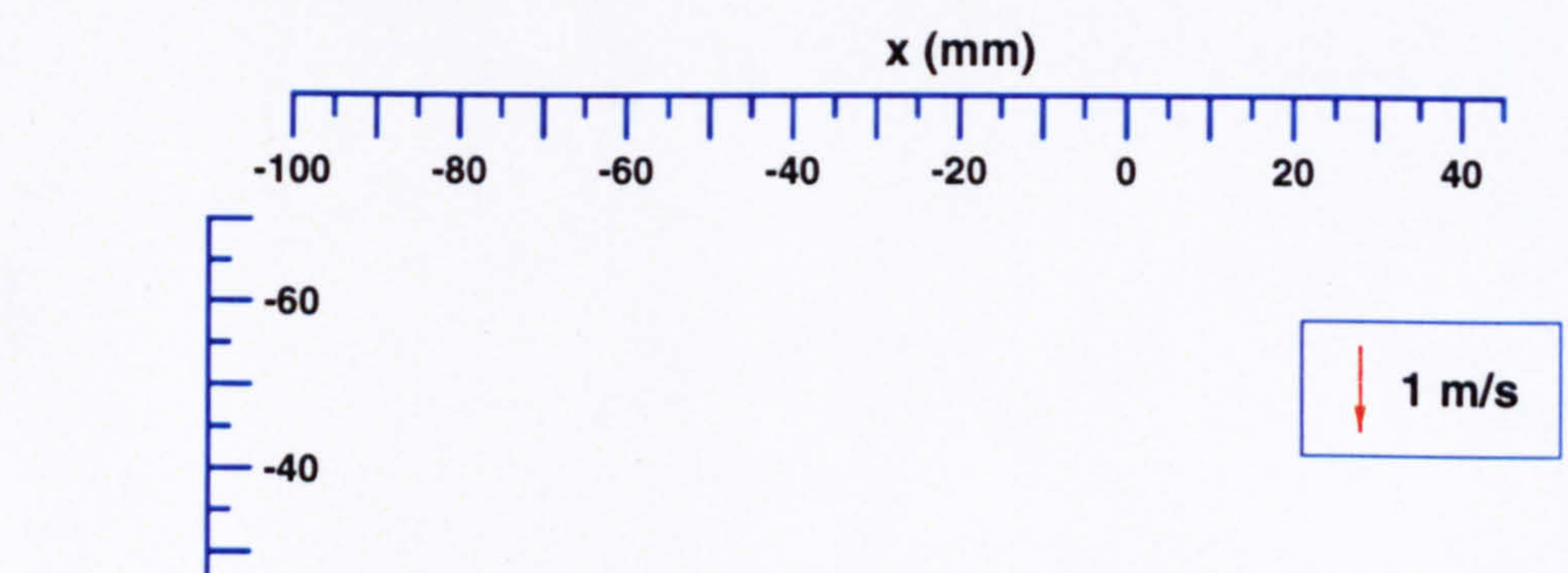

Figure 4.13(b) Profiles of mean U velocities in the vertical plane y = 0 mm with Valve 1 closed

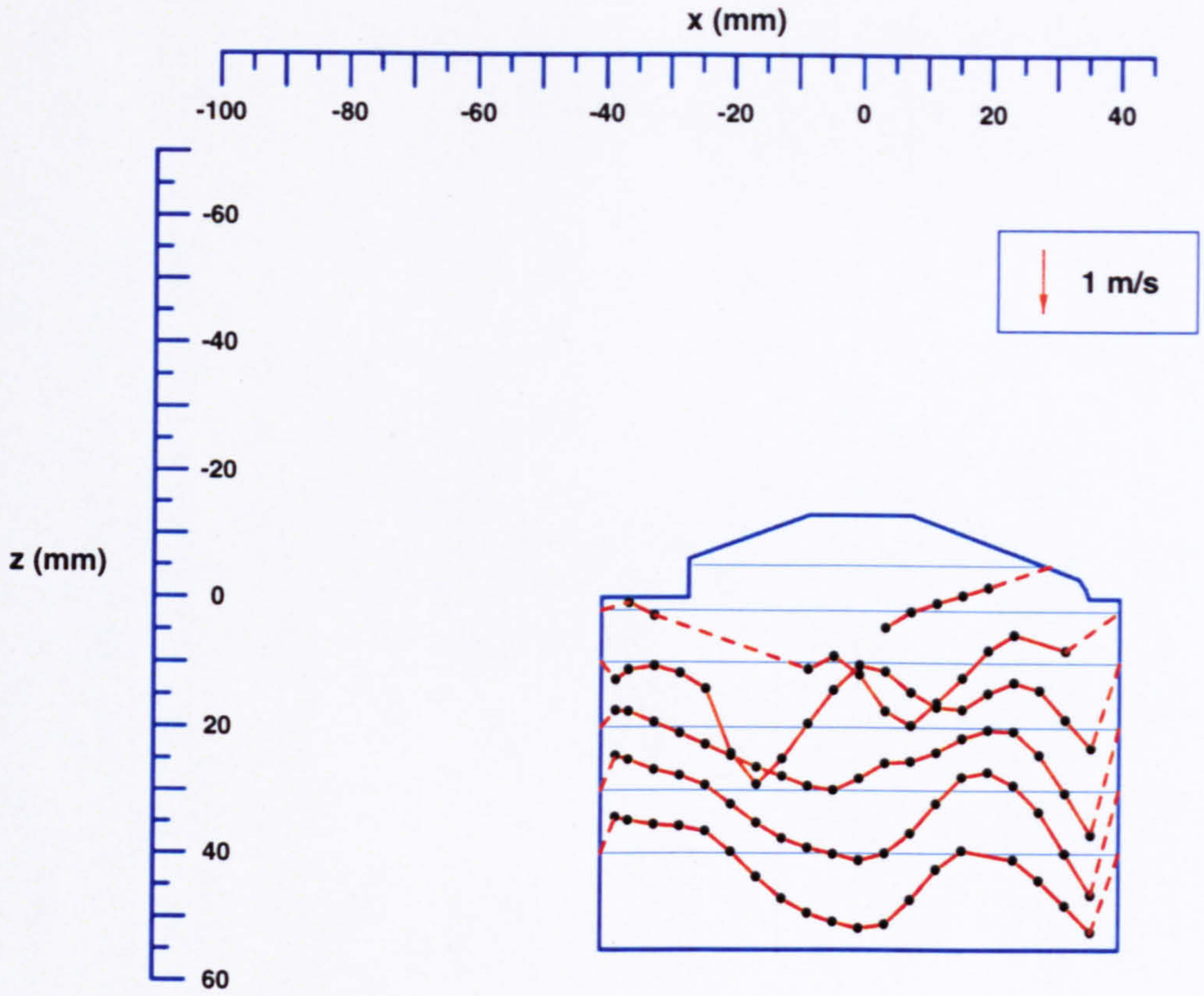

Figure 4.13(c) Profiles of mean W velocities in the vertical plane y = 0 mm with Valve 1 closed

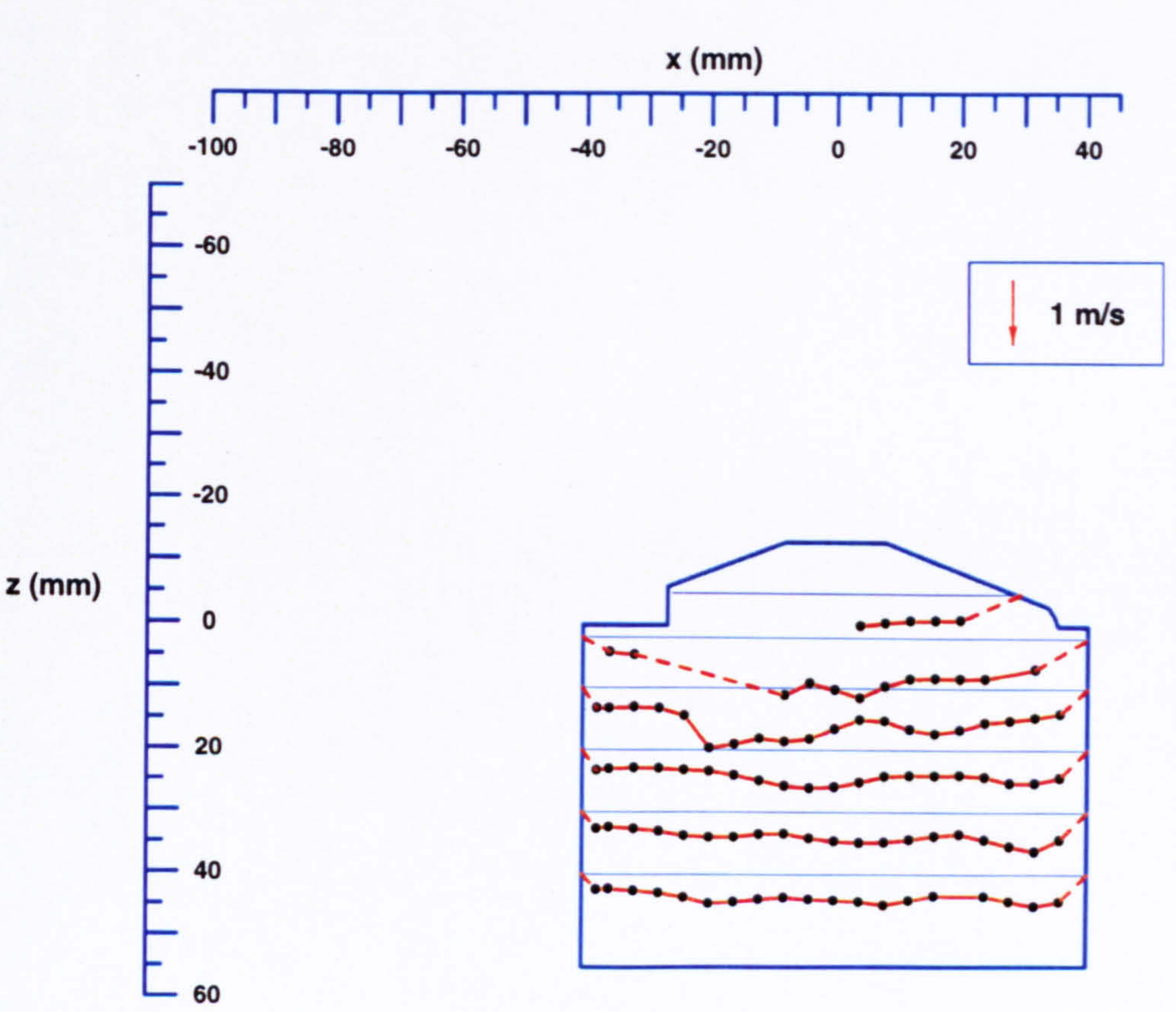

Figure 4.13(d) Profiles of r.m.s. w' velocities in the vertical plane y = 0 mm with Valve 1 closed

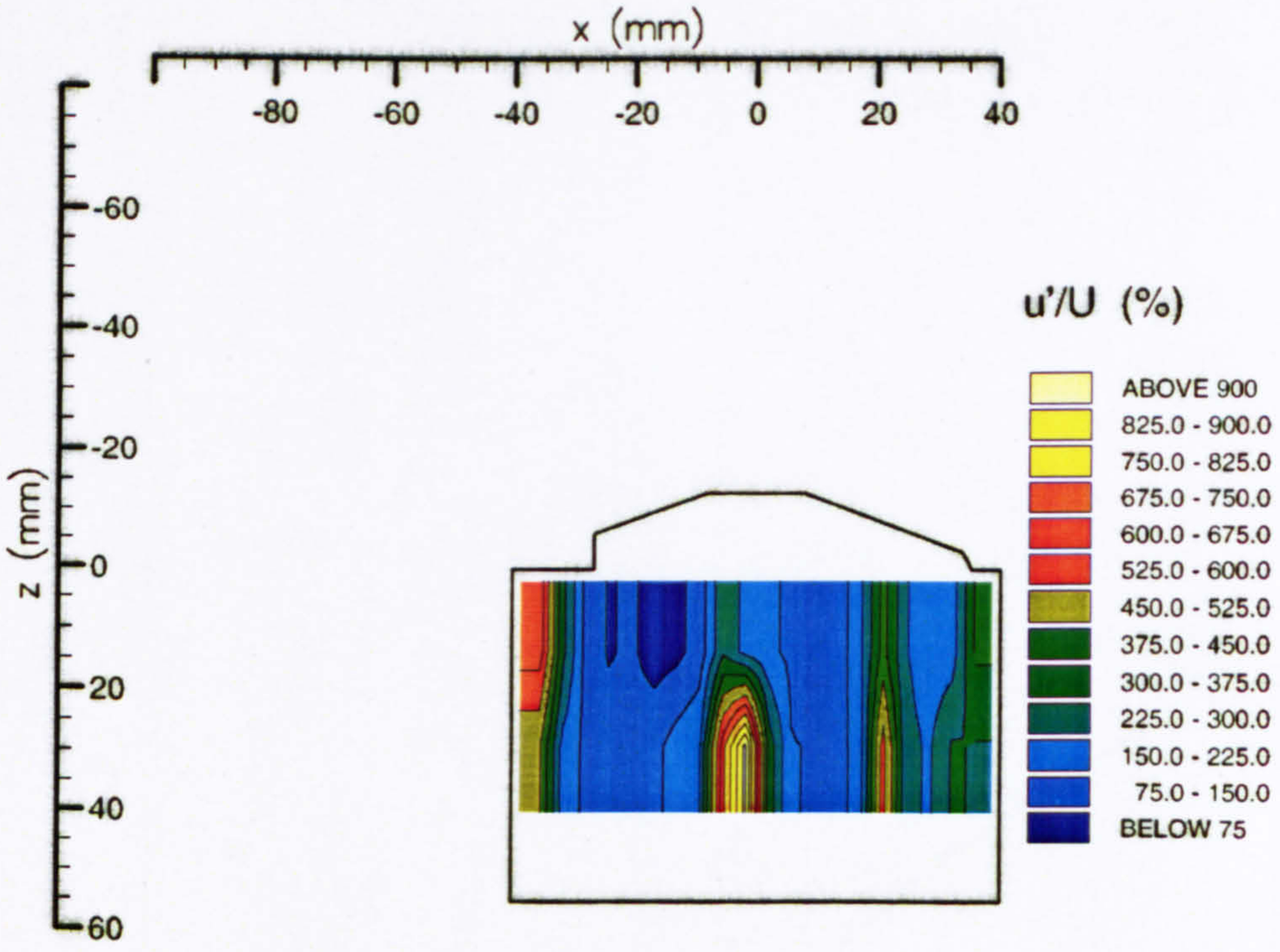

(a) Contours of u'/U

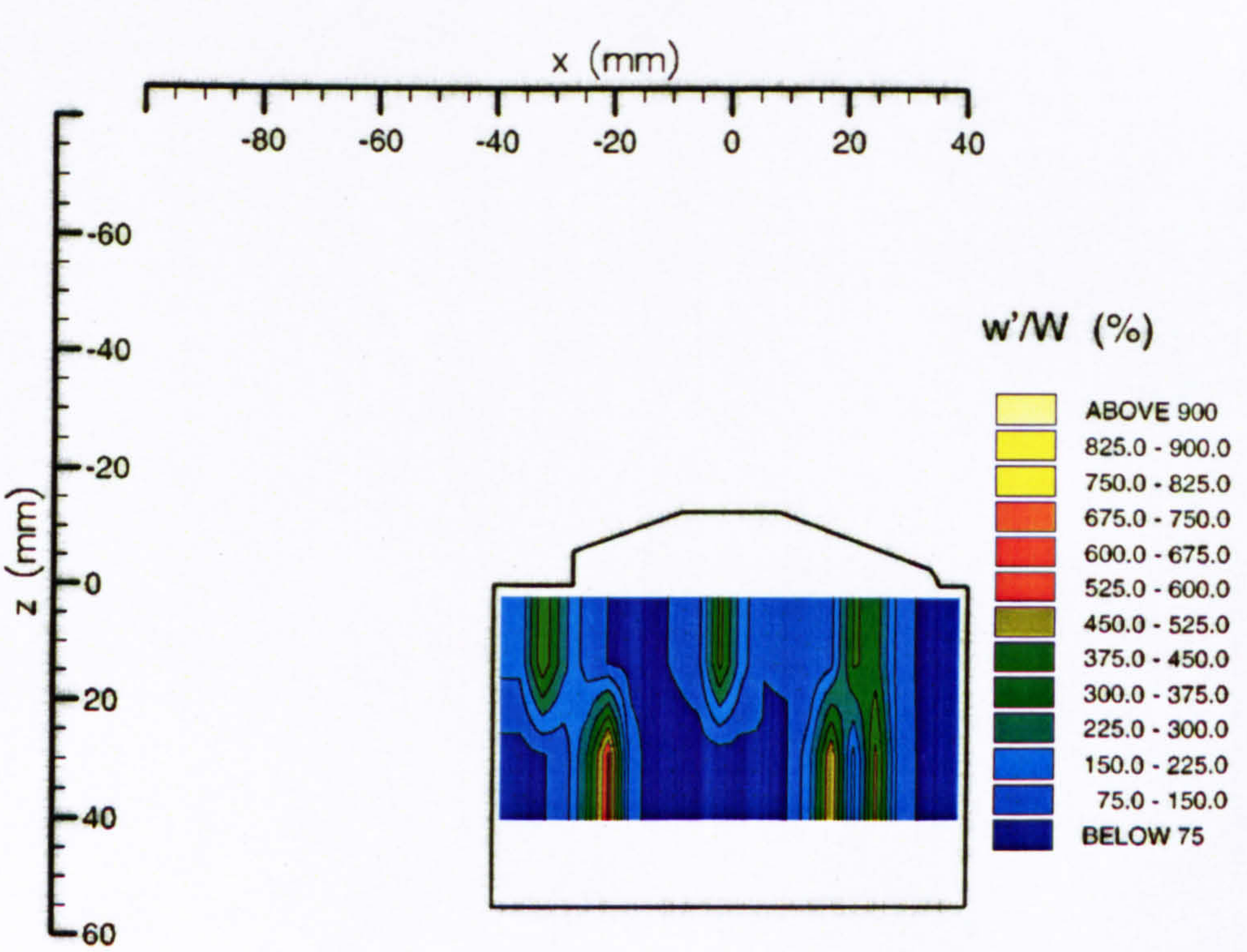

(b) Contours of w'/W

Figure 4.14 Contours of turbulence intensity for flow in the vertical plane y = 0 mm with Valve 1 closed

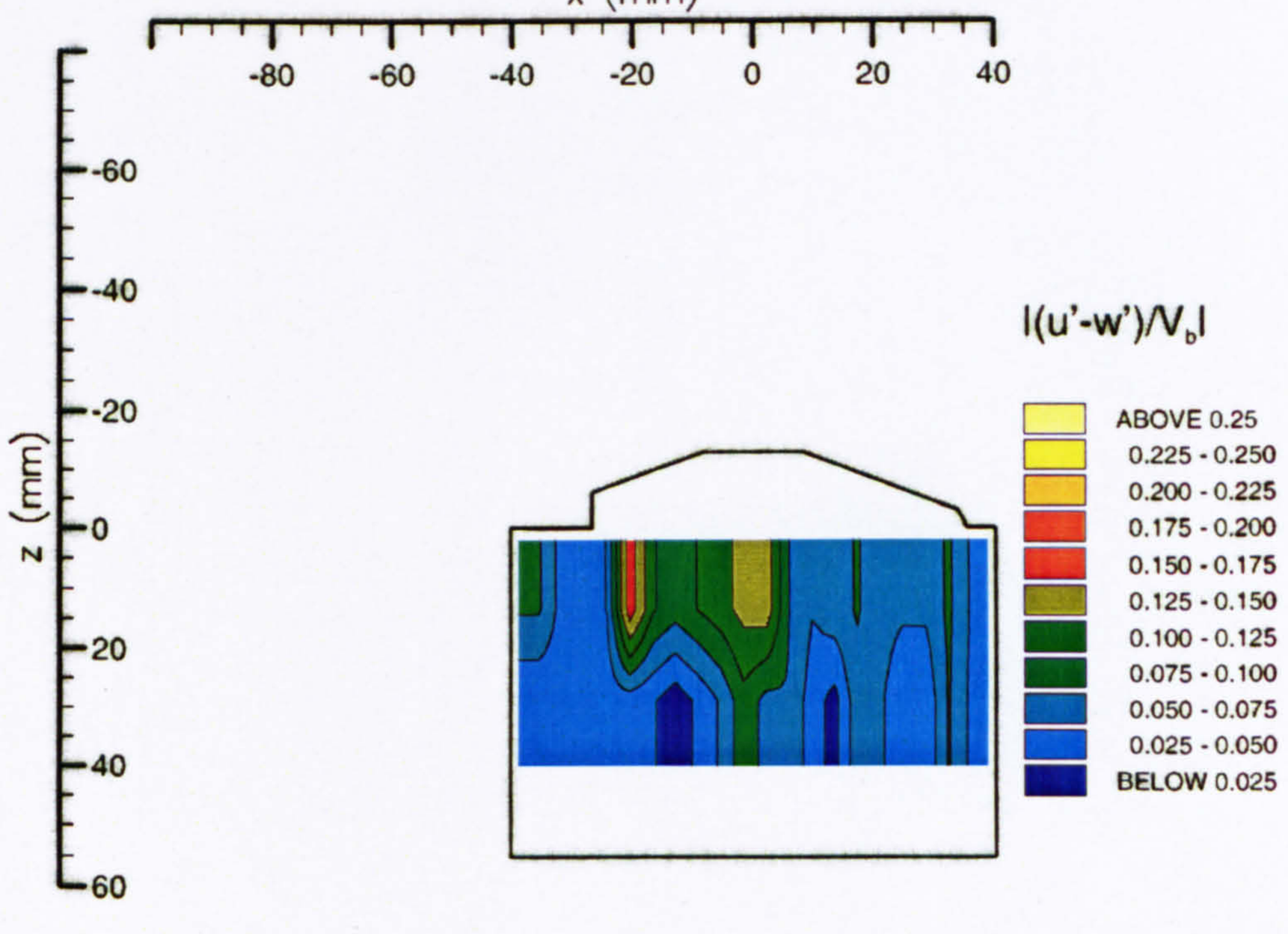

Figure 4.15 Contours of $|(u' - w')/V_b|$ for flow in the vertical plane y = 0 mm with Valve 1 closed

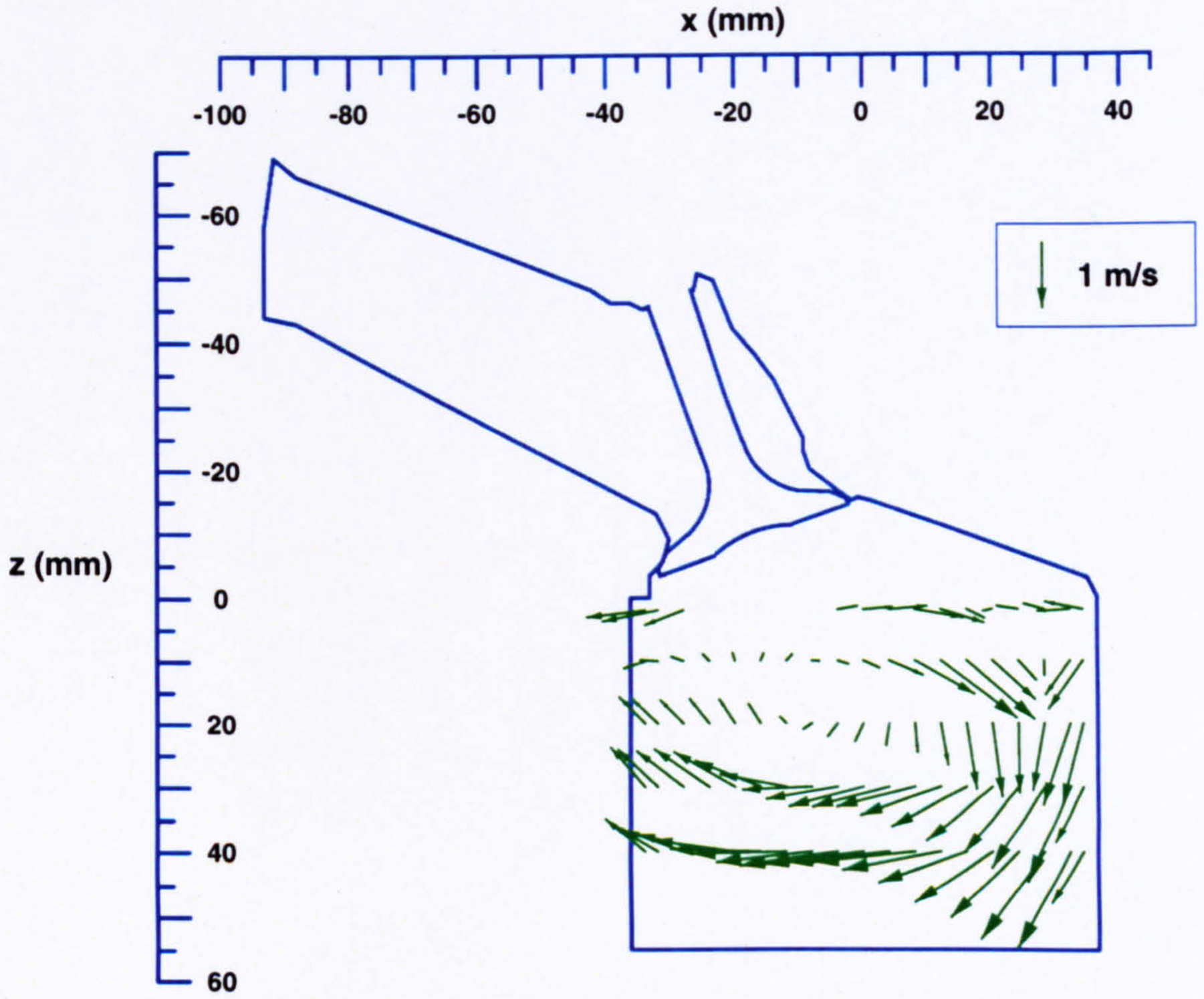

Figure 4.16 Vector plot of radial (U) and axial (W) mean velocities in the plane y = 17.6 mm with Valve 1 closed

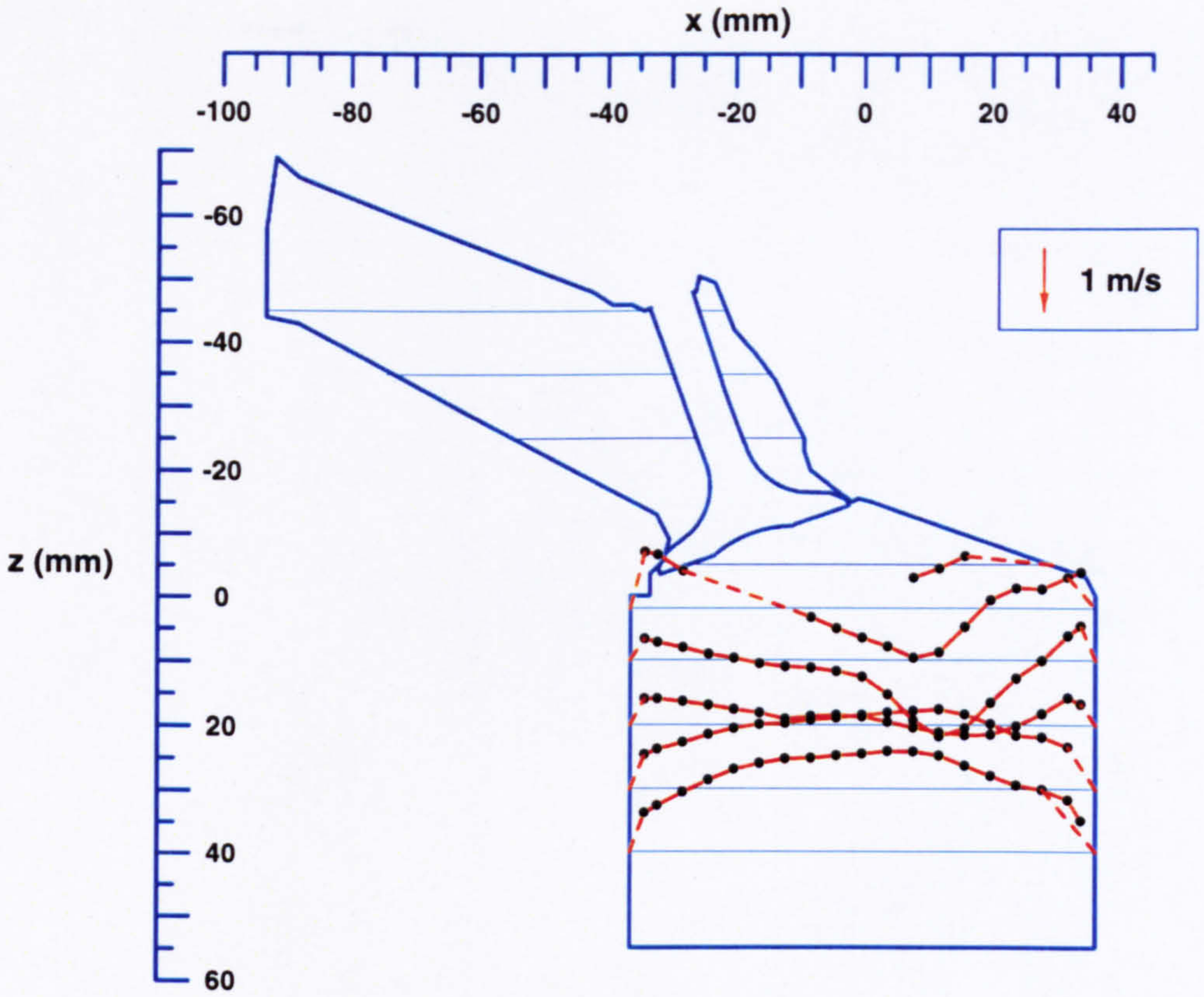

Figure 4.17(a) Profiles of mean U velocities in the vertical plane y = 17.6 mm with Valve 1 closed

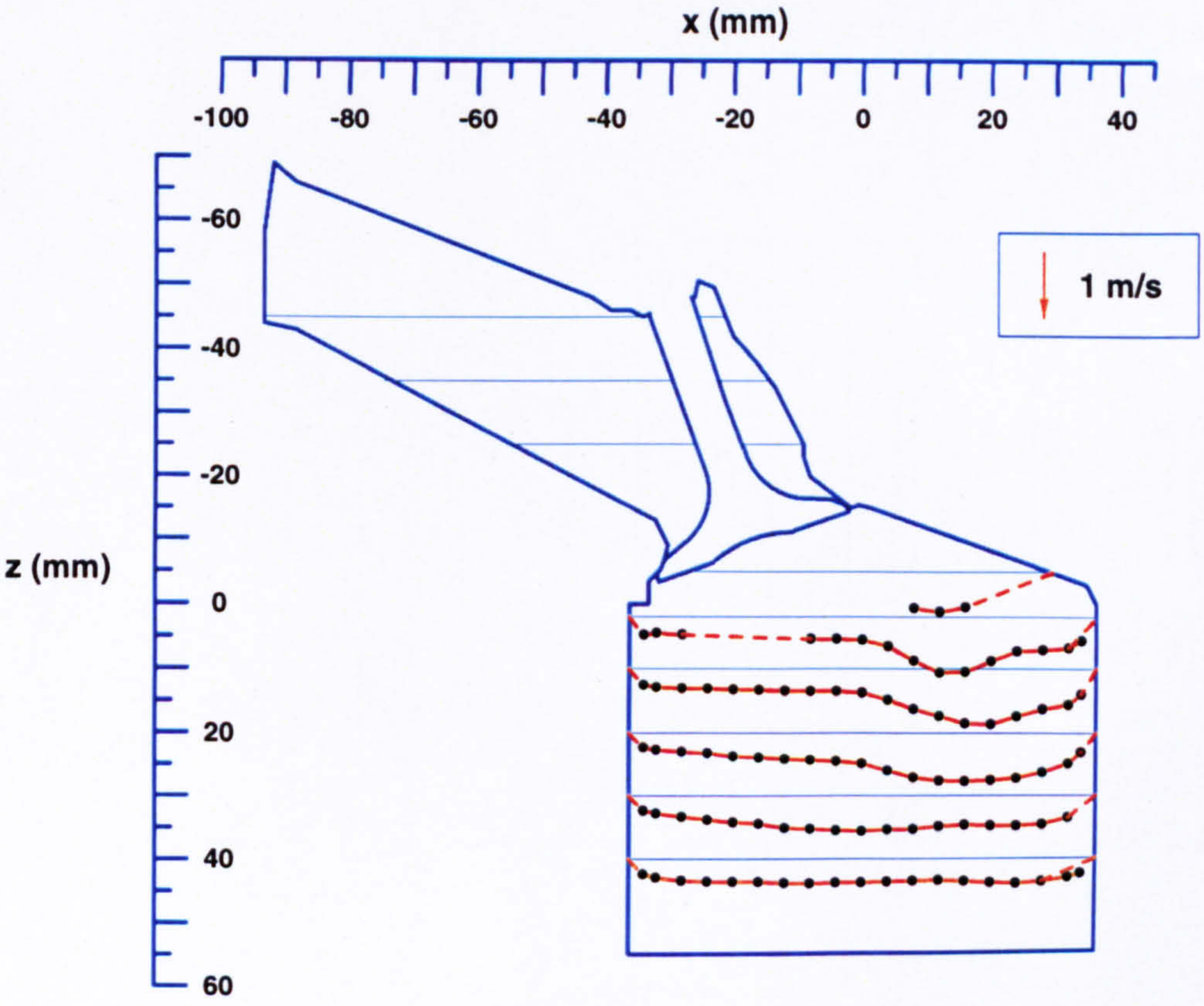

Figure 4.17(b) Profiles of r.m.s. velocities in the vertical plane y = 17.6 mm with Valve 1 closed

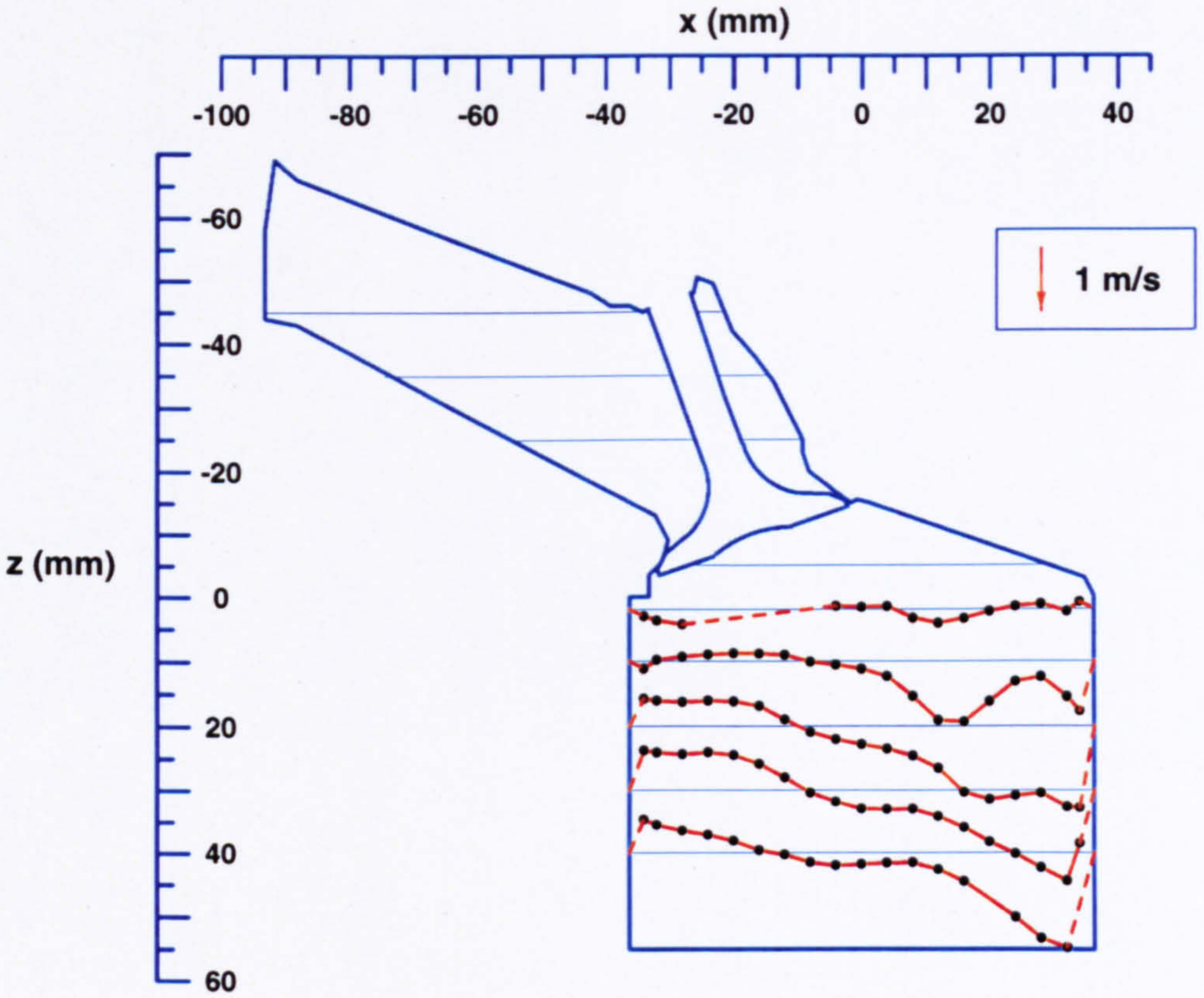

Figure 4.17(c) Profiles of mean W velocities in the vertical plane y = 17.6 mm with Valve 1 closed

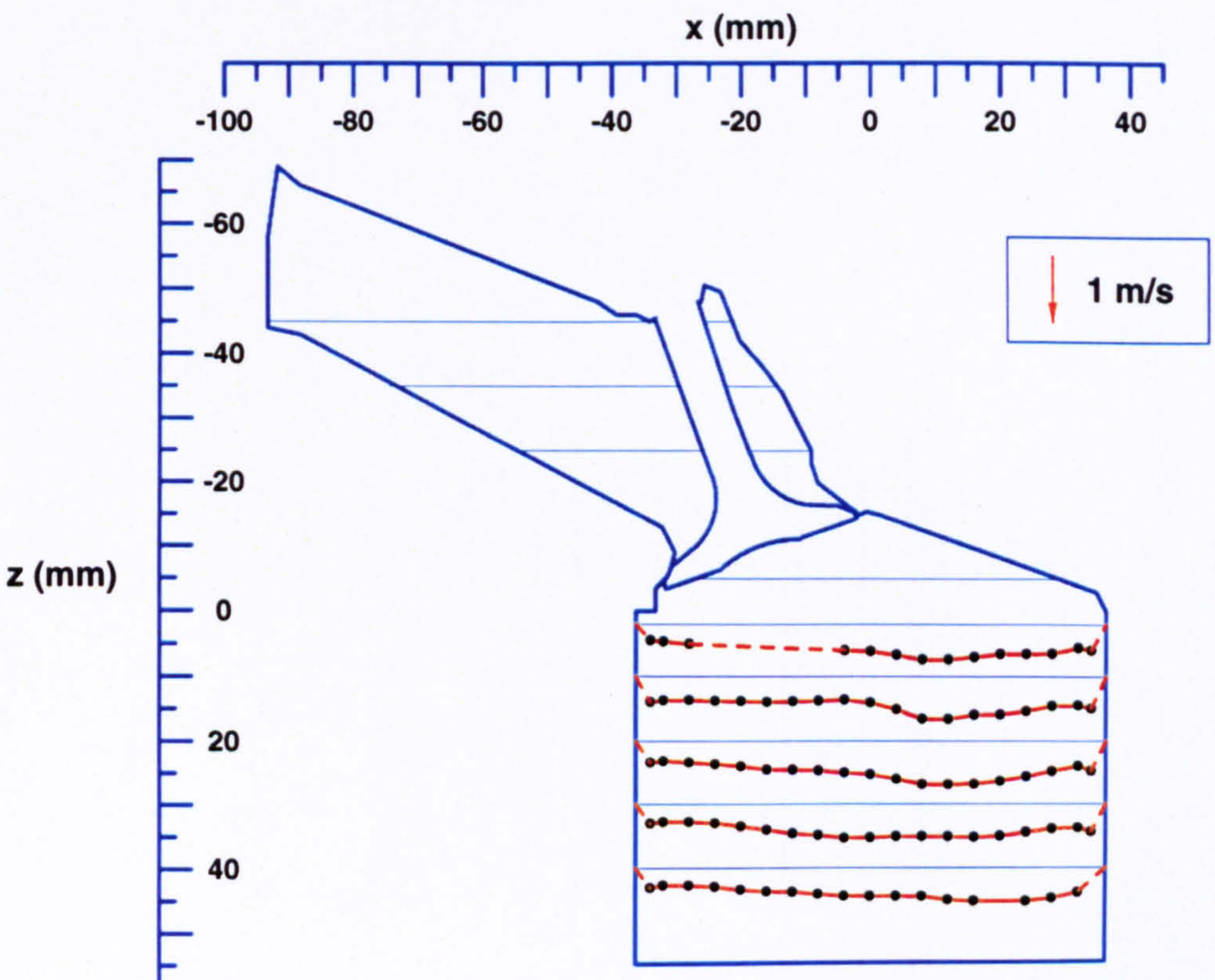

Figure 4.17(d) Profiles of r.m.s. w' velocities in the vertical plane y = 17.6 mm with Valve 1 closed

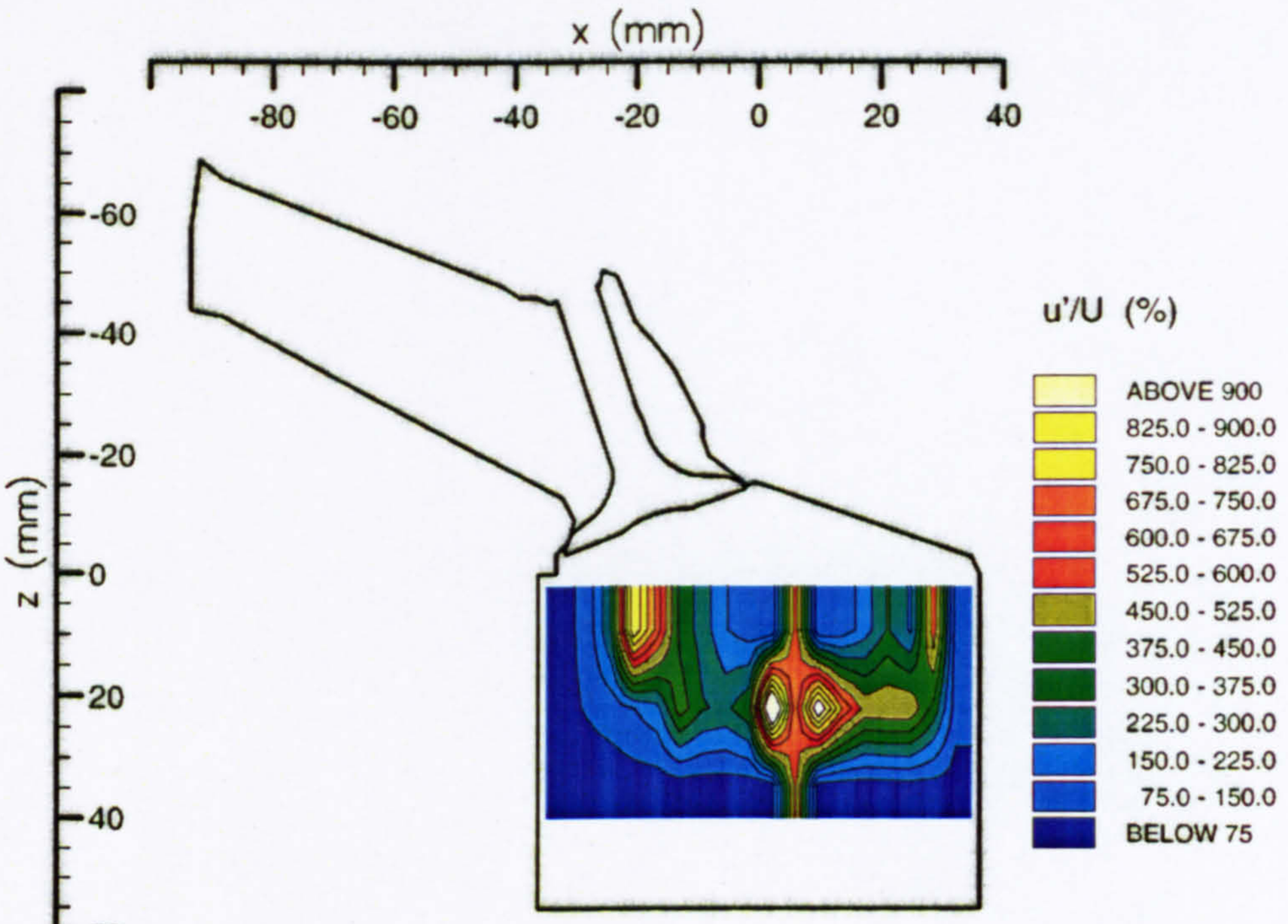

(a) Contours of u'/U

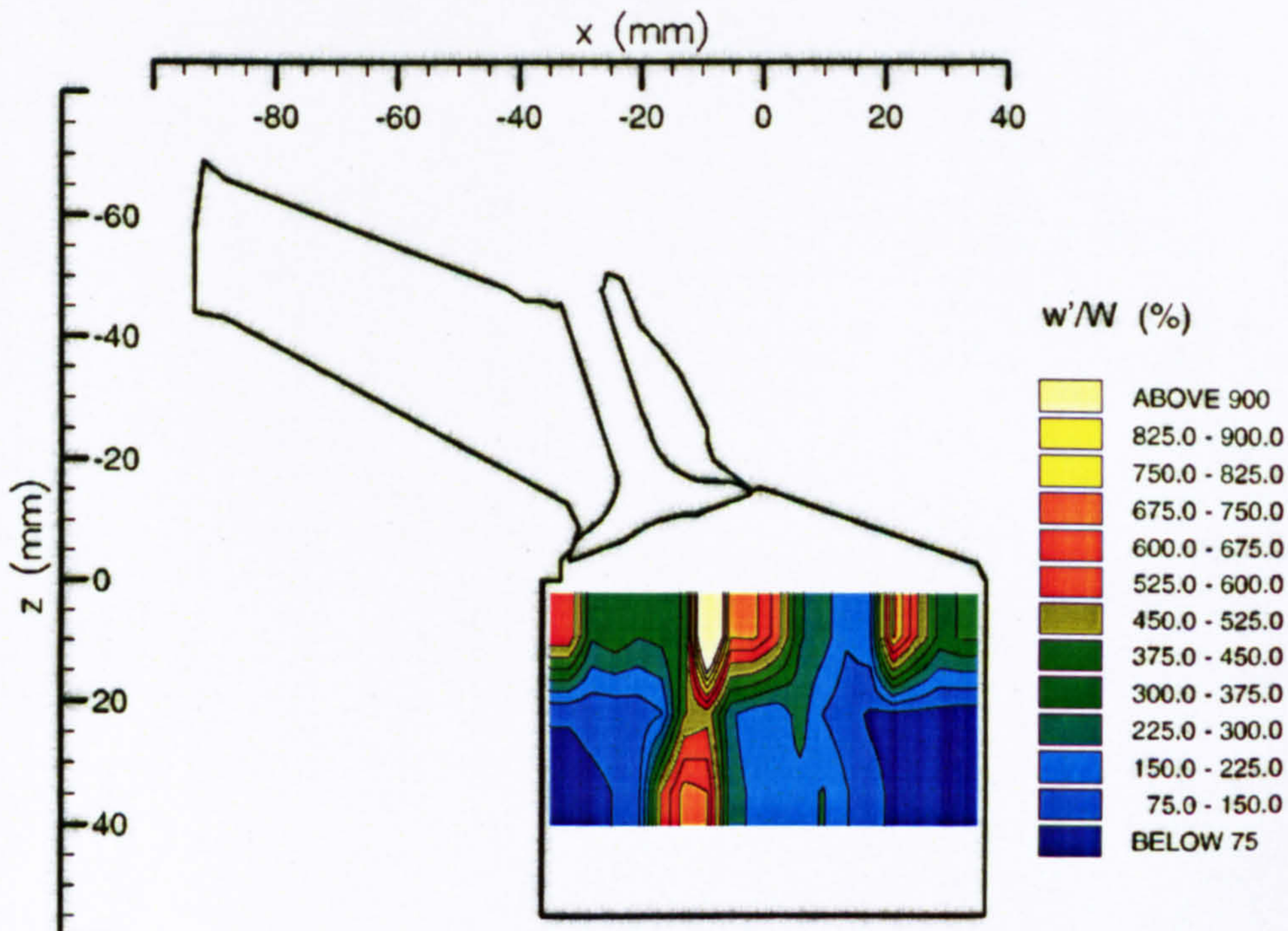

(b) Contours of w'/W

Figure 4.18 Contours of turbulence intensity for flow in the vertical plane y = 17.6 mm with Valve 1 closed

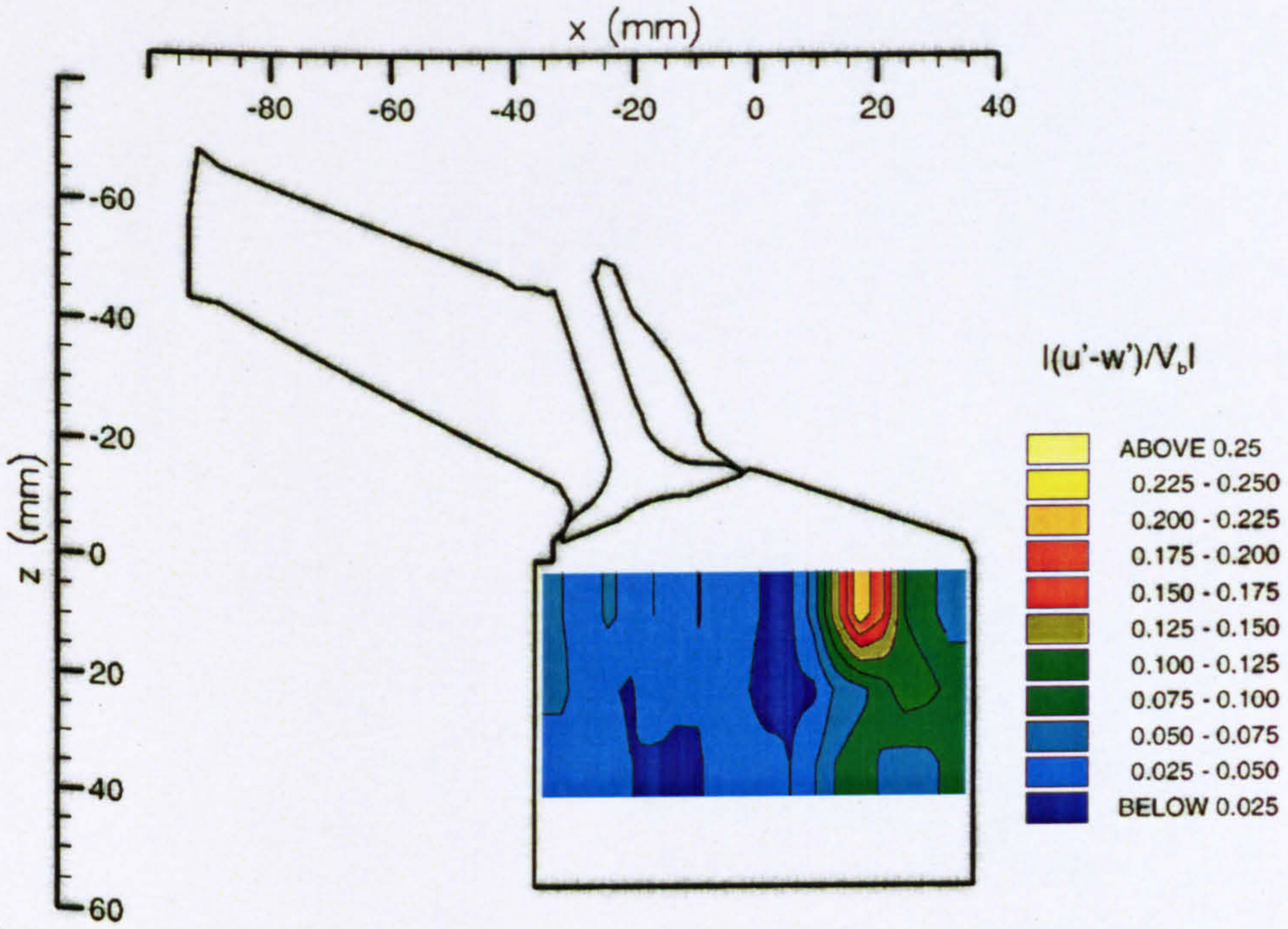

Figure 4.19 Contours of $|(u' - w')/V_b|$ for flow in the vertical plane y = 17.6 mm with Valve 1 closed

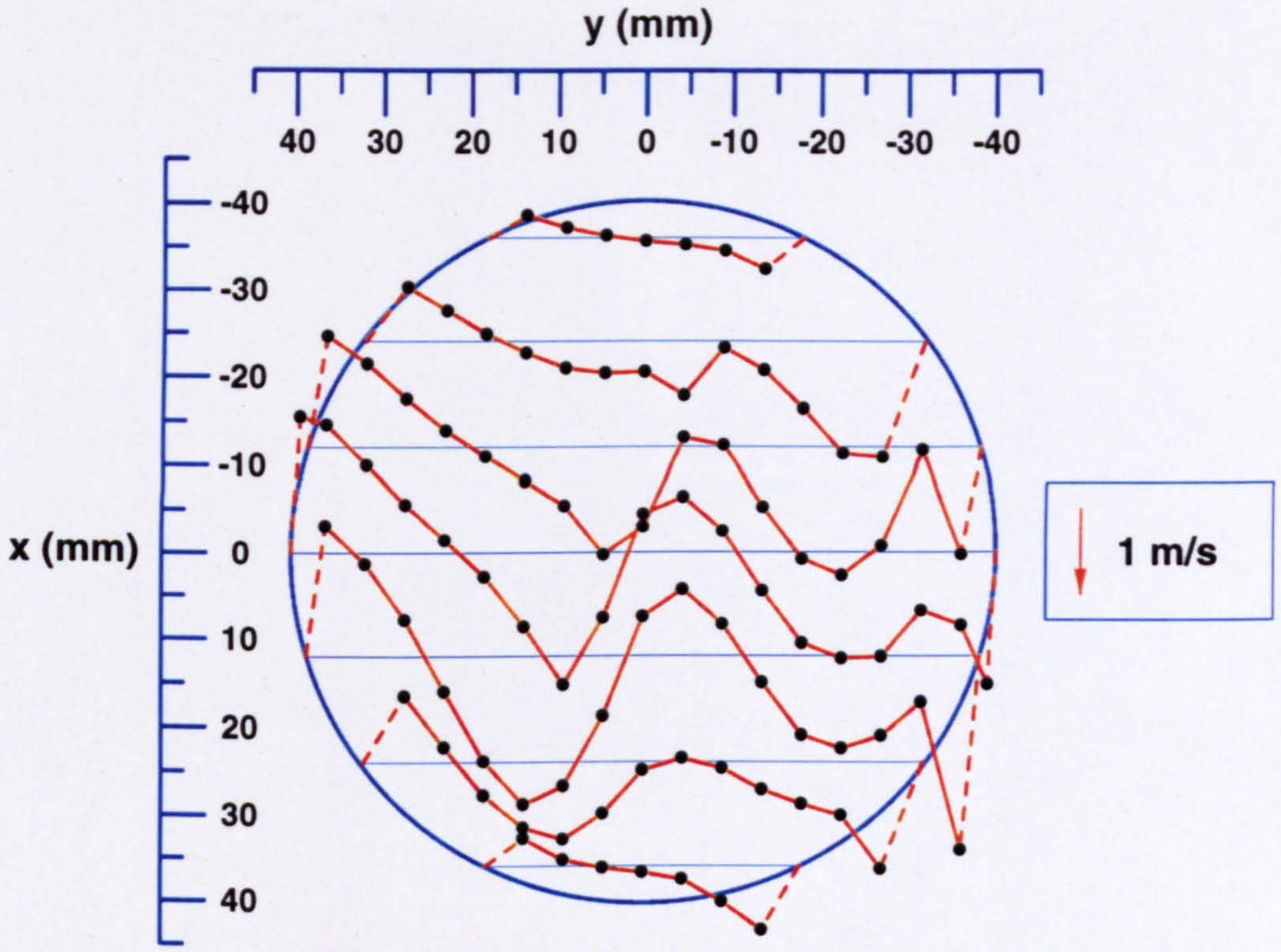

Figure 4.20(a) Profiles of U velocities in the horizontal plane z = 10 mm plane with Valve 1 closed

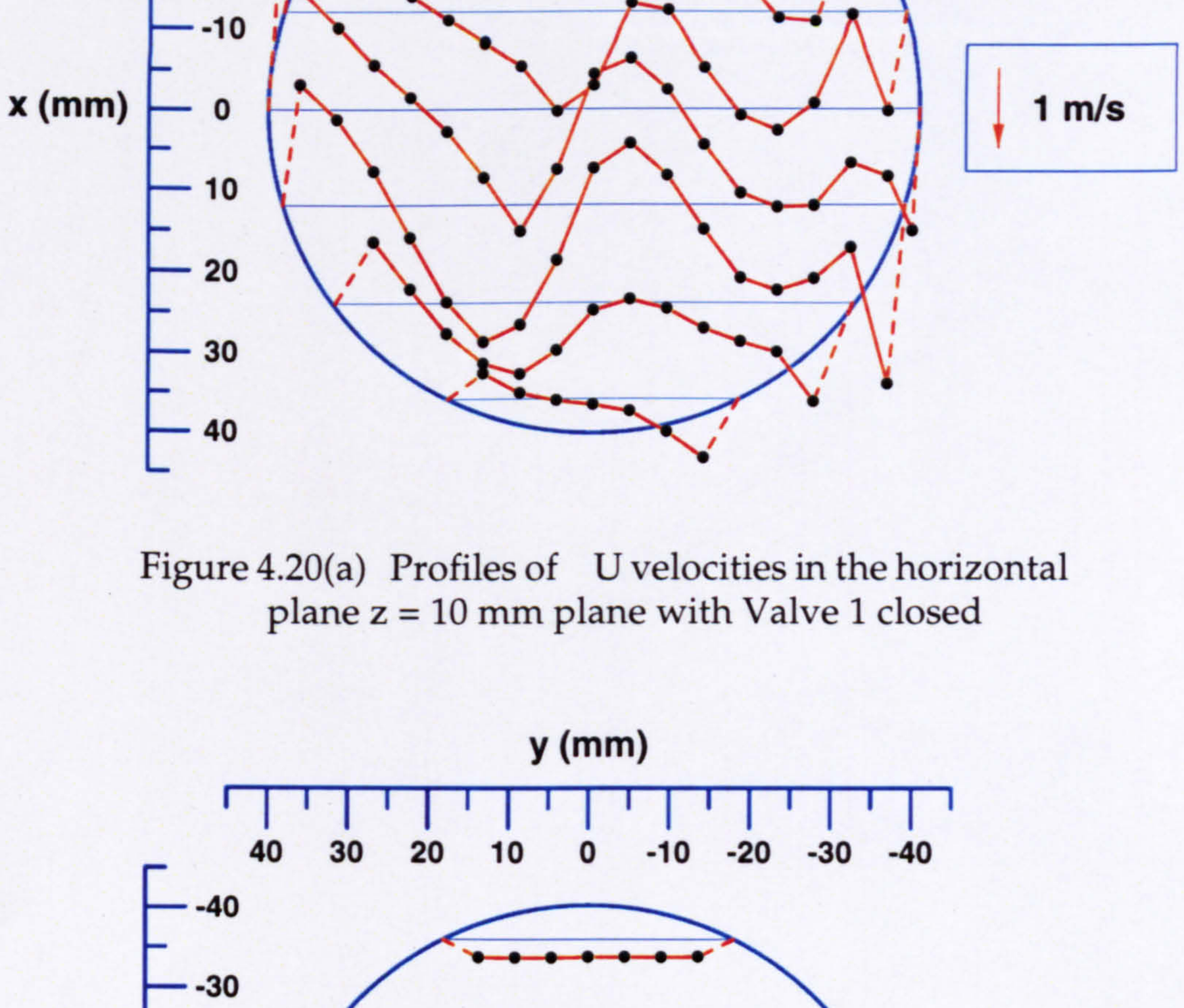

Figure 4.20(b) Profiles of u' velocities in the horizontal plane z = 10 mm plane with Valve 1 closed

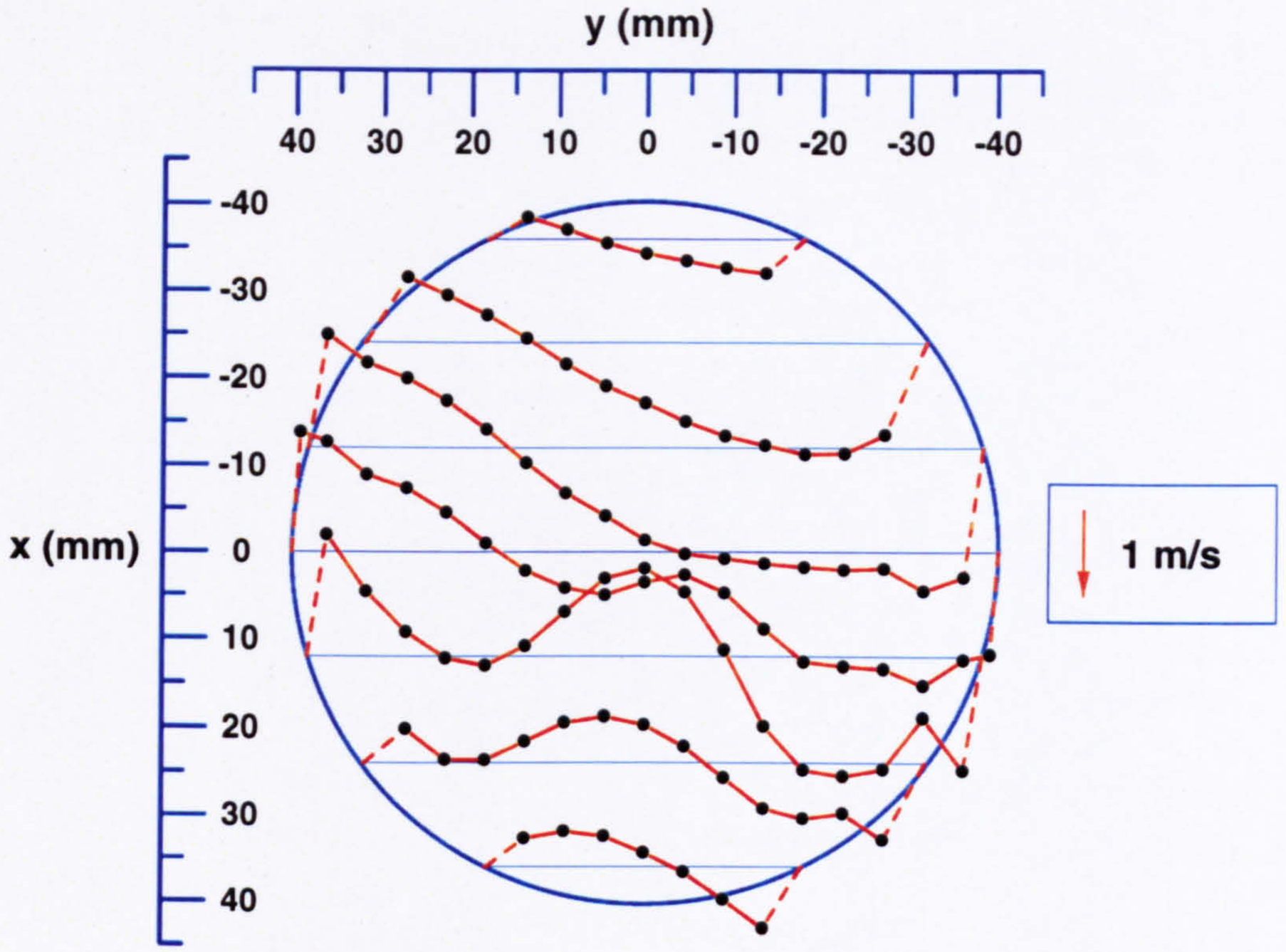

Figure 4.21(a) Profiles of U velocities in the horizontal plane z = 20 mm plane with Valve 1 closed

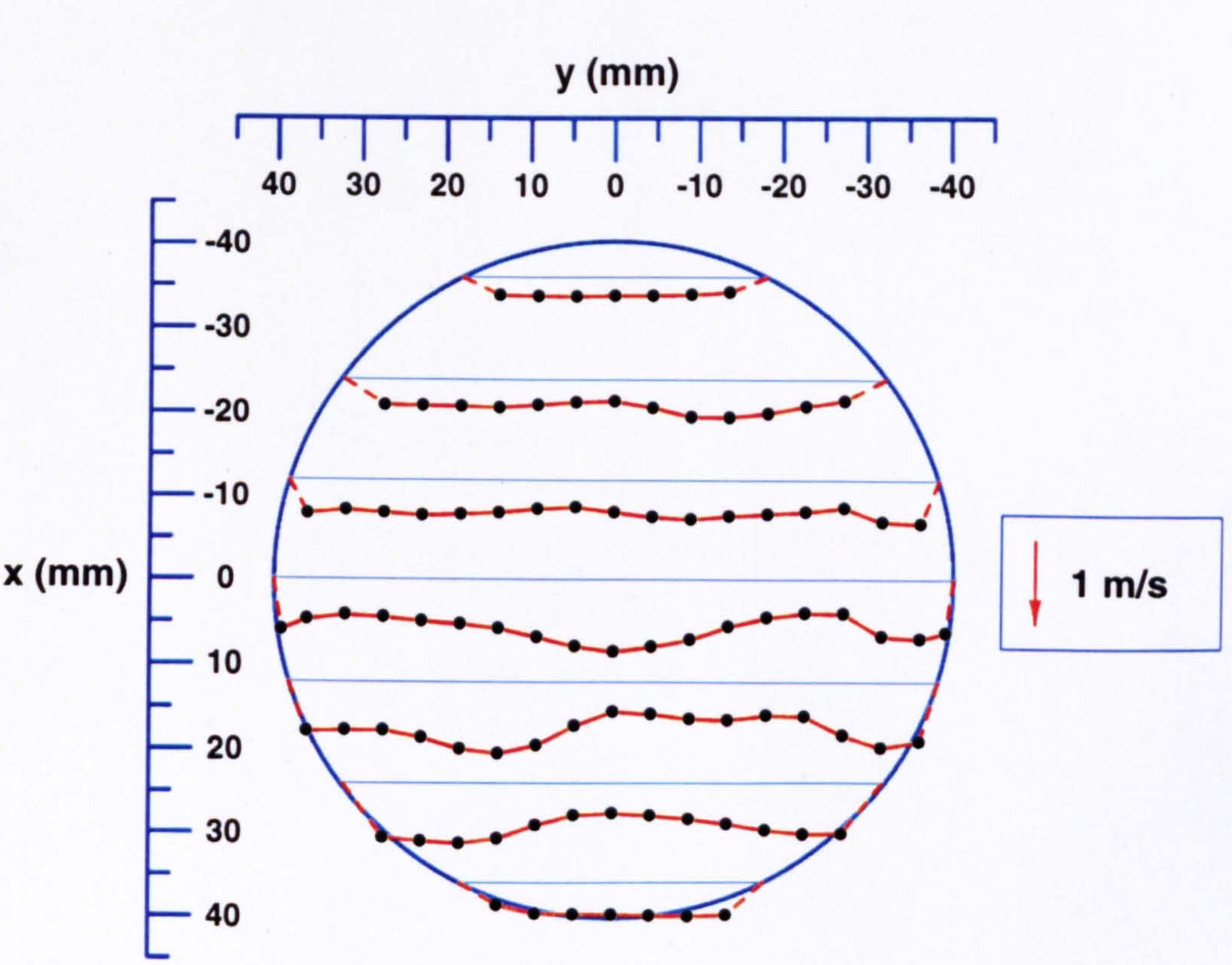

Figure 4.21(b) Profiles of u' velocities in the horizontal plane z = 20 mm plane with Valve 1 closed

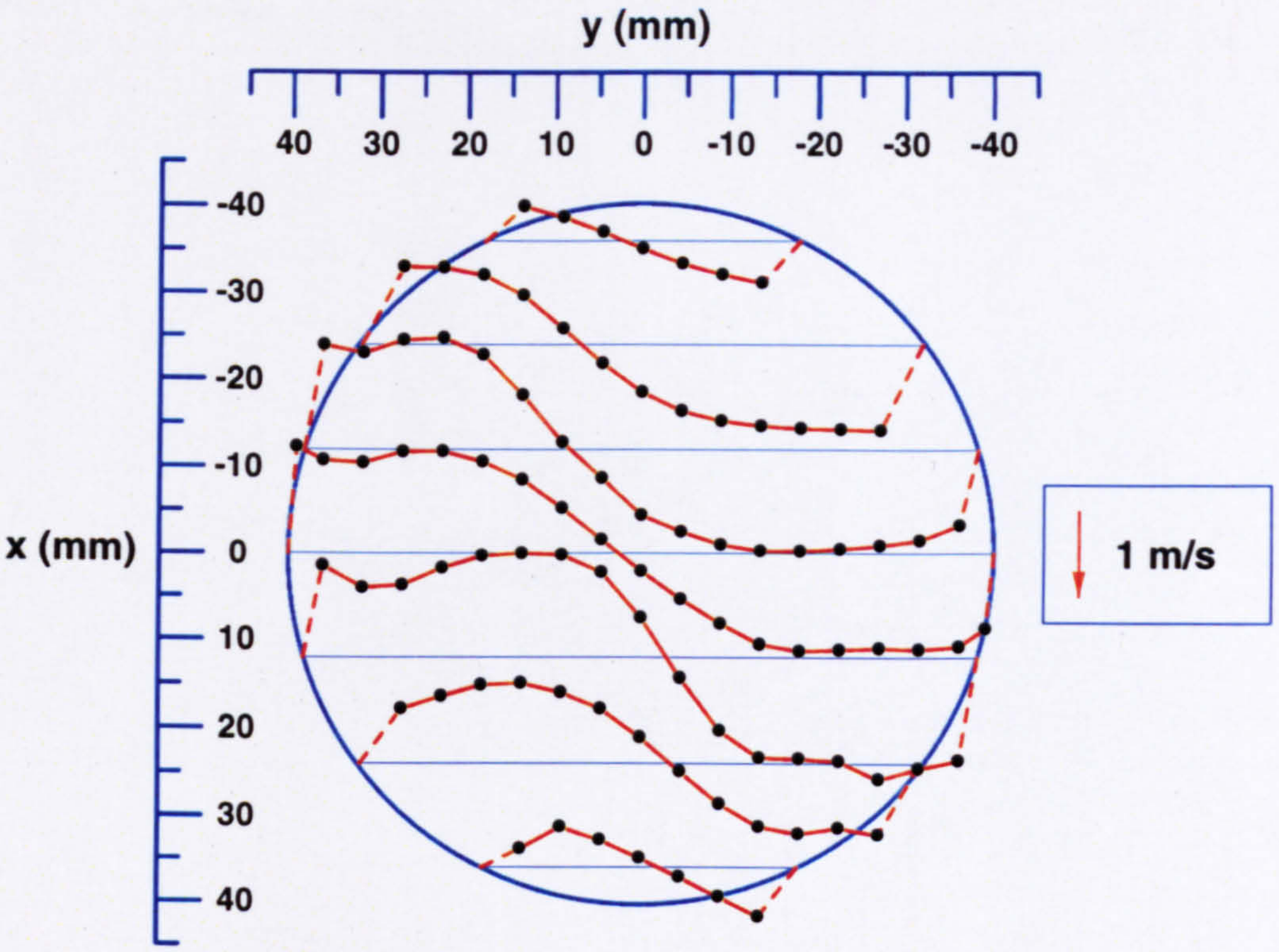

Figure 4.22(a) Profiles of U velocities in the horizontal plane z = 30 mm plane with Valve 1 closed

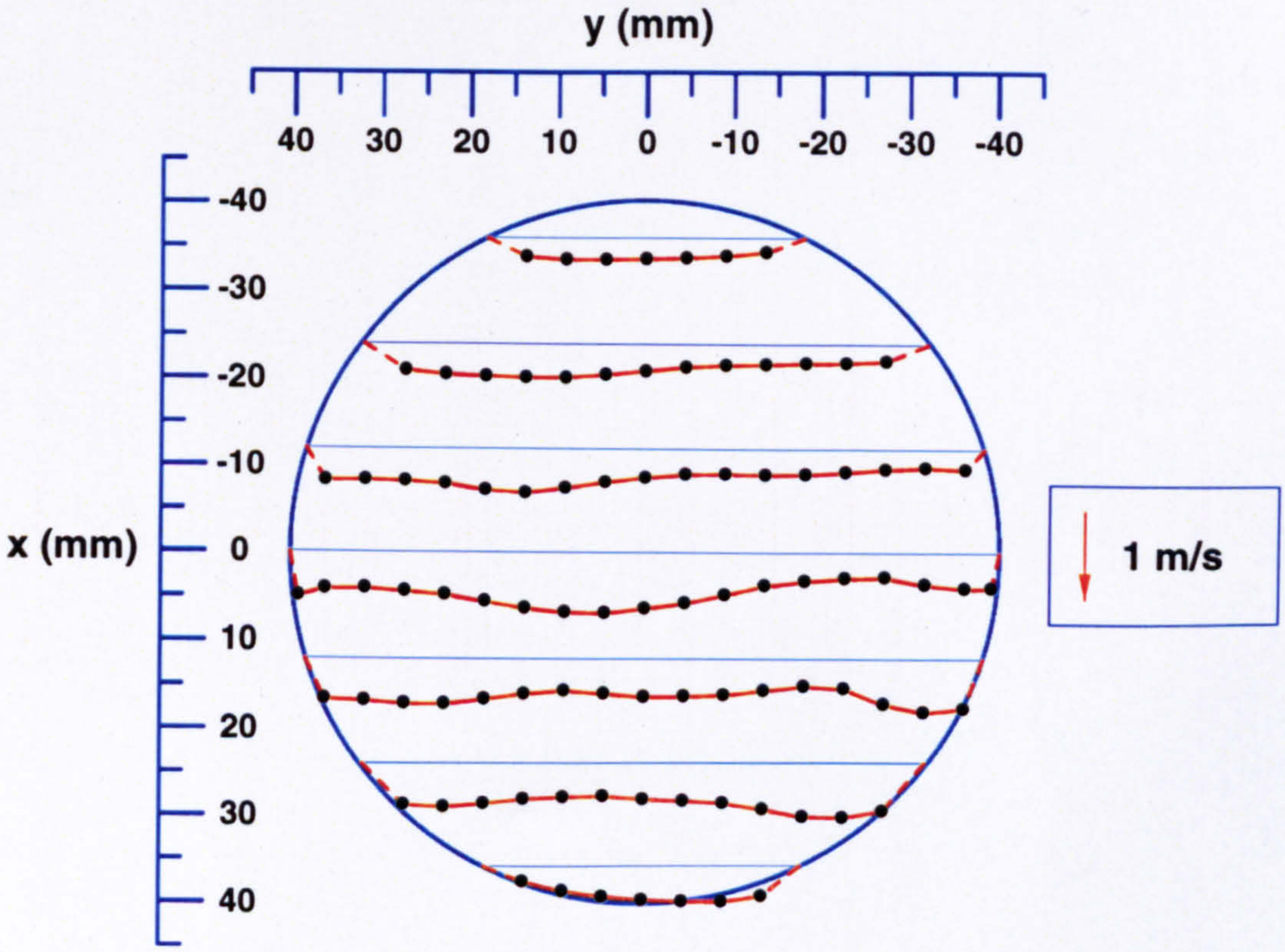

Figure 4.22(b) Profiles of u' velocities in the horizontal plane z = 30 mm plane with Valve 1 closed

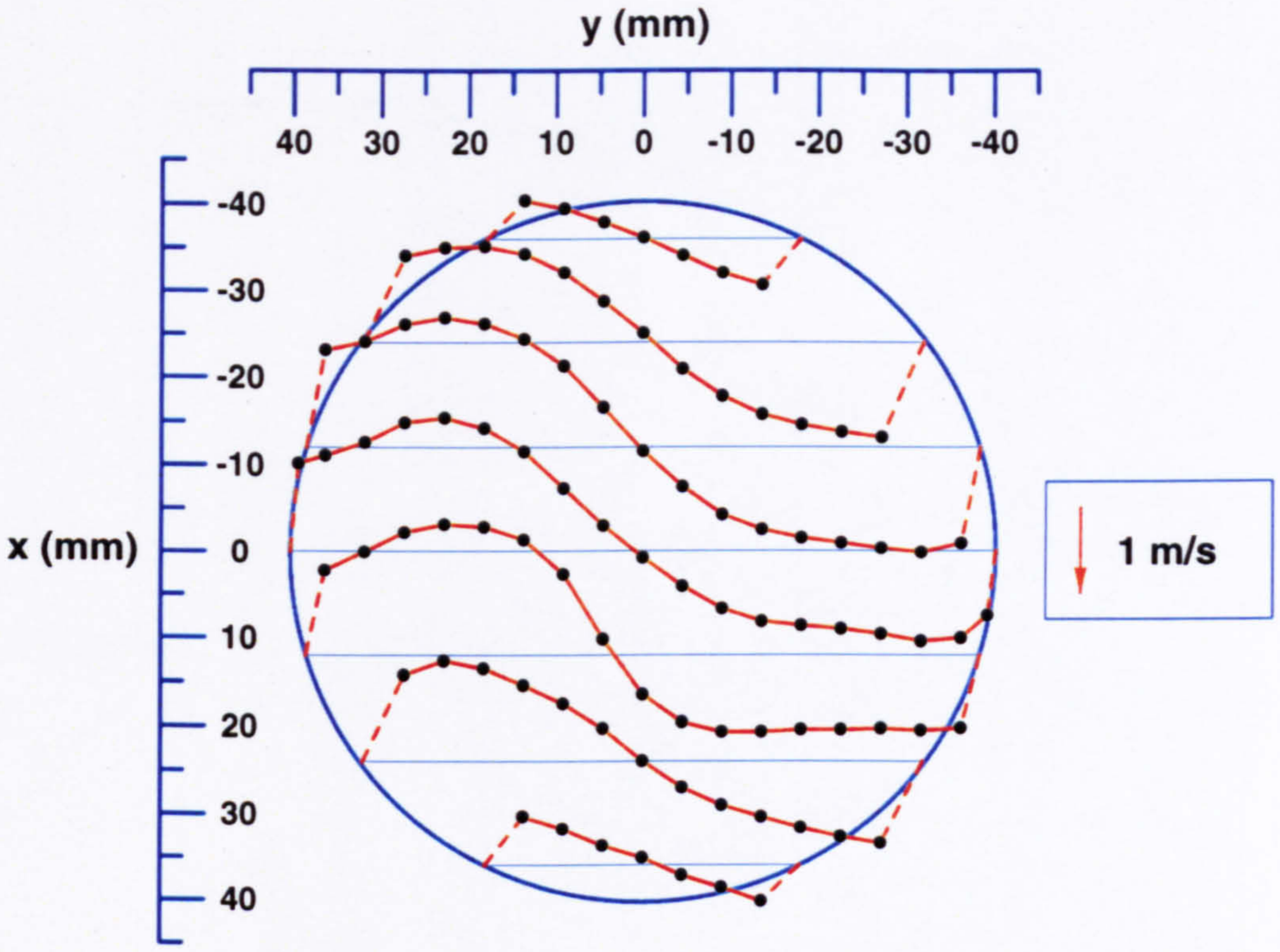

Figure 4.23(a) Profiles of U velocities in the horizontal plane z = 40 mm plane with Valve 1 closed

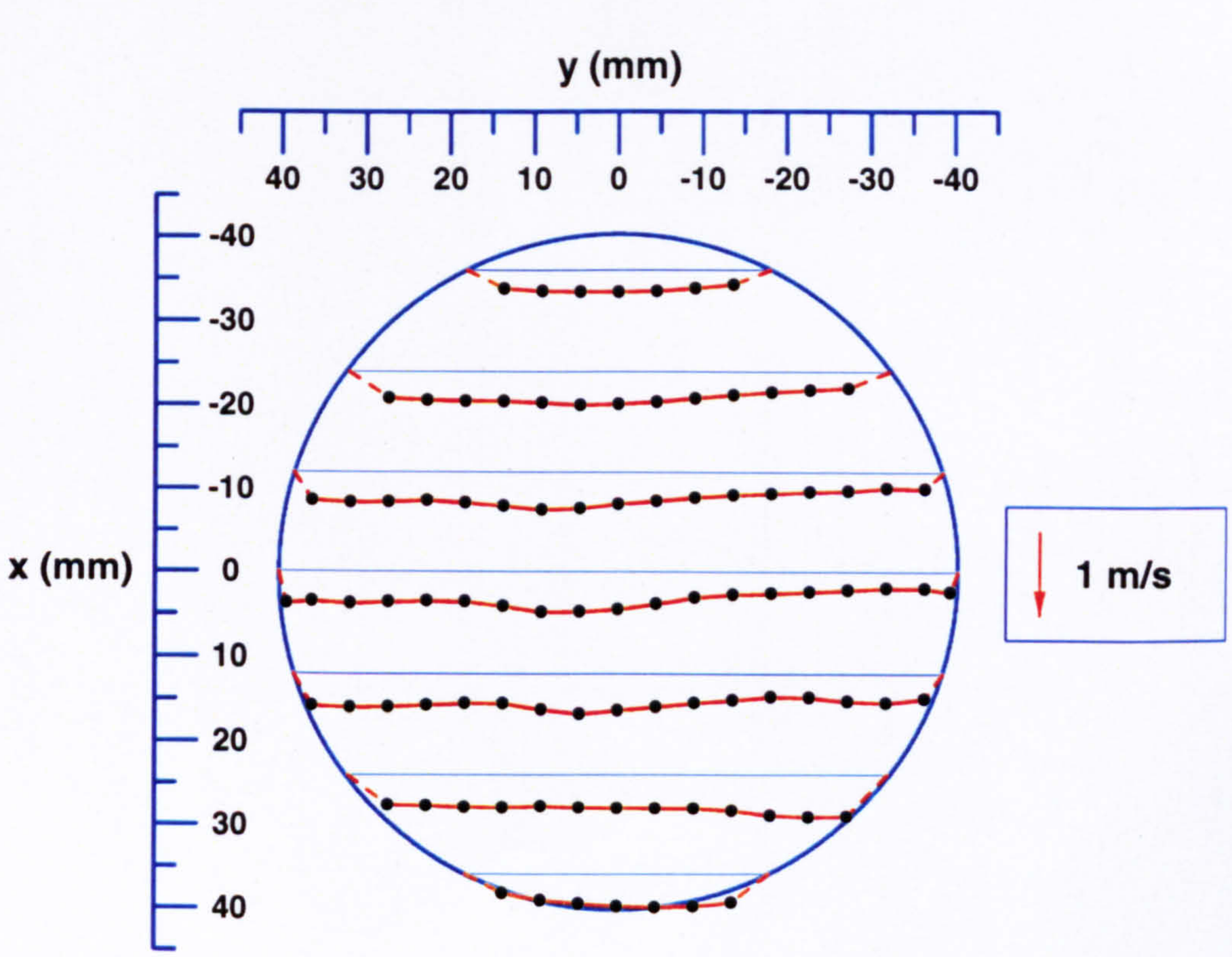

Figure 4.23(b) Profiles of u' velocities in the horizontal plane z = 40 mm plane with Valve 1 closed

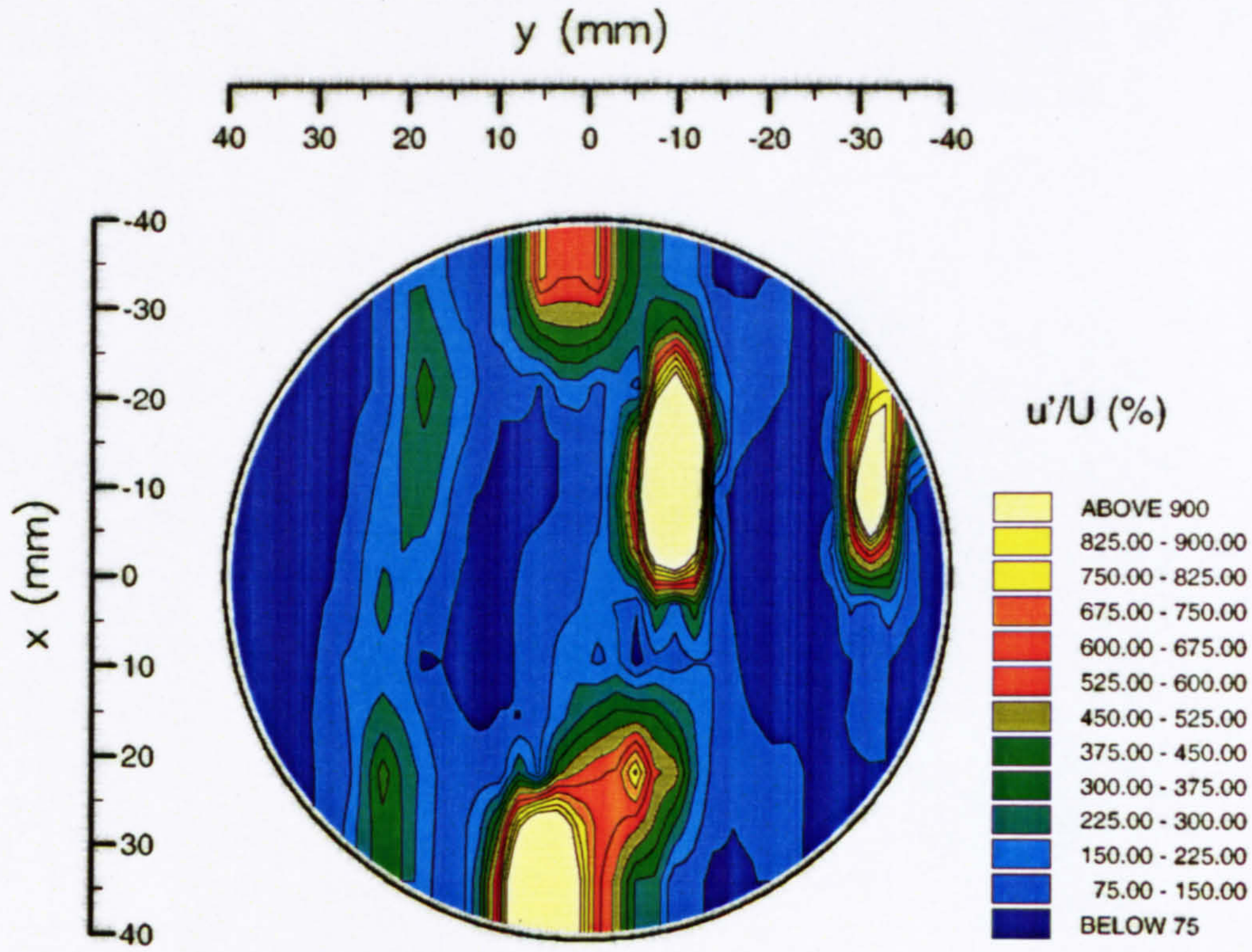

Figure 4.24(a) Contours of turbulence intensity u'/U for flow in the horizontal plane z = 10 mm with Valve 1 closed

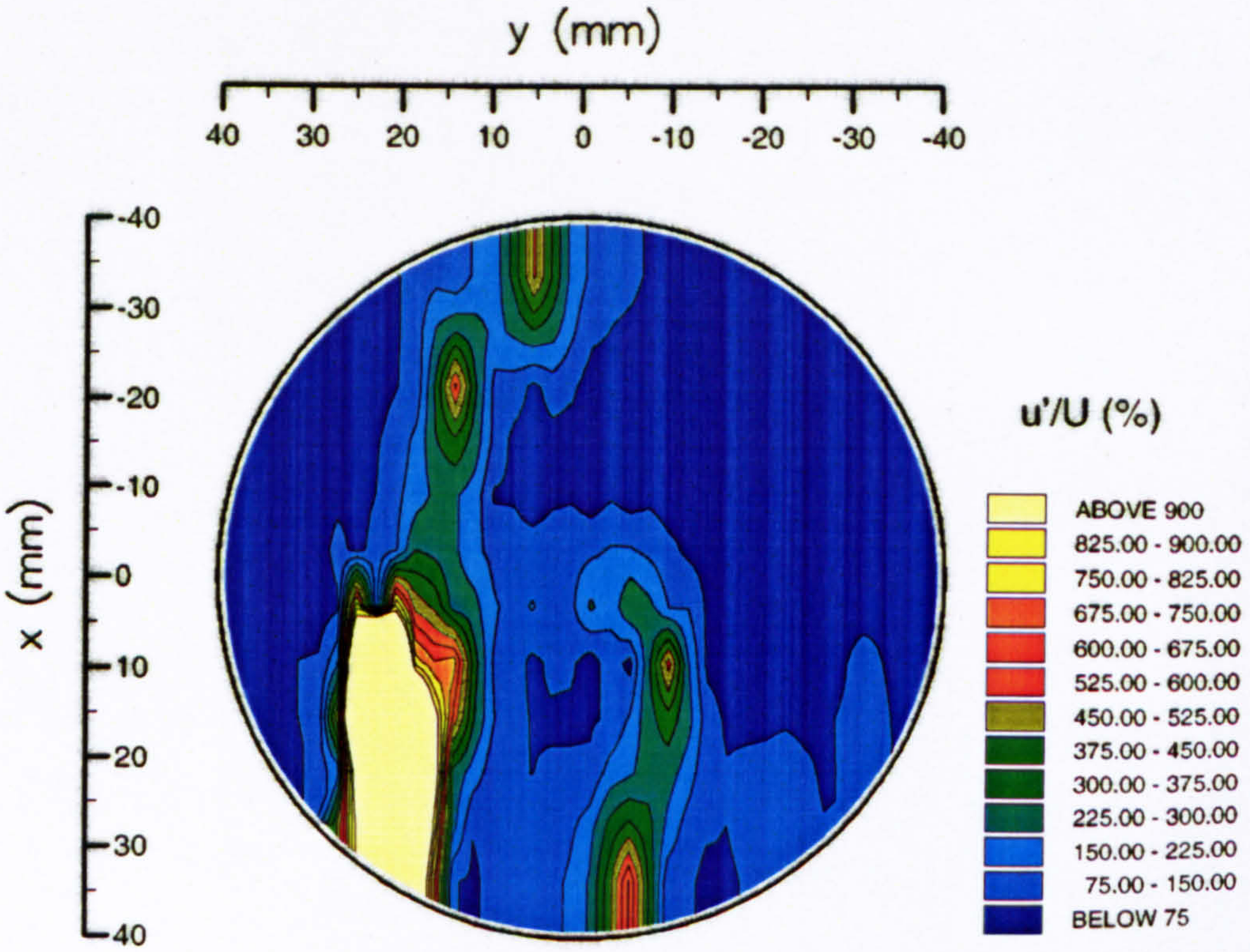

Figure 4.24(b) Contours of turbulence intensity u'/U for flow in the horizontal plane z = 20 mm with Valve 1 closed

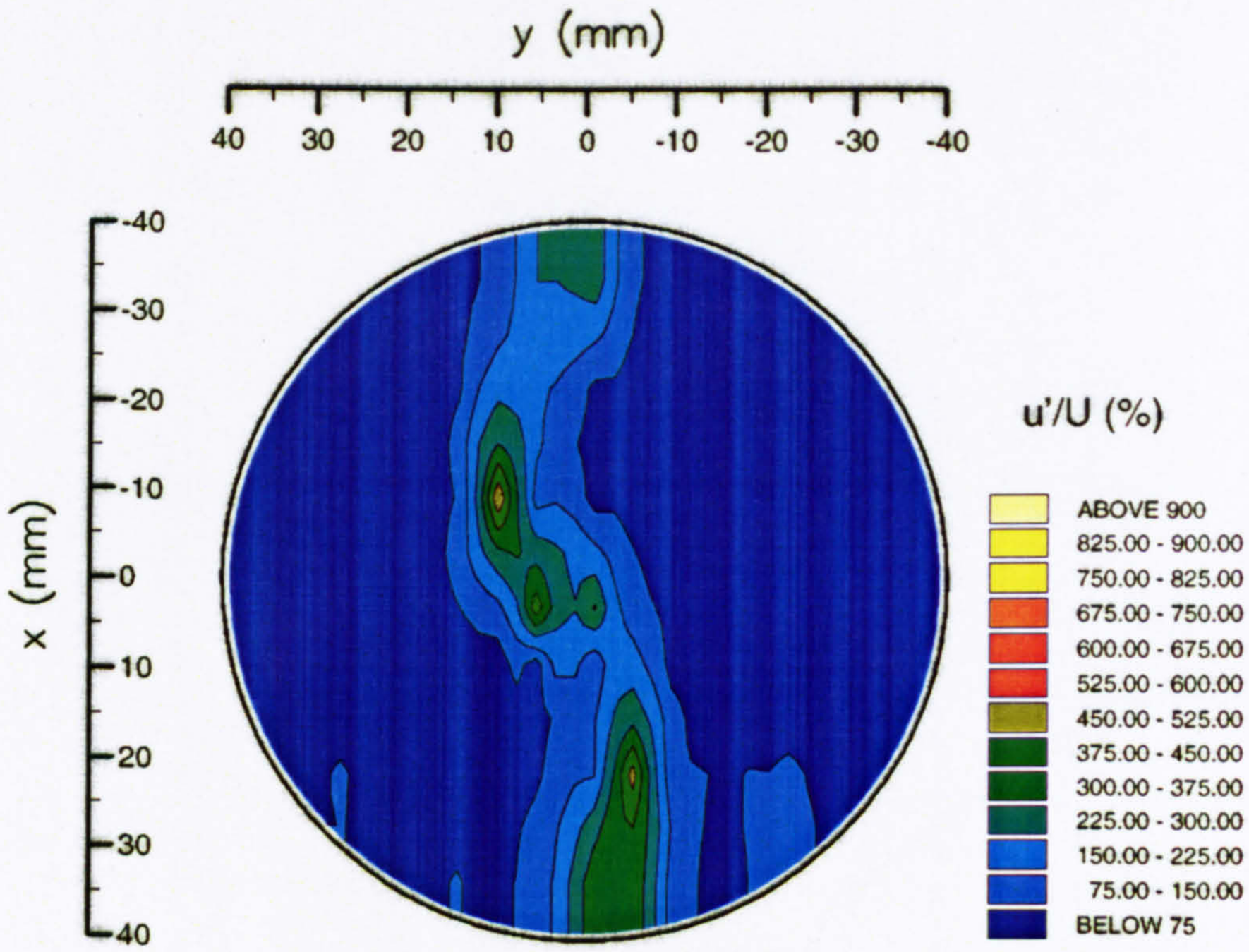

Figure 4.24(c) Contours of turbulence intensity u'/U for flow in the horizontal plane z = 30 mm with Valve 1 closed

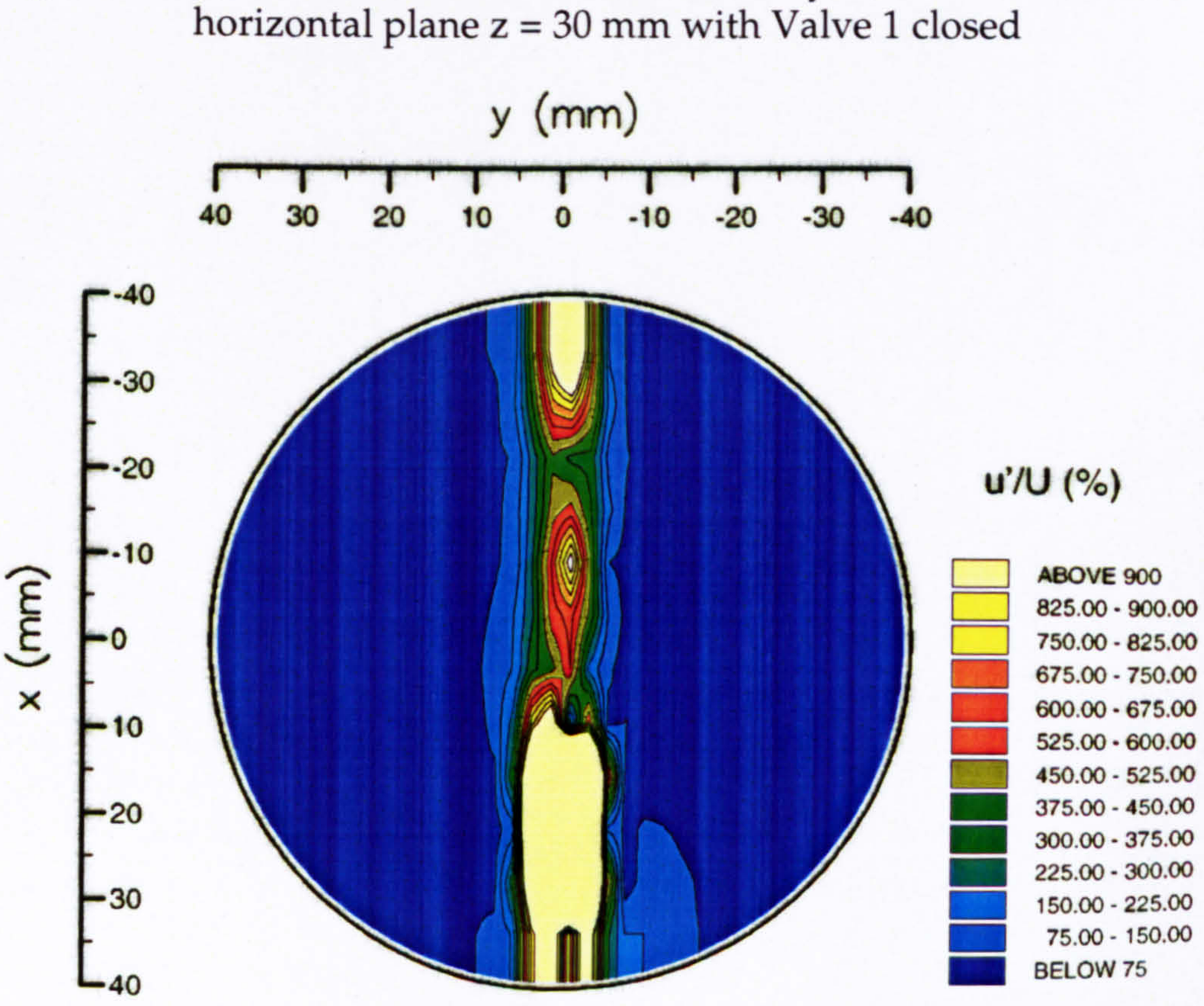

Figure 4.24(d) Contours of turbulence intensity u'/U for flow in the horizontal plane z = 40 mm with Valve 1 closed

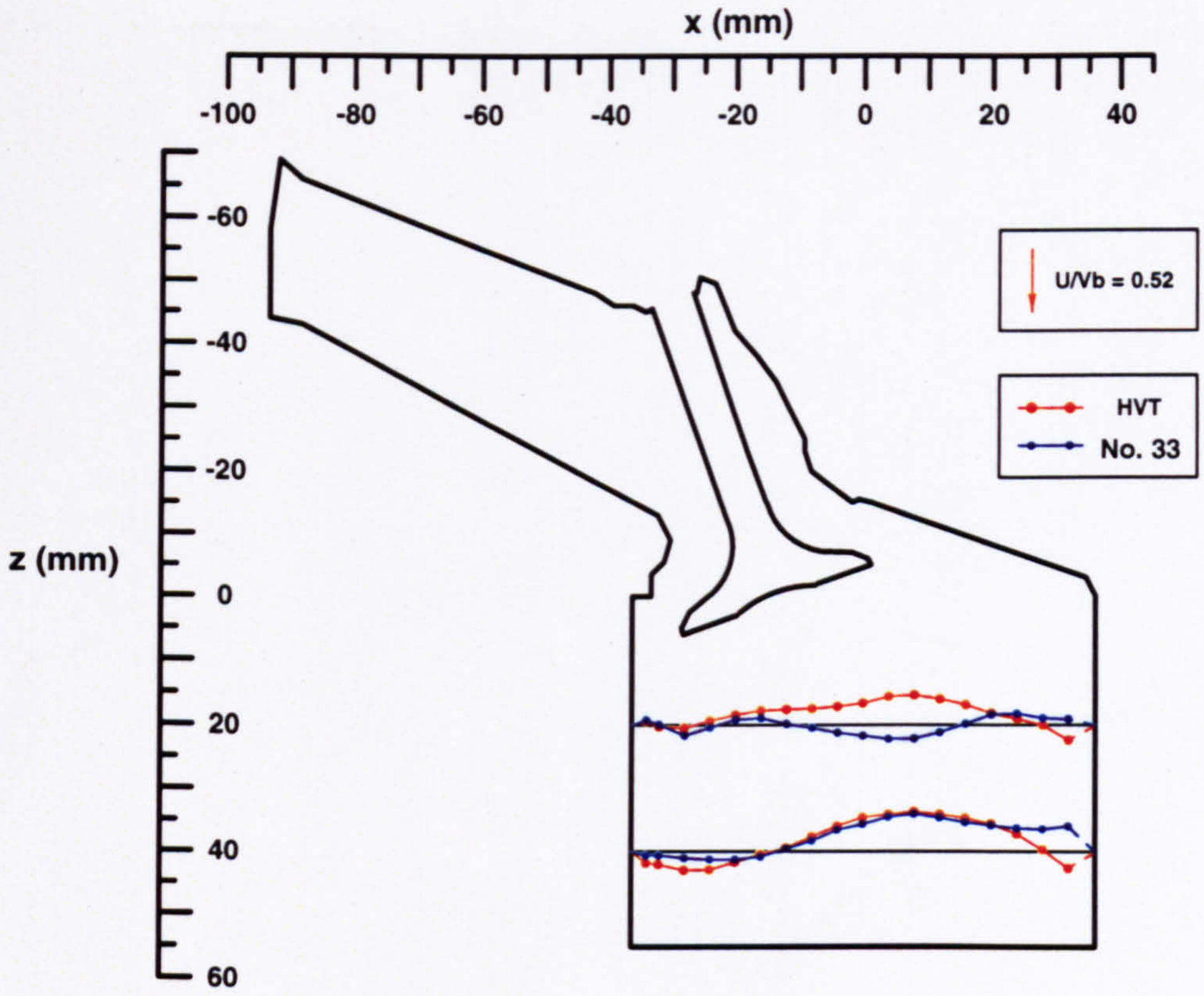

Figure 4.25(a) Comparison of normalised mean U velocities in the y = -17.6 mm plane with 10 mm valve lifts

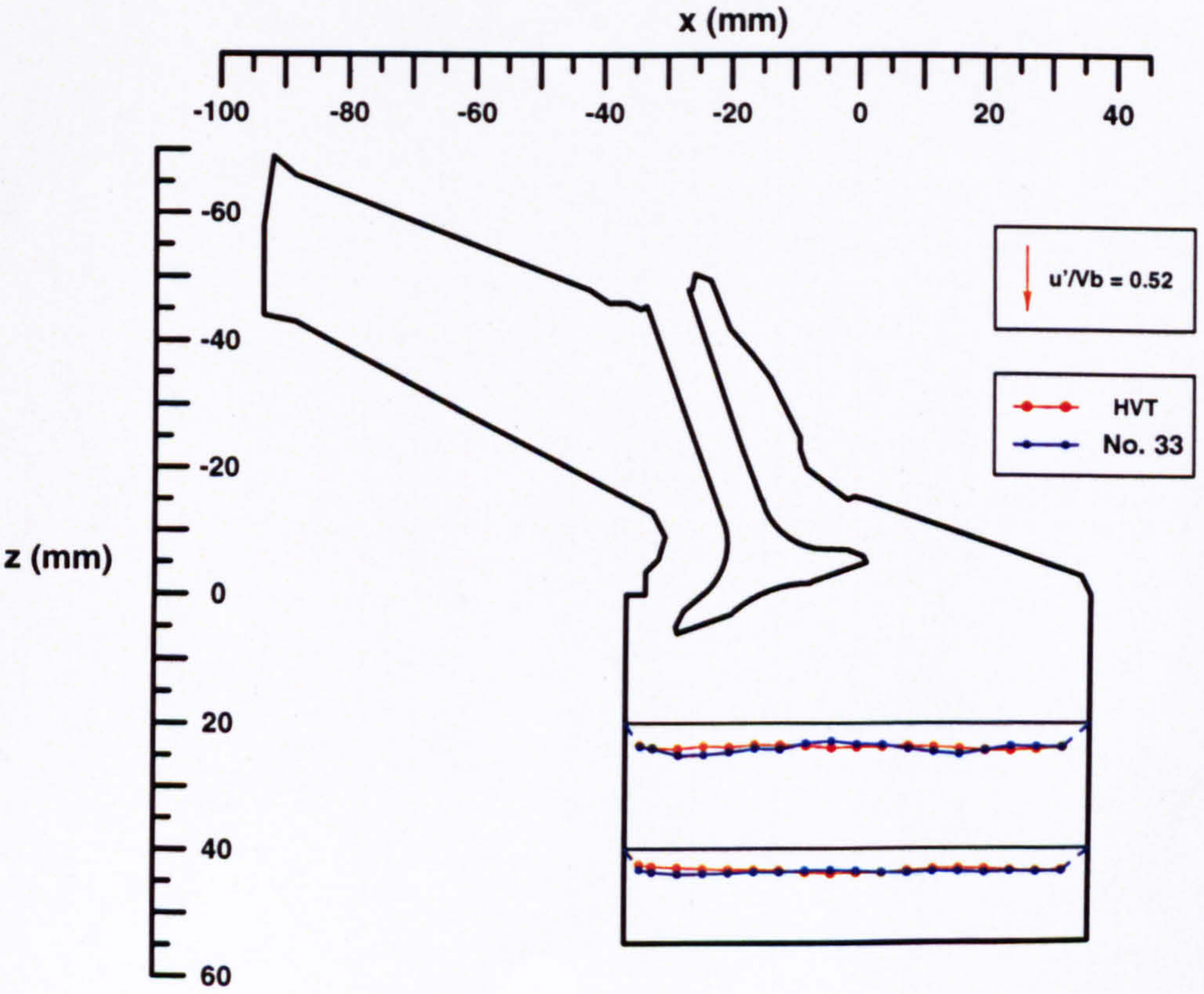

Figure 4.25(b) Comparison of normalised r.m.s. u' velocities in the y = -17.6 mm plane with 10 mm valve lifts

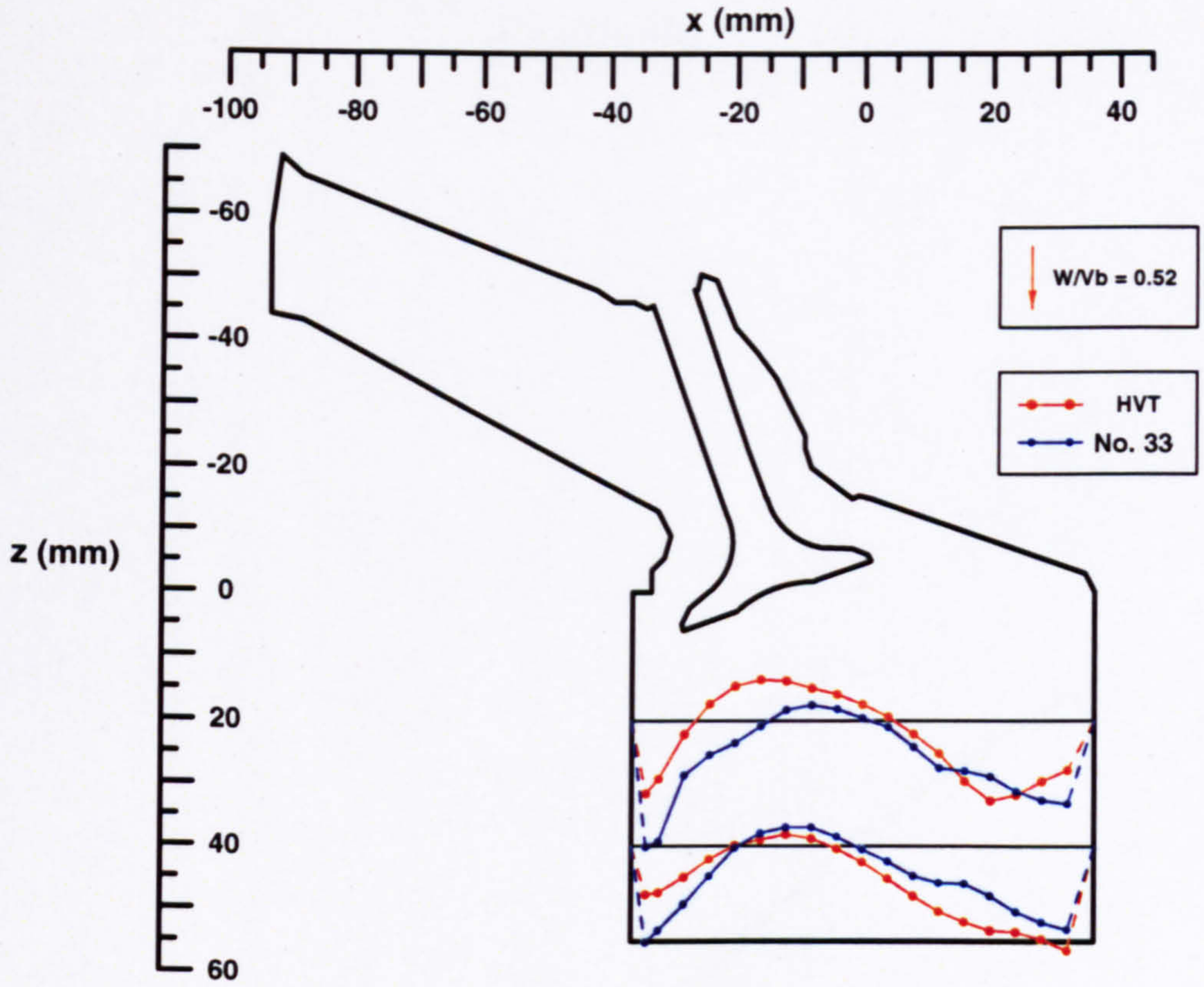

Figure 4.25(c) Comparison of normalised mean W velocities in the y = -17.6 mm plane with 10 mm valve lifts

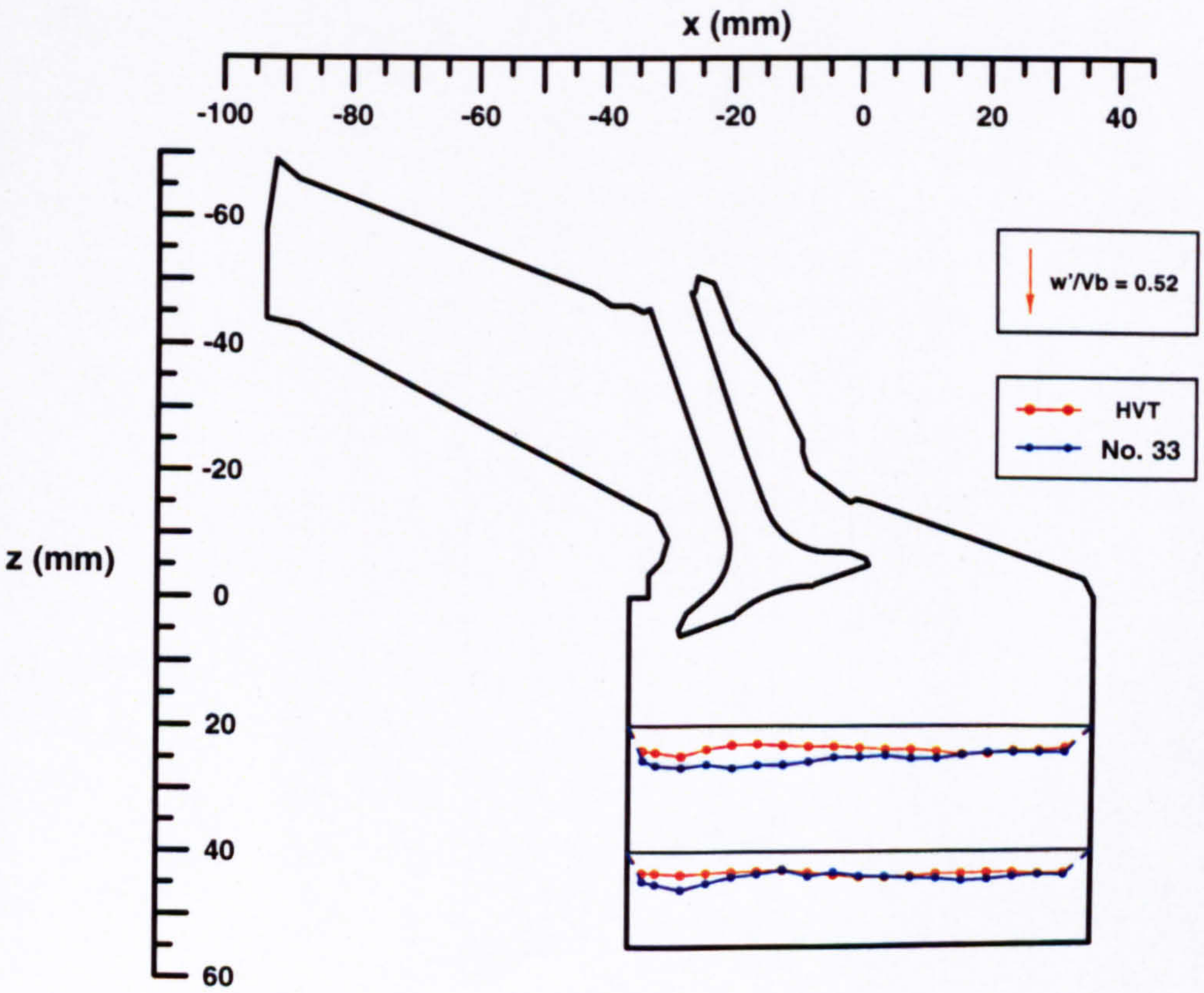

Figure 4.25(d) Comparison of normalised r.m.s. w' velocities in the y = -17.6 mm plane with 10 mm valve lifts

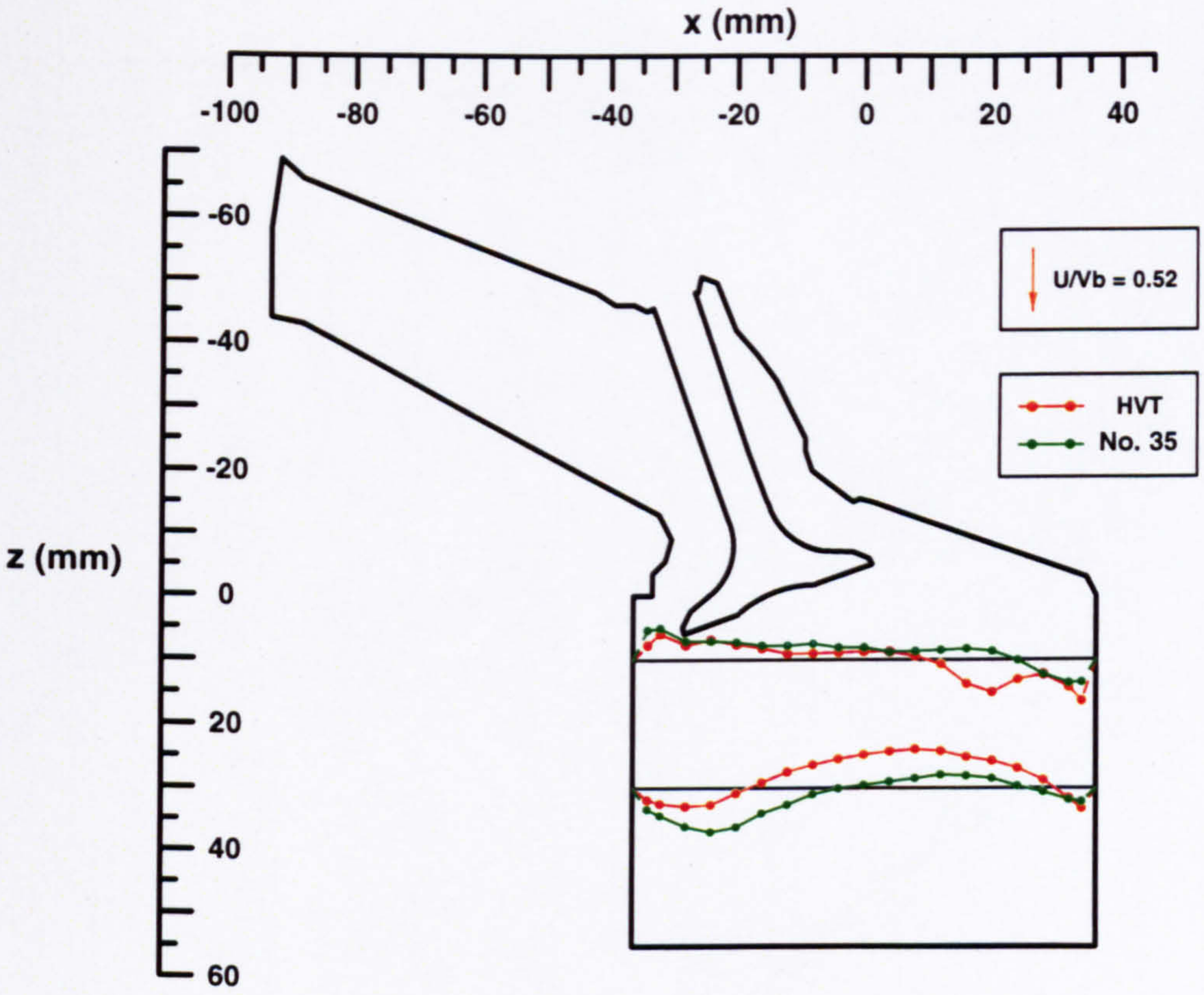

Figure 4.26(a) Comparison of normalised mean U velocities in the y = -17.6 mm plane with 10 mm valve lifts

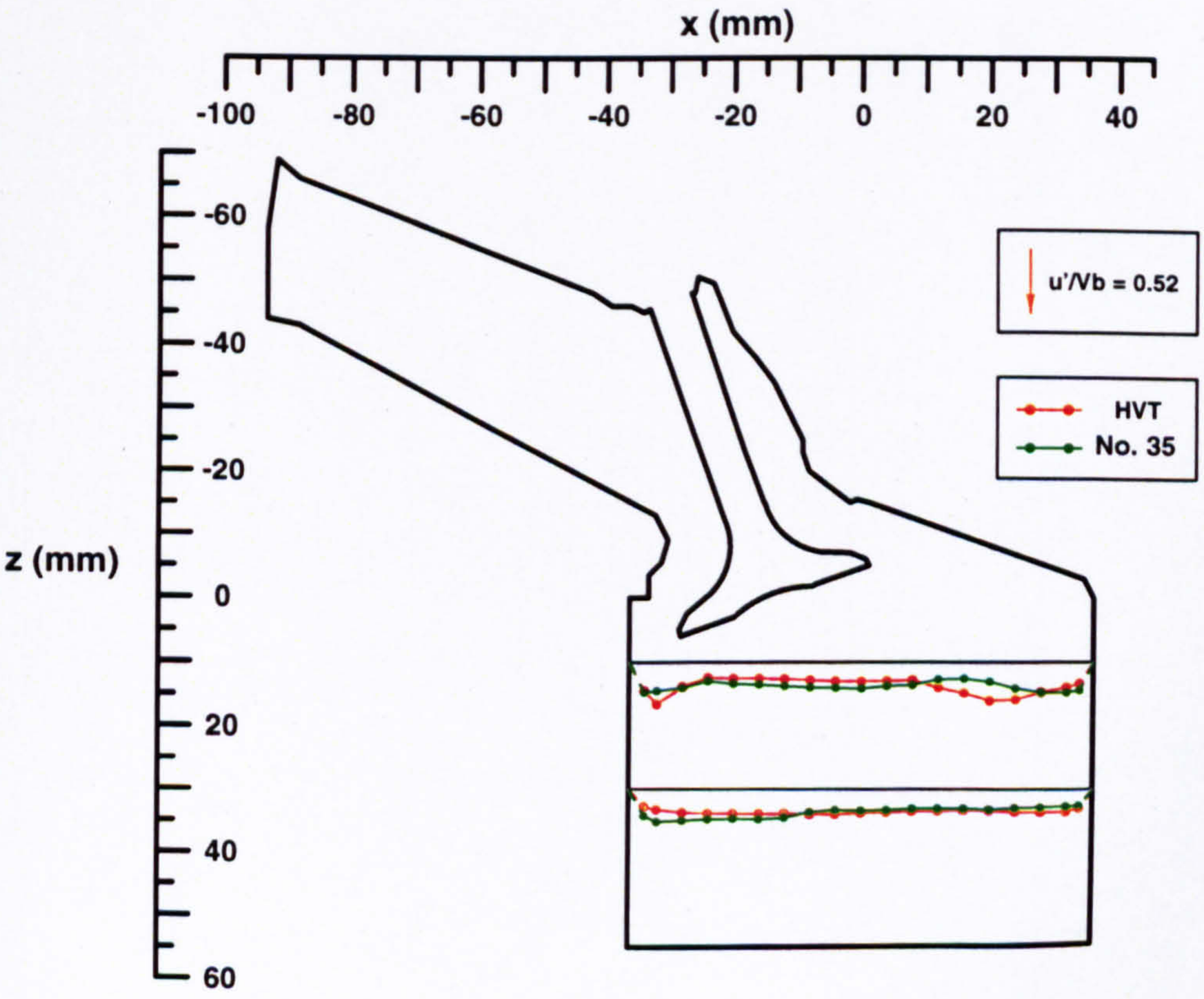

Figure 4.26(b) Comparison of normalised r.m.s. u' velocities in the y = -17.6mm plane with 10 mm valve lifts

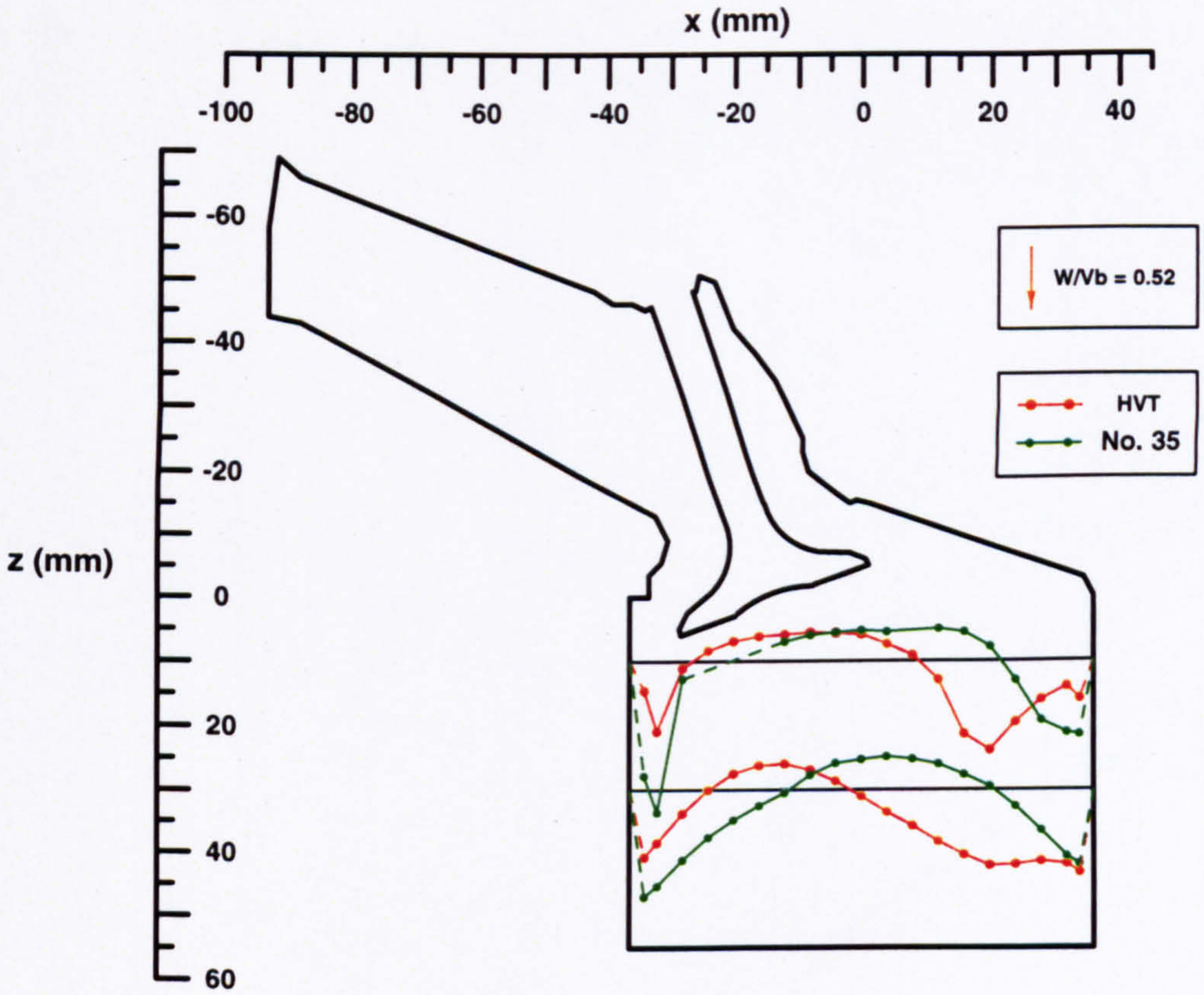

Figure 4.26(c): Comparison of normalised mean W velocities in the y = -17.6 mm plane with 10 mm valve lifts

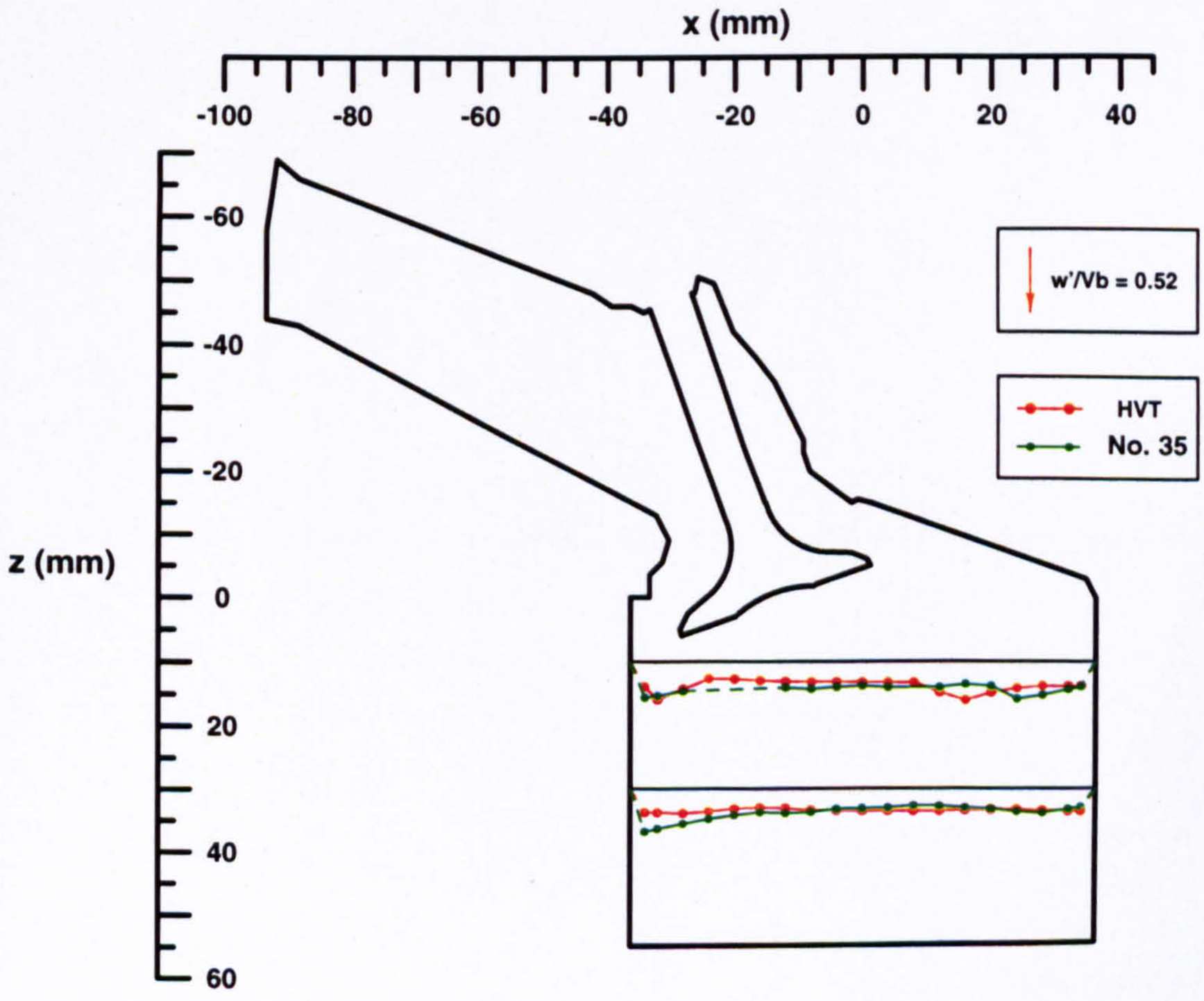

Figure 4.26(d) Comparison of normalised r.m.s. w' velocities in the y = -17.6 mm plane with 10 mm valve lifts

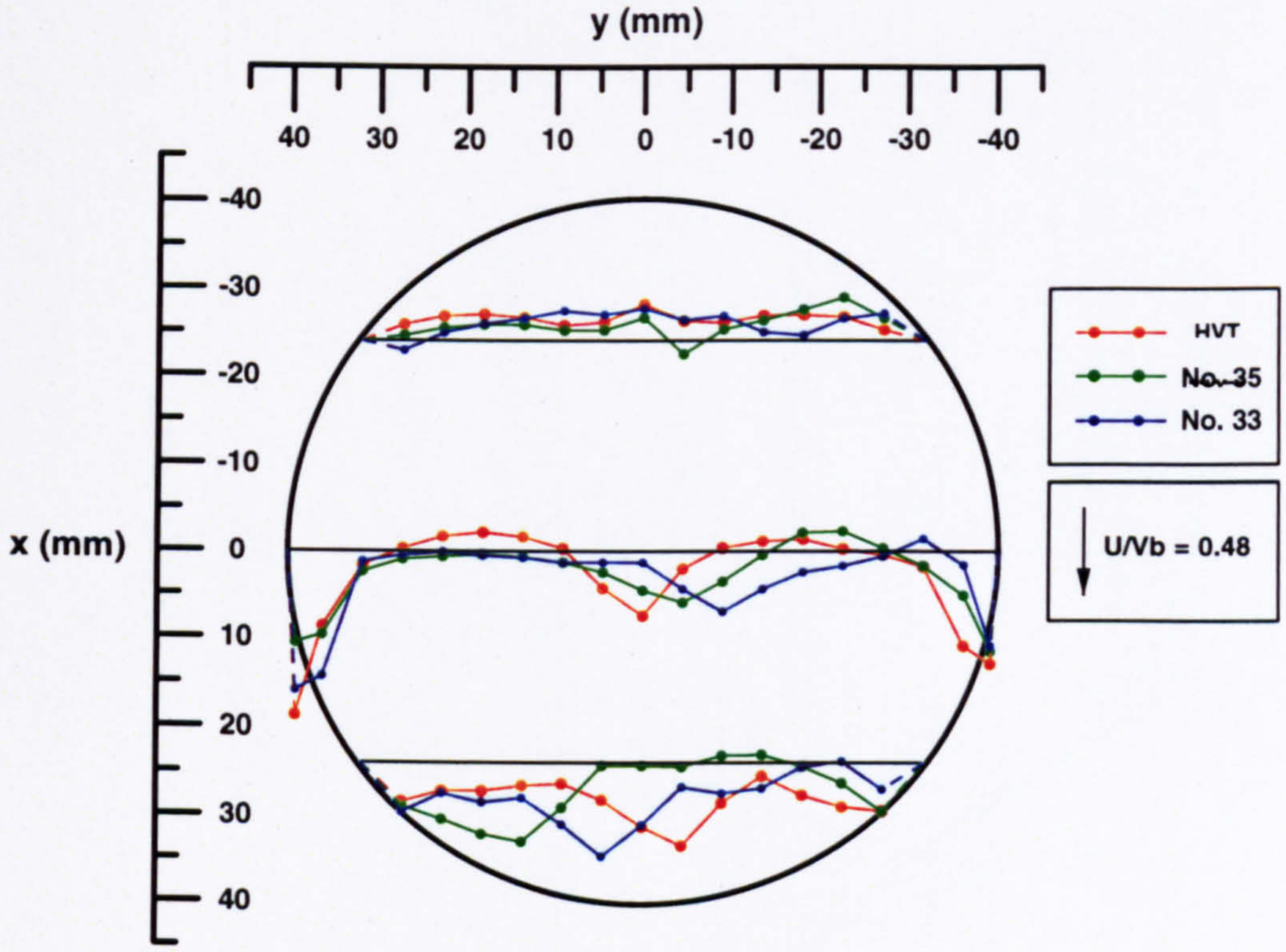

Figure 4.27(a) Comparison of normalised mean U velocities in the horizontal z = 10 mm plane with 10 mm valve lifts

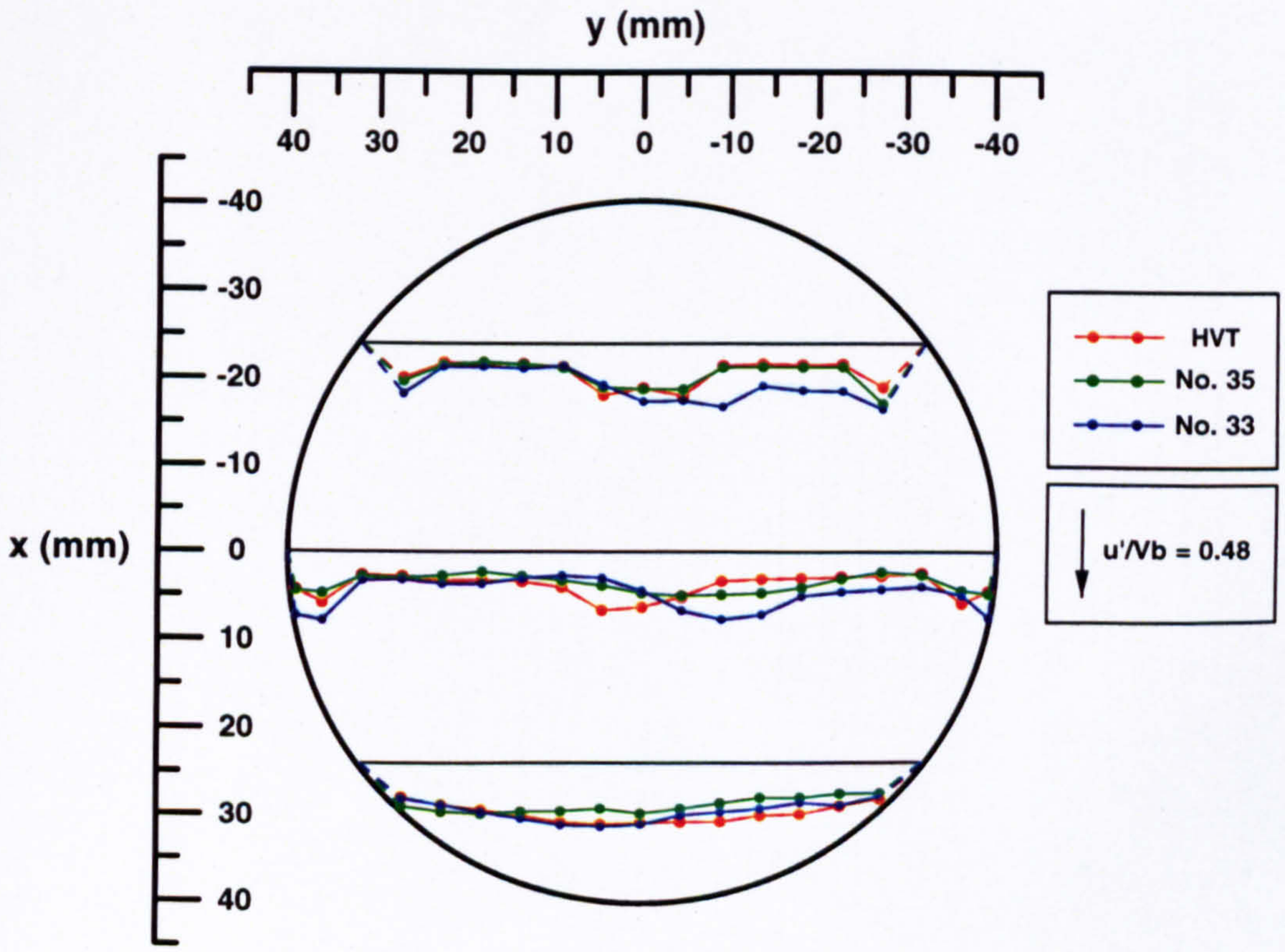

Figure 4.27(b) Comparison of normalised r.m.s. u' velocities in the horizontal z = 10 mm plane with 10 mm valve lifts

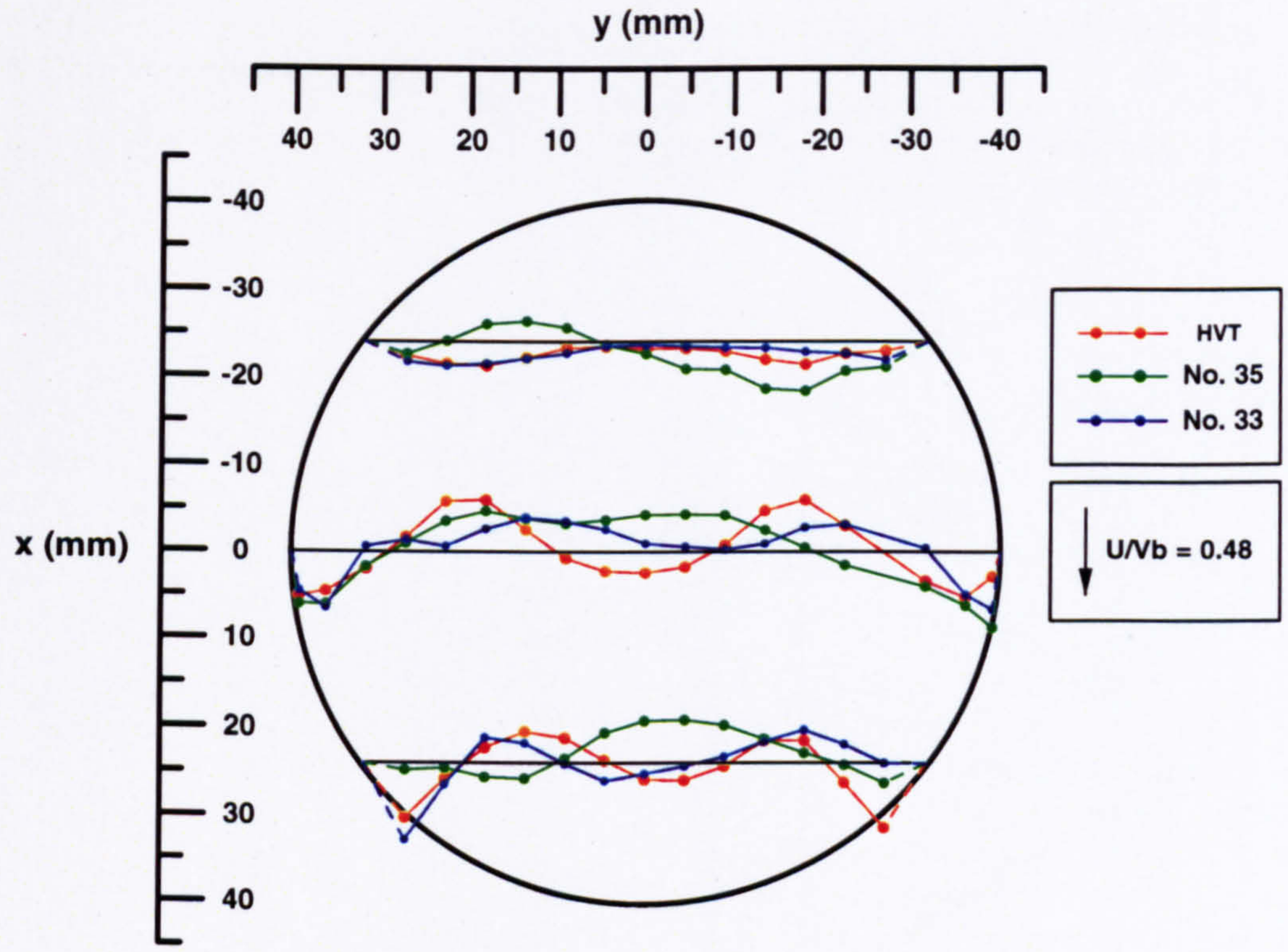

Figure 4.28(a) Comparison of normalised mean U velocities in the horizontal z = 30 mm plane with 10 mm valve lifts

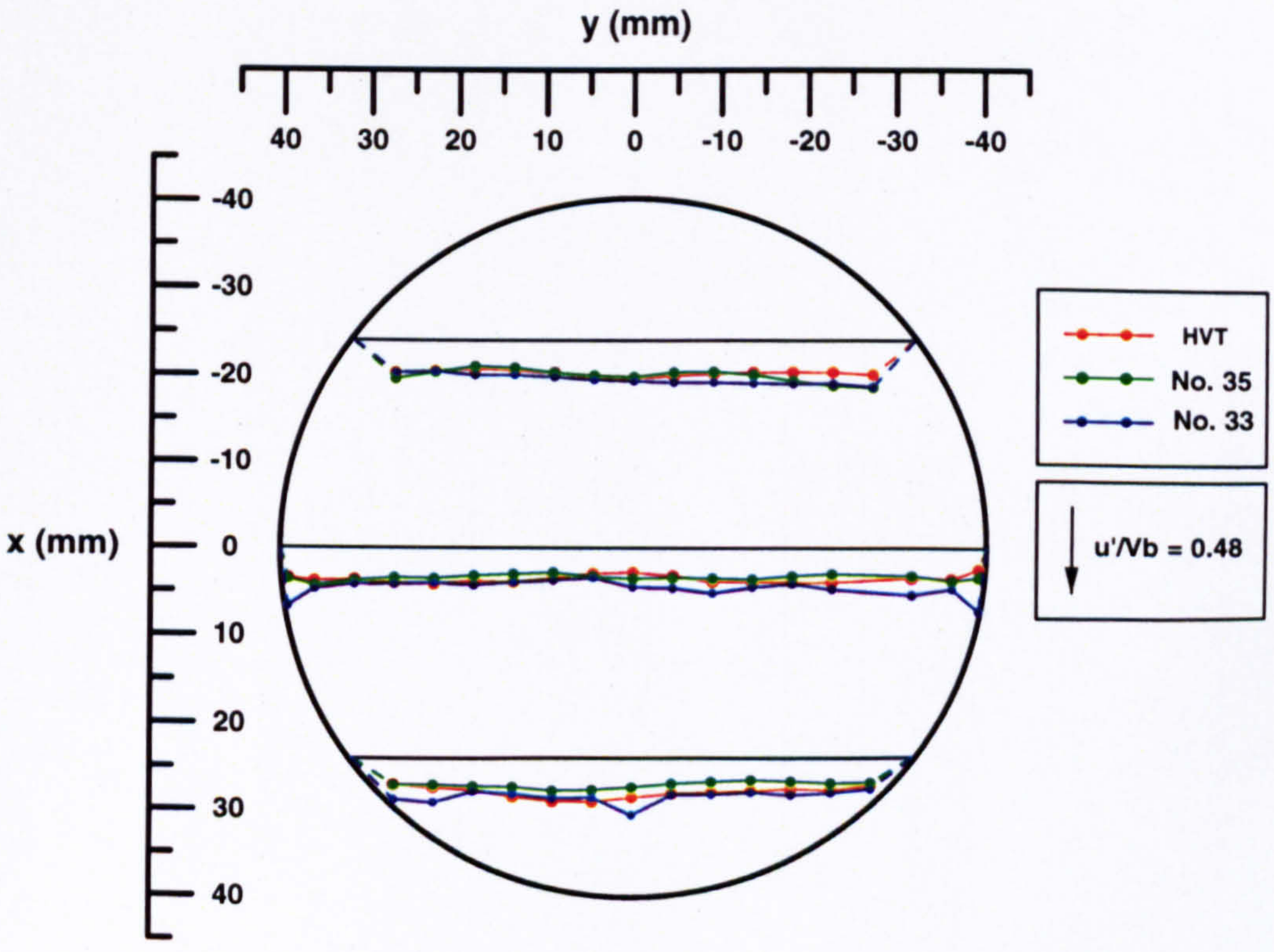

Figure 4.28(b) Comparison of normalised r.m.s. u' velocities in the horizontal z = 30 mm plane with 10 mm valve lifts

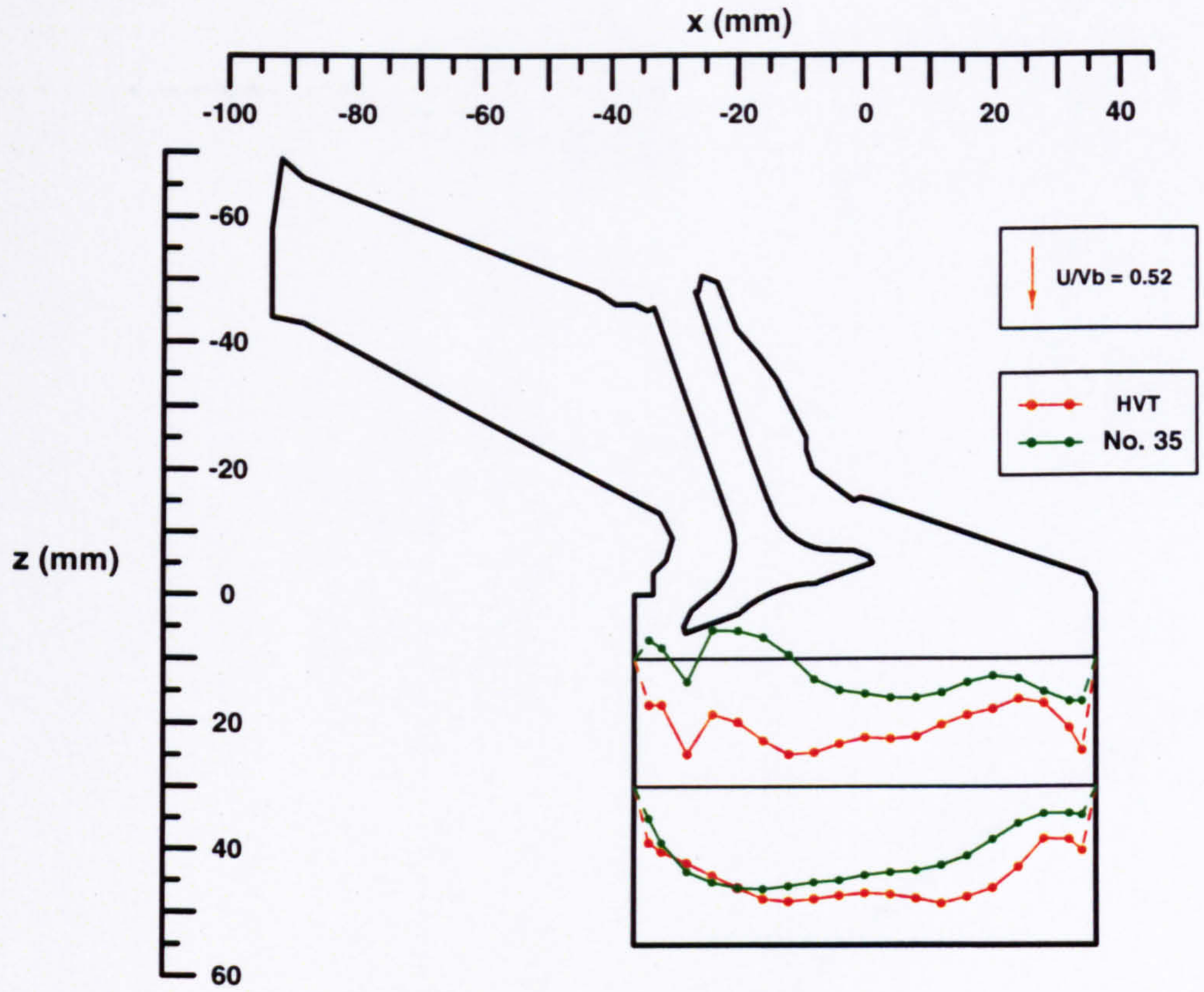

Figure 4.29(a) Comparison of normalised mean U velocities in the y = -17.6 mm plane with Valve 1 closed

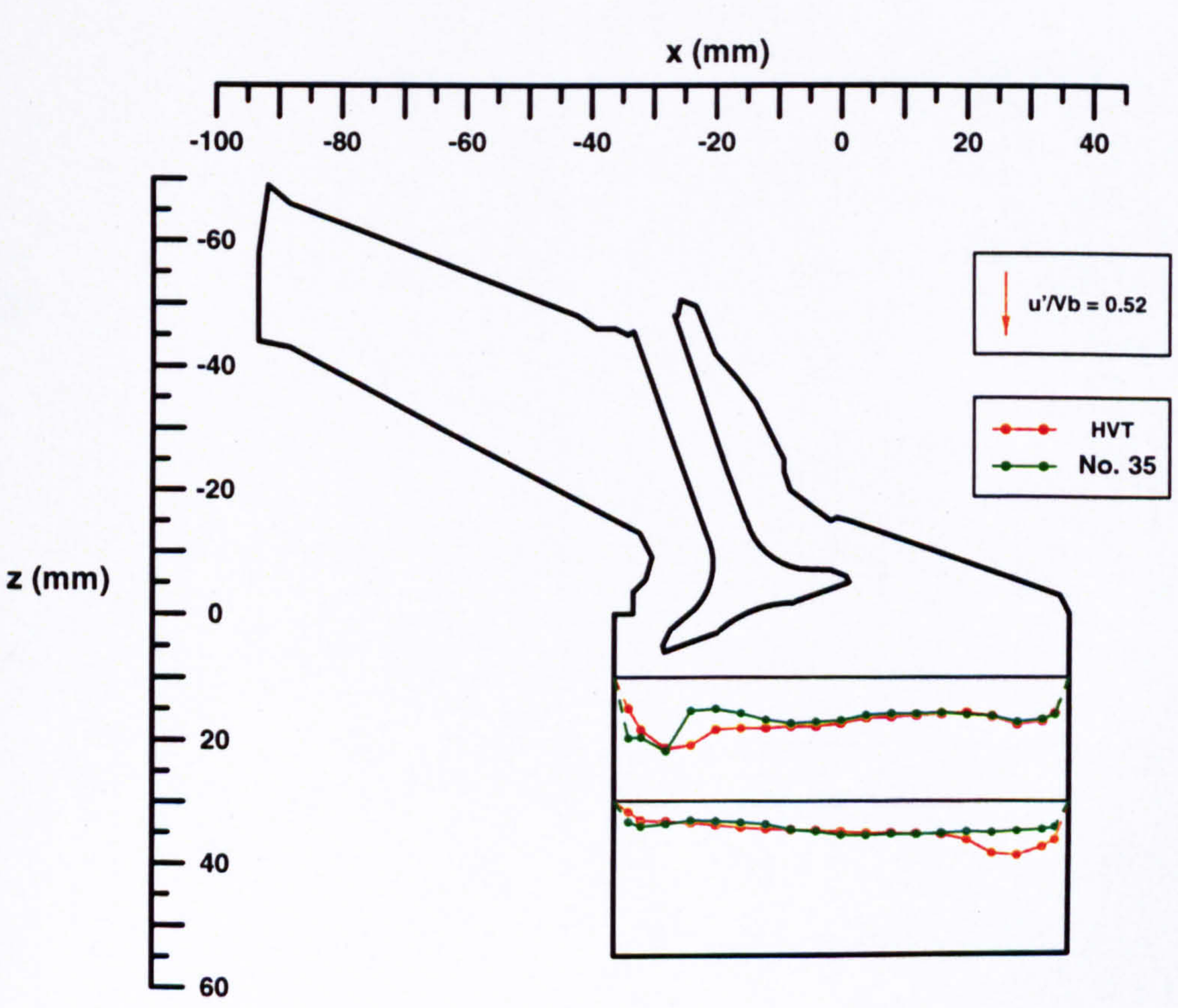

Figure 4.29(b) Comparison of normalised r.m.s. u' velocities in the y = -17.6 mm plane with Valve 1 closed

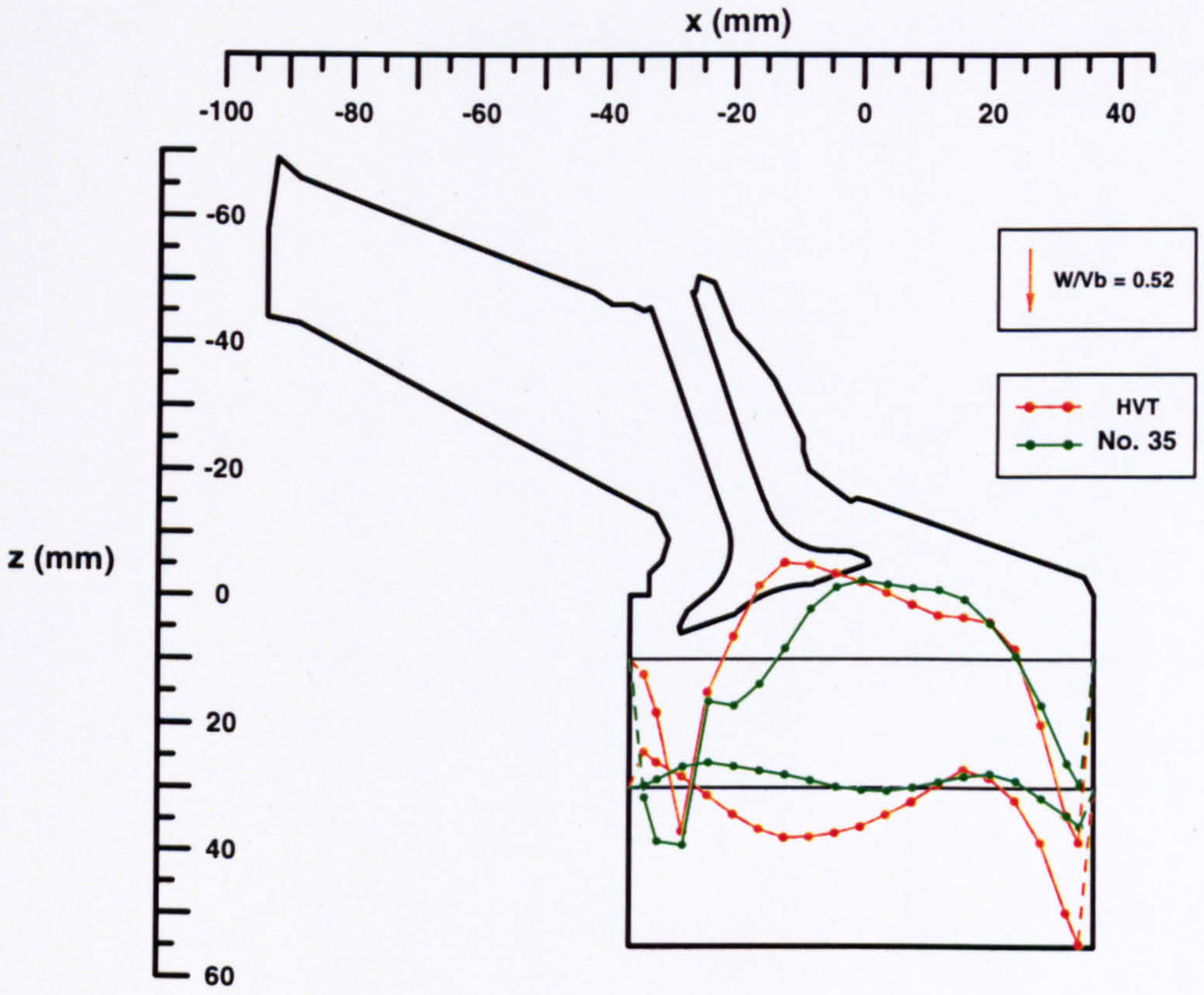

Figure 4.29(c) Comparison of normalised W velocities in the y = -17.6 mm plane with Valve 1 closed

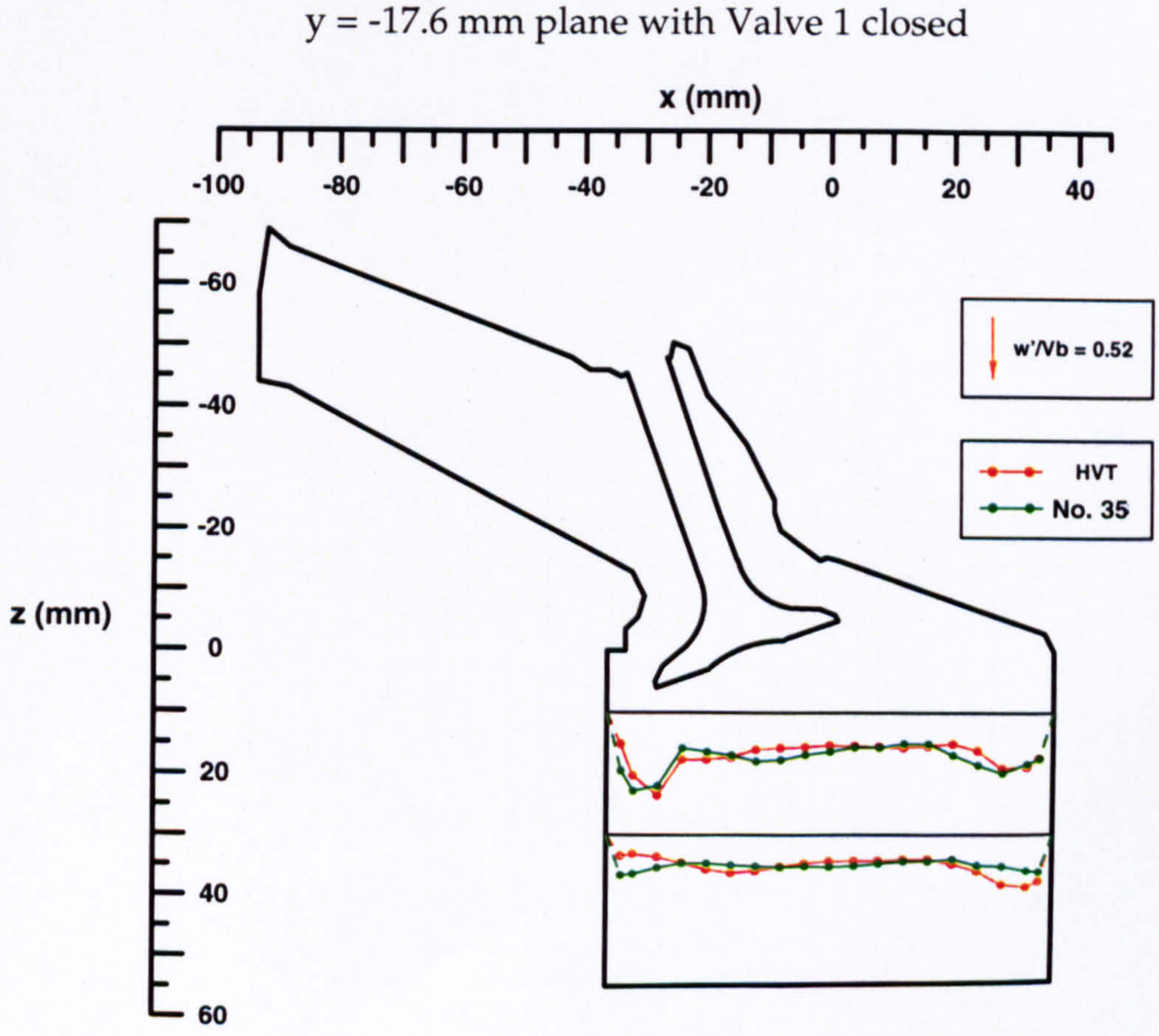

Figure 4.29(d) Comparison of normalised w' velocities in the y = -17.6 mm plane with Valve 1 closed

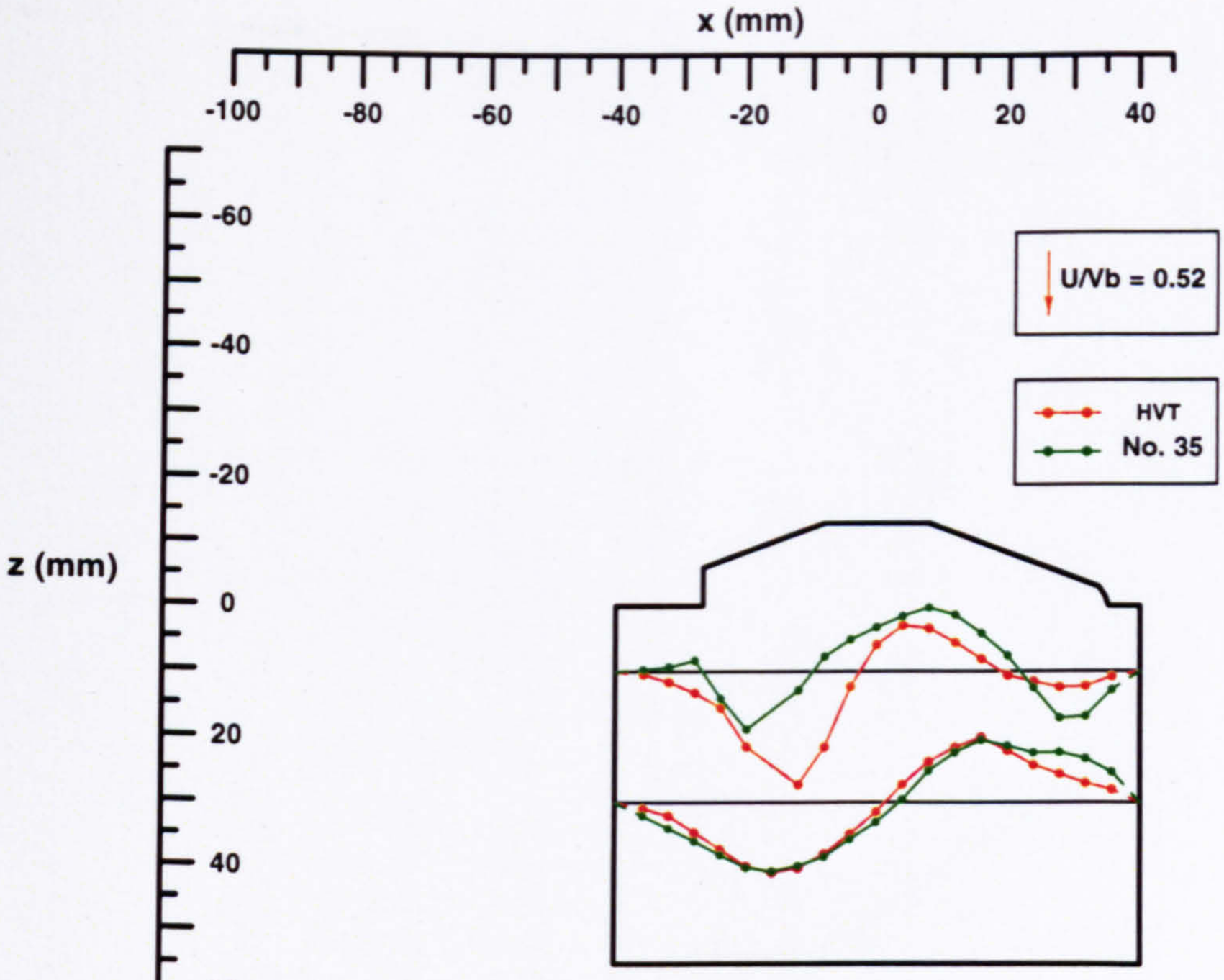

Figure 4.30(a) Comparison of normalised mean U velocities in the y = 0 mm plane with Valve 1 closed

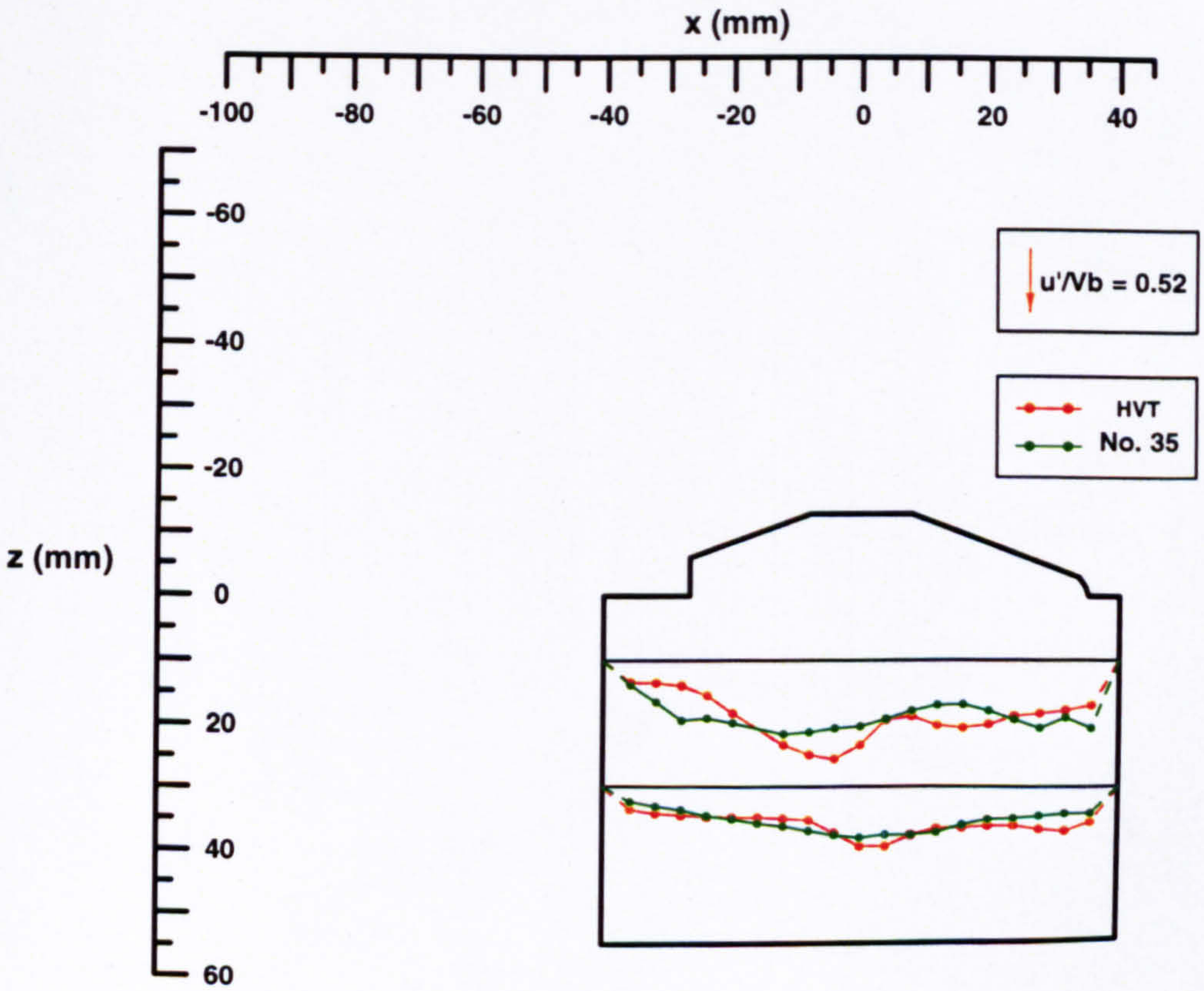

Figure 4.30(b) Comparison of normalised r.m.s. u' velocities in the y = 0 mm plane with Valve 1 closed

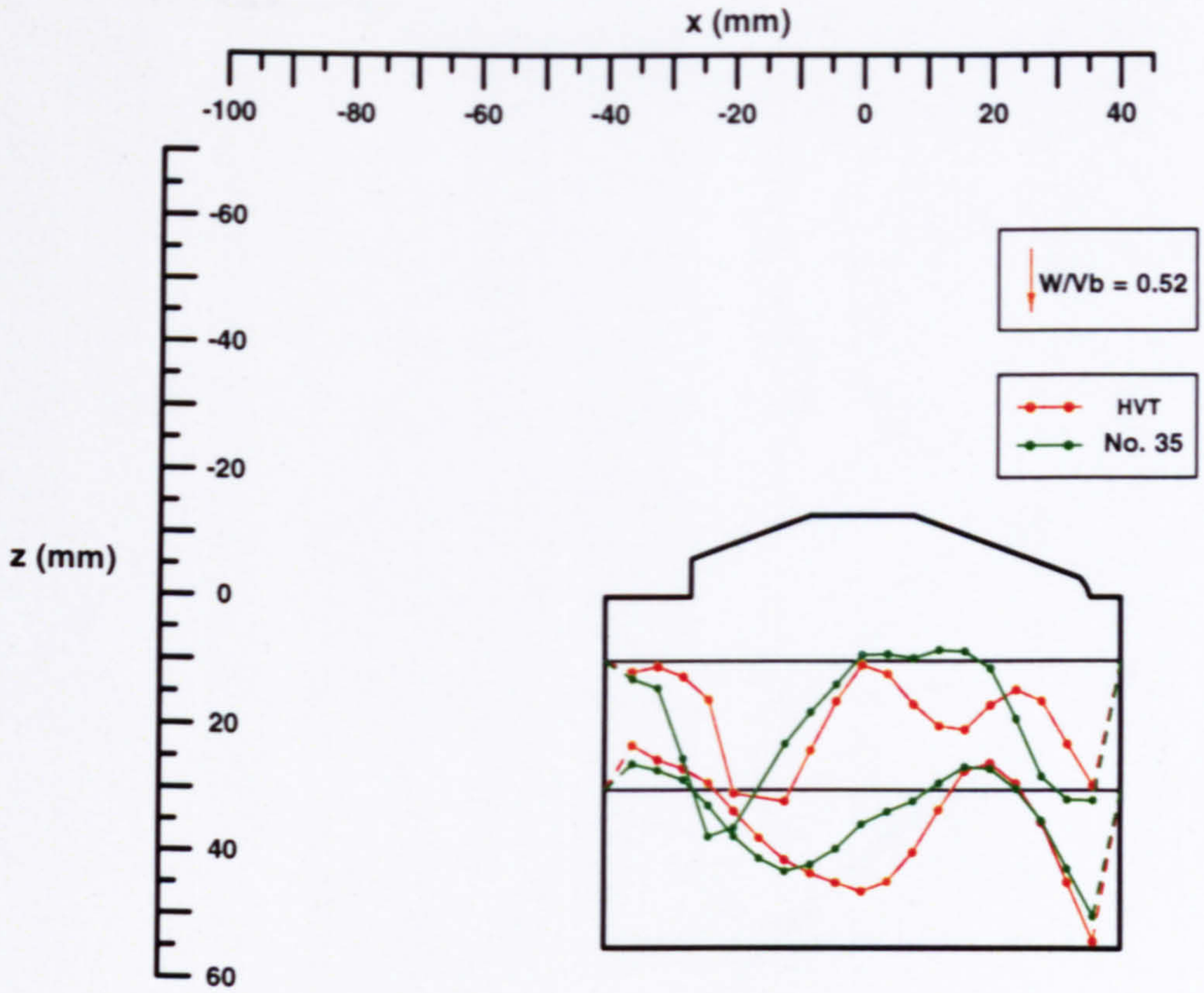

Figure 4.30(c) Comparison of normalised mean W velocities in the y = 0 mm plane with Valve 1 closed

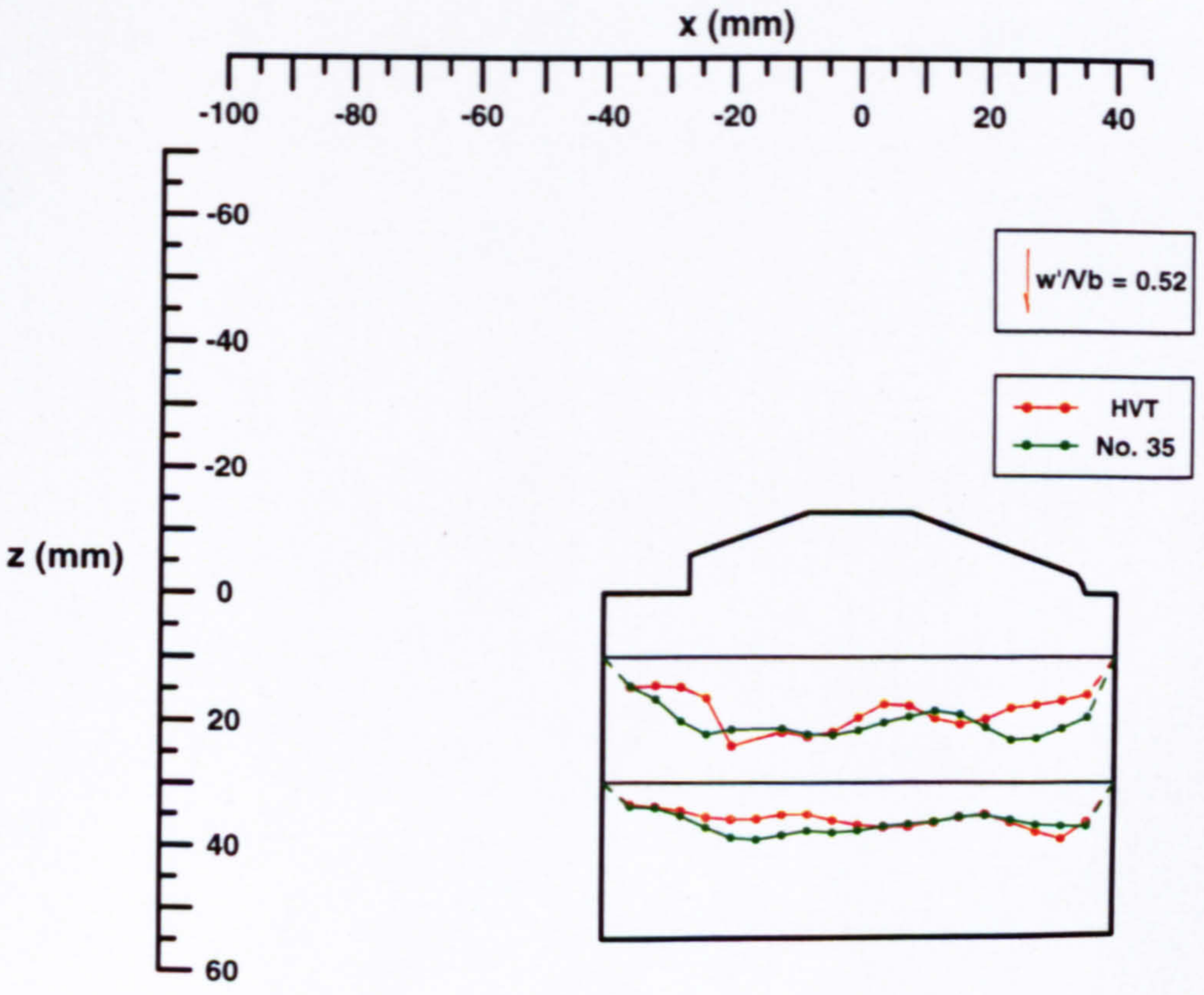

Figure 4.30(d) Comparison of normalised r.m.s. w' velocities in the y = 0 mm plane with one inlet valve closed

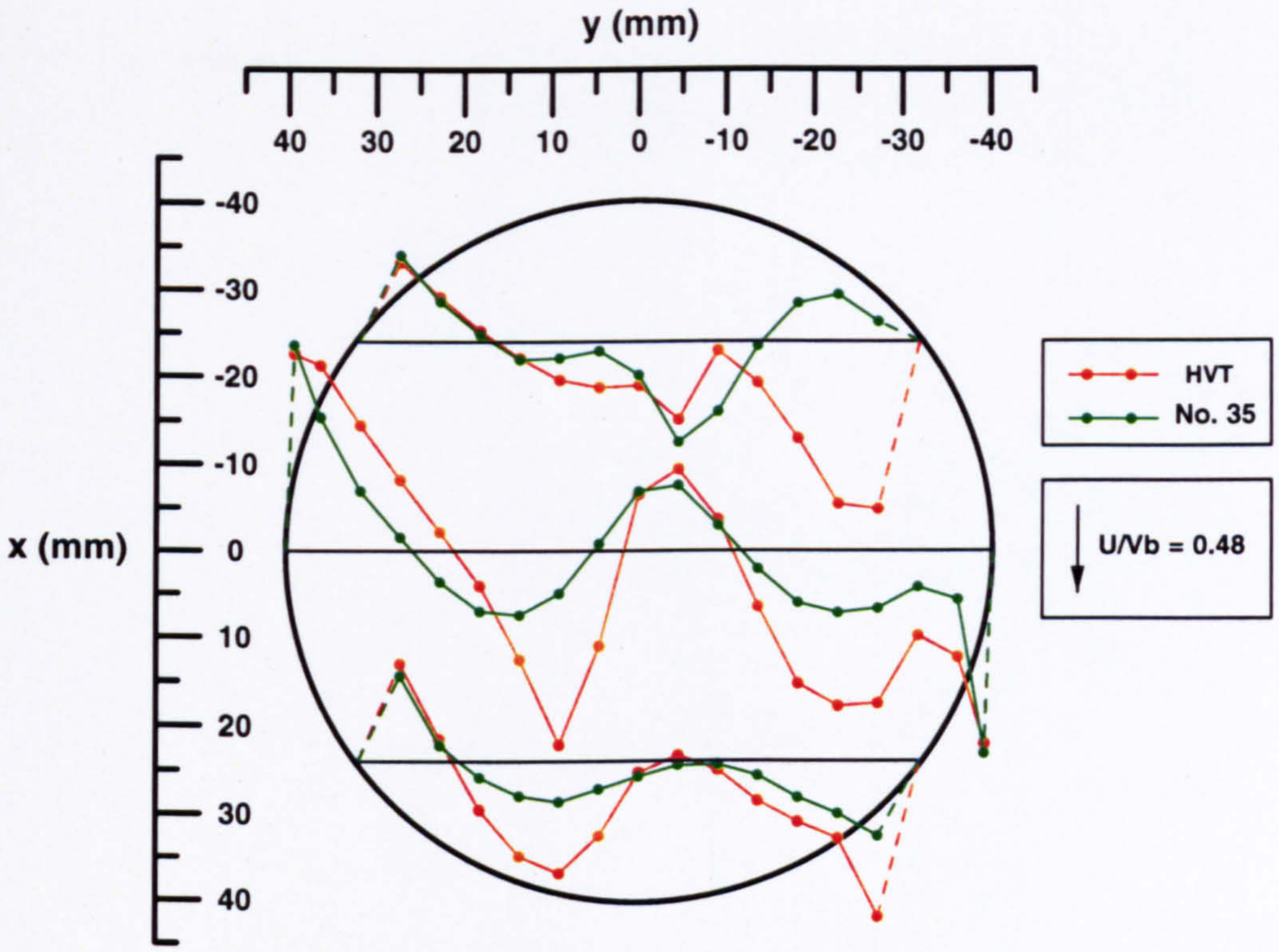

Figure 4.31(a) Comparison of normalised mean U velocities in the horizontal z = 10 mm plane with Valve 1 closed

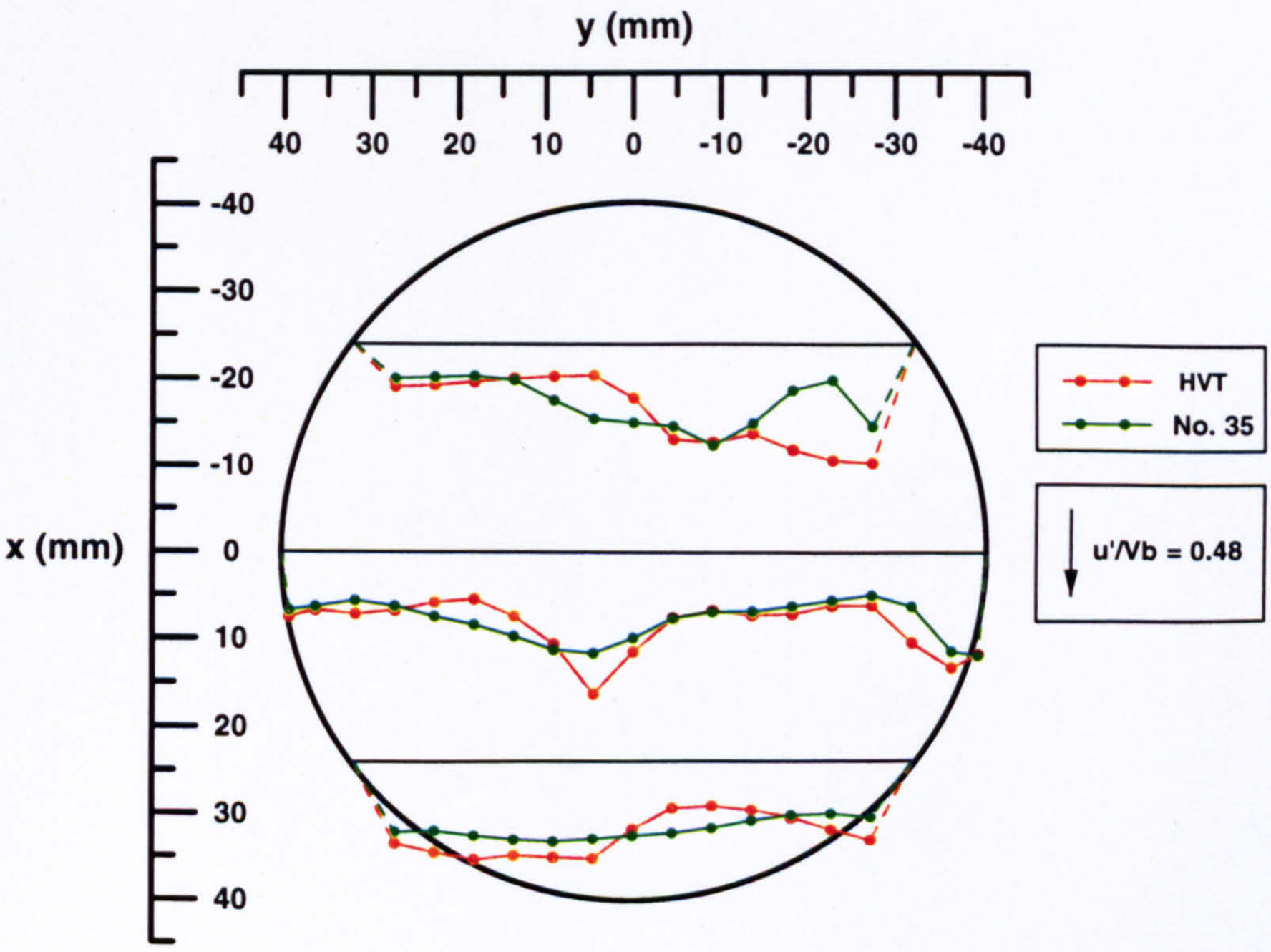

Figure 4.31(b) Comparison of normalised r.m.s. u' velocities in the horizontal z = 10 mm plane with Valve 1 closed

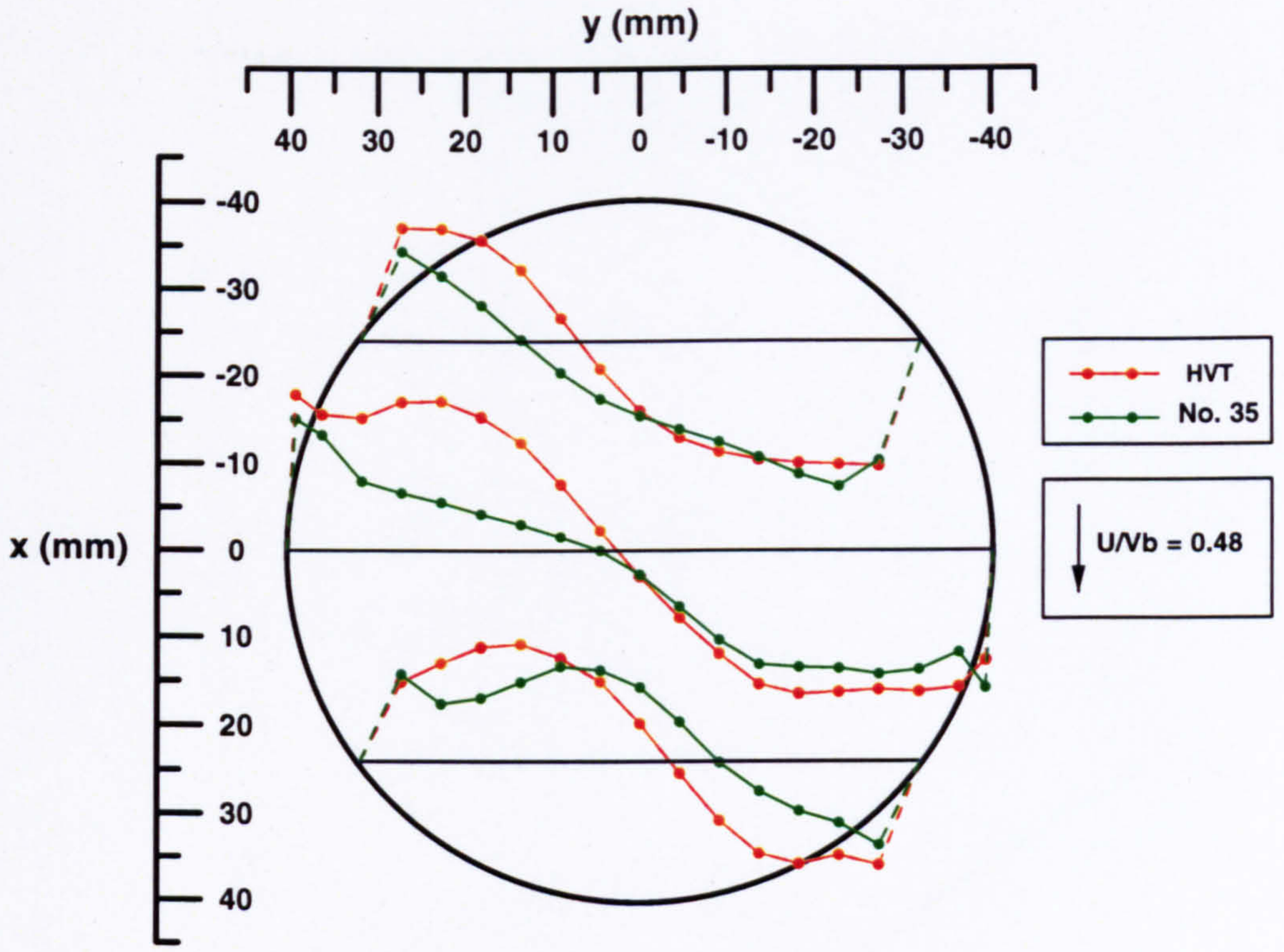

Figure 4.32(a) Comparison of normalised mean U velocities in the horizontal z = 30 mm plane with Valve 1 closed

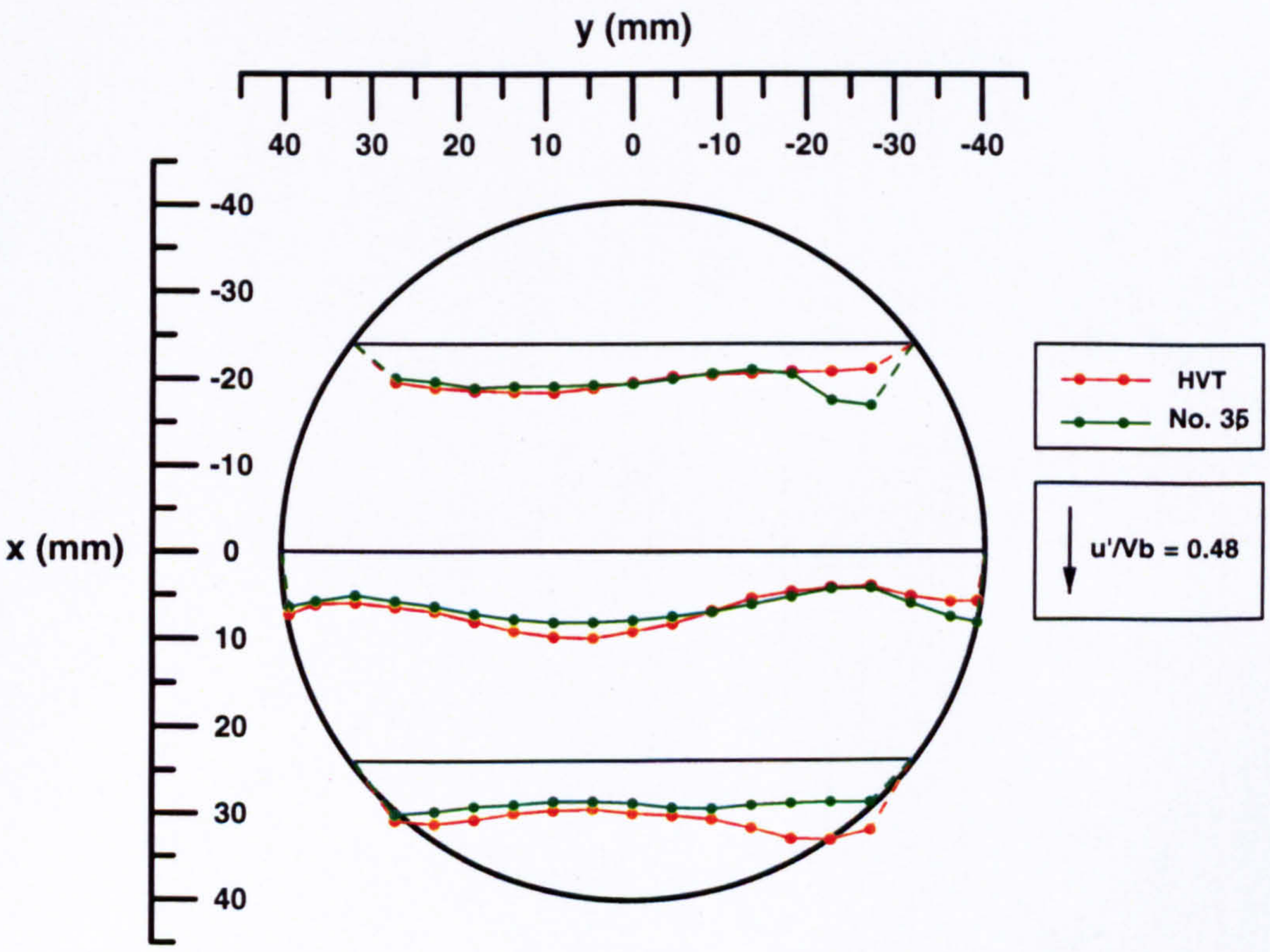

Figure 4.32(b) Comparison of normalised r.m.s. u' velocities in the horizontal z = 30 mm plane with Valve 1 closed

Chapter 5

FLOW PROCESSES IN A DYNAMIC WATER-ANALOG MODEL OF A FOUR-VALVE PER CYLINDER ENGINE

5.1 INTRODUCTION

The unsteady flow processes during the induction stroke of a 'medium output' Ford Zetec engine were modelled using a low speed water-analog rig. Laser-sheet flow visualisation was firstly employed to investigate the development of tumble and swirl motion inside the engine cylinder at various crankangle positions and in a number of vertical and horizontal planes. Following this, particle image velocimetry was applied to measure the velocity and vorticity characteristics of the flow at bottom-dead-centre of induction. The measurement data has been used to evaluate the tumble characteristics of the in-cylinder motion and the results are discussed in the context of similar published work. The measurements were performed at the Department of Mechanical Engineering, University of Brighton.

5.2 FLOW VISUALISATION

Detailed descriptions of the water-analog rig and the experimental techniques are provided in Chapter 2 of this thesis. The similarities between air flow during the induction stroke of a four-stroke engine and water-analog simulations have been discussed by Khalighi and Huebler (1988), among others. It has been shown that compressibility has a minor effect on fluid motion during induction, so that flow can be considered as incompressible without any substantial errors arising in the experiments. Therefore, water-analog rigs may be used to assess the flow generating capabilities of engine

cylinder heads with some degree of confidence. Dynamic similarity criteria require the matching of both Reynolds number and Strouhal number between the actual engine and the engine model. The Strouhal number - St = D/tV_p (D = cylinder bore, t = a timescale, V_p = piston velocity) - for both the model and the engine are automatically identical, as t is a function of the angular velocity of the crankshaft and is therefore directly proportional to the piston velocity. Reynolds number matching is given by:

$$Re = \left(\frac{\rho\ V_p\ D}{\mu}\right)_{model} = \left(\frac{\rho\ V_p\ D}{\mu}\right)_{engine} \qquad (5.1)$$

where ρ and μ have their usual meanings. The above expression can be simplified to calculate the ratio of model engine speed to actual engine speed:

$$\frac{V_{p,\,model}}{V_{p,\,engine}} = \frac{\nu_{model}}{\nu_{engine}} \qquad (5.2)$$

where ν is the kinematic viscosity of the two working fluids. In the present study the rig was operated at its maximum speed of approximately 14 rpm, which is equivalent to an actual engine speed of around 240 rpm. Although it is appreciated that the modelled speed is very low and not representative of actual engine operation, the experiments should nevertheless be useful to gain an insight into the flow field in the engine cylinder. Both inlet valves were opening identically in this study. Some relevant engine specifications for the Ford Zetec engine are provided in Table 5.1.

Displacement:	**1796 cm^3**
Bore:	**80.6 mm**
Stroke:	**88.0 mm**
Inlet valve head diameter:	**32 mm**
Exhaust valve head diameter:	**28.0 mm**
Inlet valve opening:	**6° BTDC**
Inlet valve closure:	**222° ATDC**
Max. inlet valve lift:	**8.1 mm @ 111° ATDC**

Table 5.1 Specifications of the 1.8 litre Ford Zetec engine

The laser-sheet positions in the cylinder of the engine model during flow visualisation and the co-ordinate system are indicated on Figure 5.1. Four vertical planes were chosen to investigate tumble formation in the model; (i) y = 0 mm, the mid-cylinder plane, (ii) y = 8.8 mm, (iii) y = 17.6 mm, the mid-valve plane and (iv) y = 26.4 mm. Flow in diametral planes in the model was studied in the following horizontal planes z = 10 mm, z = 25 mm, z = 40 mm and z = 80 mm. The flow features were recorded onto S.V.H.S. video tape and selected frames from the video were captured using an image grabbing and processing system. It should be noted that during both the flow visualisation and the P.I.V. experiments, the cylinder head on the water analog rig was positioned such that the cylinder axis was horizontal. The grabbed images for vertical planes have been rotated 90° clockwise to allow the flow patterns to be more easily understood. The flow structure at several cycles was compared and showed that although some cycle-by-cycle variations did exist in the size and shape of vortices, the main flow features were repeated in every cycle.

5.2.1 Development of tumble motion

Figure 5.2 presents the flow motion in the mid-cylinder plane (y = 0 mm) from early induction stroke to bottom-dead-centre. At 60° ATDC crankangle, strong intake motion is noted along the left hand edge of the image and a small vortex is formed in the plane, as indicated. A jet of fluid is also observed towards the right of Figure 5.2(a), where the two intake streams passing over the right of the inlet valves (as defined on Figure 5.1(b)) are merging. A well-defined vortical motion is being seen to develop at 90° ATDC, produced by flow along the cylinder wall and across the top of the piston. A tumble vortex is clearly present at this stage in the mid-cylinder plane; the valve lift at this crankangle is 7.9 mm, and an intense flow on the right of Figure 5.2(b) counters the main intake jet formed to the left of the valve. The flow structure at the 90° ATDC crankangle is akin to the flow patterns seen in this plane in the steady flow investigations discussed in Chapter 3, and indicates that steady and unsteady flows in engines are similar during the early part of the induction stroke. At 120° ATDC, the strong intake jet covers over half the area in the plane and well-defined fluid motion is seen over the piston top and striking the cylinder wall.

A better-defined tumble vortex is seen in the bottom right hand corner of the mid-cylinder plane at 150° ATDC, as shown on Figure 5.2(d). This

vortex occupies approximately one quarter of the area of the plane. At 180° CA - Figure 5.2(e) - the tumble vortex is slightly larger, though it stll occupies the same position in the plane. A number of previous studies suggest that a good tumble-generating four-valve cylinder head design is characterised by a large tumble vortex occupying the entire plane at bottom-dead-centre of the induction stroke [eg. Khalighi 1990] as this type of flow motion is most stable and less likely to deteriorate too early in the compression stroke. At the same time, it should be noted that these intense tumble structures reported by authors such as Khalighi (1990) were produced using shrouds and valve masking and with port de-activation. These configurations are not applicable in production engine designs as the inlet port discharge and flow coefficients are compromised with shrouding and masking. In the present case, the inlet valve lifts are 4.5 mm at B.D.C. induction. Therefore fluid is still entering the cylinder over the r.h.s. of the inlet valves and this jet opposes the main tumble motion in this plane. An identical flow structure to that in Figure 5.2(e) at B.D.C. was obtained in water-analog investigations by Trigui et al (1994) with a similar cylinder head configuration.

The flow field development in the mid-valve plane y = 17.6 mm is indicated by the images in Figure 5.3. The images at both 60° ATDC and 90° ATDC show two distinct vortices in this plane. The vortex on the left side of Figures 5.3 (a) and (b) is the tumble-like motion created by flow over the combustion chamber roof and down the cylinder wall, while the counter-rotating elliptic vortex adjacent to this is produced by flow passing over the r.h.s. of the inlet valve. Steady flow investigations using both flow visualisation and laser-Doppler anemometry also displayed these features at 7.5 mm and 10 mm valve lifts, as is discussed in Chapter 3.

At 120° ATDC crankangle, a strong jet of fluid is noted at the left of the image which produces the large tumble motion in Figure 5.3(c), which occupies most of the plane. The elliptic vortex seen in the previous images is now contained in the top right hand corner of the plane due to the development of the tumble vortex. When the piston approaches BDC (Figures 5.3(d) and (e)) the tumble motion covers over 90% of the plane.

Figure 5.4 compares the in-cylinder flow patterns in the four vertical planes at 90° ATDC. These have been chosen to help visualise the three-dimensional flow in the cylinder, which is discussed further at the end of Section 5.2. In the mid-cylinder plane (y = 0 mm) two distinct jets of fluid are apparent which collide with each other towards the right of Figure 5.4(a). Well-defined flow motion is also noted in the the y = 8.8 mm plane, and

small vortices vortices are seen. A tumble vortex is observed in the mid-valve plane y = 17.6 mm, and a smaller similar vortex is also present to the left of the y = 26.4 mm plane.

The structure of the tumble motion at BDC induction in the vertical planes is shown by the images in Figure 5.5. Each of the four images show the presence of structured flow with tumble-like vortices. The tumble motion is more clearly formed in the y = 17.6 mm plane, while at y = 26.4 mm only an ascending flow can be observed on the l.h.s. due to the three-dimensionality of the flow structure.

5.2.2 Flow in Horizontal Planes

The flow motion produced in horizontal planes (diametral) during the induction stroke was also examined with laser-sheet visualisation. Figure 5.6 presents images of the fluid motion at 60° ATDC crankangle. In both the z = 10 mm and z = 25 mm planes the flow structure is slightly asymmetric and no large swirl vortices are seen, although small vortices can be distinguished in each plane. The flow field comprises a number of jets which are travelling from the inlet valve to the exhaust valve side of the cylinder head. The inlet valve lift at 60° ATDC is 6.5 mm. The steady flow study reported in Chapter 3 of this thesis showed a slightly asymmetric flow field and the presence of two pairs of counter-rotating vortices in the horizontal planes, which were larger in size at the lower valve lifts than at the higher valve lift settings. This can also be seen in Figure 5.6. There are differences between the steady and unsteady swirling flow patterns which could be due to the presence of the piston, which encourages the development of tumble motion.

At 120° ATDC crankangle, images from the vertical planes showed that large scale tumble motion was evolving in the engine cylinder at this stage. Flow in three horizontal planes is displayed on Figure 5.7. No organised flow motion is apparent close to the engine cylinder head, as indicated by the image of the z = 10 mm plane and this is most likely due to the predominantely out-of-plane motion of the fluid. Further down the cylinder, the images in both the z = 25 mm and z = 40 mm planes both show a number of small vortices and jets describing asymmetric flow.

The most intense tumble in the engine model is observed when the piston reaches bottom-dead centre, as already discussed. Figure 5.8 illustrates the structure of fluid flow in the four horizontal planes examined. In the z = 10 mm and the z = 25 mm planes (Figures 5.8(a) and (b)) the particle streaks

to the left of the images show jets of fluid travelling from the inlet valve side to the exhaust valve side. Several counter-rotating vortices are present in the z = 40 mm plane, as shown in Figure 5.8(c). Towards the bottom of the cylinder in the z = 80 mm plane, Figure 5.8(d) shows the fluid travelling from the exhaust valve side to the inlet valve side of the image. This motion is followed by liquid passing over the surface of the piston and constitutes part of the tumble vortex.

The three-dimensional in-cylinder flow structure at 90° ATDC crankangle and at BDC has been illustrated on Figures 5.9(a) and (b). The illustrations show only one half of the flow field (that to the left of the mid-cylinder plane y = 0 mm) to improve the clarity of the presentation. In the 90° ATDC position, the 3D flow pattern over the right hand side of the cylinder comprises a toroidal (doughnut-shaped) vortex, which is produced by liquid motion over the two inlet valves. Swirl is created by flow along the cylinder wall, while tumble is the dominant motion close to the central plane. Figure 5.9(b) shows the flow pattern at BDC. This indicates the presence of a number of strong three-dimensional vortices in the cylinder. The vertical dimensions of the main tumble vortex increase in the direction of the y-axis.

5.3 PARTICLE IMAGE VELOCIMETRY

The flowfield in each of the selected vertical and horizontal planes inside the engine model was measured using particle image velocimetry. An introduction to the P.I.V. technique and a description of the hardware and software employed in the present investigation has been provided in section 2.5 of Chapter 2. As detailed in the literature review in Chapter 1 of this thesis, many previous studies into flow in four-valve per cylinder engines have established that strong tumble motion is important at bottom-dead-centre of the induction stroke, as this greatly influences the levels of turbulence generated at the point of ignition of the air/fuel mixture [eg. Endres et al 1992, Hu et al 1992]. The P.I.V. images were therefore grabbed at 180° BDC crankangle, in order to assess the in-cylinder flow in the Ford Zetec engine at the start of compression.

The captured P.I.V. images, as with the flow visualisation images presented in the preceding section, displayed the flow structure at a single instant in time and image interrogation resulted in measurement data in the form of instantaneous velocity and vorticity results. Time-averaged velocity

vector maps were obtained by computing the average of ten instantaneous maps. Although it may be argued that ten sets of measurement data are too few to determine statistically-independent velocity results, the averaged results do nevertheless indicate the important trends in the flow motion. Faure et al (1996 b) investigated the effects of the number of samples on averaged velocity results obtained using the same experimental rig and showed that at least ten samples are required and that very little change occurs in average velocity magnitudes between ten and fifty samples.

5.3.1 Velocity Characteristics in Vertical Planes

Averaged two-dimensional velocity vectors in the four vertical planes are presented on Figures 5.10 to 5.13. The quantitative flowfield at BDC in the mid-cylinder plane y = 0 mm is shown in Figure 5.10 alongside a corresponding instantaneous flow visualisation image to indicate the similarities between the two figures. The PIV vector plot confirms all the features already described in the flow visualisation study. Strong downward fluid motion is observed to the left of the plane adjacent to the cylinder wall and a tumble vortex is formed in the bottom right hand portion of the plane. The highest velocities in this plane are in the region of 0.12 m/s within the main jet flow and in the tumble vortex. The lowest velocities in this plane are below 0.01 m/s and are observed in the region underneath the inlet valves, in the top right hand corner of the vector plot.

Figure 5.11 presents the qualitative and quantitative flowfields in the y = 8.8 mm plane. Both sets of results display the prominent flow features, viz. the well-defined jet and the tumble vortex. The highest velocities in the plane are again approximately 0.12 m/s and encountered within the jet seen on the left of both figures. The smallest velocity values are present in the region above the tumble vortex and are very close to zero.

The fluid flow motion in the mid-valve plane y = 17.6 mm is shown on Figure 5.12. The flow visualisation study showed that a large vortex is present in the plane, and this is also verified by the averaged velocity results. A vortical motion is also apparent in the top right hand corner of the plot which counteracts the development of a single tumble over the entire plane. Velocity magnitudes in the plane are comparatively high throughout the plane; the highest velocity magnitude is 0.11 m/s, while the average velocity magnitude in this plane is 0.05 m/s.

In the plane y = 26.4 mm the flow visualisation study indicated that a single vortex structure exists in the plane. The vector plot in Figure 5.13 shows that fluid is directed upwards in the right of the figure, below the inlet valves with velocities in the region of 0.1 m/s, with much lower velocities to the left of the plot.

Tumble ratios (T_r) based on angular momentum have been evaluated for flow at B.D.C. in each of the vertical planes. The following expression is derived from the angular momentum equation and used to calculate the ratios [Faure et al 1996 b]:

$$T_r = \frac{8\sum_{i=1}^{n}(u_i \cdot z_i - w_i \cdot x_i)}{n\omega^2 B} \tag{5.3}$$

where x and z are the Cartesian co-ordinates of the velocity measurement locations, u and w are the radial and axial components of the fluid velocity respectively, n is the number of vectors in the plot, ω is the crank speed in rad/s and B is the cylinder bore. Faure et al (1996 b) indicate that this calculated tumble ratio value is strongly dependent on the reference location chosen as the centre of the tumble motion (i.e. the vortex centre or the centre of the mid-cylinder plane) and is sensitive to effects of flow vectors distant from that location. It does, however, provide a useful indication of the strength of the tumble motion at the end of the induction stroke. This method was also employed by Khalighi (1990) and Rönnbäck et al (1991) among others, who found very similar results inT_r with both reference locations. The values of T_r in each plane, based on the centre of the mid-cylinder plane, are listed below in Table 5.1. The above results show that the calculated values of tumble ratio are very similar for each plane, with an average value of approximately 1.1.

	Plane	Tumble Ratio
(i)	y = 0 mm	1.17
(ii)	y = 8.8 mm	1.02
(iii)	y = 17.6 mm	1.03
(iv)	y = 26.4 mm	1.10

Table 5.2 Calculated tumble ratio at B.D.C. based on the centre of the engine cylinder

As discussed in Chapter 1, previous studies into the correlations between in-cylinder flow, combustion and emissions characteristics have established that strong tumble motion leads directly to improvements in engine performance. However, the definition of the value of tumble ratio that constitutes a high-tumble engine design does vary from one researcher to another. Kent et al (1989) tested six different four-valve cylinder head configurations and describe one configuration with valve masking and giving a T_r value of 1.4 as a high-tumble design, which led to the shortest burn durations in combustion tests. Rönnbäck et al (1991) describe a cylinder head giving T_r = 1.1 at B.D.C. (similar to the present case) as the best design from among those tested and Hadded and Denbratt (1991) also found a similarT_r value (1.14) for a dual-intake valve engine with siamesed and directed ports.

In many of the previous cases where tumble ratios comparable to that calculated for the Zetec engine have been measured, the configurations have included considerable valve masking or shrouds; e.g. Trigui et al (1994) who obtained aT_r value of 1.0 at B.D.C. for a head with a high level of masking on the combustion chamber on the inlet valve side, while with a combustion chamber masking level similar to the present Zetec engine cylinder head, a value of only 0.55 was measured. Similarly, Fujimoto et al (1995) judged T_r = 1.0 to be high and this was achieved by manipulating the inlet valve opening and closing timings.

In comparison to these cases it would appear that the Zetec engine may be judged as a high-tumble cylinder head despite the fact that the velocity maps show a smaller tumble vortex in the mid-cylinder plane than some other designs report. The engine offers further potential for improvement since at present the combustion chamber masking level on the inlet valve side is small, and the port inclination angle at 24.2° is greater than that for some cylinder heads. Increasing the valve masking and reducing the port angle to closer to 20° could be two methods for achieving higher tumble ratios in the Zetec engine at B.D.C. of the induction stroke.

5.3.2 Velocity Characteristics in Horizontal Planes

Averaged two dimensional velocity vector maps for flow in the horizontal planes at B.D.C. are presented in Figures 5.14 to 5.17. In each figure the outer boundary of the plot represents the cylinder bore, while the inner circle depicts the actual area of the plane that could be observed. The

viewing restriction was due to the fact that the piston contained grooves for the piston rings. The two circles at the top of each figure indicate the position of the inlet valves.

Fluid motion in the plane z = 10 mm is shown on Figure 5.14. The vector plot displays a number of small vortices present in the flow and no large scale swirling motion is seen. In the main, the flow structure is asymmetric and the fluid is travelling from the inlet valve to the exhaust valve side of the plane, with strong jets present close to the cylinder wall. The highest velocities in the plane are 0.06 m/s, within the jets.

Similar flow features are noted in the z = 25 mm plane, as shown in Figure 5.15. High velocity flow is observed in the top half of the plot. Several swirling vortices are present in the exhaust valve side and the lowest velocities are also observed in this region. The vertical plane P.I.V. plots showed strong downward motion close to the cylinder wall due to the intake motion and therefore radial and tangential velocity magnitudes are smaller in this part of the plane.

The z = 40 mm plane shows two counter-rotating swirl vortices at the left and right sides of the vector plot, as Figure 5.16 illustrates. The flow pattern in this plane would indicate that fluid motion is almost symmetric about the y = 0 mm plane. The vectors at the top of Figure 5.15 show a high velocity motion which forms part of the top of the tumble vortex. The highest velocity magnitude in this plane is 0.07 m/s.

The flow visualisation study indicated that in the z = 80 mm plane the fluid is travelling with high velocity over the surface of the piston from the exhaust valve to the inlet valve side. Two low velocity areas are noted in the top of the corresponding velocity vector plot, Figure 5.17, where the fluid is moving up towards the cylinder head and at the bottom of the figure where downward motion is prominent. The highest velocity magnitude in this plane is around 0.13 m/s.

5.3.3 Average Vorticity Measurements

The contribution of vorticity measurements to the understanding of engine in-cylinder flows is an area which requires further research. Reuss et al (1989) indicate that vorticity has a major influence on the burning rate of laminar flames and is also thought to have an effect on the burning rate of turbulent flames.

Plots of average vorticity results for the flow field at B.D.C. are presented in this section. Vorticity (ζ) is defined as the curl of velocity and is calculated using the following expression:

$$\zeta = \frac{\partial v}{\partial x} - \frac{\partial u}{\partial y} \tag{5.4}$$

Since the present case has two-dimensional velocity results, only the out-of-plane component of the vorticity is presented.

Figure 5.18 shows 2D and 3D (topographic) contour plots of average out-of-plane vorticity in the four vertical planes. The plots indicate that vorticity is not uniformly distributed throughout each plane, but is rather found in patches, most of which directly relate to vortices seen on the vector maps. Positive values of vorticity (red areas) correspond to anti-clockwise rotating vortices while negative values (blue areas) indicate the regions with clockwise rotating vortices. In the majority of locations in all four planes, magnitudes of ζ are close to zero. The highest value is around 25 s^{-1} in the centre of the tumble vortex in the mid-cylinder plane, y = 0 mm. Maximum values of vorticity are seen to decrease in planes increasingly further away from the cylinder axis, such that ζ_{max} in the y = 26.4 mm plane is approximately half that in the mid-cylinder plane.

The above observations are also relevant to vorticity results in the horizontal planes, which are presented on Figure 5.19. Once again, the features of the vorticity maps generally correspond to an identifiable small scale structure in the plane. Maximum values of ζ are between 10 and 15 s^{-1}. Large variations in ζ are seen across the z = 80 mm plane, even though no vortices are shown on the vector plot of Figure 5.17. This may be due to the fact that the flow is travelling in many different directions in this plane.

5.4 CONCLUSIONS

The three dimensional in-cylinder flow field in the Ford Zetec engine during the induction stroke has been examined in a low-speed dynamic water-analog rig using flow visualisation and particle image velocimetry. Laser-sheet visualisation was firstly employed in a number of vertical and horizontal planes to follow the path of seeding particles during the stroke.

P.I.V. was then applied to obtain averaged vector maps of flow at B.D.C. crankangle. The results have been used to arrive at the following conclusions:

1. Images of fluid motion in the vertical planes indicated that during induction high velocity jets of fluid along the cylinder walls and across the piston surface produce strong tumble motion. At 90° ATDC, images of the mid-cylinder and mid-valve planes showed that the flow pattern was very similar to that seen in the steady flow investigations. At bottom-dead-centre, the tumble motion occupied the majority of the cylinder volume.

2. Flow images in diametral planes displayed a number of small swirling vortices in each plane, though no large-scale swirl formation was observed. The images indicated that flow was asymmetric inside the cylinder at all crankangles during induction, despite the fact that the inlet valves had been set to open with equal lifts.

3. P.I.V. measurements made in the vertical planes at B.D.C. displayed all the flow features noted through flow visualisation. The averaged vector maps showed organised tumble motion in each plane and the highest velocity magnitude was similar in all four planes, at around 0.12 m/s. Vector maps of flow in the horizontal (diametral) planes again showed the presence of a number of swirling vortices in each plane at B.D.C.

4. Values for tumble ratio were calculated using the P.I.V. results based on the angular momentum of the flow about the centre of the cylinder. A tumble ratio value of approximately 1.1 was calculated. This value was found to be comparable to tumble ratios previously reported for similar dual-intake port cylinder head designs [eg. Kent et al (1989), Hadded and Denbratt (1991), Rönnbäck et al (1991)].

5. Plots of vorticity in the selected planes at B.D.C. indicated that patches of large vorticity magnitudes generally corresponded to vortices observed in the vector plots. In other areas of the planes, magnitudes of vorticity were close to zero.

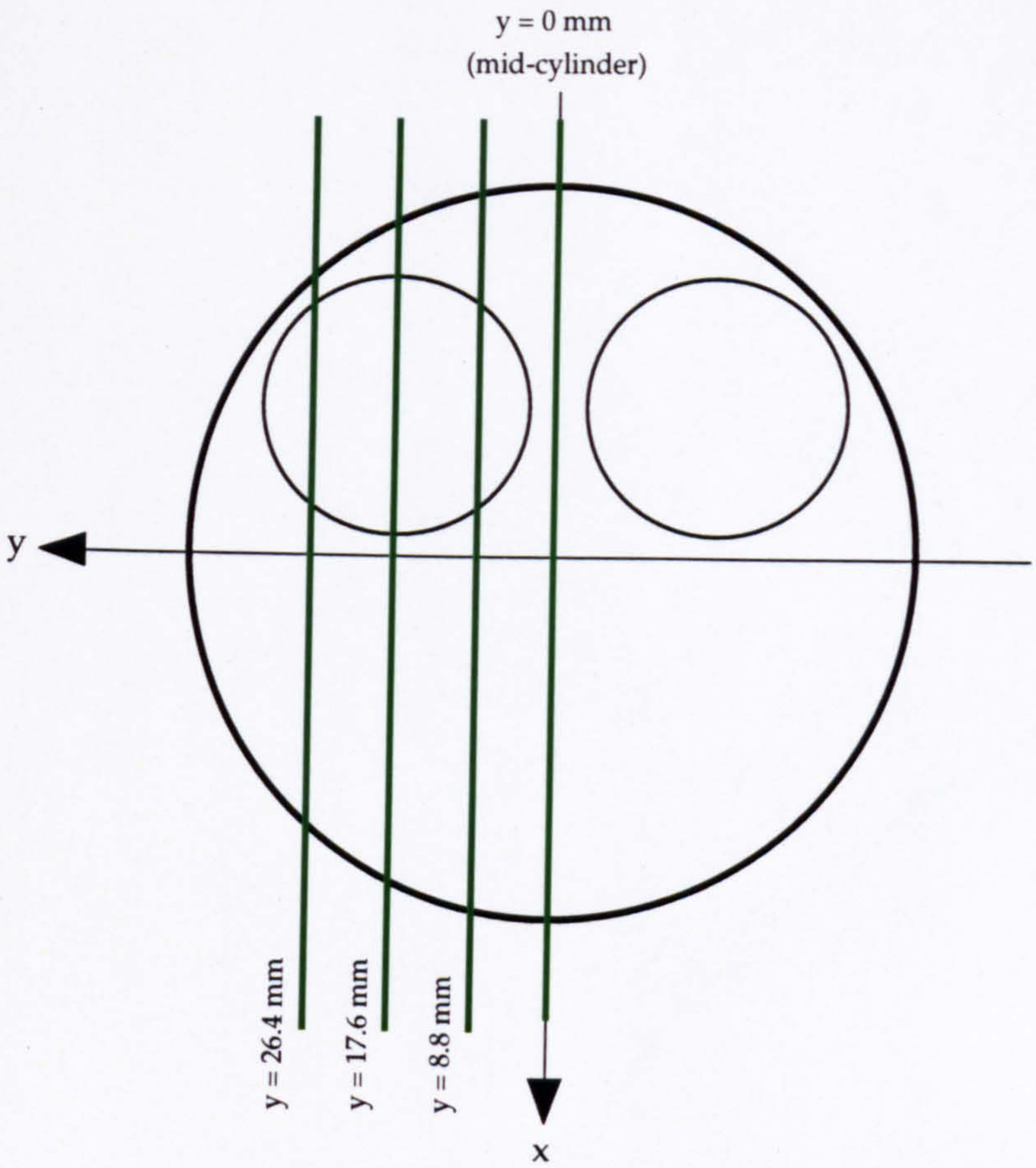

(a) Vertical plane locations

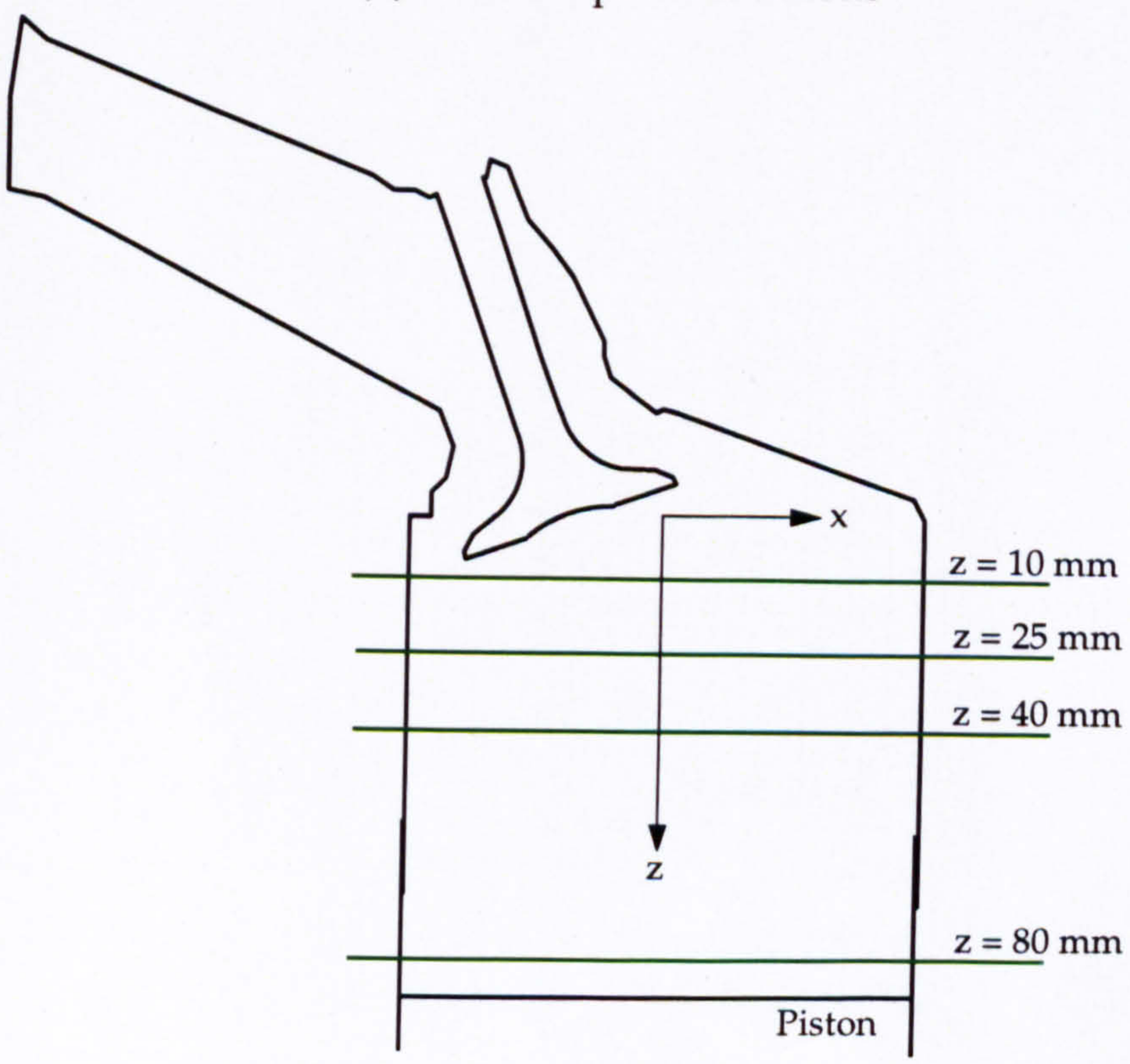

(b) Horizontal plane locations

Figure 5.1 Flow visualisation and P.I.V. measurement planes

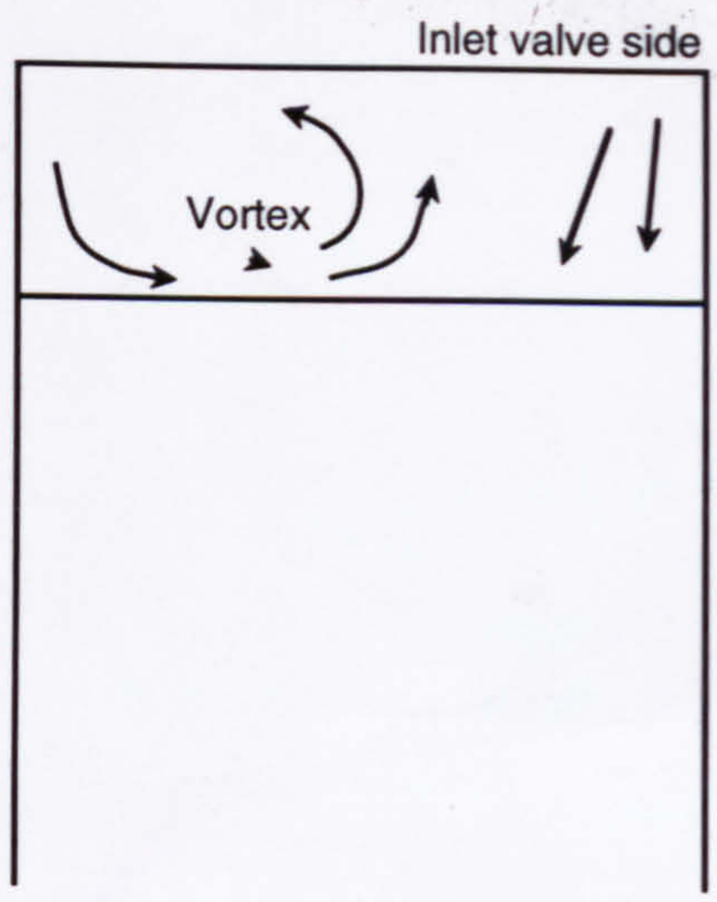
Inlet valve side
Vortex

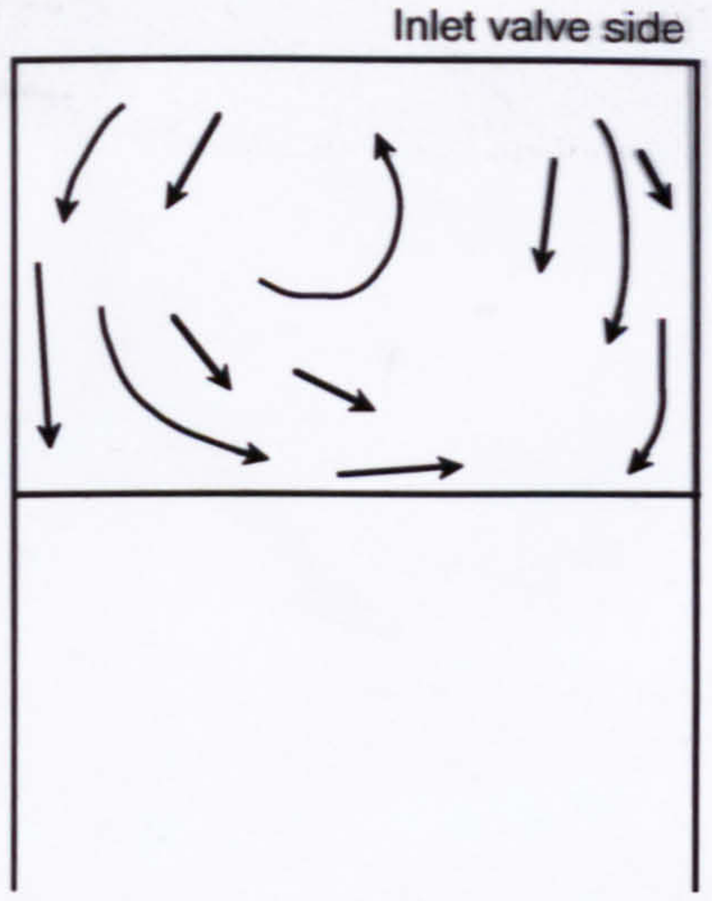
Inlet valve side

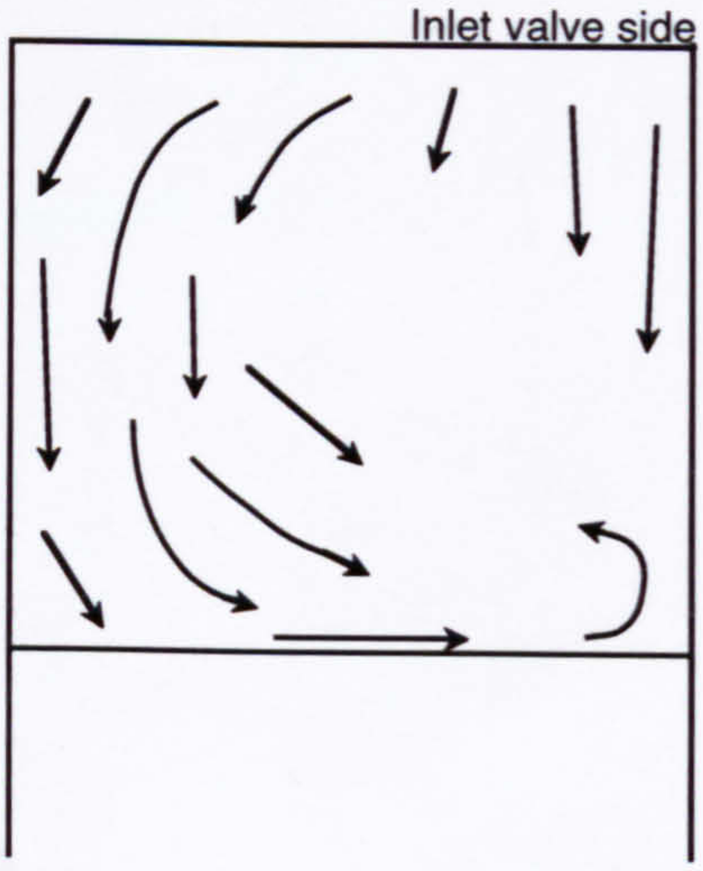
Inlet valve side

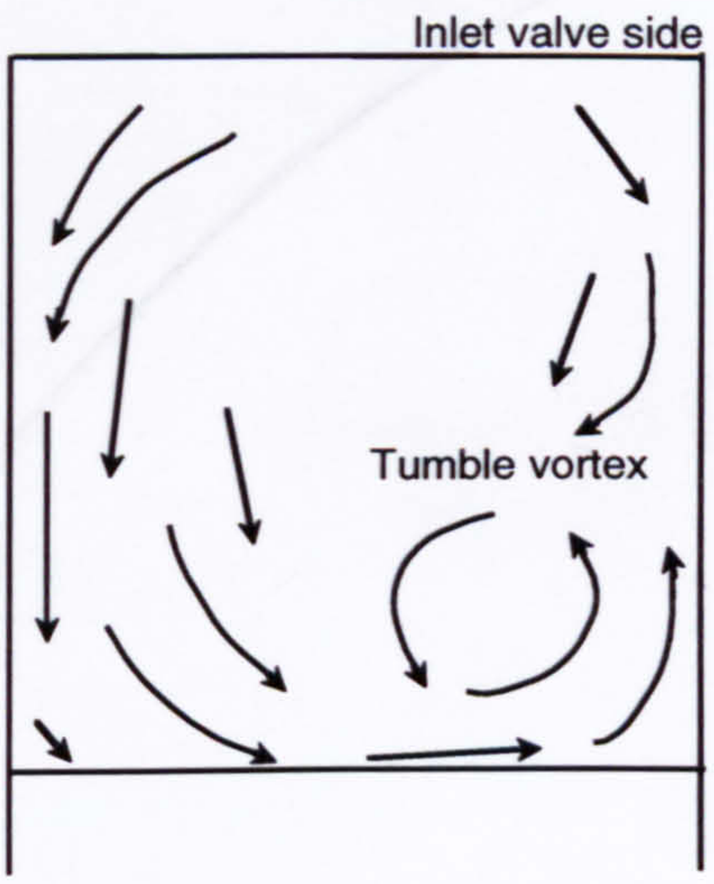
Inlet valve side
Tumble vortex

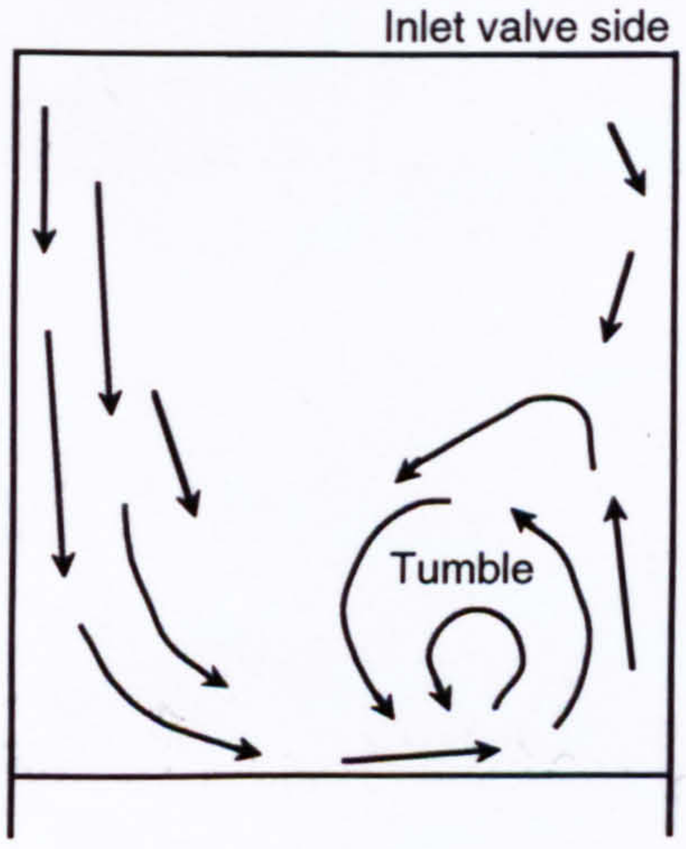
Inlet valve side
Tumble

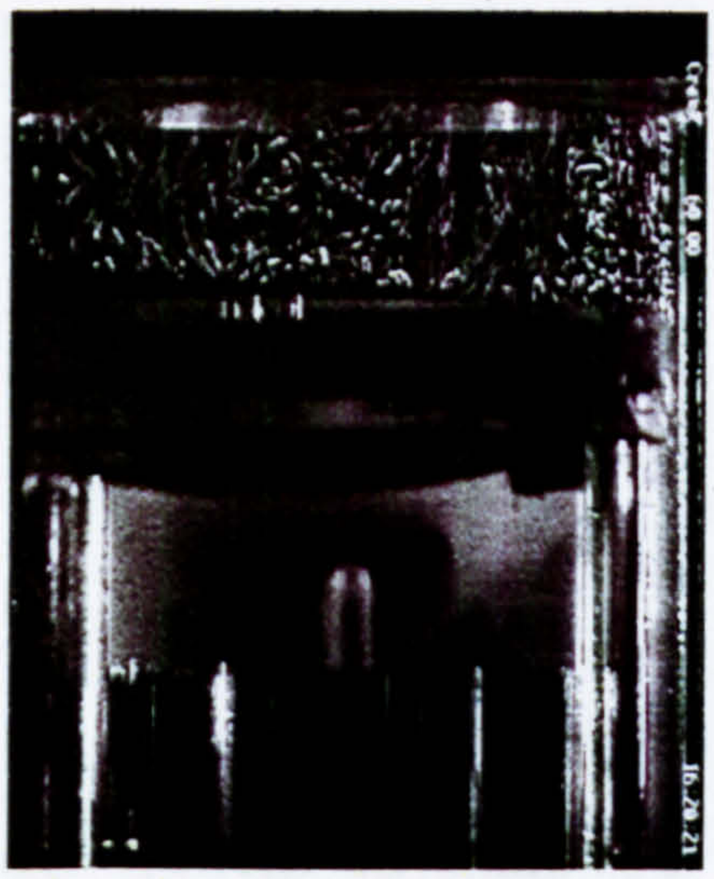

(a) 60 ° ATDC

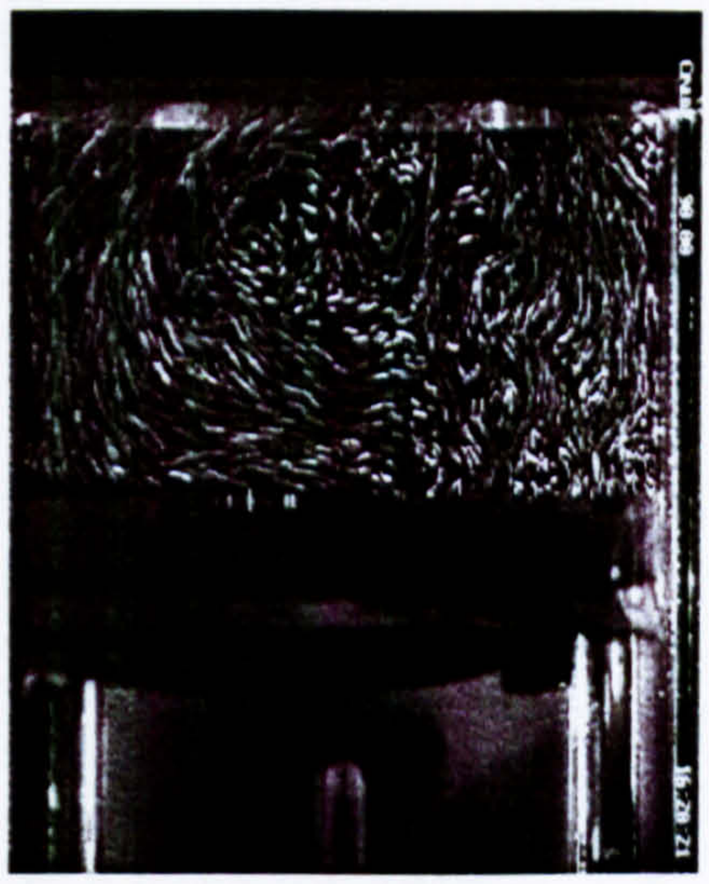

(b) 90° ATDC

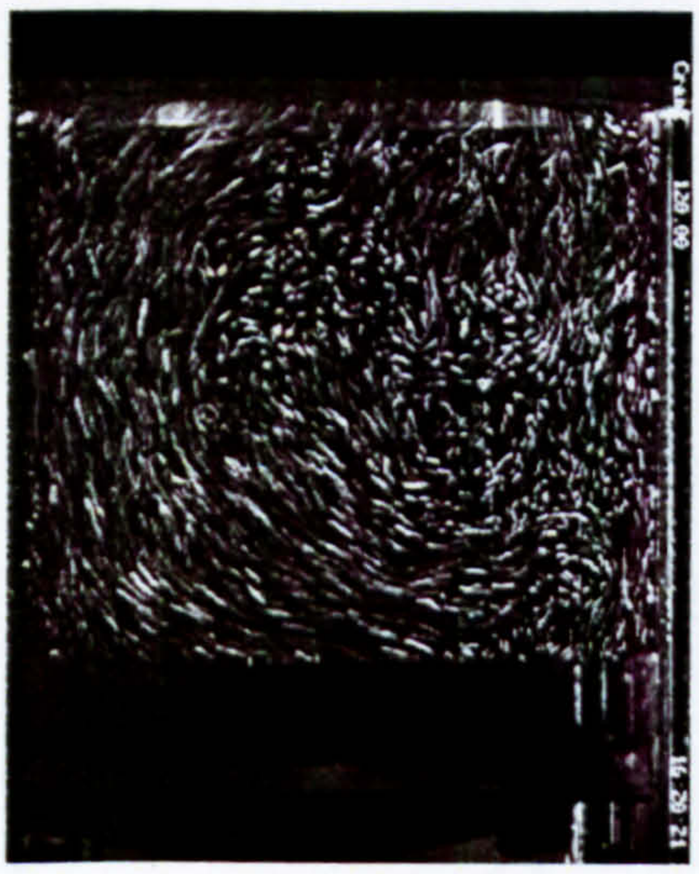

(c) 120 ° ATDC

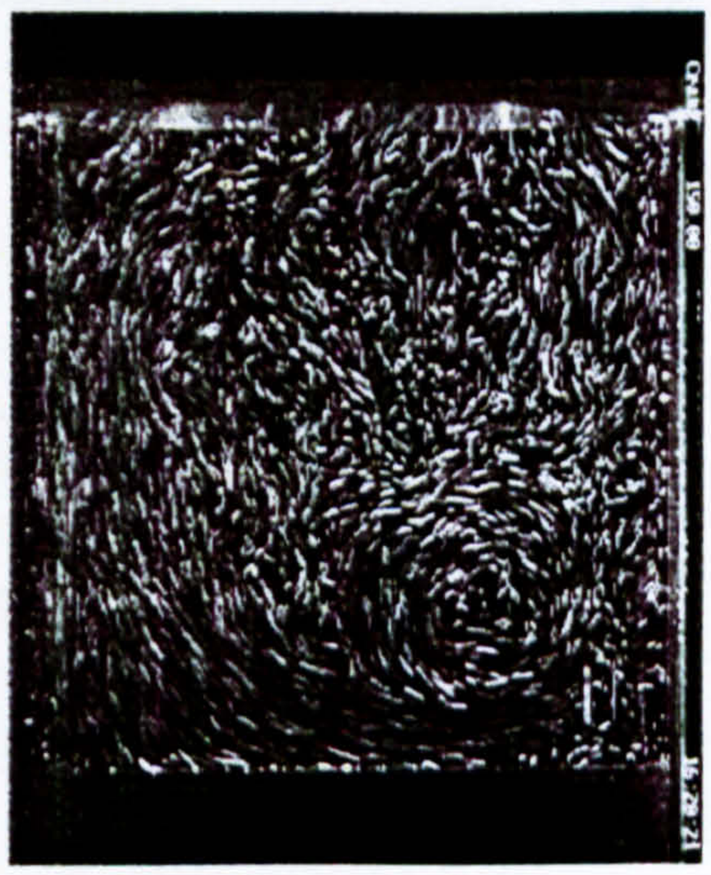

(d) 150 ° ATDC

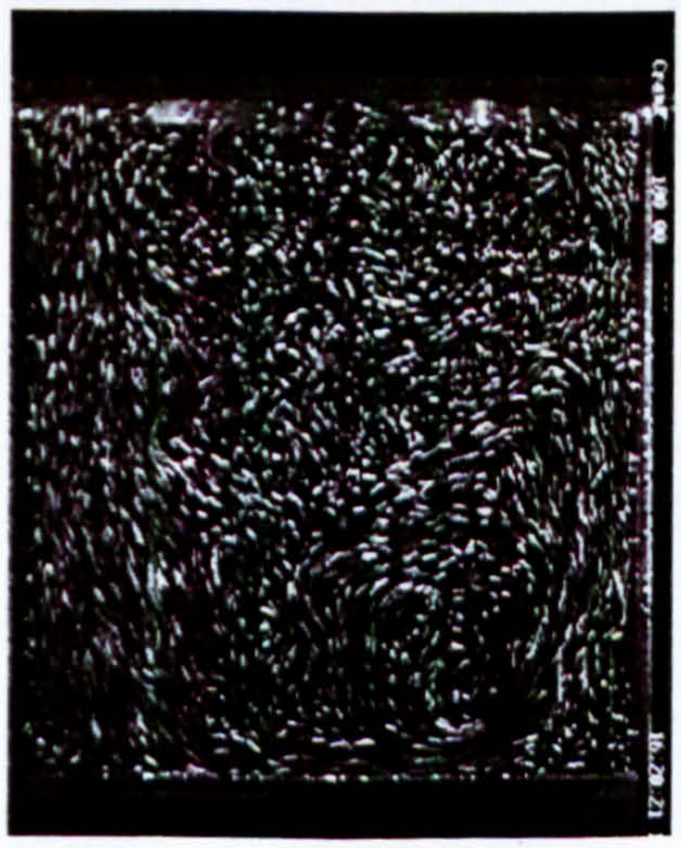

(e) 180° CA (BDC)

Figure 5.2 Development of flow in the plane y = 0 mm

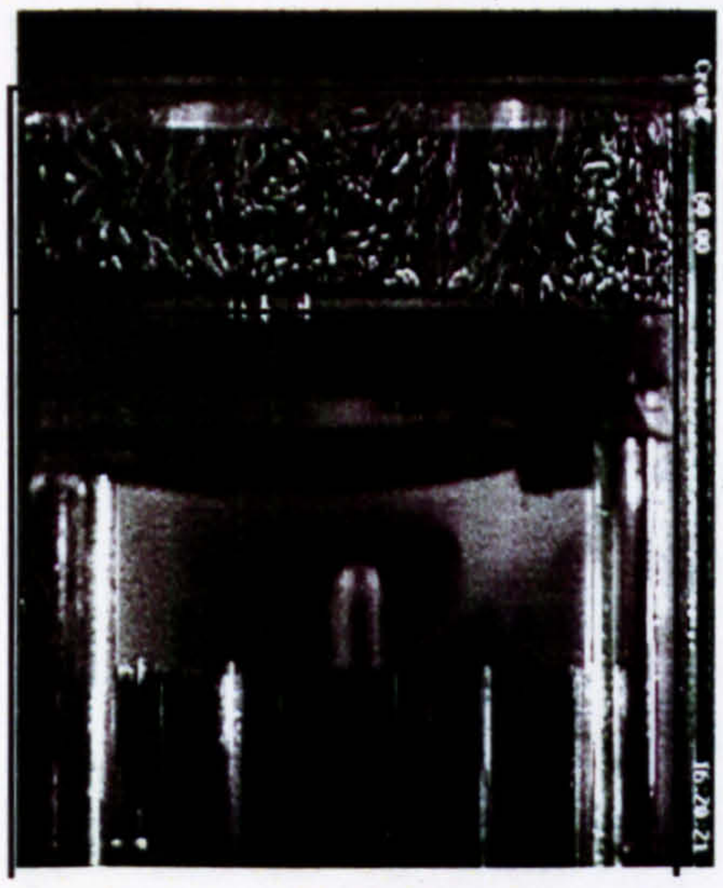

(a) 60 ° ATDC

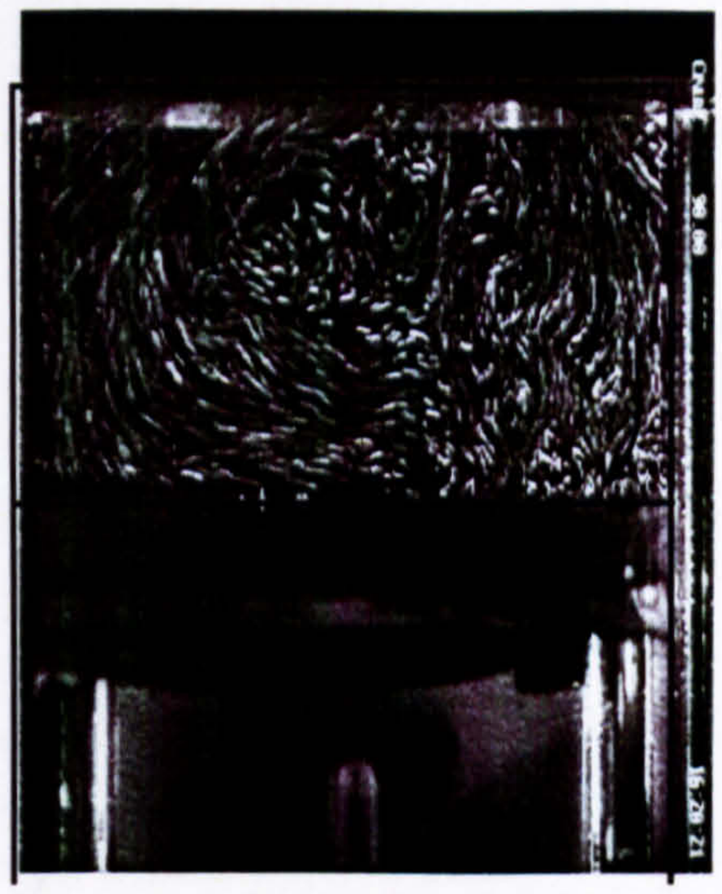

(b) 90° ATDC

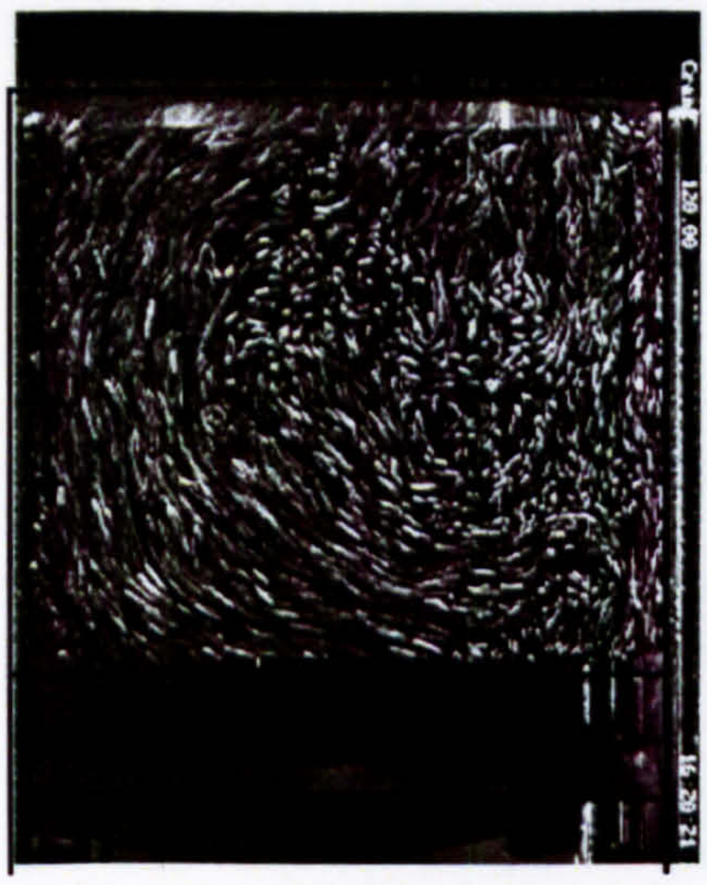

(c) 120 ° ATDC

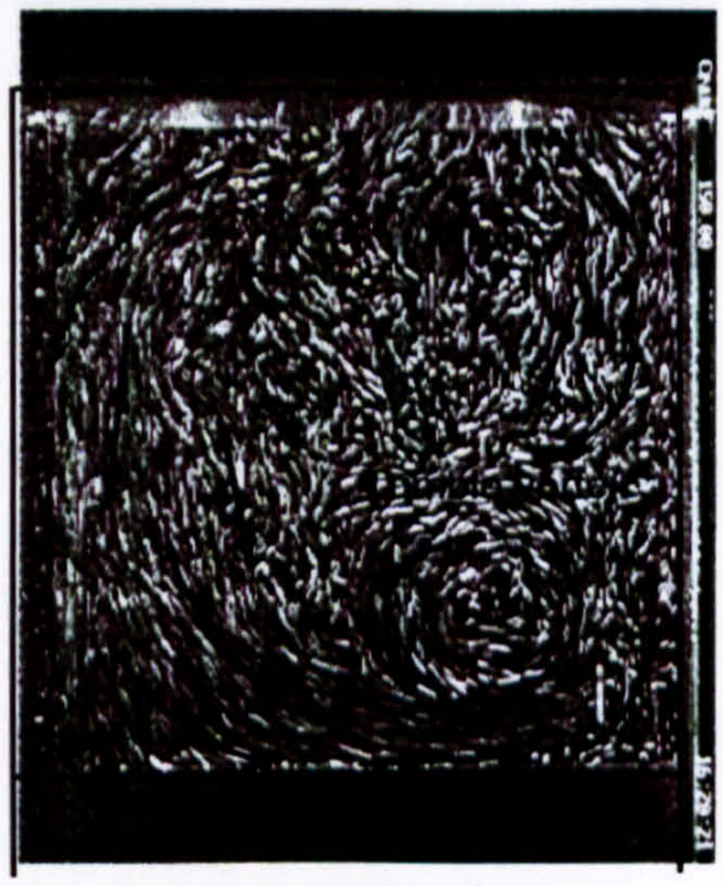

(d) 150 ° ATDC

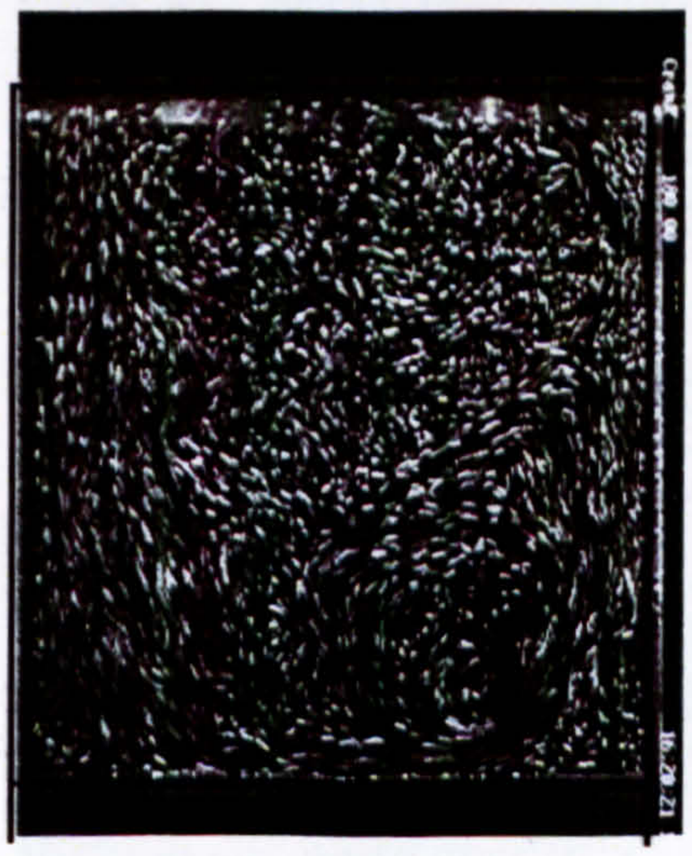

(e) 180° CA (BDC)

Figure 5.2 Development of flow in the plane y = 0 mm

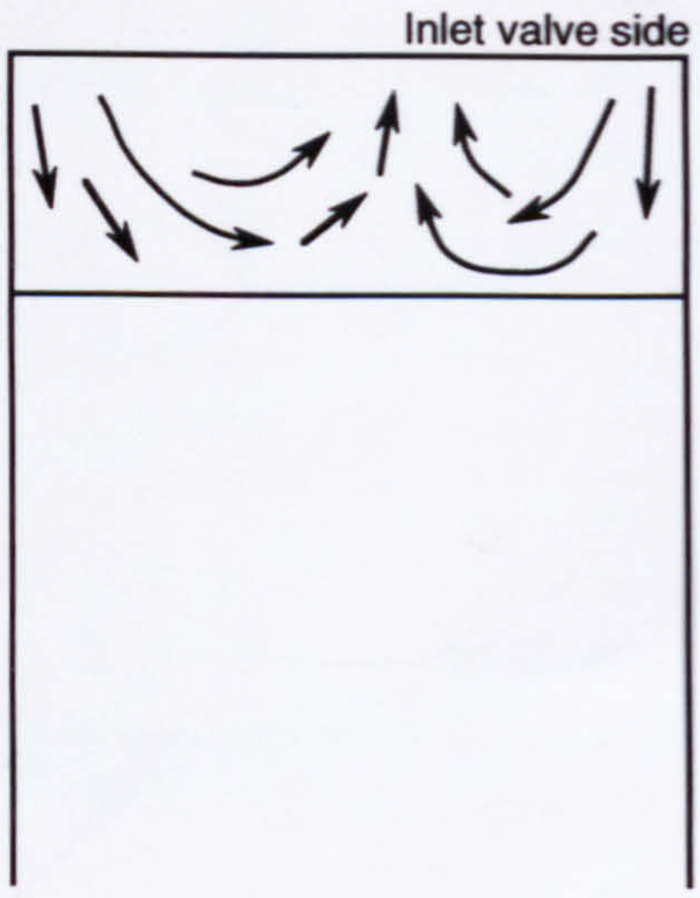
Inlet valve side

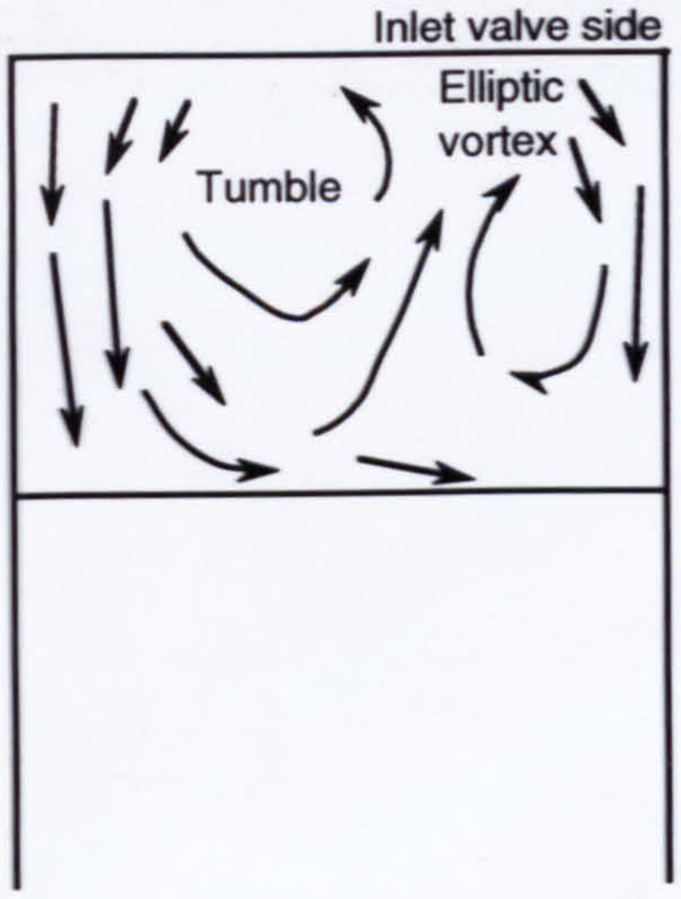
Inlet valve side
Elliptic
vortex
Tumble


Inlet valve side

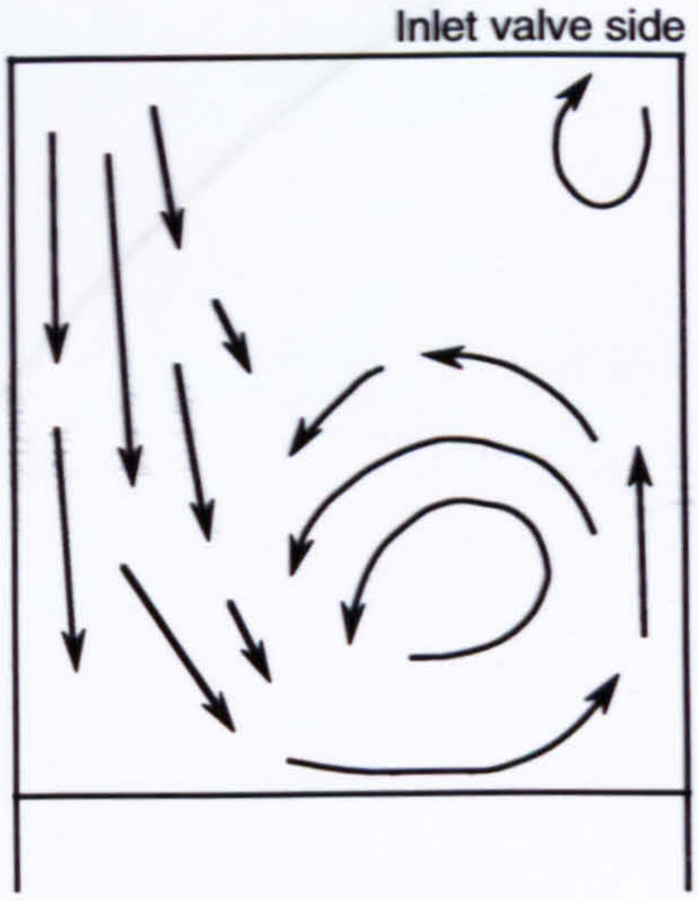
Inlet valve side

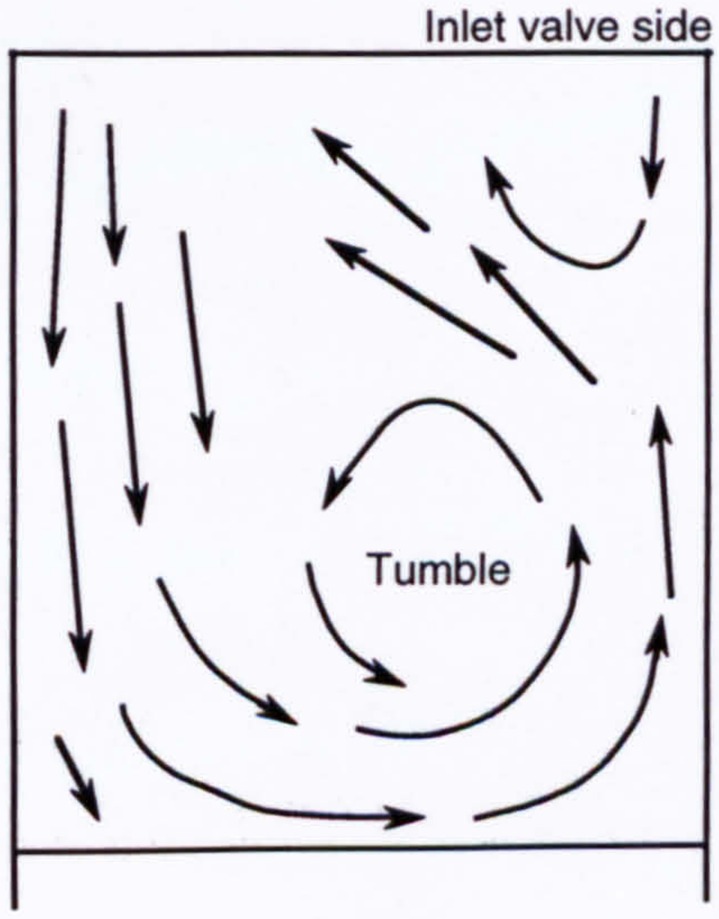
Inlet valve side
Tumble

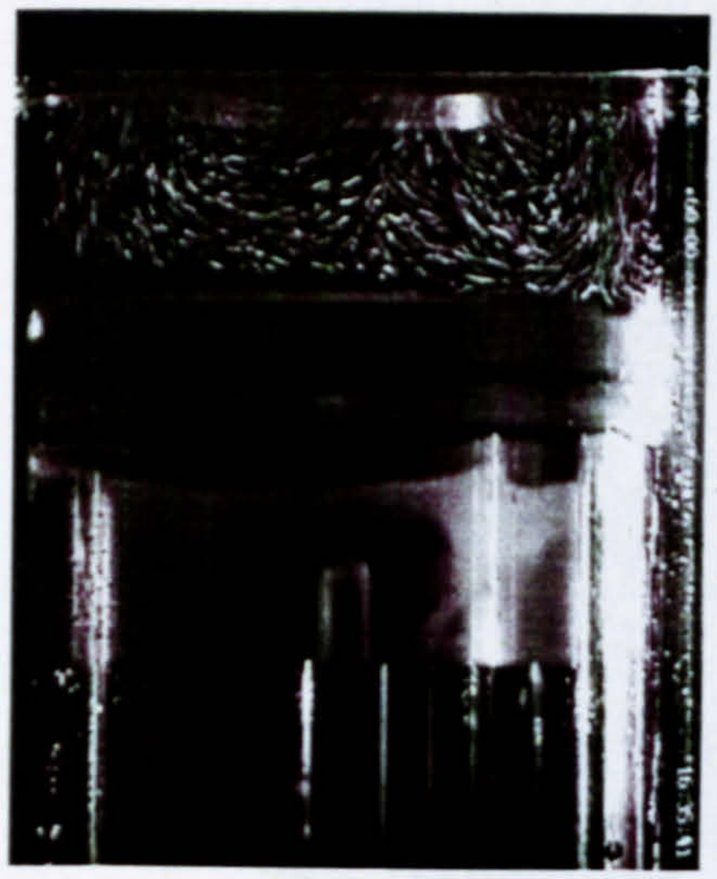

(a) 60° ATDC

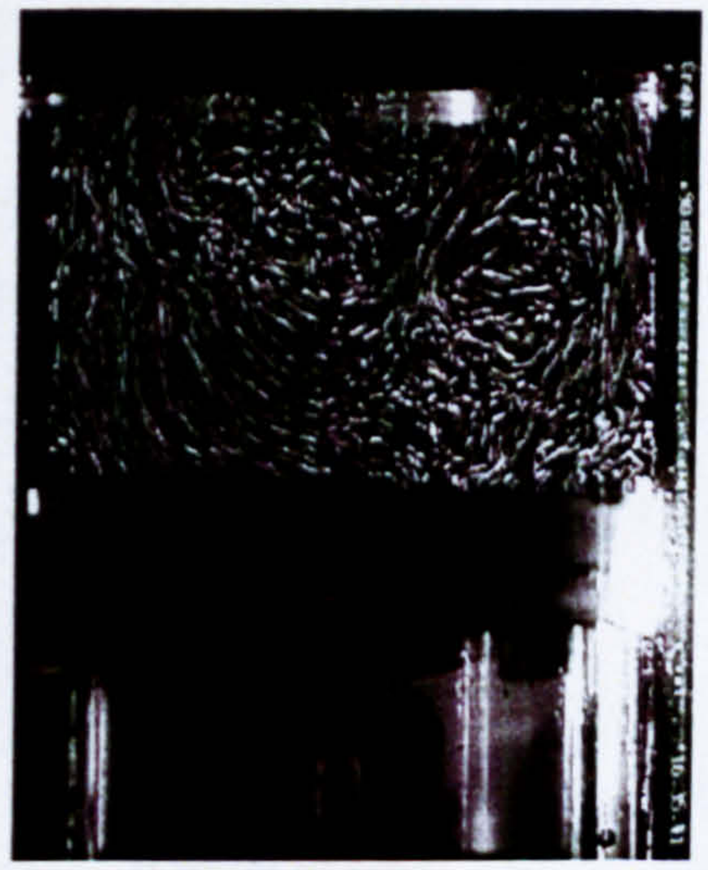

(b) 90° ATDC

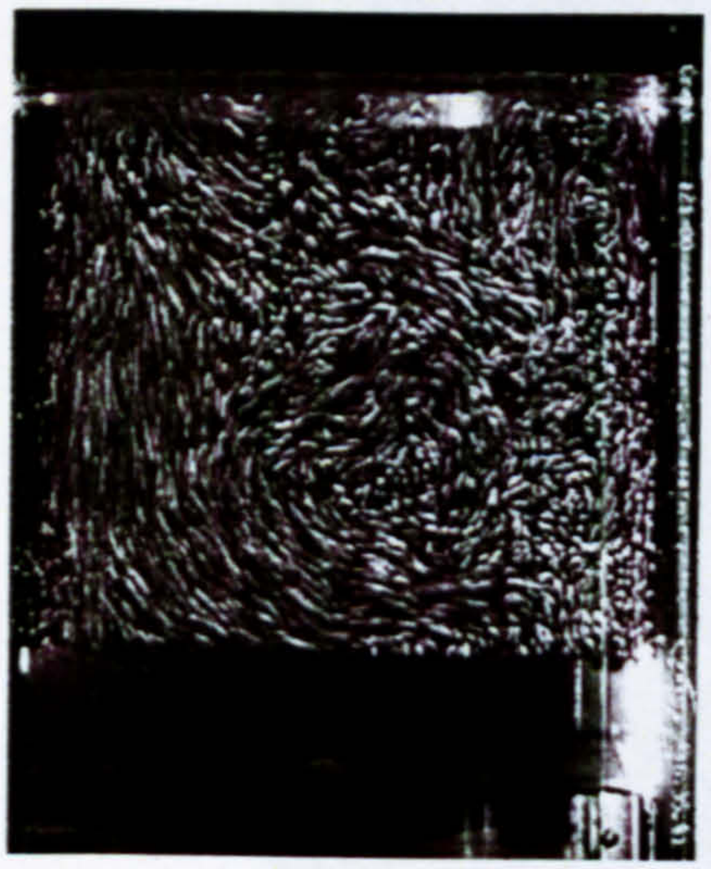

(c) 120° ATDC

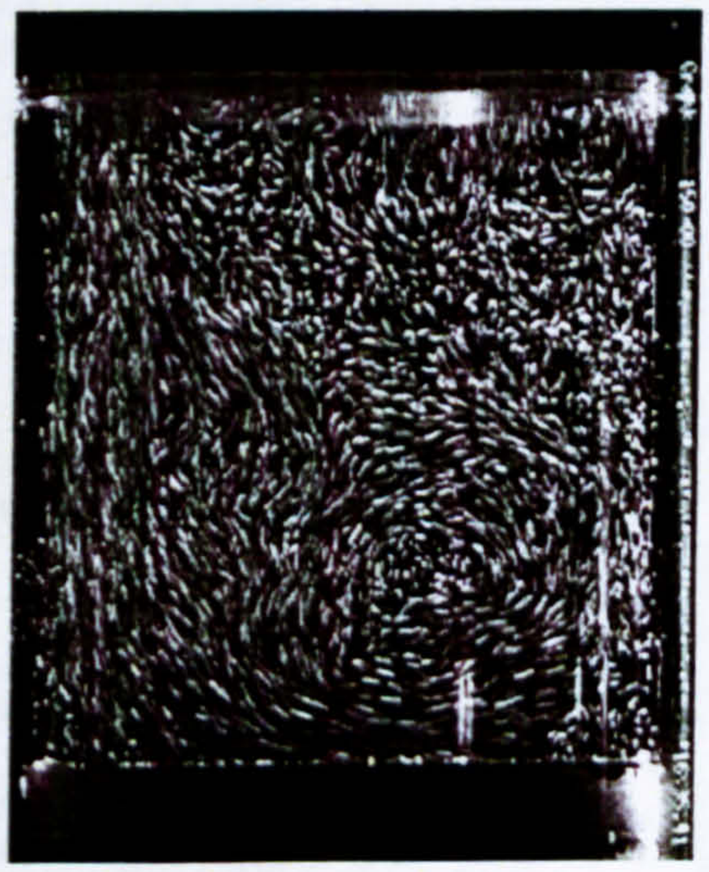

(d) 150° ATDC

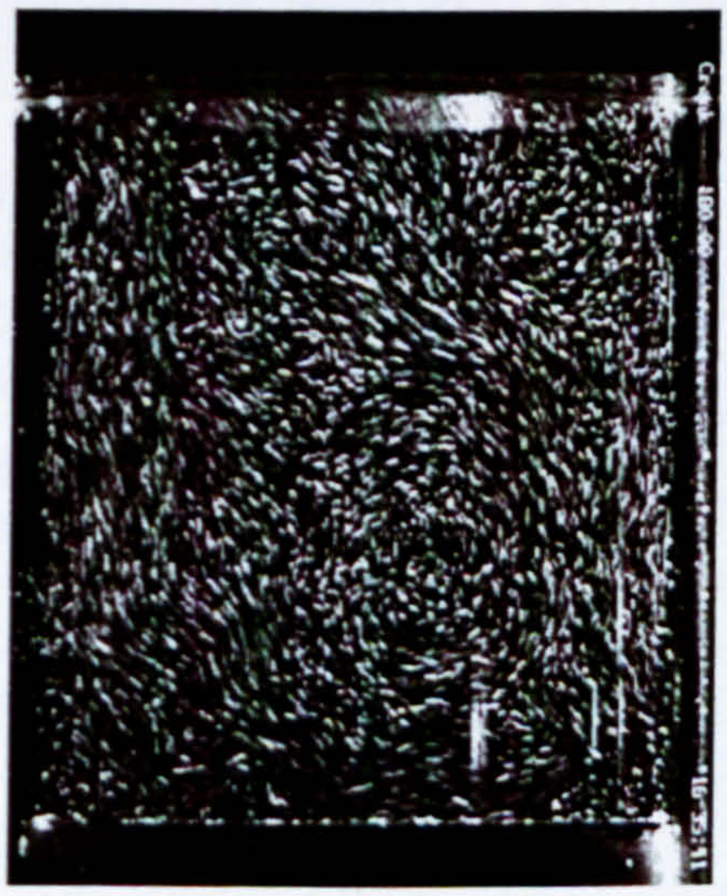

(e) 180° CA (BDC)

Figure 5.3 Development of flow in the plane y = 17.6 mm

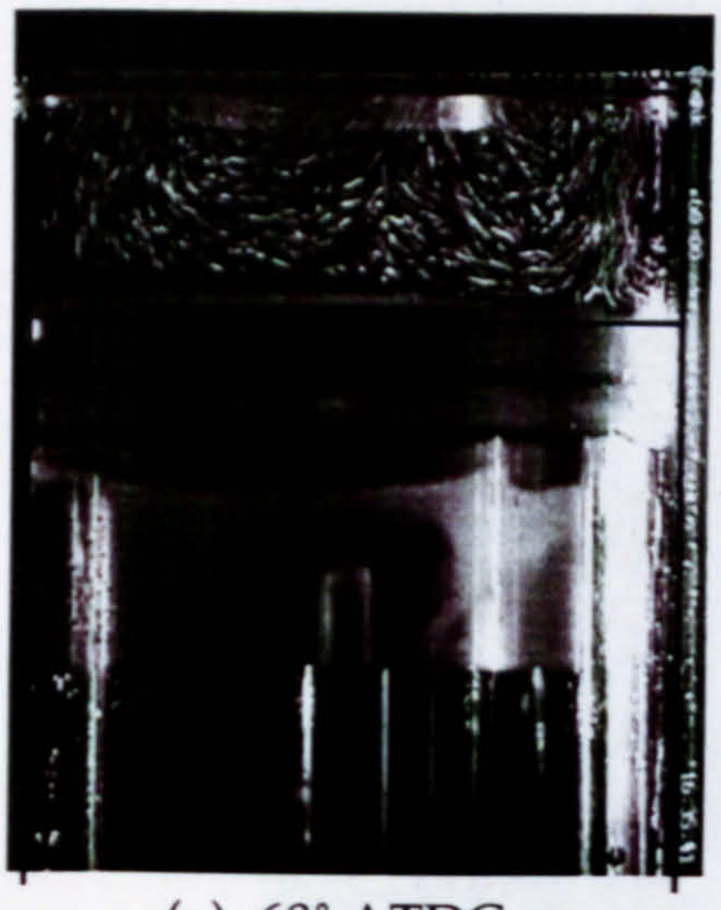

(a) 60° ATDC

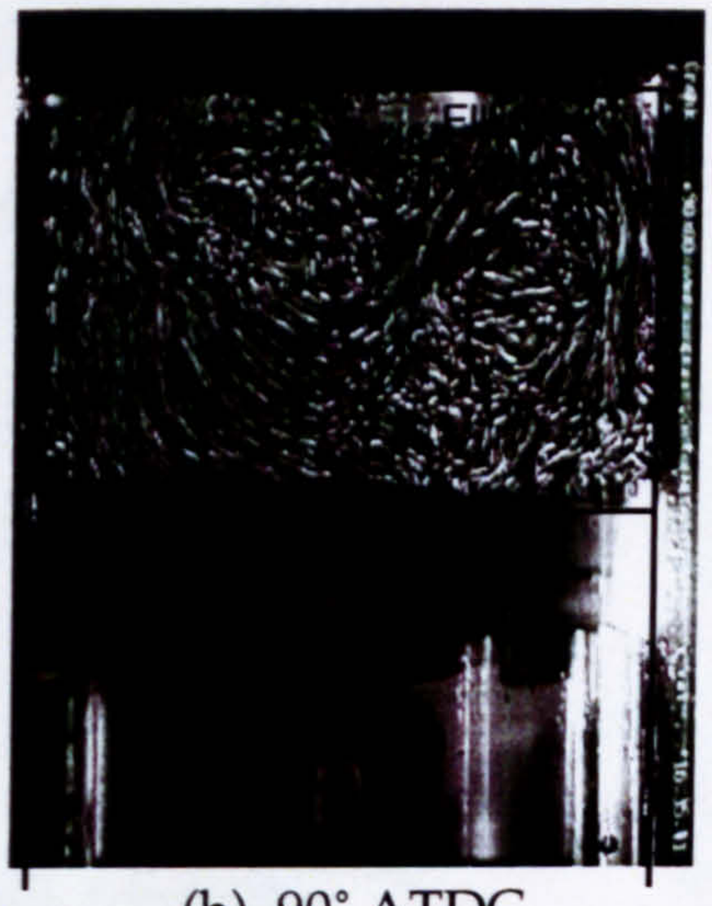

(b) 90° ATDC

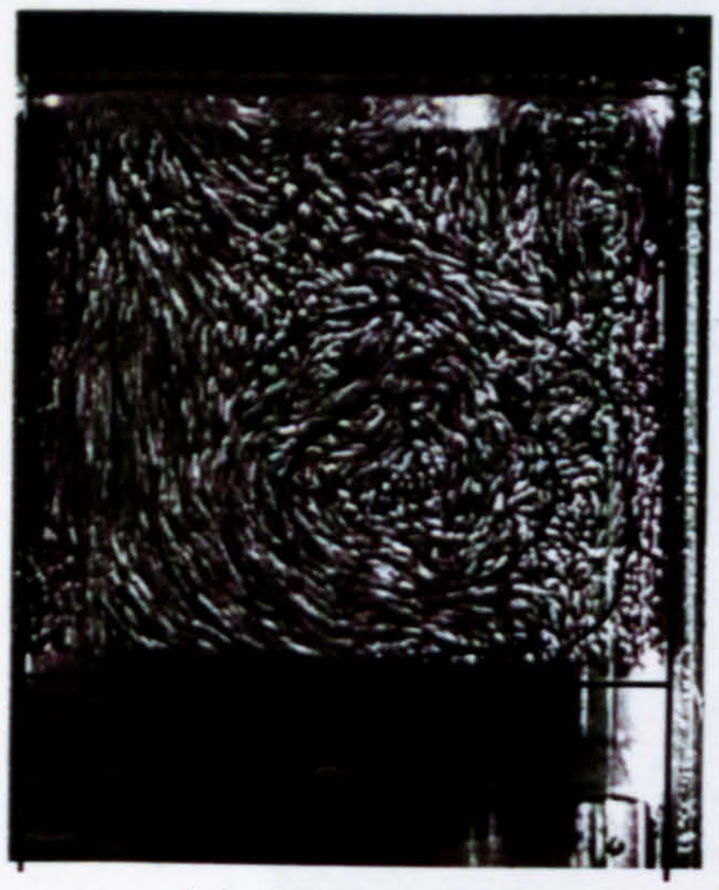

(c) 120° ATDC

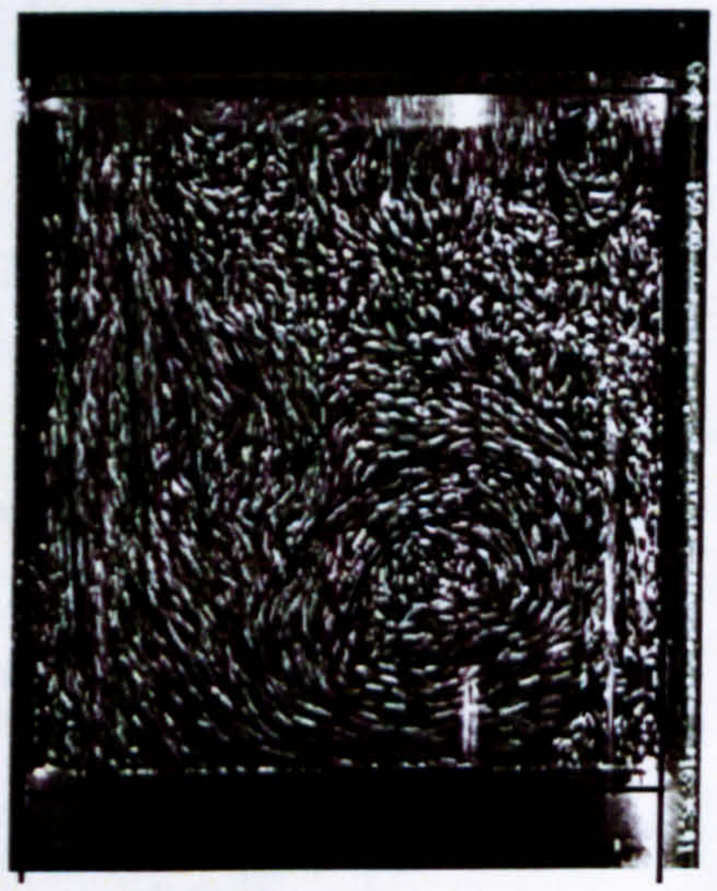

(d) 150° ATDC

(e) 180° CA (BDC)

Figure 5.3 Development of flow in the plane y = 17.6 mm

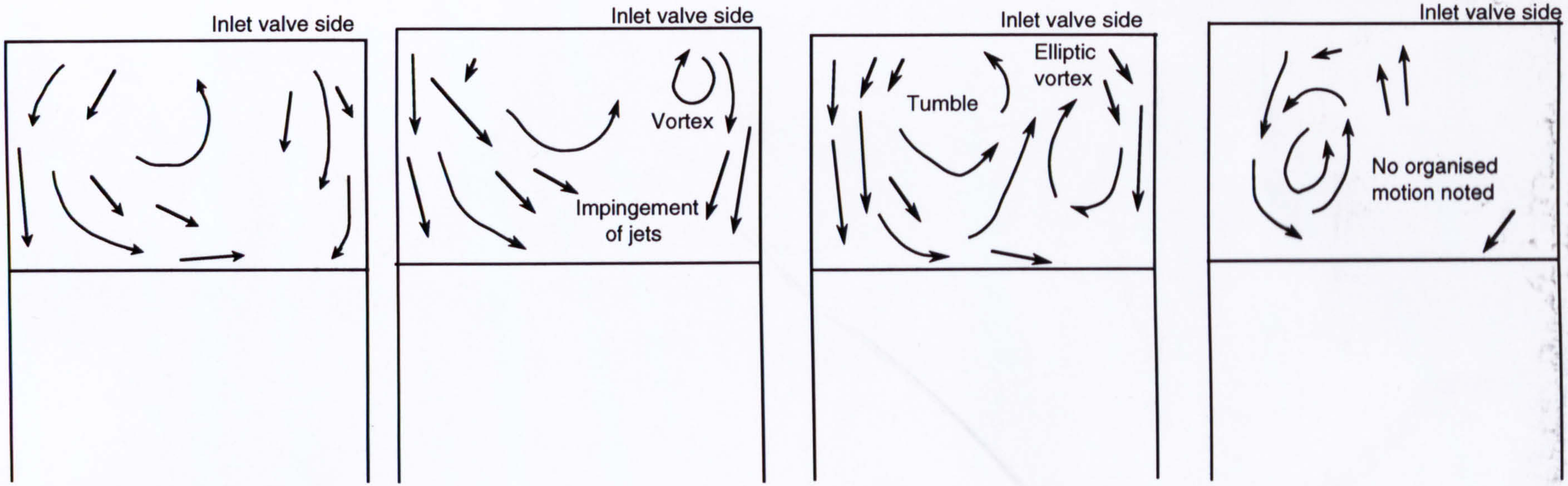
Inlet valve side
Inlet valve side
Vortex
Impingement
of jets
Inlet valve side
Tumble
Elliptic
vortex
Inlet valve side
No organised
motion noted

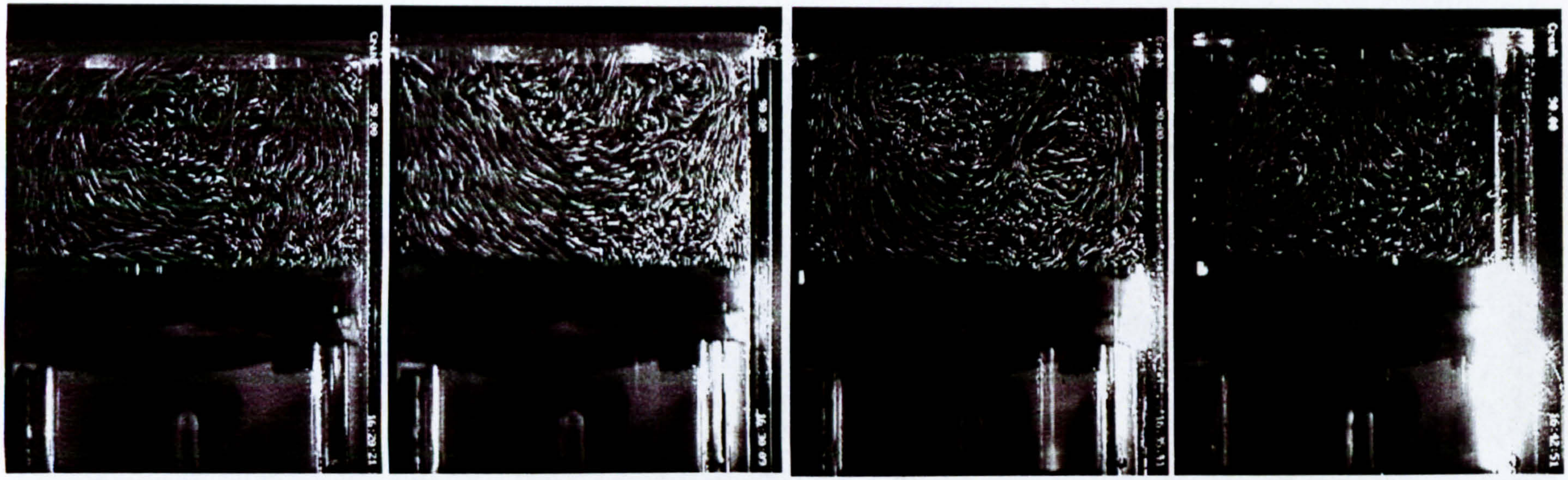

(a) y = 0 mm (b) y = 8.8 mm (c) y = 17.6 mm (d) y = 26.4 mm

Figure 5.4 Variation of in-cylinder flow across the vertical planes at 90° ATDC crankangle

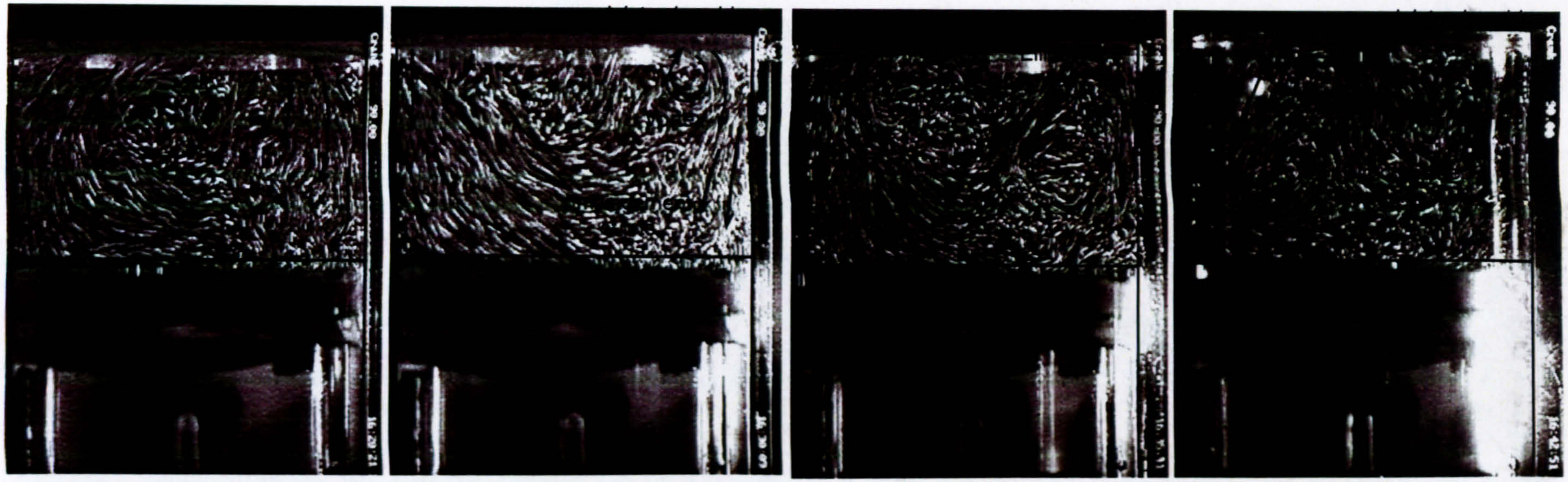

(a) y = 0 mm (b) y = 8.8 mm (c) y = 17.6 mm (d) y = 26.4 mm

Figure 5.4 Variation of in-cylinder flow across the vertical planes at 90° ATDC crankangle

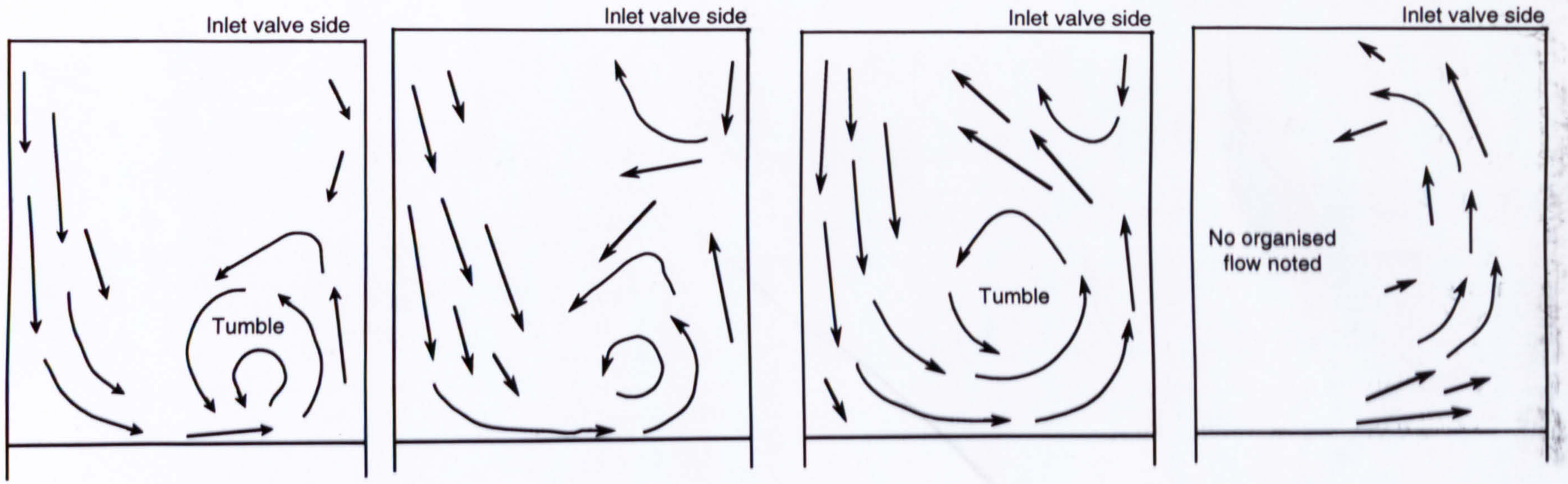
Inlet valve side
Tumble
Inlet valve side
Inlet valve side
Tumble
Inlet valve side
No organised
flow noted

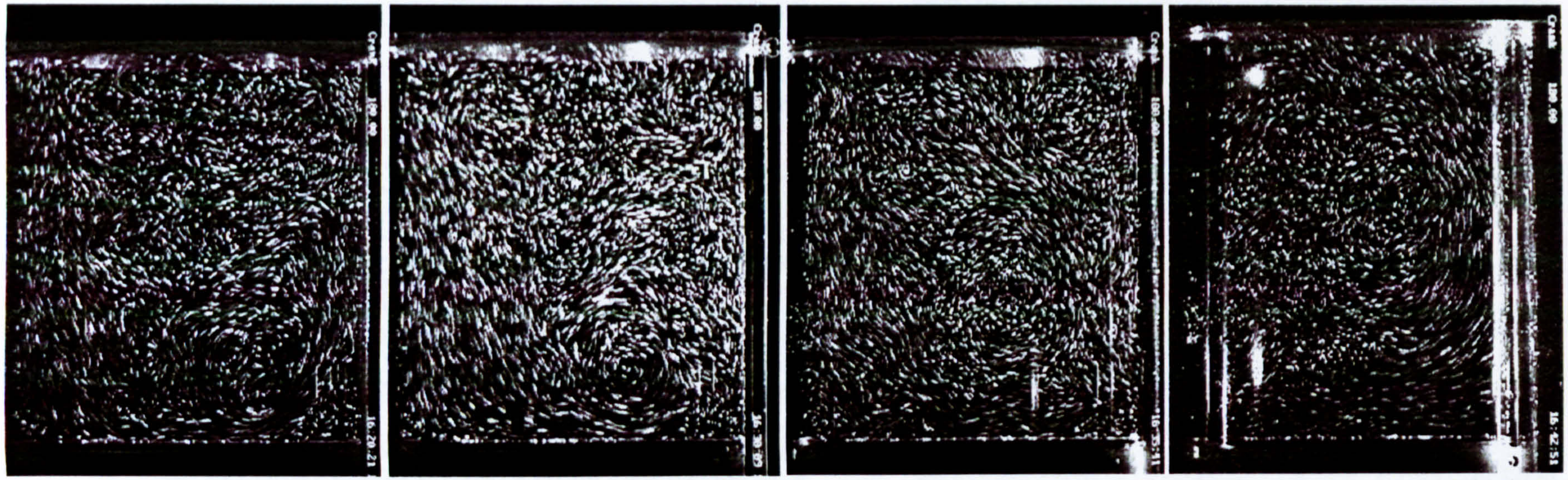

(a) y = 0 mm (b) y = 8.8 mm (c) y = 17.6 mm (d) y = 26.4 mm

Figure 5.5 Variation of in-cylinder flow across the vertical planes at 180° (BDC) crankangle

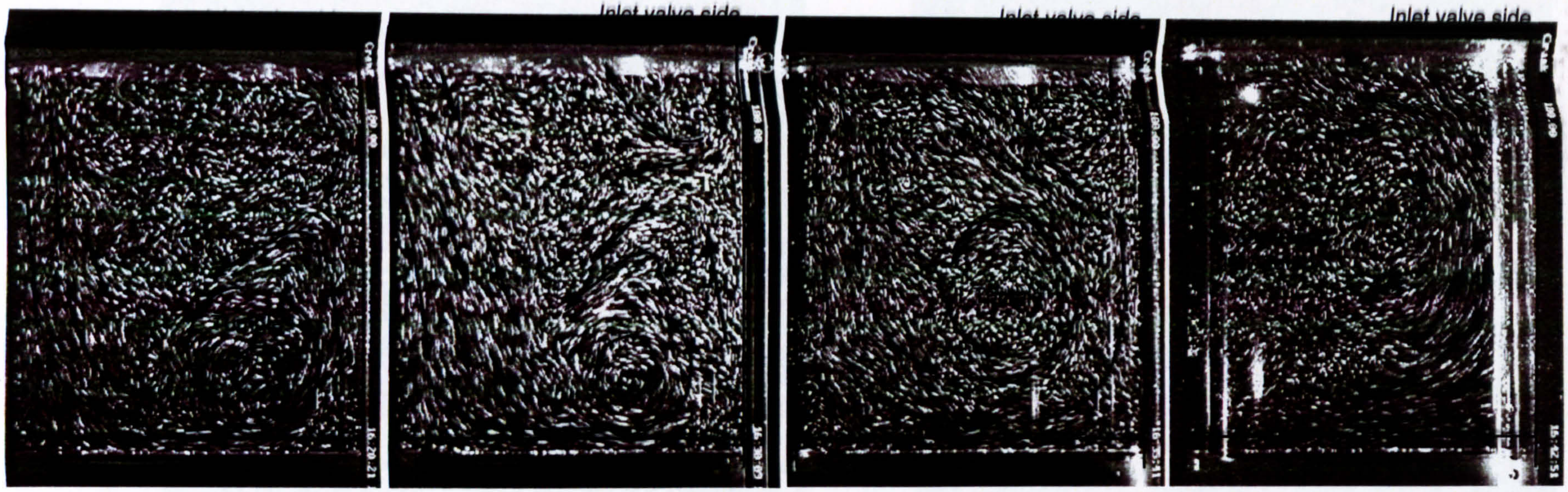

(a) y = 0 mm (b) y = 8.8 mm (c) y = 17.6 mm (d) y = 26.4 mm

Figure 5.5 Variation of in-cylinder flow across the vertical planes at 180° (BDC) crankangle

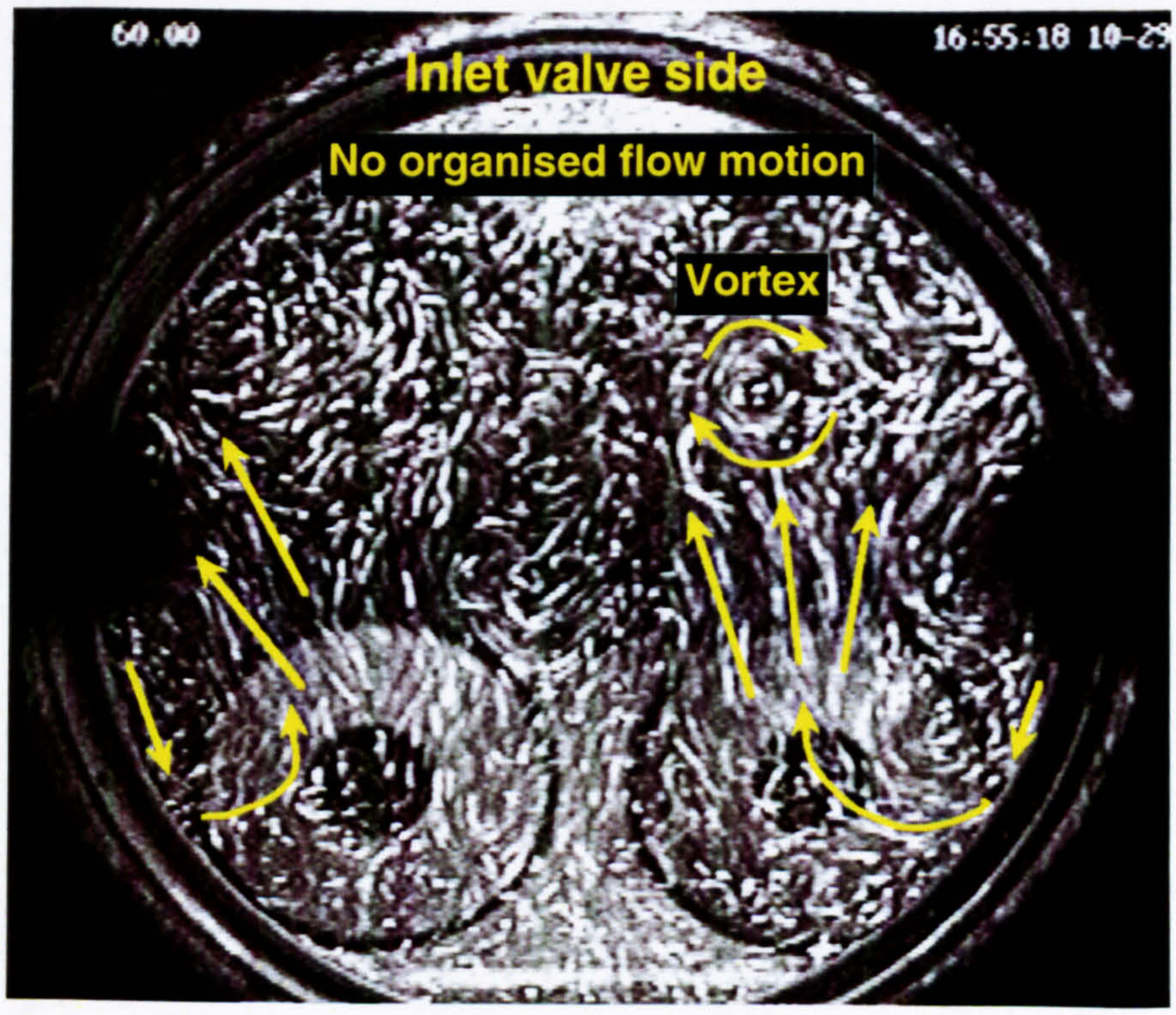

(a) Flow structure in the plane z = 10 mm

(b) Flow structure in the plane z = 25 mm

Figure 5.6 Flow structure in horizontal planes at 60° ATDC crankangle

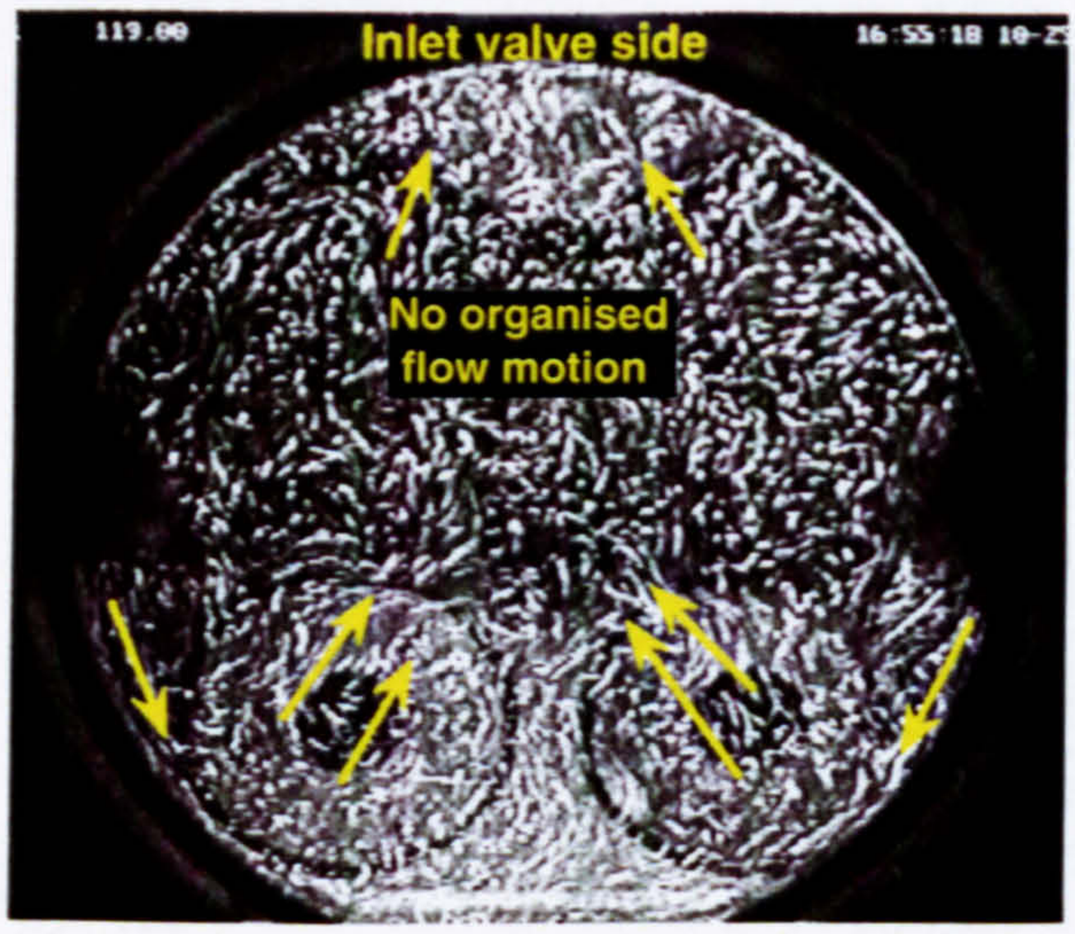

(a) Flow structure in the plane z = 10 mm

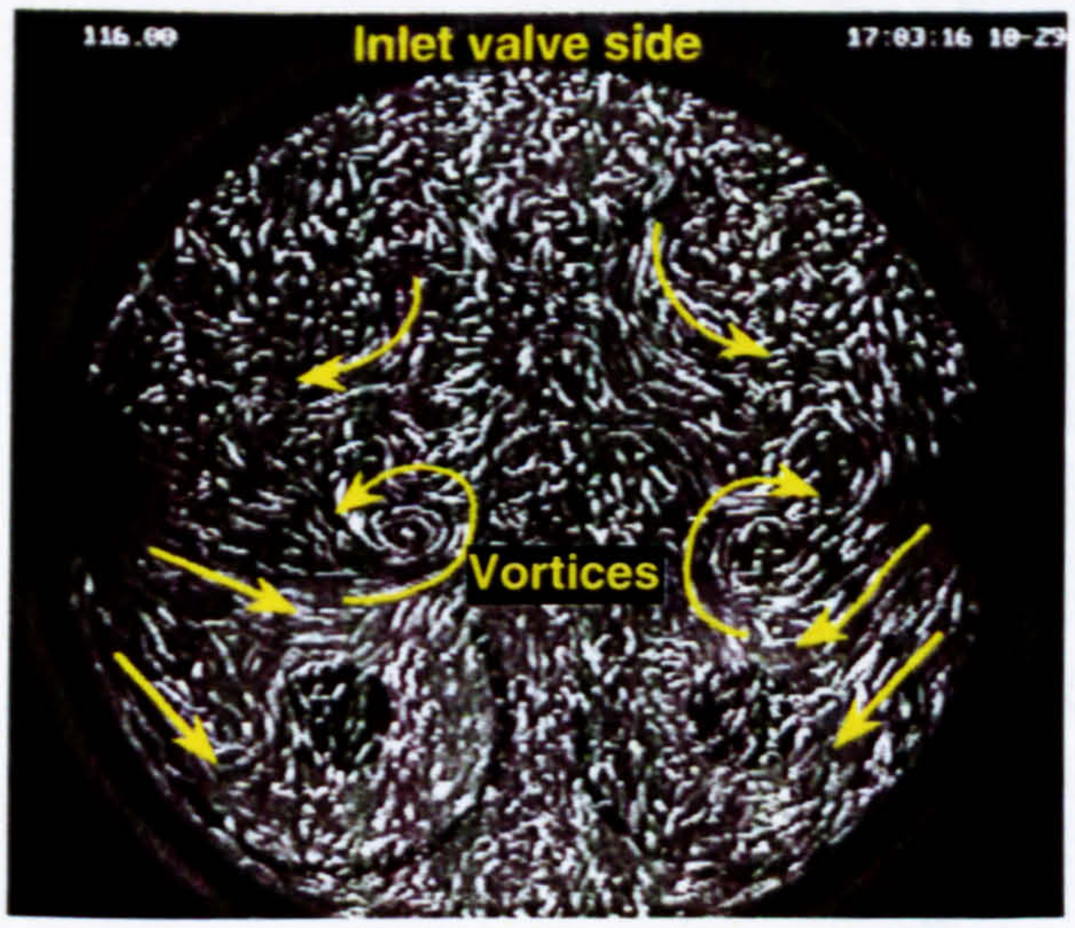

(b) Flow structure in the plane z = 25 mm

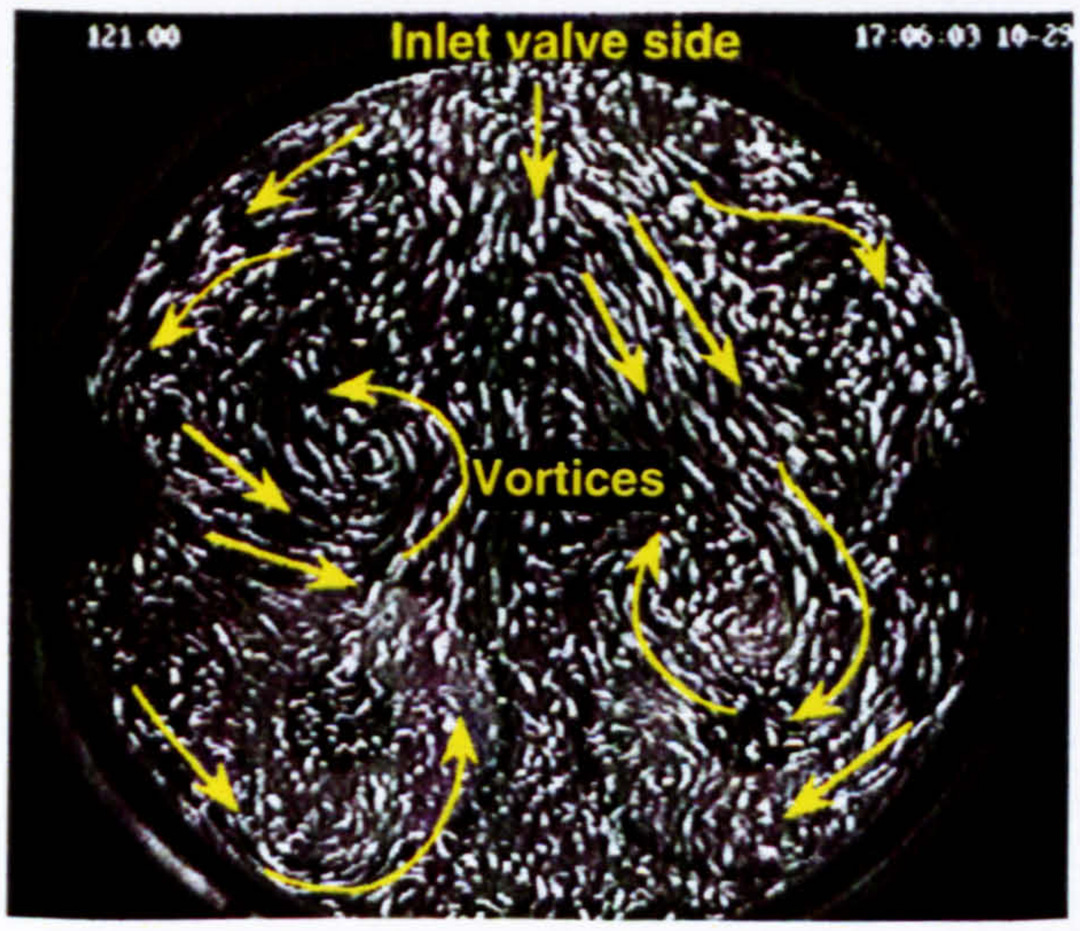

(c) Flow structure in the plane z = 40 mm

Figure 5.7 Flow structure in horizontal planes at 120° ATDC crankangle

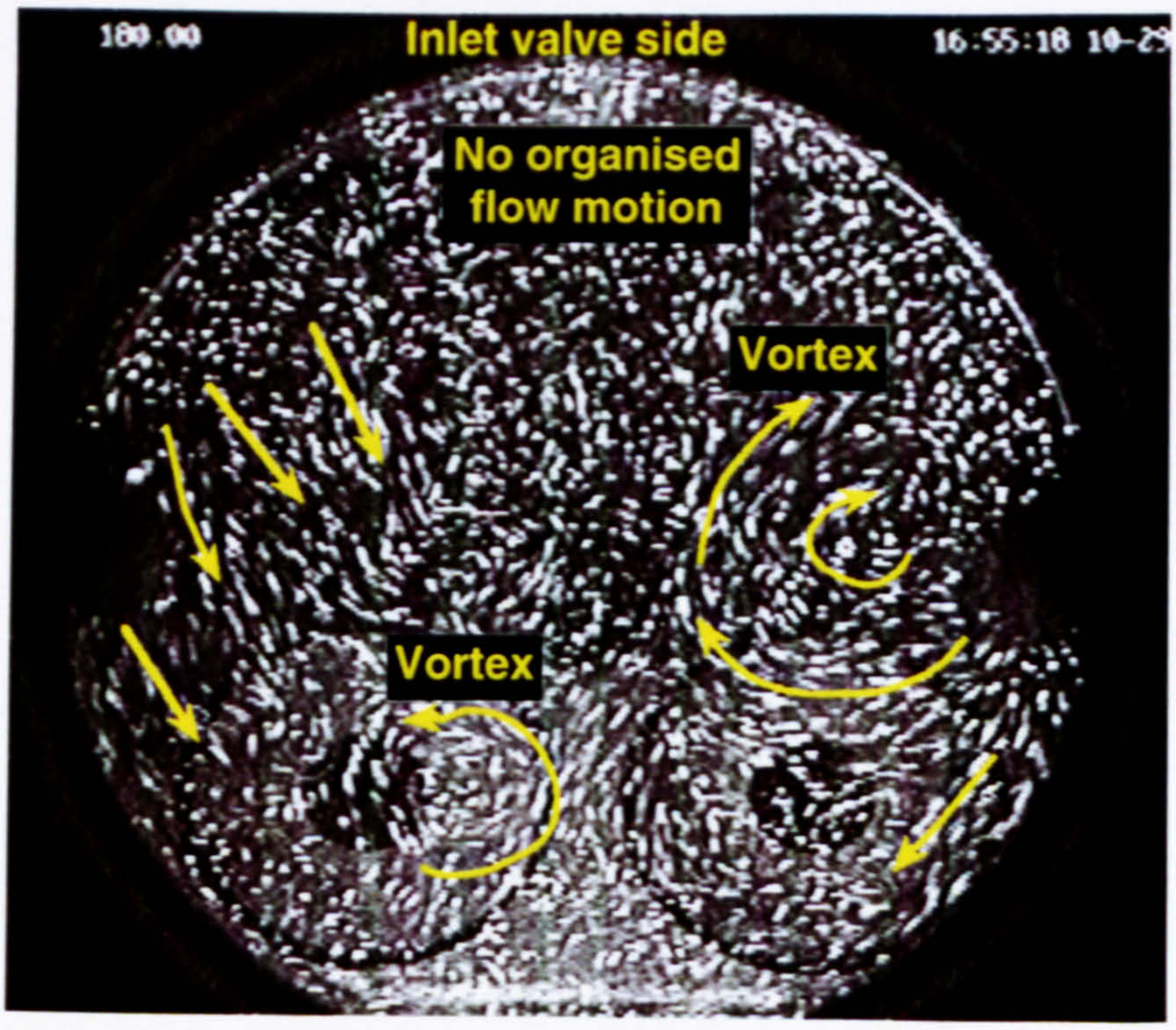

Figure 5.8(a) Flow structure in the plane z = 10 mm at 180° (BDC) crankangle

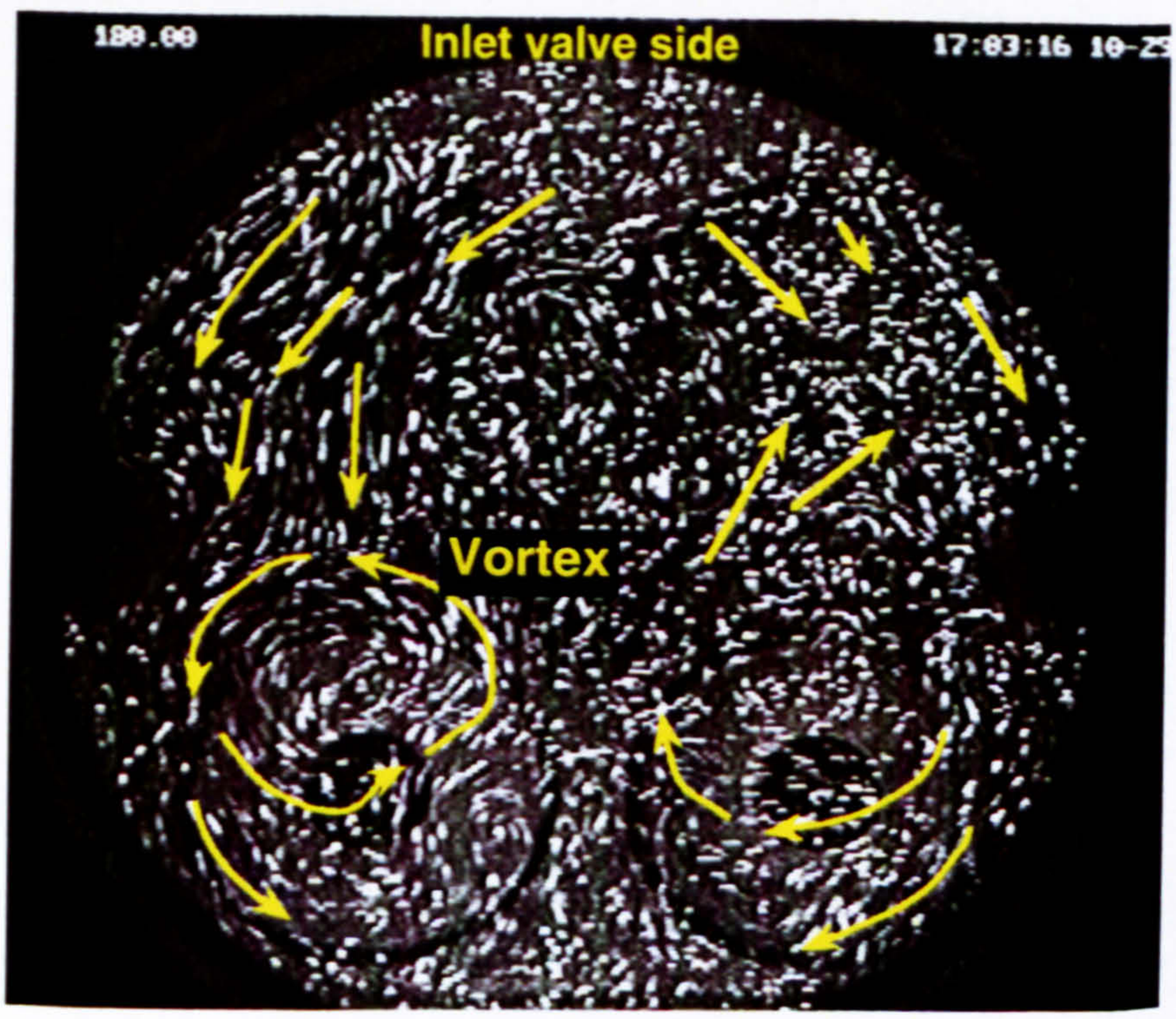

Figure 5.8(b) Flow structure in the plane z = 25 mm at 180° ATDC crankangle

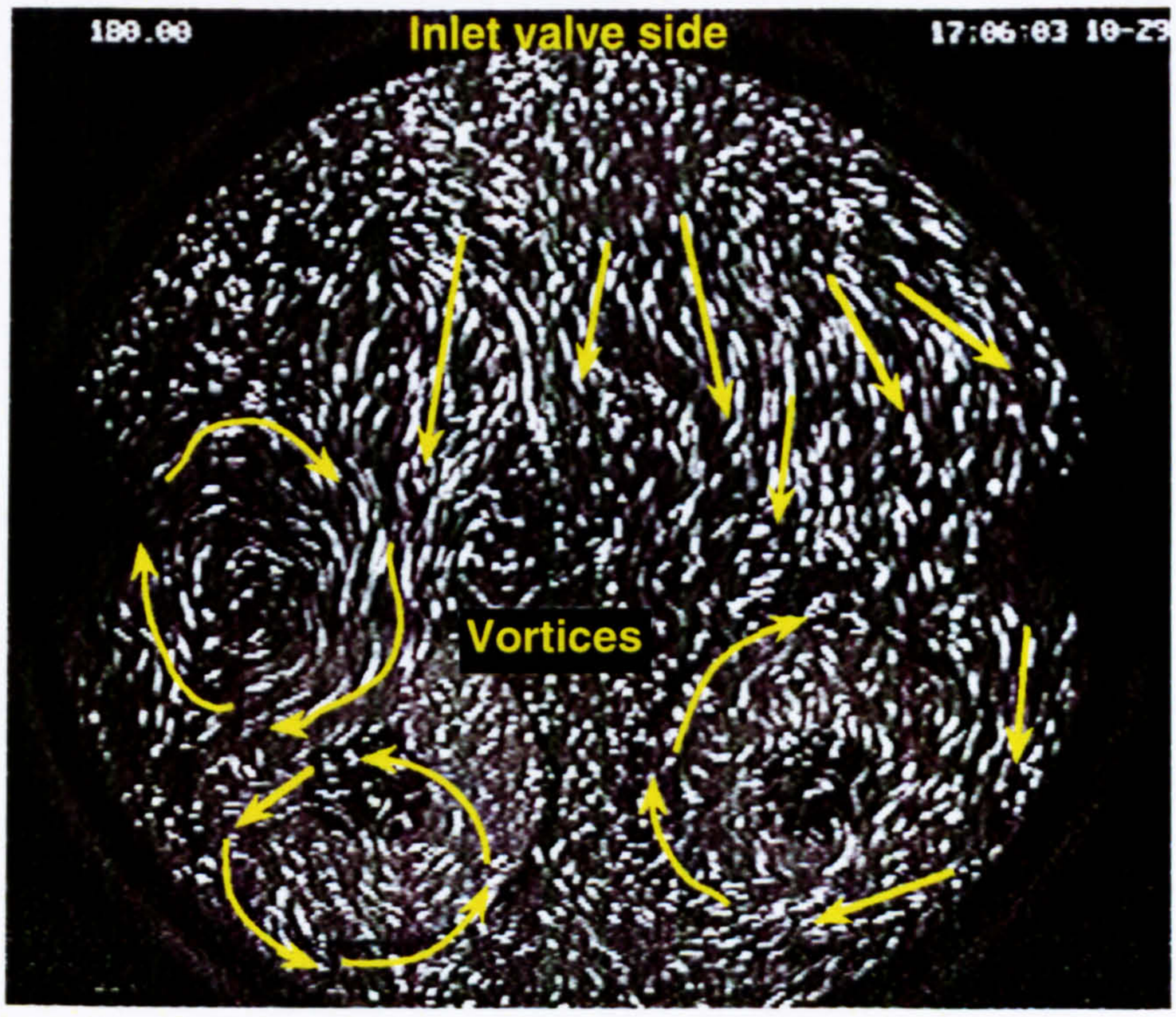

Figure 5.8(c) Flow structure in the plane z = 40 mm at 180° (BDC) crankangle

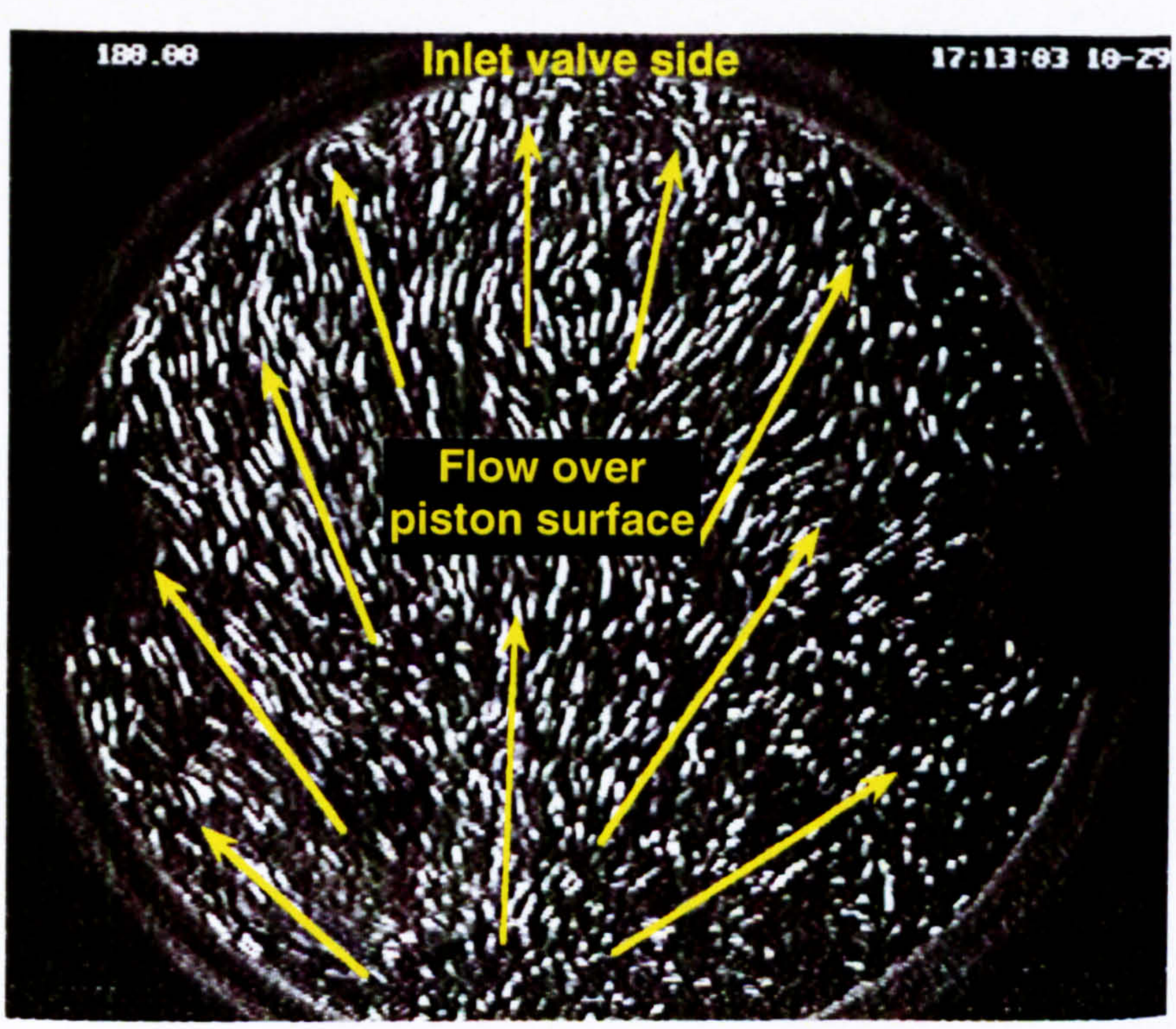

Figure 5.8(d) Flow structure in the plane z = 80 mm at 180° (BDC) crankangle

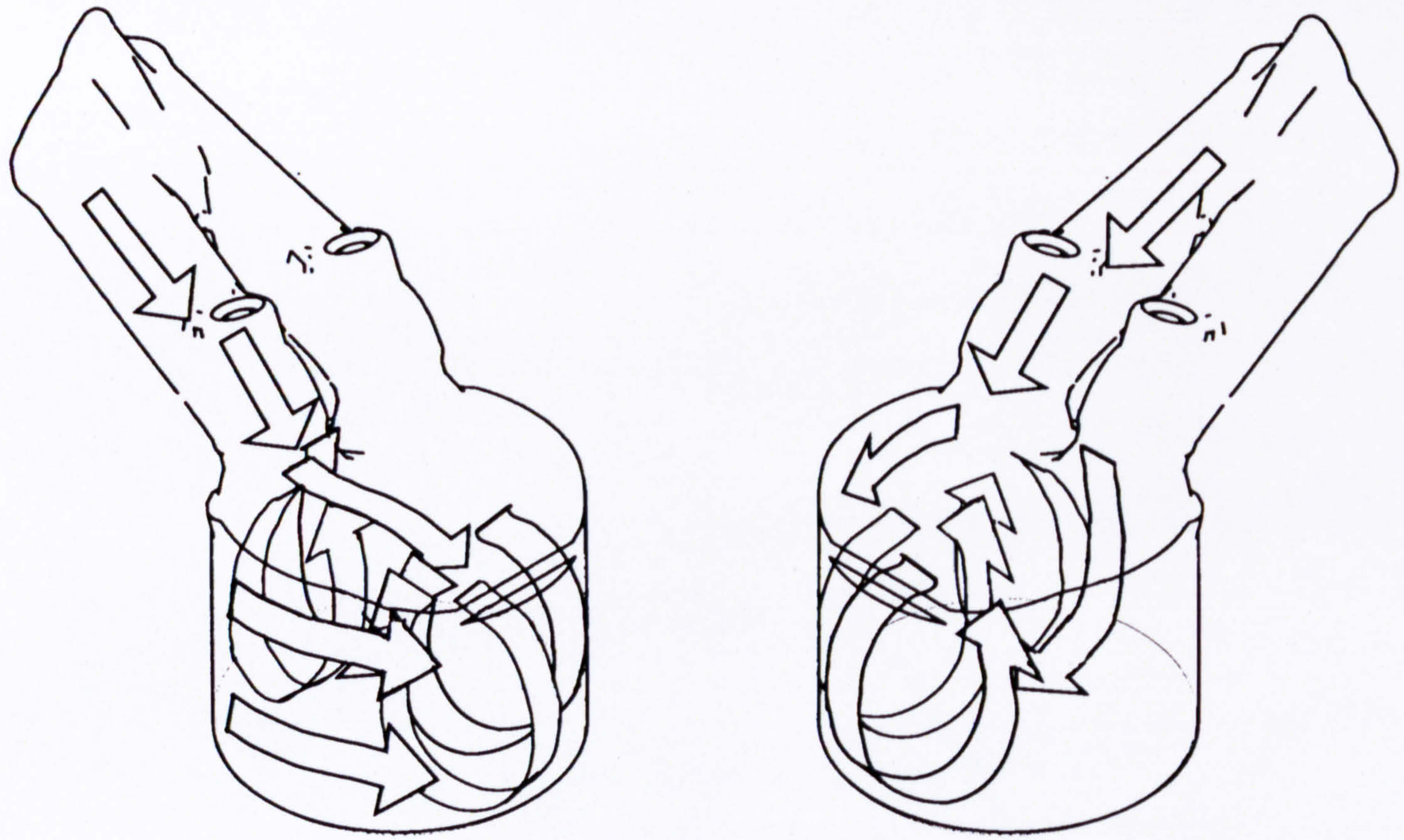

Figure 5.9(a) Three-dimensional flow pattern in the engine cylinder at 90° ATDC
(one half of the flow structure shown)

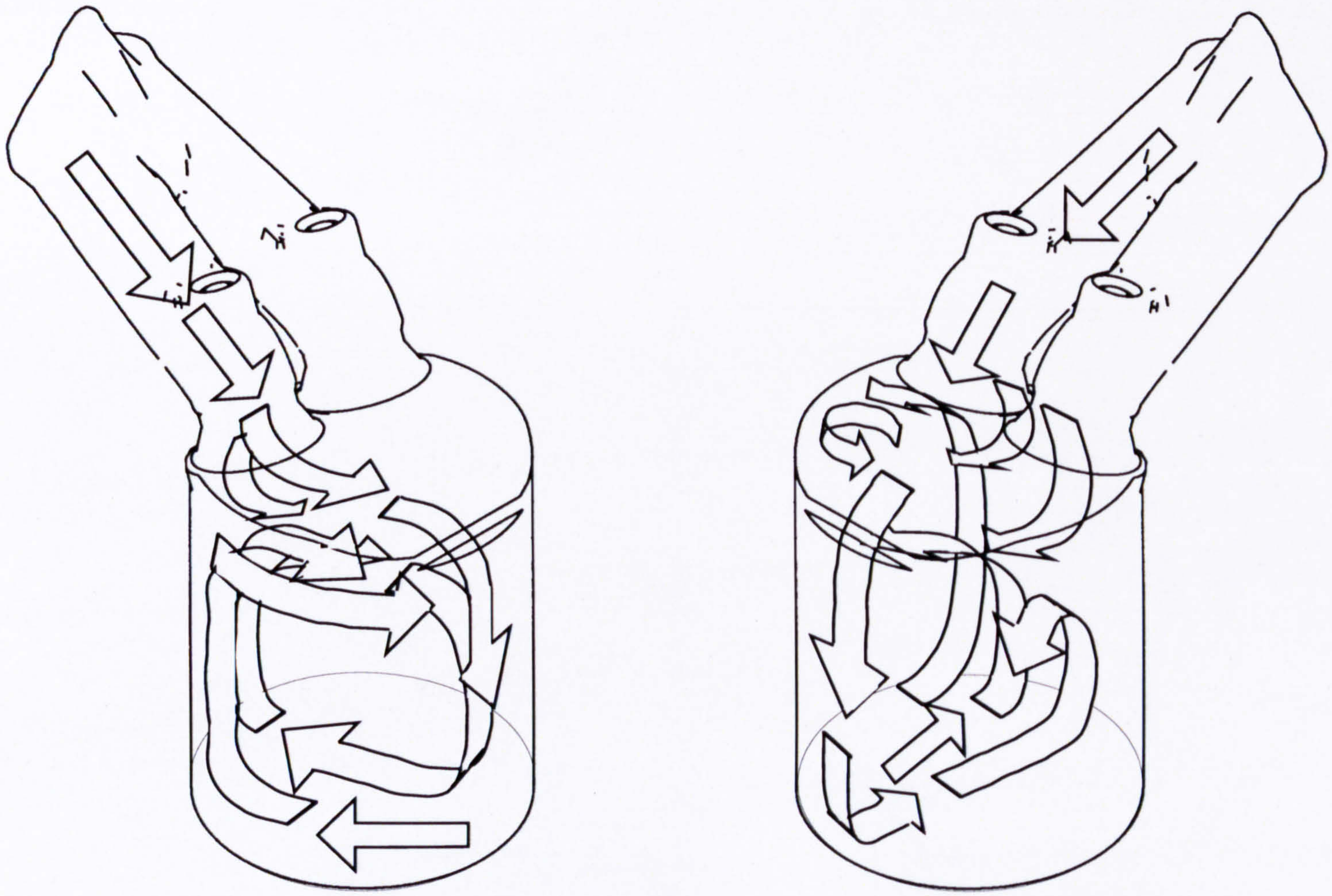

Figure 5.9(b) Illustration of the three-dimensional in-cylinder flow pattern at BDC induction (one half of the flow structure shown)

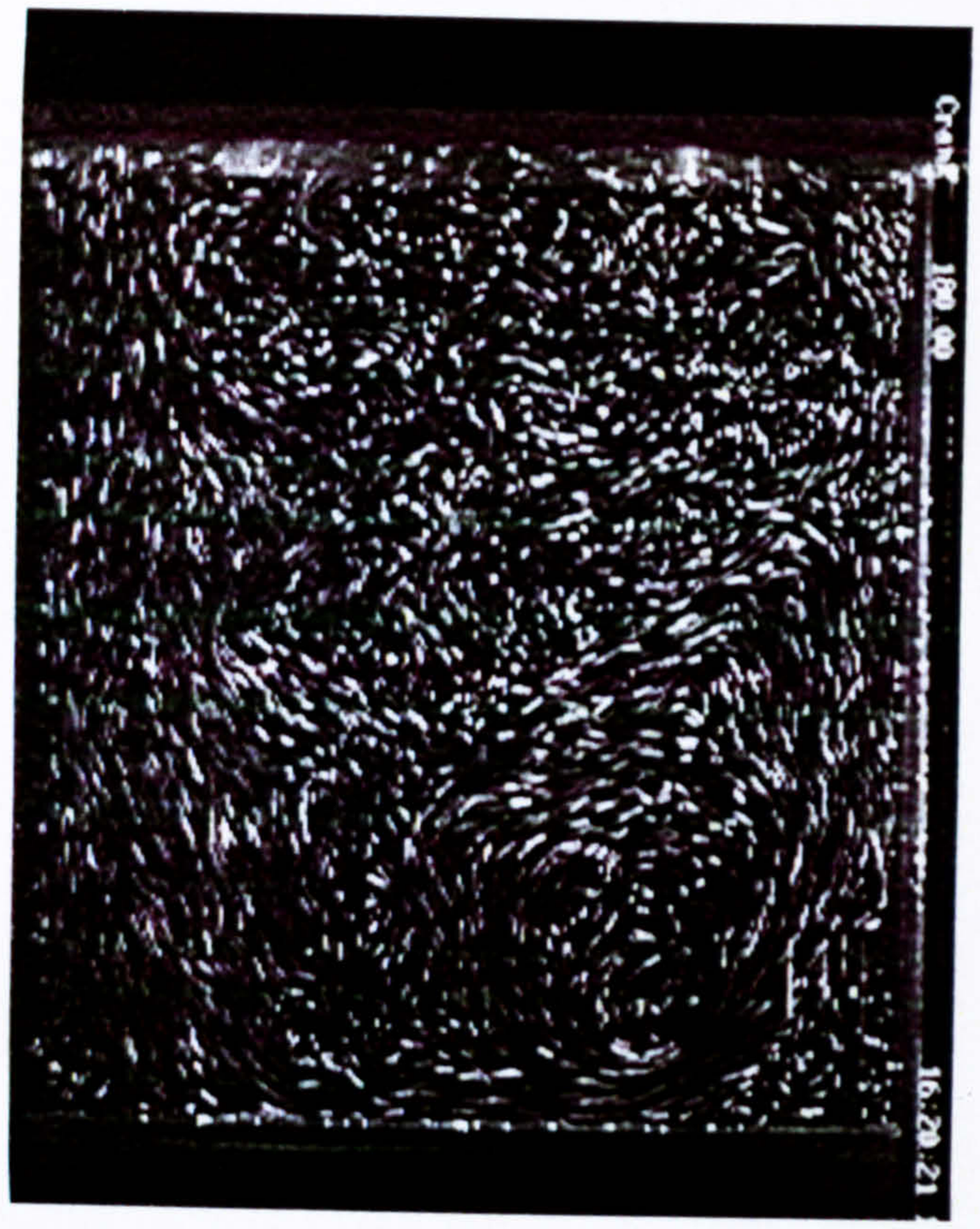

Flow visualisation image

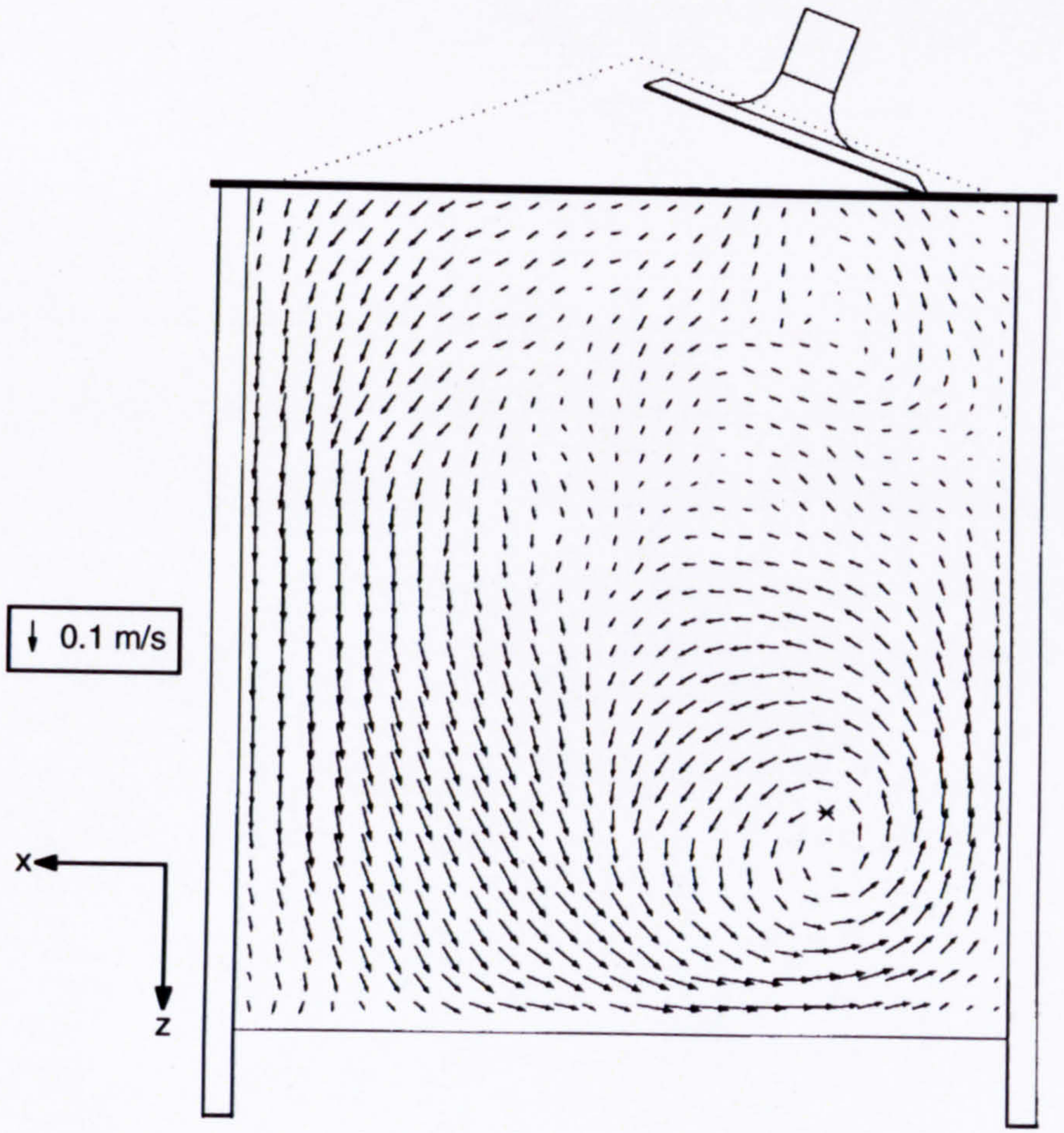

Averaged velocity vector map

Figure 5.10 Qualitative and quantitative flow field in the mid-cylinder plane y = 0 mm at 180° (BDC) crankangle

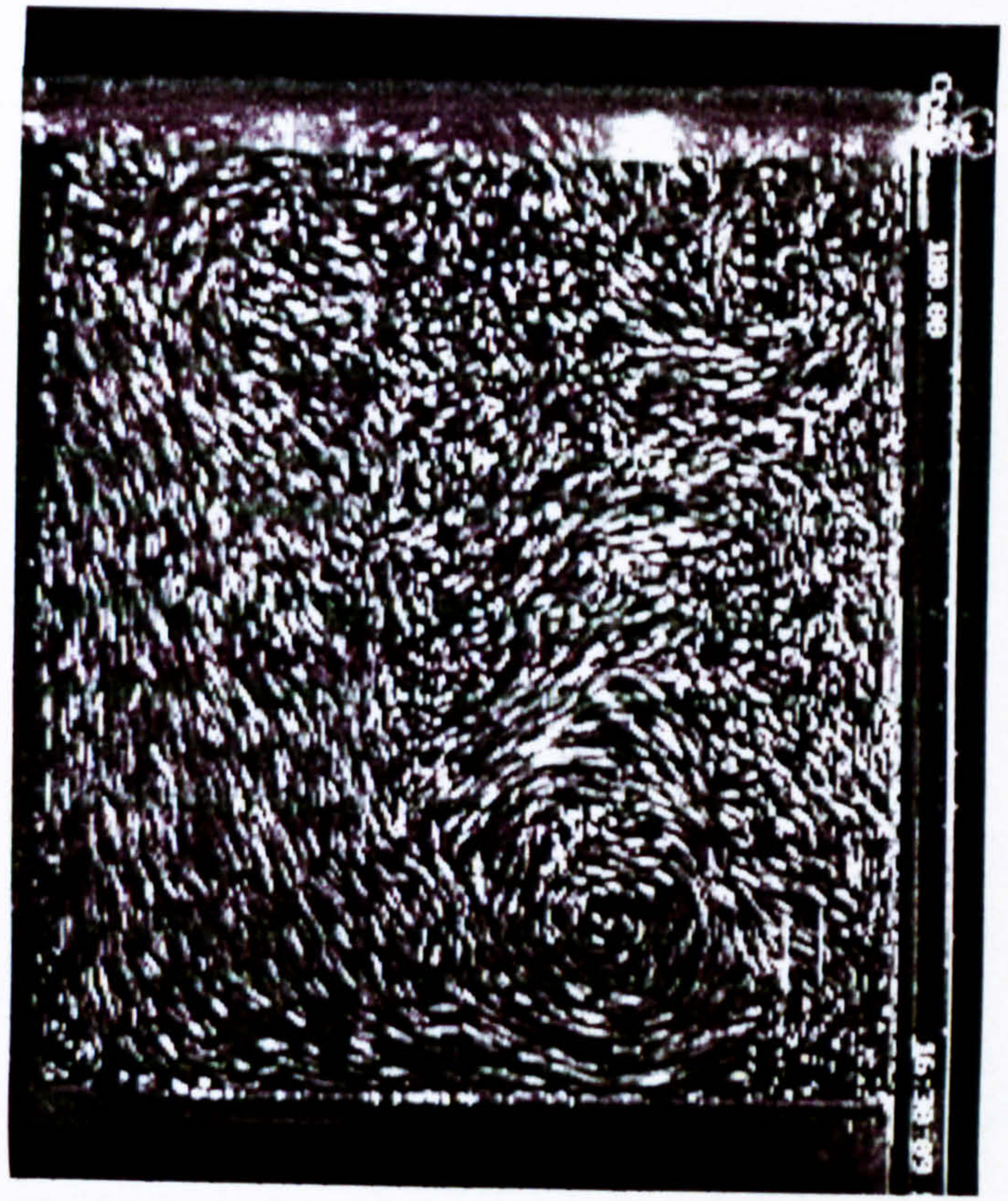

Flow visualisation image

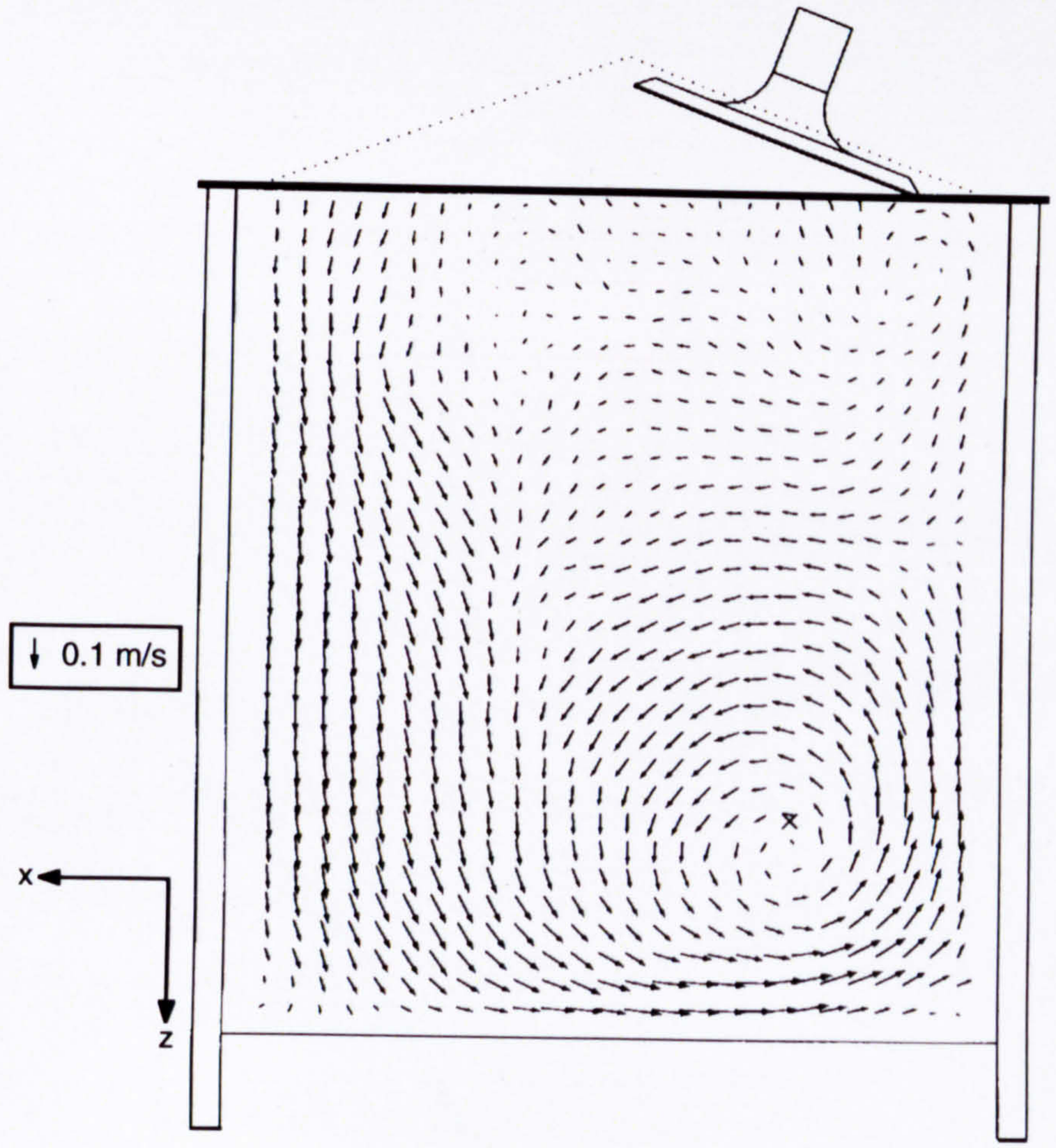

Averaged velocity vector map

Figure 5.11 Qualitative and quantitative flow field in the plane y = 8.8 mm at 180° (BDC) crankangle

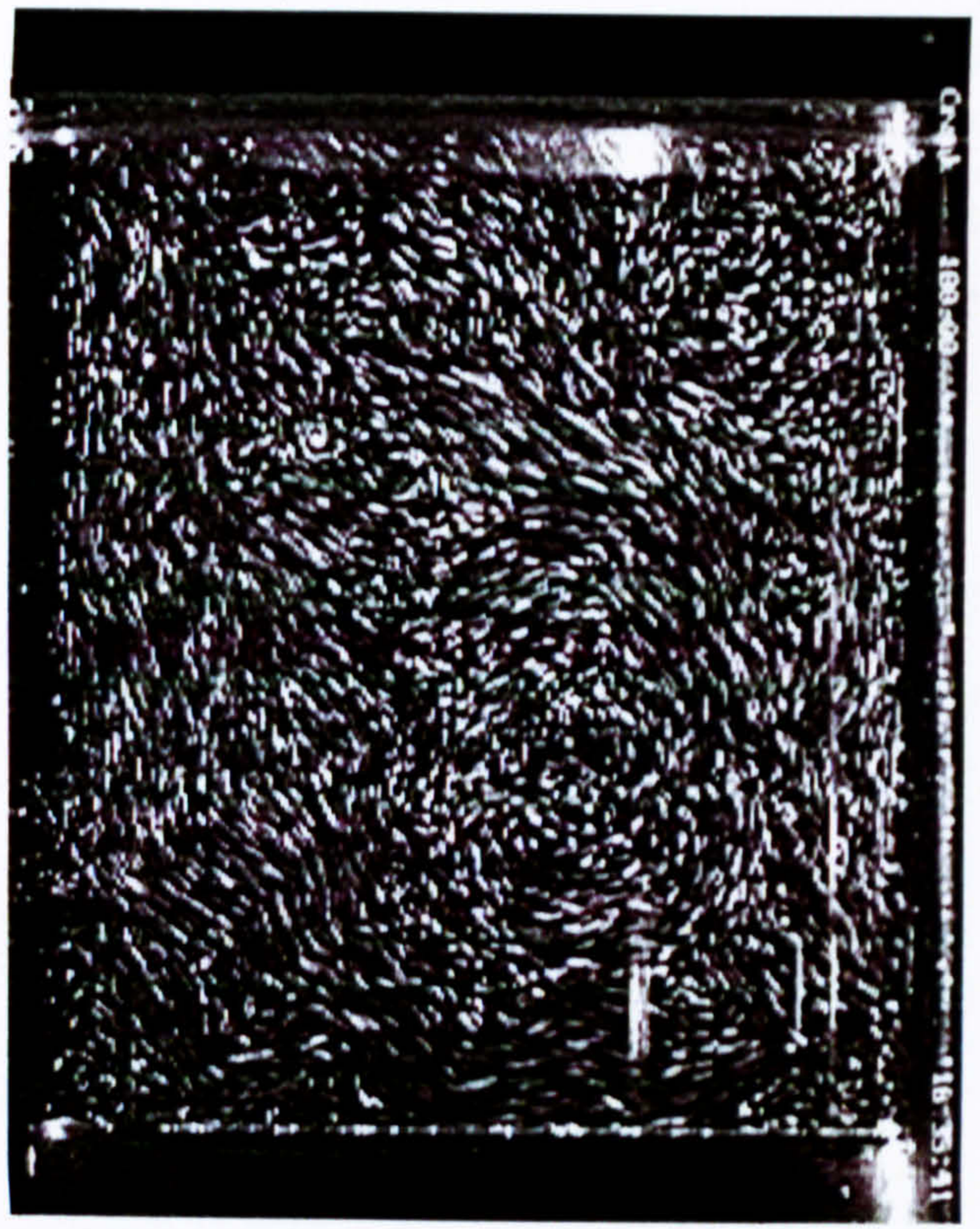

Flow visualisation image

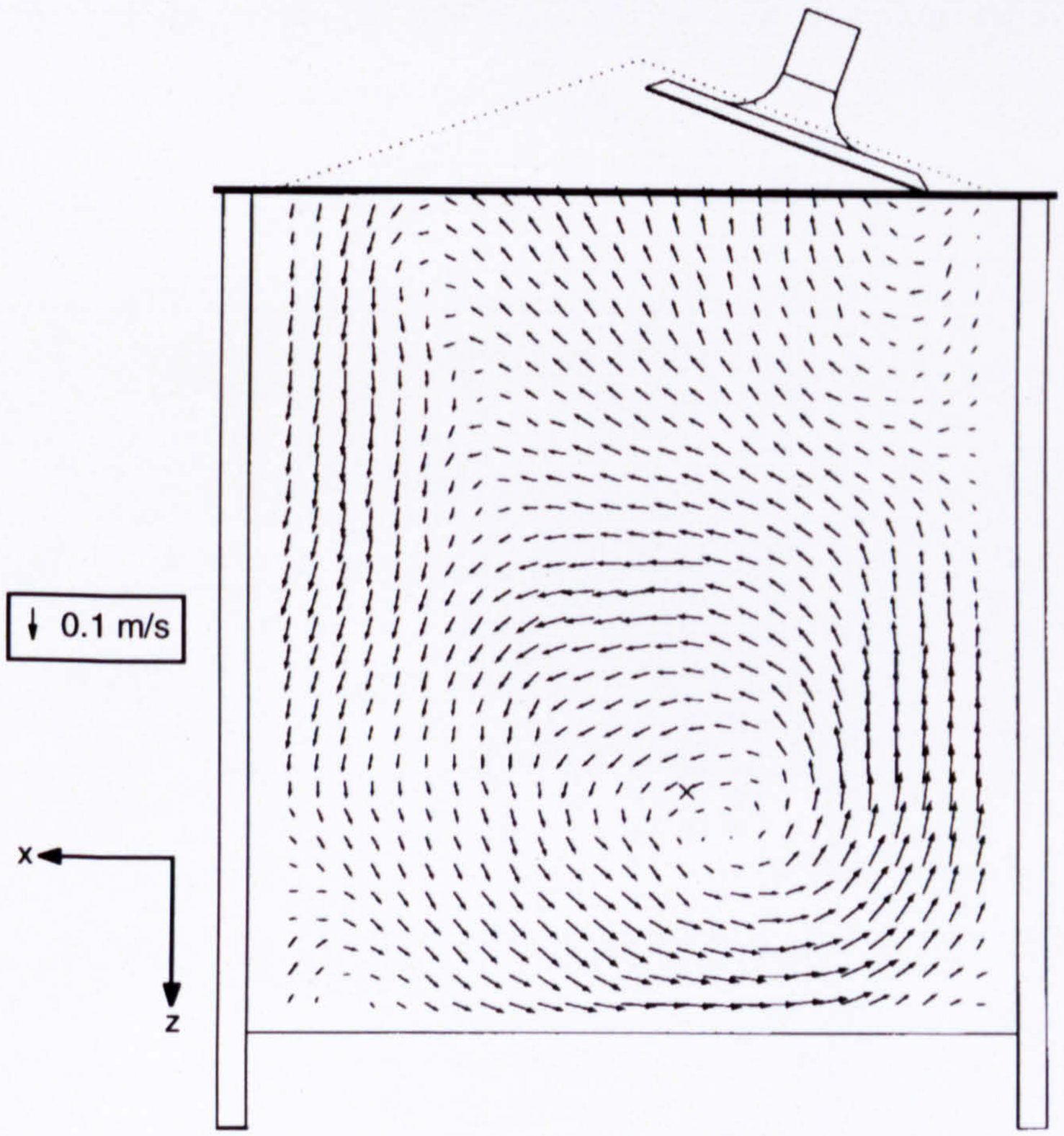

Averaged velocity vector map

Figure 5.12 Qualitative and quantitative flow field in the mid-valve plane y = 17.6 mm at 180° (BDC) crankangle

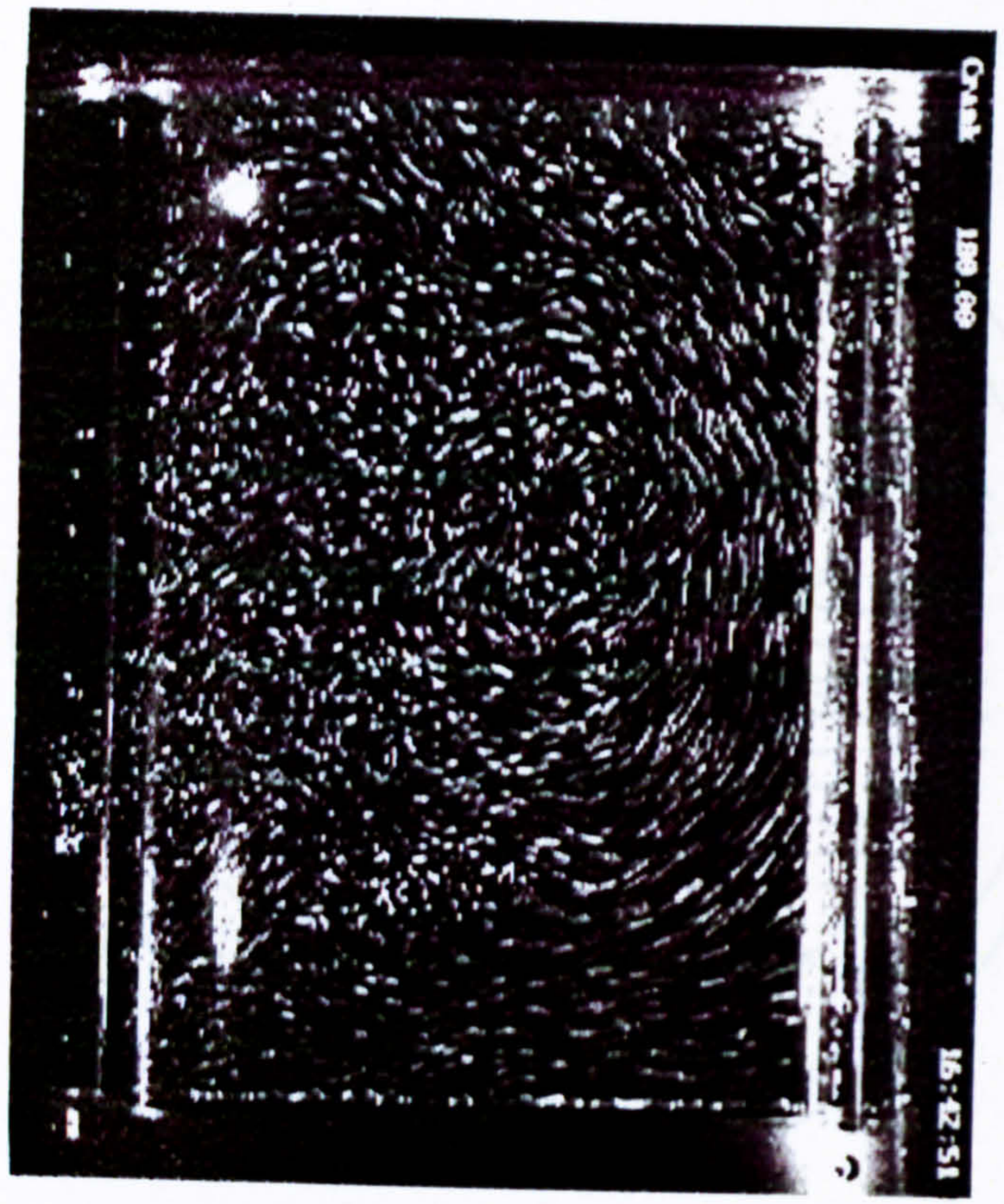

Flow visualisation image

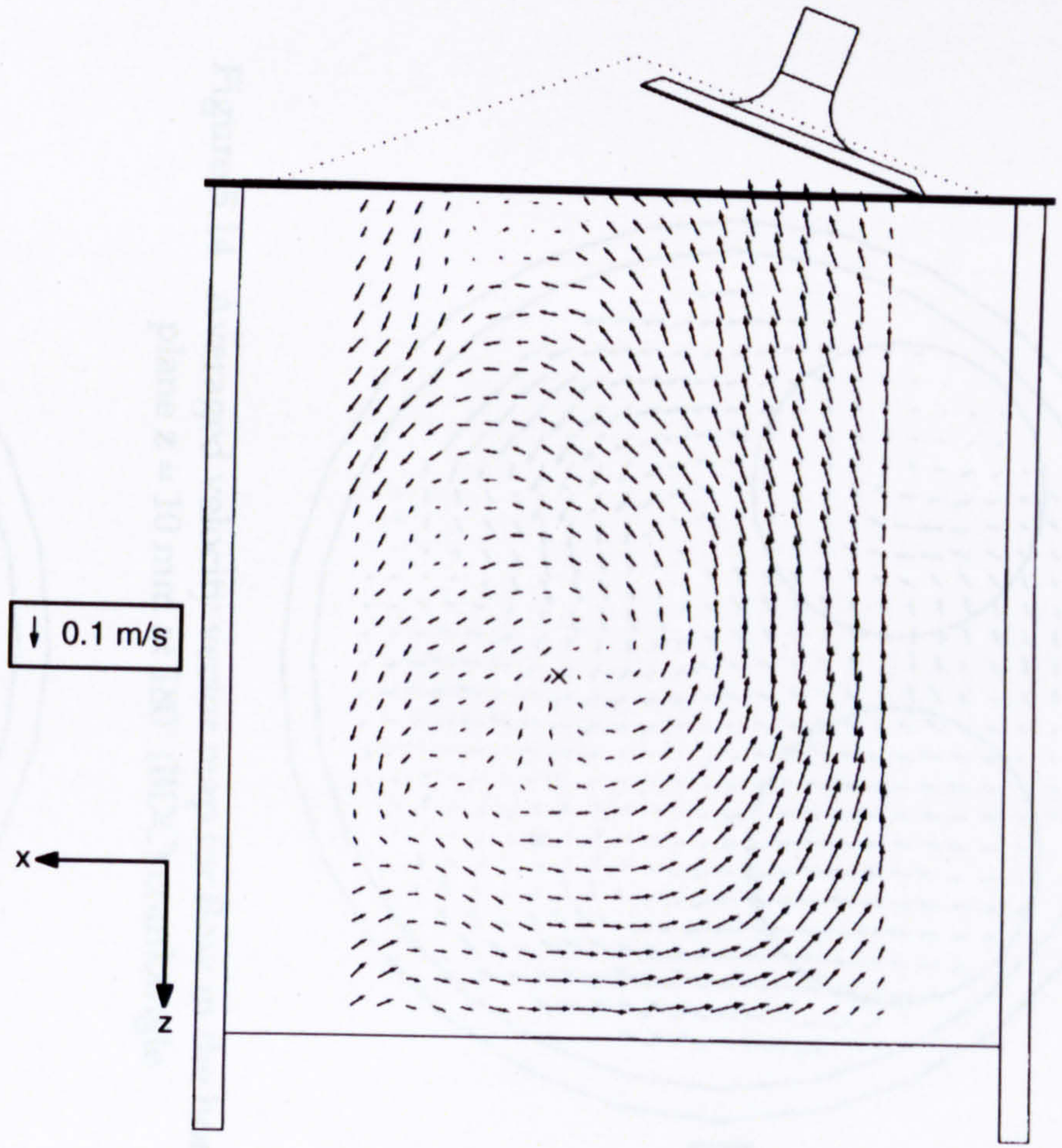

Averaged velocity vector map

Figure 5.13 Qualitative and quantitative flow field in the plane y = 26.4 mm at 180° (BDC) crankangle

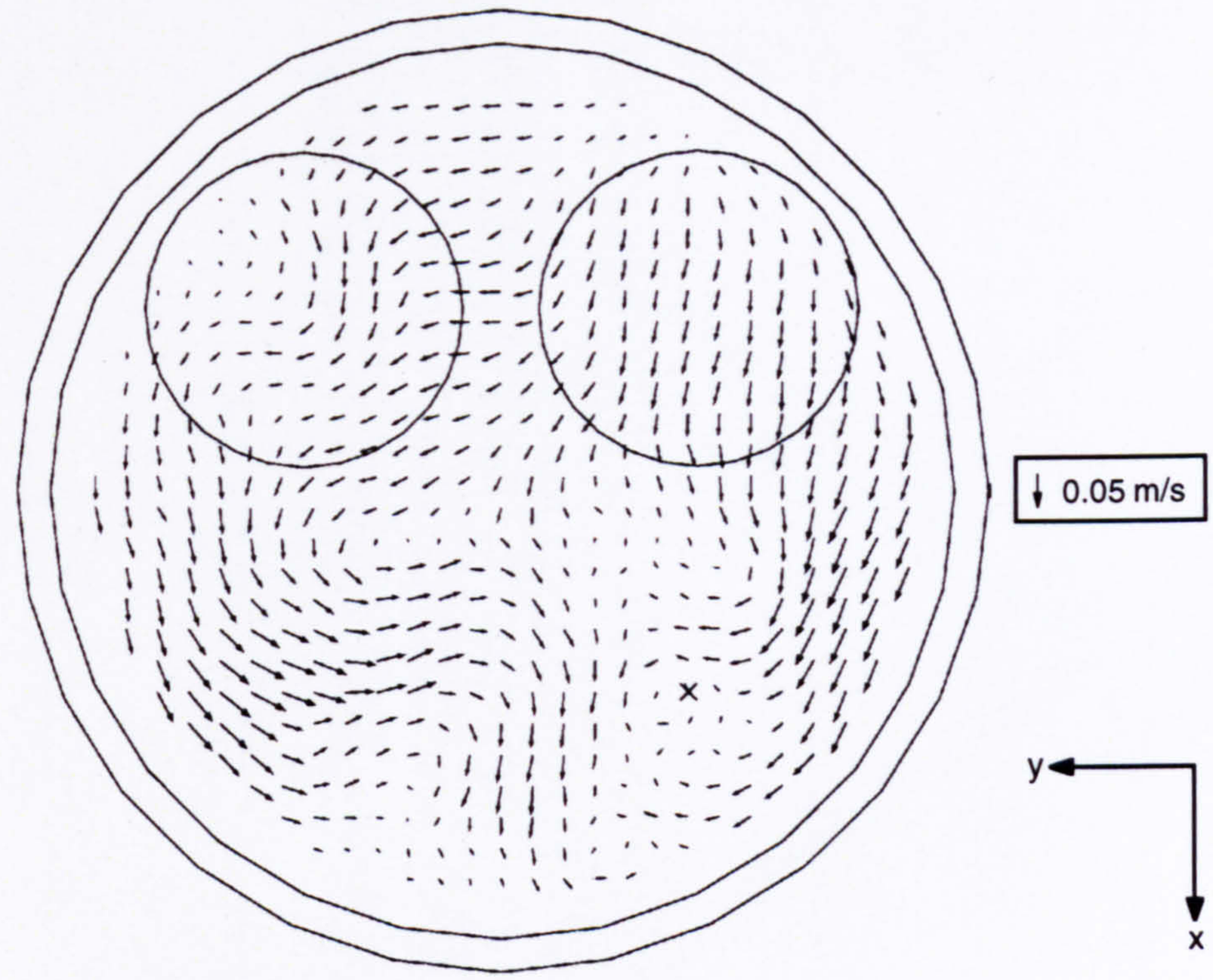

Figure 5.14 Averaged velocity vector map for flow in the horizontal plane z = 10 mm at 180° (BDC) crankangle

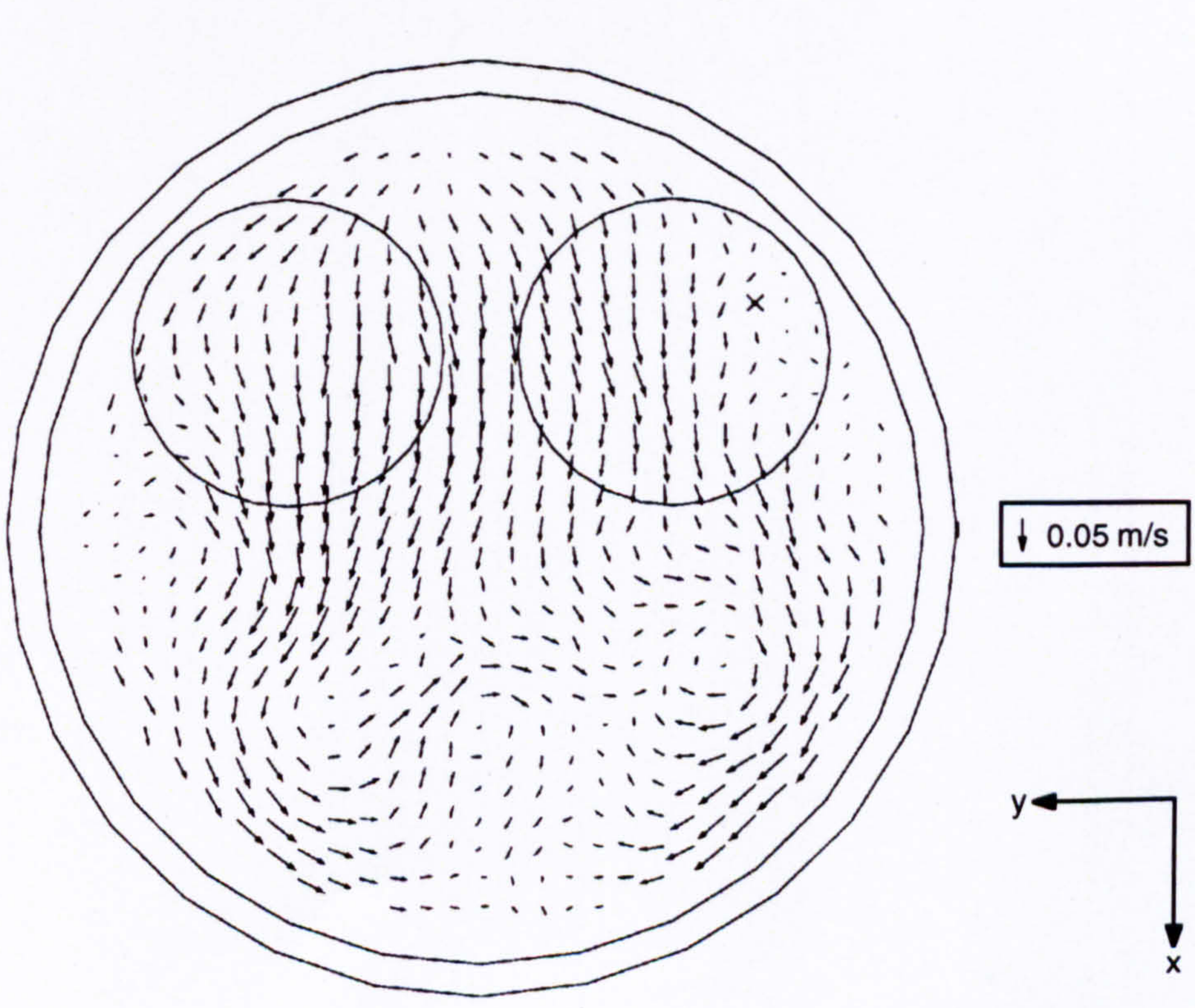

Figure 5.15 Averaged velocity vector map for flow in the horizontal plane z = 25 mm at 180° (BDC) crankangle

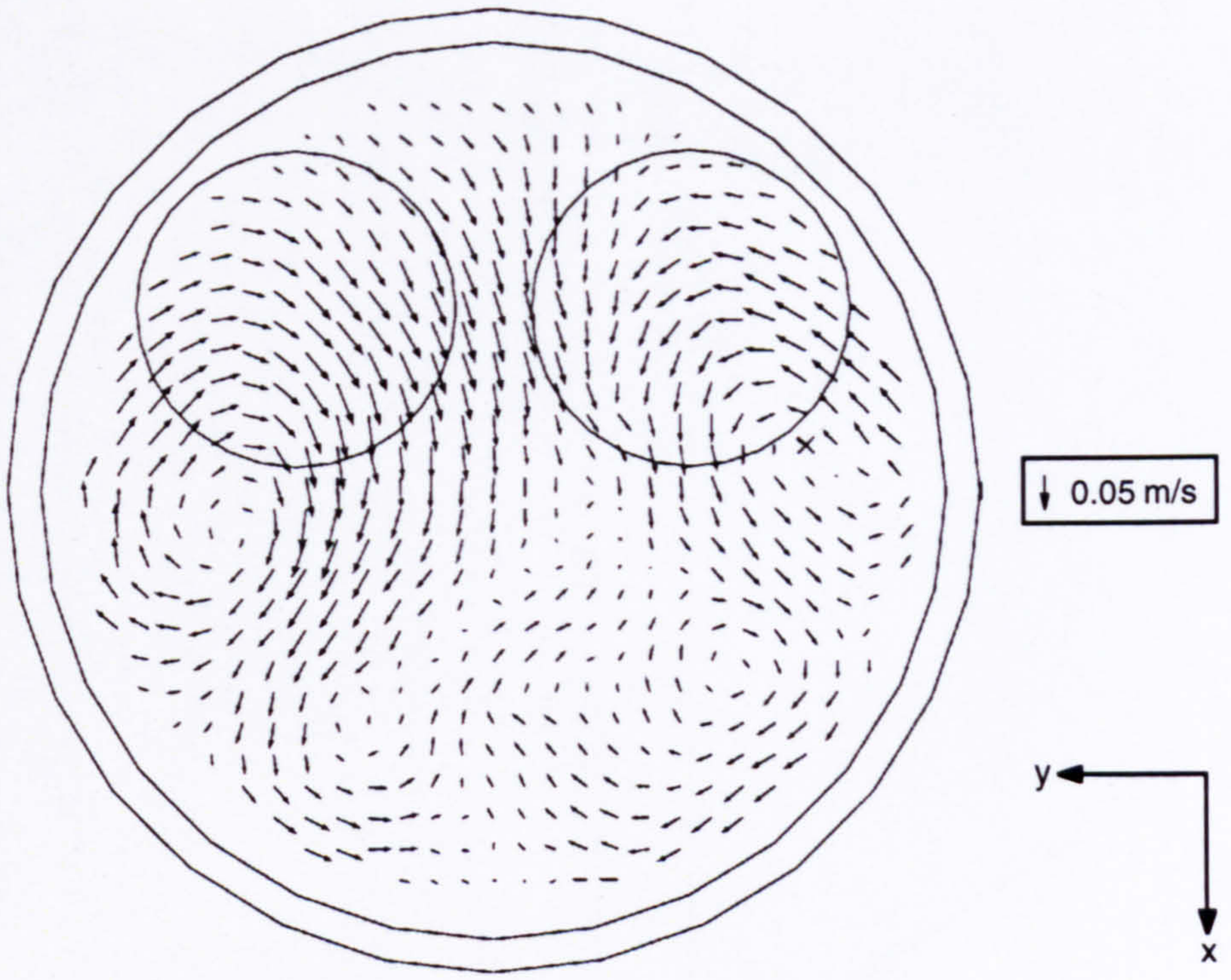

Figure 5.16 Averaged velocity vector map for flow in the horizontal plane z = 40 mm at 180° (BDC) crankangle

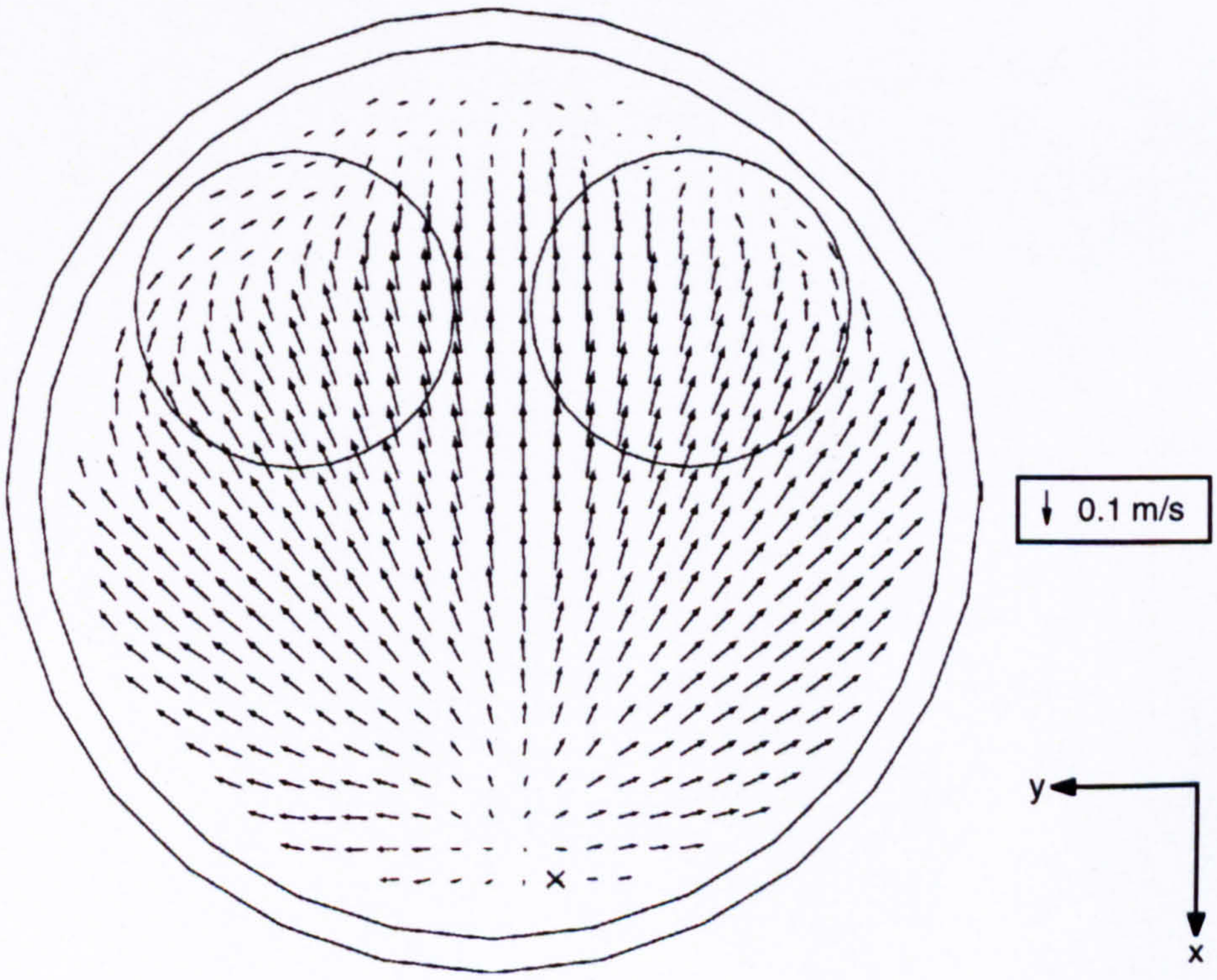

Figure 5.17 Averaged velocity vector map for flow in the horizontal plane z = 80 mm at 180° (BDC) crankangle

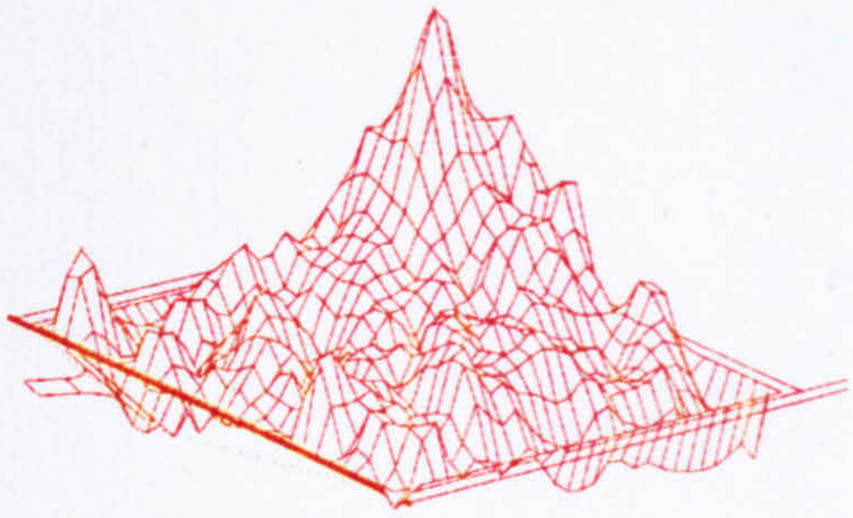

(a) Plane y = 0 mm

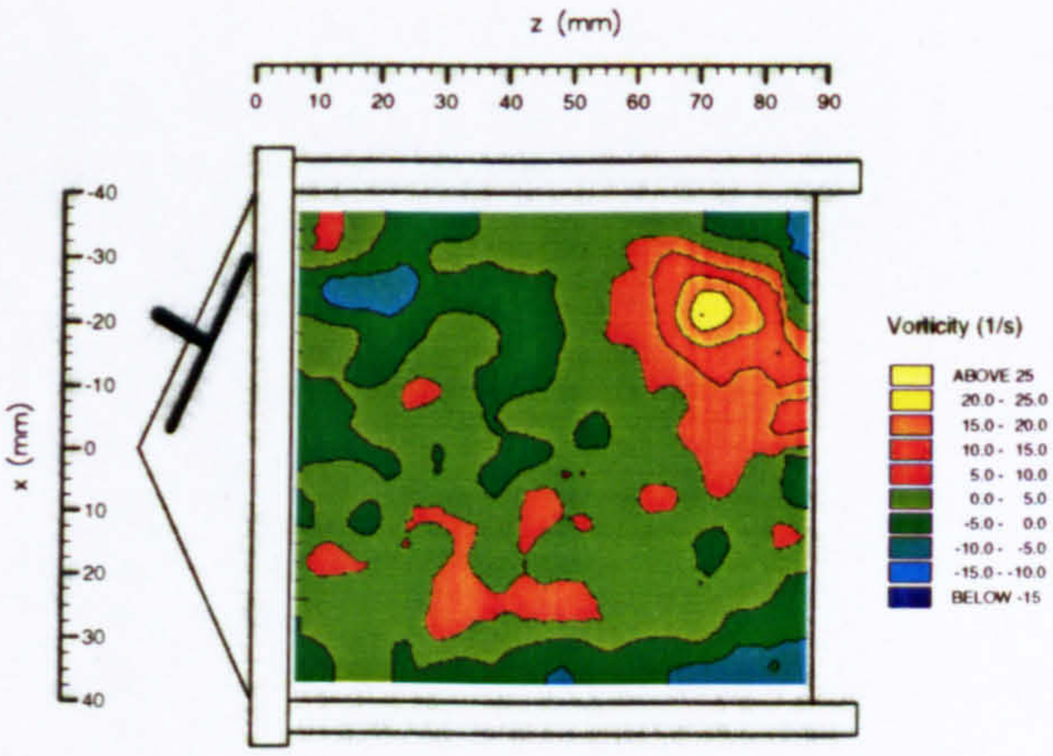

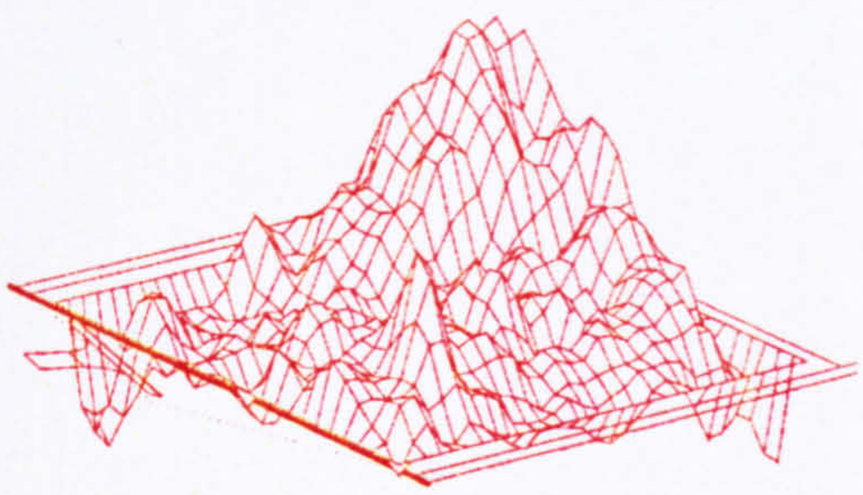

(b) Plane y = 8.8 mm

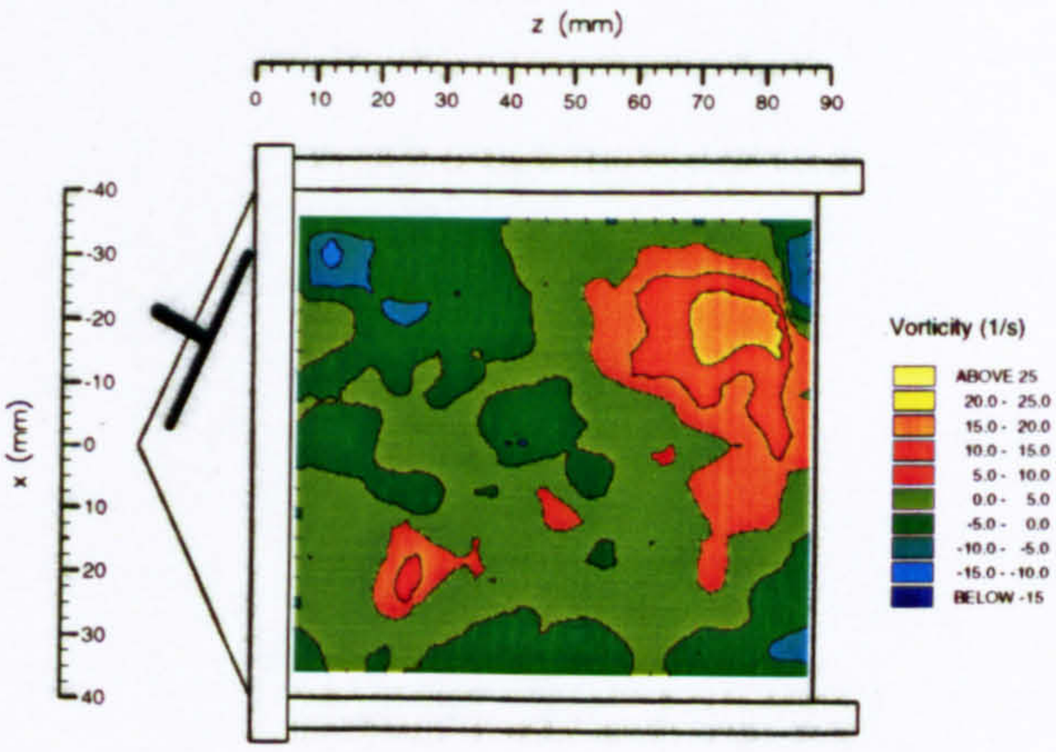

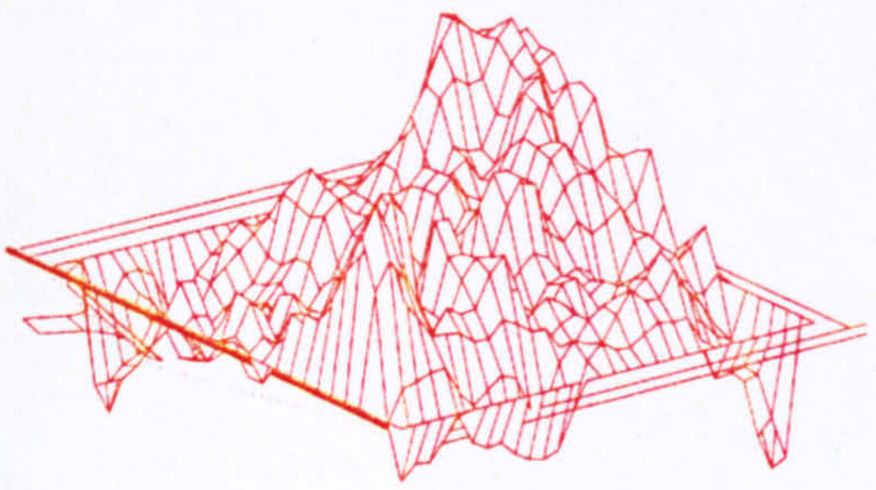

(c) Plane y = 17.6 mm

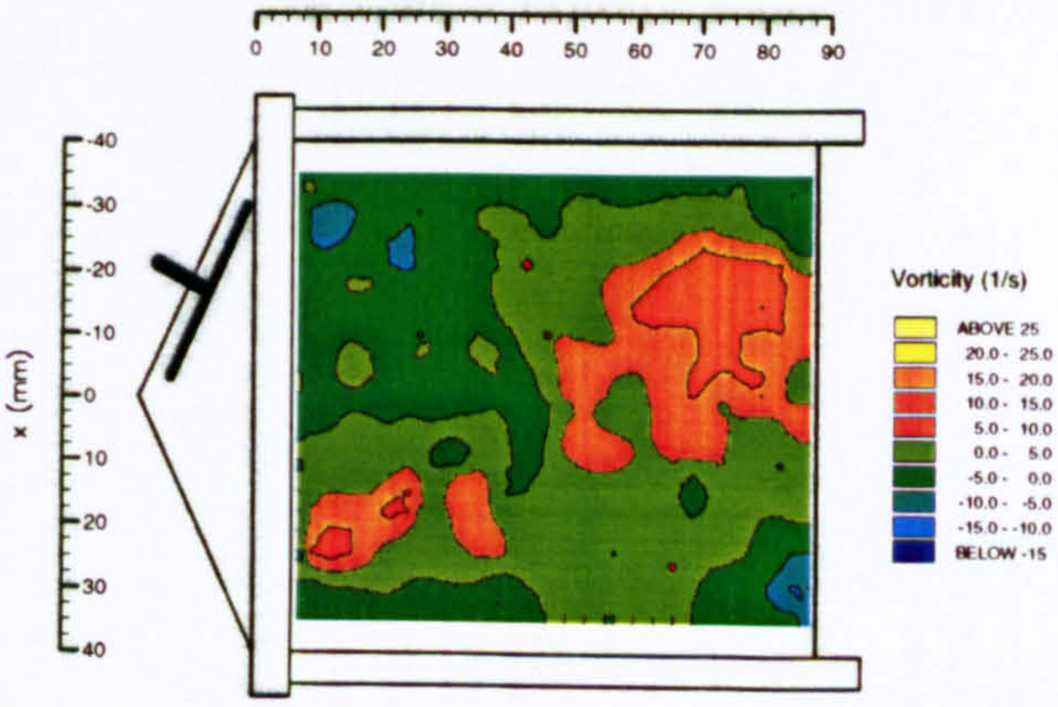

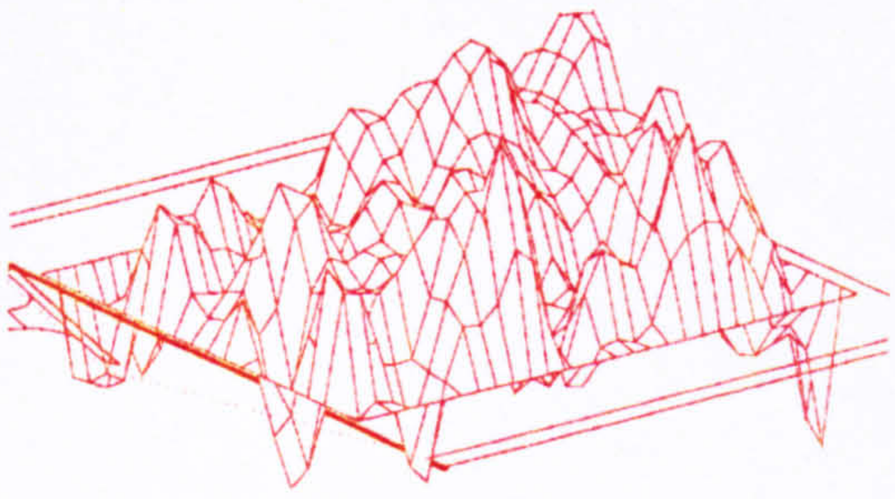

(d) Plane y = 26.4 mm

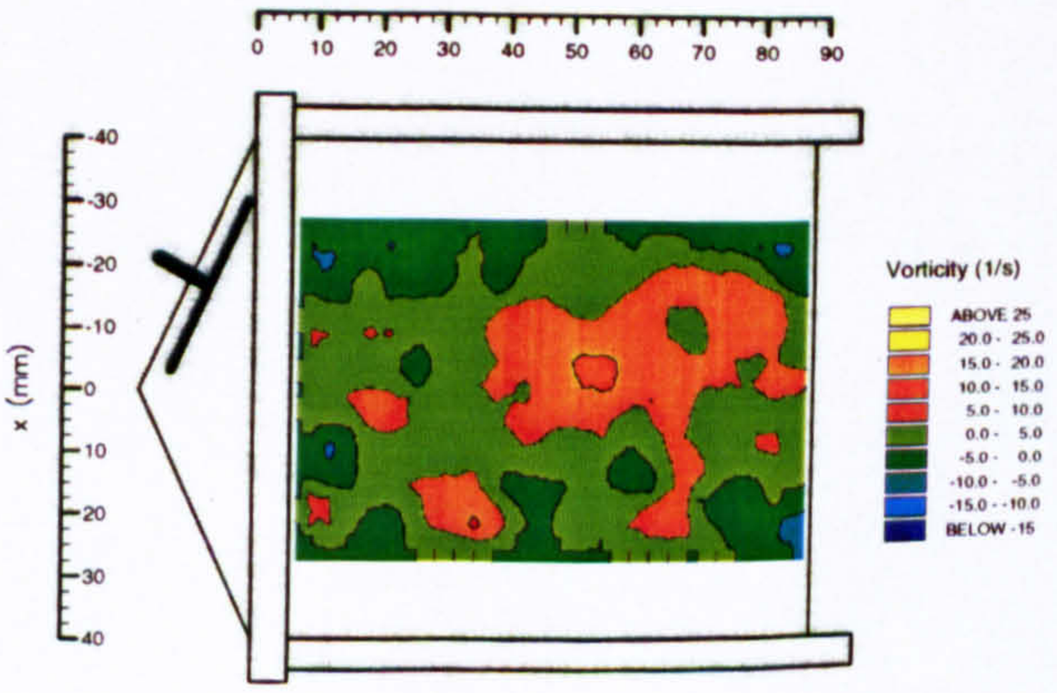

Figure 5.18 Contours of out-of-plane vorticity in the vertical planes

(a) Plane z = 10 mm

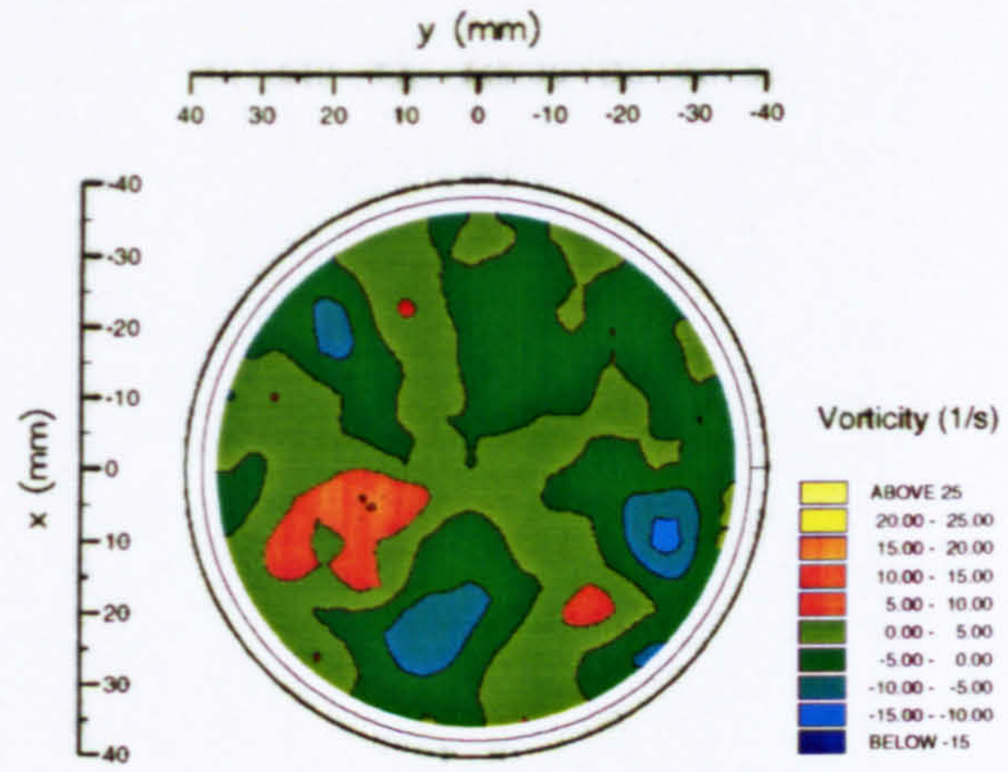

(b) Plane z = 25 mm

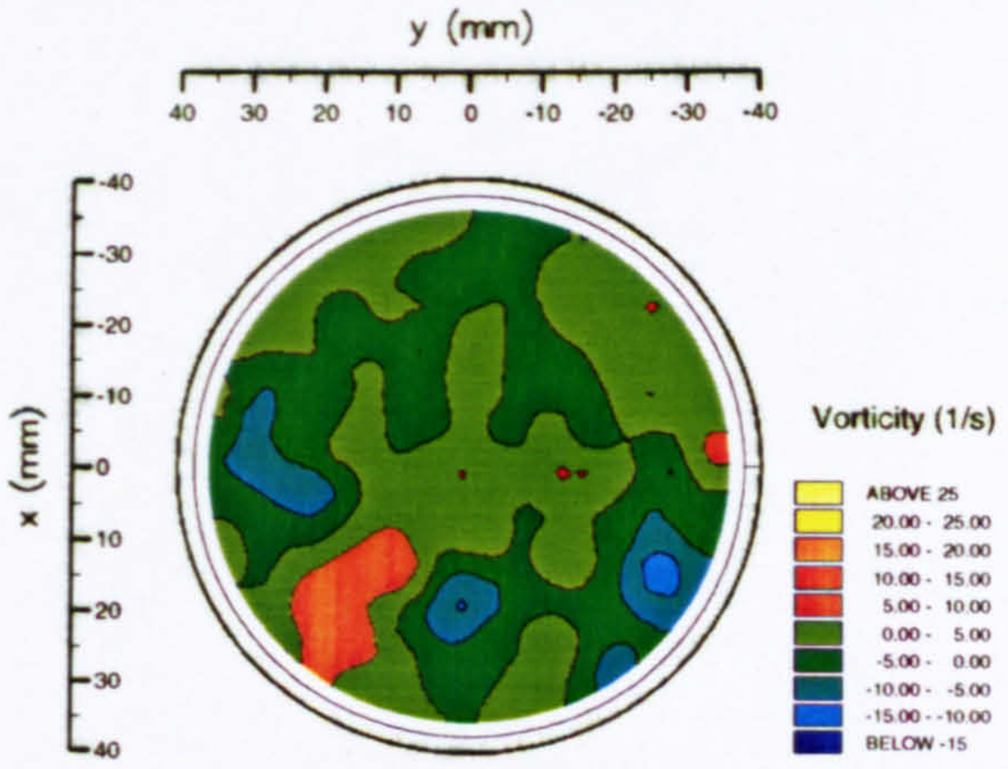

(c) Plane z = 40 mm

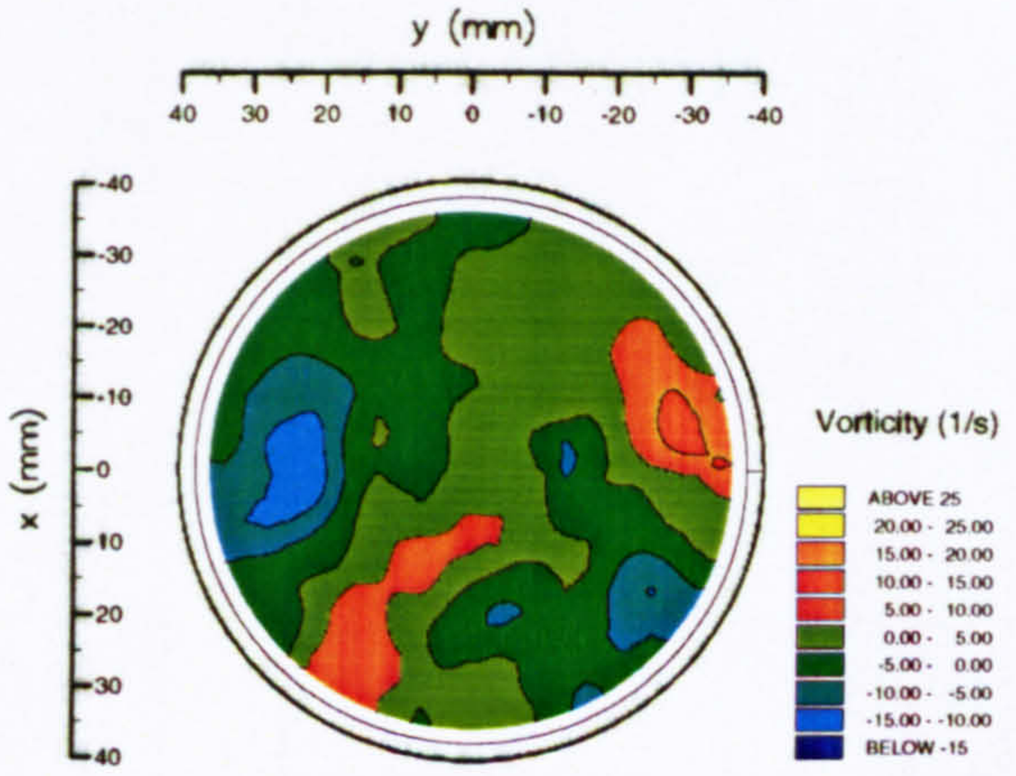

(d) Plane z = 80 mm

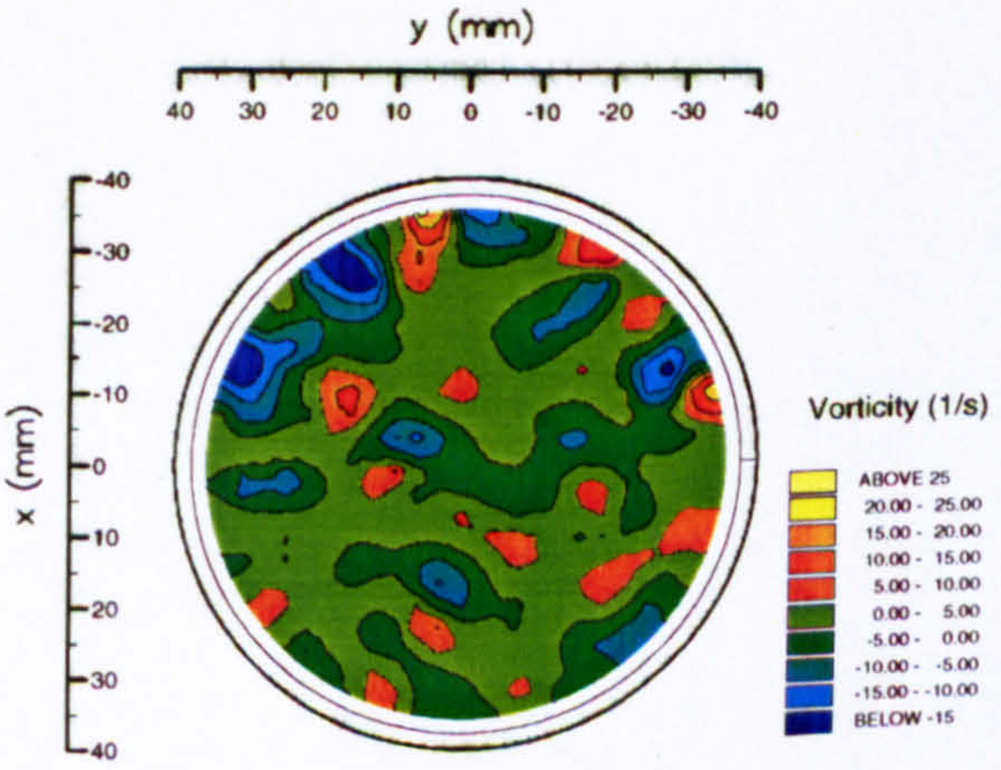

Figure 5.19 Contours of out-of-plane vorticity in the horizontal planes

Chapter 6

VISUALISATION OF THE PRE-COMBUSTION IN-CYLINDER FLOW FIELD IN A MOTORED FOUR-VALVE OPTICAL ENGINE

6.1 INTRODUCTION

The in-cylinder gas motion in a motored four-valve per cylinder optical engine was investigated using laser-sheet flow visualisation and particle tracking velocimetry. The optical engine employed sulphur hexafluoride (SF_6) gas as the working fluid and could be operated at engine speeds of 0 - 100 r.p.m. In-cylinder air motion during the induction and compression strokes in a high speed engine was simulated by pressurising the SF_6 gas to different inlet conditions and by applying dynamic similarity criteria, as described below.

The flow field was seeded with hollow glass micro-spheres and illuminated with a laser-sheet for flow visualisation purposes. In-cylinder flow patterns during induction and compression were recorded onto video tape through a stereoscopic video camera arrangement. Selected images from the video tape were grabbed and the recorded particle tracks were processed in order to evaluate velocity magnitudes and directions. A complete description of the technique and the apparatus used is provided in Chapter 2, section 2.6.

In the present study, the optical engine was motored at speeds of 56 r.p.m., 77 r.p.m. and 104 r.p.m. and with absolute inlet gas pressure conditions of 1.22 bar, 1.43 bar and 1.56 bar to simulate various engine speed and engine load conditions. Mechanical difficulties with the optical engine when operated close to its maximum engine speed, particularly at the higher

manifold pressure settings, dictated that only some of the possible pressure/engine speed combination cases from the above could be studied.

The scaling factors for equivalent engine speeds were obtained using Reynolds number matching, by calculating the ratios of the kinematic viscosities of air to SF_6 at various inlet pressure settings. Some dynamic similarity criteria are explained in section 5.2 in Chapter 5 and defined by equation 5.2. Thus, for example, at 1 atmosphere SF_6 inlet manifold pressure with the optical engine, the velocity scaling factor would be 7·0, i.e. with a model engine speed of 56 r.p.m. the equivalent engine speed is 400r.p.m. (1 atm. air pressure/full engine load). By varying the manifold pressure on the optical engine, and thereby altering the density and kinematic viscosity of the SF_6 gas, the velocity scaling factor could be altered to simulate higher equivalent engine speeds.

Section 6.2 of this chapter presents flow visualisation images which describe the flow patterns observed during induction and compression. In section 6.3 velocity vector results from different engine operating conditions are discussed and the results are summarised in section 6.4. Equivalent engine speeds with the current arrangement are given in Appendix 3.

6.2 FLOW VISUALISATION STUDY

The development of tumble flow in the Zetec engine during the induction stroke has already been described in some detail in the flow visualisation and P.I.V. study reported in Chapter 5. Therefore, for brevity only two vertical planes were chosen to examine tumble for the present investigation - the mid-cylinder (y = 0 mm) and the mid-valve (y = 17.6 mm) planes - as shown on Figure 6.1. The flow in transverse planes was not examined in this study.

6.2.1 Flow Processes During the Induction Stroke

Figure 6.2 presents flow visualisation images during the induction stroke captured from a video recording of gas motion at 77 r.p.m. engine speed and 1.22 bar inlet manifold pressure. At 57° ATDC, Figure 6.2(a) shows strong intake flow along the combustion chamber to the exhaust valve side (on the right of the image) and down the cylinder wall, as indicated by the particle streaks in the image. No vortices are apparent within the flow structure at this stage. As the piston travels further downwards, at 76° ATDC

crankangle (Figure 6.2(b)), gas motion from the right of the inlet valve across the surface of the piston produces a small vortex. The two intake jets from over the left and the right sides of the inlet valve are seen colliding with each other.

Tumble motion is beginning to form halfway down the induction stroke at 95° ATDC, as shown on Figure 6.2(c), where an elliptical vortex can be identified at the left hand side of the image. The flow patterns observed up to 95° ATDC in this plane are very similar to that noted with steady liquid flow through the Ford Zetec engine intake port model with equal valve lift settings (see Chapter 3). This, along with the results from the dynamic water-analog study presented in Chapter 5, displays the similarity between steady and unsteady flows in engine cylinders during the early part of the induction stroke, as has already been discussed earlier in this thesis.

Figure 6.2(d) illustrates the flow structure at 133° ATDC crankangle. A distinct intake jet is present at the right side of the image and across the piston surface and tumble is visible at the left of the plane, which occupies approximately one quarter of the plane at 152° ATDC, as seen in Figure 6.2(e). At bottom-dead-centre, the tumble vortex is larger in size, as shown on Figure 6.2(f). The flow pattern at BDC in the motored engine is very similar to that shown on Figure 5.2(e) in the water analog study.

Aside from showing the qualitative similarities between steady liquid flows and gas motion in a reciprocating engine during early induction, the aim of this study was to show the likeness of the flow structures produced by dynamic water analog rigs with gas motion in motored engines. The results would indicate that water analog simulations, such as those presented in Chapter 5, are very useful for examining flow processes in reciprocating engines during induction, since compressibility effects are negligible particularly in the early stages of the stroke at low Mach numbers [Ma et al (1986 a), Kent and Mikulec (1988)].

6.2.2 Flow Processes During the Compression Stroke

Although inlet port shapes and cylinder head designs can be assessed with some degree of confidence using data acquired from steady flow and water analog rigs to calculate tumble and swirl ratios, it is very difficult, if at all possible, to postulate gas motion development during the compression stroke using these techniques. Bicen et al (1985) indicate that steady and unsteady flows in intake ports and over the intake valves are very similar;

however, in-cylinder flow is highly dependent on piston movement, so that there are usually few similarities between steady and transient gas motion, particularly after the early stages of the induction stroke. The process of efficient charge combustion relies on the presence of large turbulent eddies and length scales at the time of ignition, as already discussed in Chapter 1. For this reason, knowledge of the in-cylinder flow processes from B.D.C. induction to T.D.C. compression is invaluable in assessing cylinder head designs.

Previous studies into engine flows using dynamic water-analog rigs, including those by Khalighi (1989, 1990) among others, have provided little insight into tumble motion during compression. Trigui et al (1994) used experimental data obtained at B.D.C. induction using a water-analog rig as initial conditions for a C.F.D. investigation of gas motion during compression. Although useful results were acquired through the study, the use of C.F.D. methods would in itself introduce elements of uncertainty into the data obtained, due to the assumptions present in numerical schemes and turbulence models. The low-speed optical engine used in the present investigation therefore offers the opportunity for a unique insight into in-cylinder gas motion development during the compression stroke, since the tumble flow motion has been successfully visualised.

Figure 6.3 presents selected video images showing tumble motion in the mid-cylinder plane at an engine speed of 77 r.p.m., I.M.P. = 1·22 bar in the compression stroke. The images continue directly from the same cycle shown in Figure 6.2. At 190° ATDC - Figure 6.3(a) - the flow pattern is very similar to that shown at BDC induction, since there has been little movement of the piston and of the inlet valves in between. Figure 6.3(b) shows the flow pattern at 209° ATDC. In this case the tumble vortex has increased in size from approximately one quarter of the plane to occupying two thirds of the area. However, the inlet valves are still slightly open at this crankangle, so that an intake jet can be observed at the top left hand corner of the plane which counteracts the main tumble motion. The inlet valves close at 220° ATDC and at this point the tumble vortex begins to take over the flow in the plane, as indicated on Figure 6.3(c), for 228° ATDC.

In the initial stages of compression, as already explained in Chapter 1, the tumble vortex undergoes the 'spin-up' phase as defined by Gosman et al (1985), where the rotational velocity of the vortex increases as the piston travels upwards due to conservation of angular momentum. A well-defined tumble vortex is noted at 247° ATDC - Figure 6.3(d) - with its centre offset

slightly to the right of the cylinder axis. The particle streaks in the image indicate comparatively high velocity organised gas flow inside the engine cylinder. Towards the end of the compression stroke, there is some evidence that the tumble vortex is still present in the cylinder as shown in Figure 6.3(e) which displays the flow structure at 295° ATDC crankangle.

The same observations can be made when the engine speed is increased to 104 r.p.m at 1.22 bar manifold pressure. Figure 6.4 displays three flow visualisation images from the compression stroke in the mid-valve plane for this case. In Figure 6.4(a), 206° ATDC crankangle, a tumble vortex is visible in the bottom half of the image, which occupies almost two-thirds of the plane, similar to the image shown in Figure 6.3(b). Further up the stroke at 232° ATDC, the vortex is noted to occupy the entire plane as shown on Figure 6.4(b) and at 260° ATDC crankangle - Figure 6.4(c) - tumble can again be observed. Comparisons of the flow patterns from the two engine speed cases indicate that at the higher piston velocity the tumble structures are better defined, which is particularly noticeable at the early stages of compression.

6.3 PARTICLE TRACKING VELOCIMETRY STUDY

This section presents processed results from the stereoscopic particle tracking velocimetry study of in-cylinder flow processes at several engine speed and inlet manifold pressure conditions. The results for each case are described first and then discussed relative to results and data presented in previously published investigations using similar four-valve engine designs.

It should be noted that the processed velocity vector plots represent instantaneous velocities and the raw data has not been averaged, interpolated or smoothed over the measurement planes. For this reason the results should be interpreted with care, since instantaneous velocities do not necessarily indicate any repeatable trends within the flow field.

In some plots, velocity vectors adjacent to each other are seen pointing in opposing directions, and this is due to the fluctuations and cyclic variations present in real engine flows. However, comparison of video images over a number of engine cycles showed very few differences in the flow pattern, and therefore it may be assumed that the results presented in this section do provide a useful indication of the general flow features

encountered in the engine cylinder during the induction and compression strokes.

6.3.1 Description of Results

Figures 6.5 presents vector plots from the induction stroke, shown next to the original flow visualisation images in the mid-valve plane. The engine speed was 56 r.p.m. and the inlet manifold pressure was set to 1.22 bar. At 67° ATDC crankangle, shown on Figure 6.5(a), particle streaks on the flow visualisation image indicate intake jets travelling downwards towards the piston. The longest streaks are seen close to the combustion chamber at the top of the image, indicating that the highest gas velocities are present in this region of the plane. This is confirmed by the adjacent vector plot, which illustrates velocities of approximately 0.7 to 0.8 m/s within the intake stream at the top right hand section of the plot. Gas velocities are lower close to the piston surface and the cylinder wall, at between 0.3 and 0.5 m/s. No distinct vortices are seen at this crankangle and the figure shows a number of intake jets colliding with each other.

Figure 6.5(b) shows the flow structure at 100° ATDC crankangle. The flow visualisation image again shows a strong intake jet on the right as the gas travels downwards and over the piston surface. Velocity magnitudes within the jet are around 0.2 and 0.3 m/s, while vectors up to 0.5 m/s are seen close to the combustion chamber. The figure shows an elliptic vortex on the left hand side of the plane, directly underneath the inlet valves. The largest velocity magnitudes - around 0.6 m/s - are noted at the boundaries of the vortices, with lower velocities (approximately 0.2 - 0.3 m/s) inside the vortices.

At 147° ATDC a tumble vortex is seen in the image close to the piston surface, with velocity vectors of up to 0.9 m/s in the top portion of the corresponding vector plot. In the centre of the plane, velocity values are considerably lower, in the region of 0.25 m/s.

Selected images from the compression stroke for this case are presented on Figure 6.6. At 214° ATDC crankangle, a tumble vortex is present near the bottom of the figure which includes gas velocities of around 0.3 m/s. A jet opposing the tumble vortex can be seen in the upper portion of the figure. Further into the compression stroke, at 261° ATDC (Figure 6.6(b), a single intense vortical motion is apparent in the plane, with the vectors indicating velocity magnitudes of approximately 0.3 m/s within the plane.

Figure 6.7 presents two vector plots showing in-cylinder velocities in the mid-valve plane (y = 17.6 mm) at an engine speed of 56 r.p.m. and 1.22 bar inlet manifold pressure. The flow structure at 101° ATDC crankangle is shown on Figure 6.7(a). The flow visualisation image illustrates strong intake motion on the right and velocity values are between 0.3 and 0.5 m/s in this region. The uneven distribution of the seeding particles in the left hand side of the plane, as shown by the flow visualisation image, meant that few vectors could be clearly identified in this section of the plane. At 202° ATDC crankangle Figure 6.7(b) shows tumble motion in the mid-valve plane with its centre close to the piston surface. In-cylinder velocities are lower than those shown on Figure 6.7(a), being on average around 0.25 m/s.

In order to assess the effect of inlet manifold pressure on in-cylinder flow structure to simulate higher engine load conditions, the manifold pressure was increased from 1.22 bar to 1.56 bar absolute, while maintaining the engine speed at 56 r.p.m. Figure 6.8 shows the flow field during the induction stroke in the mid-cylinder plane for this case. At 67° ATDC crankangle, Figure 6.8(a) shows a similar flow structure to that seen in Figure 6.5(a), with the lower manifold pressure. Maximum velocity magnitudes within the intake stream in the top right hand portion of Figure 6.8(a) are approaching 0.7 m/s, which is a similar level to that noted with 1.22 bar manifold pressure. The velocity magnitudes at 101° ATDC crankangle are also of the same magnitude to those seen in Figure 6.5(b) with the highest values being in the region of 0.5 - 0.6 m/s.

Few discernible differences are present in the overall flow structure, i.e. flow pattern and velocity magnitude, between the two sets of results of Figures 6.5 and 6.8. The same is noticeable when Figures 6.6 and 6.9 (with results from the compression stroke) are compared. Vectors plots from the 214° ATDC and 261° ATDC crankangle positions in each figure indicate similar orders of magnitude in the in-cylinder velocities, even though the particle streaks are in different locations in both sets of plots.

Figures 6.10 and 6.11 present the qualitative and corresponding quantitative results from flow in the mid-valve plane at 56 r.p.m. engine speed and 1.56 bar manifold pressure. Figures 6.10(a) to (c) show the development of intake motion. In-cylinder velocities are higher during the early portion of the induction stroke (67° ATDC and 147° ATDC) as has already been mentioned, and maximum values are between 0.5 and 0.7 m/s. Further down the stroke at 147° ATDC tumble motion is seen at the bottom of the plane.

At BDC in the mid-valve plane (Figure 6.11(a)) the vortex structure is akin to that noted with the dynamic water-analog study - shown on Figure 5.12. The highest gas velocities are found in the jet at the right of the planes, with magnitudes ranging from 0.4 to 0.6 m/s, while in the left hand side of the figure velocity values are around 0.2 m/s. As mentioned earlier in the chapter, large-scale tumble motion is seen inside the cylinder from close to intake valve closure and this is again noted from Figure 6.11(b). Gas velocities are between 0.2 and 0.3 m/s at 214° ATDC crankangle, which is similar to the flow pattern noted in Figure 6.7(b). A tumble vortex is also apparent at mid-compression as shown at 261° ATDC - Figure 6.11(c).

The effect of the variation of engine speed on in-cylinder flow was investigated by increasing the engine speed from 56 r.p.m. to 77 r.p.m. Figure 6.12 shows vector plots of the in-cylinder motion with 1.22 bar inlet manifold pressure in the mid-cylinder plane. Strong intake motion is observed at both sides of the plane at 67° ATDC crankangle. Velocity magnitudes in the vector plot of Figure 6.12(a) are in the region of 0.3 and 0.4 m/s. This is of a similar magnitude to velocities noted with 56 r.p.m. engine speed (Figure 6.5(a)).

At 105° ATDC crankangle the vector plot of Figure 6.12(b) also shows a distinct downward intake jet at the right of the plot. Velocities are higher across the surface of the piston than at 56 r.p.m. engine speed, being approximately 0.8 m/s. Average gas velocities are approximately 0.3 m/s at the 77 r.p.m. engine speed and this also shows little difference to the magnitudes noted at the lower speed.

Figures 6.12(d) and (e) in general show the presence of strong tumble motion during compression and velocity values are on the whole higher at 219° ATDC and 266° ATDC crankangles than seen in the plots taken from the compression stroke given in Figure 6.6, although the flow patterns are very similar for both cases.

Gas motion in the mid-valve plane at selected crankangles during the induction and compression strokes is presented on Figure 6.13. Strong intake jets can be observed in the plane as seen in each of Figures 6.13(a) to (c). Maximum velocity values are approximately 0.7 m/s in each of these plots. Whereas gas velocities during the compression stroke at the 56 r.p.m. engine speed were around 0.3 m/s in the mid-valve plane, at the higher engine speed velocities are bigger at the 219° ATDC and 266° ATDC crankangles the highest velocities in this case being up to 0.5 m/s. On average gas velocities in this plane are approximately 0.4 m/s on Figures 6.13(d) and (e).

Figure 6.14 presents three vector plots from the in the mid-cylinder plane from the induction and compression strokes at 77 r.p.m. engine speed and 1.43 bar inlet manifold pressure. In qualitative terms Figures 6.14(a) to (c) show little difference in flow pattern from previous cases, as indicated by the plots. However, the maximum in-cylinder velocities are greater, being 0.8 - 0.9 m/s within the intake jet at 67° ATDC and on average around 0.6 m/s at 105° ATDC crankangle. A large-scale tumble vortex was noted in the mid-valve plane at inlet valve closure, as shown by Figure 6.14(c).

6.3.2 Discussion of Results

The optical engine used in the present investigation, with SF_6 as the working fluid and stereoscopic flow visualisation, is a unique experimental facility and no similar results have been reported by researchers outside of Ford Motor Company Limited. The engine was developed and first put to use by Ford powertrain engineers in the United Kingdom to study three-dimensional cycle-resolved flow patterns and gas velocities in engine cylinders. Previous publications include those by Ma et al (1986 a and b) and Marko et al (1986) which looked at flow in single-intake valve engines. The lack of publications reporting similar investigations, particularly for multi-valve engine designs, complicates the task of comparing the results of this chapter in detail with previous studies.

Many of the published papers on multi-valve engine flows reviewed in Chapter 1 of this thesis have discussed the influence of intake port shape and the strength of tumble on turbulence and combustion characteristics in spark-ignition engines. The flow visualisation results and velocity vector maps of both Chapter 5 and this chapter have shown that well-defined tumble is produced inside the Ford Zetec engine cylinder, although the size of the tumble vortex at BDC induction is smaller than has been indicated previous studies. The intense tumble structures reported by Kent et al (1989), Henriot et al (1989) and Khalighi (1990) were produced using combinations of valve masking and shrouds. Although such cylinder head configurations provide an interesting insight into the nature of engine flows, they are not normally employed in production engine designs.

The tumble ratio at BDC for the Zetec cylinder head tested was calculated to be 1.1 from the P.I.V. measurements of Chapter 5 and this was noted to be comparable to the ratios given in publications by Hadded and Denbratt (1991), Rönnbäck et al (1991) and Trigui et al (1994), among others.

The design of an efficient dual-intake valve cylinder head requires a compromise in the strength of tumble, since inlet ports which produce the strongest tumble motion also reduce the port discharge flow co-efficient [Omori et al 1991, Arcoumanis et al 1993]. The flow patterns seen during compression are very similar to those noted by Kuduo et al (1992) in a high-tumble engine configuration.

The present study has shown that tumble in the Zetec engine is intensified during the compression stroke, particularly after intake valve closure, and was present in the cylinder at approximately 300° ATDC. This is near the ignition point of the engine (330° ATDC) under part load/lean burn conditions. This would ensure that the flow would have high levels of turbulent kinetic energy for combustion of the air-fuel mixture in the engine, though turbulence characteristics could not be determined with the measurement technique employed in the present study.

6.4 CONCLUSIONS

The development of tumble motion inside a Ford Zetec engine cylinder has been examined using flow visualisation and stereoscopic particle tracking velocimetry. A low-speed motored optical engine was employed with SF_6 gas as the working fluid and the engine was operated with various inlet manifold pressures and engine speeds. The experimental facility is unique when compared with water-analog rigs, since flow during the compression stroke could be studied. The measurement technique was also invaluable since it offered the complete description of gas motion in a single engine cycle, which is not possible when single-point techniques such as L.D.A are employed.

Laser-sheet flow visualisation was applied initially to the engine in order to assess the qualitative flow structures in detail. Selected stereoscopic flow visualisation images were then processed in order to determine the instantaneous velocities from the length of the particle streak lines in illuminated planes.

The results have lead to the following conclusions:

1. During the induction stroke, strong intake motion was observed in vertical planes, especially close to the cylinder wall and over the piston

surface, which developed into a distinct tumble vortex as the piston reached the bottom of the stroke.

2. During compression, the tumble vortex was seen to occupy the entire mid-valve plane after intake valve closure. Flow visualisation images indicated that the tumble structure became more intense as the piston moved upwards, and was still visible in the cylinder at approximately 300° ATDC crankangle.

3. Velocity vector plots from the 56 r.p.m. and the 77 r.p.m. engine speed cases showed that in-cylinder velocities during induction and compression were generally greater at the higher engine speed case and although only instantaneous velocities were compared, this trend was apparent from results in both mid-valve and mid-cylinder planes.

4. In the early part of the induction stroke, up to approximately 100° ATDC, the flow structures produced by the SF_6 gas were similar to those noted with steady liquid flow through the Perspex Ford Zetec engine model (see Chapter 3). This would confirm previous observations into the similarities between steady and unsteady in-cylinder flows through engine intake ports in the early stages of induction [e.g. Bicen et al (1985)].

5. The effects of engine load on in-cylinder velocities was investigated through variation of manifold pressure settings. The results from this study showed few differences in the general velocity magnitude due to pressure variation.

6. Flow processes during induction in the optical engine were also akin to those observed in the dynamic water-analog engine study presented in Chapter 5. The flow pattern similarities between the motored engine and the water-analog simulations indicated that water-analog studies are useful techniques for obtaining information on induction flows.

7. The experimental technique employed in the present study has proved to be a valuable method for assessing engine in-cylinder flow motion. In qualitative terms, the flow patterns produced inside the engine cylinder were highly representative of the structures expected from similar four-valve

cylinder head designs and corresponded with results from previous published studies, e.g. Trigui et al (1994).

The current arrangement for processing stereoscopic flow visualisation images required each pair of particle streaks to be identified and tracked manually for velocity magnitude evaluation. This limited the number of images which could be processed within a given time period. At the same time, although a knowledge of instantaneous velocities is very important for the understanding of cycle-resolved engine flow processes, time averaged velocity information would have been useful for recognising trends in the quantitative flow field and for comparing experimental data with results from C.F.D. studies.

With the present system, the evaluation of time-averaged velocities would have required considerable effort in order to obtain reliable and statistically independant data. An automated processing system would be necessary for the rapid characterisation of in-cylinder flow motion, such as the systems employed by Adamczyk and Rimai (1988), Khalighi and Huebler (1988) and Trigui et al (1994) among others. The combination of this motored optical engine with an improved image and data processing method, or other measurement techniques such as L.D.A. and P.I.V., would lead to an extremely powerful tool for engine design.

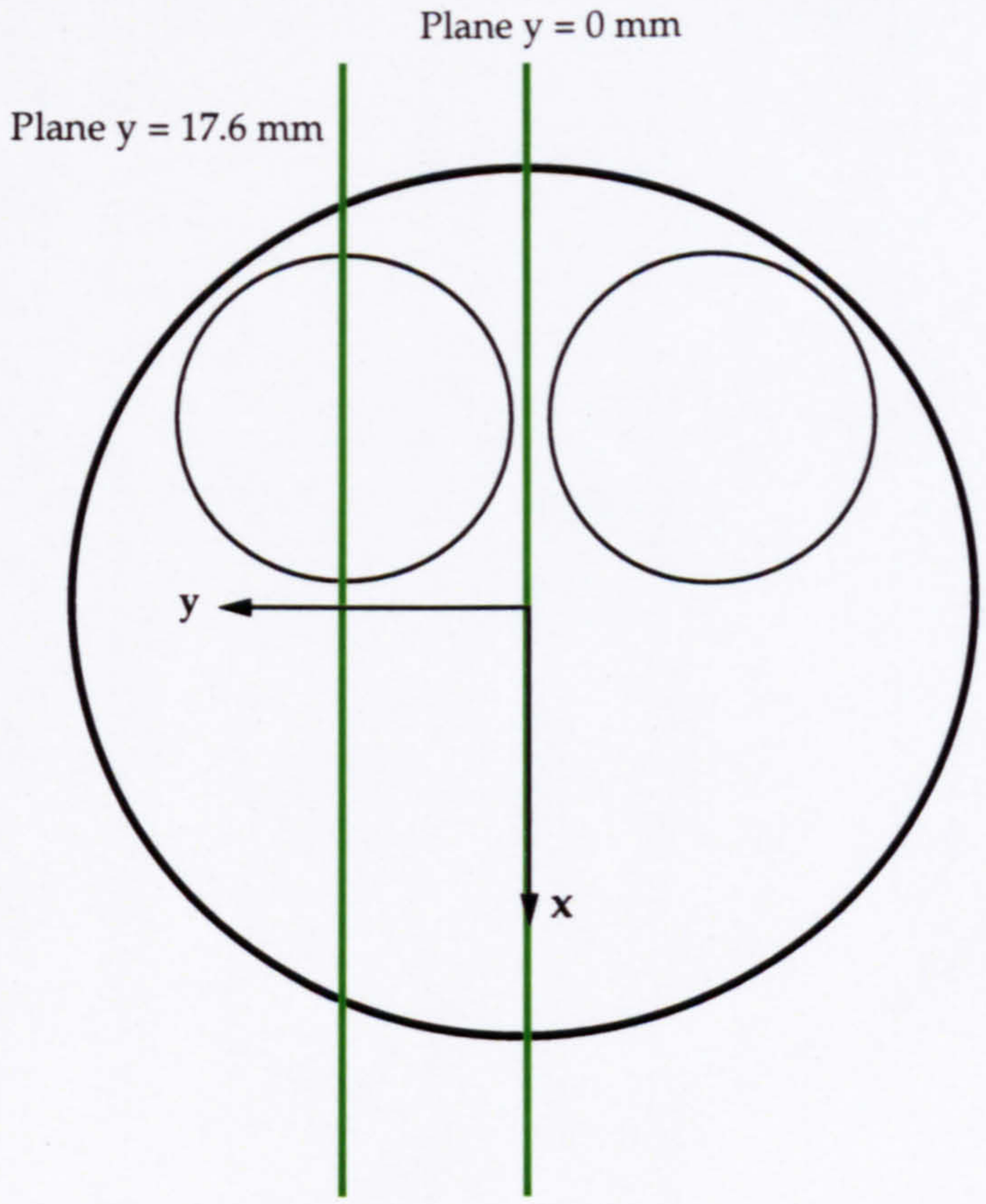

Figure 6.1 Position of laser-sheet planes selected for the study

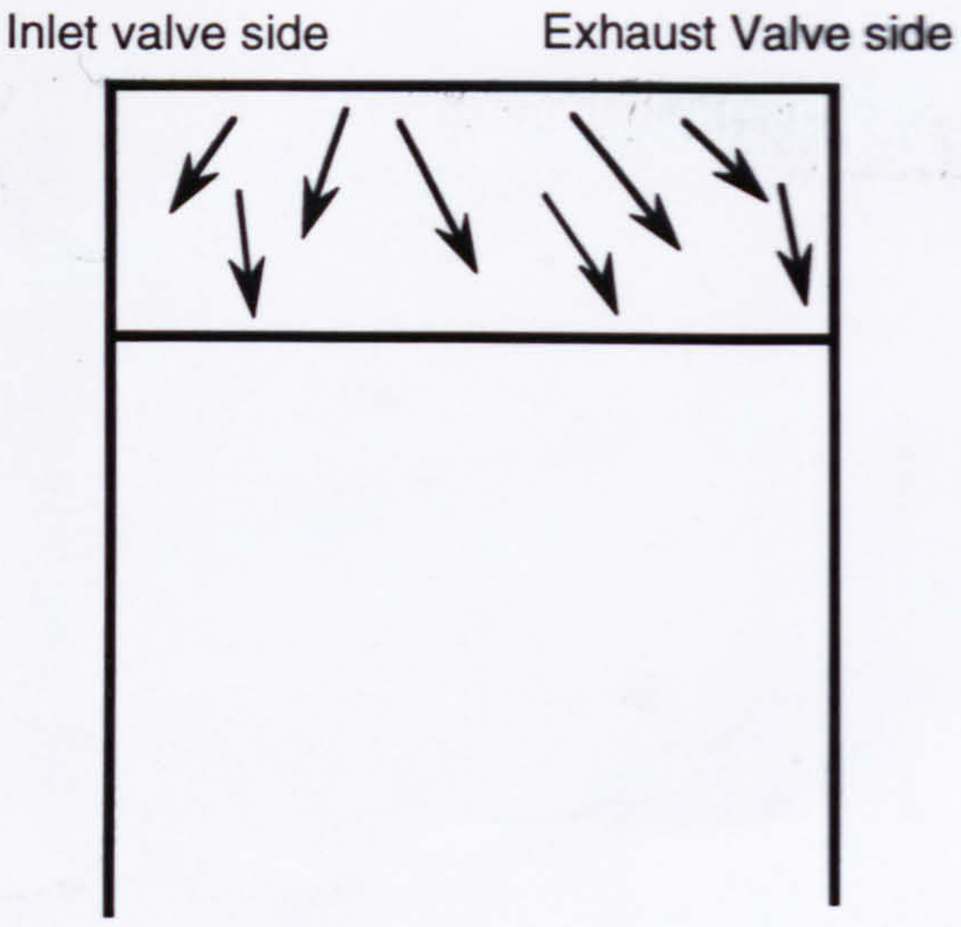
Inlet valve side
Exhaust Valve side

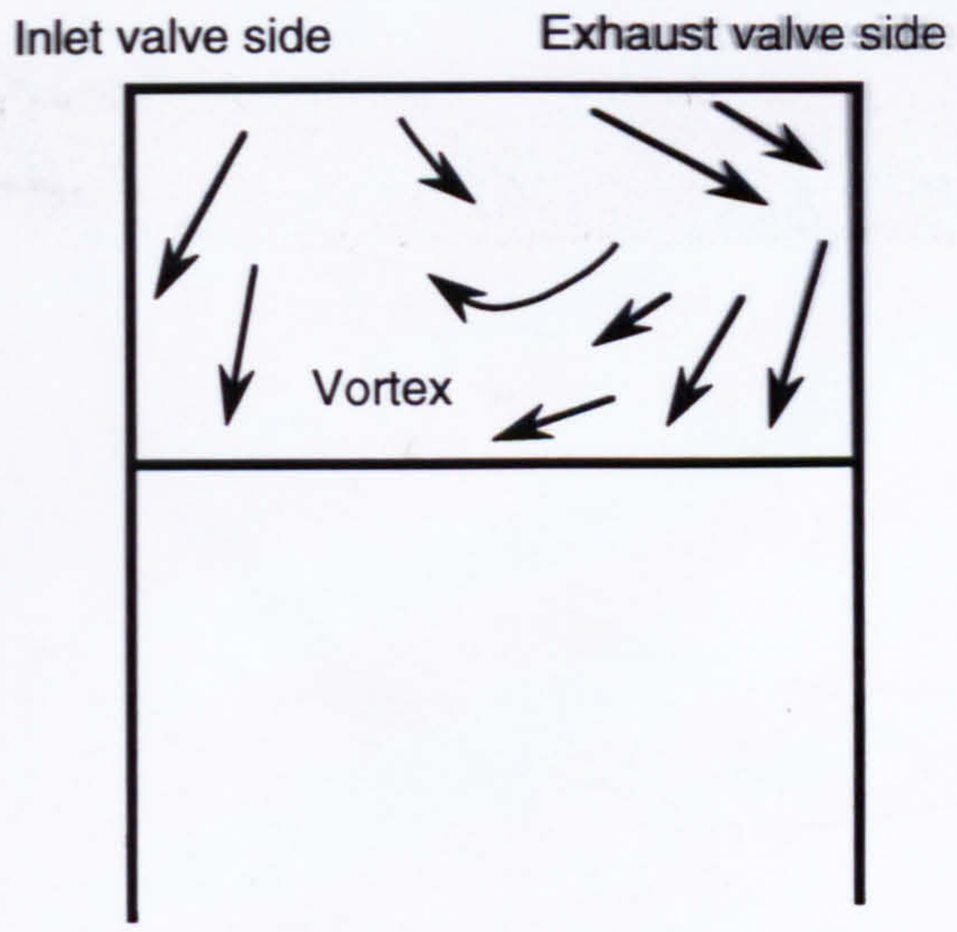
Inlet valve side
Exhaust valve side
Vortex

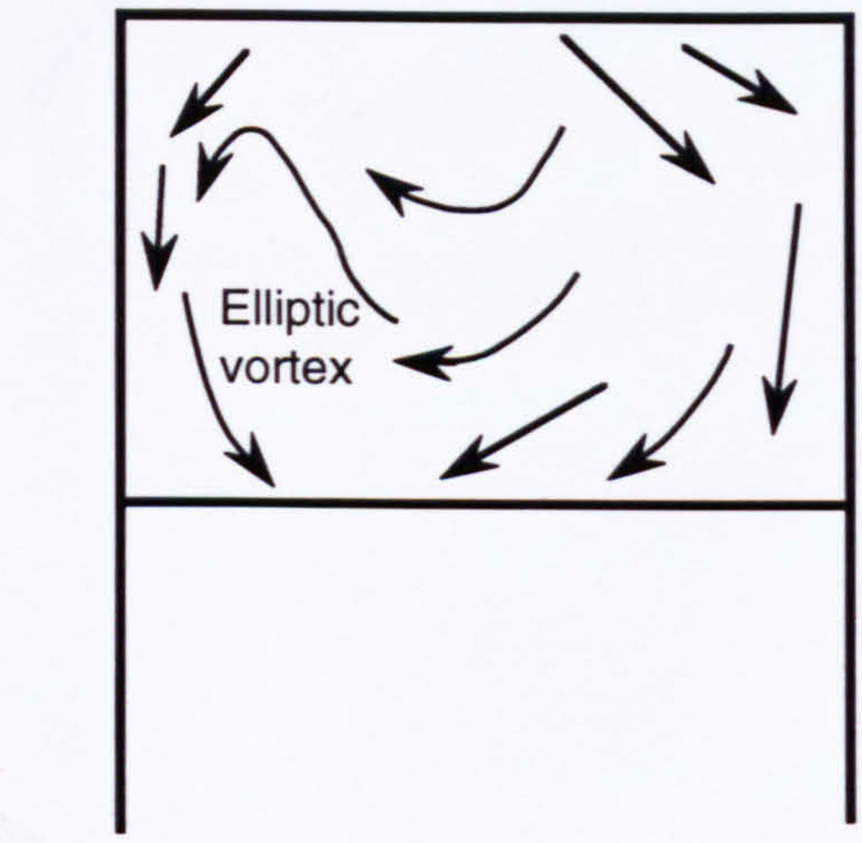
Inlet valve side
Exhaust valve side
Elliptic
vortex

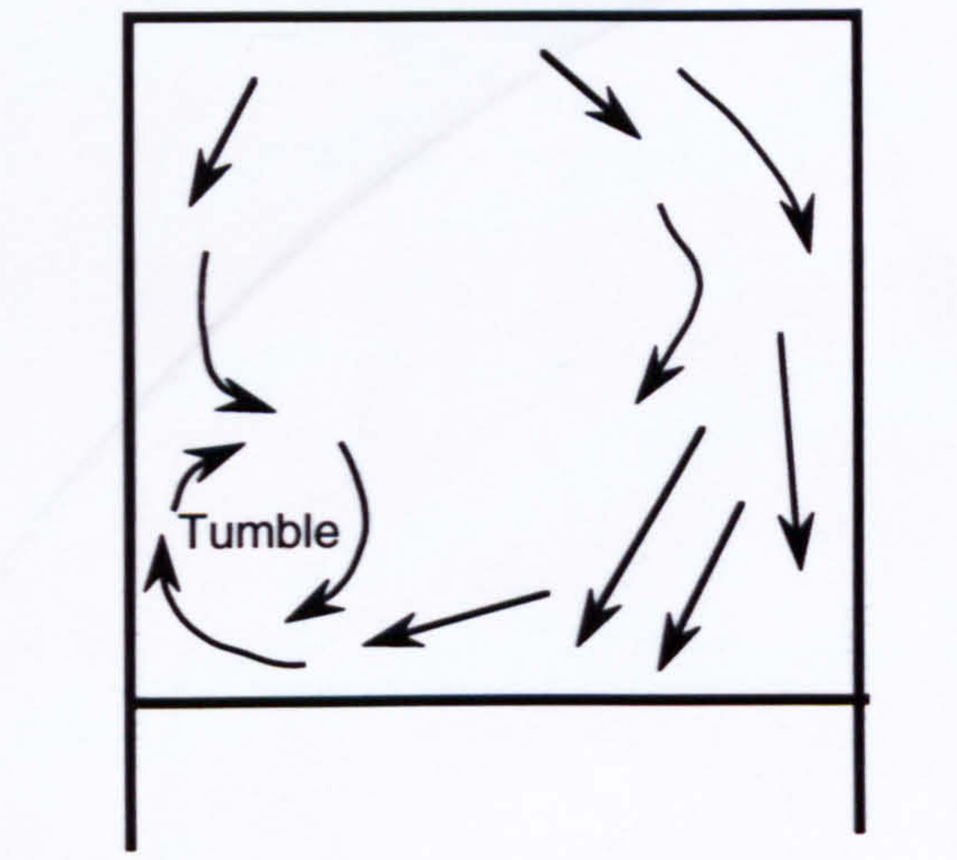
Intake valve side
Exhaust valve side
Tumble

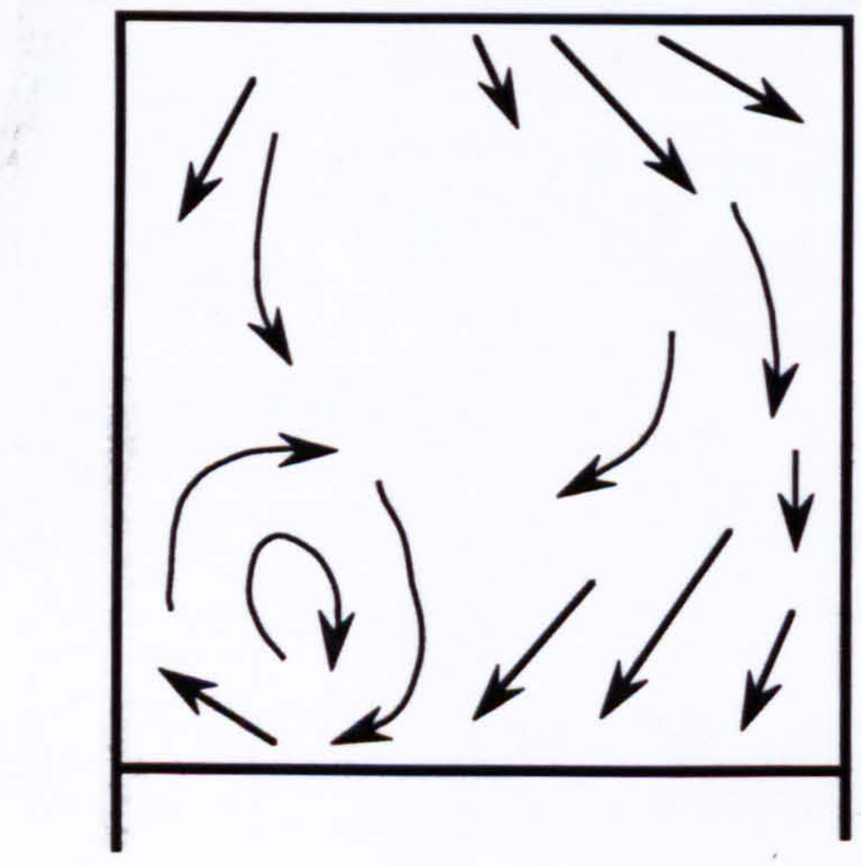
Intake valve side
Exhaust valve side

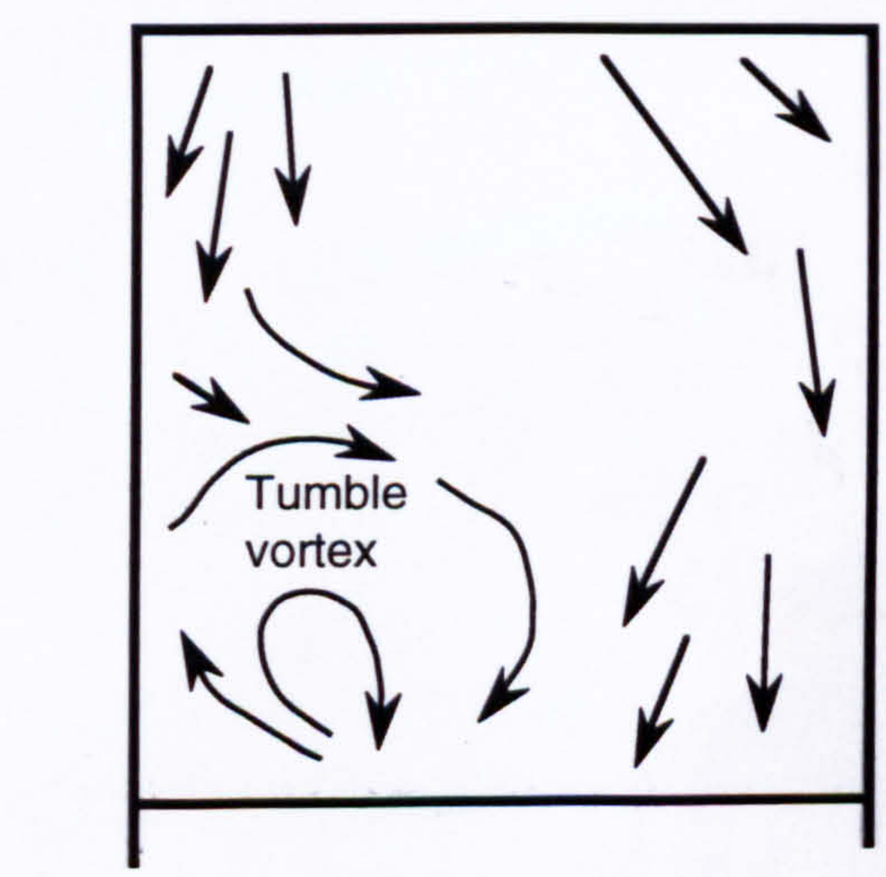
Intake valve side
Exhaust valve side
Tumble
vortex

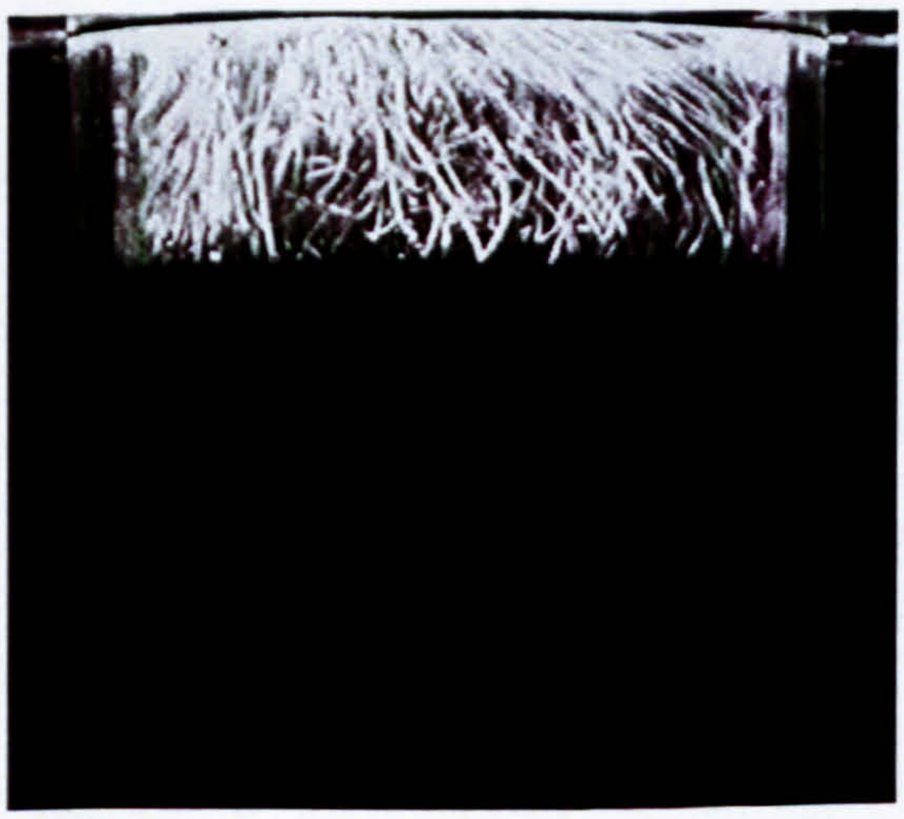

(a) 57° ATDC

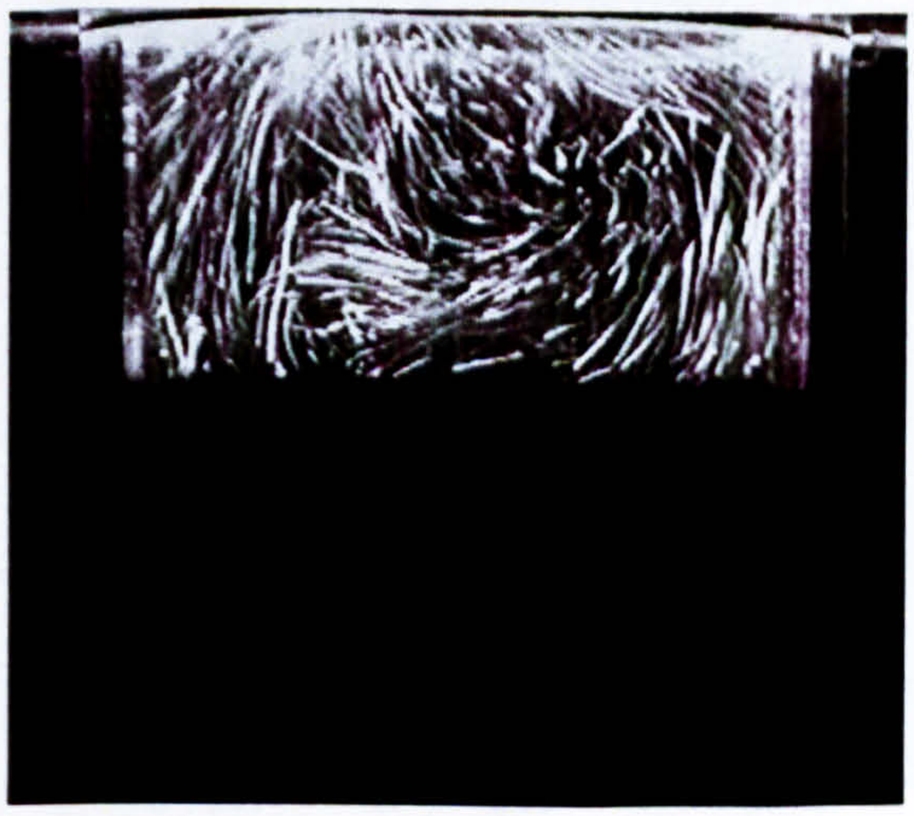

(b) 76° ATDC

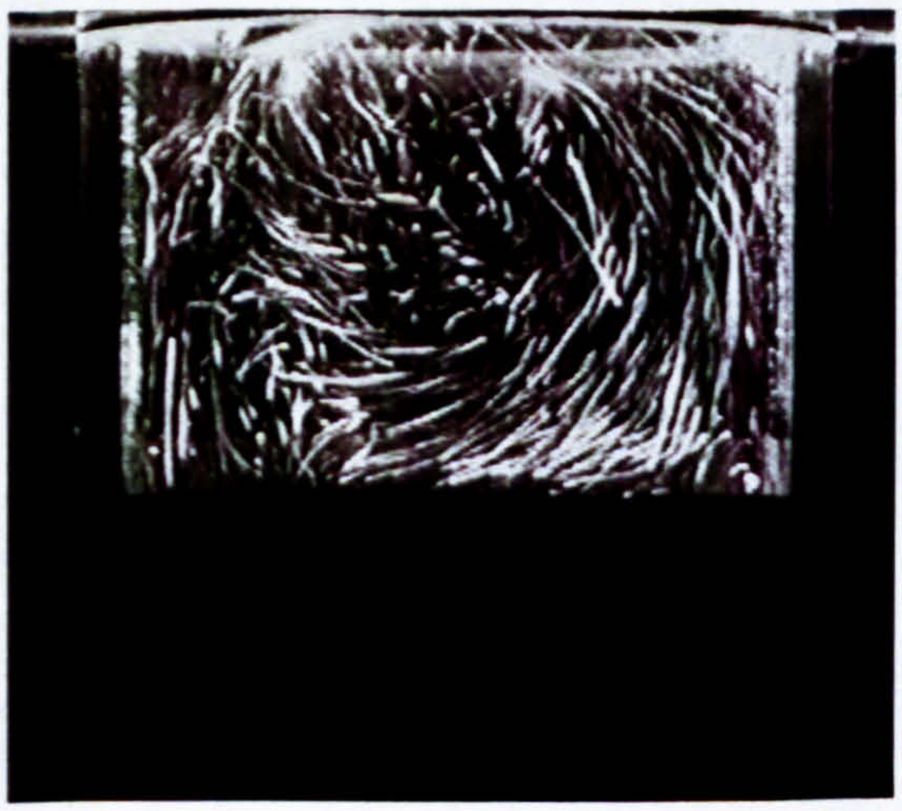

(c) 95° ATDC

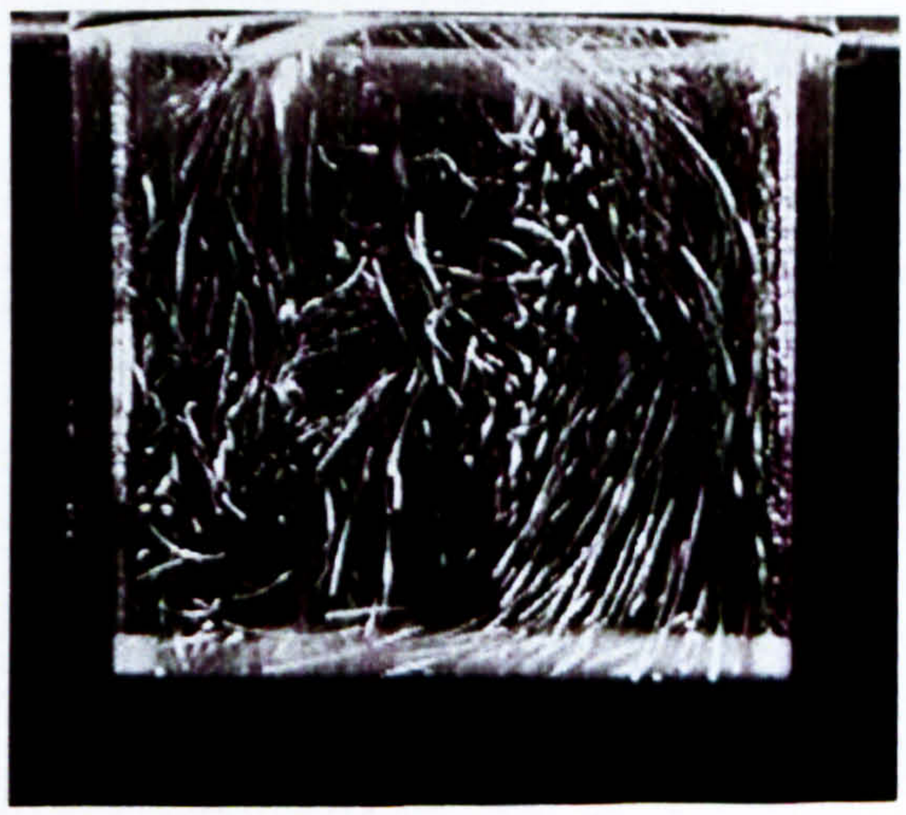

(d) 133° ATDC

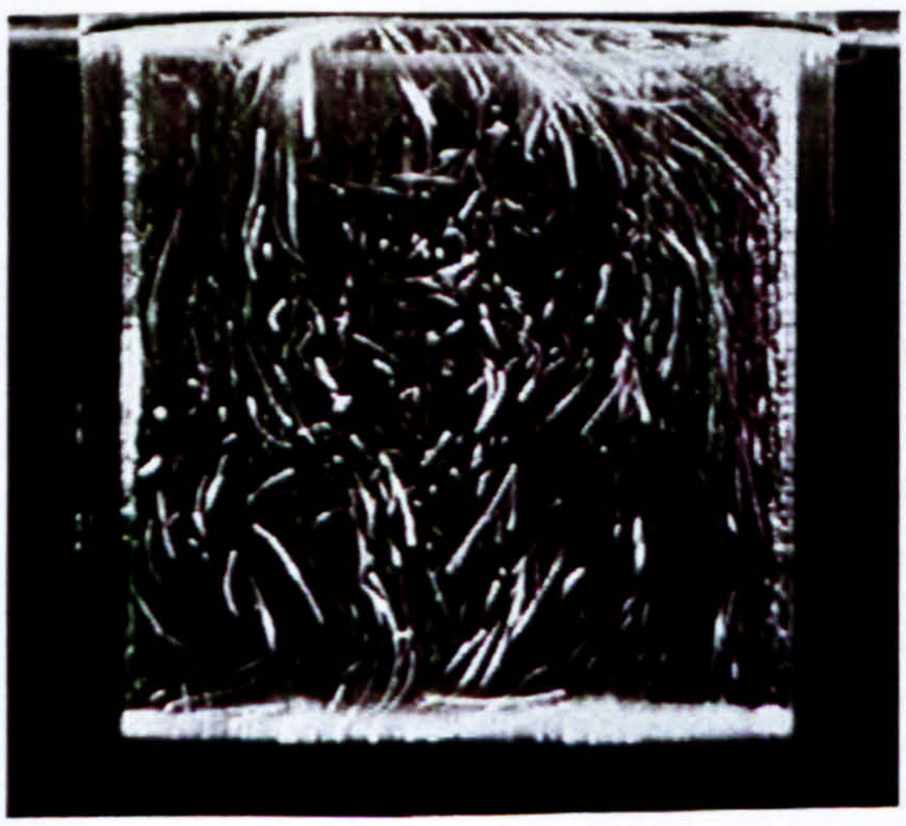

(e) 152° ATDC

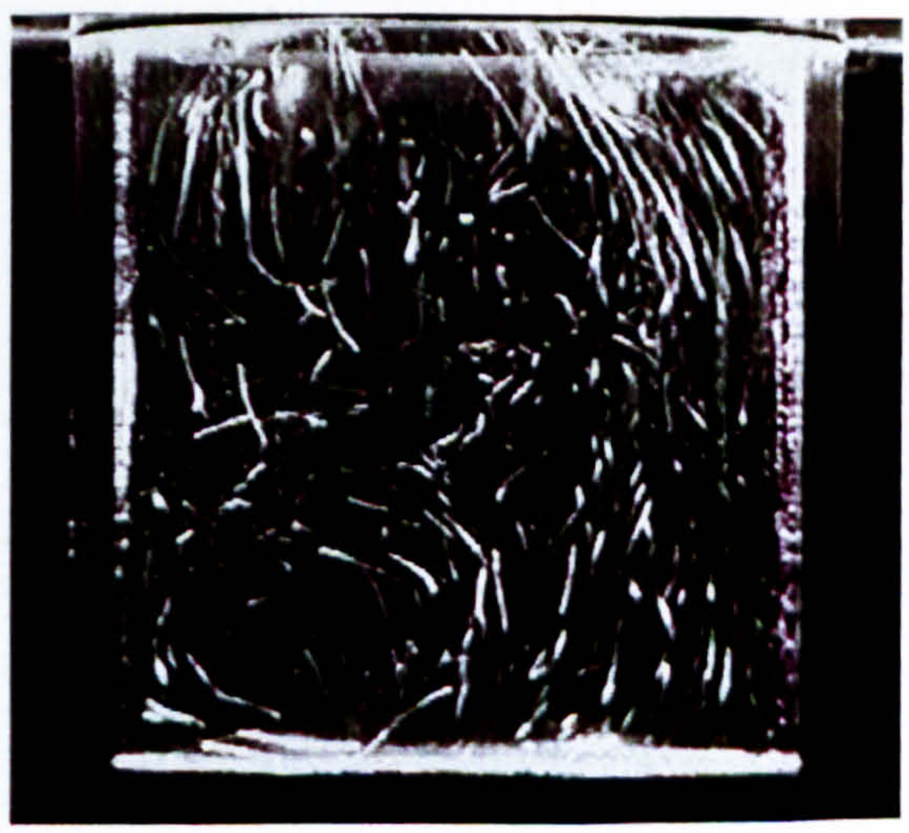

(f) 180° CA (BDC)

Figure 6.2 Development of flow motion during the induction stroke in the mid-cylinder plane y = 0 mm (Engine speed: 77 r.p.m.)

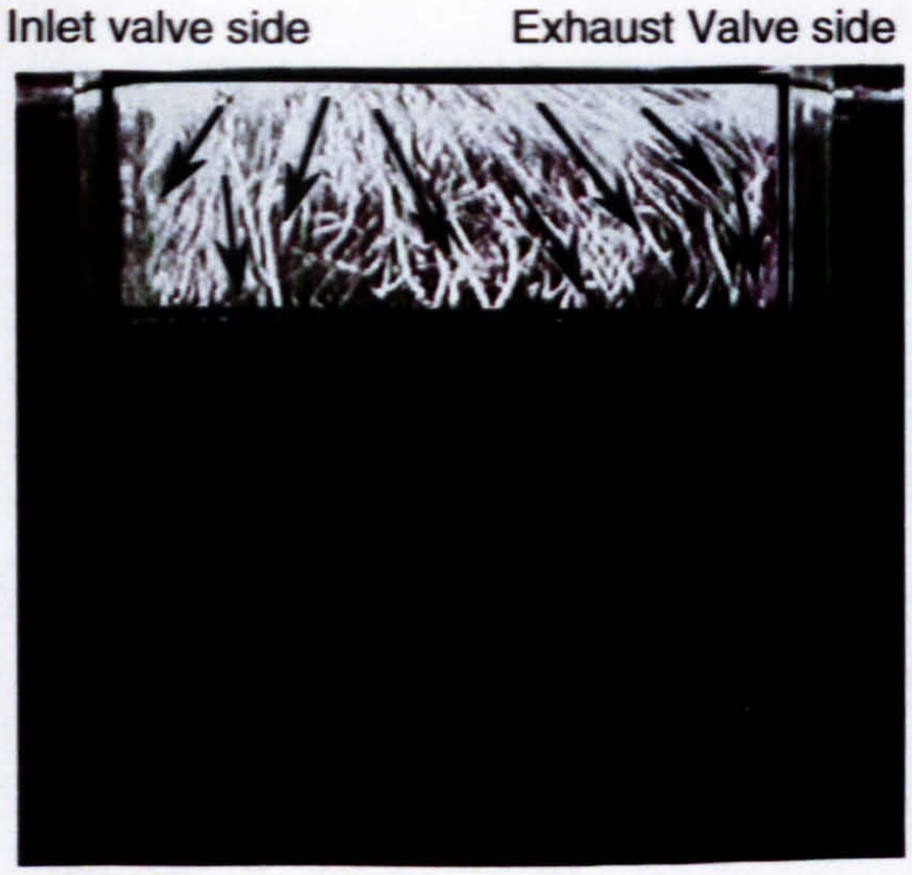

(a) 57° ATDC

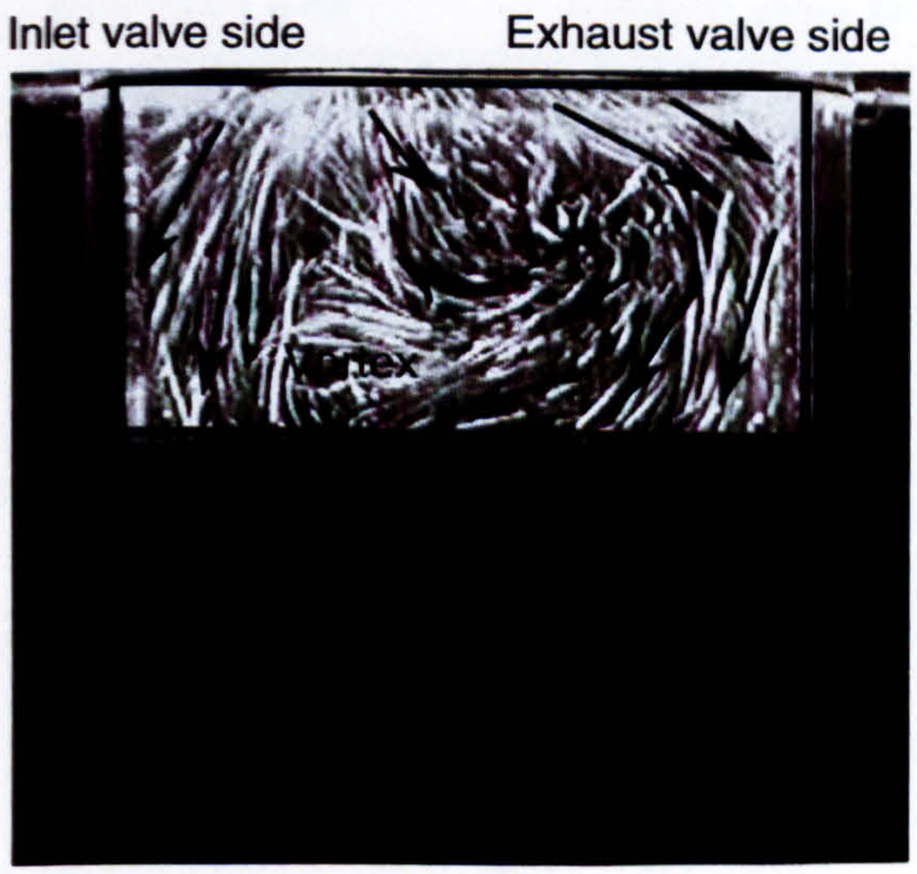

(b) 76° ATDC

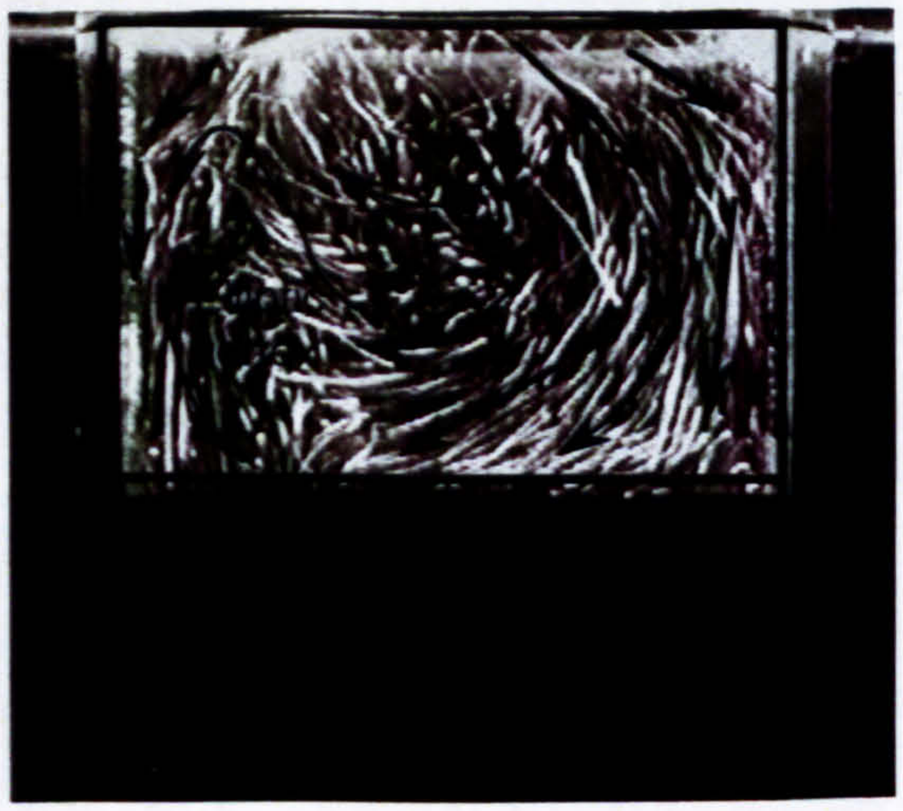

(c) 95° ATDC

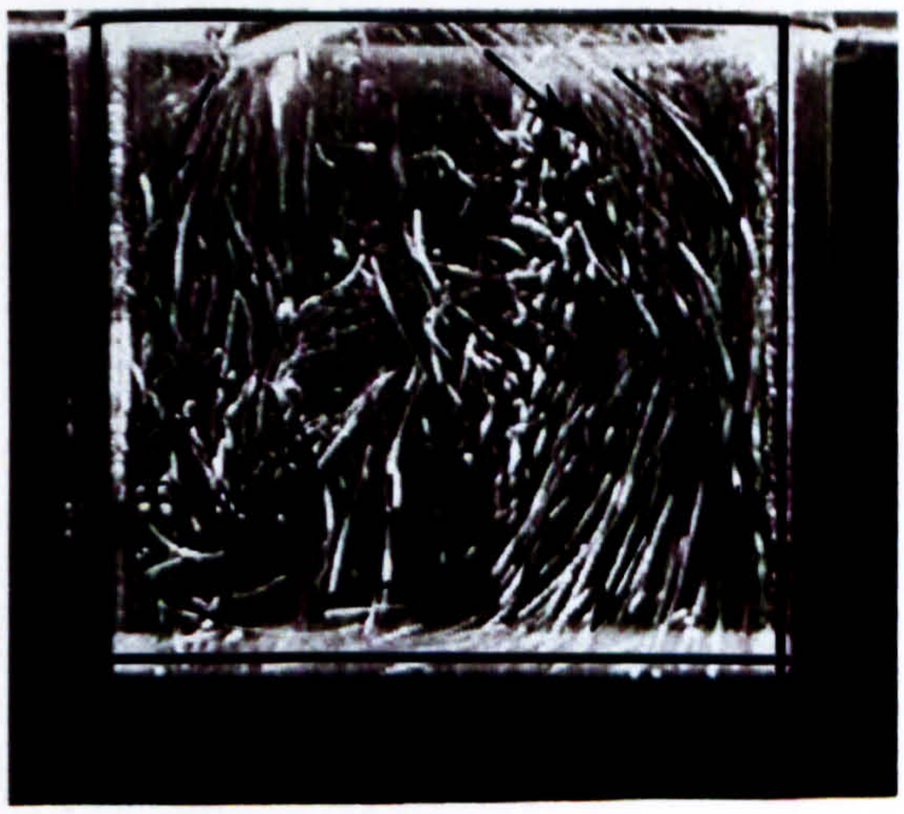

(d) 133° ATDC

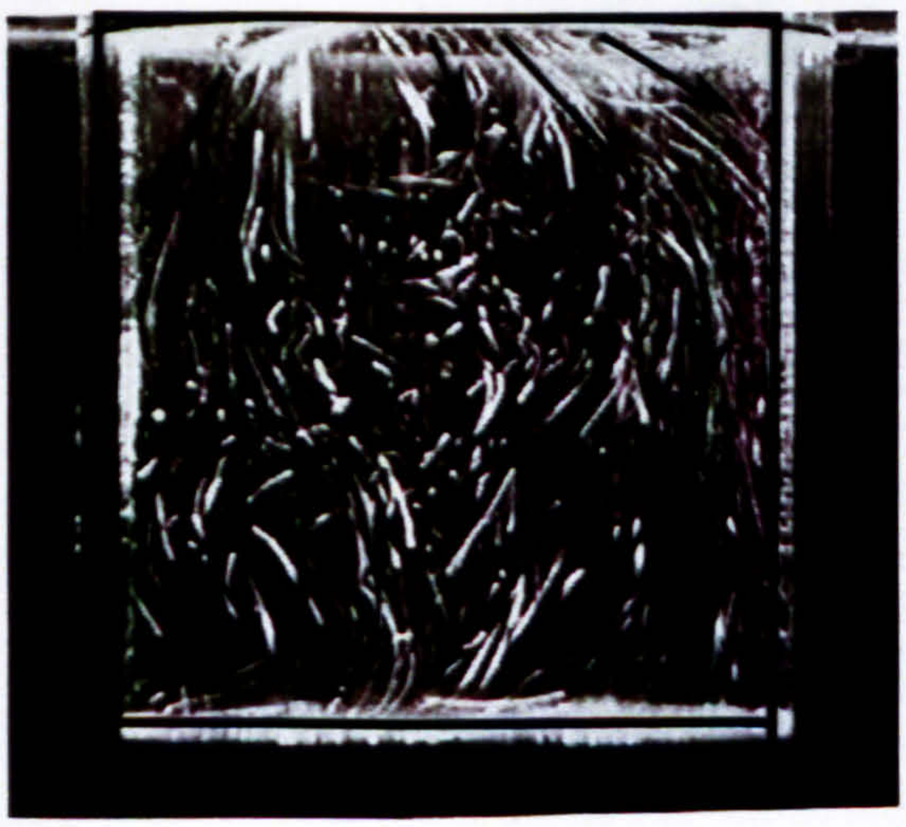

(e) 152° ATDC

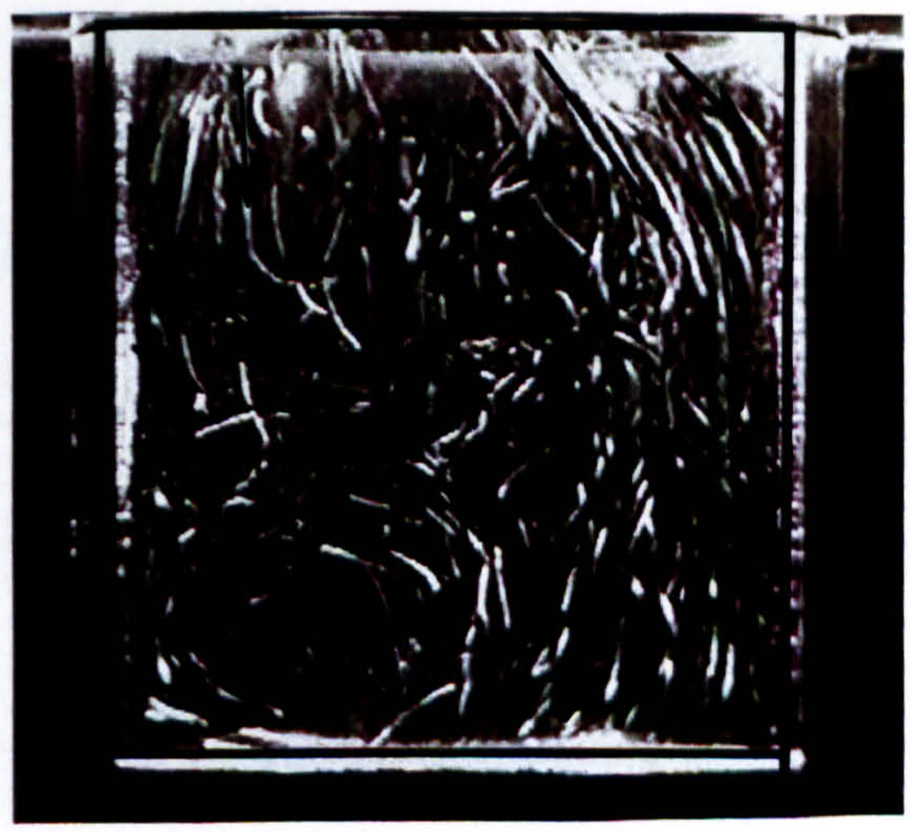

(f) 180° CA (BDC)

Figure 6.2 Development of flow motion during the induction stroke in the mid-cylinder plane y = 0 mm (Engine speed: 77 r.p.m.)

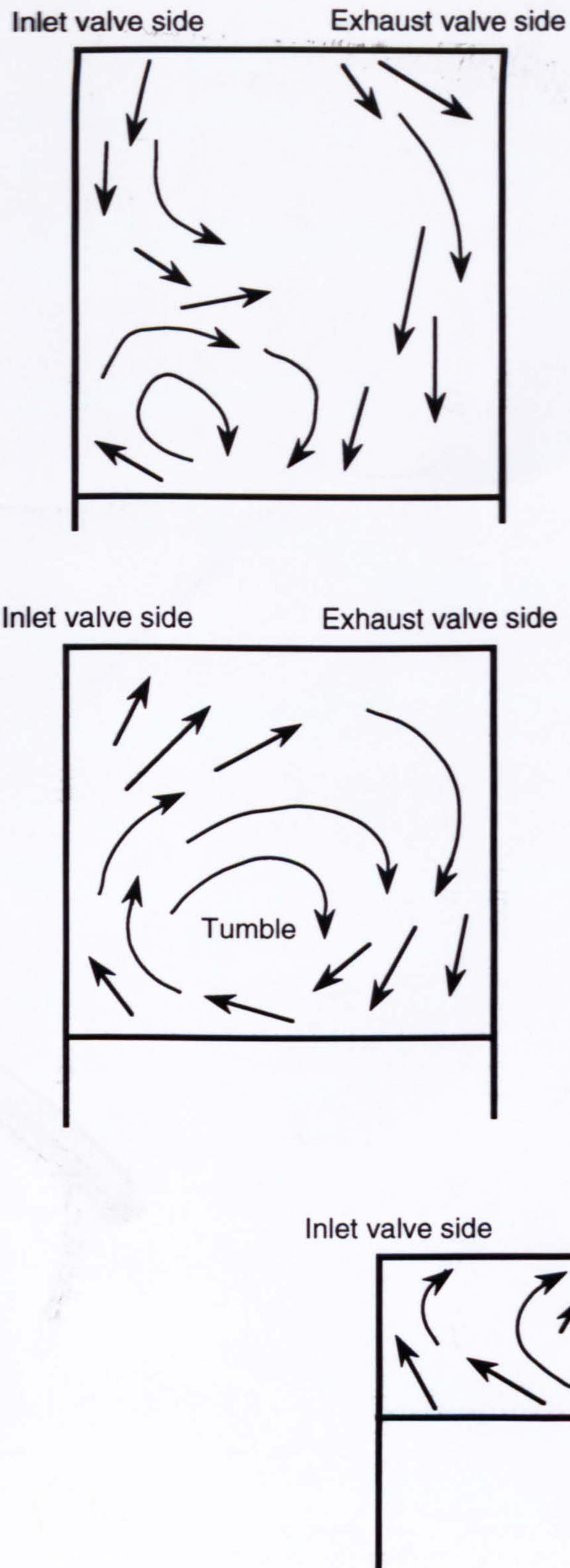
Inlet valve side
Exhaust valve side

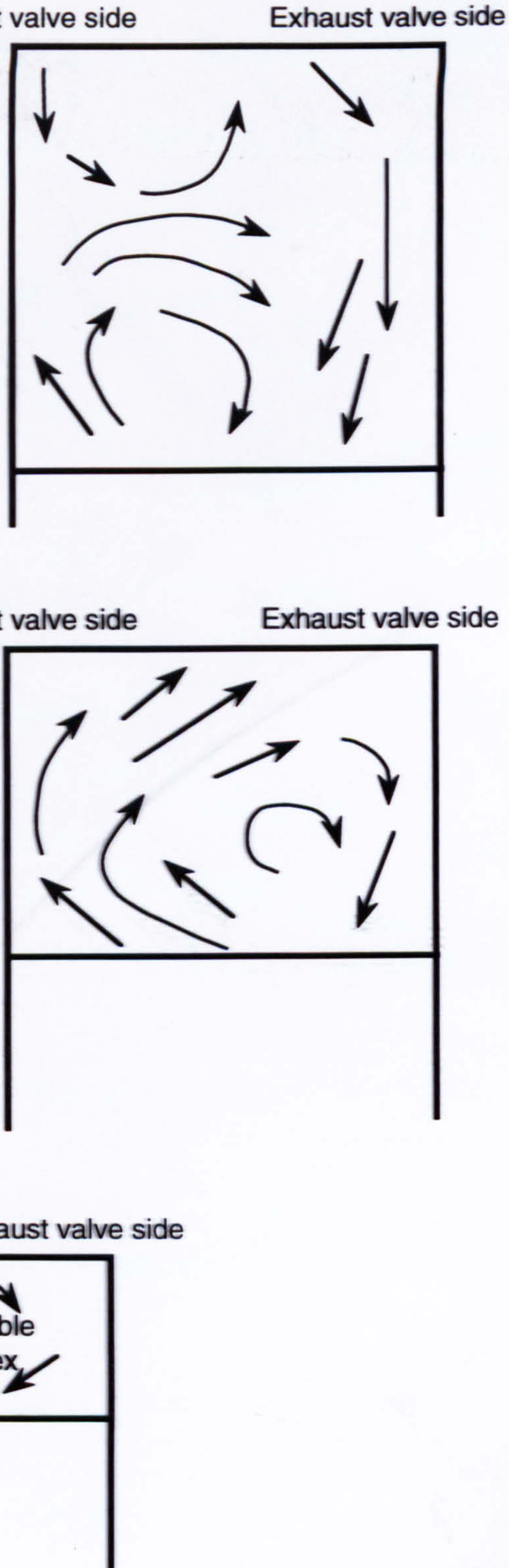
Inlet valve side
Exhaust valve side

Inlet valve side
Exhaust valve side
Tumble

Inlet valve side
Exhaust valve side

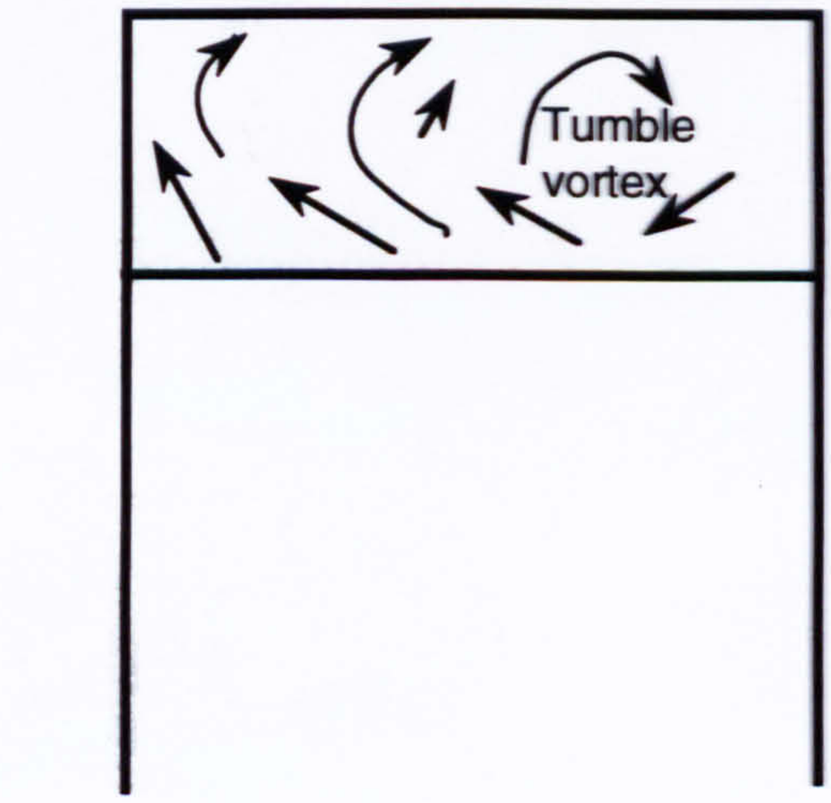
Inlet valve side
Exhaust valve side
Tumble
vortex

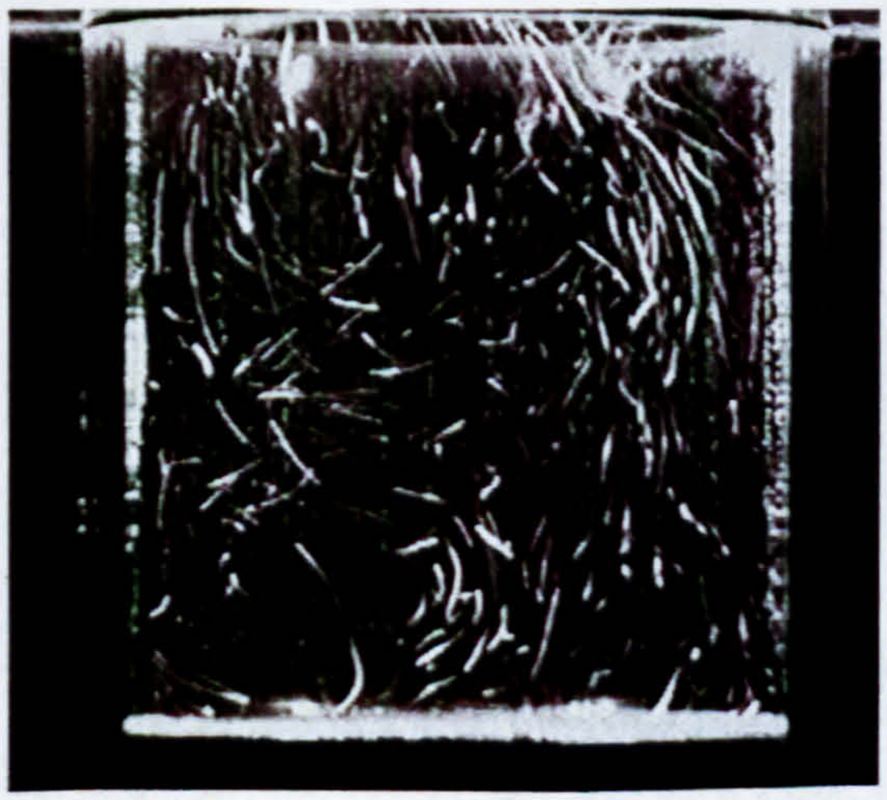

(a) 190° ATDC

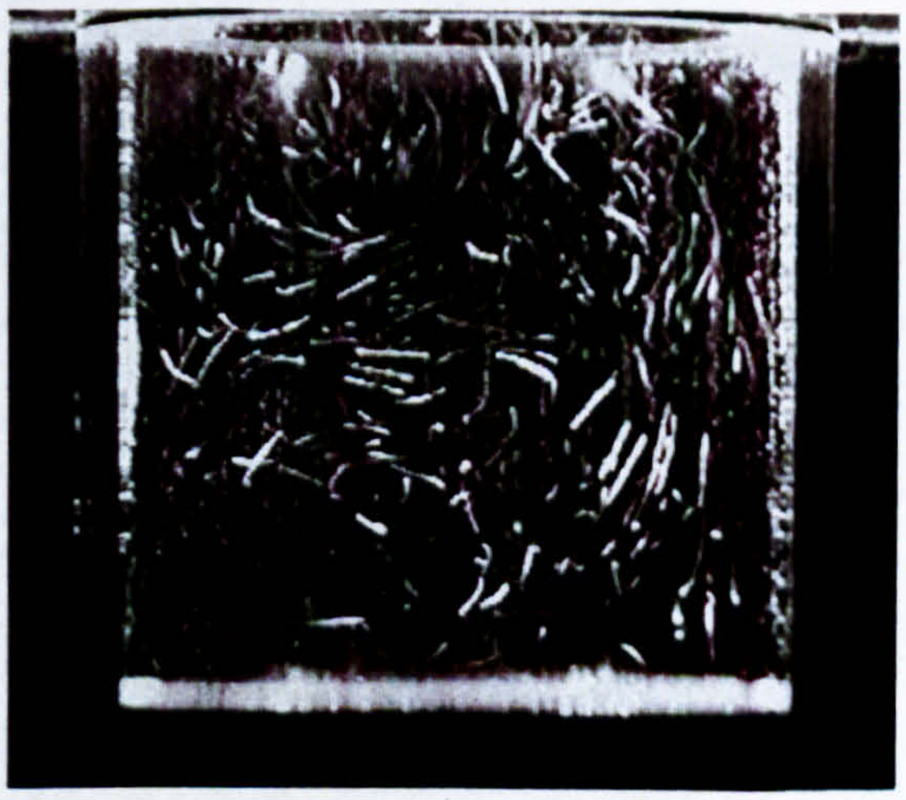

(b) 209° ATDC

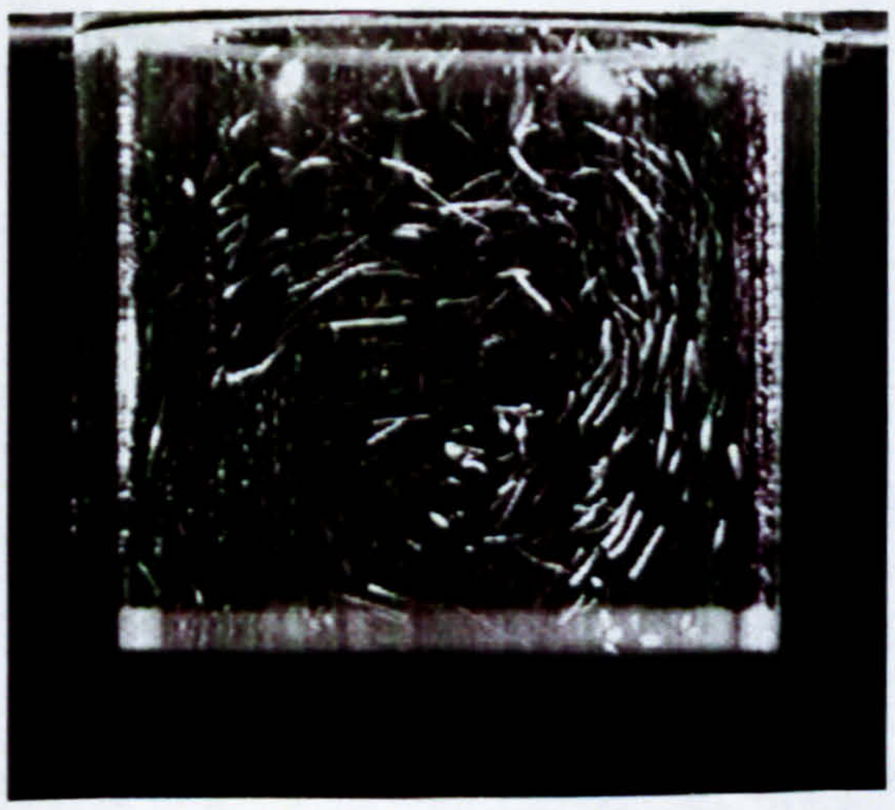

(c) 228° ATDC

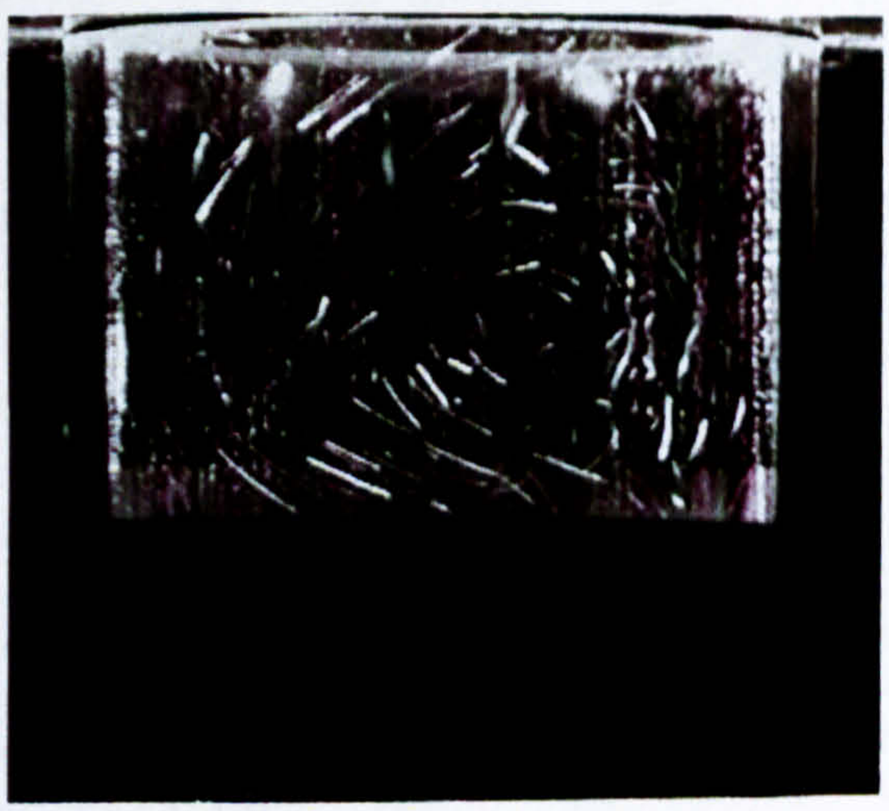

(d) 247° ATDC

(e) 295° ATDC

Figure 6.3 Development of flow motion during the compression stroke in the mid-cylinder plane y = 0 mm (Engine speed: 77 r.p.m.)

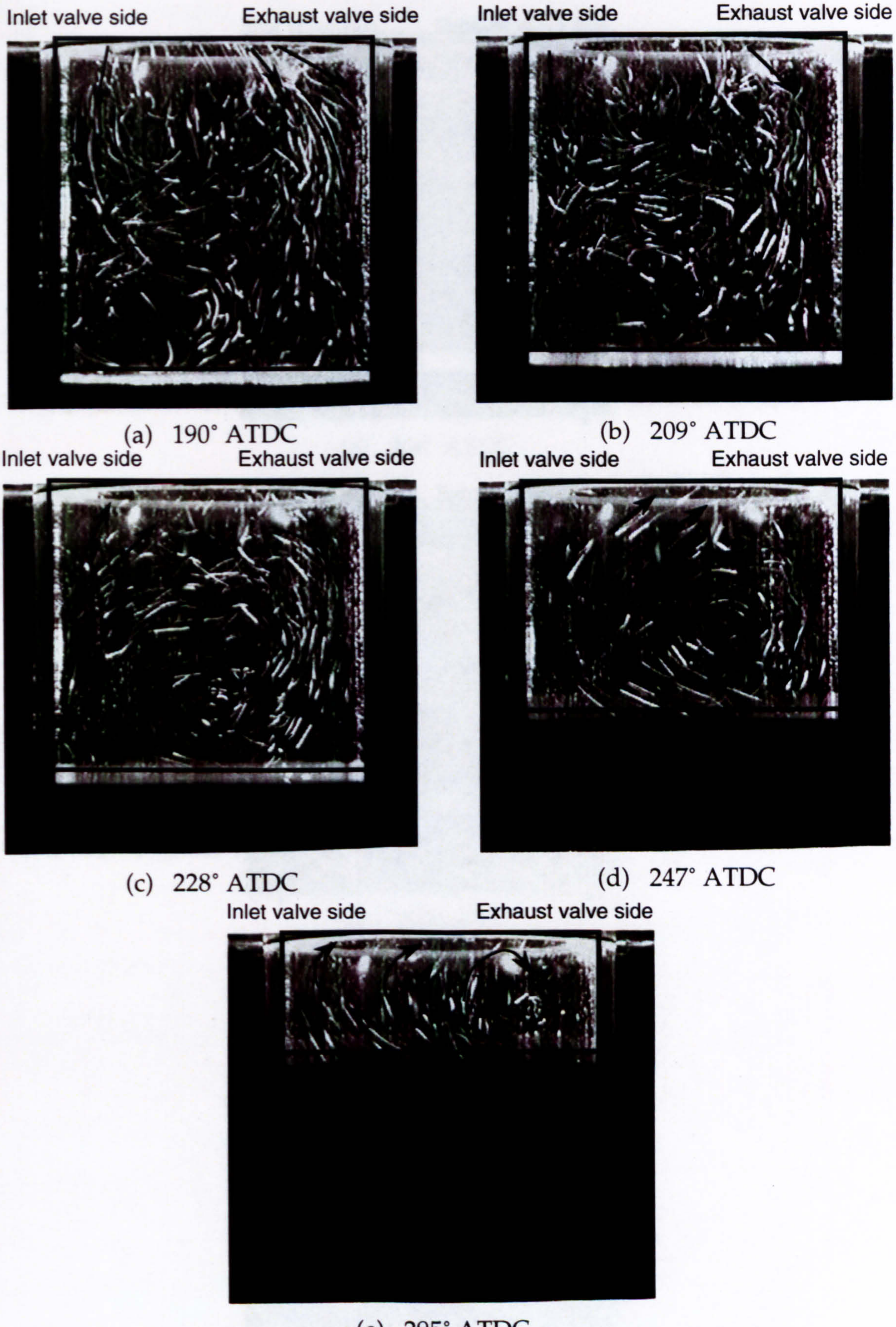

Figure 6.3 Development of flow motion during the compression stroke in the mid-cylinder plane y = 0 mm (Engine speed: 77 r.p.m.)

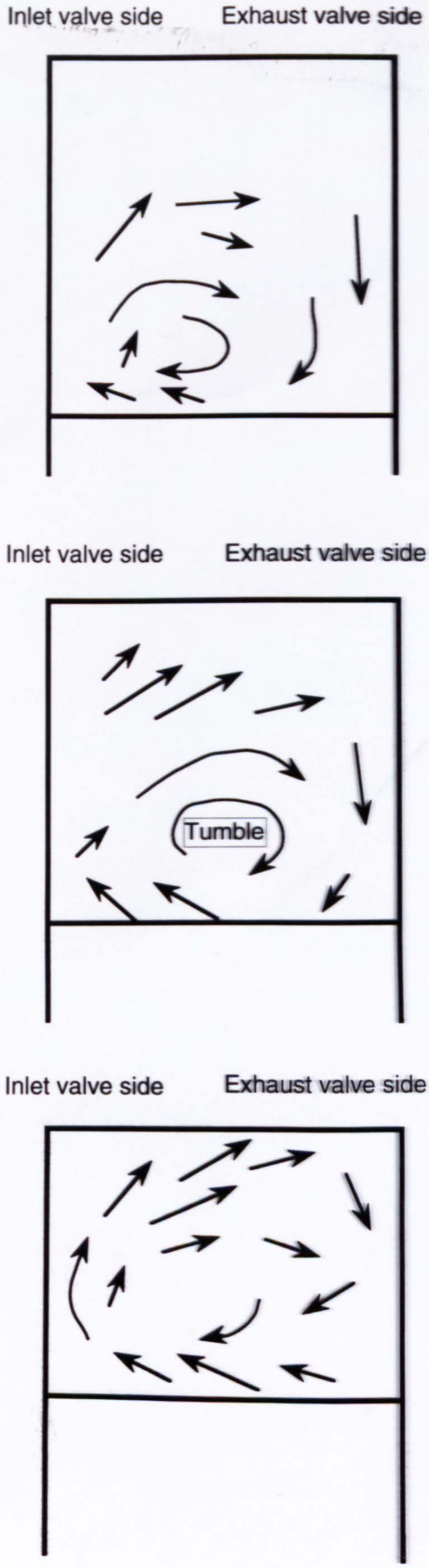
Inlet valve side
Exhaust valve side
Inlet valve side
Exhaust valve side
Tumble
Inlet valve side
Exhaust valve side

(a) 206° ATDC

(b) 232° ATDC

(c) 260° ATDC

Figure 6.4 Selected flow visualisation images from the compression stroke in the y = 0 mm (N = 104 r.p.m., IMP = 1.22 bar)

(a) 206° ATDC

(b) 232° ATDC

(c) 260° ATDC

Figure 6.4 Selected flow visualisation images from the compression stroke in the y = 0 mm (N = 104 r.p.m., IMP = 1.22 bar)

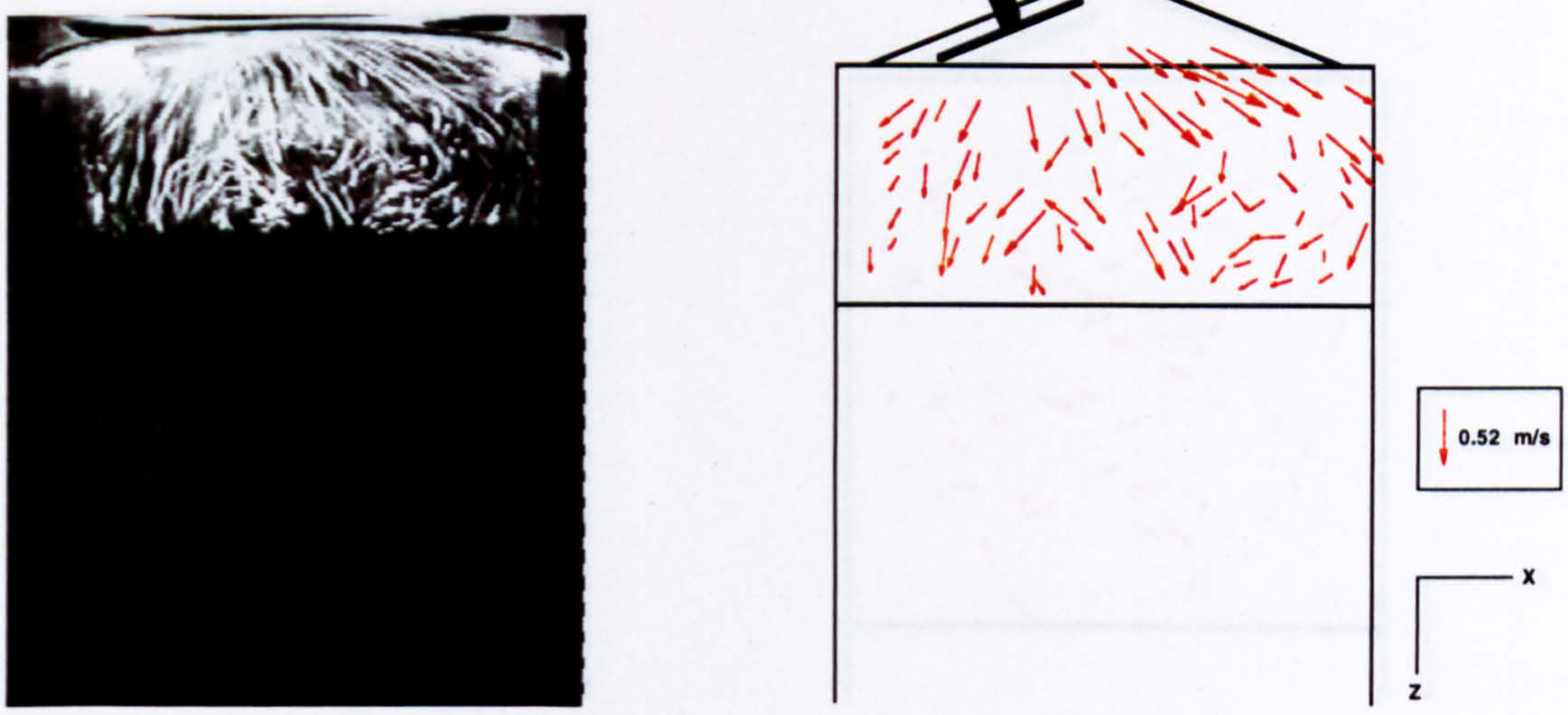

(a) 67° ATDC crankangle

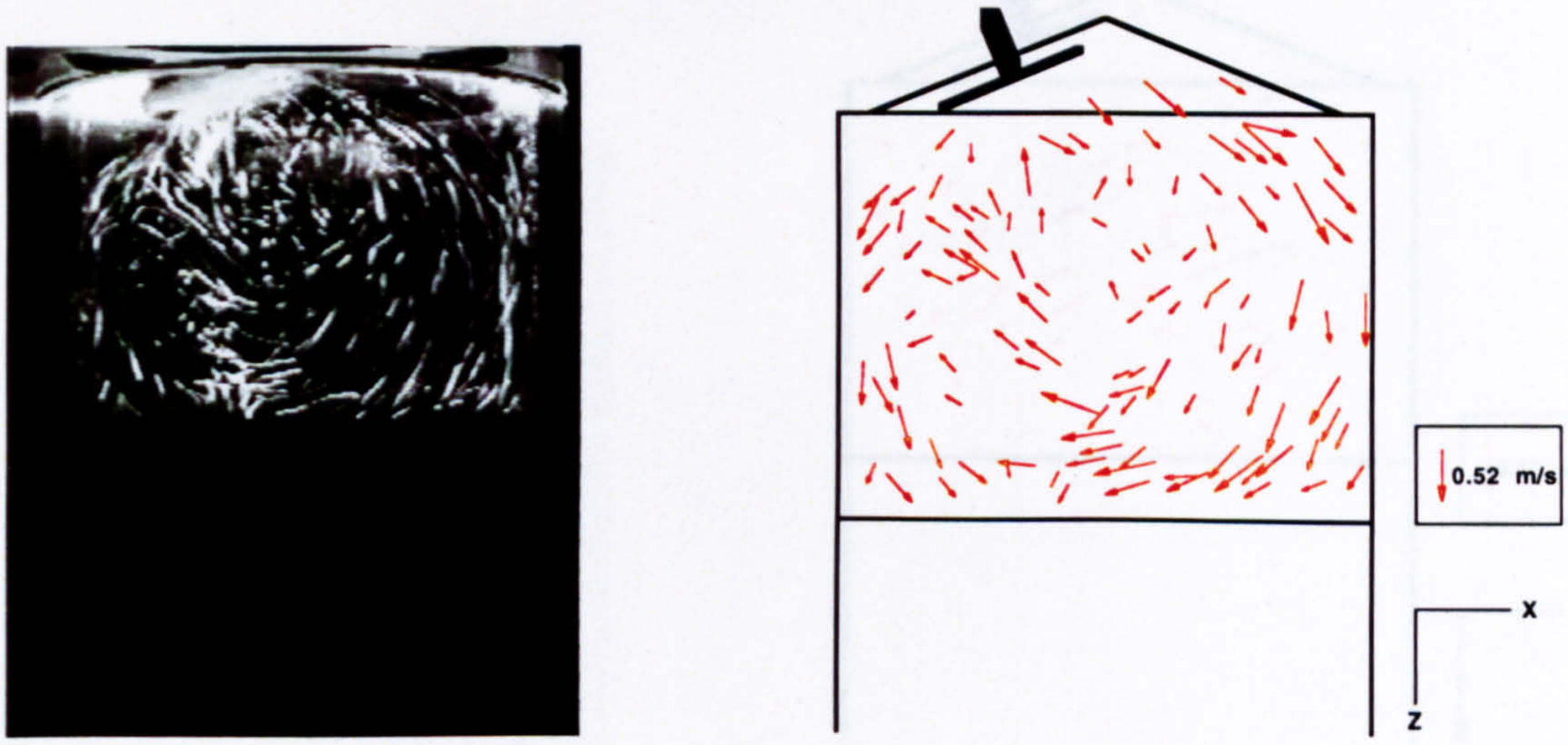

(b) 100° ATDC crankangle

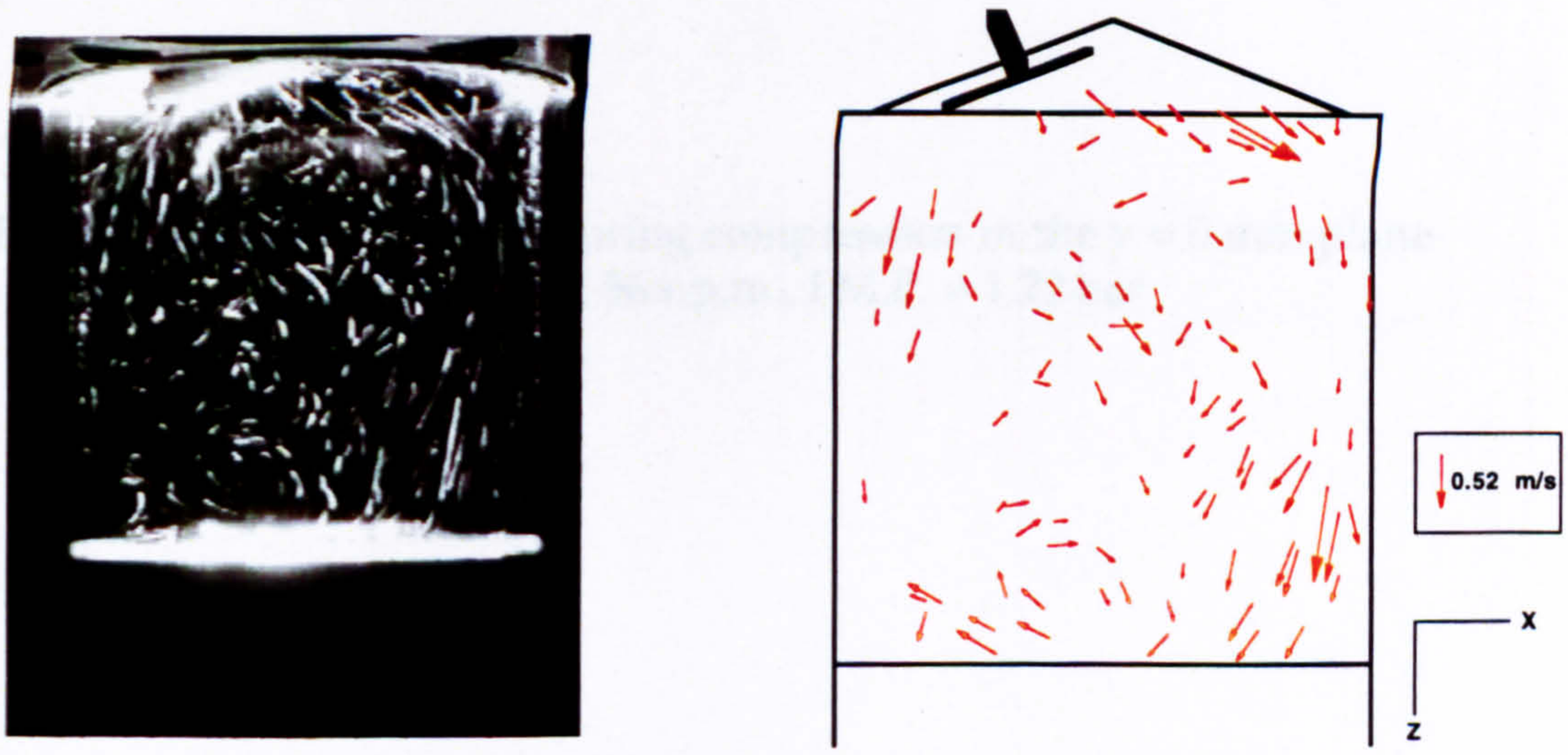

(c) 147° ATDC crankangle

Figure 6.5 Flow processes during induction in the y = 0 mm plane
Engine speed: 56 r.p.m., I.M.P. = 1.22 bar

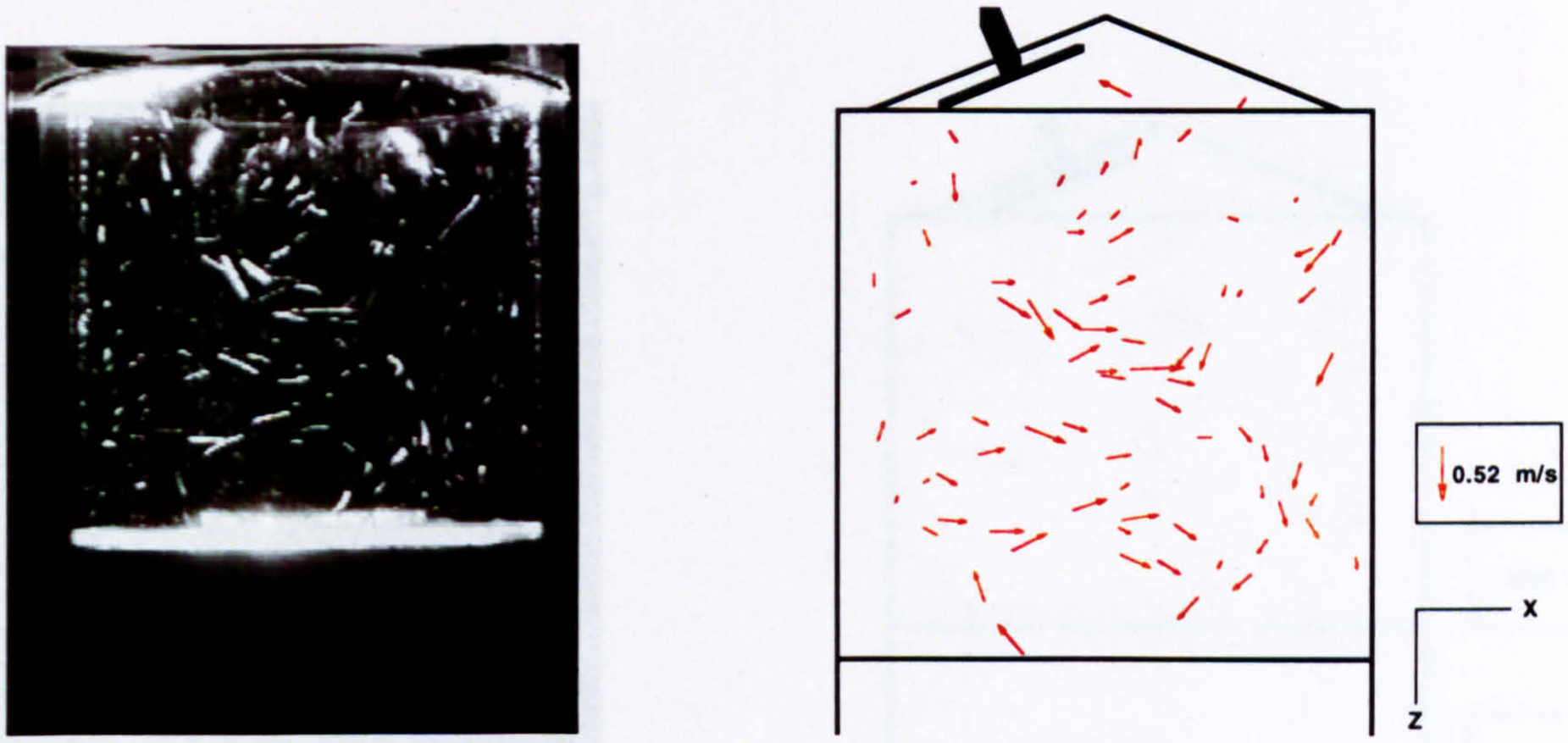

(a) 214° ATDC crankangle

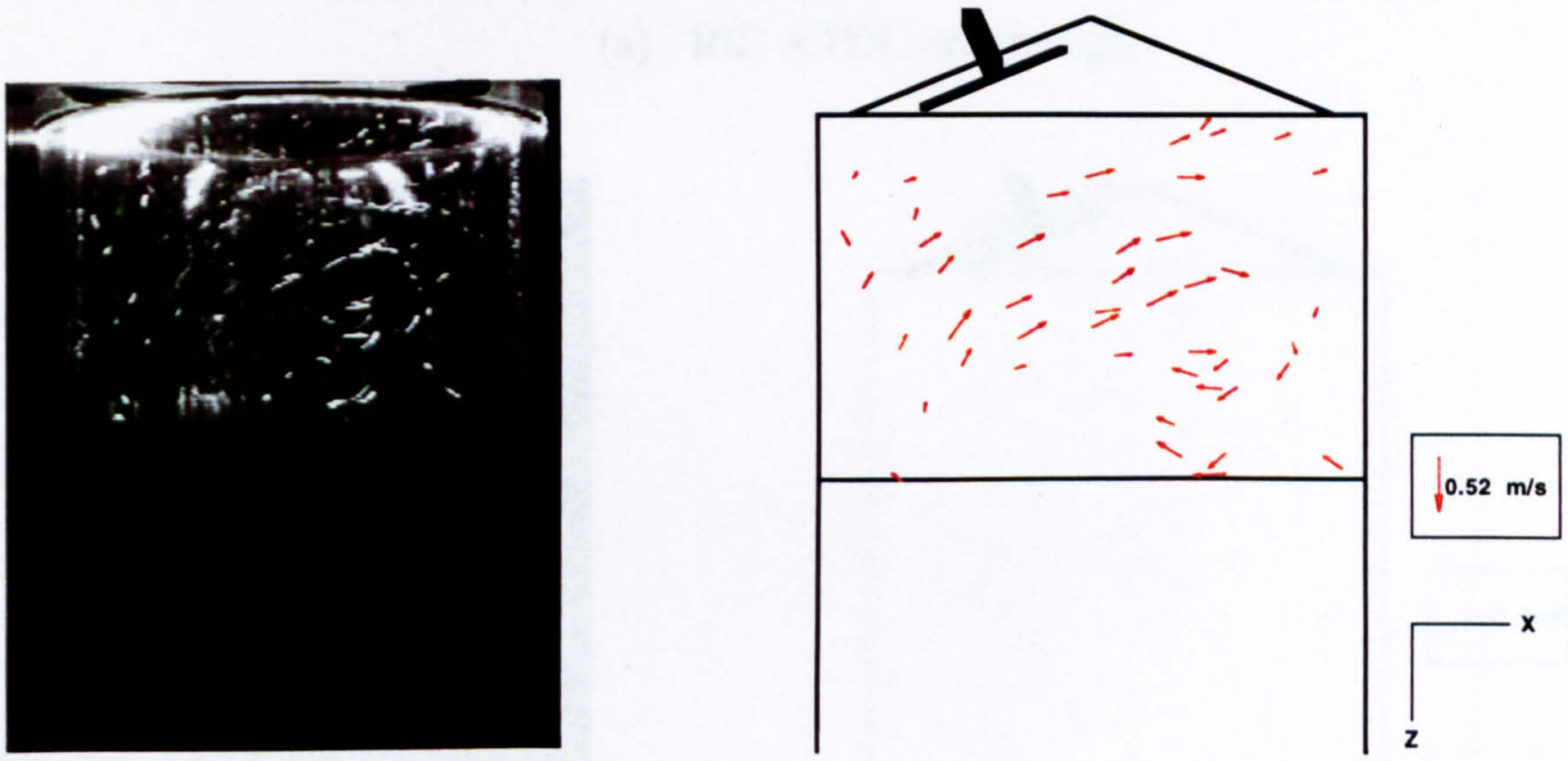

(b) 261° ATDC crankangle

Figure 6.6 Flow processes during compression in the y = 0 mm plane
Engine speed: 56 r.p.m., I.M.P. = 1.22 bar

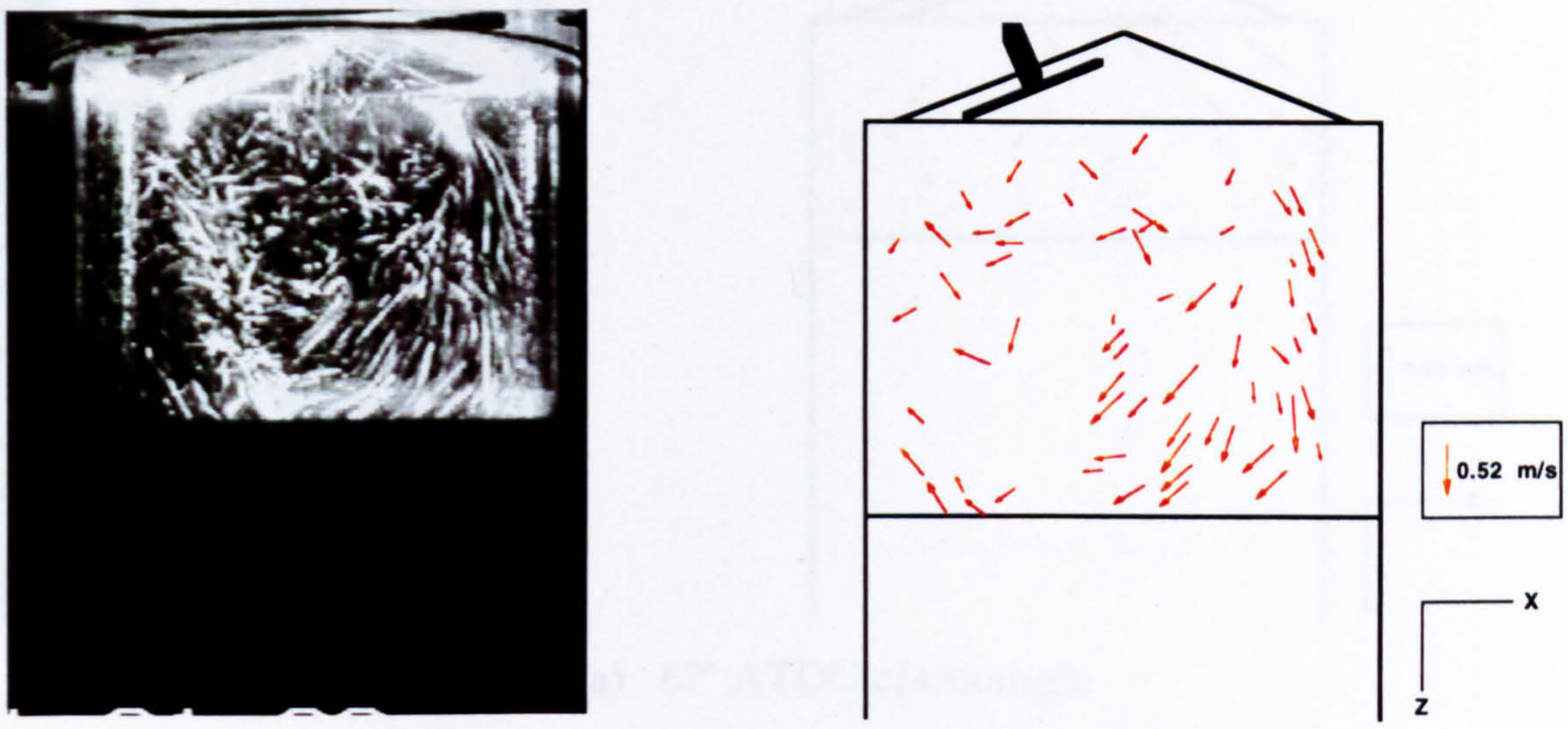

(a) 101° ATDC crankangle

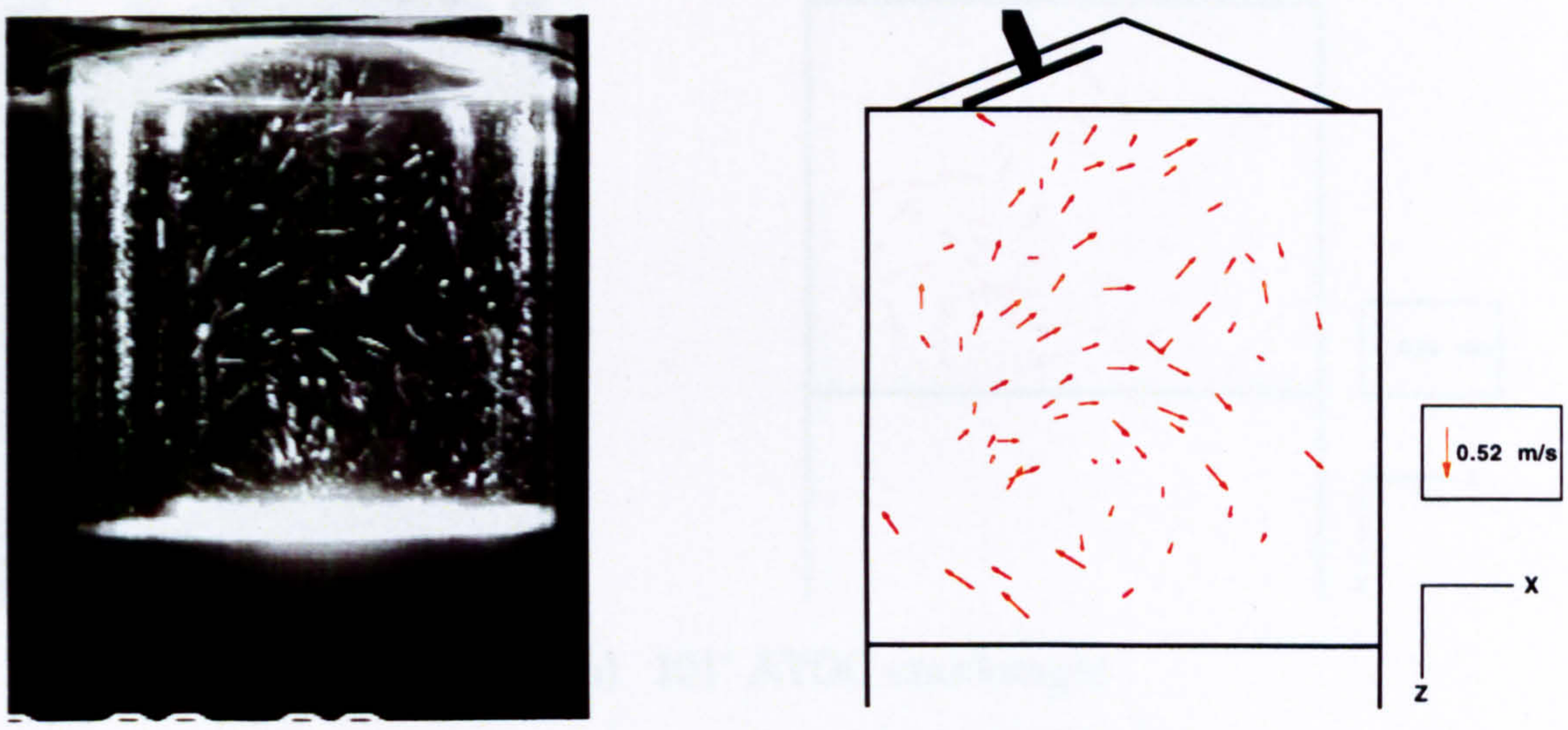

(b) 202° ATDC crankangle

Figure 6.7 Flow processes in the y = 17.6 mm plane, selected images
Engine speed: 56 r.p.m., I.M.P. = 1.22 bar

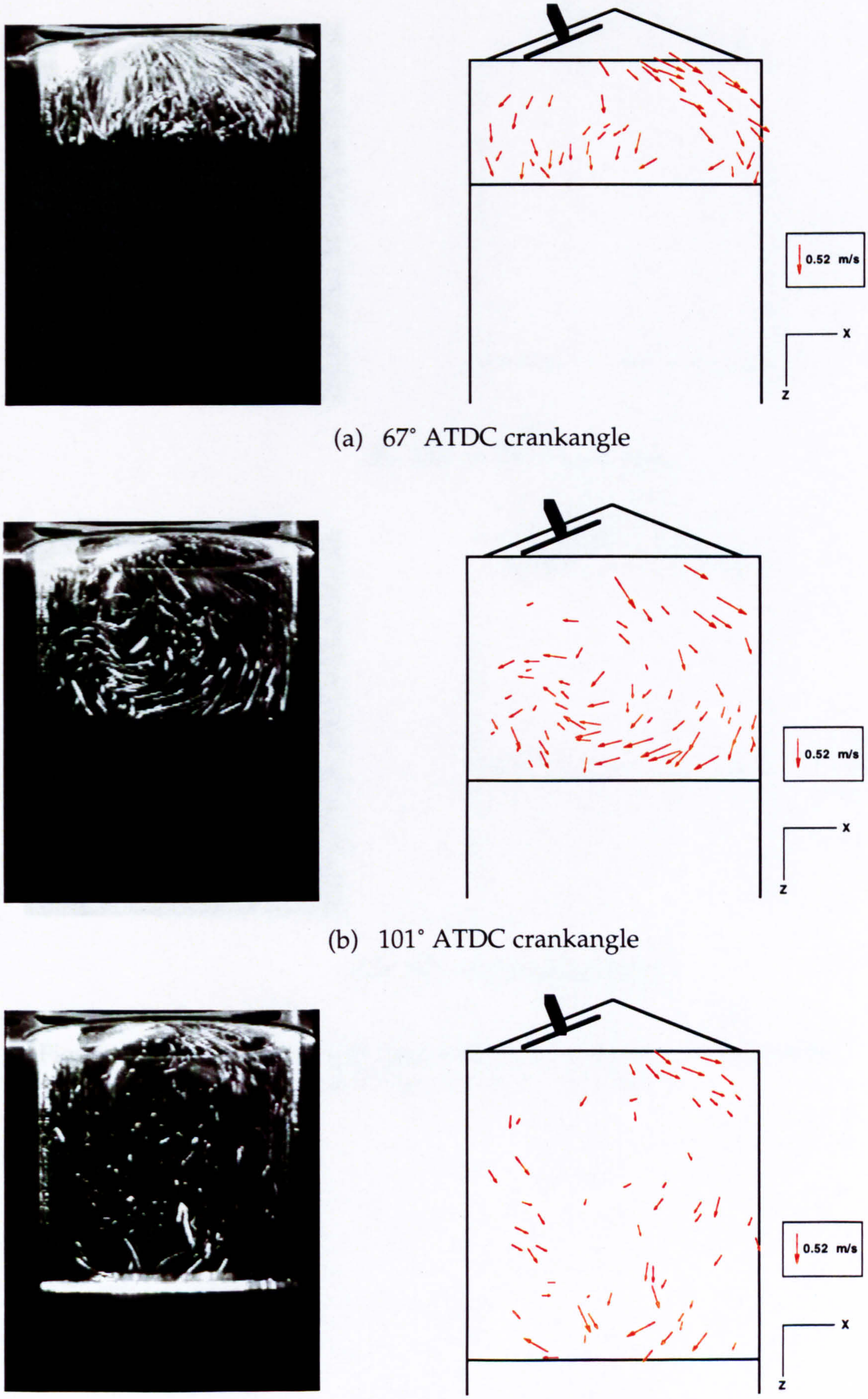

(a) 67° ATDC crankangle

(b) 101° ATDC crankangle

(c) 147° ATDC crankangle

Figure 6.8 Flow processes during induction in the y = 0 mm plane
Engine speed: 56 r.p.m., I.M.P. = 1.56 bar

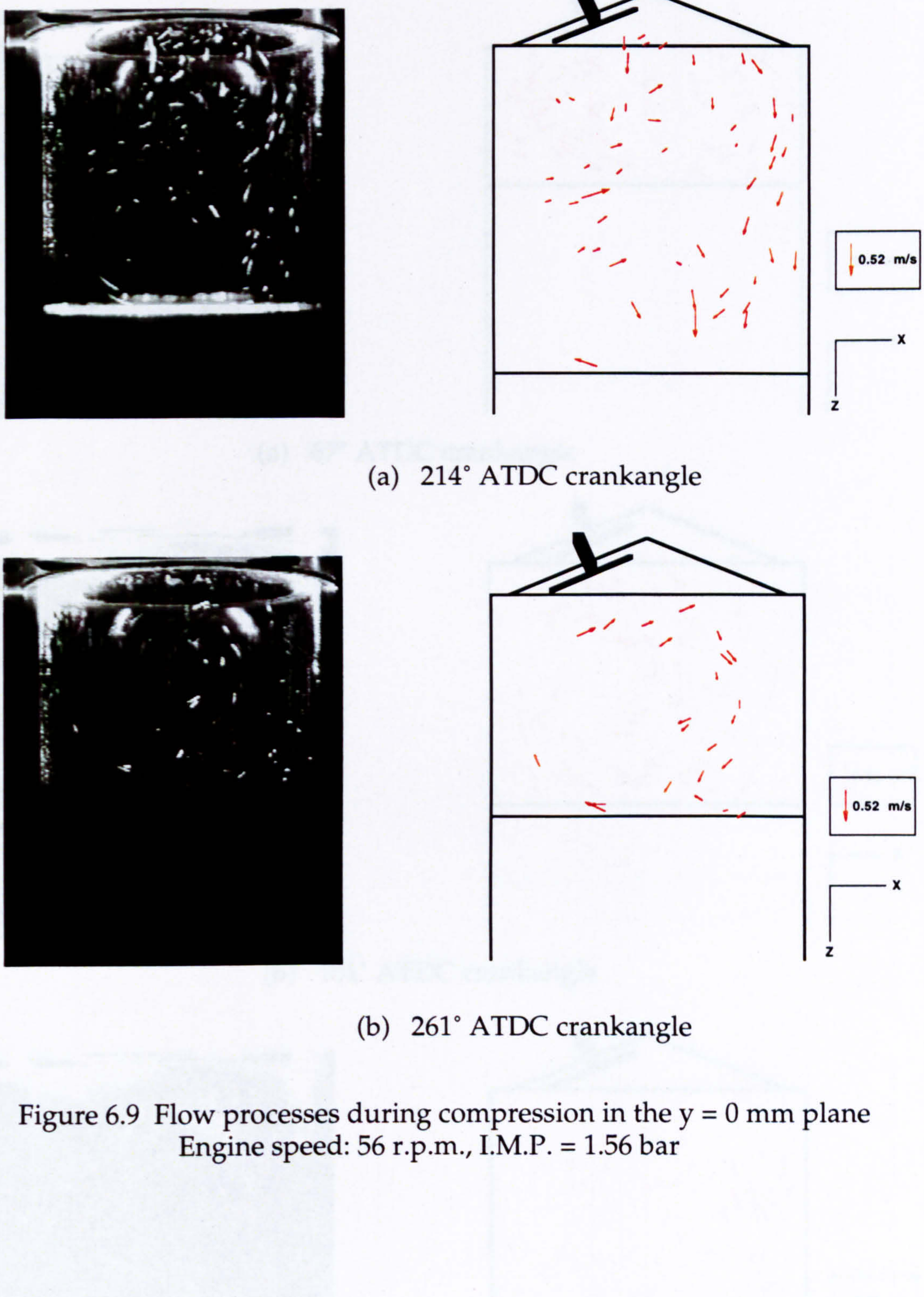

(a) 214° ATDC crankangle

(b) 261° ATDC crankangle

Figure 6.9 Flow processes during compression in the y = 0 mm plane
Engine speed: 56 r.p.m., I.M.P. = 1.56 bar

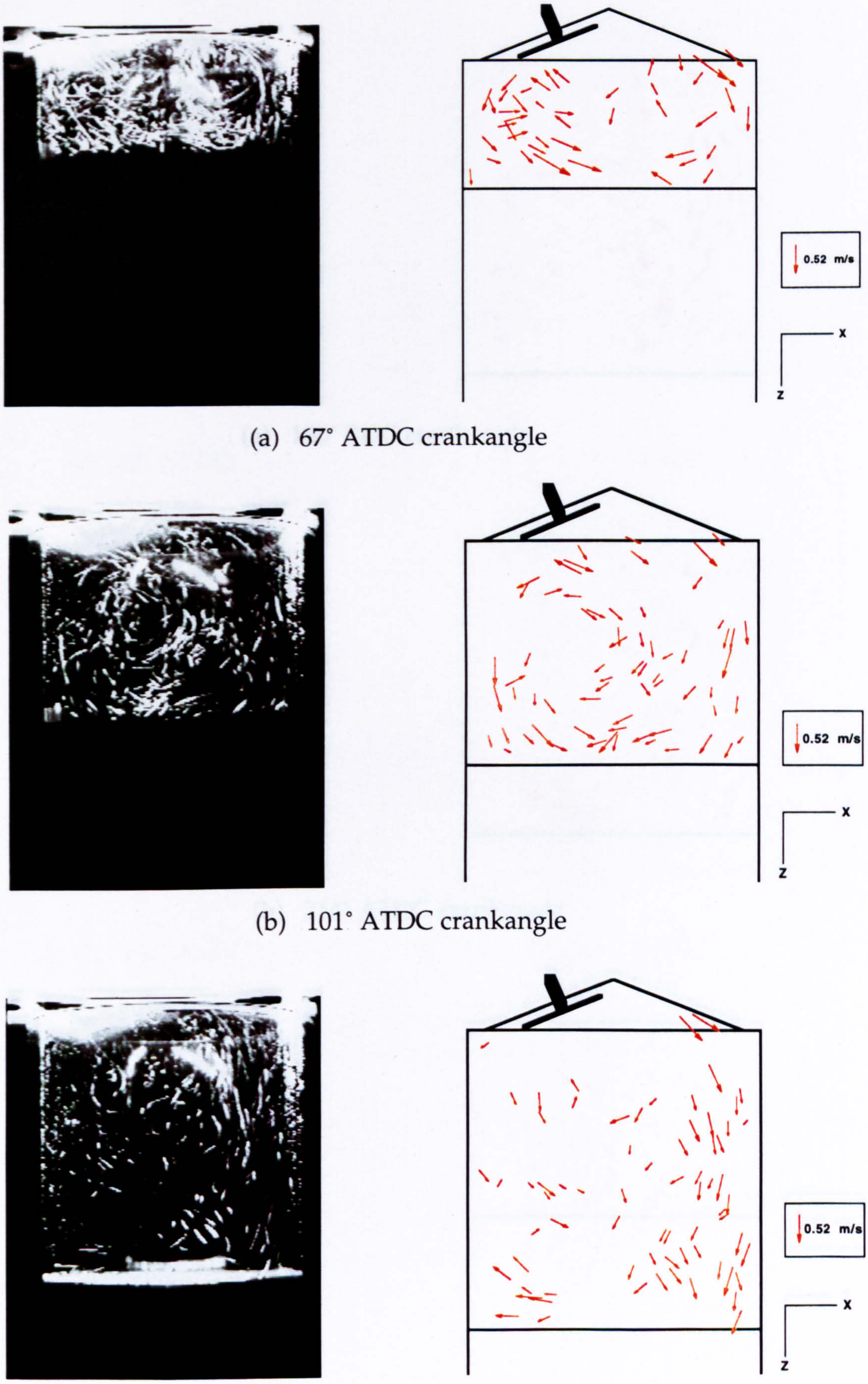

(a) 67° ATDC crankangle

(b) 101° ATDC crankangle

(c) 147° ATDC crankangle

Figure 6.10 Flow processes during induction in the y = 17.6 mm plane
Engine speed: 56 r.p.m., I.M.P. = 1.56 bar

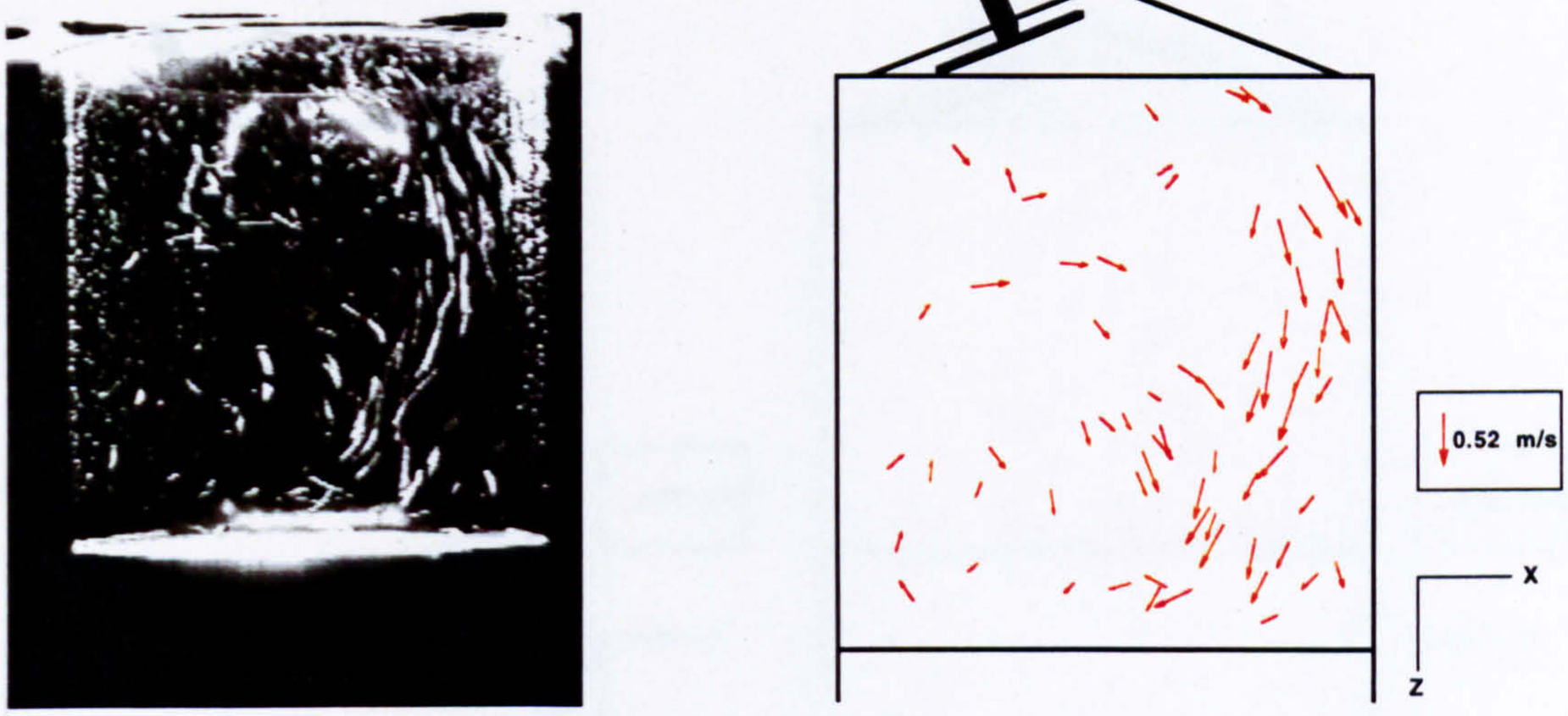

(a) 180° BDC crankangle

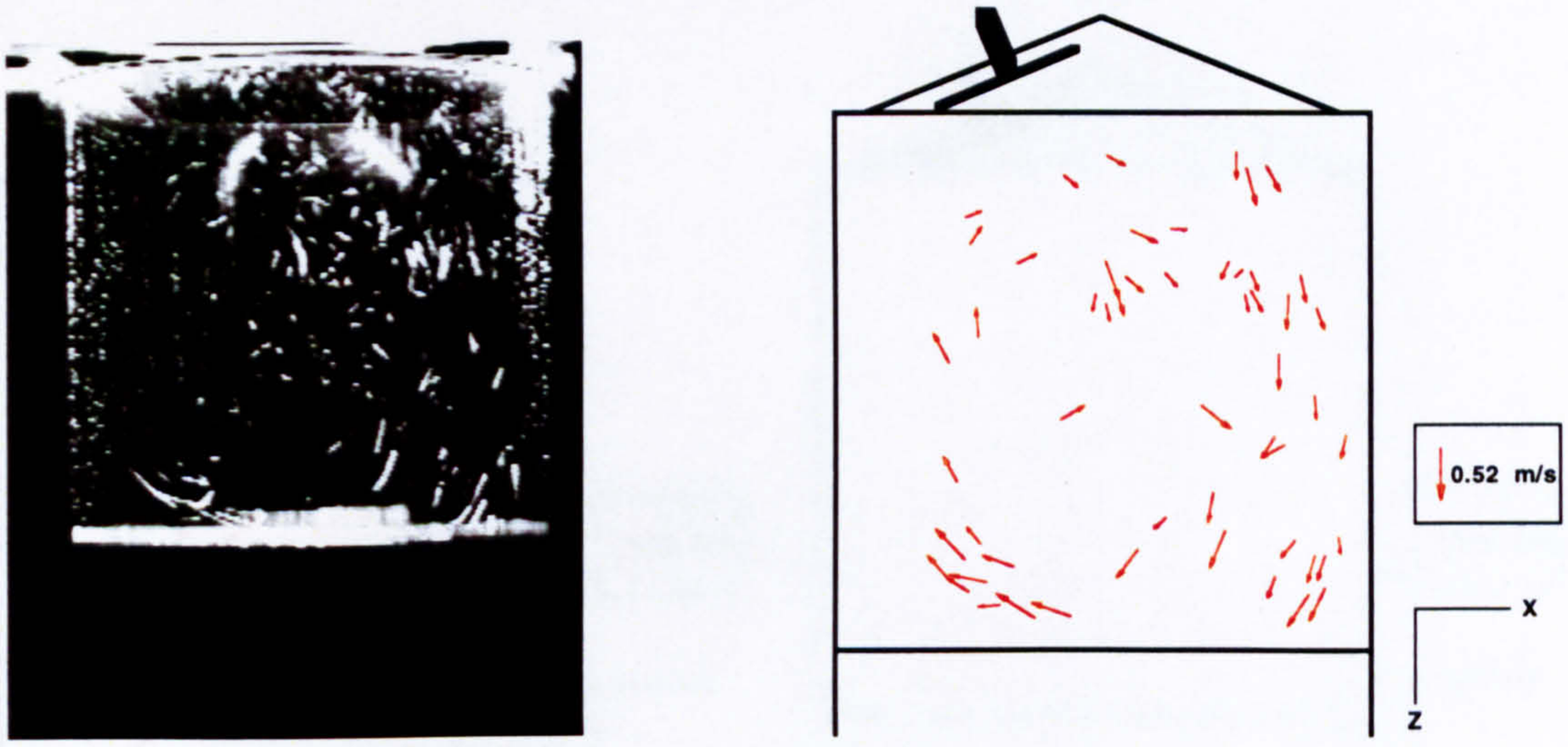

(b) 214° ATDC crankangle

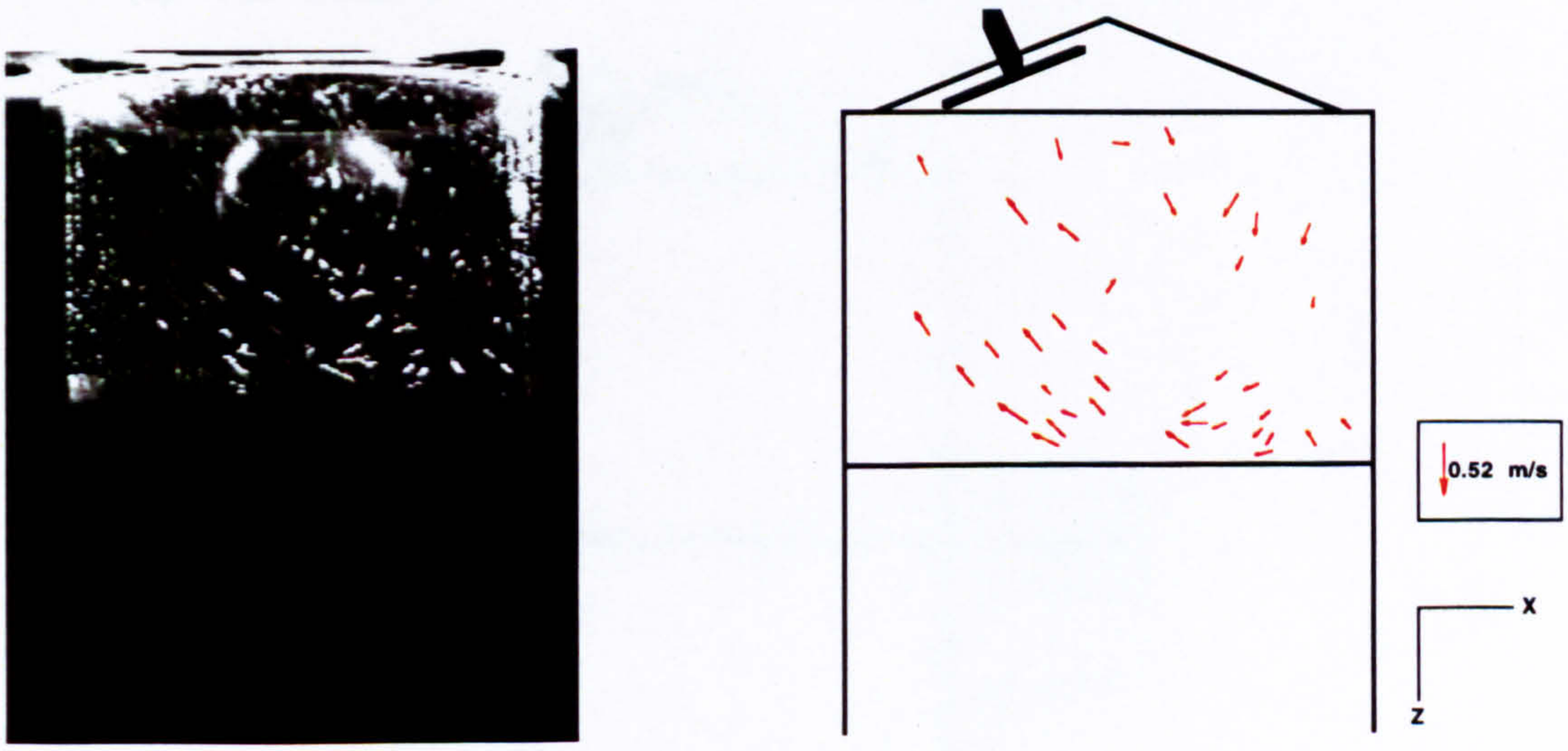

(c) 261° ATDC crankangle

Figure 6.11 Flow processes during compression in the y = 17.6 mm plane
Engine speed: 56 r.p.m., I.M.P. = 1.56 bar

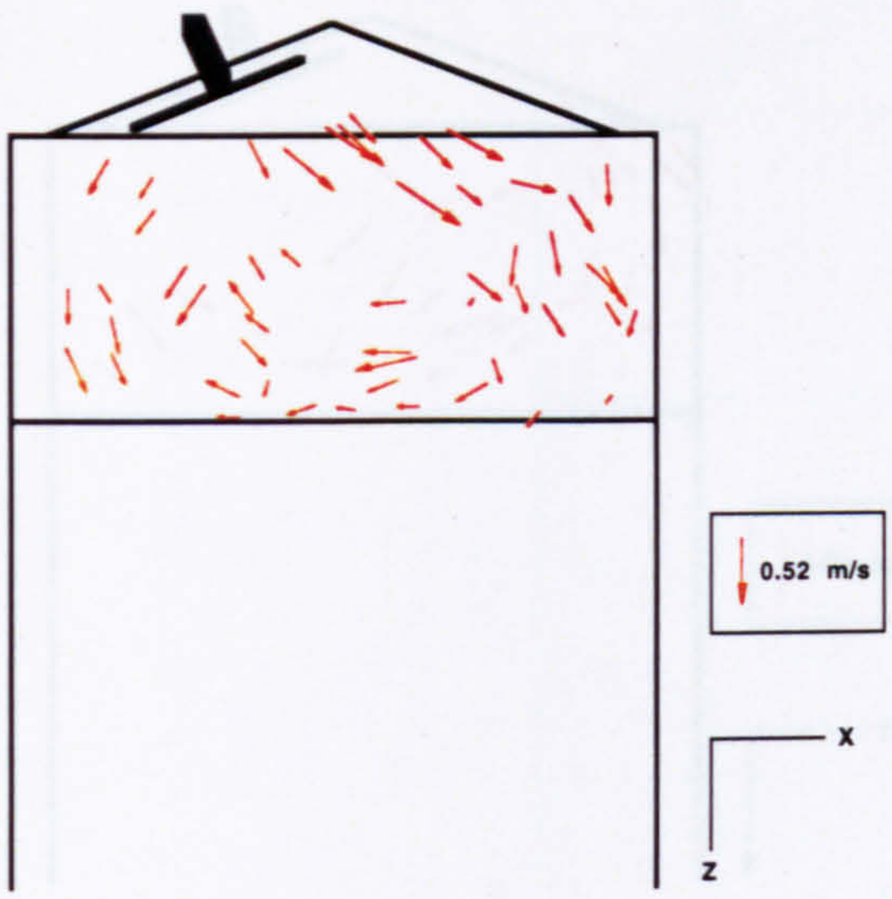

(a) 67° ATDC

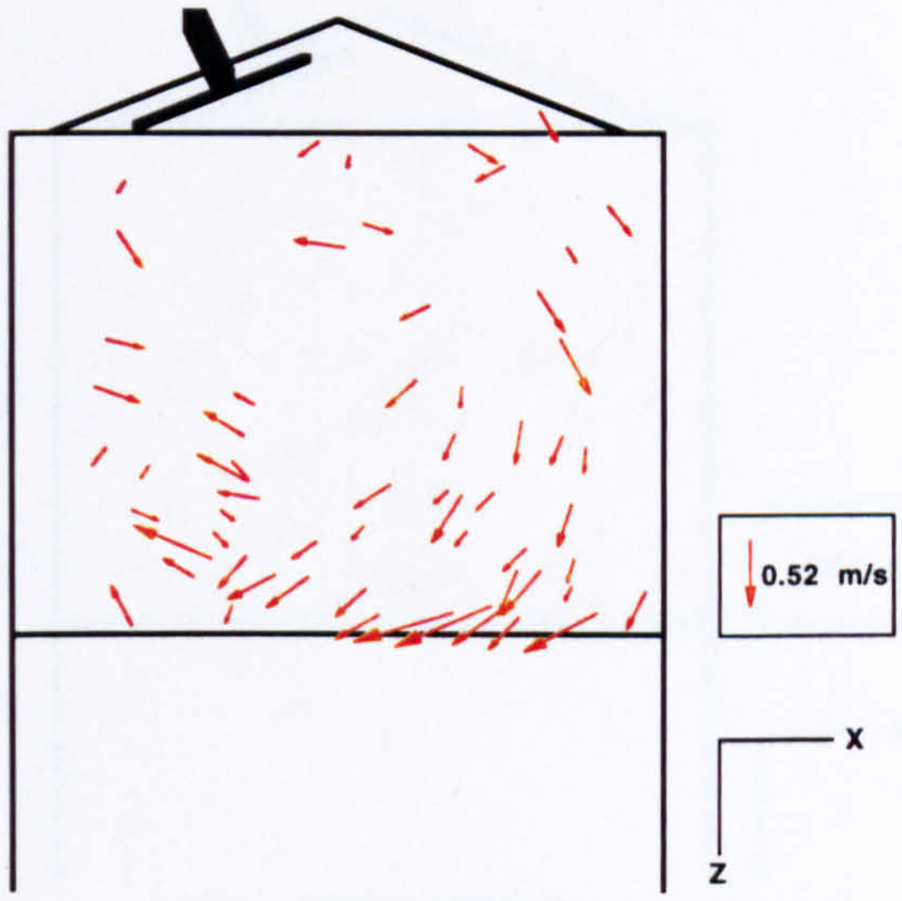

(b) 105° ATDC

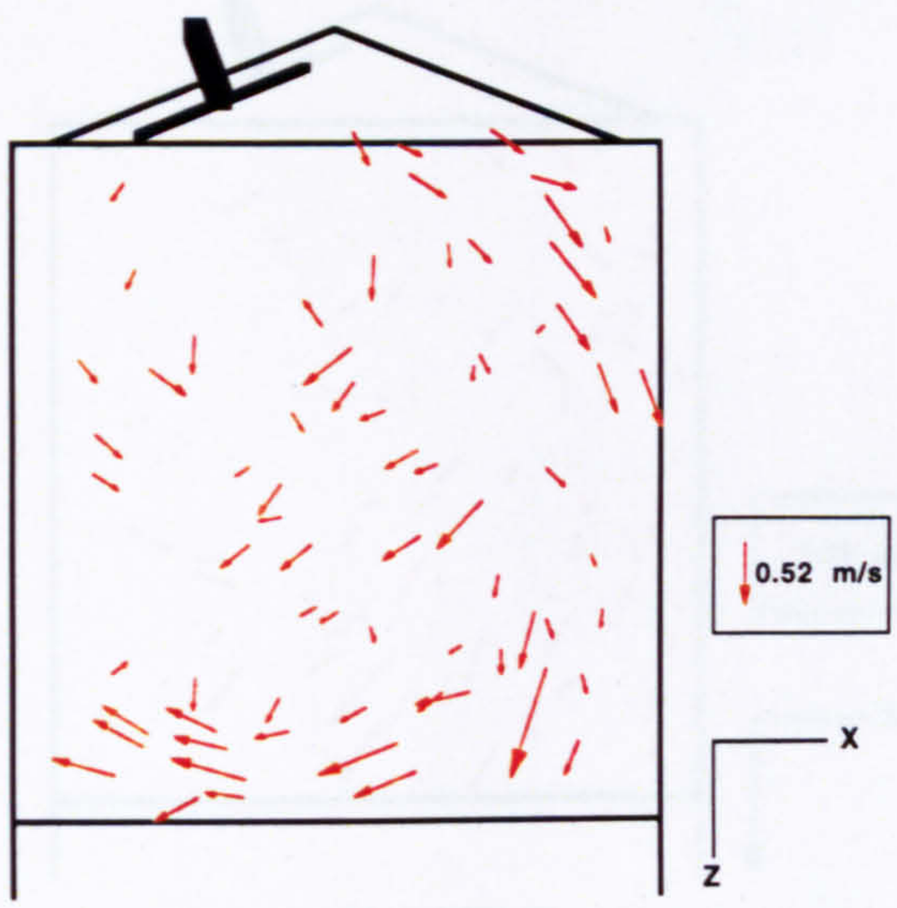

(c) 143° ATDC

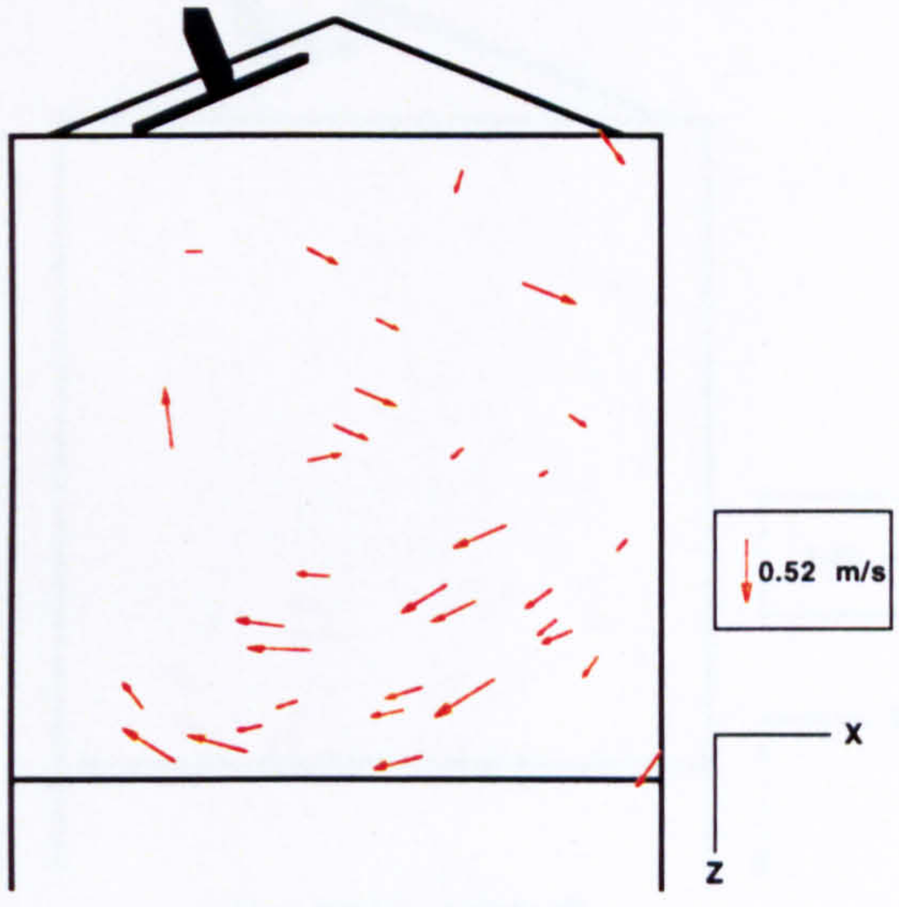

(d) 219° ATDC

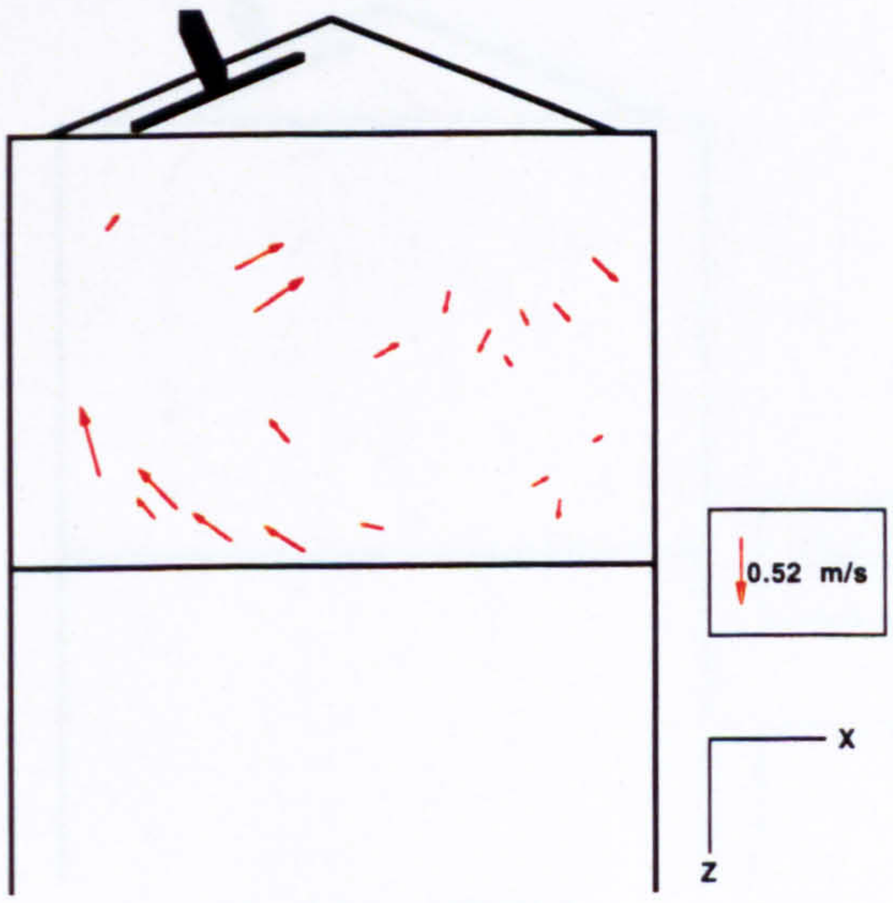

(e) 266° ATDC

Figure 6.12 Flow processes during induction in the y = 0 mm plane
Engine speed: 77 r.p.m., I.M.P. = 1.22 bar

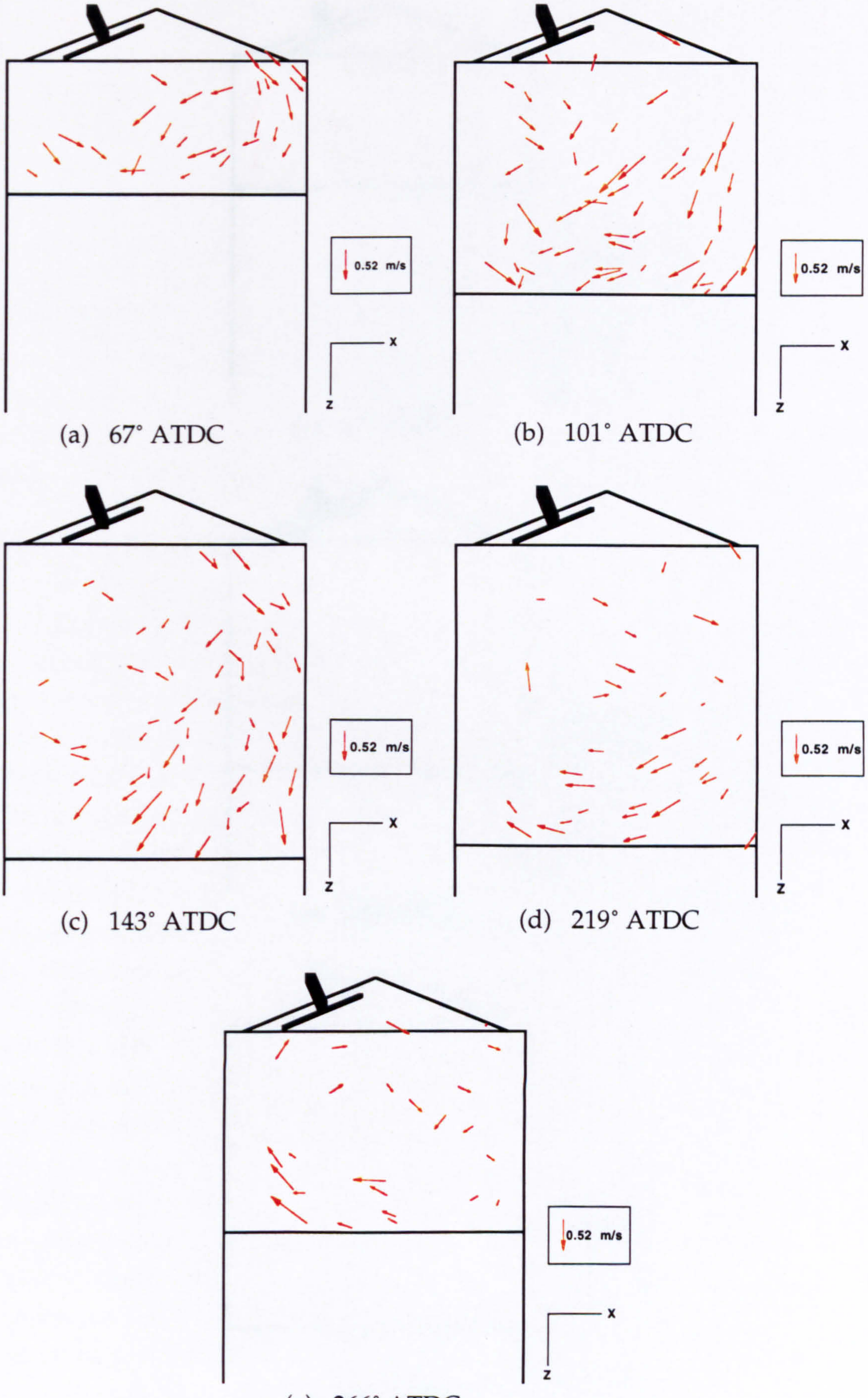

(a) 67° ATDC

(b) 101° ATDC

(c) 143° ATDC

(d) 219° ATDC

(e) 266° ATDC

Figure 6.13 Flow processes during induction in the y = 17.6 mm plane
Engine speed: 77 r.p.m., I.M.P. = 1.22 bar

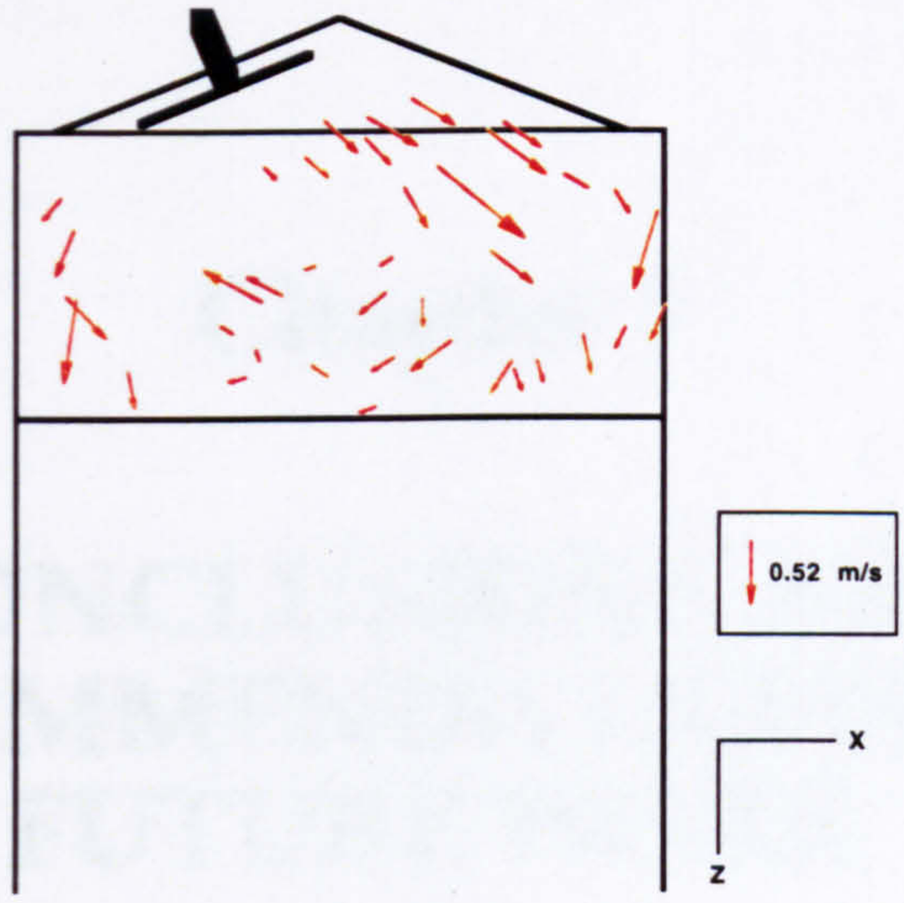

(a) 67° ATDC

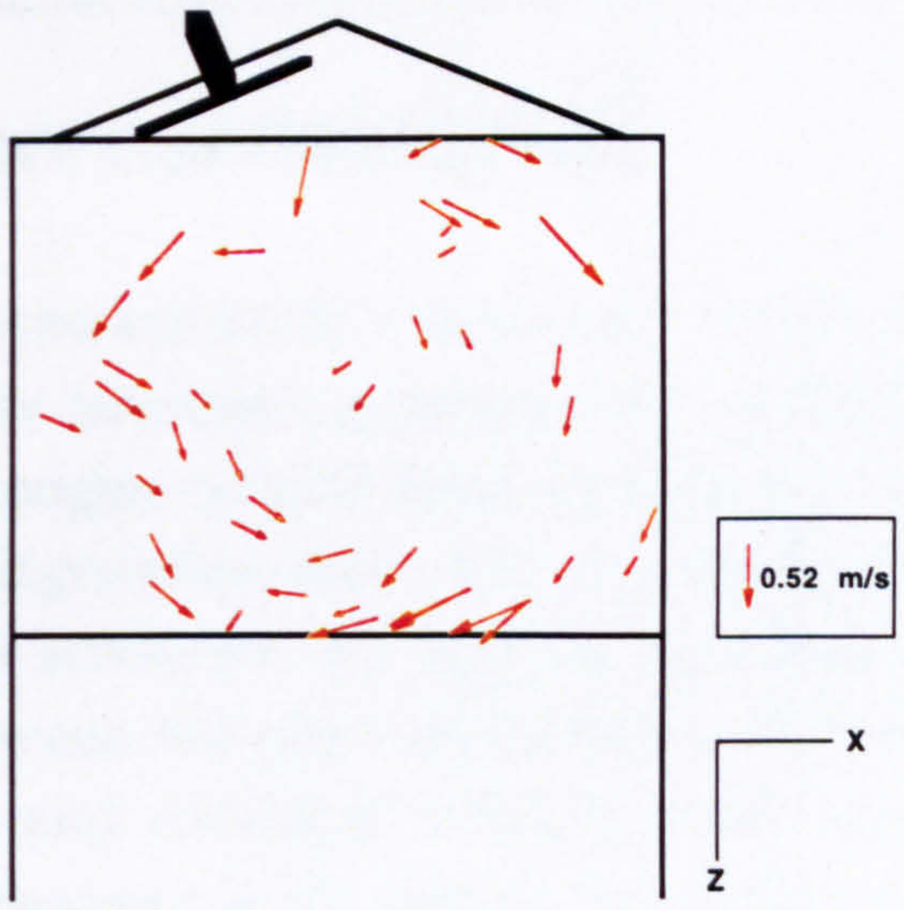

(b) 105° ATDC

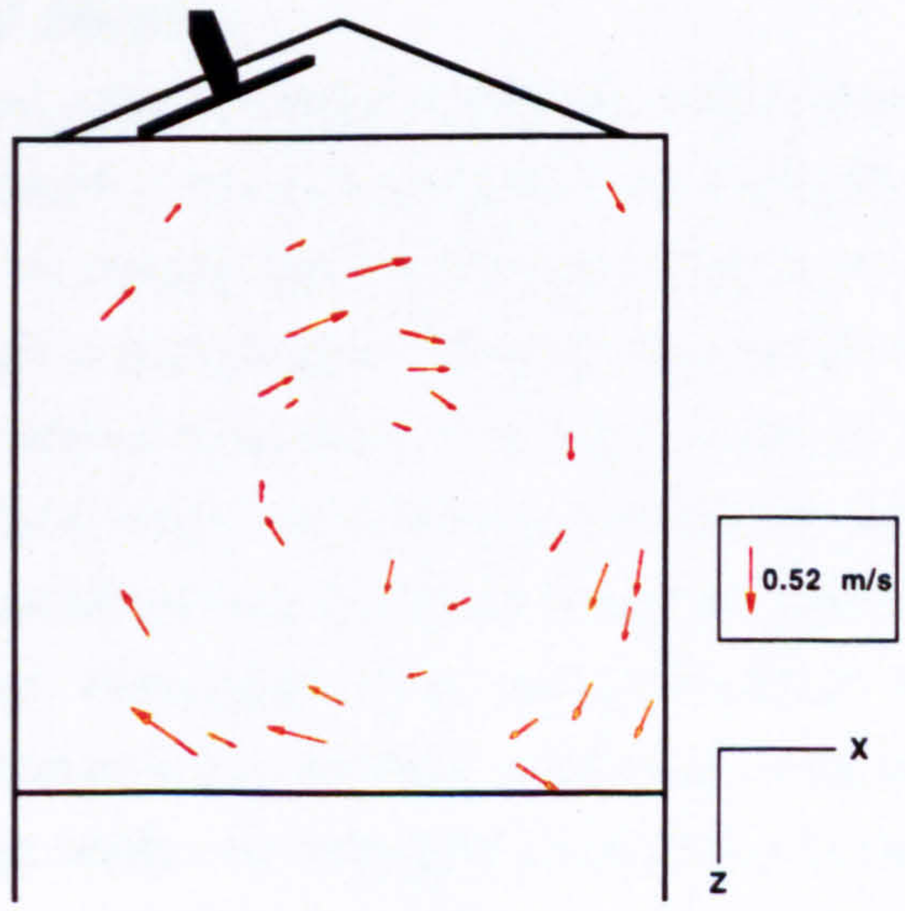

(c) 219° ATDC

Figure 6.14 Flow processes in the y = 0 mm plane, selected crankangles
Engine speed: 77 r.p.m., I.M.P. = 1.43 bar

Chapter 7

CONCLUSIONS AND RECOMMENDATIONS FOR FUTURE WORK

7.1 THE PRESENT CONTRIBUTION

The aim of the present study was to improve the understanding of the pre-combustion flow processes generated by current production spark-ignition multi-valve engine cylinder head designs. Increasingly stricter motor vehicle emissions legislation have led to considerable efforts into the development of low emissions I.C. engines by automobile manufacturers. The correlation between the pre-combustion in-cylinder gas motion and engine combustion and emissions characteristics were discussed in the literature survey presented in Chapter 1. Previous investigations into the influence of inlet port and combustion chamber design on engine flows were also described in that chapter.

Several different experimental methods were employed in this study, each of which provided a unique insight into fluid motion in engine inlet ports and cylinders. A steady flow technique was firstly used to investigate liquid motion through a transparent Perspex replica of the Ford Zetec engine inlet port and combustion chamber. The influences of inlet valve lift on in-cylinder flow structure were examined qualitatively using laser-sheet flow visualisation and quantitatively by laser-Doppler anemometry. Three Ford Zetec cylinder head configurations were studied under steady flow conditions: they included a production siamesed twin straight port design, one prototype design with one straight port and a swirl port and a second prototype configuration with twin swirl ports. Ensemble-averaged mean and r.m.s. velocity measurements were performed in the engine cylinder and, where possible, the inlet ports, using L.D.A.

The unsteady intake gas flow during the induction stroke of a four-valve engine was simulated using a low-speed dynamic water-analog rig. Laser-sheet flow visualisation and particle image velocimetry were employed to investigate the development of tumble and swirl processes from early induction to B.D.C. in a Ford Zetec engine. Averaged two-dimensional velocity vector maps of liquid motion at B.D.C. induction were produced using P.I.V. and tumble ratios and vorticity characteristics were also calculated from the P.I.V. results.

The development of tumble motion inside the cylinder of a four-valve engine during the induction and compression strokes was examined using flow visualisation and particle tracking velocimetry applied to a low-speed motored optical engine. Gas motion in a high-speed reciprocating engine was modelled using a high density gas, sulphur hexafluoride (SF_6), as the working fluid. The gas flow structures were recorded onto video tape and the particle streaks in selected video frames were processed in order to calculate instantaneous velocities at different crankangles. The effects of engine speed and engine load were examined by varying the engine speed and the pressure of the SF_6 gas in the inlet manifold.

In the following sections the results and main findings of each investigation are summarised and recommendations are made regarding further research necessary to add to the current understanding of gas flow processes in multi-valve S.I. engine cylinder head designs.

7.2 MAIN FINDINGS OF THE INVESTIGATION

The main conclusions of this experimental study are described below:

- Steady flow investigations confirmed that engine in-cylinder flows are highly complex and three-dimensional. Results from both flow visualisation and L.D.A. experiments showed large variations in flow structure as a result of changes to inlet valve lift and the geometric characteristics of the engine cylinder head. Experiments with the straight port engine configuration indicated that at low valve lift settings, swirl was the dominant flow type in the cylinder volume, while vortices in vertical planes were small. High velocity intake jets of fluid were seen at low valve lifts adjacent to the combustion chamber roof and the cylinder wall. Asymmetries and instabilities were present in the flow structure when the valve lifts were set

at 2.5 mm. This verified that asymmetries may exist in engine flows, even when engine cylinder head configurations are completely symmetric. Only small asymmetries were apparent in the flow field at higher valve lifts.

- L.D.A. measurements of mean and r.m.s. velocities inside the inlet ports showed that axial and radial velocity components at both 5 mm and 10 mm valve lifts were very similar, when the liquid mass flowrate was kept constant. Both the U and W mean velocity components inside the ports were large, while the corresponding r.m.s. components were small. Inside the cylinder volume, the highest ensemble averaged mean velocities were found within the intake jets and close to the cylinder wall. R.m.s. velocity magnitudes were the greatest in regions of high mean velocity gradients. In-cylinder turbulence levels were estimated for both 5 mm and 10 mm valve lift cases by calculating the average of r.m.s. velocities measured in horizontal planes. The flow inside the cylinder was most turbulent in regions close to the cylinder head and turbulence levels decreased at locations further downstream. Differences in the axial and radial r.m.s. components were calculated in order to obtain an indication of the anisotropy present within the flow. The largest differences between u' and w' (up to 20% of the bulk flow velocity, V_b) were found in regions of strong vortices and intake jets, while much lower variations (around 2% of V_b) were apparent in other regions.

- Steady flow L.D.A. data was compared with results from a previously reported C.F.D. study with initial conditions identical to the present experimental investigation. Good qualitative agreement between mean velocity profiles was achieved in both vertical and horizontal planes for both the 5 mm and 10 mm valve lift cases. Calculated mean velocity magnitudes were similar to the measured values at most points inside the cylinder; the largest differences between experimantal and calculated velocity data were noted at locations within the intake jets close to the cylinder wall. Experimental r.m.s. velocity values were compared with values determined from the computed turbulent kinetic energy. Measured r.m.s. values were noted to be significantly greater and this was partly attributed to assumptions present in the k-ε turbulence model and the time-averaged representation of the Navier-Stokes equations employed in the C.F.D. investigation, which do not account for instabilities present in three-dimensional turbulent flows.

• The effects of inlet valve disablement in a dual-intake port engine were examined under steady flow conditions by completely closing one of the inlet valves of the Perspex engine model. Flow visualisation and L.D.A. studies revealed that a high level of swirl is produced over a large proportion of the cylinder volume, in addition to an intense tumble vortex. The highest mean and r.m.s. velocities were found in regions close to the cylinder head, within high speed intake jets close to the open inlet valve. The average r.m.s. velocity values decreased as the fluid travelled down the cylinder. Estimations of the anisotropy of turbulence showed that the differences between the u' and w' r.m.s. components with inlet valve disablement were over twice those measured with both valves on the engine model open.

• L.D.A. measurements performed in the prototype Zetec engine models under steady flow conditions were compared with results from the production engine model. Tumble-like motion was noted to be less pronounced with configurations including swirl ports. Comparisons of normalised r.m.s. velocities showed that similar levels of turbulence were produced by the three cylinder head designs.

• Flow visualisation results from the dynamic water analog study with a production cylinder head with siamesed straight inlet ports showed that strong intake jets are produced inside the engine cylinder during the induction stroke, in both tumble and swirl planes. Similarities between steady flow images in tumble planes and fluid motion in the early part of induction were observed at around 90° ATDC crankangle. A large-scale tumble vortex was noted at BDC induction, though no distinctive swirl was apparent in diametric planes. Visualisation images showed that in-cylinder flow was asymmetric throughout the stroke.

• Averaged velocity vector maps of flow at BDC with the water-analog rig were acquired using P.I.V. The highest fluid velocities were noted in the intake flow adjacent to the cylinder wall, and within the main tumble vortex. The tumble ratio of the flow at BDC was evaluated from P.I.V. results, based on the angular momentum of fluid elements in planes about a point at the centre of the engine cylinder. The calculated tumble ratio value of 1.1 for the production Zetec engine was noted to be very similar to ratios reported in previous published studies. The largest vorticity magnitudes in the

measurement planes corresponded, as expected, to regions in the velocity vector maps with well-defined vortices.

- Results from the motored optical engine investigation showed that the strong intake gas motion produced in the engine cylinder during the induction stroke develops into a large scale tumble vortex at BDC, as was seen in the water analog study. The tumble motion was present over most of the cylinder volume during the compression stroke and was visible at crankangles close to the ignition point normally prescribed in lean burn engines. Variation of engine speed showed that in-cylinder velocities during induction and compression were larger with higher piston speeds. The effects of engine load were examined by varying the inlet manifold pressure. No major differences in velocity magnitude were identified from alteration of inlet manifold pressure.

- Similarities were noted between the unsteady flow processes through the water-analog rig and the motored engine during the early stages of the induction stroke, up to around 90° ATDC crankangle, and steady liquid flow through the Zetec engine model. This confirms statements made in earlier chapters of this thesis that steady flow techniques can be employed to quickly assess the tumble and swirl generation capabilities of intake port designs, and thereby reducing the overall time required for development of combustion systems.

Apart from the observations on multi-valve engine flows made in this thesis, the experimental methods employed during the investigation have also demonstrated the various types and amounts of qualitative and quantitative information available through laser techniques. Laser-sheet flow visualisation has been used extensively in this study to gain a general insight into in-cylinder fluid motion under both steady and unsteady flow conditions. The relative simplicity of the equipment required for flow visualisation experiments meant that fluid behaviour with different engine configurations and operating conditions could be quickly examined to select aspects which required further research using complex and often time consuming quantitative measurement techniques such as L.D.A., P.I.V. and P.T.V.

The most detailed quantitative data in this study was acquired through the use of ensemble-averaged L.D.A. Mean and r.m.s. velocity data offered

the opportunity for the complete characterisation of flow and turbulence inside the engine cylinder. Quantities including turbulent kinetic energy, energy dissipation rate and anisotropy of turbulence require detailed mean and r.m.s. velocity data, which at present is most easily acquired through L.D.A., if a two-component or three-component measurement system is available. The system used in the present study was only able to measure one velocity component at a time, and since each component required re-alignment of the diffraction grating and lens systems, time limitations restricted the number of data obtained in the steady flow investigations. A two- or three-component fibre-optic L.D.A. system requiring minimal alignment would have allowed significantly greater amounts of data to be measured within the same timespan.

The major advantage of P.I.V. over single-point techniques such as L.D.A. is that all particle velocities in a measurement plane can be evaluated at the same instant. Although P.I.V. photographic images were rapidly acquired and processed for 2D instantaneous velocity results, considerable effort was necessary in order to obtain an indication of the mean flow characteristics in measurement planes. In the present study, mean velocity results were estimated from ten instantaneous velocity vector maps, due to time limitations. In order to acquire more reliable time-averaged statistically independent velocity data in each plane, the average of a large number of P.I.V. images at each crankangle and plane would have been necessary. Unless a P.I.V. system is highly automated, it is difficult to acquire time averaged velocity without substantial effort.

The advantages of the stereoscopic P.T.V. measurement technique employed in the motored engine investigation over the L.D.A. and P.I.V. systems used included the fact that all three velocity components could be determined at the same time from the processing of stereoscopic images. However, the current system required manual processing of grabbed particle streak video images, so that only instantaneous velocities were obtained in the time available and the acquisition of time-averaged results was not attempted. This also implied that turbulence quantities could not be measured.

In summary, the multi-point fluid measurement techniques, P.I.V. and P.T.V., were found to be the most useful for the evaluation of mean flow characteristics largely due to the fact many hundreds of velocity vectors can be processed simultaneously. However, L.D.A. was the only technique used by which accurate r.m.s. velocity results and thereby turbulence

characteristics could be acquired. At the present moment, it would seem that a combination of L.D.A. and multi-point techniques is necessary in order to obtain a complete picture of engine in-cylinder flow behaviour, at least until the availability of advanced P.I.V. systems employing high-speed computers to allow acquisition of reliable turbulence data.

7.3 RECOMMENDATIONS FOR FUTURE WORK

The present investigation has shown that further research is required in two main areas in order to gain a deeper understanding of multi-valve engine in-cylinder flow processes. Firstly, accurate experimental data relating to precombustion gas motion is invaluable to the assessment of C.F.D. models, and high-density measurements of mean flow and turbulence characteristics are required, under both steady and unsteady flow conditions, as well as time-resolved data, in order to obtain values of the turbulence time and length scales and therefore the rate of dissipation of the turbulence energy.

The refractive index matching study with the Perspex model of the Zetec engine inlet ports and cylinder showed that siamesed straight intake port designs generate well-defined vortical structures in the flow. The L.D.A. study has gone some way to bridge the gap in available data on multi-valve engine flows, in terms of mean and r.m.s. velocities. Time limitations prevented more extensive three component velocity measurements in a high density grid within the cylinder. Further steady flow L.D.A. measurements with the Zetec port cylinder heads should be obtained, particularly relating to turbulence characterisation. Since the standard Zetec production intake port configuration is typical of multi-valve engine cylinder head designs, accurate experimental data could prove to be particularly useful, which would allow detailed comparisons with computed turbulence parameters to be made.

Secondly, instabilities and oscillations were seen to be present in engine flows from the steady flow study, but ensemble-averaged L.D.A. measurements were unable to quantify the fluctuations present in the flow and time-resolved L.D.A. was not attempted in the current investigation due to the low seeding density of the flow. Therefore, time-resolved L.D.A. measurements are urgently required to identify the non-random components present in the measured ensemble-averaged r.m.s. values. In addition,

different designs of inlet ports should be tested in a similar manner in future to assess their flow characteristics in comparison with those of the geometries studied in this thesis. For example, the literature survey indicated that cylinder heads with separated intake port designs, such as those employed in investigations on charge stratification by Ricardo Consulting Engineers and Mitsubishi Motors [e.g. Stokes et al 1994, Kuwahara et al 1994] among others, also produce strong tumble and swirl motions inside the engine which lead to improvements in combustion and emissions. Therefore, flow visualisation studies and L.D.A. measurements are required in order to evaluate such port designs. A steady flow investigation with the refractive index matching rig is highly recommended to compare data with the Zetec engine work reported in this thesis.

Recently, direct-injection gasoline engines have been reported to give large benefits in engine performance and emissions, due to their high E.G.R. tolerance and stratified charge capabilities. Flow processes through vertical intake port configurations should also be thoroughly examined with the refractive index matching rig in addition to motored engine investigations.

The low speed motored optical engine with SF_6 as the working fluid was found to be an invaluable tool for engine research. It would be interesting to carry out an L.D.A. study into the in-cylinder gas motion during induction and compression using this engine. Experimental data relating to the development of tumble motion during compression and turbulence characteristics close to the end of the stroke at the point of ignition is urgently required, and this facility offers the ideal opportunity to measure these quantities under greatly reduced engine speeds.

References

Adamczyk, A.A. and **Rimai, L. (1988)**
"Reconstruction of a three-dimensional flow field from orthogonal views of seed track video images"
Expts. Fluids, Vol. 6, pp. 380-386.

Adrian, R.J. (1991)
"Particle-imaging techniques for experimental fluid mechanics"
Annu. Rev. Fluid Mech., Vol. 23, pp. 261-304.

Adrian, R.J. (1992)
"The role of particle image velocimetry in fluid mechanics"
Proc. I.Mech.E. Seminar, "Optical Methods and Data Processing in Heat and Fluid Flow", pp. 1-6, London, April 1992.

Adrian, R.J. (1996)
"Chapter 4: Laser Velocimetry" in "Fluid Mechanics Measurements" (2nd ed.), edited by Goldstein, R.J.
Taylor and Francis.

Alcock, J.F. (1934)
"Air swirl in oil engines"
Proc. I.Mech.E., Vol. 128, pp. 123-193
(Cited by Gosman (1986)).

Ando, H. (1996)
"Combustion control technologies for gasoline engines"
Paper S433/001/96, Proc. I.Mech.E. Sem. 'Lean Burn Combustion Engines', pp. 3-15, London, 1996.

Aoi, K., Nomura, K. and **Matsuzaka, H. (1986)**
"Optimization of multi-valve four cycle engine design - the benefit of five valve technology"
S.A.E. Paper 860032.

Arcoumanis, C. and **Whitelaw, J.H. (1987)**
"Fluid mechanics of internal combustion engines: a review"
Proc. I.Mech.E., Vol. 201, No. C1, pp. 57-74.

Arcoumanis, C., Yianneskis, M., Williams, D.R., Baker, C.A. and **Greenhalgh, D.A. (1990 a)**
Chapter 16 - "Instrumentation for Engine Flows"
"Internal Combustion Engineering" , Edited by J.H. Weaving, Elsevier, 1990.

Arcoumanis, C., Hu, Z., Vafidis, C. and **Whitelaw, J.H. (1990 b)**
"Tumbling motion: a mechanism for turbulence enhancement in spark-ignition engines"
S.A.E. Paper 900060.

Arcoumanis, C., Hu, Z. and **Whitelaw, J.H. (1993)**
"Steady flow characterization of tumble-generating four-valve cylinder heads"
Proc. I.Mech.E., "Journal of Automobile Engineering", vol. 207, No. D3.

Arcoumanis, C., Bae, C.-S. and **Hu, Z. (1994 a)**
"Flow and combustion in a four-valve spark-ignition optical engine"
S.A.E. Paper 940475.

Arcoumanis, C., Hull, D.R. and **Whitelaw, J.H. (1994 b)**
"An approach to charge stratification in lean-burn spark-ignition engines"
S.A.E. Paper 941878.

Arcoumanis, C., Gold, M.R., Whitelaw, J.H. and **Xu, H.M. (1996)**
"Local charge stratification in spark-ignition engines"
Paper S433/006/96, Proc. I.Mech.E. Sem. 'Lean Burn Combustion Engines', pp. 79-99, London, 1996.

Balabani, S. (1996)
"An experimental investigation of the crossflow over tube bundles"
Ph.D. Thesis, King's College London, Univerity of London.

Barker, D.B. and **Fourney, M.E. (1977)**
"Measuring fluid velocities with speckle patterns"
Opt. Lett., Vol.1, pp. 135-137.

Benjamin, S.F. (1988)
"The development of the GTL "Barrel Swirl" combustion system with application to four-valve spark-ignition engines"
Paper C54/88, Proc. I.Mech.E. Conf. "Combustion in Engines" , 1988.

Bicen, A.F. (1981)
"Refraction correction for LDA measurements in flows with optical boundaries"
Internal Report No. FS/87/12, Mechanical Engineering Department, Imperial College, London.

Bicen, A.F., Vafidis, C. and **Whitelaw, J.H. (1985)**
"Steady and unsteady flow through the intake valve of a reciprocating engine"
A.S.M.E. J. Fluids Eng., Vol. 107, pp. 413-419.

Bradshaw, P. (1971)
"An Introduction to Turbulence and its Measurement"
Pergamon Press (Cited by Frost and Moulden (1977)).

Buchhave, P. (1992)
"Particle image velocimetry - status and trends"
Expt. Therm. Fluid Sci., Vol. 5, pp. 586-604.

Budwig, R. (1994)
"Refractive index matching methods for liquid flow investigations"
Expts. Fluids, Vol.17, pp. 350-355.

Chen, A., Mahmood, Z., Yianneskis, M. and Ganti, G. (1996)
"Three-dimensional simulation of the flow through a twin-intake port engine"
Paper C499/055/96, Proc. I.Mech.E. Conf. "Computers in Reciprocating Engines and Gas Turbines", pp. 239-248, London, 9-10 Jan. 1996.

Cheung, R.S.W. (1989)
"An investigation of flow patterns inside inlet ports"
Ph.D. Thesis, King's College London, University of London.

Cheung, R.S.W., Nadarajah, S., Tindal, M.J. and Yianneskis, M. (1990)
"An experimental study of velocity and Reynolds stress distributions in a production engine inlet port under steady flow conditions"
S.A.E. Paper 900058.

Clerk, D. (1912)
Fifth Report Gaseous Explosions Committee, British Association Report, (Reported in Bone, W.A. and Townend, D.T. (1927) - "Flame and Combustion in Gases", Longman Green and Company), London, 1912 (Cited by Gosman (1986)).

Coupland, J.M. and Halliwell, N.A. (1992)
"Three dimensional particle image velocimetry"
Proc. I.Mech.E. Seminar, "Optical Methods and Data Processing in Heat and Fluid Flow", pp. 7-18, London, April 1992.

Davies, J.T. (1972)
"Chapter 1 - Velocities and Stresses in Turbulent Flows", Turbulence Phenomena, Academic Press.

De Boer, C.D., Johns, R.J.R., Grigg, D.W., Train, B.M., Denbratt, I. and Linna, J.-R. (1990)
"Refinement with performance and economy for four-valve automotive engines"
Paper C394/053, Proc. I.Mece.E. Conf. "Automotive Power Systems - Environment and Conservation", September 1990.

De Boer, C.D., Stokes, J. and Lake, T.H. (1993)
"Advanced gasoline combustion systems for fuel economy and emissions"
Proc. I.Mech.E. Seminar "Worldwide Engine Emissions Standards and How to Meet Them", London, 25-26 May, 1993.

Deschamps, B., Snyder, R. and **Baritaud, T. (1994)**
"Effect of flow and gasoline stratification on combustion in a four-valve S.I. engine"
S.A.E. Paper 941993.

Downing, I.C. and **Bale, C.J.C. (1990)**
"The design and development of a unique five-valve cylinder head"
Paper 905156, Proc.XXIII FISITA Congress, pp. 301-308, Torino, Italy, May 1990.

Drain, L.E. (1980)
"The Laser-Doppler Technique"
John Wiley and Sons.

Dudderar, T.D. and **Simpkins, P.G. (1977)**
"Laser speckle photography in a fluid medium"
Nature, Vol. 270, pp. 45-47.

Durao, D.F.G. and **Whitelaw, J.H. (1975)**
"The influence of sampling procedures on the velocity bias in turbulent flows"
Proc. Symp. on "The Accuracy of Flow Measurements using Laser-Doppler Methods", Copenhagen, 1975.

Durst, F., Melling, A. and **Whitelaw, J.H. (1981)**
"Principles and practice of laser-Doppler anemometry"
Academic Press.

Eckchian, A. and **Hoult, D.P. (1979)**
"Flow visualization study of the intake process of an internal combustion engine"
S.A.E. Paper 790095.

Endres, H., Neusser, H.-J. and **Wurms, R. (1992)**
"Influence of swirl and tumble on economy and emissions of multivalve engines"
S.A.E. Paper 920576.

Faure, M.A., Heikal, M.R. and **Jackson, N.S. (1996 a)**
"Three-dimensional in-cylinder flow maps using two-dimensional P.I.V. system"
Paper C516/049/96, Proc. I.Mech.E. Seminar, "Optical Methods and Data Processing in Heat and Fluid Flow", pp. 147-156, London, April 1996.

Faure, M.A., Heikal, M.R. and **Jackson, N. (1996 b)**
"P.I.V. measurements and characterisation of in-cylinder flows in combustion engines"
Proc. 8th Int. Symp. "Applications of Laser Techniques to Fluid Mechanics", pp. 22.3.1-22.3.8, Lisbon, Portugal, July 1996.

Frost, W. and **Moulden, T.H. (1977)**
"Handbook of Turbulence - Volume 1"
Plenum Press.

Fujii, H., Takagi, Y. and **Urushihara T. (1989)**
"A study of in-cylinder gas flow in 4-valve engine based on 3-dimensional numerical simulations and L.D.V. measurements"
J.S.A.E. Review, Vol. 10, No. 4.

Fujimoto, H., Nakagawa, T., Kudo, H., Wakisaka, T. and **Shimamoto Y. (1995)**
"A study on the formation of vertical vortex in the cylinder of an I.C. engine using C.F.D.: Effect of intake valve closing timing"
J.S.A.E. Review, Vol. 16, pp. 349-355.

Furuno, S., Iguchi, S., Oishi, K. and **Inoue, T. (1990)**
"The effects of "inclination angle of swirl axis" on turbulence characteristics in a 4-valve lean-burn engine with SCV"
S.A.E. Paper 902139.

George, W.K. and **Lumley, J.L. (1973)**
"The laser-Doppler velocimeter and its application to the measurement of turbulence"
J. Fluid Mech., Vol. 60, Part 2, pp. 321-362.

Gosman, A.D., Tsui, Y.Y. and **Vafidis, C. (1985)**
"Flow in a model engine with a shrouded valve - a combined experimental and computational study"
S.A.E. Paper 850498.

Gosman, A.D. (1986)
Chapter 11, "Flow Processes in Cylinders"
"The Thermodynamics and Gas Dynamics of Internal Combustion Engines",
Vol. 2, Edited by Horlock, J.H. and Winterbone, D.E., Clarendon Press, 1986.

Gray, C. (1992)
"The evolution of particle image velocimetry"
Proc. I.Mech.E. Seminar, "Optical Methods and Data Processing in Heat and Fluid Flow", pp. 19-36, London, April 1992.

Grousson, R. and **Mallick, S. (1977)**
"Study of flow pattern in a fluid by scattered laser light"
Appl. Opt., Vol. 16, pp. 2334-2336.

Gruden, D., Richter, W. and **Wurster, W. (1984)**
"Combustion chamber investigations at Porsche - paving the way for the 4-valve engine"
Paper 845005, Proc. XX FISITA Congress, pp. 1.41-1.47, Vienna, May 1984.

Hadded, O. and **Denbratt, I. (1991)**
"Turbulence characteristics of tumbling air motion in 4-valve S.I. engines and their correlations with combustion parameters"
S.A.E. Paper 910478.

Hadded, O., Stokes, J. and **Grigg, D.W. (1995)**
"Low emission vehicle technology for ultra low emissions vehicle and European stage 3 emissions standards"
Proc. I.Mech.E., Vol. 209, Part D, pp. 159-170.

Haradalupas, Y. and **Laker, J.R. (1993)**
"Description of the Thermofluids Section 'Model 3' phase Doppler counter"
Internal Report No. TF/93/15, Mechanical Engineering Department, Imperial College, London.

Heckmann, W., Merzkirch, W. and **Wintrich, H. (1992)**
"Particle image velocimetry using a C.C.D. camera for direct recording and image processing"
Proc. I.Mech.E. Seminar, "Optical Methods and Data Processing in Heat and Fluid Flow", pp. 37-40, London, April 1992.

Henriot, S., Le Coz, J.F. and **Pinchon, P. (1989)**
"Three dimensional modelling of flow and turbulence in a four-valve spark-ignition engine - comparisons with LDV measurements"
S.A.E. Paper 890843.

Heywood, J.B. (1987)
"Fluid motion within the cylinder of internal combustion engines - the 1986 Freeman Scholar Lecture"
ASME Journal of Fluids Engineering, Vol. 109/3.

Hirsch, W. (1991)
"The Ford Zeta Engine Family - Engine Design"
Paper C427/242, Proc. I.Mech.E. Sem. "Autotech '91", pp. 1-9, November 1991.

Hoesel, W. and **Rodi, W. (1977)**
"New biasing elimination method for laser-Doppler velocimeter counter processing"
Rev. Sci. Instrum., Vol. 48, No. 7.

Hu, Z., Vafidis, C., Whitelaw, J.H., Chapman, J. and **Head R.A. (1992)**
"Correlation between in-cylinder flow, performance and emissions characteristics of a Rover pentroof four-valve engine"
Paper C448/026, Proc. I.Mech.E. Conf. "Combustion in Engines", December 1992.

Iwamoto, Y., Danno, Y., Hirako, O., Fukui, T. and **Murakami, N. (1992)**
"The 1.5 Liter Vertical Vortex Engine"
S.A.E. Paper 920670.

Jackson, N.S., Stokes, J., Heikal, M.R. and **Downie, J.H. (1995)**
"A dynamic flow visualisation rig for automotive combustion system development"
S.A.E. Paper 950728.

Jackson, N.S., Stokes, J., Whitaker, P.A. and **Lake, T.H. (1996)**
"A direct injection stratified charge gasoline combustion system for future European passenger cars"
Proc. I.Mech.E. Sem. 'Lean Burn Combustion Engines', London, Dec. 1996.

Kang, K.-Y., Oh, S.-M., Lee, J.-W., Jeong, D.-S., Lee, K.-H. and **Bae, C.-S. (1996)**
"The effect of intake port design in lean burn S.I. engines"
Paper S433/009/96, Proc. I.Mech.E. Sem. 'Lean Burn Combustion Engines', pp. 135-147, London, 1996.

Keane, R.D. and **Adrian, R.J. (1993)**
"Theory of cross-correlation analysis of P.I.V. images" in "Flow Visualisation and Image Analysis", edited by Nieuwstadt, F.T.M.
Kluwer Academic Publishers.

Kent, J.C. and **Mikulec, A. (1988)**
"Visualization of low mach number gas flows using water analog simulation"
Proc. ICALEO, Vol. 67, pp. 139-147.

Kent, J.C., Mikulec, A., Adamczyk, A.A., Mueller, S.R., Stein, R.A. and **Warren, C.C. (1989)**
"Observations on the effects of intake-generated swirl and tumble on combustion duration"
S.A.E. Paper 892096.

Khalighi, B. and **Huebler, M.S. (1988)**
"A transient water analog of a dual-intake valve engine for intake flow visualization and full-field velocity mesurements"
S.A.E. Paper 880519.

Khalighi, B. (1989)
"Quantitative fluid velocity measurements by automatic analysis of flow visualization images"
Expts. Fluids, Vol.7, pp. 142-144.

Khalighi, B. (1990)
"Intake generated swirl and tumble motions in a 4-valve engine with various intake configurations - flow visualization and Particle Tracking Velocimetry"
S.A.E. Paper 900059.

Kiyota, Y., Akishino, K. and **Ando, H. (1992)**
"Concept of lean combustion by barrel-stratification"
S.A.E. Paper 920678.

Kuduo, H., Yamamoto, H. and **Iida, Y. (1992)**
"A study about in-cylinder flow and combustion in a 4-valve S.I. engine"
S.A.E. Paper 920574.

Kühn, M., Abthoff, J., Kemmler, R. and **Kaiser, T. (1996)**
"Influence of the inlet port and combustion chamber configuration on the lean-burn behaviour of a spark-ignition gasoline engine"
S.A.E. Paper 960608.

Kume, T., Iwamoto, Y., Iida, K., Murakami, M., Akishino, K. and **Ando, H. (1996)**
"Combustion control technologies for direct-injection S.I. engine"
S.A.E. Paper 960600.

Kuwahara, K., Watanabe, T., Takemura, J., Omori, S., Kume, T. and **Ando, H. (1994)**
"Optimization of in-cylinder flow and mixing for a centre-spark four-valve engine employing the concept of Barrel-Stratification"
S.A.E. Paper 940986

Lake, T.H., Stokes, J., Christie, M.J., Horada, O. and **Shimotani, K. (1994)**
"Preliminary investigation of solenoid activated in-cylinder injection in stoichiometric engines"
S.A.E. Paper 940483.

Le Coz, J.F., Henriot, S. and **Pinchon, P. (1990)**
"An experimental and computational analysis of the flow field ina four-valve spark-ignition engine - focus on cycle-resolved turbulence"
S.A.E. Paper 900056.

Lee, D.W. (1939)
"A study of the airflow in engine cylinders"
NACA Report No.. 653, 1939
(Cited by Gosman (1986)).

Liou, T.-R., Hall, M., Santarivea, D.A. and **Bracco, F.V. (1984)**
"Laser-Doppler velocity measurements in valved and ported engines"
S.A.E. Paper 840375.

Lourenco, L. and **Krothapalli, A. (1995)**
"On the accuracy of velocity and vorticity measurements with P.I.V."
Expts. Fluids, Vol. 18, pp. 421-428.

McLaughlin, D.K. and **Tiederman, W.G. (1973)**
"Biasing correction for individual realization of laser anemometer measurements in turbulent flows"
Phys. Fluids, Vol. 16, No. 12, pp. 2082-2088.

Ma, T.H., Davies, M. and **Collings, N. (1986 a)**
"Low speed dynamic similarity modelling in internal combustion engines"
S.A.E. Paper 860239.

Ma, T.H., Marko, K., Li, P. and **Davies, M. (1986 b)**
"Dynamic similarity helps laser flow visualisation for in-cylinder measurements"

Paper 865036, Proc. XXI FISITA Congress, pp. 1.259-1.264.

Mahmood, Z. and Yianneskis, M. (1994)
"Laser-sheet visualisation of the flow processes in a Ford 'Zeta' engine cylinder under steady-flow conditions"
Internal Report, No. EM/94/07, Mech. Eng. Dept., King's College London.

Mahmood, Z. and Yianneskis, M. (1995)
"Velocity and turbulence characteristics of the steady flow processes in the inlet ports and cylinder of a Ford Zetec engine"
Internal Report, No. EM/95/02, Mech. Eng. Dept., King's College London.

Mahmood, Z., Chen, A., Yianneskis, M. and Ganti, G. (1996 a)
"On the structure of steady flow through dual-intake engine ports"
Int. J. Num. Meth. Fluids, Vol. 23, pp. 1085-1109.

Mahmood, Z., Ng, K. and Yianneskis, M. (1996 b)
"Characteristics of flows through the inlet ports of multi-valve engines"
Proc. 8th Int. Symp. "Applications of Laser Techniques to Fluid Mechanics", pp. 16.2.1 - 16.2.8, Lisbon, Portugal, July 1996.

Marko, K. and Rimai, L. (1985)
"Video recording and qualitative analysis of seed particle track images in unsteady flows"
Appl. Optics, Vol.24, pp. 3666-3672.

Marko, K.A., Li, P., Rimai, L., Ma, T. and Davies, M. (1986)
"Flow field imaging for quantitative cycle resolved velocity measurements in a model engine"
SAE Paper 860022.

Matekunas, F.A. (1983)
"Modes and measures of cyclic combustion variability"
S.A.E. Paper 830337.

Melling, A. (1975)
"Investigation of flows in non-circular ducts and other configurations by laser-Doppler anemometry"
Ph.D. Thesis, Imperial College, University of London.

Melling, A. (1977)
"Axisymmetric turbulent flow in a motored reciprocating engine"
Internal Report No. CHT/77/4, Mechanical Engineering Department, Imperial College London.

Meynart, R. (1983 a)
"Instantaneous velocity field measurements in unsteady gas flow by speckle velocimetry"
Appl. Opt., Vol. 22, pp. 535-540.

Meynart, R. (1983 b)
"Speckle velocimetry study of vortex pairing in a low Re unexcited jet"

Phys. Fluids, Vol. 26, pp. 2074-79.

Morse, A., Whitelaw, J.H. and **Yianneskis, M. (1980)**
"The influence of swirl on the flow characteristics of a reciprocating piston-cylinder assembly"
ASME Journal of Fluids Engineering, Vol. 102, pp. 478-480.

Nadarajah, S. (1992)
"An experimental investigation of flows through inlet ports and valves"
Ph.D. Thesis, King's College London, University of London.

Nakanishi, K., Iguchi, S., Okano, H., Okomura, T. and **Furuno, S. (1992)**
"Development of a new intake system for a 4-valve lean burn engine"
Paper C389/243, Proc. XXIV FISITA Congress, London, 7-11 June 1992.

Neusser, H.-J., Spiegel, L. and **Ganser, J. (1995)**
"Particle tracking velocimetry - a powerful tool to shape the in-cylinder flow of modern multi-valve engine concepts"
S.A.E. Paper 950102.

Neusser, H.-J. and **Geiger, J. (1996)**
"Continuous variable tumble - a new concept for future lean burn engines"
S.A.E. Paper 960607.

Newton, K., Steeds, W. and **Garrett, T.K. (1989)**
Chapter 4 - "Constructional details of the engine"
"The Motor Vehicle" - Eleventh Edition, Butterworths International, 1989.

Ohm, I.-Y., Ahn, H.-S., Lee, W.-J., Kim, W.-T., Park, S.-S. and **Lee, D.-U. (1993)**
"Development of HMC axially stratified lean combustion engine"
S.A.E. Paper 930879.

Ohrnberger, G. and **Mann, M. (1994)**
"The Audi 5-valve cylinder head concept"
Paper 945004, Proc. XXV FISITA Congress, pp. 36-44, Beijing, China, Oct. 1994.

Ohsuga, M., Yamaguchi, J., Kawabe, R. and **Momono, M. (1995)**
"In-cylinder air fuel ratio and combustion control for spark ignition engines"
S.A.E. Paper 950076.

Omori, S., Iwachido, K., Motomochi, M. and **Hirako, O. (1991)**
"Effect of intake flow pattern on the in-cylinder tumbling airflow in multivalve S.I. engines"
S.A.E. Paper 910477.

Prasad, A.K. and **Adrian, R.J. (1993)**
"Stereoscopic particle image velocimetry applied to liquid flows"
Expts. Fluids, Vol. 15, pp. 49-60.

Quader, A.A. (1982)
"The axially-stratified-charge engine"
S.A.E. Paper 820131.

Queenan, K.B., Nightingale, C.J.E. and **Bennett, J. (1996)**
"The design and testing of an arrangement to achieve stratified charge through port injection"
Paper S433/002/96, Proc. I.Mech.E. Sem. 'Lean Burn Combustion Engines', pp. 17-33, London, 1996.

Reeves, M., Garner, C.P., Dent, J.C. and **Halliwell, N.A. (1996)**
"Particle image velocimetry measurements of in-cylinder flow in a multi-valve internal combustion engine"
Proc. I.Mech.E., Vol. 210, Part D, pp. 63-70.

Reuss, D.L., Adrian, R.J., Landreth, C.C.French, D.T. and **Fansler, T.D. (1989)**
"Instantaneous planar measurements of velocity and large-scale vorticity and strain rate in an engine using particle image velocimetry"
S.A.E. Paper 890616.

Rönnbäck, M., Le, W.X. and Linna, J.-R. (1991)
"Study of induction tumble by particle tracking velocimetry in a 4-valve engine"
S.A.E. Paper 912376.

Rouland, E., Vottier, S., Lecordier, B. and **Trinite, M. (1994)**
"Cross-correlation P.I.V. development for high speed flow with a standard C.C.D. camera"
Paper C485/039, Proc. I.Mech.E. Seminar, "Optical Methods and Data Processing in Heat and Fluid Flow", pp. 9-20, London, April 1994.

Saito, F., Misumi, M., Komatsu, K., Mitobe, N. and **Nagao, A. (1994)**
"Mazda advanced lean burn engine with new three-way catalyst"
Paper 945006, Proc. XXV FISITA Congress, pp. 52-59, Beijing, China, Oct. 1994.

Saneyoshi, K., Hanawa, K., Kaneko, M. and **Kobayashi, H. (1991)**
"Gas flow investigation by stereography in spark ignition engine"
S.A.E. Paper 910476.

Stokes, J., Lake, T.H., Christie, M.J. and **Denbratt, I. (1994)**
"Improving the NOx/fuel economy trade-off for gasoline engines with the CCVS combustion system"
S.A.E. Paper 940482.

Stone, C.R., Carden, T.R. and **Podmore, I. (1993)**
"Analysis of the effect of inlet valve disablement on swirl, combustion and emissions in a spark-ignition engine"
Proc. I.Mech.E. "Journal of Automobile Engineering", Vol. 207, No. D4.

Suen, K.O. and **Yianneskis, M. (1988)**
"A laser anemometry system for the investigation of in-cylinder flows"
Proc. I.Mech.E. Seminar: "Experimental Methods in Engine Research and Development", 10th March 1988.

Suen, K.O. (1992)
"Investigation of gas flow in a motored high-speed diesel engine by laser-Doppler anemometry"
Ph.D. Thesis, King's College London, University of London.

Sykes, R. (1995)
"Development of a 5 valve per cylinder variant of the Ford Duratec 2.5 litre V6 engine"
Paper C498/22/174, Proc. I.Mech.E. Sem. 'Autotech 95'.

Tabata, M., Kataoka, M., Fujimoto, M. and Noh, Y. (1995)
"In-cylinder fuel distribution, flow field and combustion characteristics of a mixture injected S.I. engine"
S.A.E. Paper 950104.

Taylor, A.M.K.P., Whitelaw, J.H. and Yianneskis, M. (1982)
"Developing flow in S-shaped ducts. Part 2: Circular cross-section duct"
Internal Report No. FS/82/7, Mechanical Engineering Department, Imperial College, London.

Tennekes, H. and Lumley, J.L. (1972)
"A First Course in Turbulence"
M.I.T. Press.

Tindal, M.J. and Williams, T.J. (1977)
"An investigation into gas motion in the direct-injection diesel engine"
S.A.E. Paper 770405

Tindal, M.J., Brown, P.G. and Kyriakides, S.C. (1982)
"An investigation of swirl and turbulence in the cylinder of direct-injection diesel engines"
Paper C127/82, Proc. I.Mech.E. Conf. "Diesel Engines for Passenger Cars and Light Duty Vehicles", 1982.

Tindal, M.J., Cheung, R.S. and Yianneskis, M. (1988)
"Velocity characteristics of steady flows through engine inlet ports and cylinders"
S.A.E. Paper 880383.

Trigui, N., Leep, L.J. and Kent, J.C. (1994)
"Rapid characterization of I.C. engine in-cylinder flow at spark: a synergistic approach using experimental and numerical simulations"
S.A.E. Paper 941934.

Urushihara, T., Murayama, T., Takagi, Y. and Lee, K.-H. (1995)
"Turbulence and cycle-by-cycle variation of mean velocity generated by swirl and tumble flow and their effects on combustion"
S.A.E. Paper 950813.

Vafidis, C. and Whitelaw, J.H. (1986)
"Intake valve and in-cylinder flow development in a reciprocating model engine"

Proc. I.Mech.E., Vol. 200, No. C2, pp. 143-152.

Willert, C.E. and **Gharib, M. (1991)**
"Digital particle image velocimetry"
Expts. Fluids, Vol. 10, pp. 181-193.

Wilson, N.D., Watkins, A.J. and **Dopson, C. (1993)**
"Asymmetric valve strategies and their effect on combustion"
S.A.E. Paper 930821.

Wirth, M., Piock, W.F. and **Fraidl, G.K. (1996)**
"Actual trends and future strategies for gasoline direct injection"
Paper S433/005/96, Proc. I.Mech.E. Sem. 'Lean Burn Combustion Engines', pp. 65-77, London, 1996.

Witze, P.O. (1980)
"A critical comparison of hot-wire anemometry and laser-Doppler anemometry for I.C. engine applications"
S.A.E. Paper 800132.

Yanta, W.J. (1973)
"Turbulence measurements with a laser-Doppler velocimeter"
Report NOLTR 73-94, Naval Ordnance Labs, White Oak, Silver Spring. U.S.A.

Yianneskis, M. (1982)
"Flows in reciprocating engine cylinders and curved ducts"
Ph.D. Thesis, Imperial College, University of London.

Yianneskis, M., Cheung, R.S.W. and **Tindal, M.J. (1988)**
"A method of investigating flows in inlet ports of complex shape"
Paper C62/88, Proc. I.Mech.E. Conf. "Combustion in Engines", pp. 51-58, London, May 1988.

Ziegler, P.M. and **Königstein, A. (1993)**
"The potential of an alternative load concept for S.I. engines"
Proc. I.Mech.E. Sem. "Worldwide Engine Emissions Standards and How to Meet Them", London, 25-26 May 1993.

Appendices

Appendix 1

CALCULATION OF 3D VELOCITY VECTORS FROM STEREOSCOPIC IMAGES

A 1.1 Definition of System Parameters

(a) **Focal length (f):** focal length of video cameras

(b) **Camera separation (t + 2h):** measured separation distance between two video cameras

(c) **Sensor width (w):** width of C.C.D. sensor in video cameras

(d) **Screen width (W):** width of stereoscopic monitor screen

(e) **Calculated magnification (M):**

$$M = \frac{\text{Screen width}}{\text{Sensor width}} = \frac{W}{w}$$

(f) **Viewer to screen distance (V):** recommended distance to view 3D view of image on stereoscopic monitor

(g) **Convergence distance (u):** distance from camera lens to point where camera viewing axes meet

(h) **Calculated lens back focal distance (v):**

$$v = \frac{1}{\left[\frac{1}{f} - \frac{1}{u}\right]}$$

(i) **Calculated lens offset (h):**

$$h = \frac{v\,(t + 2h)}{2\,(u + v)}$$

(j) **Calculated lens separation (t):**

C.L.S. = measured camera separation - 2 (calculated lens offset)

$$t = \text{camera separation} - 2h$$

(k) Scaling ratio (pixel no. / target mm):

$$S.R. = \frac{810}{\text{Sensor width}} = \frac{810}{w}$$

(l) Time integration interval (T): Time interval between successive video frames.

(m) Camera constant (C.C.):

C.C. = Calc. lens back focal dist x Calc. lens separation

C.C. = v x t

A 1.2 Formulae for 3D Track Positions and Velocities

A 1.2.1 Abbreviations

XLH = x-coordinate of vector head on left hand image
YLH = y-coordinate " " " " " "
XLT = x-coordinate of vector tail on left hand image
YLT = y-coordinate " " " " " "

XRH = x-coordinate of vector head on right hand image
YRH = y-coordinate " " " " " "
XRT = x-coordinate of vector tail on right hand image
YRT = y-coordinate " " " " " "

ZH = z-coordinate of 3D vector head
YH = y-coordinate " " " "
XH = x-coordinate " " " "

ZT = z-coordinate of 3D vector tail
YT = y-coordinate " " " "
XT = x-coordinate " " " "

xlh = XLH/scaling ratio;
xlt = XLT/scaling ratio;
xrh = XRH/scaling ratio;
xrt = XRT/scaling ratio;

ylh = YLH/scaling ratio;
ylt = YLT/scaling ratio;
yrh = YRH/scaling ratio;
yrt = YRT/scaling ratio;

A 1.2.2 3D Vector Positions

$$ZH = \frac{v\,t}{(xrh - xlh) + 2h} - u$$

$$ZT = \frac{v\,t}{(xrt - xlt) + 2h} - u$$

$$YH = \frac{ylh\,[ZH + u]}{v}$$

$$YT = \frac{ylt\,[ZT + u]}{v}$$

$$XH = \frac{(u + ZH)(xlh - h)}{v} + \frac{t}{2}$$

$$XT = \frac{(u + ZT)(xlt - h)}{v} + \frac{t}{2}$$

A 1.2.3 3D Velocities

$$X = \frac{XT - XH}{T}$$

$$Y = \frac{YT - YH}{T} \quad (m/s)$$

$$Z = \frac{ZT - ZH}{T}$$

Note: X, Y and Z velocities correspond to the x-, y- and z- coordinate directions specified in the Super 3D™ software.

Appendix 2

CALCULATION OF REYNOLDS NUMBER FOR ENGINE CYLINDER HEAD FLOWS

The Reynolds number for flow through each cylinder head was based on the flow area at the inlet plane of the cylinder head, upstream of the inlet ports. This was the same for each design. The bulk flow velocity, V_b, was also evaluated for flow through this area.

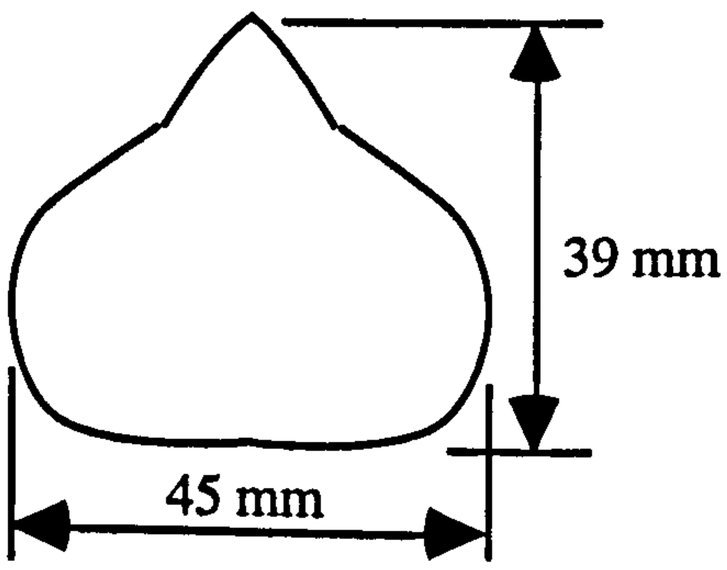

Cross-sectional area: CSA = 1253 mm^2
Wetted perimeter: WP = 136 mm

For hydraulic diameter:

$$D_h = \frac{4 \times \text{Cross-Sectional Area}}{\text{Wetted Perimeter}}$$

$$= \frac{4 \times 1.253 \times 10^{-3}}{0.136}$$

$$= 0.037 \text{ m}$$

i.e. hydraulic diameter of flow passage = 37 mm.

For bulk flow velocity (at 1.54 kg/s mass flowrate):

$$V_b = \frac{m}{\rho \times CSA}$$

$$= \frac{1.54}{893.5 \times 1.253 \times 10^{-3}}$$

$$= 1.376 \text{ m/s}$$

Hence the bulk flow velocity with m = 1.54 kg/s is 1.376 m/s.

For Reynolds number:

$$R_e = \frac{V_b D_h}{\nu}$$

$$= \frac{1.376 \times 0.037}{1.71 \times 10^{-6}}$$

$$= 29763$$

Thus, the Reynolds number based on the flow area at entry to the cylinder head is approximately 30000 when the liquid mass flowrate is set at 1.54 kg/s.

Similarly, when m = 1.26 kg/s, V_b = 1.125 m/s and R_e = 24600.

Appendix 3

VELOCITY REDUCTION FACTORS ACHIEVED WITH SF_6 GAS

The use of SF_6 gas as the working fluid in the optical engine was based on the principles of kinematic similarity. By equating the Reynolds numbers between gas motion in the model engine with air flow in an engine with identical geometric characteristics, the equivalent engine speed was determined.

Now, for Reynolds number matching:

$$\left(\frac{\rho V D}{\mu}\right)_{air} = \left(\frac{\rho V D}{\mu}\right)_{SF_6}$$

which can be reduced to:

$$\frac{V_{air}}{V_{SF_6}} = \frac{\nu_{air}}{\nu_{SF_6}}$$

where

V_{air} is the equivalent engine speed,

V_{SF} is the model engine speed,

ν_{air} is the kinematic viscosity of air at the required pressure and temperature,

ν_{SF} is the kinematic viscosity of SF_6 gas at the required pressure and temperature.

At 1 atm. gas pressure and 20°C temperature,

$$\frac{V_{air}}{V_{SF_6}} = \frac{1.505\times10^{-5}}{2.143\times10^{-6}} = 7.023$$

Hence, at 1 atm. gas pressure, 20°C, the velocity reduction factor (V.R.F.) is 7.

At 1.22 bar SF_6 pressure, V.R.F. = (1.22/1.01325) x 7 = 8.5

At 1.43 bar SF_6 pressure, V.R.F. = (1.43/1.01325) x 7 = 9.9

At 1.56 bar SF_6 pressure, V.R.F. = (1.56/1.01325) x 7 = 10.8

Therefore, the equivalent engine speeds (E.E.S.) for the cases described in Chapter 6 are as follows:

N = 56 r.p.m., I.M.P. = 1.22 bar: E.E.S. = 56 x 8.5 = 480 r.p.m. (full load).

N = 56 r.p.m., I.M.P. = 1.56 bar: E.E.S. = 56 x 10.8 = 605 r.p.m. (full load).

N = 77 r.p.m., I.M.P. = 1.22 bar: E.E.S. = 77 x 8.5 = 650 r.p.m. (full load).

N = 77 r.p.m., I.M.P. = 1.43 bar: E.E.S. = 77 x 9.9 = 760 r.p.m. (full load).

N = 104 r.p.m., I.M.P. = 1.22 bar: E.E.S. = 104 x 8.5 = 880 r.p.m. (full load).

If detailed small scale turbulence characteristics during compression are required, especially towards the end of the stroke, then it should be noted that because the isentropic index for SF_6 is lower than that for air, then pressure and temperature in the model engine will not scale with air. In this case, presssure and temperature values would have to be calculated at a particular crankangle for both air and SF_6, in addition to density and viscosity data. The equivalent engine speed would then be determined from these values.

Ma et al (1986 a) indicate that the process of the generation of large scale eddies and mean flow characteristics is unaffected by the differences in the isentropic index if the Reynolds number is matched at the inlet conditions, as in the present study.